JOURNAL OF THE
MYANMAR ACADEMY OF
ARTS AND SCIENCE

Chemistry and Industrial Chemistry

Vol. XIX, No.2B, January, 2023

Myanmar Academy of Arts and Science

Journal of the Myanmar Academy of Arts and Science

Vol. XIX, No.1B

Contents

Section (i), Chemsitry

Journal of the Myanmar Academy of Arts and Science

Vol. XIX, No.1B

Contents

Section (ii), Industrial Chemistry

STUDY ON PHYTOCHEMICAL CONSTITUENTS, NUTRIENTS AND ISOLATION OF FATTY ACIDS FROM THE LEAF OF *CLINACANTHUS NUTANS* L. (SNAKE-GRASS)

Ei Ei Chaw[1], Kay Khine Nyunt[2] , Saw Hla Myint[3]

Abstract

Plants are the main source of natural products that are used in medicine. *Clinacanthus nutans* (Arcathanceae), was collected from Yangon University Campus, Yangon Region and identified by the botanist, Department of Botany, University of Yangon. According to the preliminary phytochemical tests, it was found that glycosides, flavonoids, phenolic compounds, saponins, tannins and terpenoids were present in the dried leaves powders. Qualitative elemental analysis by EDXRF revealed that the leaves of *Clinacanthus nutans* contained K (2.204 %) and Ca (2.25 %) as major elements and Fe, S, Mn, Zn, Cu and Rb as trace elements. The nutritional values determined by AOAC method indicate the percentage of moisture (13.95), ash (19.27), fat (2.01), fibre (28.45), protein (18.12) and carbohydrate (18.2) in the leaves of *Clinacanthus nutans*. From the ethyl acetate fraction of 95 % ethanol extract of the leaf of *Clinacanthus nutans*, carboxylic acids were isolated after three successive column chromatographic methods, namely vacuum liquid chromatography (VLC), flash chromatography, using medium pressure, and micro-column chromatography using pasteur pipette giving a single spot on TLC. Carboxylic acids were characterized as long chain fatty acids by TLC staining and FTIR. Three fatty acids were further identified by GC-MS in C, namely linoleic acid (or) (*Z, Z*)-9,12-octadecadienoic acid (**C-1**), 11,14-octadecadienoic acid (**C-2**) and 11,14-eicosadienoic acid (**C-3**).

Keywords: *Clinacanthus nutans*, nutritional values, long chain fatty acids, linoleic acid

Introduction

Plants are used as medicine at least to the middle period, since 60 000 years ago. The genus *Clinacanthus nutans* (family Acathaceae) consists of two species. *Clinacanthus nutans* is a small shrub about one meter tall native to tropical Asia and it is used in traditional system of medicine.

Botanical Aspect of *Clinacanthus nutans*

Family : Acanthaceae
Genus : *Clinacanthus*
Species : *nutans*
Scientific name : *Clinacanthus nutans*
Common name : Snake- grass

Figure 1 *Clinacanthus nutans* (snake-grass) plant and leaf

[1] Lecturer, Department of Chemistry, Dagon University
[2] Dr, Lecturer, Department of Chemistry, University of Yangon
[3] Dr, Professor and Head (Retired), Department of Chemistry, University of Yangon

A mixture of nine cerebrosides and a monoacyl monogalatosylglycerol are present from the ethyl acetate soluble fraction of the ethanol extract of the leaves (Tuntiwachwuttikul, 2004). The structures of the cerebrosides were characterized as 1-*O*-b-D-glucosides of phytosphingosines, which comprised a common long-chain base, (2*S*, 3*S*, 4*R*, 8*Z*)-2-amino-8(*Z*)-octadecene-1,3,4-triol with nine 2-hydroxy fatty acids of varying chain lengths (C16, C18, C20-26) linked to the amino group. Fatty acids are widely occurring in natural fats and dietary oils and they play an important role as nutritious substances and metabolites in living organisms.

The leaves are also consumed as raw vegetable or mixed with other juices (apple, sugarcane or green tea) or served as fresh drink or refreshing beverage in Thailand. The decoction of the dried leaves is applied on the affected part to treat herpes infection and envenomation (Kapoor, 2001).

Materials and Methods

Sample Preparation

The collected fresh leaves sample was washed with distilled water and air dried at room temperature for one week and the dry leaves were ground into powder and then stored in the air tight container. The plant sample was identified at Department of Botany, Yangon University.

Preliminary Phytochemical Screening

In order to classify the secondary metabolites present in the leaf sample, preliminary phytochemical tests were carried out according to the appropriate reported methods.

Determination of Nutrients

The determination of percentage of the nutrients in the powdered sample was carried out according to the Chemical Analysis of Food Method. Protein content was determined by using Macro-Kjeldahl's method. Fat content was determined by the Soxhlet Extraction method. Fiber content was determined by Fiber-cap method.

Extraction and Isolation of Compounds

Ethyl acetate soluble fraction of a 95% ethanolic extract was prepared and submitted to three successive separations by vacuum liquid chromatography, flash chromatography and micro-column chromatography using Pasteur pipette to finally obtain carboxylic acids mixture C, giving a single spot on TLC.

Vacuum Liquid Chromatography

The vacuum liquid chromatography (VLC) employed in the present work is a modification of the Dry Column Vacuum Chromatography (DCVC) (Pedersen & Rosenbohm, 2001). In DCVC, Silica Gel 60 (15–40 μm) is used whereas in VLC of the present work Silica Gel 60 (63–200 μm) was used. Another difference is the use of a normal glass column instead of a sintered glass funnel, and also a usual wet packing of the column instead of a dry packing. Fractions of 70 mL each of PE: EA 9:2, 9:4, 9:6, 9:8, EA only, EA:MeOH 9:1, 1:1 and MeOH only were collected, and 10 fractions were obtained. Each of the fractions was concentrated by evaporating the solvent and monitored by TLC. The ethyl acetate sub fraction from the VLC was rechromatographed by flash chromatography (Still *et al.*, 1978). The solvent system chloroform: methanol (9:1) which gave good separation and also moved the major component to $R_f = 0.35$ on analytical TLC was chosen. Further purification on a micro-column (Millar, 2012) yielded C.

Rapid Methylation of Isolated Compound C

The isolated compounds by micro-column chromatography was identified as acid by TLC with reagent bromocresol green (yellow spots against blue background), and C was converted to its methyl ester for GC-MS analysis by a rapid methylation method (Ichihara and Fukubayashi, 2010).

Results and Discussion

The results of preliminary photochemical tests of *Clinacanthus nutans* showed that the leaves contain alkaloids, flavonoids, glycosides, organic acids, tannins, phenolic compounds and terpenoids were present in Table 1.

Table 1 Results of Phytochemical constituents on the Leaves of *Clinacanthus nutans*

No.	Phytochemical tests	Extracts	Test reagents	Observation	Remark
1	Alkaloids	1% HCl	Mayer's reagent Dragendroff's reagent Wagner's reagent Sodium picrate	White ppt Orange ppt Reddish brown ppt Yellow ppt	+ + + +
2	α-amino acids	H_2O	Ninhydrin	Purple spot	+
3	Carbohydrate	H_2O	10% α-naphtnol + Conc: H_2SO_4	Red ring	+
4	Cyanogenic glycosides	H_2O	Conc: H_2SO_4 and Sodium picrate	No color change	-
5	Flavonoids	EtOH	Conc: HCl and Mg turning	Pink color	+
6	Glycosides	EtOH	10% Lead acetate	White ppt	+
7	Organic acid	H_2O	Bromocresol green solution	Yellow colour	+
8	Phenolic compound	EtOH	$K_3Fe(CN)_6$ + 1% $FeCl_3$	Brown ppt	+
9	Reducing sugars	H_2SO_4	Benedict's solution	No brick red ppt	-
10	Saponins	H_2O	Distilled water	Frothing	+
11	Starch	H_2O	I_2 solution	Blue black	+
12	Steroids	PE	Acetic-anhydride & conc: H_2SO_4	Red colour	+
13	Tannins	EtOH	1% gelatin	Brown	+
14	Terpenoids	$CHCl_3$	Acetic anhydride	Pink	+

(+) = Presence, (-) = Absence, (ppt) = Precipitate

Analysis of Nutrients in the Leaves of *Clinacanthus nutans*

According to the results, the ash, carbohydrate, fat, fibre, moisture and proteins were found to be 19.27 %, 18.20 %, 2.01 %, 28.45 %, 13.95 % and 18.12 %, respectively, (Table 2).

Table 2 Nutritional Values for the Leaves of *Clinacanthus nutans*

No.	Parameter	Contents (%)
1	Ash	19.27
2	Carbohydrate	18.20
3	Fat	2.01
4	Fiber	13.95
5	Moisture	18.12
6	Protein	28.45
7	Energy values (kcal/100g)	163.37

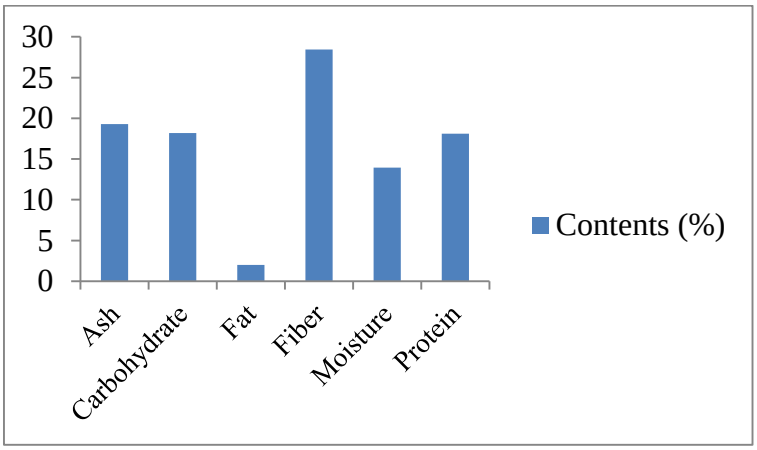

Figure 2 Bar graph showing nutrients in the leaves of *Clinacanthus nutans*

Qualitative Elemental Analysis by EDXRF

In this study relative abundance of elements present in the leaf of *Clinacanthus nutans* was determined by EDXRF. Qualitative elemental analysis by EDXRF spectrometry revealed that the leaves of *Clinacanthus. nutans* was found to contain K (2.204%) and Ca (2.251%,) as major elements and Fe, S, Mn, Zn, Cu and Rb as trace elements, (Figure 3 and Table 3).

Table 3 Relative Abundance of Elements in Leaves of *Clinacanthus nutans* by EDXRF

No.	Elements	Relative abundance (%)
1	K	2.204
2	Ca	2.251
3	P	-
4	S	0.513
5	Fe	0.037
6	Mn	0.005
7	Zn	0.003
8	Ti	0.006
9	Sr	0.004
10	Rb	0.004
11	Cu	0.001
12	Br	0.001

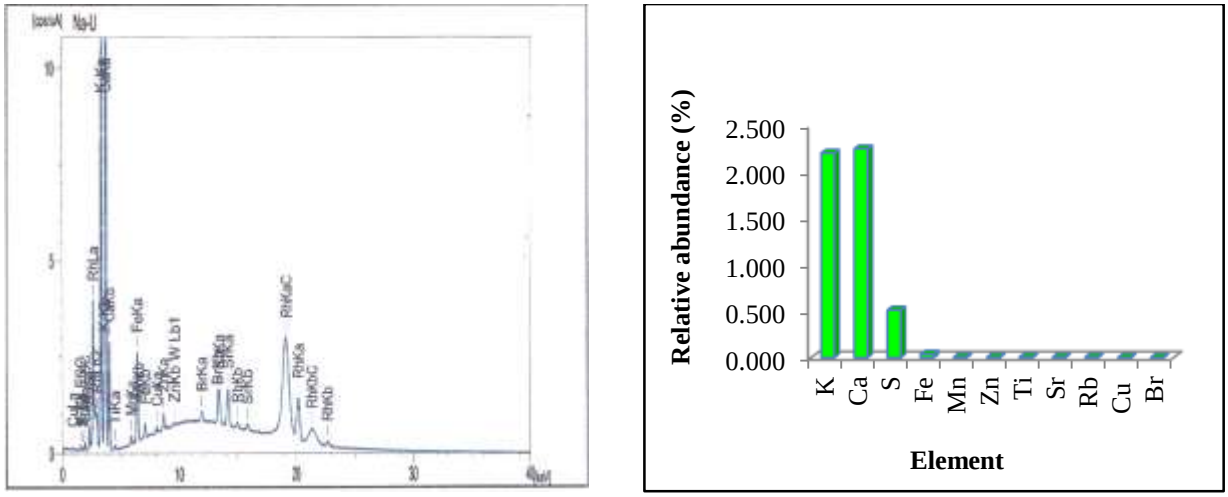

(a) (b)

Figure 3 EDXRF spectrum (a) and bar graph showing the elements (b) of *Clinacanthus nutan* leaf

Isolation of Carboxylic Acids

The ethyl acetate soluble fraction of ethanol extract was subjected to vacuum liquid chromatography (VLC) by applying suction elution using a vacuum pump, collecting 70 mL fractions. Common column silica gel (63 – 200 µm) was used. Due to the rapid flow rate under suction, the running time was shortened considerably. Next the selected eluted fraction from the column was further separated by flash chromatography (Still *et al.*, 1978) on a finer silica gel (40–63 µm) in which positive pressure elution was employed using compressor. Purer fraction containing compound was obtained in a short time due to the increased flow rate used. The small fraction was further purified on a micro-column (Millar, 2012) using a pasteur pipette filled with common column silica gel (63 – 200 µm) and a rubber bulb for pressure elution, collecting 1 mL fractions. Finally, fraction containing C was obtainedwhich gives single spot on TLC was obtained. If the finer silica gel (15–40 µm) used in dry column vacuum chromatography (DCVC) (Pedersen and Rosenbohm, 2001) were available, the purification could have been done by a single column.

Analysis of the Carboxylic Acids Composition of C by GC-MS

The observed IR bands may be explained as follows: the broad O-H stretching band with maximum at 3365cm^{-1}, characteristic of a carboxyl group, with the carbonyl C=O stretching band at 1720 cm^{-1} indicates a carboxylic group. The CH_3 asymmetric and symmetric stretching bands at 2957 and 2858 cm^{-1}, the CH_3 asymmetric and symmetric bending bands at 1461 and 1380 cm^{-1} indicate presence of methyl groups. Furthermore, the methylene rocking band at 731 cm^{-1} suggests a long-chain fatty acid rather than a pentacyclic triterpenic acid (Table 4). Thus from the TLC reagent tests and the FT IR spectrum (Figure 4), **C** is a long-chain fatty acid. The presence of linoleic acid (palmitic acid) in the leaf of *Clinacanthus nutans* has also been reported on page 5 of a review article on *Clinacanthus nutans* (Khoo *et al.*, 2018).

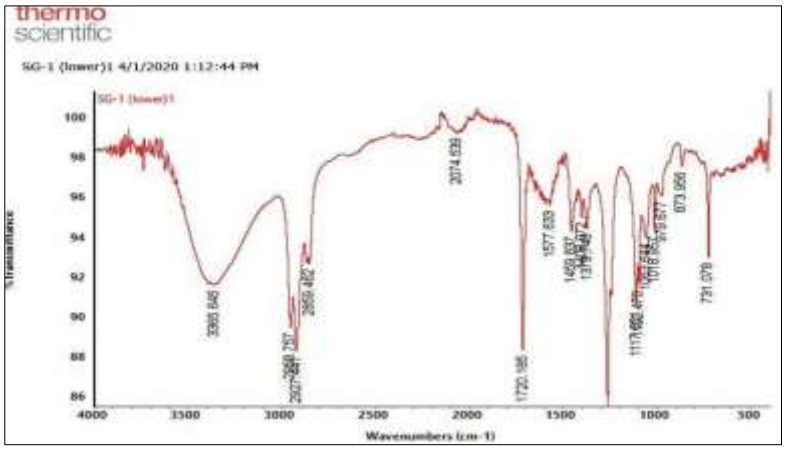

Figure 4 FT IR spectrum of the isolated compound

Table 4 FT IR Band Assignment of Isolated Compound C

Wavenumber (cm^{-1})	**Vibrational Mode**	**Assignments**
3500-2500 (very broad)	ν O-H	OH of carboxyl
2957	ν_{as} CH_3	CH_3
2927	ν_{as} CH_2	CH_2
2858	ν_{sy} CH_3	CH_3
1720	ν C=O	carboxyl
1461	δ CH_2, δas CH_3	CH_3, CH_2
1380	δ_{sy} CH_3	CH_3
1266, 1117, 1063, 1018	ν C-O	C-O
731	□ CH_2	$(CH_2)_n$ with $n \geq 4$

C can be a mixture of fatty acids since it is usually impossible to isolate individual acids on a silica gel column or by TLC. Therefore the carboxylic acid composition and their structures in C was analysed by GC-MS after preparation of the methyl ester. In the present method used for the preparation of fatty acid methyl esters (Ichihara and Fukubayashi, 2010), the methanolysis reaction is improved by enhancement of the solubility of hydrophobic acids and esters, if any, by adding toluene, and the use of heating in the sealed tube condition 100 °C shortened significantly the reaction time. The desired groups of methyl esters is the reaction mixture after further workup procedure were separated from other products by micro-column and then by PTLC.

Three fatty acids have been identified by GC-MS in isolated compound. From the selected peaks in the TIC chromatogram, Figure 5, linoleic acid (or) (*Z, Z*)-9,12-octadecadienoic acid (**C-1**) (RT 16.861 min) (Figure 6) was observed as free fatty acid (FFA) in the GC-MS. The second is 11,14-octadecadienoic acid (**C-2**) as its methyl ester (RT 19.511 min), Figure 7 and 11,14-eicosadienoic acid (**C-3**) as its methyl ester (RT 21.835 min) Figure 8. All the mass spectra show the low mass ion series corresponding to the formula C_nH_{2n-3}, namely 53, 67, 81, 95, 109,123, 137, 151 etc., suggesting a long chain hydrocarbon containing two double bonds, which is present in all the three compounds. A diagnostic peak at m/z 73 for a long chain fatty acid can be observed in the mass spectrum of **C-1**.

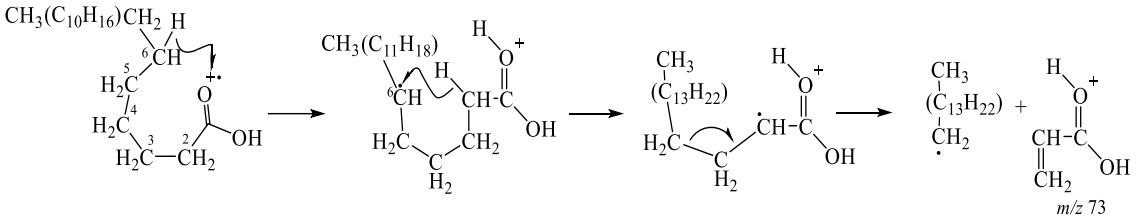

In the mass spectra of the fatty acid methyl esters of **C-2** and **C-3**, *m/z* 263 and 291 peaks for [M-31] corresponding to [M-OCH_3] by loss of methoxyl radical are very small. Refined search in the total ion chromatogram (TIC) may give better mass spectra for these esters.

C-1
Linoleic acid (or)
(*Z*,*Z*)-9,12-octadecadienoic acid

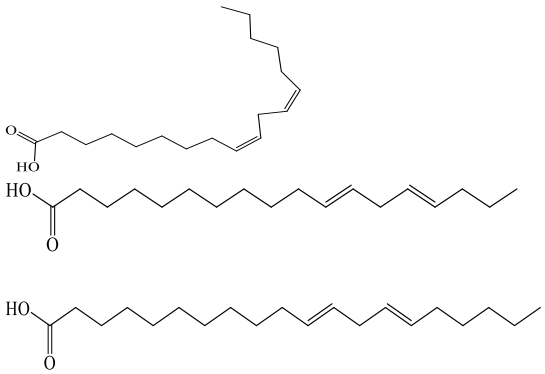

C-2
11,14-octadecadienoic acid

C-3
11,14-eicosadienoic acid

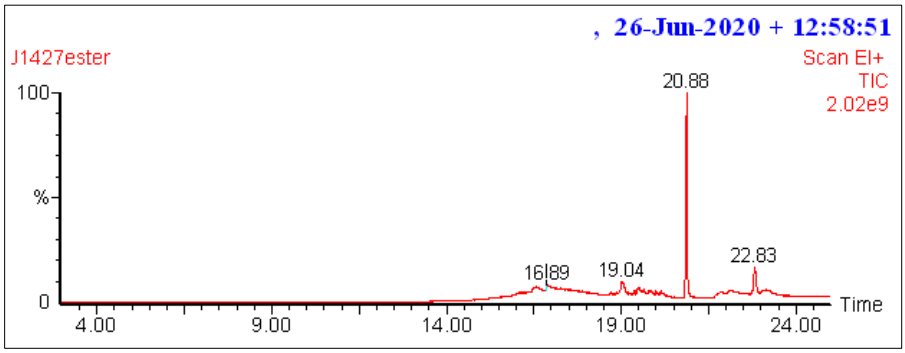

Figure 5 Total ion chromatogram (TIC) of isolated compound

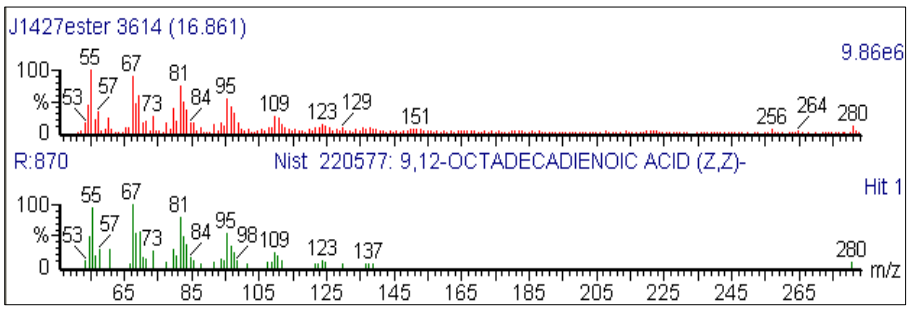

Figure 6 Comparison of the EI mass spectra of C-1 (upper) and 9,12- octadecadienoic acid

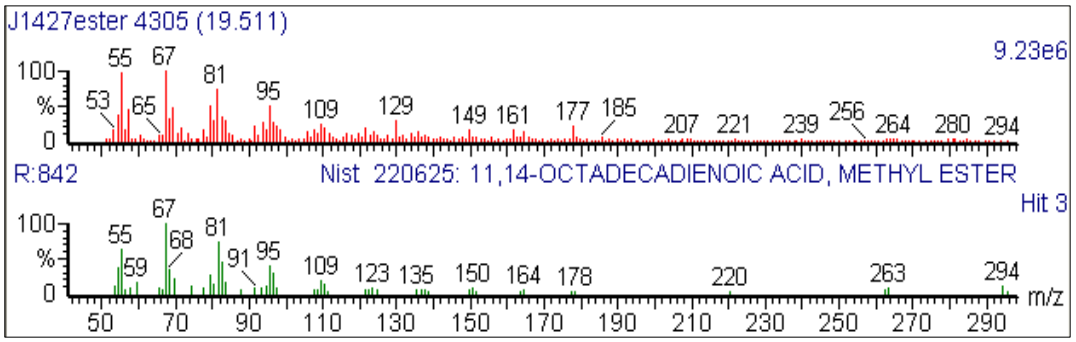

Figure 7 Comparison of the EI mass spectra of C-2 methyl ester (upper) and methyl 11,14-octadecadienoate (lower)

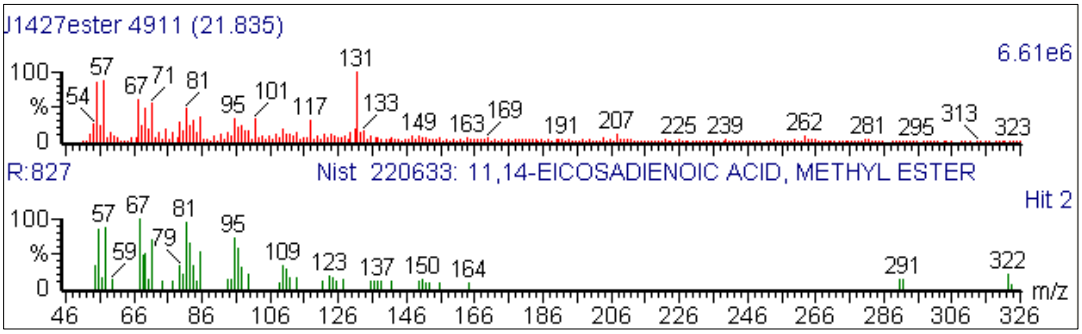

Figure 8 Comparison of the EI mass spectra of C-3 methyl ester (upper) and methyl 11,14-eicosadienoate (lower)

Conclusion

From the leaves of *Clinacanthus nutans*, carboxylic acids **C** were isolated after passing through different column chromatographic techniques. **C** giving a single spot on TLC was deduced as long-chain fatty acids by the FT IR and physicochemical characteristics. Three fatty acids have been further identified by GC-MS in **C**, namely linoleic acid (or) (*Z,Z*)-9,12-octadecadienoic acid (**C-1**), 11,14-octadecadienoic acid (**C-2**) and 11,14-eicosadienoic acid (**C-3**).

Acknowledgements

The authors would like to thank to the Myanmar Academy of Art and Science and its Editors, Ministry of Education in Myanmar, for giving us the opportunity to present this research paper. We also would like to thank to the Department of Higher Education, Ministry of Education in Myanmar, for providing us the research facilities during this research. Thanks are also due to Research and Innovation Department, the Government of the Republic of the Union of Myanmar, Myanmar for the GC-MS.

References

AOAC**.** (1984). *Official Methods of Analysis.* Washington, DC: 13th Ed., Association of Official Analytical Chemists

Ichihara, K. and Y. Fukubayashi. (2010). "Preparation of Fatty Acid Methyl Esters for Gas-liquid Chromatography." *Journal of Lipid Research*. vol.51, pp. 635-640

Kapoor, L.D, (2001). *CRC Handbook of Ayurvedic Medicinal Plants.* New York, Herbal Reference Library, CRC Press.Khoo, L.W., S.A. Kow, M.T. Lee, C.P. Tan, K. Shaari, C.L. Tham, and F. Abas. (2018). "A Comprehensive Review on Phytochemistry and Pharmacological Activities of *Clinacanthus nutans* (Burm.f.) Lindau". *Evidence-Based Complementary and Alternative Medicine,* vol.1. pp. 1-39

Khoo, L.W., S.A. Kow, M.T. Lee, C.P. Tan, K. Shaari, C.L. Tham, and F. Abas. (2018). "A Comprehensive Review on Phytochemistry and Pharmacological Activities of *Clinacanthus nutans* (Burm.f.) Lindau". *Evidence-Based Complementary and Alternative Medicine,* vol.1, pp. 1-39

Pedersen, D. S and C. Rosenbohm. (2001). "Dry Column Vacuum Chromatography", *Synthesis*, vol.16. pp. 2431-2434

Millar, S. (2012). "Tips and Tricks for the Lab: Column Troubleshooting and Alternatives", Weinheim:Wiley-VCH Verlag GmbH & Co.KGaA

(https://www.chemistryviews.org/details/education/2345141/Tips_and_Tricks_for_the_Lab_Column_Troubleshooting_and_Alternatives.html

(accessed 11.4.2020))

Still, W. K., M. Kahn, and A. Mitra. (1978). "Rapid Chromatographic Technique for Preparative Separations with Moderate Resolution". *J. Org. Chem.,* vol. 43. pp. 2923-2925

Tuntiwachwuttikul, P., Y. Pootaeng., P. Phansa and W.C. Taylor. (2004). "Cerebrosides and Amonoacylmonogalactosylglycerol from *Clinacanthus nutans*". *Chem. Pharma. Bull*, vol.52. pp. 27-32

INVESTIGATION OF SOME PHYTOCHEMICAL CONSTITUENTS AND BIOACTIVITIES OF LEAF EXTRACTS OF *MENTHA SPICATA* L. (PU SI NAN)

Mar Mar Win[1], Swe Zin Myint[2], Ni Ni Than[3]

Abstract

The present work focused on the investigation of nutritional values, antimicrobial activity, antioxidant activity and some phytoconstituents in the leaf extracts of *Mentha spicata* L. (Pu Si Nan). The preliminary phytochemical tests revealed the presence of alkaloids, α-amino acids, carbohydrates, cyanogenic glycosides, flavonoids, glycosides, organic acids, phenolic compounds, reducing sugars, saponins, steroids, tannins and terpenoids. However, starch was absent. The nutritional values were determined by AOAC method providing proteins 23.68 %, ash 25 %, fibers 11.49 %, water content 15.15 %, carbohydrates 17.04 %, fats 7.64 % and energy value (232 kcal /100 g). *Invitro* screening of antimicrobial activity by agar well diffusion method on five different microorganisms (*Escherichia coli, Enterococcus faecalis, Staphylococcus aureus, Bacillus cereus, Candida albicans*) on PE, EtOAc, EtOH, $CHCl_3$ and H_2O extracts of the leaf of *Mentha spicata* L. (Pu Si Nan), PE, EtOH, $CHCl_3$ and EtOAc extracts showed antimicrobial activity on four strains of microorganisms (except *E. coli*). Watery extract was observed activity against on *E. faecalis*, *S. aureus* and *B. cereus*. The highest inhibition zone was observed 20.50 ± 0.35 mm on *Bacillus cereus* by EtOAc extract of sample. The antioxidant activity of watery and ethanol extracts of the leaf sample was determined by DPPH assay. The IC_{50} values of watery and ethanol extracts were found to be 127 and 38 μg/mL respectively. Ethanol extract of the leaf sample was observed that higher antioxidant activity than watery extract but weaker activity than BHT (IC_{50} of BHT=11.71 μg/mL). Essential oils from the leaf of the sample were extracted by steam distillation method and analyzed by GC-MS spectroscopic method. According to the results, the components (3-carene, D-limonene, *trans*-carveol, D-carvone, 2-cyclohexen-1-one, 3-methyl-6-(1-methylethylidene), beta-bourbonene and alpha-copaene) were investigated in the extracted essential oils of leaf of *Mentha spicata* L. (Pu Si Nan).

Keywords: *Mentha spicata* L., phytochemical tests, nutritional values, antioxidant activity, antimicrobial activity, essential oils

Introduction

Mint, commonly known as "Pudina" in most Indian languages, belongs to the genus *Mentha* in the family Lamiaceae. There are 25-30 species within the genus *Mentha*, including *spearmint*, *peppermint*, *wild mint*, *corn mint*, *curled mint*, *bergamot*, *American mint*, *Korean mint*, etc. of which spearmint is the most common of all (Kumar *et al*., 2006).

Spearmint (*Mentha spicata* L.) belongs to the family Lamiaceae (Tetika *et al.*, 2013). The plants of this family are a rich source of polyphenols and thus possessing strong antioxidant properties (Robinson, 1983).

Mentha spicata possesses several biological activities and is used in folkloric medicine as a carminative, antispasmodic, diuretic, antibacterial, antifungal and antioxidant agent and for treatment of colds and flu, respiratory tract problems, gastralgia, hemorrhoids, and stomachache (Boukef, 1986 and Leporatti and Gheira, 2009).

[1] Lecturer, 1 PhD, Department of Chemistry, Dagon University
[2] Dr, Lecturer, Department of Chemistry, Dagon University
[3] Dr, Professor & Head, Department of Chemistry, University of Yangon

Materials and Methods

Collection and Preparation of Plant Sample

In the present research, the leaf of *Mentha spicata* L. was chosen to be studied. The plant of Pu Si Nan was collected from North Dagon Township, Yangon Region on June, 2018. The collected leaves were washed with water to remove impurities. They were dried at room temperature. The dried sample was made to powder in electric grinder and stored in air-tight container. The dried powdered sample was used to investigate for chemical and biological activities.

Botanical Identification of Collected Sample

Botanical name of collected plant was identified by authorized taxonomist at the Botany Department, Dagon University.

Preliminary Phytochemical Test

Phytochemical investigation of the leaf of *Mentha spicata* L. was carried out according to the standard procedures to investigate the presence or absence of phytochemicals such as alkaloids, α-amino acids, carbohydrates, cyanogenic glycosides, flavonoids, glycosides, organic acids, phenolic compounds, reducing sugars, saponins, starch, steroids, tannins and terpenoids (Harborne, 1984 and Marini-Bettolo *et al*., 1981).

Determination of Nutritional Values

Nutritional values such as moisture content, ash content, fat content, fiber content, protein content, carbohydrate content and energy value of the selected sample were determined by AOAC method (AOAC, 1990 and Liu, 2003).

Evaluation of Antimicrobial Activity

The experiment to evaluate the antimicrobial activity of leaf extracts was carried out at the Pharmaceutical Research Laboratory, Biotechnology Research Department (BRD), Kyaukse District, Mandalay Region, Myanmar.

Sample

EtOH, Pet Ether, CHCl3, EtOAc and H2O extracts of Mentha spicata L. leaf

Tested microorganisms

One Gram-negative bacterium (*Escherichia coli*), three Gram-positive bacteria (*Staphylococcus aureus, Enterococcus faecalis* and *Bacillus cereus*) and one fungal strain (*Candida albicans*) were used as the tested microorganisms for this experiment. Some bacterial strains were kindly supported by Public Health Laboratory (PHL), Mandalay.

Procedure

The agar well diffusion method was used for antimicrobial activity evaluation by modifying the method described. Tested microorganisms were inoculated in Mueller Hinton broth at 37 °C for overnight. On the next day, the overnight broth culture was diluted with normal saline to obtain the OD_{600} at 0.08 to 0.1 with the approximate cell density of $1.5x10^8$ CFU/mL. Mueller Hinton agar plates were prepared and sterilized by autoclaving at 121 °C for 15 min. The broth inoculums were evenly spread out with sterile cotton swabs on the Mueller Hinton agar plates to obtain the uniform inoculums. After the plate was inoculated, 8-mm diameter wells were made on the agar

medium by using a sterile cork borer. The wells then filled with 50 µL of different plant extracts with the concentration of 25 mg per 50 µL. Ethanol (70 %) was used to prepare the extracts and as a solvent control. Tetracycline hydrochloride 30 µg/well was used as the positive control. Then, the plates were placed in an incubator at 37 °C for 16 to 18 hours. After incubation, the plates were examined and zone diameters of complete inhibition were measured and recorded to the closest millimeter (Snoussi *et al.,* 2015).

Screening of Antioxidant Activity

DPPH (1, 1-diphenyl-2-picryl-hydrazyl) radical scavenging assay was chosen to assess the antioxidant activity of selected simple. This assay has been widely used to evaluate the free radical scavenging effectiveness of various flavonoids and polyphenols in food system (Leea *et al*., 2002).

In this experiment, the antioxidant activity was studied on 95 % ethanol extract and watery extract from leaf sample.

Procedure

DPPH radical scavenging activity was determined by UV spectro-photometric method. The control solution was prepared by mixing 1.5 mL of 60 µM DPPH solution and 1.5 mL of 95 % ethanol using shaker. The sample solution was also prepared by mixing thoroughly 1.5 mL of 60 µM DPPH solutions and 1.5 mL of test sample solution. The solutions were allowed to stand at room temperature for 30 minutes. After 30 minutes, the absorbance of these solutions was measured at 517 nm by using (UV-2550) UV-Visible spectrophotometer. Absorbance measurements were done in triplicate for each solution and then mean values so obtained were used to calculate percent inhibition of oxidation and the IC_{50} (50 % inhibitory concentration) values were also calculated by linear regressive excel program (Snoussi *et al.,* 2015).

Extraction of Essential Oils

Procedure

Fresh leaves (500 g) of Pu Si Nan were cut into pieces and mixed with 500 mL of distilled water. The mixture was placed in the 1 liter round-bottomed flask and then connected to a steam generator on one side and a water condenser on the other. The distilled water in the flask was heated and a current of steam was passed into the mixture. The mixture of hot vapours was collected and condensed in order to produce a liquid in which the oil and water form two distinct layers. The upper layer of essential oils was carefully drawn out by a syringe and dried over anhydrous Na_2SO_4 and kept in the freezer. This procedure was done about three times to collect more amounts of essential oils (Basim *et al.,* 2000).

Analysis of Essential Oils by GC-MS Spectroscopy

GC conditions

Source temp	-	200 °C
Inlet line temp	-	270 °C
Injector temp	-	250 °C
Injection volume	-	1.0 µL
Column type	-	Elite5 MS (5% diphenyl 95% dimethyl polysiloxane) 30.0 mL, 0.25 mm, 0.25 µm (thickness)
Oven program	-	Flow 20 °C/ min 80 °C to 210 °C hold 1 min Flow 8.0 °C/ min 210 °C to 250 °C hold 2 min Flow 10 °C/ min 250 °C to 280 °C hold 5 min
Carrier gas	-	Helium (flow rate: 1.0 mL/ min)

MS conditions

Mass Range	-	50 to 550 amu
MS mode	-	Full Scan and Selected Ion Monitoring (SIM)
Delay time	-	3.0 min

Results and Discussion

Preliminary phytochemical investigation was carried out to know the types of phytochemical constituents present in the leaf of *Mentha spicata* L. (Pu Si Nan). According to these results, alkaloids, α-amino acids, carbohydrates, cyanogenic glycosides, flavonoids, glycosides, organic acids, phenolic compounds, reducing sugars, saponins, steroids, tannins and terpenoids were found to be present but starch was absent.

The water content was found to be 15.15 %. The ash content was observed as 25.00 %. The main purpose of protein is to build the body and to require by the body can be used to provide. It was found that the protein content was 23.68 %. The fat content was found to be 7.64 %. Fats are important dietary requirement and provide energy. The fiber was observed as 11.49 %. Fiber reduces the risk of type 2 diabetes. The carbohydrate content was determined by subtraction method. If was found to be 17.04 % and energy value was 232 kcal/100 g of the sample. Carbohydrates are major source of fuel for metabolism, being used both as an energy source and in biosynthesis.

In the present work, antimicrobial activity of PE, EtOH, $CHCl_3$, EtOAc and H_2O extracts obtained from the leaf of (Pu Si Nan) was investigated on five different strains of microorganisms such as *Staphylococcus aureus, Bacillus cereus, Enterococcus faecalis, Escherichia coli* and *Candida albicans* by agar well diffusion method. The measurable diameter, including the well diameter, shows the degree of antimicrobial activity. The well diameter is 8 mm in this experiment. The antimicrobial activity was observed for the extracts of PE, EtOH, $CHCl_3$ and EtOAc against on four strains of microorganisms (except *E. coli*). Watery extract did not show antimicrobial activity on *E. coli* and *C. albicans*. The highest inhibition zone was observed 20.50 ± 0.35 mm on *Bacillus cereus* by EtOAc extract of sample leaf.

The absorbance of different concentrations (6.25, 12.5, 25, 50, 100 and 200 µg/mL) of tested sample was measured as 517 nm by using UV-2550 spectrophotometer. It was found that as the concentrations were increased, the absorbance values were decreased. The larger the % RSA indicates the higher antioxidant activity. In contrast, the lower the IC_{50} indicates the more effective antioxidant activity. The antioxidant activity is expressed as % radical scavenging activity (% RSA) and 50 % inhibition concentration (IC_{50}) value (Cheeseman and Slater, 1993). From the experimental results, IC_{50} values of ethanol and watery extracts of leaf of Pu Si Nan were 38 and 127 µg/mL respectively. According to the results, the ethanol extract was found to be more antioxidant potency than watery extract. Antioxidant potency of ethanol and watery extracts were observed that weaker than compared to the potency of standard BHT (IC_{50}=11.71 µg/mL).

From the analysis of essential oils by Gas Chromatography with Mass Spectrometer, it was observed that the phytoconstituents (3-carene, D-limonene, *trans*-carveol, D-carvone, 2-cyclohexen-1-one, 3-methyl-6-(1-methylelthylidene), beta-bourbonene and alpha-copaene) were investigated in the essential oils of the selected sample leaf.

Table 1 Nutritional Values of the Leaf of *Mentha spicata* L. (Pu Si Nan)

No.	Nutrients	Content %
1	Proteins	23.68
2	Ash	25.00
3	Fibers	11.49
4	Water content	15.15
5	Carbohydrates	17.04
6	Fats	7.64
7	Energy value (kcal/100 g)	232

Table 2 Inhibition Zone Diameters of Various Crude Extracts of *Mentha spicata* L. Leaf Against on Five Microorganisms

Sample	Inhibition Zone Diameter (mm)				
	Staphylococcus aureus	***Bacillus cereus***	***Enterococcus faecalis***	***Escherichia coli***	***Candida albicans***
(1) PetEther Extract	15.50 ± 0.35	15.50 ± 0.35	13.50 ± 1.06	0	15.00 ± 0.00
(2) EtOH Extract	12.00 ± 0.00	17.50 ± 0.35	18.00 ± 0.71	0	13.00 ± 0.71
(3) $CHCl_3$ Extract	13.00 ± 0.71	17.50 ± 0.35	15.50 ± 0.35	0	14.50 ± 0.35
(4) EtOAc Extract	15.50 ± 0.35	20.50 ± 0.35	18.00 ± 0.00	0	15.00 ± 0.00
(5) H_2O Extract	11.00 ± 0.00	14.00 ± 1.41	15.00 ± 0.00	0	0
70% Ethanol	0	0	0	0	0
Tetracycline Hydrochloride	11.67 ± 0.19	23.67 ± 0.51	16.00 ± 0.67	27.67 ± 0.19	24.33 ± 0.19

Values are means ± SEM of duplicate results.
Agar well diameter = 8mm

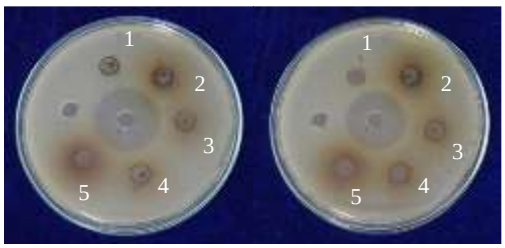

Figure 1 Inhibition zones of various crude extracts against on *Escherichia coli*

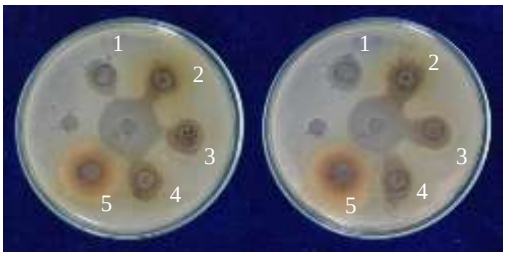

Figure 2 Inhibition zones of various crude extracts against on *Candida albicans*

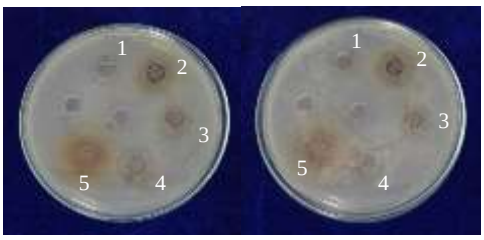

Figure 3 Inhibition zones of various crude extracts against on *Enterococcus faecalis*

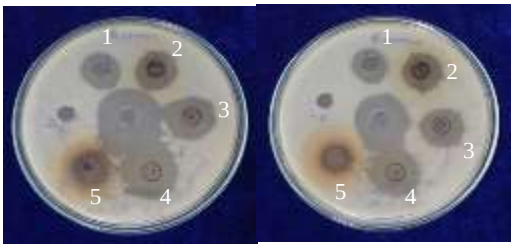

Figure 4 Inhibition zones of various crude extracts against on *Bacillus cereus*

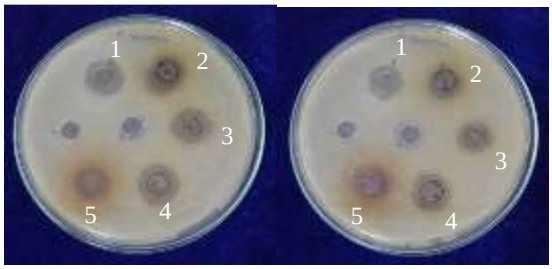

Figure 5 Inhibition zones of various crude extracts against on *Staphylococcus aureus*

Sample Code
(1) = Pet Ether Extract
(2) = EtOH Extract
(3) = $CHCl_3$ Extract
(4) = EtOAc Extract
(5) = H_2O Extract
-C = 70% Ethanol
+C = Tetracycline Hydrochloride

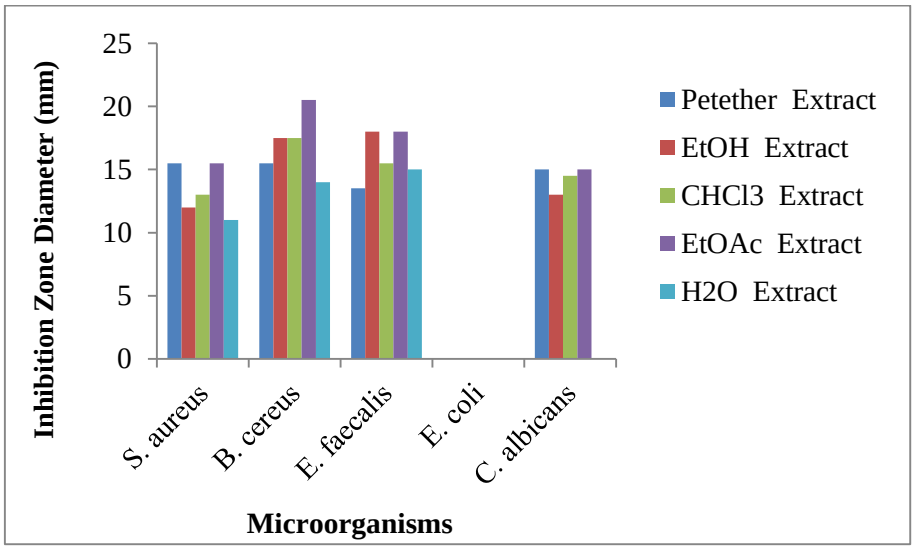

Figure 6 Comparison of inhibition zone diameters for various crude extracts against on five microorganisms

Table 3 Radical Scavenging Activity (% RSA) of Ethanol and Watery Extracts of Leaf of Pu Si Nan and Standard BHT

Extracts	% RSA±SD at Different Concentration (µg/mL)					
	6.25	**12.5**	**25**	**50**	**100**	**200**
EtOH	18.02±003	26.11±0.002	40.02±0.012	58.96±0.005	80.85±0.01	92.68±0.016
H_2O	6.16±0.001	9.1±0.160	16.4±0.002	26.51±0.011	44.98±0.007	63.57±0.003
BHT	33.43±0.010	52.38±0.005	62.14±0.001	68.37±0.011	74.06±0.002	82.34±0.007

Table 4 IC_{50} Values of Ethanol and Watery Extracts of Leaf of Pu Si Nan and Standard BHT

Sample Extracts	IC_{50} (µg/mL)
Ethanol	38
Water	127
BHT	11.71

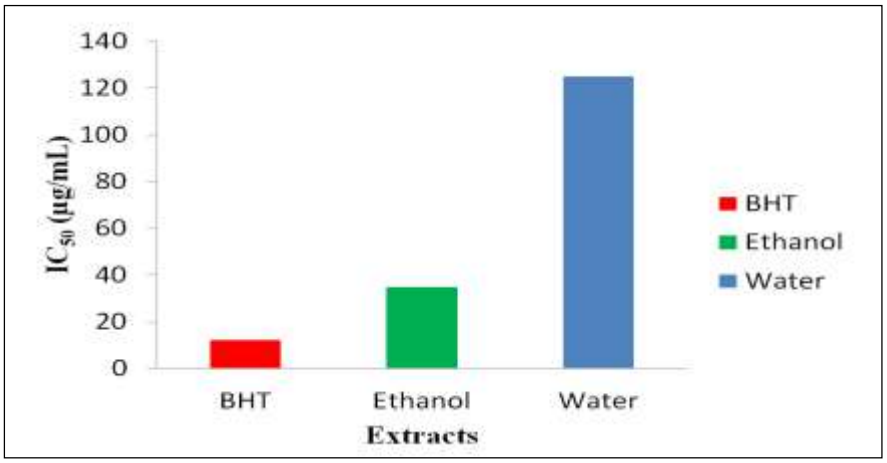

Figure 7 IC_{50} values of ethanol and watery extracts of leaf of Pu Si Nan and standard BHT

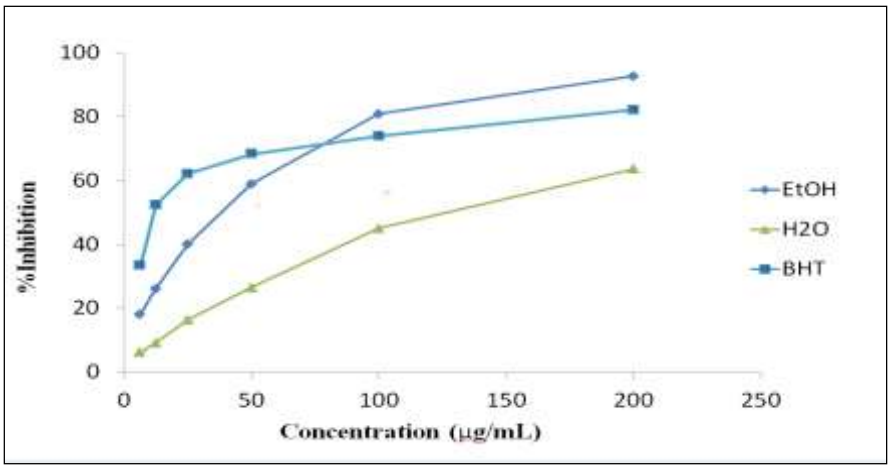

Figure 8 A plot of % RSA of ethanol and watery extracts of leaf of Pu Si Nan and standard BHT on antioxidant activity

Table 5 Phytochemical Constituents in the Essential Oils of Leaf of *Mentha spicata* L. (Pu Si Nan) by GC – MS Spectroscopy

No	
1	3-carene
2	D-limonene
3	*trans*-carveol
4	D-carvone
5	2-cyclohexen-1-one, 3-methyl-6- (1-methylelthylidene)
6	beta-bourbonene
7	alpha-copaene

(a)

(b)

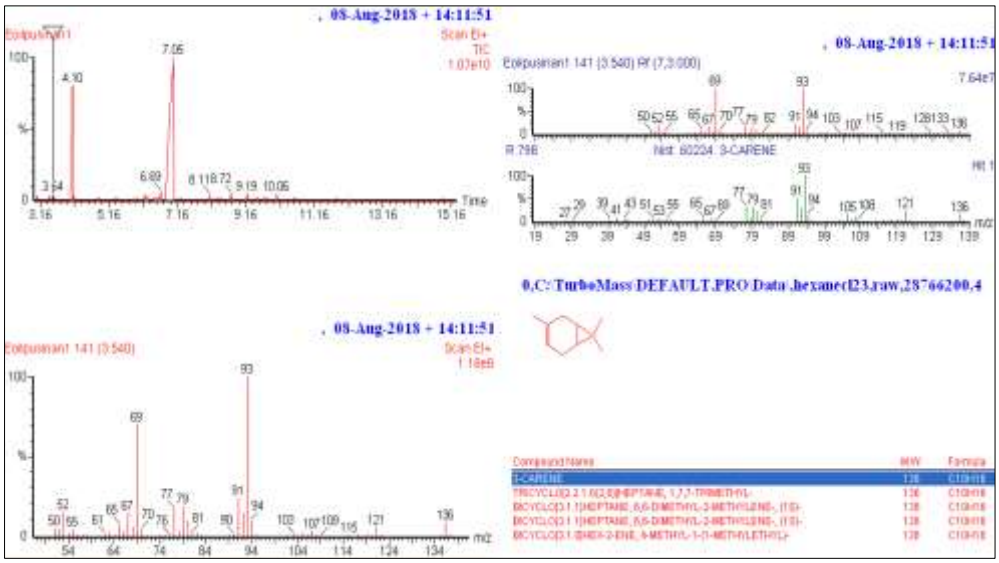

Figure 9 (a) Gas chromatogram and (b) mass spectrum of 3-carene

(a)

(b)

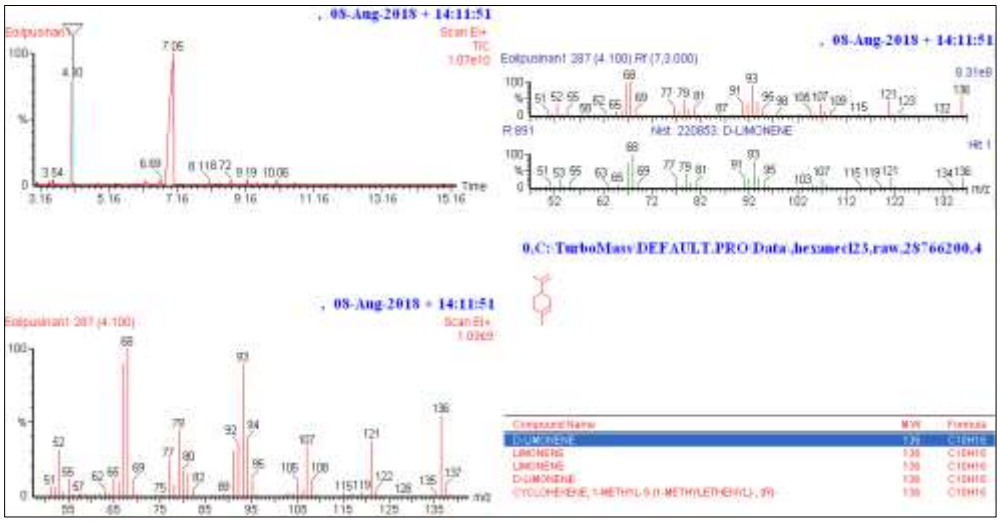

Figure 10 (a) Gas chromatogram and (b) mass spectrum of D-limonene

(a)

(b)

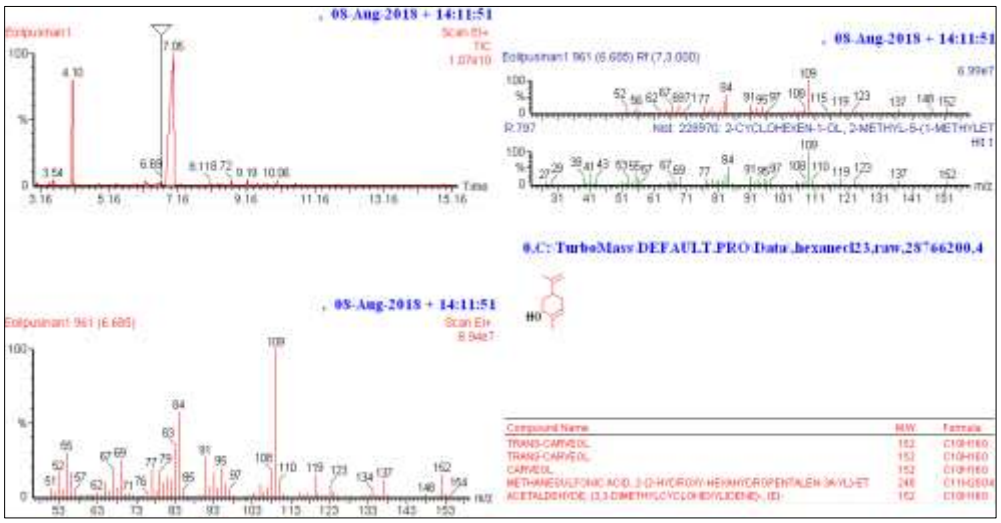

Figure 11 (a) Gas chromatogram and (b) mass spectrum of *trans*-carveol

(a)

(b)

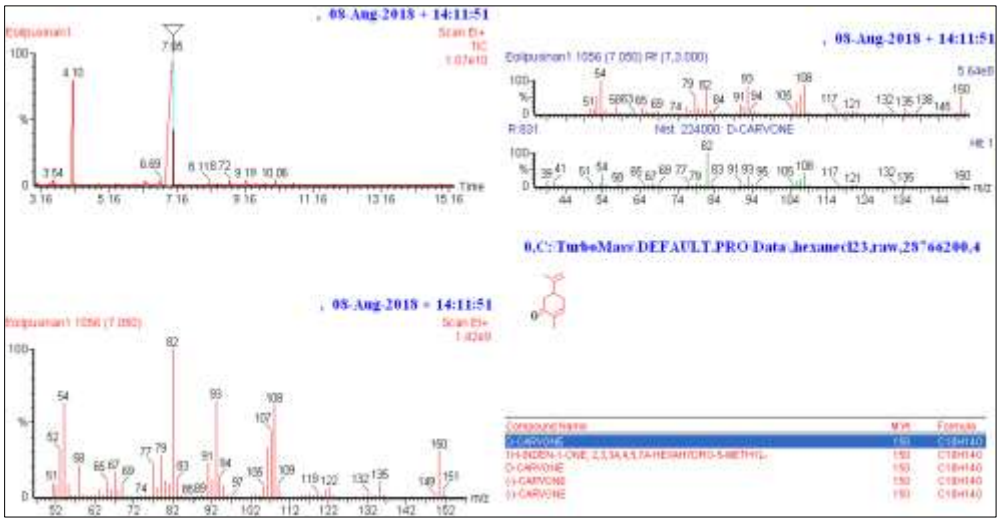

Figure 12 (a) Gas chromatogram and (b) mass spectrum of D-carvone

(a)

(b)

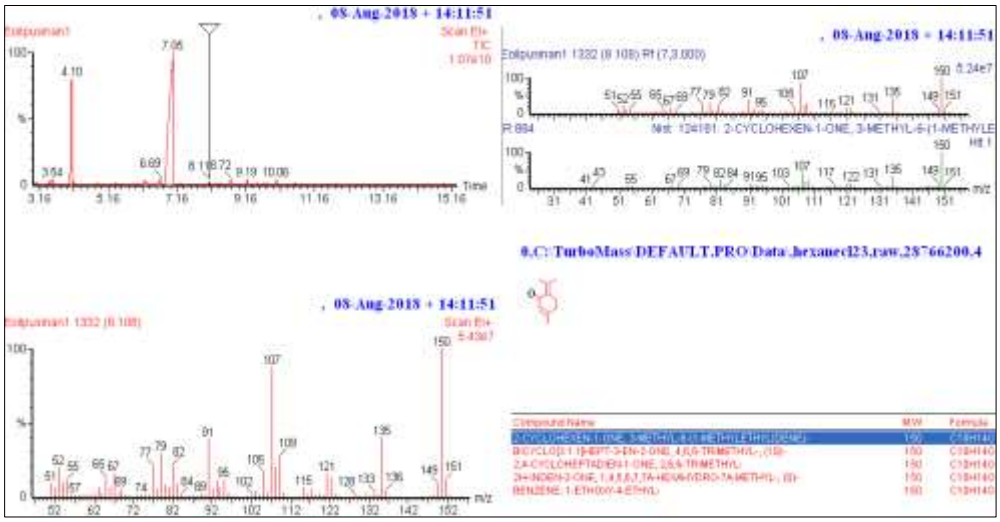

Figure 13 (a) Gas chromatogram and (b) mass spectrum of 2-cyclohexen-1-one, 3-methyl-6 (1-methylethylidene)

(a)

(b)

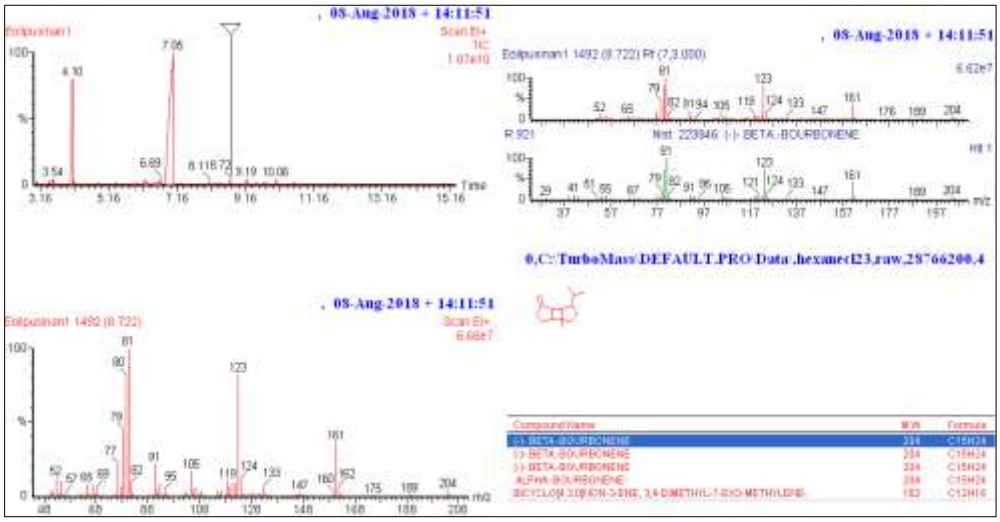

Figure 14 (a) Gas chromatogram and (b) mass spectrum of beta-bourbonene

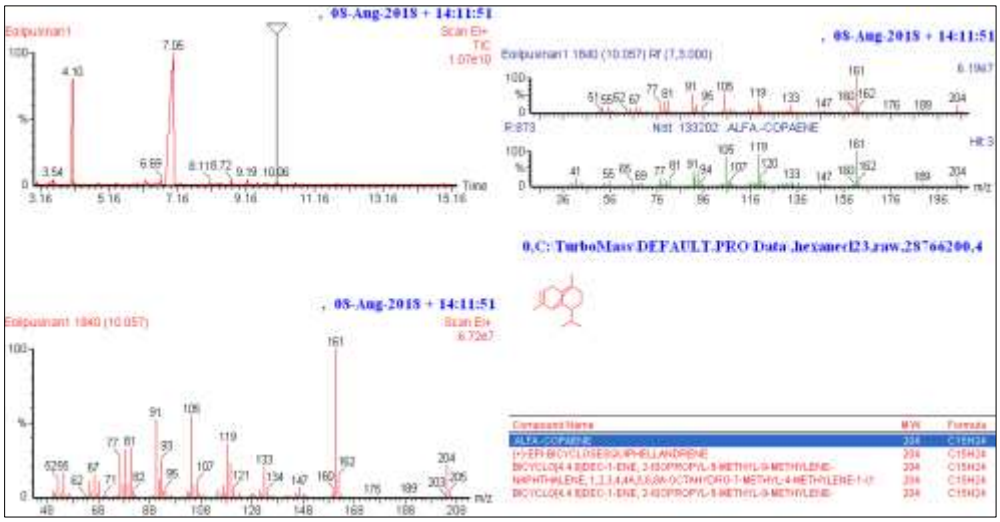

Figure 15 (a) Gas chromatogram and (b) mass spectrum of alpha-copaene

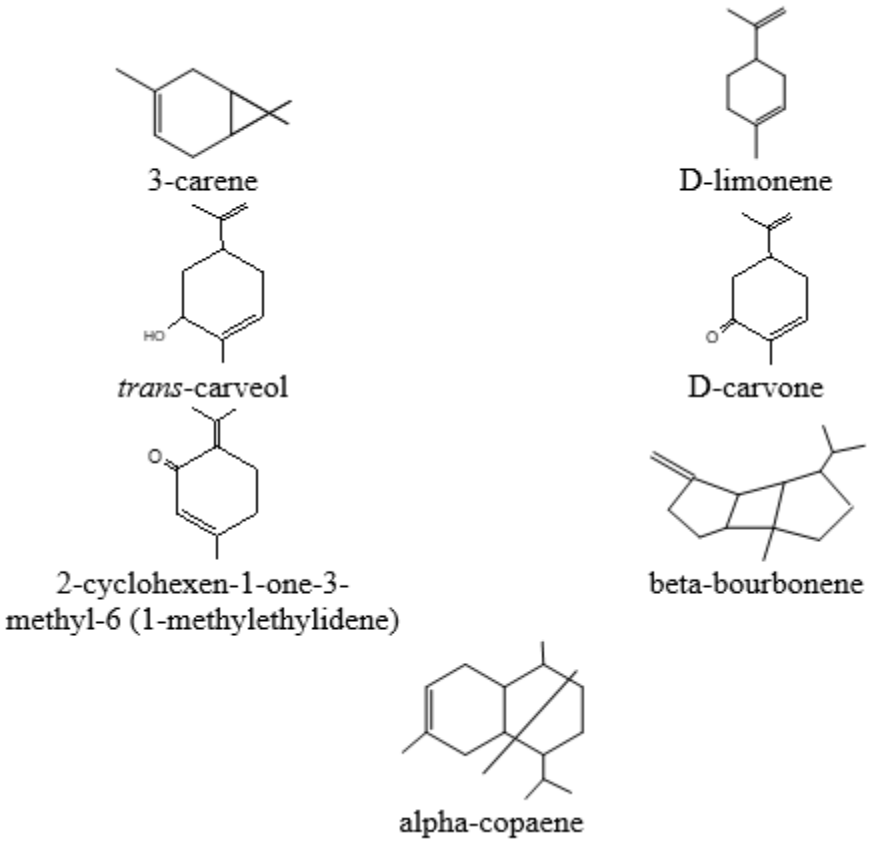

Figure 16 Molecular structures of phytochemical constituents in the essential oils of *Mentha spicata* L. (Pu Si Nan) leaf

Conclusion

From the overall assessment of chemical and biological investigation of the selected plant, *Mentha spicata* L. leaf, the following inferences could be deduced. Preliminary phytochemical tests performed by test tube method indicated that the presence of alkaloids, α-amino acids, carbohydrates, cyanogenic glycosides, flavonoids, glycosides, organic acids, phenolic compounds,

reducing sugars, saponins, steroids, tannins and terpenoids in the leaf of Pu Si Nan whereas starch was absent in the sample.

The nutritional values of the leaf of sample were evaluated by using AOAC method. It was suggested that the sample contained proteins (23.68 %), ash (25.00 %), fibers (11.49 %), water content (15.15 %), carbohydrates (17.04 %), fats (7.64 %) and energy value (232 kcal/100 g). So the leaf of Pu Si Nan is rich source of protein.

The antimicrobial activity of the PE, EtOAc, EtOH, $CHCl_3$ and H_2O extracts of the leaf of Pu Si Nan was screened by using agar well diffusion method against on 5 bacterial strains namely *Staphylococcus aureus, Bacillus cereus, Enterococcus faecalis, Escherichia coli, Candida albicans*. All extracts did not show antimicrobial activity on *E. coli*. Watery extract was not observed activity against on *C. albicans*. PE, EtOH, $CHCl_3$ and EtOAc extracts showed antimicrobial activity on *S. aureus, B. cereus, E. faecalis* and *C. albicans*. EtOAc extract showed highest activity against *Bacillus cereus* (ID = 20.50 ± 0.35mm). The leaf sample can be used to treat diarrhea, emetic toxin, nausea and vomiting.

The antioxidant activity of ethanol and watery extracts of the leaf of Pu Si Nan was evaluated by DPPH free radical scavenging method. In the study of antioxidant activity, the IC_{50} values of ethanol and watery extracts of the leaf part of Pu Si Nan were observed as 38 μg/mL and 127 μg/mL respectively. The ethanol extract of *Mentha spicata* L. leaf was observed that potent antioxidant activity than watery extract but weak activity than standard BHT (IC_{50}= 11.71 μg/mL).

Some phytochemical constituents (3-carene, D-limonene, *trans*-carveol, D-carvone, 2-cyclohexen-1-one, 3-methyl-6-(1-methylethylidene), beta-bourbonene and alpha-copaene were extracted from the essential oils of *Mentha spicata* L. leaf (Pu Si Nan).

Acknowledgements

The authors would like to thank the Department of Higher Education (Yangon office), Ministry of Education, Yangon, Myanmar, for the permission of doing this research and for allowing to write this paper. Our deepest gratitude is expressed to Dr Nu Nu Yi and Dr Nay Thwe Kyi, Prorectors, Dagon University, for their invaluable advices.

References

AOAC. (1990). "Official Method of Analysis of the Association of Official Analytical Chemists", Ed. Helrich, K. Virgenia; 15th Ed. 1, AOAC Inc.

Basim, H., Yegen, O. and Zeller, W. (2000). "Antibacterial Effect of Essential oil of Thymbra *spicata* L. var. *spicata* on some Plant Pathogenic Bacteria". *Zeitschrift fur Pflanzenkr. Pflanzenschutz*, vol. 108, pp. 279-284

Boukef, M. K. (1986). "Traditional Medicine and Pharmacopoeia". *Plants in the Traditional Tunisian Medicine*; Agency of cultural and Technical Copperation: Paris, France, pp. 195-206

Cheeseman, K. H. and Slater, T. F. (1993). "Introduction to Free Radical Biochemistry". *British Medical Bulletin*, vol. 49 (3), pp. 481-493

Harborne, J. B. (1984). *Phytochemical Methods, "A Guide to Modern Techniques of Plant Analysis"*, New York: 2nd Ed., Chapman and Hall, pp. 120-126

Kumar, A., Choudhury, R. P. and Garg, A. N. (2006). "Analysis of Indian Mint (*Mentha spicata*) for Essential, Trace and Toxic Elements and its Antioxidant Behaviour". *Journal of Pharmaceutical and Biomedical Analysis*, vol. 41, pp. 825-832

Leea, E. L., Vitaly, I. V., Myaung-Woo, B. and Cherl-Ho, L. (2002). "Detection of Free Radicals in Gamma-irradiated Soybean Paste and Model System by Electron Spin Resonance Spectroscopy". *Radiation Physics and Chemistry*, vol. 64, pp. 61-66

Leporatti, M. L. and Gheira. K. (2009). "Comparative Analysis of Medicinal Plants Used in Traditional Medicine in Italy and Tunisia". *J. Ethnobiol. Ethnomed*, vol. 5, pp. 31-39

Liu, R. H. (2003). "Health Benefits of Phytochemicals". *Journal of Clinical Nutrition*, vol. 78, pp. 5175-5205

Marini-Bettolo, G. B., Nicolettic, M. and Patamia, M. (1981). "Plant Screening by Chemical and Chromatographic Procedure under Field Conditions". *J. Chromato*., vol. 213, pp. 113-127

Robinson, T. (1983). "*The Organic Constituents of Higher Plant"*. North Amberst: 5th Ed. Cordus Press, pp. 285-286

Snoussi, M., Noumi, E., Trabelis, N., Flanini, G., Papetti, A. and Feo, Y. D. (2015). "*Mentha spicata* Essential Oil, Chemical Composition, Antioxidant and Antibacterial Activities against Planktonic and Biofilm Cultures of *Vibrio* spp. Strains". *Molecules*, vol. 20, pp. 14402-14424

Tetika, F., Civelek, S. and Cakileioglu, U. (2013). "Traditional Uses of Some Medicinal Plants in Malatya (Turkey). *J. Ethnopharma col*, vol. 146, pp. 331-346

SOME APPLICATION OF NATURAL DYE EXTRACTED FROM *EUCALYPTUS GLOBULUS* LABILL (EUCALYPTUS) BARK ON COTTON

Zin Mar Oo[1], Nwe Nwe Aung[2], Mya Theingi[3]

Abstract

The raw sample barks (Eucalyptus) were collected from Aunglan Township, Magway Region. Natural dyes were extracted from the bark of Eucalyptus by water. The prepared natural dye was characterized by FT IR. The phytochemical tests of extracted natural dye were carried out. The maximum wavelength (λ_{max}) of Eucalyptus dyes extracted with water at 483 nm was determined by UV-spectrophotometer. The percentage of bio-mordants was determined. And then, the effect of dyeing time was studied by using colour densitometer at three mordanting methods. The extracted natural dyes were also used on cotton cloth by three mordanting methods. Extracted dye though Specifically identified, from Eucalyptus bark was as adsorbate. Cotton cloth was used as adsorbent. The colour intensities of these dyed cotton cloth was determined by Reflection Transmission Colour Densitometer. Depending on the type of mordant, such as onion peel, jengkol peel and tea waste (bio-mordants), colour fastness of the dyeing cotton cloth were studied. And then, cotton can also be dyed by using post mordanting methods. In addition, the antimicrobial activities of Eucalyptus dye were investigated by Agar Disc Diffusion method on six tested organisms.

Keywords: Natural dye, Eucalyptus bark, mordants, dyeing process

Introduction

The natural dyes have been traditionally extracted from animal and plant sources for use in colouring food substrate, leather, wood and natural fibers such as silk, cotton and flax from time immemorial. The main advantage of using natural dyes is the fact that their source is renewable, biodegradable and reduces environmental impact. They produce very uncommon, soothing and soft shades which are refreshingly different from the strong bright colour produced by synthetic dyes (Chengeto *et al.,* 2016)

Dyes are a kind of magic, a delight to the eye and a joy to use. Even a brief inquiry into the early discoveries and uses of these colouring agents conveys a sense of mystery and glamour. Primitive people in many different parts of the world discovered that certain root, leaf or bark material could be treated to produce colour in a fluid form. Its application was both religious and functional the embellishment of body, clothing and utensils. A dye is a colourant that penetrates the actual fiber and appears to become a part of it. The best colour fastness is attributed to those dyes which must successfully colour the total fiber (Joshi *et al.,* 2015). Most of the natural dyes have no substantively on cellulose or other textile fibers without the use of a mordant. Aqueous extraction of natural dyes was most preferred method by textile dyers. The standardized dyeing techniques are needed for the better commercialization of natural dyes.

Natural dyes have less substantivity to the fiber and have poor fastness properties, hence require a mordant to improve their fixation in the fiber by forming a mordant- dye complex through chemical bonds. Mordants are metal salts which produce affinity between dye and the fiber. Mordants not only help in dye uptake and colour fastness, it also helps in achieving different colour shades in the textiles (Samanta *et al.,* 2009)

The majority of natural dyes need a mordanting chemical (preferably metal salt or suitably coordinating complex forming agents) to create an affinity between the fiber and dye or the pigment molecules of natural colourant. These metallic salts as mordant form metal complexes

[1] PhD Candidate, Department of Chemistry, University of Yangon
[2] Lecturer, Department of Chemistry, University of Yangon
[3] Associate Professor, Department of Chemistry, Taunggoke Degree College

with the fibers and the dyes (Samanta *et al.,* 2011). Bio-mordants are onion peel, jengkol peel and tea waste. Tannin is a widely used as bio-mordant. Tannin was used for dyeing and printing by people from onion peel, jengkol peel and tea waste. Nowadays in most of the countries, natural dyeing is practiced only as a handcraft and synthetic dyes are being used in all commercial dyeing processes. However, with the worldwide concern over the use of eco-friendly and biodegradable materials, the use of natural dyes has once again gained interest (Geetha *et al.,* 2013). Natural dyes are known to exhibit better biodegradability, less toxicity, eco-friendly alternative to synthetic dyes and some dyes also medicinal properties.

Materials and Methods

Sample Collection

Eucalyptus bark is the sample used in this study for extraction of dye, which was collected from the Aunglan Township, Magway Region. The part used for the dye extraction was only bark. And then, they were washed with distilled water and dried at room temperature, and made into fine powder. Cotton cloth was purchased from Shwetaung Myoema Market, Bago Region. Bio–mordents (onion, jengkol and tea waste) and cottons were collected from Mindom Myoma Market.

Extraction of Dyes with Water

The barks of Eucalyptus were collected, chopped, dried and ground to fine powder to allow for most intimate contact with solvent. Air dried powder Eucalyptus (10 g) were extracted with each 100 mL of solvent (water) in Sonicator for 3 times each 30 min and filtered. The filtrates were evaporated by distillation semi-dried solid mass at temperature 100˚C. And then, they were dried in oven and were crushed in mortar and pestle for semi-dried solid mass and sieved with 90 μm aperture size. Finally, dye powders of water extract was 38 %.

Determination of Physicochemical Properties and Characterization of Dyes

Physicochemical Properties

Eucalyptus bark powders were washed with water to remove the adhering dirt and impurities. They were dried at room temperature and weighed. The physicochemical characteristics of Eucalyptus bark powder such as moisture content, ash content were determined by AOAC method and pH was determined by pH meter.

Phytochemical Investigation of Eucalyptus Dye

Phytochemical investigation of Eucalyptus dye was performed to determine the presence or absence of phytochemical compounds according to the methods and procedures expressed in the Phytochemical Bulletin of Botanical Society of America (Harborne, 1998).

FT IR Spectroscopy

FT IR measurements were carried out to determine the functional group of natural dye extracted from Eucalyptus. All measurements were carried out in the range of 400-4000 cm^{-1}. The dye samples were measured by using Prekin Elmer GX system, FT IR spectrophotometer.

Determination of Antimicrobial Activities of Natural Dye

The extracted dye solutions were tested with *Aspergillus flavus, Bacillus subtilis, Candida albicans, Pseudomonas fluorescens, Xanthomonas oryzae* and *Echerichia coli* species to investigate the nature of antimicrobial activities by agar disc diffusion Method**.**

Dyeing the Extracted Natural Dye with Cotton Cloth

The pretreated cotton cloth was dyed using extracted dyes (water) from Eucalyptus. The concentration of (1000 ppm) dye solution dyeing on cotton cloth was studied in terms of temperature and pH. The temperature was varied in 40-90 °C and pH was changed in the value of 3-9 by using UV-visible spectrophotometer. And then, the most suitable conditions for dyeing on cotton cloth were selected. The amount of adsorption at equilibrium q_t (mg/g) and Eucalyptus dyes were calculated by this equation:

$$q_t\,(\text{mg/g}) = \frac{\text{Co}-\text{Ce (mg/L)}}{\text{unit mass of } adsorbent\ (g)} \times \text{volume of solution (L)}$$

where, q_t = adsorption capacity (mg/g), C_o = initial concentration (mg/L)

C_e = equilibrium concentration (mg/L), unit mass of adsorbent = 1 g

Effect of Temperature

Bath adsorption experiments were conducted by 1 g of cotton cloth to 100 mL of dye solutions with water in a 250 mL beaker with a temperature control of 80 °C ± 5 °C. The original pH was used. A 100 mL dye solution in a 250 mL beaker was put in water bath. Natural dye solution dyeing on cotton cloth was allowed to reach the equilibrium for 60 min in a water bath at 40, 50, 60, 70, 80 and 90 °C. At 10 min intervals, the dye solution was taken out from the beaker. The remaining dye concentration was determined by UV-visible spectrophotometer at λ_{max} 483 nm for watery extracted dye. The results were shown in Figure 3.

Effect of pH

The effect of pH on dyeing the cotton cloth with the extracted dye was conducted by the same procedure for equilibrium over a range of pH values (3, 4, 5, 6, 7, 8 and 9) which were adjusted with HCl and NaOH. The results were illustrated in Figure 4.

Extraction of Bio-mordants

The raw onion, tea waste and jengkol peel (10 g) each was extracted with distilled water (1 L) and then setup was kept for 60 min boiling. The extracted tannin was filtered and was used for mordanting.

Pretreatment of Cotton Cloth

The cotton cloth was soaked in mixture of 1g / L of sodium carbonate and 2.5 g / L of detergent at 80 °C for 30 min and then washed with running tap water to remove the natural impurities and improve the texture of cotton cloth for dyeing.

Determination of Dyeing Time on Cotton Cloth by Three Mordanting Methods

The dyeing time were studied by using three mordanting methods (pre-mordanting, simultaneous mordanting and post mordanting). The dyeing time were determined by using colour densitometer. The suitable dyeing time were selected for dyeing methods.

Dyeing Procedure for Cotton Cloth

The pretreated cotton cloth was dyed using water extracted dye from Eucalyptus bark and selected 20 % of bio-mordant (onion peel, jengkol peel and tea waste) at the optimum temperature 80 °C, dyeing time 60 min and pH 6 by using pre-mordanting, simultaneous mordanting and post-mordanting methods.

Determination of Colour Density for Dyeing Cotton on Colour Fastness

The colour density of dyeing cotton cloth before and after sun exposure and washing were determined by Reflection Transmission Colour Densitometer at Universities' Research Centre, Yangon (cf. section 3.6)

Some Application of Natural Dye Extracted from Eucalyptus Bark Dyeing on Yarn

The cotton was collected from Mindom Myoma Market, Magway Region. Firstly, the cotton was soaked with water to remove the dirty and impurity at overnight. The cotton (2 g) was dyed with 20 % onion peel, jengkol peel and tea waste (bio-mordants) and 3 g w/v of extracted dye powder at 80 °C for 1 hr by firing. And then, the cotton was dried in sunlight at 4 hr and the dried yarn was trampled with rice to stiff for weave. The next is firmed step. Finally, the firm fibers were obtained. The weaving steps were shown in Figure 9.

Results and Discussion

The physicochemical characteristics of Eucalyptus bark powder and phytochemical investigation of water extracted dye sample were determined. Table 1 indicates that the results of 7.45% w/w moisture content, 3.25 % w/w ash content and pH 6.50 in raw sample were observed.

Table 1 Physicochemical Properties of Eucalyptus Bark Powder

No.	Characteristic	Content
1	Moisture Content (%)	7.45
2	Ash Content (%)	3.25
3	pH	6.50

Phytochemical Constituents of Eucalyptus Dye

According to the results of phytochemical analysis, it was found that alkaloids, flavonoids, glycosides, phenolic compounds, tannins, α-amino acids and saponins were present in the extracted Eucalyptus dye sample whereas carbohydrates, steroids and starch were absent in this extracted dye sample.

FT IR Analysis

Figure 1 show the FT IR spectrum of natural dyes extracted from Eucalyptus with water. The characteristic absorption bands at 3300, 2885, 1616, 1444 and 1049 cm^{-1} were observed. These peaks correspond to the groups present in the sample and are indicated to O-H stretching, C-H stretching, C=O stretching, C-H bending and C-O stretching which is the good correlation with that of literature. These bands were confirmed the presence of alkaloids, tannins and flavonoids in natural dye (Silverstein *et al.*, 2003).

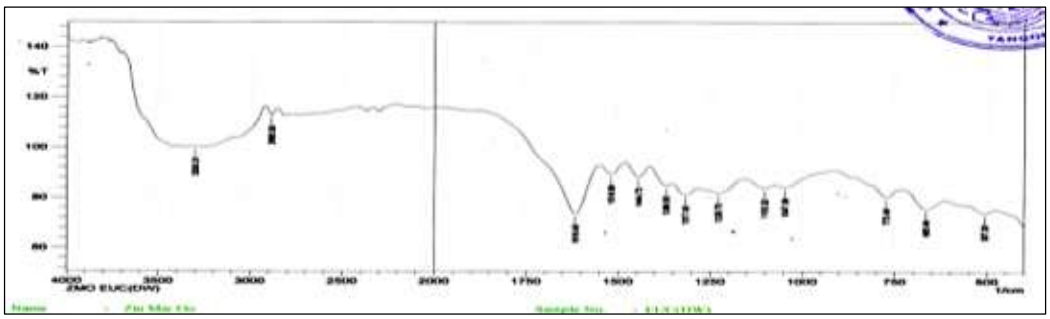

Figure 1 FT IR spectrum of natural dyes extracted from Eucalyptus with water

Antimicrobial Activities of the Extracted Dye from Eucalyptus

It was important to study the antimicrobial activity on dyes extracted from Eucalyptus because natural dyes showed inhibition effect against test bacterial in solution. The results were shown in Table 2 and Figure 2. Among these solvents, watery extract did not show antimicrobial activity against test organisms. Petroleum ether extract showed the highest activity while acetone, ethyl acetate and methanol extract exhibited the lowest activity against six types of microorganisms. The antimicrobial activity might be due to ellagic acid and tannin components.

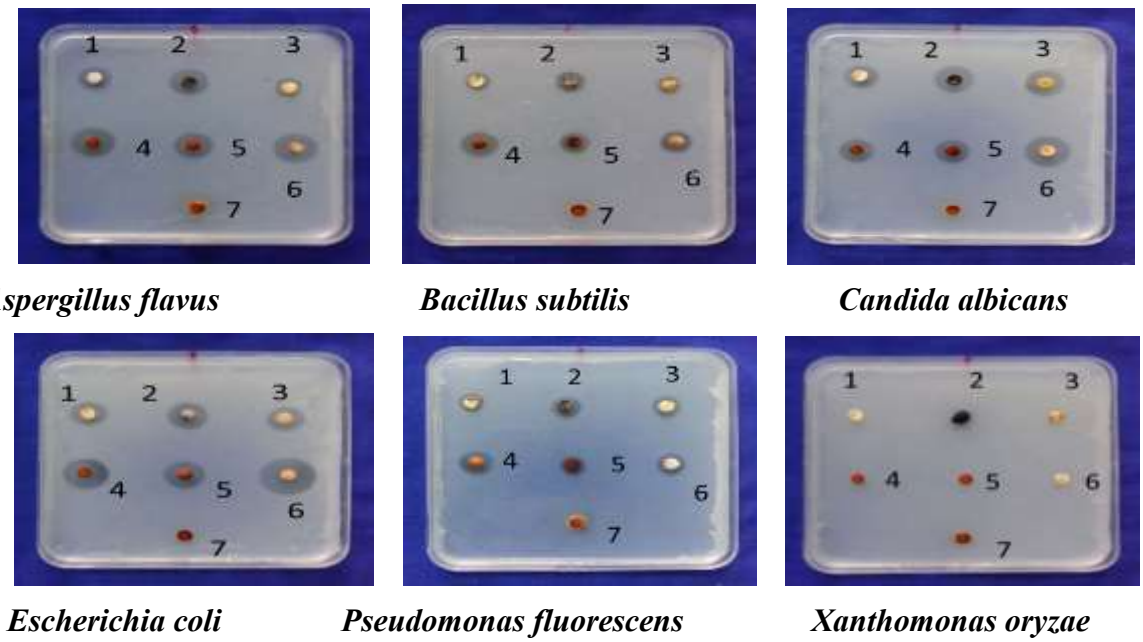

Aspergillus flavus ***Bacillus subtilis*** ***Candida albicans***

Escherichia coli ***Pseudomonas fluorescens*** ***Xanthomonas oryzae***

Figure 2 `Antimicrobial activities of various solvent extracts of Eucalyptus dye (1.acetone 2.chloroform, 3.ethylacetate, 4.ethnaol, 5.methanol, 6.pet.ether and 7. water)

Table 2 Antimicrobial Activities of Eucalyptus Dye

No.	Test Organisms	Acetone	$CHCl_3$	EtOAc	EtOH	MeOH	Pet.eth	H_2O
1	*Aspergilus flavous*	+(10)	+(12)	+(8)	+(14)	+(12)	+(14)	-
2	*Bacillus subtilis*	+(8)	+(10)	+(8)	+(14)	+(10)	+(12)	-
3	*Candida albicans*	+(12)	+(14)	+(14)	+(12)	+(12)	++(16)	-
4	*Escherichia coli*	+(14)	++(16)	+(14)	++(18)	++(16)	+++(22)	-
5	*Pseudomonas fluorescens*	+(8)	+(10)	+(10)	+(12)	+(8)	+(10)	-
6	*Xanthomonas oryzae*	-	-	-	-	-	-	-

Agar Disc Diffusion Method -6 mm, 6 mm ~ 12mm (+), 15 mm ~ 19mm (++), 20 mm above (+++), No activity (-)

Sorption of the Extracted Natural Dye from Eucalyptus on Cotton Cloth

Effect of temperature

The adsorption properties of water extracted dye were studied at different temperatures (40-90 °C). In dyeing, the optimum temperature of extracted natural dyes on cotton cloth was 80 °C.

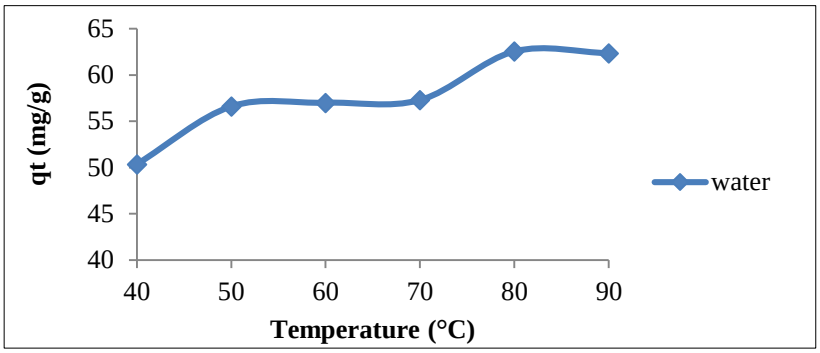

Figure 3 Effect of temperature on dyeing of Eucalyptus dyes extracted by water

Effect of pH

The original pH of extracted dyes (water) was 6.50. The pH values of extracted natural dye were adjusted with 1 % HCl and 1 % NaOH to reach the pH values of 3, 4, 5, 6, 7, 8 and 9. The optimum pH of extracted natural dyes was 6.

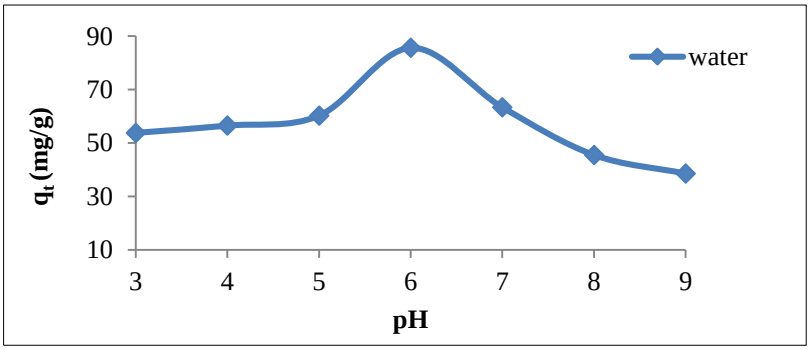

Figure 4 Effect of pH on dyeing of Eucalyptus dyes extracted by water

Determination of Dyeing Time by Three Mordanting Methods

Table 3 shows the suitable percent of bio-mordants. According to the Tables (4, 5, 6 and 7), the effect of dyeing time were studied by using three mordanting methods (pre-mordanting, simultaneous mordanting and post mordanting). The suitable amount of dyeing time was observed at 60 min for three mordanting methods.

Table 3 Colour Density of Extracted Natural Dye with Different Bio-mordants

No.	Volume of Natural dye (mL)	Percentage of Bio-mordants (%) v/v	Colour density/ mordant		
			Onion peel	Jengkol peel	Tea waste
1	100	10	0.35	0.38	0.36
2	100	**20**	**0.76**	**0.74**	**0.70**
3	100	30	0.41	0.44	0.42

- Suitable percent of bio-mordants, size of cotton=3.5”length x 3.5’’ wide,

  Dyeing temperature= 80 °C

Table 4 Effect of Dyeing Time on the Amount of Extracted Eucalyptus Dye on Cotton Cloth Using Direct Dyeing Method

No.	Volume of Natural Dye (mL)	Dyeing Temp (°C)	Dyeing Time (min)	Colour densities
1	100	80	40	0.32
2	100	80	50	0.33
3	100	80	**60**	**0.36**
4	100	80	70	0.34

- Suitable dyeing time, Amount of bio-mordants =20 %, size of cotton =3.5" length x 3.5' wide

Table 5 Effect of Dyeing Time on the Amount of Extracted Eucalyptus Dye on Cotton Cloth Using Pre-mordanting Method

No.	Volume of Natural Dye (mL)	Dyeing		Colour Densities		
		Temp (°C)	Time (min)	Onion peel S_2	Jengkol peel S_3	Tea waste S_4
1	100	80	40	0.36	0.32	0.34
2	100	80	50	0.38	0.35	0.35
3	100	80	60	**0.47**	**0.42**	**0.38**
4	100	80	70	0.42	0.39	0.36

- Suitable dyeing time, Amount of bio-mordants =20 %, size of cotton =3.5" length x 3.5' wide

Table 6 Effect of Dyeing Time on the Amount of Extracted Eucalyptus Dye on Cotton Cloth Using Simultaneous Mordanting Method

No.	Volume of Natural Dye (mL)	Dyeing		Colour Densities		
		Temp (°C)	Time (min)	Onion peel S_2	Jengkol peel S_3	Tea waste S_4
1	100	80	40	0.46	0.40	0.36
2	100	80	50	0.48	0.42	0.38
3	100	80	**60**	**0.50**	**0.43**	**0.41**
4	100	80	70	0.47	0.37	0.39

- Suitable dyeing time, Amount of bio-mordants =20 %, size of cotton =3.5" length x 3.5' wide

Table 7 Effect of Dyeing Time on the Amount of Extracted Eucalyptus Dye on Cotton Cloth Using Post Mordanting Method

No.	Volume of Natural Dye (mL)	Dyeing		Colour Densities		
		Temp (°C)	Time (min)	Onion peel S_2	Jengkol peel S_3	Tea waste S_4
1	100	80	40	0.45	0.42	0.37
2	100	80	50	0.47	0.43	0.38
3	100	80	**60**	**0.53**	**0.45**	**0.42**
4	100	80	70	0.50	0.41	0.40

- Suitable dyeing time, Amount of bio-mordants =20 %, size of cotton =3.5" length x 3.5' wide

Colour Fastness Properties of Eucalyptus Dye Extracted with Water Dyeing on Cotton Cloth

Colour density on the cotton cloth was increased significantly when a mordant was used. The size of cotton was used 3.5" length x 3.5' wide for dyeing process. The colour fastness cotton cloth samples were prepared using pre-mordanting, simultaneous mordanting and post mordanting, 20 % v/v dye concentration, pH 6, temperature at 80 °C and 60 min dyeing time because those conditions resulted in the highest colour strength for cotton cloth. The suitable amount of bio-mordants was selected by colour densities. The effect of dyeing time on the amount of extracted Eucalyptus dye on cotton cloth were studied by using direct dyeing method, pre-mordanting, simultaneous and post mordanting method. Among three mordanting methods, post-mordanting method was the best for dyeing process. In this, the maximum dyeing time were also studied by colour densities. And then, using the above optimum conditions, the colour density for Eucalyptus dye extracted with water solution dyeing on cotton cloth before and after colour fastness testing were compared in Figures 5, 6,7 and 8. For the dyeing on cotton cloth, the dyed cotton cloth without mordant was seen the lowest colour density. Among mordants, natural mordant (onion peel) was the highest colour density whereas jengkol and tea waste were nearly equal colour density. It was also found that onion peel was good in colour fastness (Li *et al*., 2016).

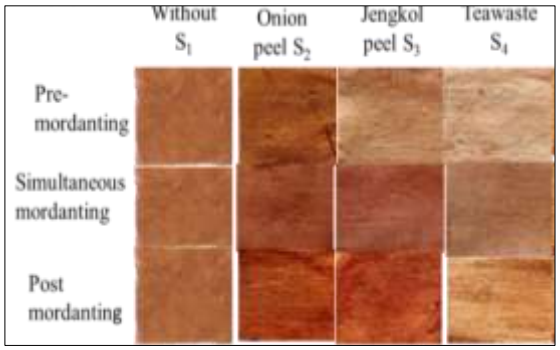

Figure 5 Colour of cotton cloth dyeing water extract of Eucalyptus dye (i)pre-mordanting, (ii)simultaneous mordanting and(iii) post mordanting

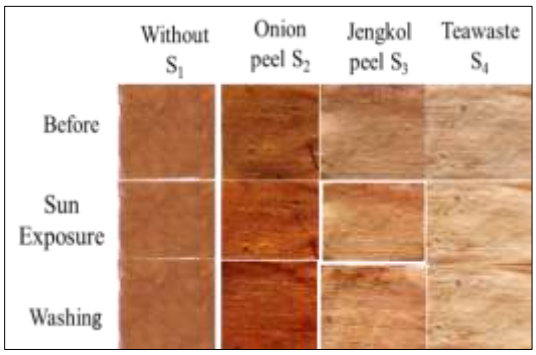

Figure 6 Colour of cotton cloth dyeing water extract of Eucalyptus dye by pre- mordanting method

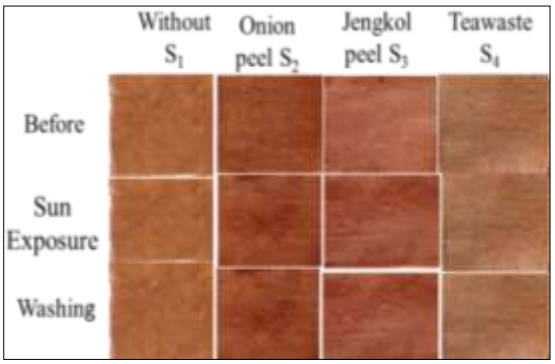

Figure 7 Colour of cotton cloth dyeing water extract of Eucalyptus dye by simultaneous mordanting method

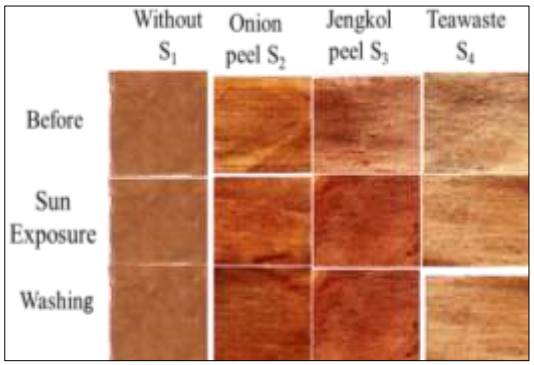

Figure 8 Colour of cotton cloth dyeing water extract of Eucalyptus dye by post mordanting method

Some Application of Natural Dye Extracted from Eucalyptus using Bio-mordants on Cotton

Cotton was dyed, using three types of bio-mordants with dyes obtained from Eucalyptus and colour fastness was compared. They were applied to dye not only cotton cloth but also pure cotton. Post mordanting method was used that gives the outcome of the best colour fastness and the dyed cotton can be seen in Figure (c). After that, stiffen the cotton using rice for weaving is as shown in Figure (d). In Figures (e) and (f), the cotton for weaving is knotted to a tie. The cotton weaved by using three types of bio-mordants are shown in Figure (g). The two courses of dyeing process show that weaving cotton cloth with purely dyed cotton is lighter in tone than to dye cotton cloth after weaving.

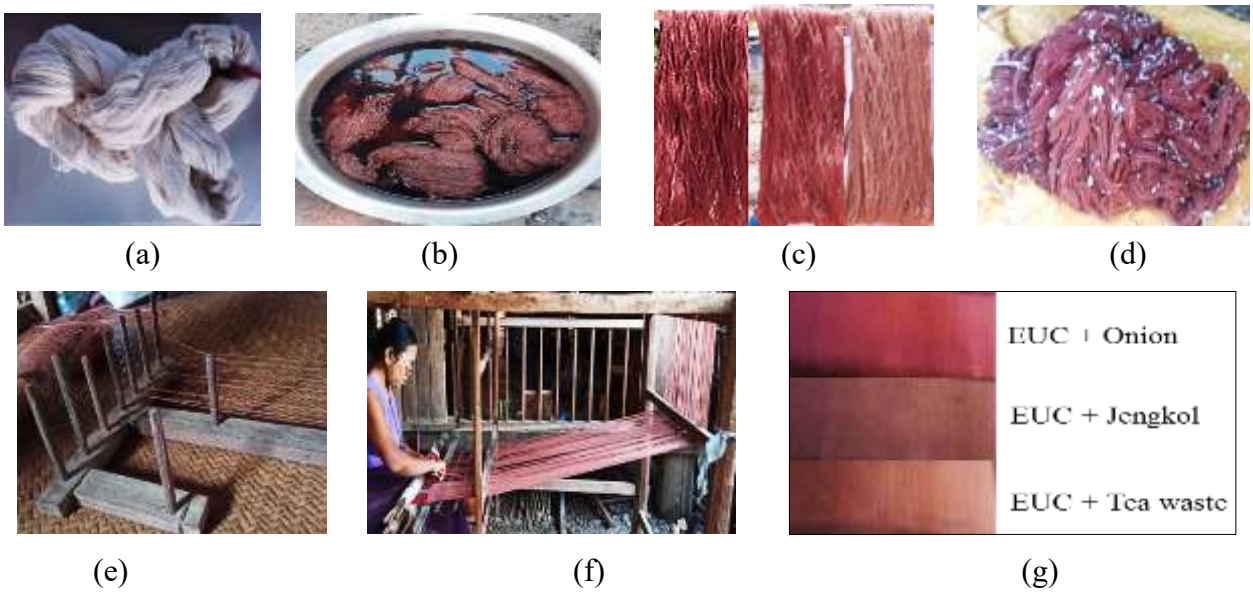

(a) (b) (c) (d)

(e) (f) (g)

Figure 9 Weaving steps of the cotton by the extracted natural dye from Eucalyptus with water (a) cotton (b) dyeing, (c) drying, (d) trample, (e) tiding, (f) weaving and (g) cloth

Conclusion

Natural dyes were extracted from Eucalyptus bark powder with water. The physicochemical properties of Eucalyptus raw bark were investigated. In phytochemical test, tannins, steroids, alkaloids, flavonoids, glycosides, phenolic compounds, saponins and α-amino acids were observed in the extracted dyes of water whereas carbohydrates and starch were absent in this extracted dye. According to the FT IR analysis, Eucalyptus dyes extracted by water, functional groups of O-H, C-H, C=O (stretching), - CH bending and C-O stretching were observed. . Furthermore, antimicrobial activities of acetone, chloroform, ethyl acetate, ethanol, methanol, petroleum ether and water extracted dye from Eucalyptus were investigated by agar disc diffusion method. Among these extracted dyes, watery extract did not show antimicrobial activity in all test organisms. If the dyed cotton wears, there were not be toxic on human skin and other effectives. Thus antimicrobial activities were also tested. The maximum absorption wavelength (λ_{max}) of Eucalyptus dyes extracted by water was 483 nm. The suitable amounts of bio-mordants were selected by colour densities. The effect of dyeing time on the amount of extracted Eucalyptus dye on cotton cloth were studied by using direct dyeing method, pre-mordanting, simultaneous and post mordanting method. The colour fastness of dyed samples was determined by three mordanting methods. Among three mordanting methods, post-mordanting method was the best for dyeing process. For the dyeing on cotton, the dyed cotton without mordant was seen the lowest colour density. Among mordants, bio-mordants (onion) were highest colour density whereas jengkol and tea waste were nearly equal colour density. Further, cotton can be dyed by traditional methods. The cotton is

steadier colour than cotton cloth. Thus, not only the cotton cloth but also cotton can be dyed. Nowadays most of the natural dyers are interested to use the natural dye materials in the same ways used for synthetic dyes.

Acknowledgements

The authors would like to express their profound gratitude to the Department of Higher Education, Ministry of Education, Yangon, Myanmar, for provision of opportunity to do this research and Myanmar Academy of Arts and Science for allowing to present this paper.

References

Ali, S., Nisar, N. and Hussain, T. (2006). "Dyeing Properties of Natural Dyes Extracted from Eucalyptus". *J. Text. Inst.*, vol. 98, pp. 559-562

Chengeto, Z., Cathrine, C., Clever, K. M., Vernon, M., Felicity, P., Bettina, B., Mafika, K.N. and Joel, T. (2016). Yellow Dye Extraction from Eucalyptus Grandis Bark". *Am. J. Eng. Res.*, vol. 5,pp. 10-18

Geetha, B. and Judia Harriet Sumathy, V. (2013). "Extraction of Natural Dyes from Plants*". International Journal of Chemistry and Pharmaceutical Sciences,* vol. 1(8), pp. 502-509

Harborne, J.B. (1998). *Phytochemical Methods, A Guide to Modern Technique of Plant Analysis*. New York; 3rd Ed., Chapman and Hall, pp. 120-160.

Joshi, S., Sunseeta, G.R., Chandarkar, R. and Madan, S. (2015). "Use of Plant Dyes in Textiles Industries". *Indian JL. Sci,* vol. 5(1), pp.111-114

Li, Y.V., Malensek, N., Sarkar, A.K. and Xiang, C. (2016). "Colour fastness Properties of Persimmon Dye on Cotton and Wool Fabrics". *Clothing and Textile Research Journal*, vol. 34(3), pp. 223-234.

Samanta, A. K and Konar, A. (2011). *Dyeing of Textiles with Natural Dyes, Institute of Jute Technology, University of Calculta India*, pp.29-56

Samanta, A.K. and Agarwal, P. (2009). "Application of Natural Dyes on Textiles". *Indian Journal of Fiber and Textile Research,* vol. 34, pp. 384-399.

Silverstein, R.M., Webster, F.X. and Kiemle, D. J. (2003). *Spectrometric Identification of Organic Compounds*, New York: 7th Edition, John Willey and Sons, Inc.

PURIFICATION AND CHARACTERIZATION OF PHOSPHOLIPASE FROM CABBAGE LEAF (*BRASSICA OLERACEA* L.)

Mar Mar Soe[1], San San Myint[2], Kyaw Naing[3]

Abstract

Phospholipase (EC 3.1.4.4) is wide spread distribution in animals and plants. Phospholipase can occur naturally in cabbage leaves, peanut seeds, rat liver, human liver, snake liver, etc. Phospholipase enzyme catalyzed the hydrolysis of phospholipids to phosphatidic acid and the corresponding free base. Phospholipase activities are present in all organisms from bacteria to mammals. Phospholipase enzyme from cabbage leaves was with sodium chloride salt solution, successive ammonium sulphate (40 and 60%), finally crude phospholipase extract (250 mL) was obtained. Further purification was carried by using Sephadex G-200 gel filtration technique. The eluents (fraction numbers) were analyzed for protein content (280 nm) and phospholipase activity (558 nm). The fraction (32-42) showing the highest phospholipase activity were pooled and subsequent studies were done using this pooled solution. The protein contents of the enzyme was determined by using Biuret method. The wavelength of maximum absorption of copper-protein complex in Biuret method was found to be 550 nm. After purification, the specific activity, the relative purity of the enzyme, increased about (7) folds from crude to final purification step. In this research, the molecular weight of the purified phospholipase enzyme was determined by using SDS-PAGE Technique. The purity and homogenity of the phospholipase enzyme were confimed as a single band on gel electrophoresis chromatogram. In this research, effect of metal ions (Mn^{2+}, K^{+}, Na^{+}, Ca^{2+}, Co^{2+}, Zn^{2+}, Cu^{2+}, Pb^{2+} and Hg^{2+}) on phospholipase activities were stud~~ied~~. The Ca^{2+} ion showed the highest activating effect on phospholipase activities. The Pb^{2+} and Hg^{2+} lead to the total denaturing of the enzyme proteins.

Keywords: Phospholipase, cabbage leaf, phosphatidyl choline, SDS-PAGE, phospholipids, Sephadex G-200 gel chromatograph~~y~~

Introduction

The aim of this work is to study isolation, purification and some enzymic characterization of phospholipase from cabbage leaf. The cabbage (*Brassica oleracea* Capitata Group) is a plant of the family *Brassicaceae or Cruciferae*. It is an herbaceous, biennial, and dicotyledonous flowering plant with leaves forming a characteristic compact cluster. Cabbages grown late in autumn and in the beginning of winter are called coleworts. Cabbage is a leaf vegetable. Cabbage has a long history of use both as a food and a medicine. Cabbage is an excellent source of vitamin C. It is also a very good source of fiber, manganese, folate, vitaminB6, potassium and omega-3 fatty acids. Cabbage is also a good source of thiamin (vitamin B1), riboflavin (vitamin B2), calcium, potassium, magnesium, vitamin A and protein. Cabbage also contains phytochemicals called indoles and sulforaphane, the breakdown products of compounds called glucosinolates (Ensminger, 1986). Cabbage leaves are used to treat acute inflammation. A paste of raw cabbage may be placed in a cabbage leaf and wrapped around the affected area to reduce discomfort. Some that it is effective for relieving painfully engorged breasts in breastfeeding women. Cabbage contains significant amounts of glutamine, amino acids, which has anti-inflammatory properties. It is a source of indol-3-carbin or I3C, a compound used as an adjuvent therapy for recurrent respiratory papillomatosis, a disease of the head and neck caused by human papilloma virus (usually type 6 and 11) that causes growths in the airway that can lead to death (Alison, 2006).

[1] Assistant Lecturer, Department of Chemistry, Dagon University
[2] Associate Professor, Department of Chemistry, Pyay University
[3] Deputy Permanent Secretary, Ministry of Education, Myanmar

Phospholipase

A phospholipase is an enzyme that converts phospholipids into fatty acids and other lipophilic substances. There are four major classes, termed A, B, C, D.

Phospholipase A_1**:** A fungal enzyme.

Phospholipase A_2**:** a) This enzyme removes the acyl group at C-2 for prostaglandin and leukotriene synthesis. This enzyme is also present in snake venom. Large amount of lysolecithin is produced after snake bite and acts as a potent haemolytic agent.

b) The enzyme lecithin cholesterol acyl transferase (LCAT) uses this acyl group for esterification of cholesterol.

c) The acyl group at C-2 is mostly unsaturated and prone to oxidation change.

Phospholipase B**:** Also acts at this site but its substrate is a lysophospholipid and not a phospholipid.

Phospholipase C**:** This is membrane bound enzyme. It is activated by certain hormones, generating into sitol-P_3 and diacylglycerol which modify activities of certain enzymes.

Phospholipase D**:** Basically, a plant enzyme is getting the attention of biotechnologists due to its very interesting applications (Dennis, 1991).

These enzymes are distinguished by the type of reaction they catalyze**:**

Phospholipase A

PL A_1- cleaves the SN-1 acyl chain

PL A_2- cleaves the SN-2 acyl chain

Phospholipase B- cleaves both SN-1 and SN-2 acyl chain, also known as lysophospholipase.

Phospholipase C- cleaves before the phosphate, releasing diacylglycerol and a phosphate – containing head group. Phospholipase C plays a central in signal transduction, releasing the second messenger Inositol triphosphate.

Phospholipase D-cleaves after the phosphate, releasing phosphatidic acid and an alcohol.

Occurrences of Phospholipase

Phospholipase D (PLD, phosphatidylcholine phosphatido-hydrolase, EC 3.1.4.4) has a very broad distribution in living organisms. It was first isolated in various kind of cabbage and has since been recognized in a number of plants including *ricinus*, castor beans, spinach leaves, soy beans and others (Madorey, 1997). Numerous bacterial sources are rich in PLD. The enzyme can be obtained in the culture broth of various *Streptomyces* (Ulbrich, 2003).

Phospholipase-catalyzed Reaction

Phospholipase enzyme exhibits two types of reaction are hydrolysis and transphosphatidylation. When this enzyme hydrolyzes phospholipids, such as phosphatidyl-choline (PC), it forms phosphatidic acid (PA) and choline (Liscovitch, 2000). Phosphatidic acid is an important second messenger in mammalian signal transduction pathways. Many PLDs, in the presence of an alcohol, are able to catalyze the exchange of the polar head group in addition to the hydrolysis product. Transphosphatidylation occurs with different degree of selectivity depending on the enzymatic source, the nature of the alcohol and its concentration (Yang, 1967).

Application of PLDs, PLs and PAs

Phospholipids are present in all living organisms. They are a major component of all biological membranes, along with glycolipids and cholesterol. Enzymes aimed at modifying phospholipids, namely, phospholipase, are consequently wide spreading nature. Phospholipase (A_1, A_2, C and D) are a complex and crucially important group of enzymes that hydrolyze phospholipids (PLs) releasing a variety of products, like for example lyso-phospholipids, free fatty acids (FFAs), diacylglycerols (DGs), choline phosphate and phosphatidates, depending on the site of hydrolysis. They play crucial roles in many biochemical processes related among others, digestion and inflammation (Shimizu *et al*, 2006). The use in industrial processes is increasing through the ability of optimizing the enzyme by protein engineering. Nowadays, phospholipase play key roles in bread making, egg yolk industry (emulsification for different applications) and refinement of vegetable oils (degumming). Phospholipids (PLs) are the constituents of all biological membranes. Due to their superior emulsification properties, phospholipids and their partial hydrolysis products, lysophospholipids, have numerous applications in food, cosmetics, pharmaceutical and other industries (Vance, 2002). Their properties depend on the fatty acid components and the polar component bound to the glycerol backbone. By changing the hydrophilic/lipohilic balance of phospholipids using lipase or phospholipases, it is possible to produce tailor made lecithin for specific applications (Cichowiez, 1993). Phosphatidic acid (PA) is a useful starting material for chemical synthesis of phospholipids. The chemical acylation of sn-glycrol-3-phosphate is the simplest way for preparing desaturated phosphatidic acid species. The most common methods for the preparation of phosphatidic acid containing unsaturated fatty acids are the extraction from wheat germ and the enzymatic degradation of phospholipids. This last reaction is catalyzed by phospholipase D (Hajdu, 2007).

Materials and Methods

In this research, cabbage sample was collected from local market. The mixture of light green inner leaves of cabbage (200 g) small pieces and 40% of sodium chloride solution were placed in a blender to blend this mixture. The solution mixture was filtered through a filter paper (first filtrate). The filtrate was taken and mixed with 50 g of sodium chloride. And then the solution mixture was filtered through a filter paper (second filtrate). A 72.68 g of ammonium sulphate was added into the 300 mL of filtrate to get 40% saturation. The solution was allowed to stand for 1hr and then filtration was carried out (third filtrate). The 250 mL of filtrate was fractionated by adding 32.5 g of solid ammonium sulphate to give 60 % saturation (fourth filtrate). The extract solution was placed in the refrigerator at 4·C. Phospholipase activity in the fourth filtrate enzyme solution fraction was determined by mixing 0.5mg/mL phosphatidyl choline, 0.3 mM sodium dodecyl sulphate, 0.1 mM phenol red and 40 mM calcium chloride in a test tube and incubating at room temperature for 10 min, and absorption spectra were recorded between 500 to 600 nm by UV-visible spectrophotometer (Hoppe, 1992). The maximum phospholipase activity was found at fourth filtrate. The wavelength of maximum absorption of copper-protein complex ~~was~~ determined by Biuret method was found at 550 nm. Crude phospholipase 2.0 mL was applied to a Sephadex G-200 gel filtration column previously equilibrated with the same medium. The flow rate was adjusted to 2 mL per 5 min. After collection of 2 mL fraction, the protein content of each tube was checked by measuring the absorbance at 280 nm wavelength using a UV-visible spectrophotometer. The enzyme in each test tube was also measured for phospholipase activity. The fraction which had the highest phospholipase activity was pooled. The pooled phospholipase fraction was measured for protein content by the Biuret method.

In this research, determination of molecular weight of the purified phospholipase was carried out by using sodium dodecyl sulphate-polyacrylamide gel electrophoresis techniques in

European molecular biology Laboratory, Heidelberg, Germany. Before electrophoresis, purification of the crude phospholipase was carried out by Sephacryl S-200 Gel and Sepharose 6-B chromatographic technique. Activating and inhibiting effect of metal ions (Na^+, K^+, Mn^{2+}, Ca^{2+}, Co^{2+}, Zn^{2+}, Cu^{2+}, Pb^{2+}, Hg^{2+}) 1 x 10^{-2} M on phospholipase activities was determined by UV-visible spectrophotometric method.

Results and Discussion

Extraction of Phospholipase from Cabbage Leaf

Phospholipase was first identified in plants (Heller, 1978). Phospholipase is a widely distributed enzyme, occurring in various bacteria, fungi, animals and unrelated plants as cabbage, soy beans and maple trees, etc. (Tookey, 1956). The phospholipids of seeds disappear during germination, reappearing as water–soluble choline and other compounds, thus suggesting a general role for the enzyme in the utilization of reserve phospholipid. Plant phospholipase has the great potential for industrial applications such as food additives, industrial reagents and medical applications (Woodman, 2003). In this work, phospholipase enzyme was extracted from cabbage leaves by using the sodium chloride solution (40%) and two successive ammonium sulphate precipitations (40 and 60 %). Since ammonium sulphate has little effect on enzyme activity and in some cases stabilizes the enzyme, it is useful as the salt of choice in most isolation of enzyme (Seamen, 1963). Thus, it was used in the present isolation.

Phospholipase Activity of the Enzyme Solution

Phospholipase activity was determined spectrophotomatically using phosphatidyl choline (lecithin) as substrate. Figure 1 showed the reaction of phospholipase. Phospholipase enzyme catalyzed the hydrolysis of phospholipids to phosphatidic acid and the corresponding free base. In this research, the spectrophotometric assay was applied using phenol red indicator. The rate of the disappearance of the indicator was used to measure the rate of hydrolysis of the phosphatidyl choline substrate. Hydrolysis of lecithin can affect to decrease the pH due to the ionization of the new phosphate group, causing the indicator to change colour from red to yellow. Figure 2 showed absorption spectra of phenol red solutions under different concentrations. The wavelength of maximum absorption phenol red was found at 558 nm when 0.1 mL of phospholipase enzyme solution was added into the phenol red solution, spectra changed (after 10 min, 20 min, 30 min, 1 h and 2 h in different reaction time). Phospholipase activity was defined as changes of 0.001 absorbance unit at 558 nm per mL of enzyme solution per min of reaction time.

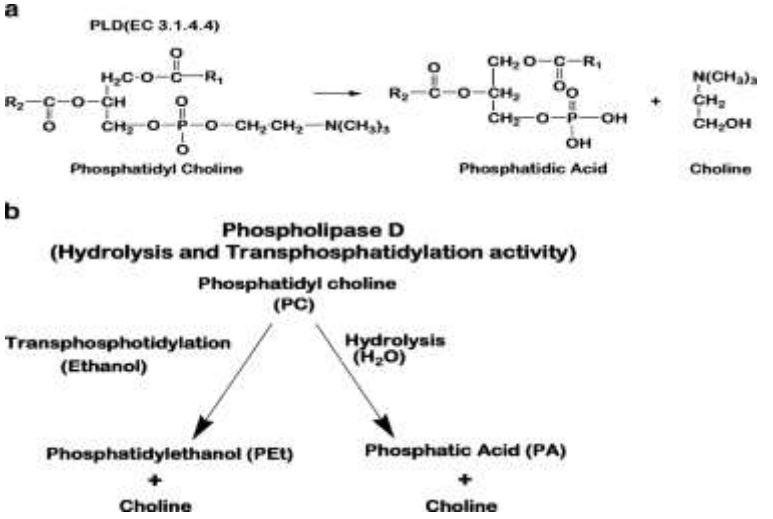

Figure 1 Reaction of phospholipase

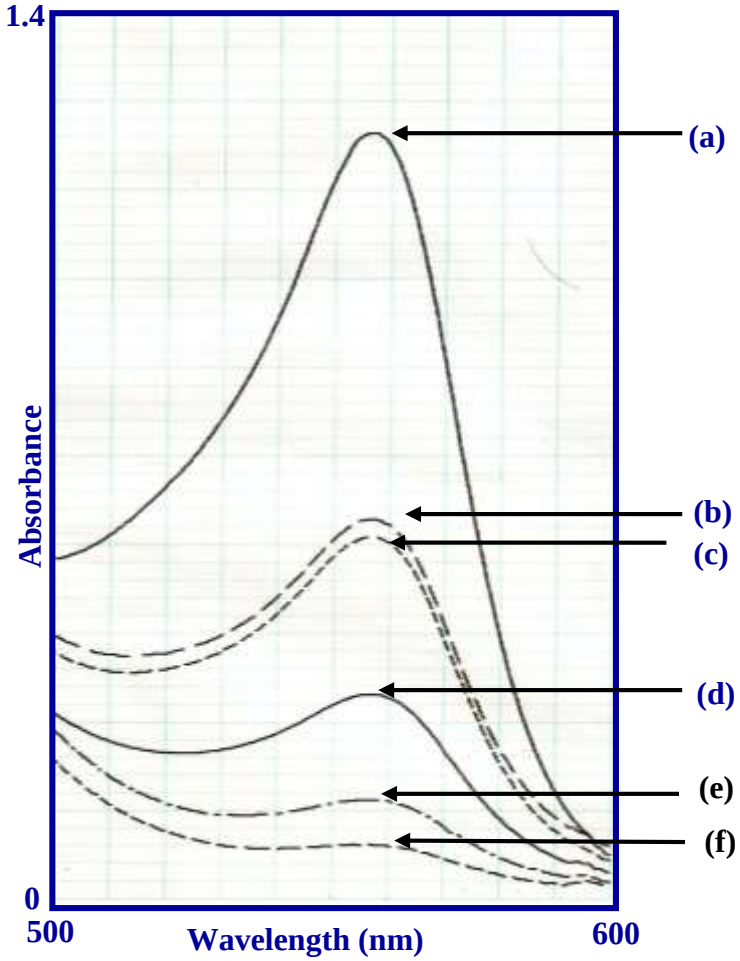

Figure 2 Absorption spectra of phenol red solution
(a) before adding enzyme solution
(b) after adding enzyme solution of crude extract (0.1) mL (reaction time 10 min)
(c) after adding enzyme solution of crude extract (0.1) mL (reaction time 20 min)
(d) after adding enzyme solution of crude extract (0.1) mL (reaction time 30 min)
(e) after adding enzyme solution of crude extract (0.1) mL (reaction time 1 h)
(f) after adding enzyme solution of crude extract (0.1) mL (reaction time 2 h)

Phospholipase Activity, Protein Content and Specific Activity of the Enzyme Solutions

In this research, Sephadex G-200 gel chromatographic purification was carried out. The phospholipase activity was determined by using the spectrophotometric method and protein content of the enzyme solution was determined by using the Biuret method at final purification step. The phospholipase activity was found to be 2.265 EU per gram of cabbage leaf and specific activity was 271.37 μmol min^{-1} mg of protein. Table 1 showed phospholipase activity, protein contents and specific activity of the enzyme solution at different purification steps. Table 2 showed variation of protein absorbance at 280 nm and phospholipase activity with fractions numbers in Sephadex G-200 chromatography. Figure 3 showed the purification of crude phospholipase enzyme by G-200 gel filtration chromatography.

Table 1 Phospholipase Activities, Protein Contents and Specific activities of Enzyme Solutions at Different Purification Steps

No	Purification Steps	Protein Content (mg/mL)	Phospholipase Activity (μmol min^{-1} mL^{-1})	Total Phospholipase Activity (μmol min^{-1} mL^{-1})	Specific Activity (μmol min^{-1} mg^{-1})	Protein Recovery (%)	Degree of Purity (fold)
1	Crude extract	4.257	370	55500	39.93	100	1
2	After purification with 40% ammonium sulphate	2.877	439	52680	152.59	94.92	3.61
3	After purification with 60% ammonium sulphate	2.760	564	50760	204.35	91.46	4.84
4	After passing the Sephadex G-200 column (32-42)	1.404	381	3733.8	271.37	6.73	6.80

Table 2 Variation of Protein Absorbance at 280 nm and Calculated Phospholipase Activity with Fractions Numbers in Sephadex G- 200 Gel Chromatography

Fraction Number	Protein Absorbance at 280 nm	Phospholipase Activity (μmol min^{-1} mL^{-1})
1	0.005	0
3	0.007	0
5	0.008	0
7	0.016	0
9	0.046	0
11	0.072	0
13	0.082	0
15	0.126	1
17	0.487	5
19	0.616	10
21	0.516	103
23	0.273	105
25	0.358	110
27	0.323	118
29	0.355	145
31	0.303	175
33	0.277	204
35	0.308	227
37	0.210	253
39	0.261	222
41	0.334	95

Fraction Number	Protein Absorbance at 280 nm	Phospholipase Activity (μmol min^{-1} mL^{-1})
43	0.233	101
45	0.240	97
47	0.249	98
49	0.235	89
51	0.205	23
53	0.185	0
55	0.087	0
57	0.085	0
59	0.080	0
61	0.007	0

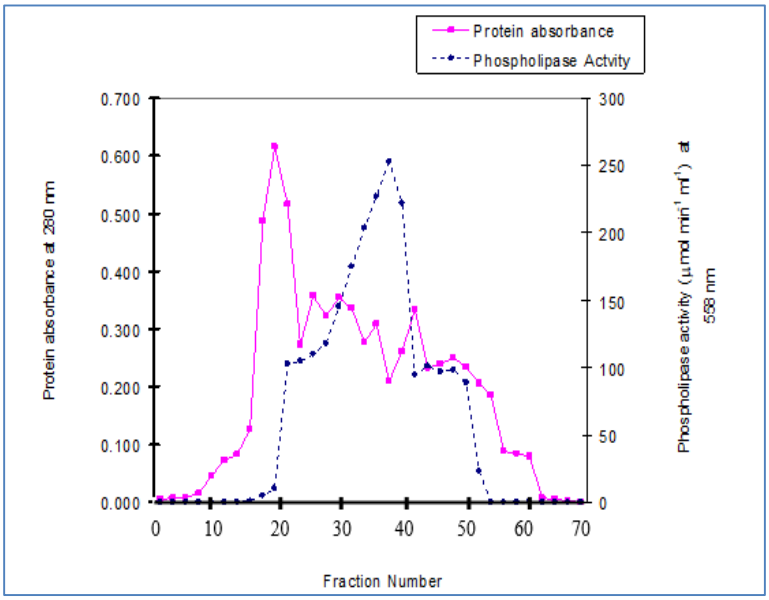

Figure 3 Purification of crude phospholipase enzyme by gel filtration chromatography

Molecular Weight of Purified Phospholipase Enzyme

The molecular weight of a protein may be determined by a variety of methods (Murray, 1993). The most accurate molecular weights are those obtained from sequence studies, a procedure hardly suitable in routine studies. Usually, molecular weight is obtained by methods involving the analytical ultracentrifuge and other methods; gel filtration, osmotic pressure, light scattering, electron microscopy, etc., have been employed (Scopes, 1994). Molecular weights are best determined when both the band of interest and the standards appear as sharp, narrow bands so that there is no mistake as to where to measure the migration distance. Maximal resolution is obtained with low protein loads. In this study, protein from the pharmacia high molecular weight (HMW) calibration kit: thyroglobulin (667,500), ferritin (439,000), urease trimer (230,000), β-glactosidase (139,000) and fructose-6-phosphate kinase (66,500) were used for molecular weight determination by SDS-PAGE (Table 3, Figure 4). The homogeneity of the purified phospholipase was confirmed by (SDS-PAGE). The use of polyacrylamide gel electrophoresis for determining protein molecular weights has become a routine laboratory technique (Pharmacia Inc, 1987). The molecular weight of a protein under investigation is determined by comparing its electrophoretic mobility with that of protein standards of known molecular weights. The principal limitation of the method, as related to protein work, appears to be its relatively low molecular weight exclusion characteristics. The

purified phospholipase enzyme showed a single band on SDS-PAGE where the molecular weight of purified phospholipase was located near the standard protein (mol.wt. 230,000). The molecular weight of purified phospholipase was measured according to the method of Halim and Smith (Smith, 1975). An estimated molecular weight of purified phospholipase from cabbage leaves sample was found as 158,489 Daltons from the log of known HMW marker proteins vs R_f values from SDS-PAGE (Figure 5).

Table 3 Relationship between Log of Molecular Weight of Standard Marker Proteins and Relative Mobility (R_f) Value Obtained from SDS – PAGE

No	Standard HMW marker proteins	MW (Daltons)	Log of MW	R_f
1	Thyroglobulin	667,500	5.8244	0.04
2	Ferritin	439,000	5.6425	0.13
3	Urease trimer	230,000	5.3617	0.33
4	β-Glactosidase	139,000	5.1430	0.44
5	Fructose-6-phosphate kinase	66,500	4.8228	0.63

The R_f of phospholipase was found to be 0.39 so that the molecular weight was determined to be 158, 489 Daltons (Figure 5).

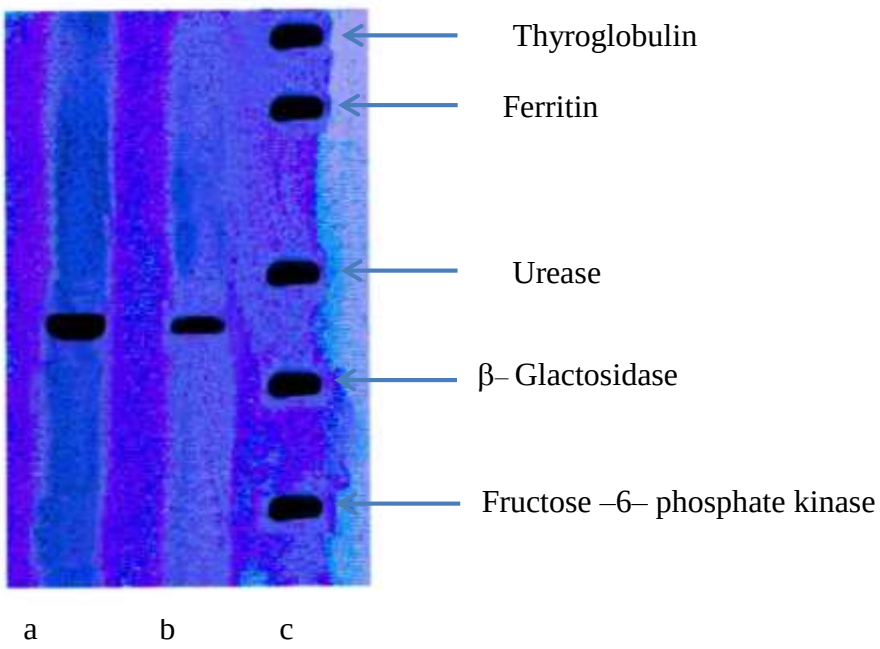

Figure 4 Photograph of sodium dodecyl sulphate polyacrylamide gel electrophoresis
a. Purified phospholipase fraction obtained from Sephadex G-200
b. Purfied phospholipase fraction obtained after successive purifications with Sephacryl S–200 and Sepharose 6–B
c. High molecular weight marker proteins

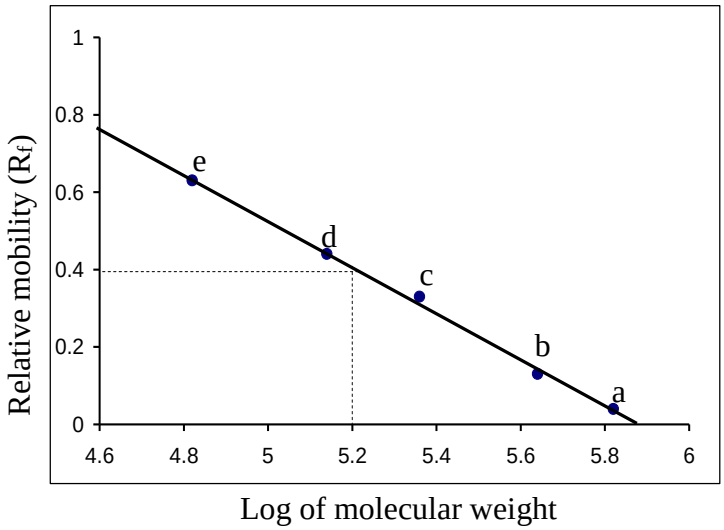

Figure 5 Plot of log of molecular weight of high molecular weight (HMW) marker proteins as a function of relative mobility (R_f) obtained from SDS – PAGE
(a) Thyroglobulin
(b) Ferritin
(c) Urease trimer
(d) β– Glactosidase
(e) Fructose – 6 – phosphate kinase

Effect of Some Metals Ions on Phospholipase Activity

In this research, effect of some metal ions (Mn^{2+}, K^{+}, Na^{+}, Ca^{2+}, Co^{2+}, Zn^{2+}, Cu^{2+}, $Pb^{2+}$and Hg^{2+}) on phospholipase activity was studied. The metal ions; Mn^{2+}, K^{+}, Na^{+}, and Ca^{2+} were found to be activators (Table 4, Figure 7). Among them, Ca^{2+} showed highest degree of activation (20.64%). In general, salt solutions of alkali and alkaline earth metal ions can stabilize the native structure of enzyme protein in solution. Therefore, phospholipase activity increased in the presence of alkali and alkaline earth metal ions. A Co^{2+}, Zn^{2+}, Cu^{2+}, Pb^{2+}, and Hg^{2+} ions exhibited as inhibitors. In the presence of 1 x 10^{-2} M Pb^{2+} and Hg^{2+} ions, phospholipase activity became zero due to the denaturing of enzyme protein by these metal ions. Heavy metals can bind to the –SH, -NH_2, and –OH groups in the protein structure of the enzyme. As a result, deformation occurred in native structure of enzyme protein and the phospholipase activity decreased.

Table 4 Relationship between Metal Ions and Degree of Activation (+)/Inhibition (-)

No	Metal ions	Δ A at 558nm	Phospholipase activity (10^2 μmol $min^{-1}mL^{-1}$)	Degree of activation /inhibition
1	Without	0.281	2.81	-
2	Mn^{2+}	0.293	2.93	+4.27
3	K^+	0.304	3.04	+8.19
4	Na^+	0.336	3.36	+19.85
5	Ca^{2+}	0.339	3.39	+20.64
6	Co^{2+}	0.172	1.72	-38.79
7	Zn^{2+}	0.164	1.64	-41.64
8	Cu^{2+}	0.072	0.72	-74.38
9	Pb^{2+}	0	0	-100
10	Hg^{2+}	0	0	-100

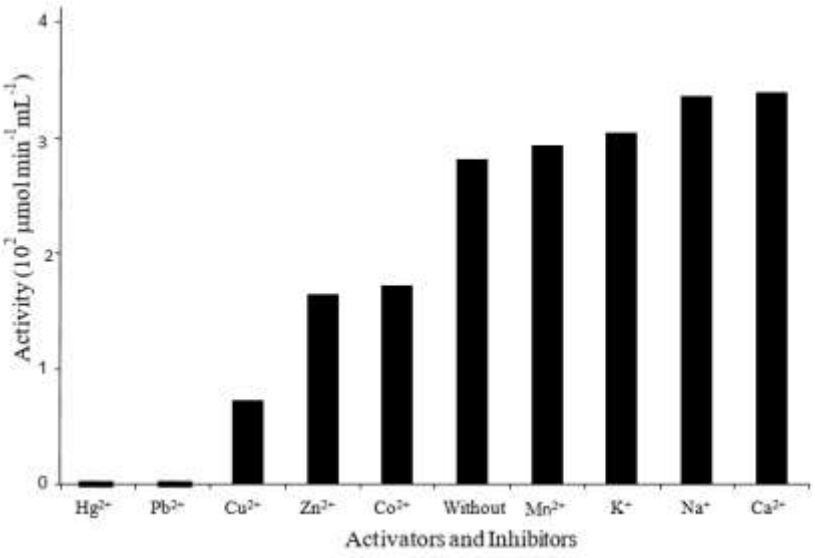

Figure 7 Phospholipase activities in the presence of various inhibitors and activators (1 x 10^{-2} M)

Conclusions

In this research, crude phospholipase enzyme was extracted from cabbage leaf and crude phospholipase extract solution (250 mL) was obtained from 200 g of cabbage leaf. The phospholipase activity in crude extract was to be 2.265 EU per gram of cabbage leaf. After Sephadex G-200 gel chromatographic separation, the specific activity (the relative purity of the enzyme) increased about (7) folds from crude to final purification step. The specific activity was found to be 271.37 EU per mg of enzyme protein at final purification step. The purity of the enzyme was confirmed by SDS-PAGE as a single band. The molecular weight of the purified enzyme as determined by SDS-PAGE technique was 158,489 Dalton. The Mn^{2+}, K^+, Na^+ and Ca^{2+} showed the activating effect on phospholipase activity, whereas Co^{2+}, Zn^{2+}, Cu^{2+}, Pb^{2+} and Hg^{2+} exhibited the inhibitory effect on phospholipase activity. The Ca^{2+} ion ($1x10^{-2}$ M) showed the highest activating effect (20.6%) on phospholipase activity. The Pb^{2+} and Hg^{2+} ($1x10^{-2}$ M) lead to the total denaturing of the enzyme protein and therefore phospholipase activity became zero. Degrees of activation were found to be 4.27%, 8.19%, 19.58% and 20.64% for 0.01 M of Mn^{2+}, K^+, Na^+ and Ca^{2+} ions, respectively. The inhibitory effect of Zn^{2+} ion on phospholipase activity was found to be

non-competitive type (enzyme denature) and degrees of inhibition were found to be 38.79%, 41.64%,74.38%, 100% and 100% for 0.01M of Co^{2+}, Zn^{2+}, Cu^{2+}, Pb^{2+} and Hg^{2+} ions, respectively.

Acknowledgements

The authors would like to express their profound gratitude to the Department of Higher Education, Ministry of Education, Myanmar, for provision of opportunity to do this research and also to the Myanmar Academy of Arts and Science for allowing to present this paper.

References

Alison, M. (2006). "Cabbage Leaves Can Help Inflammation of Any Body Part". *J. British Medical.*, vol. 12, pp 10-15

Cichowicz, D. J. (1993). "The Hydrolysis of Phosphatidycholine by an Immobilize Lipase: Optimization of Hydrolysis in Organic Solvents". *J. Am. Oil Chem. Soc*., vol. 70, pp. 111-117

Dennis, E. A. (1991). "Phospholipase. Methods in Enzymology''. New York: Academic Press, vol. 197, pp. 300-310

Dixon, M. and Webb, E. C. (1964). "Enzymes". London: Longmans Green Co. Ltd, pp. 193-200

Ensminger, A, H. (1986). *A Nutrition Encyclopedia: Food for Health*, Clovis: Pegus Press, pp. 748-773

Hajdu, J. (2007). "A New Synthesis of Lysophosphatidylcholines and Related Derivatives". *J. Org. Chem*., vol. 72, pp 1691-1698

Heller, M. (1978). "Phospholipase D". *Adv. Lipid Res*., vol.16, pp. 267 – 284

Hoppe, S. (1992). "Purification and Activity of Phospholipase D". *J. Biochem*., vol. 373, pp. 81-88

Liscovitch. M. (2000). "Phospholipase D: Molecular and Cell Biology of a Novel Gene Family". *J. Biochem*., vol 345, pp. 401-415

Madoery, R. R. (1997). "Silica-immobilized Phospholipase D from Daucus Carota". *Inf. Technol*., vol **8**, pp. 23-29

Murray, R. K. and Roodwell, V. W. (1993). "Harper's Biochemistry". Connecticut: Appleton and Lange Co. Ltd, pp. 78-83

Pharmacia Inc. (1987). "Electrophoresis Calibration Kits Instruction Manual". Uppsala: pp. 62-68

Scopes, R. K. (1994). "Proteins Purification". Principles and Practice, Berlin: Springer-Verlag, pp. 89-94

Seaman, G. R. (1963). "Experiments in Microbial Physiology and Biochemistry". New York: Burgress Pub, Co. Ltd, 54

Shimizu, T., Ohto, T and Kita Y. (2006). "Phospholipase from A Pharmaceutical Perspective". *J. Appl. Micro. Biotechnol*., vol. 74, pp. 290-300

Smith, I. (1975). "Chromatographic and Electrophoresis Techniques". London: Williams Heinemann Medical Books Ltd, 2: pp. 153

Tookey, S. and Gupta, M. N. (2004). "Purification of Phospholipase D by Two Phase Affinity Extraction". *J. Chromatography*., vol. 1025, pp. 297-301

Ulbrich, H. R. (2003). "Enzyme-catalyzed Transphosphatidylation". *Eur. J. Lipid Sic. Technol*., vol. 105, pp. 305-308

Vance, D.E. (2002). "Biochemistry of Lipids, Lipoproteins and Membranes". Amsterdam: 4th Ed., Elsevier Science, pp. 315-340

Woodman, H.M. (2003). "Cabbage Leaves are Poor Man's Poulitice". *J. British Medical*., vol. 327, pp 450-452

Yang, S. F. (1967). "Transphosphatidylation by Phospholipase D". *J. Biochem*., vol. 242, pp. 477- 484

SEASONAL CHANGES ON EUTROPHICATION LEVELS OF THE COASTAL SEA WATER AROUND THE KAYINDAUNG IN TANINTHARYI COASTAL AREA

May Hnin Aye[1], Thida[2], Win Aung[3], Kyaw Naing[4]

Abstract

The aim of this paper is to study the seasonal changes of eutrophication levels of coastal sea water around the Kayindaung in Tanintharyi Coastal Area. Sea water samples were collected from three different sites around Kayindaung in Tanintharyi Coastal Area. Sampling sites were recorded with GPS detector. Some chemical properties such as DO, orthophosphate (inorganic phosphate), organic phosphate, total phosphate and total nitrogen were determined. In this paper, the measured DO values were in the range of 6.86 ppm to 8.21 ppm. The values of orthophosphate, organic phosphate and total phosphate were found to be in the range of 0.014 ppm to 0.186 ppm, 5.311 ppm to 7.838 ppm and 5.325 ppm to 7.969 ppm in seasonally and annually collected sea water samples, respectively. The total nitrogen value in the studied area was found in the range of 0.560 ppm to 1.586 ppm for seasonally and annually collected samples. For eutrophication assessment, the determination of nutrient levels of all sea water samples in hot season were low nutrient-enrichment (oligotropic) and in rainy and cold season were medium nutrient-enrichment (mesotropic) for both seasonally and annually collected samples.

Keywords: Coastal sea water, Kayindaung in Tanintharyi Coastal Area, DO, total phosphate, total nitrogen, Eutrophication level

Introduction

Eutrophication is the most studied form of coastal marine pollution. Eutrophic waters are characterized by excessive algal growth as a consequence of nutrient enrichments of coastal surface waters. This problem, that is high nutrient concentration and algal biomass is commonly called eutrophication. If the coastal waters are nutrient poor with low productivity are characterized as "oligotrophic" whereas, nutrient rich waters with high algal biomass are characrerized as "eutrophic". The intermediate conditions characterize "mesotrophy". The impacts of eutrophication in the marine environment vary according to the enrichment level: slight increase of phytoplankton biomass is followed by changes in community structure (Karydis, 2009).

Biomass production in coastal waters - the conversion of light and carbon dioxide into living organic matter - is mainly limited by availability of nitrogen and/or phosphorus (light is a limiting factor in turbid zones). Eutrophication leads to increased biomass production that disturbs the natural ecological balance in the coastal zone, with serious detrimental consequences for biodiversity, ecosystem resilience, recreational activities and fisheries (Caitlin, 2020).

Materials and Methods

In this research, sea water samples were collected from Kayindaung in Tanintharyi Coastal Area seasonally and annually during 2011-2014. Figure 1 shows the sampling sites of sea water samples by the GPS detector. All samples were collected at a depth of 2m below the surface of sea water. Some chemical properties such as DO, orthophosphate, organic phosphate, total phosphate and total nitrogen were determined. The dissolved oxygen of sea water samples were measured in the field by using a DO meter-Temperature sensor probe HANNA Instrument. Orthophosphate and

[1] Dr, Lecturer, Department of Chemistry, Bago University
[2] Dr, Associate Professor, Department of Chemistry, University of Yangon
[3] Dr, Associate Professor, Department of Chemistry, Pakokku University
[4] Dr, Deputy Director General, Retired, Ministry of Higher Education (Naypyitaw Office)

total phosphate were determined by UV-visible spectrophotometric method. Total nitrogen of sea water samples were determined by Azo Dye method.

Figure 1 Satellite image of the sample collection sites (Site A 97 ° 35.966'E, 15° 56.969'N, Site B 97 ° 35.256'E, 15 ° 56.969'N, Site C 97 ° 35.440'E, 15 ° 56.726'N)

Results and Discussion

Dissolved Oxygen in Sea Water Samples

Monitoring dissolved oxygen will provide indication of water quality in coastal areas and used as a tool in ecosystem integrity. Dissolved oxygen is essential to the respiratory metabolism of most aquatic organisms. In this research work, dissolved oxygen content of the sea water samples were found to be in the range of 6.86 ppm to 8.21 ppm for seasonally and annually. Higher dissolved oxygen concentration (8.21 ppm) observed during rainy season (2013) might be due to the cumulative effect of higher wind velocity coupled with heavy rainfall and the resultant freshwater mixing. Optimum concentration of dissolved oxygen is essential for maintaining aesthetic qualities water as well as for supporting life. The value of dissolved oxygen (6.86 ppm) during hot season (2014) is lower due to higher temperature and high rate of microbial decomposition of organic matter. The measured DO values were within the permissible level of ASEAN standard (> 5ppm) (Table 1 and Figure 2).

Table 1 Seasonal Changes of the Dissolved Oxygen Contents in Sea Water Sample

Sr No.	Year	Season	Sampling Sites	Dissolved Oxygen (DO) ppm
1.	2011	Rainy	A	7.41
			B	7.85
			C	7.62
2.	2012	Hot	A	7.65
			B	7.34
			C	7.22
		Rainy	A	7.83
			B	7.79
			C	7.72
		Cold	A	7.71
			B	7.69
			C	7.65
3.	2013	Hot	A	7.15
			B	7.35
			C	7.24
		Rainy	A	8.11
			B	8.05
			C	8.21
		Cold	A	7.72
			B	7.58
			C	7.64
4.	2014	Hot	A	7.09
			B	6.86
			C	7.22
		Rainy	A	7.99
			B	7.81
			C	7.93
		Cold	A	7.72
			B	7.45
			C	7.54
EPA Standard (2009)				>4
ASEAN Standard (2010)				>5

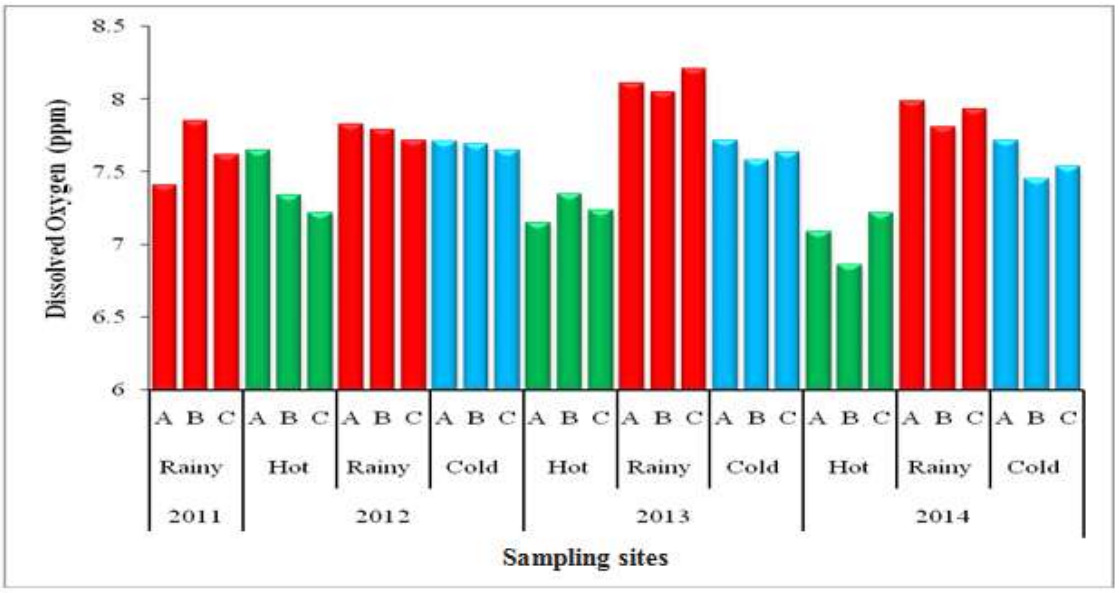

Figure 2 Seasonal changes of the dissolved oxygen values in the sea water samples from the Kayindaung in Tanintharyi Coastal Area

Orthophosphate, Organic Phosphate and Total Phosphate in Sea Water Samples

Phosphorous is an essential element for all life including plant growth and photosynthesis in algae. Phosphorous is considered to be the most significant component among the nutrients responsible for eutrophication of a water body. Phosphate is the most important nutrient for the production of phytoplankton in sea water which is primary food for many of the commercial fishes (Mihajlovie *et al*., 2007).

In water bodies, the phosphorus may be present in various forms. All forms of phosphorus are not readily available to plants. Total phosphate is a measure of all forms of phosphorous (dissolved or suspended) found in water. The soluble reactive phosphorous is a measure of orthophosphate (inorganic phosphate) that is the form directly taken up by plant cells. While monitoring the water bodies, the latter form of phosphorus would be of special significance to determine the stage of eutrophy and oligotrophy (Kyaw Naing, 2011). Agriculture runoff containing phosphate fertilizers as well as the wastewater containing the detergents etc. tend to increase phosphate pollution in water.

In the present work, the orthophosphate concentration of sea water samples were found to be in the range of 0.061 ppm to 0.184 ppm in rainy season (2011), 0.014 ppm to 0.027 ppm in hot season, 0.109 ppm to 0.142 ppm in rainy season, 0.043 ppm to 0.052 ppm in cold season (2012), 0.029 ppm to 0.035 ppm in hot season, 0.131 ppm to 0.186 ppm in rainy season, 0.063 ppm to 0.078 ppm in cold season (2013), 0.027 ppm to 0.034 ppm in hot season, 0.132 ppm to 0.143 ppm in rainy season and 0.039 ppm to 0.058 ppm in cold season (2014), respectively (Table 2 and Figure 3).

The high amount of orthophosphate (0.186 ppm) observed during rainy season (2013) could be due to turbulence and mixing in water column, while the low amount (0.014 ppm) observed during hot season (2012) could be due to the limited flow of fresh water, high salinity and utilization of phosphate by phytoplankton.

The highest and lowest values of organic phosphate were 7.838 ppm and 5.311 ppm. The lowest value (5.311 ppm) was found in hot season, 2012 and the highest value (7.838 ppm) was found in rainy season, 2013 (Table 2 and Figure 4).

Total Phosphate concentration of sea water samples were found to be in range of 5.325 ppm to 7.969 ppm (Table 2 and Figure 5). The highest value of total phosphate was found in rainy season 7.969 ppm (2013). This may be due to the nutrient inputs to aquatic ecosystem, especially agricultural wastes.

Table 2 Seasonal Changes of the Orthophosphate, Organic Phosphate and Total Phosphate in Sea Water Samples

Sr No.	Year	Season	Sampling sites	Ortho phosphate (ppm) Mean ± SD	Organic phosphate (ppm) Mean ± SD	Total phosphate (ppm) Mean ± SD
1.	2011	Rainy	A	0.061 ± 0.003	6.360 ± 0.058	6.421 ± 0.058
			B	0.123 ± 0.005	7.835 ± 0.047	7.958 ± 0.047
			C	0.184 ± 0.005	7.664 ± 0.063	7.848 ± 0.063
2.	2012	Hot	A	0.014 ± 0.002	5.311 ± 0.051	5.325 ± 0.051
			B	0.018 ± 0.003	6.547 ± 0.026	6.565 ± 0.026
			C	0.027 ± 0.003	6.440 ± 0.063	6.467 ± 0.063
		Rainy	A	0.109 ± 0.005	6.680 ± 0.026	6.789 ± 0.026
			B	0.128 ± 0.003	6.627 ± 0.026	6.755 ± 0.026
			C	0.142 ± 0.002	6.645 ± 0.090	6.787 ± 0.090
		Cold	A	0.052 ± 0.003	6.613 ± 0.026	6.665 ± 0.026
			B	0.043 ± 0.003	6.611 ± 0.053	6.654 ± 0.053
			C	0.046 ± 0.005	6.591 ± 0.090	6.637 ± 0.090
3.	2013	Hot	A	0.029 ± 0.002	5.516 ± 0.029	5.545 ± 0.029
			B	0.032 ± 0.003	5.406 ± 0.045	5.438 ± 0.045
			C	0.035 ± 0.003	5.454 ± 0.029	5.489 ± 0.029
		Rainy	A	0.131 ± 0.004	7.838 ± 0.062	7.969 ± 0.062
			B	0.179 ± 0.005	7.655 ± 0.058	7.834 ± 0.058
			C	0.186 ± 0.005	7.670 ± 0.048	7.856 ± 0.048
		Cold	A	0.075 ± 0.004	6.697 ± 0.047	6.772 ± 0.047
			B	0.063 ± 0.003	6.785 ± 0.047	6.848 ± 0.047
			C	0.078 ± 0.003	6.747 ± 0.053	6.825 ± 0.053
4.	2014	Hot	A	0.033 ± 0.003	5.546 ± 0.064	5.579 ± 0.064
			B	0.034 ± 0.003	5.418 ± 0.058	5.452 ± 0.058
			C	0.027 ± 0.002	5.485 ± 0.027	5.512 ± 0.027
		Rainy	A	0.132 ± 0.005	6.449 ± 0.047	6.581 ± 0.047
			B	0.139 ± 0.004	6.293 ± 0.072	6.432 ± 0.072
			C	0.143 ± 0.005	6.369 ± 0.047	6.512 ± 0.047
		Cold	A	0.058 ± 0.004	6.068 ± 0.029	6.126 ± 0.029
			B	0.045 ± 0.004	6.194 ± 0.043	6.239 ± 0.043
			C	0.039 ± 0.003	6.209 ± 0.055	6.248 ± 0.055
EPA Standard (2009)				-	-	-
ASEAN Standard (2010)				0.015	NC	<0.05

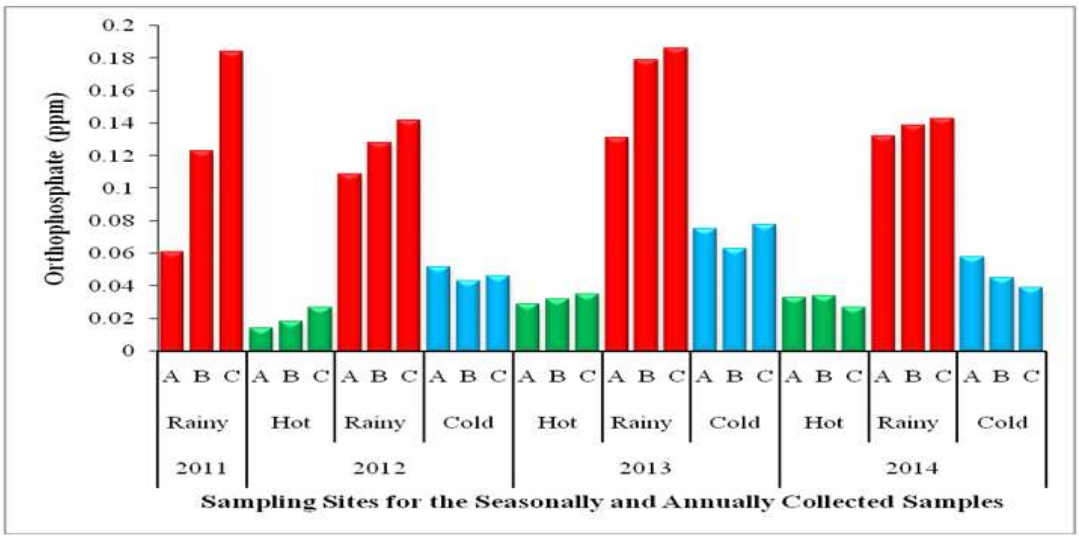

Figure 3 Seasonal changes of the orthophosphate values in the sea water samples from the Kayindaung in Tanintharyi Coastal Area

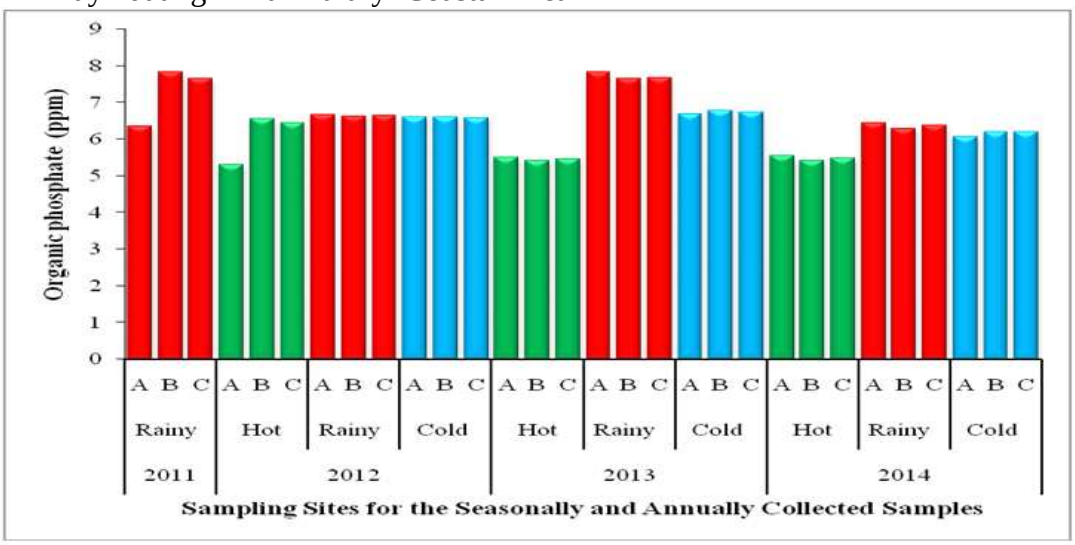

Figure 4 Seasonal changes of the organic phosphate values in the sea water samples from the Kayindaung in Tanintharyi Coastal Area

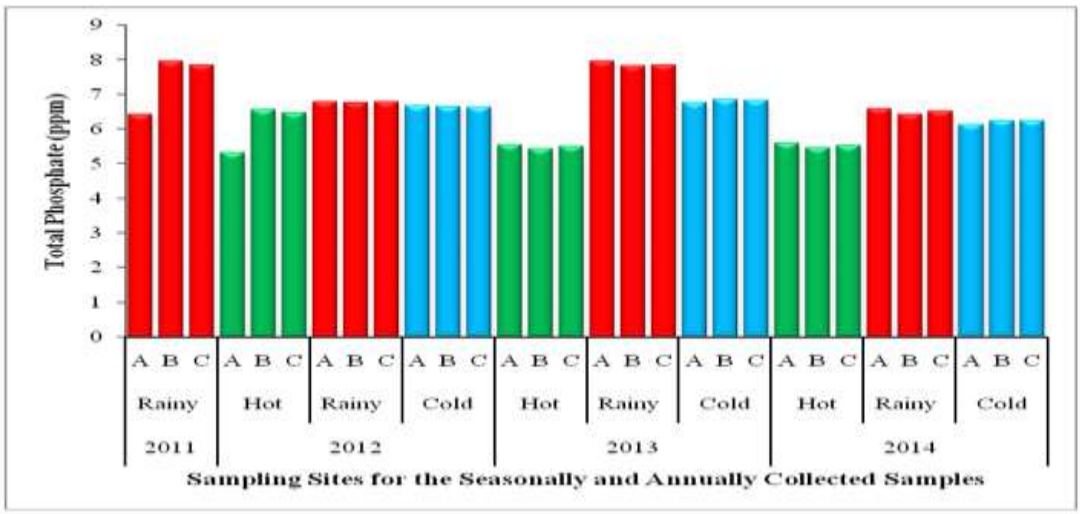

Figure 5 Seasonal changes of total phosphate values in the sea water samples from the Kayindaung in Tanintharyi Coastal Area

Total Nitrogen in Sea Water Samples

Nitrogen refers to all inorganic forms of nitrogen present in water (ammonia, ammonium nitrate and nitrite). Nitrogen concentrations in water can be reported as total nitrogen or as nitrogen in the form that it is present in solution. When nitrogenous organic matter is destroyed by microbiological activity, ammonia is produced and is therefore found in many surface and ground waters. Higher concentrations occur in water polluted by sewage, fertilizers, agricultural wastes or industrial wastes containing organic nitrogen, free ammonia or ammonium salts (Al-Safady, 2012).

In this research, total nitrogen concentration of sea water samples were in the range of 0.660 ppm to 1.320 ppm in rainy season (2011), 0.560 ppm to 0.920 ppm in hot season, 1.218 ppm to 1.425 ppm in rainy season, 0.956 ppm to 1.124 ppm in cold season (2012), 0.822 ppm to 0.992 ppm in hot season, 1.432 ppm to 1.586 ppm in rainy season, 1.185 ppm to 1.235 ppm in cold season (2013), 0.752 ppm to 0.915 ppm in hot season, 1.323 ppm to 1.445 ppm in rainy season, 0.987 ppm to 1.182 ppm in cold season (2014), respectively (Table 3 and Figure 6). The recorded high value (1.586 ppm) of total nitrogen during rainy season (2013) could be due to the organic materials received from the catchment area during ebb tide. The recorded low value (0.560 ppm) during hot season (2012) may be due to its utilization by phytoplankton as evidenced by high photosynthesis activity and the dominance of neritic sea water having a negligible amount of nitrate.

The high concentrations of total nitrogen in sea water causes a phenomenon known as "Eutrophication", which means an excessive growth of the algae in water which consumes the oxygen gas dissolved in water causing the death of fishes in that water.

Table 3 Seasonal Changes of the Total Nitrogen in the Sea Water Samples

Sr No.	Year	Season	Sampling sites	Total Nitrogen (ppm) Mean ± SD
1.	2011	Rainy	A	0.660 ± 0.015
			B	1.200 ± 0.015
			C	1.320 ± 0.020
2.	2012	Hot	A	0.560 ± 0.025
			B	0.780 ± 0.015
			C	0.920 ± 0.021
		Rainy	A	1.339 ± 0.012
			B	1.425 ± 0.012
			C	1.218 ± 0.015
		Cold	A	1.124 ± 0.016
			B	1.058 ± 0.026
			C	0.956 ± 0.022
3.	2013	Hot	A	0.935 ± 0.018
			B	0.822 ± 0.021
			C	0.992 ± 0.018
		Rainy	A	1.586 ± 0.017
			B	1.432 ± 0.020
			C	1.524 ± 0.020
		Cold	A	1.185 ± 0.023
			B	1.235 ± 0.015
			C	1.224 ± 0.018

Sr No.	Year	Season	Sampling sites	Total Nitrogen (ppm) Mean ± SD
4.	2014	Hot	A	0.752 ± 0.012
			B	0.915 ± 0.012
			C	0.832 ± 0.015
		Rainy	A	1.445 ± 0.017
			B	1.323 ± 0.015
			C	1.349 ± 0.022
		Cold	A	0.987 ± 0.012
			B	1.097 ± 0.015
			C	1.182 ± 0.012
EPA Standard (2009)				-
ASEAN Standard (2010)				-

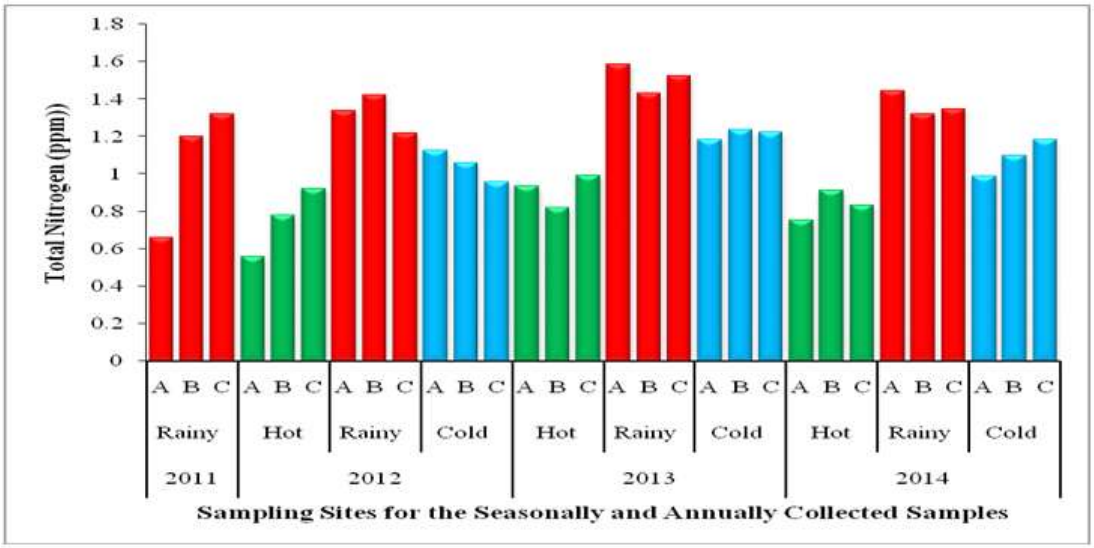

Figure 6 Seasonal changes of total nitrogen values in the sea water samples from the Kayindaung in Tanintharyi Coastal Area

Eutrophication Levels of Coastal Sea Water

Water eutrophication is mainly caused by excessive loading of nutrients into water bodies like nitrogen and phosphorus. Excessive nutrients come from both point pollution such as waste water from industry and municipal sewage, and non-point pollution like irrigation water, surface runoff water containing fertilizer from farmland, etc (Yang, 2008). Although nutrients are essential for the growth and survival of an estuary's plants, an excess of nitrogen and phosphorus may trigger a string of events that seasonally deplete dissolved oxygen (DO) in the water (Ronald and Ohrel, 2006).

In this research work, the eutrophication level of sea water samples were determined by the values of DO, orthophosphate and total nitrogen. From the experimental data of these three values were compared with criteria for evaluation degree of nutrient over-enrichment (Table 4(a)), indicated that which season for sample A, B and C were low-nutrient enrichment (oligotropic), medium-nutrient enrichment (mesotropic) and high-nutrient enrichment (eutropic). For example, in hot season (2012), nitrogen concentrations were in the range of 0.560 ppm to 0.920 ppm (within >0.1 ppm - <1.0 ppm, medium), orthophosphate concentrations were in the range of 0.014 ppm to 0.027 ppm (<0.03 ppm, low) and DO values were in the range of 7.22 ppm to 7.65 ppm (≥ 5 ppm, low). So, the samples A, B and C for hot season (2012) is low-nutrient enrichment (oligotropic).

In the present work, during 2011 to 2014 it was found that all samples for rainy season and cold season were medium-nutrient enrichment (mesotropic) and all samples for hot season were low-nutrient enrichment (oligotropic) for annually collected samples are shown in Table 4(b). So it is satisfied for the protection of aquatic life.

Table 4(a) Criteria for Evaluating Degree of Nutrient Over-Enrichment

Parameters	low	medium	high
Nitrogen (ppm)	≤0.1	>0.1 - <1.0	≥1.0
PO_4^{3-}(ppm)	<0.03	>0.03 - <0.3	≥0.3
DO (ppm)	≥5	>2 - ≤5	0 - ≤2

(Tong and Deocadiz, 1999)

Table 4(b) Evaluation of Nutrient Levels of Sea Water Samples

Sr No	Year	Season	Sampling sites	Dissolved Oxygen (ppm)	Ortho phosphate (ppm) Mean ± SD	Total Nitrogen (ppm) Mean ± SD	Nutrient Enrichment
			A	7.41	0.061 ± 0.003	0.660 ± 0.015	medium**
1.	2011	Rainy	B	7.85	0.123 ± 0.005	1.200 ± 0.015	medium**
			C	7.62	0.184 ± 0.005	1.320 ± 0.020	medium**
			A	7.65	0.014 ± 0.002	0.560 ± 0.025	low*
		Hot	B	7.34	0.018 ± 0.003	0.780 ± 0.015	low*
			C	7.22	0.027 ± 0.003	0.920 ± 0.021	low*
			A	7.83	0.109 ± 0.005	1.339 ± 0.012	medium**
2.	2012	Rainy	B	7.79	0.128 ± 0.003	1.425 ± 0.012	medium**
			C	7.72	0.142 ± 0.002	1.218 ± 0.015	medium**
			A	7.71	0.052 ± 0.003	1.124 ± 0.016	medium**
		Cold	B	7.69	0.043 ± 0.003	1.058 ± 0.026	medium**
			C	7.65	0.046 ± 0.005	0.956 ± 0.022	medium**
			A	7.15	0.029 ± 0.002	0.935 ± 0.018	low*
		Hot	B	7.35	0.032 ± 0.003	0.822 ± 0.021	low*
			C	7.24	0.035 ± 0.003	0.992 ± 0.018	low*
			A	8.11	0.131 ± 0.004	1.586 ± 0.017	medium**
3.	2013	Rainy	B	8.05	0.179 ± 0.005	1.432 ± 0.020	medium**
			C	8.21	0.186 ± 0.005	1.524 ± 0.020	medium**
			A	7.72	0.075 ± 0.004	1.185 ± 0.023	medium**
		Cold	B	7.58	0.063 ± 0.003	1.235 ± 0.015	medium**
			C	7.64	0.078 ± 0.003	1.224 ± 0.018	medium**
			A	7.09	0.033 ± 0.003	0.752 ± 0.012	low*
		Hot	B	6.86	0.034 ± 0.003	0.915 ± 0.012	low*
			C	7.22	0.027 ± 0.002	0.832 ± 0.015	low*
			A	7.99	0.132 ± 0.005	1.445 ± 0.017	medium**
4.	2014	Rainy	B	7.81	0.139 ± 0.004	1.323 ± 0.015	medium**
			C	7.93	0.143 ± 0.005	1.349 ± 0.022	medium**
			A	7.72	0.058 ± 0.004	0.987 ± 0.012	medium**
		Cold	B	7.45	0.045 ± 0.004	1.097 ± 0.015	medium**
			C	7.54	0.039 ± 0.003	1.182 ± 0.012	medium**

* Identified as oligotropic, ** Identified as mesotropic

Conclusion

The values of dissolved oxygen in the course of this research work for all sea water samples were in the slight variation and the range between 6.86 ppm to 8.21 ppm. The measured DO values were within the permissible level of ASEAN standard (> 5ppm).The values of orthophosphate, organic phosphate and total phosphate were found to be in the range of (0.014 ppm to 0.186 ppm), (5.311 ppm to 7.838 ppm) and (5.325 ppm to 7.969 ppm), respectively for both seasonally and annually collected samples. The total nitrogen values in the studied area were found in the range of 0.560 ppm to 1.586 ppm. From the results of water analysis of all sea water samples seasonally and annually indicated that the eutrophication level ranged from low to medium levels. This clearly revealed that the sea water of the studied area is not polluted and aquatic creatures are well protected from DO depletion due to eutrophication.

Acknowledgements

The authors would like to express their profound gratitude to the Department of Higher Education (Yangon Office), Ministry of Education, Yangon, Myanmar, for provision of opportunity to do this research and Myanmar Academy of Arts and Science for allowing to present this paper.

References

Al-Safady, M.Y.M. (2012). *Physico-chemical and Microbiological Characteristics of Sea water in Nothern Part of Gaza Strip, Palestine*. Deanship of Postgraduate and Science Research, Gaza: Institute of Water Environment (IWE), Al- Azhar University, Palestine, pp. 37 - 45

ASEAN Marine Environmental Managment. (2010). *Water Quality Criteria and Standards for Fresh Water and Marine Aquaculture.* North Vancouver: Environmental Consultants Ltd., pp. 171-189

Caitlin P. (2020). *Eutrophication in Coastal Environments*. http:// www. coastal wiki. org /wiki /Eutrophication in coastal environments. (Accessed 12. July.2020)

EPA. (2009). *Nutrient Water Quality Standards*. Washington, DC: Office of Water Research

Karydis. M. (2009)."Eutrophication Assessment of Coastal Waters Based on Indicators: A Literature Review". *Global NEST Journal*, vol. 11(4), pp. 373-390

Kyaw Naing. (2011). *National Report of Myanmar on the Coastal Pollution Loading and Water Quality Criteria (Land-based sources of Marine Pollution)*. Rome: FAO, Bay of Bengal Large Marine Ecosystem Project of the Food and Agriculture Organization of the United Nations, pp. 1-53

Mihajlove, R.P., Kalijevic, V.M., Vukasinovic M.P. and Pantic, L.D. (2007). "Spectrophtometric Method for the Determination of Phosphorous in Natural Waters Using the Bismuth-phosphomolybdate Complex." *Water SA.*, vol. 33, pp. 513-517

Ronald L. and Ohrel, Jr. (2006). *Volunteer Estuary Monitoring: A Methods Manual*. US: 2nd Edition, The Ocean Conservancy, pp. 10-14

Tong, S.L. and Deocadiz, E.S. (1999). *Principles for Developing ASEAN Marine Water Quality Criteria.* Malaysia: ASEAN Marine Water Quality Criteria, Department of Fisheries, pp. 1-12

Yang, X. (2008). "Mechanisms and Assessment of Water Eutrophication: Review". *J Zhejiang Univ Sci B*, vol. 9(3), pp. 197-209

ISOLATION AND CHARACTERIZATION OF URSANE AND OLEANANE TYPE TRITERPENES FROM THE ROOTS OF *STREPTOCAULON TOMENTOSUM*. WIGHT & ARNOTT (‖r i;p*e) (ASCLEPIADACEAE) IN MYANMAR

Myint Myint Khine[1]

Abstract

The aim of this paper is to study the NMR spectroscopic characterization of seven triterpenes from *Streptocaulon tomentosum* Wight & Arnott (Asclepiadaceae). Four ursane type triterpenes and three oleanane type triterpenes were isolated from the roots of *Streptocaulon tomentosum*. by column chromatography and identified by NMR spectroscopy. Comparative studies on NMR spectra of ursane type and oleanane type triterpenes were done. Four ursane type triterpenes were identified as α-amyrin acetate (compound 2),2α,3α,23-trihydroxy-urs-12-en-28-oic-acid (compound 3), 2α,3β-dihydroxy-urs-12-en-28-oic-acid (compound 4), and 2α,3β,23-trihydroxy-urs-12-en-28-oic-acid (compound 6). Three oleanane type triterpenes were identified as β-amyrin acetate (compound 1), 2α,3β-dihydroxy-olean-12-en-28-oic-acid (compound 5) and 2α,3β,23-trihydroxy-olean-12-en-28-oic-acid (compound 7).

Keywords: *Streptocaulon tomentosum*, Asclepiadaceae, ursane, oleanane, triterpenes

Introduction

The roots of *Streptocaulon tomentosum* are used in Myanmar in traditional medicine for the treatment of anticancer, dysentery and stomach-ache, and the leaves are used externally for the treatment of snake poisoning and abscesses. The triterpenoids, having a C_{30} skeleton, constitute a large, diverse group of natural products derived from squalene or, in the case of 3β-hydroxy triterpenoids, the 3*S*-isomer of squalene 2,3-epoxide. In excess of 4000 triterpenoids have been isolated so far and more than 40 skeletal types have been identified. Oleananes and ursanes often occur together and, in the past decade, have been reported from a wide range of families including the Araliaceae, Asclepiadaceae, Bignononiaceae, Cactaceae, Campanulaceae, Celastraceae, Compositae, Ericaceae, Fagaceae, Labiateae, Leguminosae, Phytolaccaceae, Primulaceae, Rosaceae, Rubiaceae, Sapotaceae, Theaceae, Umbelliferae and Urticaceae (Dey & Harborne, 1991). The biological activities of triterpenoids and triterpenoid saponins are immunostimulation (Press *et al*., 2000), anti-tumor-promoting activity (Konoshima & Takasaki, 2000), anti-inflammatory activity and anti-insect activity (Connolly & Hill, 2002). This paper focused on the NMR spectroscopic characterization of ursane and oleanane types triterpenes isolated from the roots of *Streptocaulon tomentosum* Wight and Arn. (Asclepiadaceae).

Materials and Methods

Sample Collection and Identification of Plant Samples

Streptocaulon tomentosum Wight and Arn. (Asclepiadaceae), roots collected in May 2002 from Mawlamyine Township, Myanmar by Dr Daw Hla Ngwe. The species was identified by Prof. Dr Aung Aung Min, Department of Botany, University of Yangon. A voucher specimen of the clamberer (No. Y.H.V. 1004) is deposited in University of Yangon.

[1] Dr, Professor, Department of Chemistry, University of Yangon

Spectral Studies

1D NMR spectra (^{1}H, ^{13}C) were recorded on a Varian Mercury 300 at 300.94 MHz for 1H, and at 100.57 MHz for ^{13}C NMR. Chemical shifts in ppm were referenced to internal TMS (δ =0) for 1H and C_5D_5N (δ 149.81, 135.48, 123.50 ppm) for ^{13}C, respectively.

Isolation of Triterpenes from the Roots of *Streptocaulon tomentosum*

Dried powdered root of *Streptocaulon tomentosum* (Asclepiadaceae) (1 kg) was extracted with 80% EtOH (1 L × 3) for one week. The solvent was evaporated to the remaining water layer. Then the water layer was successively partitioned between organic solvents (*n*-hexane, ethyl acetate, *n*-butanol 300 mL × 3) and water. The *n*-hexane fraction (48 g) was chromatographed over silica gel 60 (70-230 mesh, Merck), using a stepwise gradient of *n*-hexane: ethyl acetate (9.5:0.5, 9:1, ...2:1, increasing polarity) to give four fractions. Fraction 1 (8 g) and fraction 2 (4 g) were rechromatographed on silica gel 60 column (230-400 mesh, column size id 2 cm × 60 cm) with the solvent system *n*-hexane: chloroform (3:1) and (9:1-4:1) to give β-amyrin acetate (**1**), and α-amyrin acetate (**2**). The ethyl acetate fraction (12 g) was separated on a silicagel column (70-230 mesh, column size id 3 cm × 60 cm) and eluted with *n*-hexane: ethyl acetate: methanol (increasing polarity 9:1:0, 7:3:0.5, ...to pure MeOH) to give 23 fractions (each about 300 mg). Fractions 5-11 were rechromatographed on silica gel 60 (230-400 mesh, column size 1.5 cm × 40 cm) using $CHCl_3$: MeOH (9.5:0.5; 4.7:0.3) to give compounds **3-7.**

Identification of Ursane and Oleanane Types Triterpenes

The structures elucidations were determined by ^{1}H NMR, ^{13}C NMR, ESI-MS, FT-IR, GC-MS and confirmed by comparison with the literature values (Matsunaga *et al*., 1988; Chen *et al*., 1993; Hisham *et al*., 1993; De Pascual Teresa *et al*., 1987).

Results and Discussion

Structure Elucidation of Ursane and Oleanane Type Triterpenes

The *n*-hexane fraction was repeatedly chromatographed on a silica gel column and β-amyrin acetate (**1**), and α-amyrin acetate (**2**). The structures elucidations were determined by ^{1}H NMR, ^{13}C NMR, ESI-MS, GC-MS and confirmed by comparison with the literature values.

Compound 1: β-amyrin acetate

colourless needles Yield: 100 mg, 0.01%

mp.: 242-243 °C

$[\alpha]_D$: + 80.1 ° (c = 1.10, $CHCl_3$)

TLC: R_f = 0.47 (system T_1, violet colour with vanillin/H_2SO_4, inactive under UV)

IR: (KBr), ν_{max}= 1730, 1635, 1240, 812 cm^{-1}

^{1}H NMR: (300 MHz, $CDCl_3$): δ 0.84 (3H, *s*, H-28), 0.88 (12H, *s*, H-23, 24, 29, 30), 0.98 (6H, *s*, H-25, 26), 1,14 (3H, *s*, H-27), 2.07 (3H, *s*, OAc), 4.54 (1H, *dd*, *J* 11.6 Hz, H-3α), 5.21 (1H, *t*, *J* 3.5 Hz, H-12)

GC-MS: RT = 18.03 min, 468 $[M]^+$, 453 (33), 408 $[M\text{-}HOAc]^+$ (5), 393 (40), 281 (70), 218 (100), 203 (68), 69 (90)

EI-MS: (70 ev) *m/z* (rel. int): 468 $[M]^+$, 453 (2), 408 $[M\text{-}HOAc]^+$ (5), 218 (100), 203 (20)

Compound 2: α- amyrin acetate

Colourless needles, Yield: 1.5 g, 0.15%

mp.: 243 °C

$[\alpha]_D$: + 76 ° (c = 1.0, $CHCl_3$)

TLC: R_f = 0.47 (system T_1, violet colour with vanillin/H_2SO_4, inactive under UV)

IR: (KBr), ν_{max}= 1730, 1380, 1370, 1250, 1030, 1000, 985, 960 cm^{-1}

^1H NMR: (300 MHz, $CDCl_3$): δ0.79 (3H, *s*, H-28), 0.88 (12H, *s*, H-23, 24, 29, 30), 0.98 (3H, *s*, H-26), 1.01 (3H, *s*, H-25), 1,07 (3H, *s*, H-27), 2.05 (3H, *s*, OAc), 4.50 (1H, *dd*, *J* 9.7 Hz, H-3α), 5.12 (1H, *t*, *J* 3.6 Hz, H-12)

GC-MS: RT = 18.85 min, 468 $[M]^+$, 453 (45), 408 [M- HOAc]$^+$ (38), 393 (40), 281 (100), 218 (80), 203 (30), 69 (98)

EI-MS: (70 ev) *m/z* (rel. int): 468 $[M]^+$, 453 (10), 408 [M- HOAc]$^+$ (20), 218 (100), 203 (10)

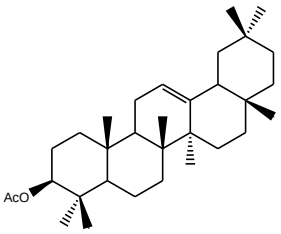

Compound 1
(Oleanane type)

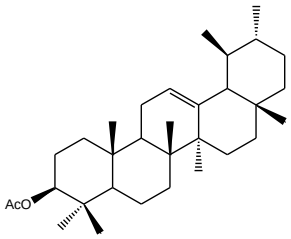

Compound 2
(Ursane type)

Compound **3-7** were isolated from fraction 5-11 of the ethyl acetate extract after repeated column chromatography on silica gel. Identification of these known compounds was based on 1D and 2D NMR, MS and comparison of their spectroscopic data with literature values (Sashida *et al*., 1992; Kojima & Ogura, 1986; Yaguchi, 1988).

In the compounds **3, 6** and **7** the molecular formula is $C_{30}H_{48}O_5$ by means of HR-ESI-MS. In compound **4** and **5** the molecular formula is $C_{30}H_{48}O_4$. Their mass spectra present ions at *m/z* 248 resulting from the retro-Diels-Alder fragmentation characteristic of the ursane and oleane skeletons. Furthermore they possess an ion at *m/z* 203 characteristic of Δ^{12}- triterpenoids (Budzikiewicz *et al*., 1963). In the ^1H NMR (C_5D_5N) spectra of these compounds, the signal of H-18 permitted the distinction between the oleane and ursane skeletons. The H-18 signal appears at δ2.6 ppm in the ursane skeleton and at δ3.3 ppm in the oleane skeleton. The proton signals of H-29 and H-30 in the ursane skeletons appears as a doublet, but in oleane as a singlet. The chemical shifts of C-12 and C-13 (δ125 and 139 ppm in ursane, δ122 and 144 ppm in oleane) and H-12 (δ5.20-5.4 ppm) suggests that these compounds are Δ^{12}-unsaturated triterpenoids. The ^{13}C NMR spectra (table. 1) clearly exhibited the difference in the chemical shifts of C-12, C-13, C-17, C-18, C-19, C-20, C-22, C-27, C-29 and C-30 between the ursane group (**3, 4, 6**) and the oleane group (**5, 7**). The coupling constant of H-3 (*J* 2.3 Hz) in **3** suggested that two OH groups at C-2 and 3 were at the *cis* position. Besides, the ROESY correlation between H-3 and H-2, H-23, H-24 also confirmed the β-configuration of H-2 and H-3. However, the coupling constant of H-3 (*J* 9.4 Hz) in **4-7** showed that the two OH groups at C-2 and C-3 were in *trans* position and there was no ROESY correlation between H-3 and H-2 (**see HMBC, ROESY in table 2**).

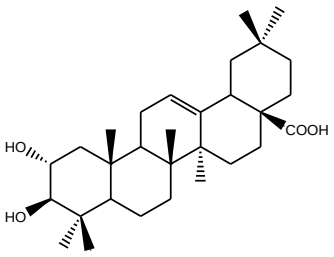

compound 5

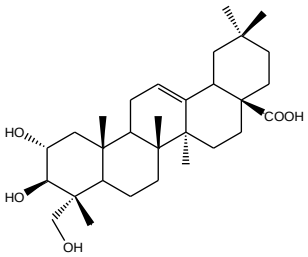

compound 7

Figure 1 Oleanane type triterpenes

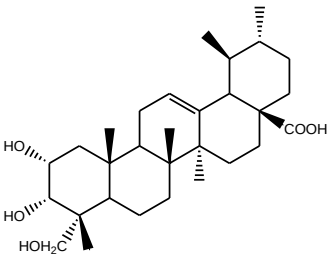

compound 3

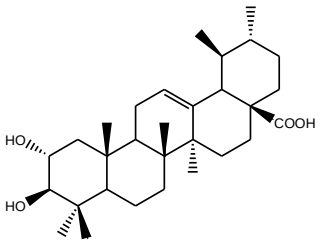

compound 4

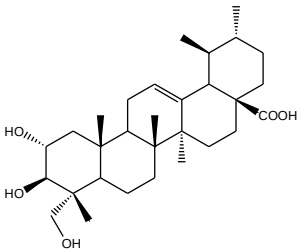

compound 6

Figure 2 Ursane type triterpenes

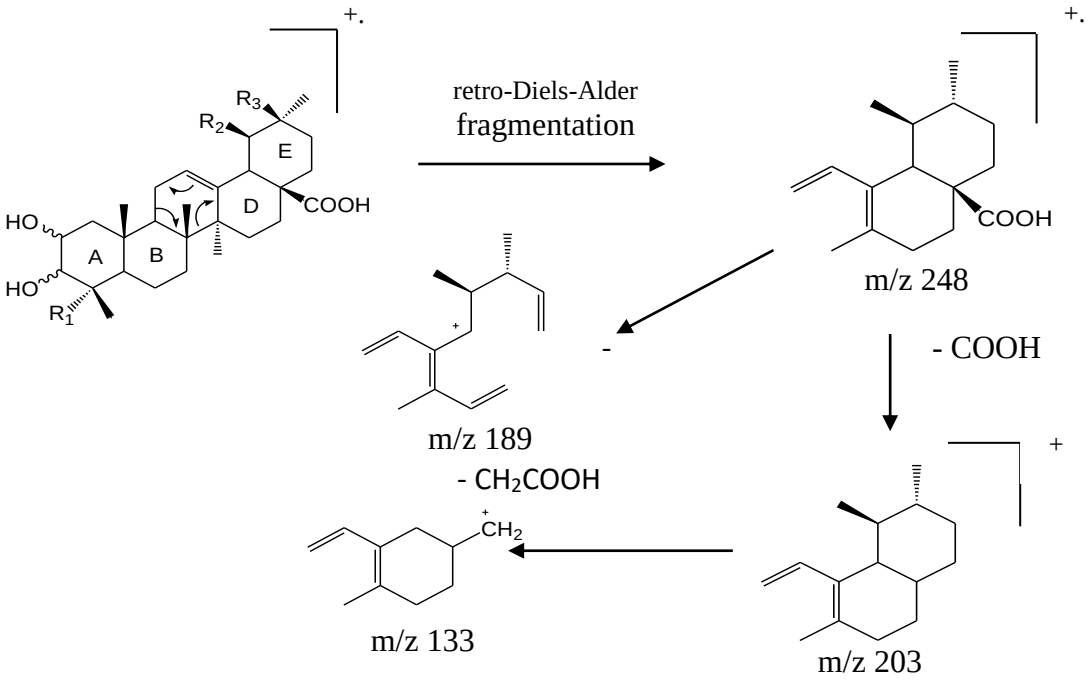

Figure 3 Proposed EI mass spectral fragmentation of triterpenoids **1-7**

Table 1 ^{13}C NMR spectral data of triterpenoid 2-7

(300, 500 MHz, 2 in $CDCl_3$; 3-5 in C_5D_5N; 6-7 in CD_3OD)

C-Atom	δ_C [ppm]					
	2	**3**	**4**	**5**	**6**	**7**
1	38.5	42.8	47.9	47.7	48.0	47.9
2	23.4	66.2	68.6	68.6	69.7	69.7
3	80.9	78.9	83.8	83.8	78.1	78.1
4	37.7	41.9	40.0	40.0	44.1	44.1
5	55.3	43.5	55.9	55.9	48.1	48.1
6	18.3	18.3	18.8	18.8	19.1	19.1
7	32.9	33.2	33.2	33.2	33.6	33.6
8	39.7	40.1	39.8	39.8	40.8	40.5
9	47.7	47.9	48.1	48.1	48.2	48.2
10	36.8	38.3	38.4	38.5	39.0	39.0
11	22.8	23.7	23.7	23.7	24.5	24.5
12	124.2	125.5	125.5	122.4	126.6	123.4
13	139.5	139.3	139.3	144.7	139.8	145.4
14	42.1	42.5	42.5	42.2	43.4	43.0
15	28.2	28.6	28.6	28.2	29.1	28.8
16	26.7	24.9	24.9	23.9	24.6	24.0
17	33.8	48.0	48.0	46.6	48.9	47.6
18	59.0	53.5	53.5	41.9	54.3	42.7
19	39.7	39.4	39.4	46.4	40.4	47.2
20	39.7	39.4	39.3	30.9	40.4	31.8
21	31.3	31.0	31.0	33.5	31.6	33.3
22	41.6	37.4	37.4	34.2	38.1	34.9
23	28.1	71.2	29.4	29.3	66.2	66.2
24	15.8	17.8	17.7	17.7	13.9	13.9
25	14.2	17.1	16.9	16.9	17.5	17.5
26	16.8	17.5	17.5	17.7	17.8	17.7
27	17.6	23.8	23.9	26.1	24.1	26.5
28	28.8	179.9	179.9	179.9	181.7	181.5
29	23.3	17.5	17.5	33.2	17.7	33.6
30	21.4	21.3	21.4	23.7	21.6	24.0
COMe	21.5					
CO	170.8					

Table 2 NMR data of triterpenoids 3-7 (500 MHz, 3-5 in C_5D_5N; 6-7 in CD_3OD)

H-Atom	δ_H [ppm]					HMBC	ROESY
	3	**4**	**5**	**6**	**7**	**(3-7)**	**(3-7)**
1	1.82, 1.94 (*m*)	1.28, 2.26 (*m*)	1.28, 2.26 (*m*)	0.88, 1.96 (*m*)	0.88, 1.96 (*m*)	C-2, 3, 25	
2	4.289 (*m*)	4.115 (*ddd*, 11/9.4/4.4)	4.115 (*ddd*, 11/9.4/4.4)	3.687 (*m*)	3.687 (*m*)	C-3	H-3 (in **3**), 25, 24
3	4.168 (*d*, 2.3)	3.420 (*d*, 9.4)	3.420 (*d*, 9.4)	3.350 (*dd*,9.7/2.4)	3.350 (*dd*,9.7/2.4)	C-24, 4, 1	H-2 (in **3**), 23, 24
5	2.02-2.08 (*m*)	1.04 (*m*)	1.04 (*m*)	1.28 (*m*)	1.28 (*m)*	C-25, 10, 4	
6	1.34, 1.60 (*m*)	1.36, 1.54 (*m*)	1.36, 1.54 (*m*)	1.38 (*m*)	1.38 (*m*)	C-25, 5	
7	1.34, 1.72 (*m*)	1.84, 2.04 (*m*)	1.84, 2.04 (*m*)	1.54, 1.74 (*m*)	1.54, 1.74 (*m*)	C-26, 8, 14	
9	1.94 (*m*)	1.76 (*m*)	1.76 (*m*)	1.66 (*m*)	1.66 (*m*)	C-25, 11, 10, 8, 5,	H-25, 26
11	1.96-2.08 (*m*)	1.98 (*m*)	1.98 (*m*)	1.94 (*m*)	1.94 (*m*)	C-12, 13, 9, 8, 10	
12	5.480 (*brs*)	5.476 (*m*)	5.476 (*m*)	5.242 (*m*)	5.242 (*m*)	C-11, 14, 9, 18, 13	H-18, 29
15	1.14-2.36 (*m*)	1.18, 2.36 (*m*)	1.18, 2.36 (*m*)	1.08 (*m*)	1.08 (*m*)	C-27, 26, 16, 8, 14	
16	1.98-2.06 (*m*)	2.00, 2.12 (*m*)	2.00, 2.12 (*m*)	1.94 (*m*)	1.94 (*m*)	C-15, 17	
18	2.626 (*br d*, 11.3)	2.641 (*br d*, 11.4)	3.314 (*dd*, 13.9, 4.0)	2.202 (*d*, 11.2)	2.849 (*dd*, 13.6, 3.9)	C-9, 16, 19, 20, 14, 17, 12, 13, 28	H-29, 20 (in ursane type), 12
19	1.42 (*m*)	1.46 (*m*)	1.28, 1.80 (*m*)	1.38 (*m*)	1.14, 1.70 (*m*)	C-29, 30, 22, 20, 17, 18	
20	1.00 (*m*)	1.04 (*m*)		0.98 (*m*)		C-30, 21 (in ursane type)	
21	1.34, 1.44 (*m*)	1.40 (*m*)	1.36, 1.56 (*m*)	1.36, 1.52 (*m*)	1.28, 1.66 (*m*)	C-29, 30, 22, 20, 17,	
22	1.96 (*m*)	1.98 (*m*)	1.18, 1.46 (*m*)	1.66 (*m*)	1.20, 1.40 (*m*)	C-17, 28	
23	3.77, 3.94 (*d*, 10.8)	1.291 (*s*)	1.291 (*s*)	3.261 (*d*, 11.0)	3.261 (*d*, 11.0)	C-24, 2, 3, 4, 5	H-3
24	0.87 (*s*)	1.092 (*s*)	1.092 (*s*)	0.692 (*s*)	0.690 (*s*)	C-25, 4, 5, 23, 3	H-25,2, 3, 23
25	1.00 (*s*)	0.991 (*s*)	0.991 (*s*)	1.042 (*s*)	1.028 (*s*)	C-24, 11, 10, 4, 5, 9, 1	H-24, 26, 3
26	1.07 (*s*)	1.060 (*s*)	1.032 (*s*)	0.846 (*s*)	0.813 (*s*)	C-25, 7, 8, 14, 9	
27	1.14 (*s*)	1.220 (*s*)	1.275 (*s*)	1.132 (*s*)	1.175 (*s*)	C-15, 8,14, 18, 12, 13	
29	0.965 (*d*, 6.4)	0.995 (*d*, 4.9)	0.954 (*s*)	0.865 (*d*, 6.4)	0.907 (*s*)	C-19, 20	
30	0.925 (*d*, 6.2)	0.960 (*d*, 5.9)	1.014 (*s*)	0.967 (*d*, 6.0)	0.941 (*s*)	C-21, 19, 20	

Conclusion

Oleanane and ursane type triterpenes are rich in the roots of *Streptocaulon tomentosum* Wight. Literature survey showed that oleanane and ursane typetriterpenes possess anti-tumor-promoting activity, anti-inflammatory activity and anti-insect activity. So the roots of *Streptocaulon tomentosum* Wight may be useful for the treatment of anticancer.

Acknowledgements

The authors acknowledge Dr Pho Kaung, Rector, University of Yangon for his kind permission to carry out this research and also thank to Dr Ni Ni Than (Professor and Head), Department of Chemistry, University of Yangon.

References

Budzikiewicz, H., Wilson, J. M., Djerassi, C. (1963). ″Mass Spectrometry in Structural and Stereochemical Problems. XXXII.1 Pentacyclic Triterpenes″, *J. Am. Chem. Soc.* vol. 85, pp. 3688.

Connolly, J. D., Hill, R. A. (2002). "Triterpenoids", Nat. Prod. Rep. vol. 19, pp. 494-513.

De Pascual Teresa, J., Urones, J. G., Marcos, I. S., Basabe, P., Sexmero Cuadrado, M. J., Fernandez Moro, R. (1987). "Triterpenes from Euphorbia broteri", *Phytochemistry*. vol. 26, pp. 1767-1776.

Dey, P. M., Harborne, J. B. (1991). *Methods in Plant Biochemistry*. vol. *7*, pp. 341-342.

Hisham, A., Kumar, G. J., Fujimoto, Y., Hara, N. (1995). "Salacianone and salacianol: two triterpenes from Salacia beddomei ", *Phytochemistry*. vol. 40, pp. 1227.

Kojima, H., Ogura, H. (1986). "Triterpenoids from *Prunella vulgaris*", *Phytochemistry*. vol. 25, pp. 729-733.

Konoshima, T., Takasaki, M. (2000). **"**Cancer-chemopreventive effects of natural sweeteners and related compounds", *Stud. Nat. Prod. Chem*. vol. 24, pp. 607.

Matsunaga, S., Tanaka, R., Akagi, M. (1988). "Triterpenoids from *Euphorbia maculata*", *Phytochemistry*. vol. 27, pp. 535-537.

Press, J. B., Reynolds, R. C., May, R. D., Marciani, D. J. (2000). "Structure/function relationships of. immunostimulating saponins". *Stud. Nat. Prod. Chem.* Vol. *24*, pp. 131–174.

Sashida, Y., Ogawa, K., Mori, N., Yamanouchi, T. (1992). "Triterpenoids from the fruit galls of *Actinidia polygama* "*Phytochemistry* vol. 31, pp. 2801-2804.

Yaguchi, Y., Sakurai, N., Nagai, M., Inoue, T. (1988). "Constituents of Myrica rubra. III: Structures of Two Glycosides of Myricanol", *Chem. Pharm. Bull*. vol. 36, pp. 1419-1424.

ANTIMICROBIAL, HYPOGLYCEMIC AND ANTIOXIDANT ACTIVITIES OF THE STEM OF *DRACAENA ANGUSTIFOLIA* (MEDIK.)ROXB.

Thin Yu Mar,[1] Hta Hta Win,[2] Kyu Kyu Maw[3]

Abstract

In this research work the stem of *Dracaena angustifolia* (Medik.) Roxb., Myanmar named Nant thar ku was selected for determination of antimicrobial, hypoglycemic and antioxidant activities. The stem of the selected plant was collected from Loikaw Township, Kayah State, in January, 2019. The aim of this research is to investigate the stem of *Dracaena angustifolia* (Medik.) Roxb. chemically and pharmaceutically. Preliminary phytochemical tests were performed by test tube method which gave positive for flavonoid, alkaloid, phenolic compound, polyphenol, glycoside, saponin, terpene, reducing sugar and tannin compounds. Antimicrobial activity of various solvent (*n*-hexane, ethyl acetate, acetone, ethanol, methanol) extracts was determined by agar well diffusion method and tested on six microorganisms such as *Bacillus subtilis, Staphylococcus aureus, Pseudomonas aeruginosa, Bacillus pumilus, Candida albicans and Escherichia coli*. Ethanol, acetone and ethyl acetate extracts responded high activity on all tested organisms. Moreover, a potent hypoglycemic activity of the stem of this plant was examined by adrenaline induced diabetic mice model method. Glibenclamide was used as standard drug. This plant showed remarkable inhibitory activity. Antioxidant activity of the stem of selected plant was measured by DPPH (2,2-diphenyl-1-picryl-hydrazyl-hydrate) assay method. IC_{50} value of selected plant was 3.17μg/mL by comparing with standard ascorbic acid 0.90μg/mL.

Keywords: *Dracaena angustifolia* (Medik.) Roxb., antimicrobial activity, hypoglycemic activity, antioxidant activity

Introduction

Dracaena angustifolia (Medik.) Roxb., family Asparagaceae is a herbaceous plant, forming large climbing shrubs with few ascending branches or small Slender tree with weak pendulous twigs, and 1-3 m tall (Flora of China,2000). The stems of this plant are simple or few branches, greyish and smooth. Leaves of this plant are born in dense rosettes, followed by yellow flowers in terminal racemes (Gupta, 2008). *Dracaena angustifolia* (Medik.) Roxb., Myanmar named Nant thar ku is one of the medicinal plants in Myanmar traditional medicine. It is one of Dragon blood trees. Dragon blood is a deep red resin, which has been used as a famous medicine in ancient times. Local people in Loikaw Township, Kayah State, Myanmar use the stem of Nant thar ku for the treatment of hypertension, diabetic, dysentery, anemia and diarrhea. And then this plant is used as tonic and diuretic. Hence, the stem of *Dracaena angustifolia* (Medik.) Roxb. is selected for chemical and pharmaceutical investigation.

In this research work, antimicrobial activity of various solvent (*n*-hexane, ethyl acetate, acetone, ethanol and methanol) extracts, hypoglycemic and antioxidant activities of ethanol extract from the stem of *Dracaena angustifolia* (Medik.) Roxb. were evaluated. Antimicrobial activity of various solvent extracts was determined by agar well diffusion method and tested on six microorganisms. Hypoglycemic activity of the stem of this plant was determined by adrenaline induced diabetic mice model method. Glibenclamide was used as standard drug. Antioxidant activity of the selected sample was measured by DPPH assay method and ascorbic acid was used as standard antioxidant.

[1] Dr, Associate Professor, Department of Chemistry, Magway University
[2] Dr, Associate Professor, Department of Chemistry, Panglong University
[3] Dr, Lecturer, Department of Chemistry, Magway University

Botanical description (Flora of China, 2000)

Genus	:	*Dracaena*
Species	:	*D. angustifolia*
Botanical name	:	*Dracaena angustifolia* (Medik.) Roxb.
Myanmar name	:	Nant thar ku
Part used	:	Stem
Medicinal uses	:	Hypertension, antibacterial, antifungal, diuretic, anti-diabetes, dysentery, diarrhea, purgative, anemia (Local people in Loikaw Township, Myanmar)

Figure 1 Flowers and plant of *Dracaena angustifolia* (Medik.) Roxb.

Materials and Methods

A. Sample Collection and Preparation

The stem of the *Dracaena angustifolia* (Medik.) Roxb. was collected from Loikaw Township, Kayah State, Myanmar in January, 2019. The plant sample was verified at the Botany Department of the University of Mandalay. They were cut into small pieces and air dried at room temperature for about one month. Then, the air-dried sample was stored in a well stoppered bottle, and used throughout the experiment.

Extraction:

The stems of the air-dried plant were percolated with ethanol. After two weeks, the mixture solution was filtered; filtrate was evaporated with rotary evaporator. Ethanol extract was obtained. This ethanol extract was used for the determination of antioxidant and hypoglycemic activities.

B. Preliminary Phytochemical Screening

Phytochemical evaluation for major phytochemicals was done using standard qualitative methods (Harbone, 1984). Tests for presence of alkaloids, carbohydrates, flavonoids, glycosides, phenolic compounds, and polyphenols, reducing sugars, saponins, tannins, steroids and terpenes were carried out.

C. Determination of Antimicrobial Activity

Antimicrobial activity of various solvent extracts from the stem of *Dracaena angustifolia* (Medik.) Roxb. was determined by agar well diffusion method and tested on six microorganisms such as *Bacillus subtilis, Staphylococcus aureus, Pseudomonas aeruginosa, Bacillus pumilus, Candida albicans* and *Escherichia coli* respectively. This determination was performed at Myanmar Pharmaceutical Industrial Enterprise, Ministry of Industry, Yangon.

1. Samples: The crude extracts of the sample were prepared by extracting the sample with different solvents like *n*-hexane, ethyl acetate, acetone, ethanol and methanol by

percolating method. The extracts (1g each) were introduced into sterile petri-dishes and 1mL of their respective solvent.

2. Procedure: The antimicrobial activity of the crude extracts from the selected sample was determined against six strain microorganisms by the agar well diffusion method. The extract 1g was introduced into sterile petri-dish and dissolved in 1mL or with least amount of its respective solvent till it was dissolved. The bacteria suspension from trypticase soy broth was done evenly onto the surface of the trypticase soy agar slants immediately after hardening of the agar-well were made with a 10 mm sterile cork borer from each extract's agar. After inoculums had dried for 5 minutes, the agar discs were removed and the wells were filled with sample to be tested. And then, the plates were incubated at 37°C. After overnight incubation at 37°C the diameter of inhibition zone including 10mm wells was measured. This method was used to test antimicrobial action of the extracts on 24 hours broth culture of the organism used. The extracts from sample were tested with six microorganisms. The observation was done the inhibition zone diameters and the measurements were recorded (Fransworth, 2005; Cowan, 1999).

D. Determination of Hypoglycemic Activity

The hypoglycemic activity of the ethanol extract from the stem of the selected plant was determined by adrenaline induced diabetic mice model method (Balssells *et.al*, 2015; Cryper, 1981; Pimenta, 2006; Kitabchi *et.al*, 2009; Verbene *et.al*, 2016). This experiment was done at Department of Biotechnology, Mandalay Technological University.

1. Selection of the mice:

The strain of ICR albino mice was used in this study. The mice with 50-60 g of body weight and age of 10-12 weeks were selected to use and kept separately.

2. Induction of the diabetes to mice:

The selected mice were prepared to cause hyperglycemic effect by using adrenaline injection. For giving adrenaline injection, the selected mice were fasted overnight. The animals were given intraperitoneally with adrenaline 0.2 mL/kg body weight in distilled water as shown in Figure 2(a). They were kept for 4 hours after injection and then they were given 0.5 mL of glucose solution orally at hourly interval to prevent hypoglycemic shock. They were offered unlimited amounts of standard laboratory diet food and water. After one week, the mice were used to test the hypoglycemic activity.

3. Determination of normal fasting blood glucose level:

In order to determine the normal blood glucose level, the mice were fasted overnight before the commencement of the experiment, to ensure stable blood sugar resulting blood drops were tested by Glucometer and test strips as shown in Figure 2(b) and (c).

4. Experimental design of groups of selected mice:

The selected mice were divided into 4 groups for the determination of hypoglycemic activity. They are tested plant sample, positive and negative control and normal group. Each group contained five mice and gave them markers by using sodium picrate solution.

5. Administration of the selected plant extracts, standard drug and water as treatment:

A total of 15 fasted mice were used to give orally for the determination of hypoglycemic activity. Group I mice were administered with the plant sample extracts of 1 g/kg of body weight. Group II mice were kept as a positive control, the standard drug; Glibenclamide was administered

0.5 mg/kg of body weight. The remaining group was given orally with water 0.2 mL to each mouse. No fasting and no adrenaline injection group of mice were used as normal group.

6. Second induction of diabetes to mice:

After administration of the tested sample and the controls, all group mice were injected with adrenaline.

7. Screening of blood glucose level:

During the experimental procedure, three observations were performed at five times of 45 minutes interval after injection of the adrenaline by using Glucometer. The results were collected from each group for the data analysis.

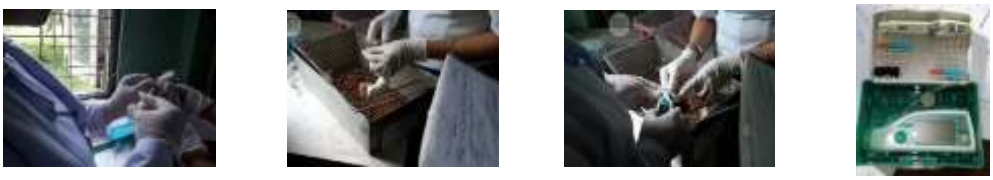

(a) (b) (c) (d)

Figure 2 Detection of hypoglycemic activity

(a) Induction of diabetes to mouse (b) Cutting the tail to collect blood

(c) Determination of blood glucose level and (d) Glucometer

E. Determination of Antioxidant Activity

Antioxidant activity of the ethanol extract from the stem of selected plant was determined by DPPH assay method by using APEL UV/Vis spectrophotometer. This determination was performed at Department of Chemistry, Panglong University.

1. Preparation of reagents:

In this experiment three solutions were prepared. They are DPPH solution, standard ascorbic acid solution and various concentrations of sample solution.

2. Preparation of 100 μM DPPH solution:

DPPH powder 0.004 g (4 mg) was weighed and it was thoroughly and gently dissolved in 100 mL of ethanol and stored in brown colored volumetric flask. It must be kept in the fridge for no longer than 24 hours before use.

3. Preparation of standard ascorbic acid solution:

Ascorbic acid (2mg) was dissolved in 20 mL of ethanol (Analar grade). This solution was thoroughly mixed at room temperature to obtain 100 μg/mL of standard solution. The various concentrations of standard solution (0. 25, 0. 5, 1, 2 and 4 μg/mL) were determined by using two-fold dilution methods. 1 mL of ascorbic acid and 3 mL of DPPH solutions were thoroughly mixed for about 15 min at room temperature. The absorbance of the mixture was measured at 517 nm.

4. Preparation of test sample solution:

Sample (0.01 g) was dissolved in 20 mL ethanol (Analar grade). This solution was thoroughly mixed at room temperature for 15 minutes to obtain 500 μg/mL of sample solution. The various concentrations of sample solution (0.625, 1.25, 2.5, 5 and 10 μg/mL) were prepared by using two-fold dilution method. 1 mL of sample solution and 3 mL of DPPH solution were

thoroughly mixed for about 15 minutes at room temperature. The absorbance of the mixture was measured at 517 nm.

5. Two-fold serial dilutions:

A two-fold dilution reduces the concentration of a solution by a factor of two that is reduced the original concentration by one half. A series of two-fold dilutions is described as two-fold serial dilutions.

$$\% \text{ inhibition} = \frac{\text{Absorbance of control} - \text{Absorbance of sample}}{\text{Absorbance of control}} \times 100$$

This formula is the calculation of percent inhibition of (IC_{50}) value. The half maximal inhibitory concentration (IC_{50}) is a measure of the effectiveness of a substance in inhibiting a specific biological or biochemical function (Lee *et.al*, 2004; Vertuani, 2004).

Results and Discussion

A. Preliminary Phytochemical Test of the Stem of *Dracaena angustifolia* (Medik.) Roxb.

Preliminary phytochemical tests were carried out by standard qualitative methods. These results are shown in Table 1.

Table 1 Preliminary Phytochemical Test of the Stem of *Dracaena angustifolia* (Medik.) Roxb.

No.	Test	Reagent used	Observation	Results
1.	Alkaloid	Dragendorff's reagent	Orange ppt	+
2.	Flavonoid	EtOH, Conc: HCl, Mg ribbon	Pink color solution	+
3.	Glycoside	10 % Lead acetate	White ppt	+
4.	Phenolic	10 % $FeCl_3$	Green color solution	+
5.	Polyphenol	1 % $K_3[Fe(CN)_6]$, 1 % $FeCl_3$	Greenish blue color solution	+
6.	Lipophilic	0.5 N KOH solution	Deep blue color solution	+
7.	Saponin	Shaked with H_2O	Frothing	+
8.	Sugar	Benedict's solution	Brick red ppt	+
9.	Steroid	$(CH_3CO)_2O$, Conc.H_2SO_4	Blue color solution	+
10.	Terpene	$(CH_3CO)_2O$, $CHCl_3$, Conc.H_2SO_4	Reddish brown color solution	+
11.	Tannin	1% $FeCl_3$	Yellowish brown ppt	+

(+) present of constituents, (–) absence of constituents, (ppt) precipitate

B. Antimicrobial Activity of Crude Extracts of the Stem of *Dracaena angustifolia* (Medik.) Roxb.

Antimicrobial activity of various solvent extracts of the stem of *Dracaena angustifolia* Medik.) Roxb. was determined by applying agar well diffusion method and tested on six selected microorganisms. These results are tabulated in Table (2) and Figure (3). As the results of antimicrobial activities, ethyl acetate, ethanol and acetone extracts responded high activity on all tested organisms. Methanol extract showed high activity on *Bacillus subtilis, Candida albicans, Escherichia coli* and medium activity on *Pseudomonas aeruginosa, Bacillus pumius*. *n*-Hexane extract revealed no activity on all tested organisms. Consequently, resulting data can be shown that the stem of *Dracaena angustifolia* Medik. possess the potency for the treatment of diseases related to microorganisms tested.

Table 2 Antimicrobial Activity of the Stem Bark of *Dracaena angustifolia* (Medik.) Roxb. (Nant thar ku)

Solvent extracted	Inhibition zones (diameter, mm)					
	B. subtilis	***S. aureus***	***B. pumilus***	***P. aeruginosa***	***C. albicans***	***E. coli***
MeOH	20 (+++)	18 (++)	17 (++)	17 (++)	20 (+++)	20 (+++)
EtOH	25 (+++)	25 (+++)	21 (+++)	25 (+++)	25 (+++)	25 (+++)
Acetone	24 (+++)	24 (+++)	21 (+++)	21 (+++)	25 (+++)	25 (+++)
EtOAc	35 (+++)	40 (+++)	38 (+++)	40 (+++)	40 (+++)	42 (+++)
n-hexane	-	-	-	-	-	-

10 mm ~ 14 mm (+) - low activity, 15 mm ~ 19 mm (++) - medium activity, 20 mm above (+++) - high activity

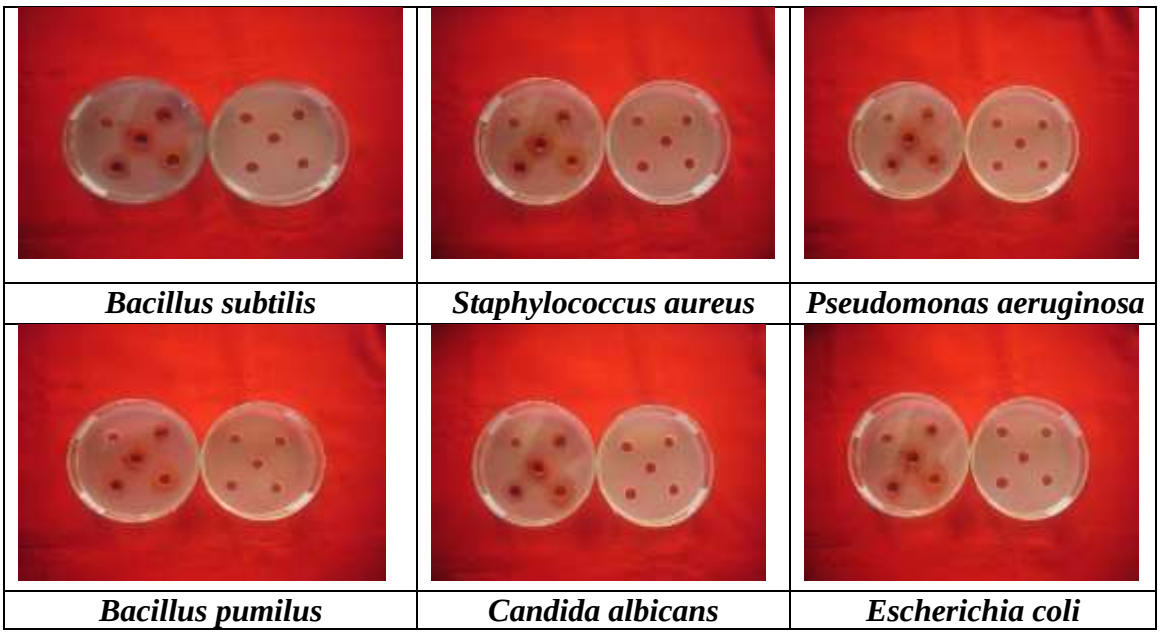

Figure 3 Antimicrobial activities (inhibition zones) of *Dracaena angustifolia* (Medik.) Roxb.

C. Determination of the Hypoglycemic Activity of Crude Extract on Adrenaline Induced Mice

The blood glucose levels of fasted animals at five times of 45 minutes intervals after adrenaline injection measured. From the measured glucose levels, the mean blood glucose values were calculated as shown in Table 3 which was also graphically presented in Figure 4. The significant hypoglycemic activity was observed in *Dracaena angustifolia* (Medik.) Roxb. and comparable to diabetic control. According to the results of the experimental carried out on diabetic mice, it had been shown that the ethanol plant extract has highly significant activity than the negative control (water) and consistent hypoglycemic effect. Positive control (Glibenclamides) was also highly significant than the water. The ethanol plant extract has highly significant activity than the negative control (water) and also effective as positive control (Glibenclamide). Therefore, ethanol plant extract has potential to use as routine drug like the positive control.

Table 3 Hypoglycemic Activity of Plant Extract, Positive Control (Glibenclamide) and Negative Control (Water)

Groups	Dose	Blood Glucose Level (mg/dL)					
		0 min	45 min	90 min	135 min	180 min	225 min
Sample extract (Nant thar ku)							
1	1 g/kg	130	153	130	104	84	70
2	1 g/kg	128	150	116	101	86	72
3	1 g/kg	124	146	122	103	82	68
4	1 g/kg	132	152	128	98	81	69
5	1 g/kg	125	148	132	95	79	67
Mean		128	150	126	100	82	69
Positive control (Glibenclamide)							
1	0.5 mg/kg	122	144	98	75	62	50
2	0.5 mg/kg	114	147	102	80	63	52
3	0.5 mg/kg	120	143	103	81	64	56
4	0.5 mg/kg	117	140	102	82	65	55
5	0.5 mg/kg	118	148	108	83	60	48
Mean		118	144	102	80	63	52
Negative control (Water)							
1	0.2 mL/kg	131	156	136	122	114	103
2	0.2 mL/kg	115	152	128	112	102	94
3	0.2 mL/kg	121	158	132	118	105	96
4	0.2 mL/kg	118	155	127	115	101	93
5	0.2 mL/kg	114	149	130	116	99	91
Mean		120	154	131	116	104	95

Table 4 Hypoglycemic Activity of Ethanol Extract of Selected Plant, Positive Control (Glibenclamide) and Negative Control (Water)

Groups	Dose	Blood Glucose Level Mean ± SD (mg/dL)					
		0 hr	45 min	90 min	135 min	180 min	225 min
Ethanol plant extract (Nant thar ku)	1 g/kg	128 ±3.35	150 ±2.87	126 ±6.56	100 ±3.71	82 ±2.71	69 ±1.94
Glibenclamide (Standard drug)	0.5 mg/kg	118 ±3.04	144 ±5.96	102 ±3.64	80 ±3.12	63 ±1.94	52 ±3.5
Diabetic negative control (water only)	0.2 mL/kg	120 ±6.80	154 ±3.53	131 ±3.60	116 ±3.39	104 ±5.89	95 ±4.64

SD = Standard Deviation

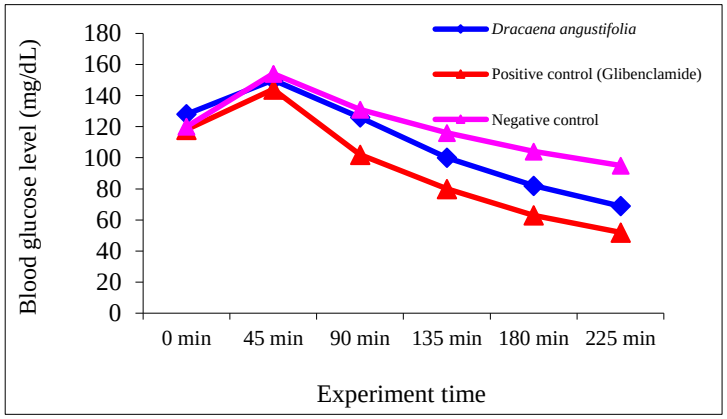

Figure 4 Level of fasting blood sugar during hypoglycemic activity test with *Dracaena angustifolia*, positive control and negative control

D. Determination of Antioxidant Activity of Stem of *Dracaena angustifolia* (Medik.) Roxb

Antioxidant activity of ethanol extract of stem of *Dracaena angustifolia* (Medik.) Roxb. was expressed as percentage of DPPH radical inhibition and IC_{50} values (μg/mL). Free radical scavenging activities values of ascorbic acid and sample extract in percentage range from 47.39% to 57.86 % and 31.25 % to 76.25 % respectively. The results of antioxidant activity using DPPH assay method in sample extract and ascorbic acid used as a positive control are shown in Figures 5 and 6 and Tables 5 and 6.

Table 5 Absorbance Values and % Inhibition of Standard Ascorbic Acid

Standard	Concentration (μg/mL)	% Inhibition	IC $_{50}$ value(μg/mL)
Ascorbic acid	0. 25	47.39	0.90
	0.50	49.58	
	1.00	51.49	
	2.00	51.67	
	4.00	57.86	

Table 6 Absorbance Values and % Inhibition of Sample Extract

Sample	Concentration (μg/mL)	% Inhibition	IC $_{50}$ value(μg/mL)
Dracaena angustifolia	0.625	31.25	3.17
	1.250	44.42	
	2.500	49.69	
	5.000	63.58	
	10.000	76.25	

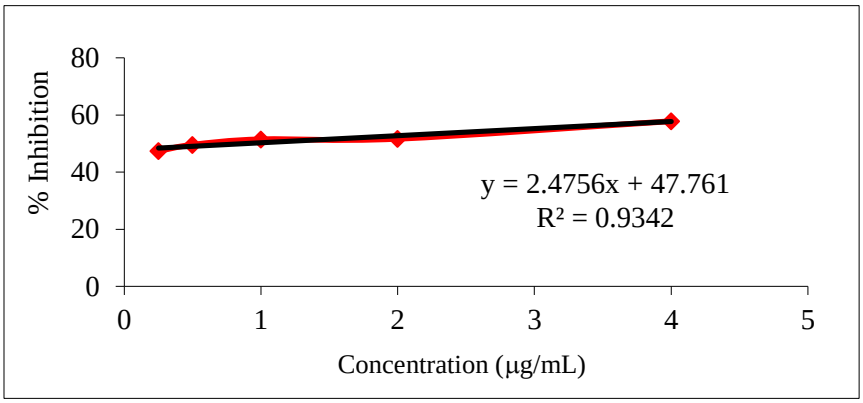

Figure 5 Plot of % inhibition vs concentration of standard ascorbic acid

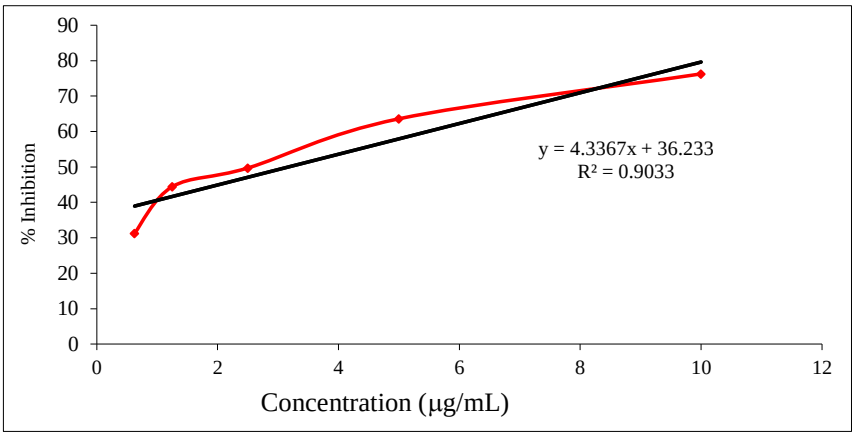

Figure 6 Plot of % inhibition vs concentration of ethanol extract of *Dracaena angustifolia* (Medik.) Roxb.

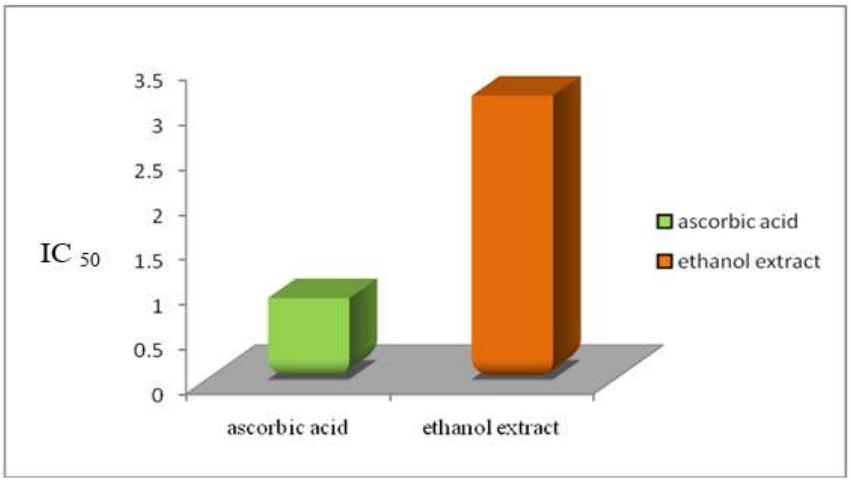

Figure 7 Comparison of IC_{50} values of standard ascorbic acid and ethanol extract of *Dracaena angustifolia* (Medik.) Roxb.

The IC_{50} value is a parameter used to measure antioxidant activity and it is defined as the sample extract concentration required for 50 % scavenging of DPPH radicals under experimental condition employed. The smaller IC_{50} value corresponds to a higher antioxidant activity. According to above IC_{50} values, the ethanol extract of the stem of *Dracaena angustifolia* (Medik.) Roxb. was found to exhibit significant antioxidant property which is comparable to standard ascorbic acid. Moreover, in accordance with Figure 5 and 6, increase in concentration implies

increase in % inhibition of oxidation. From these results, it is also observed that increase in concentration shows to increase in % inhibition, it means that increase the free radical scavenging activity.

Conclusion

In this research work one of Myanmar traditional medicinal plants, *Dracaena angustifolia* (Medik.) Roxb. was chosen for chemical and pharmaceutical investigation. Preliminary phytochemical screening showed that the selected plant has valuable phytochemical constituents. In accordance with antimicrobial activity determination, the selected plant has effective antimicrobial activity. So, various solvent extracts of the selected sample should be used for treatment of microorganism infections. The significant findings were that the test plant extract possessed high remarkable hypoglycemic effects like the standard drug, glibenclamide. It was found to possess effective hypoglycemic activity, which supports the traditional application of this plant in treatment of diabetic. IC_{50} value of the ethanol plant extract has greater than standard ascorbic acid. But the free radical scavenging activity of plant extract has effective activity like that of standard ascorbic acid. Therefore, the ethanol extract of selected plant should be used as antioxidant for maintaining of human health, protection of cancer, improve blood circulation and regulate blood pressure. From the results of experimental data, the stem of *Dracaena angustifolia* (Medik.) Roxb. has effective bioactivities. So, with the good quality control of the pharmaceutical preparation from the stem of *Dracaena angustifolia* (Medik.) Roxb., it may be used for a variety of medicinal purposes.

Acknowledgments

The authors would like to thank the Myanmar Academy of Art and Science for allowing to present this paper. We are extremely grateful to Dr Khin May Aung, Pro-Rector, Dr Nyan Tun, Professor and Head, Dr Myat Sandar Hla, Professor, Department of Chemistry, Panglong University, for their permitting and valuable advises on this research.

References

Balsells, M., Garcia-Patterson, A., Sola, I., Roque, M., Gich, I. and Corcoy, R. (2015). "Glibenclamide, Metformin, and Insulin for the Treatment of Gestational Diabetes: A Systematic Review and Meta-Analysis". *British Medical Journal* (Clinical Research ed.), pp. 350

Cowan, M. M. (1999). "Plant products as antimicrobial agents", *Clinical Microbiology Review*, pp. 564- 582

Cryper, P. E. (1981). "Glucose Counter regulation in Man Diabetes". vol.30, pp. 261-264

Flora of China Editorial Committee. (2000). "*Flora of China*". Science Press & Missouri Botanical Garden Press, Beijing & St. Louis. vol.24, pp. 425-431

Fransworth, N. R. (2005). *Review on Biological and Phytochemical Screening of Plants*, 5th edition,pp. 250-270

Gupta, D., Bleakley, B. and Gupta, R. K. (2008). "Dragons blood: Botany, chemistry and therapeutic uses": *Review journal of Ethnopharmacology*, vol. 115, pp. 361-380

Harbone, J. B. (1984). *Phytochemical methods:* A Guide to Modern Techniques of Plant Analysis, 2nd edition, Chapman and Hill Ltd, U.S.A.

Kitabchi, A. E., Umpierrez, G. E., Miles, J. M. and Fisher, J. N. (2009). "Hyperglycemic Crises in Adult Patients with Diabetes" *Diabetes Care.* vol.32 (7), pp. 1335-1343

Lee, S., Son, D., Ryu, J., Lee, Y.S., Jung, S. H., Lee, S. Y. and Shin, K. H. (2004). "Antioxidant activities of Acanthopanax senticosus stems and their lignan components". *Archives of Pharmacal Research,* vol.27, pp.106-110

Pimenta, A. M., Montenegro, M. C., Ara Ujo, A. N. and Martinez, J. C. (2006). "Application of sequential injection analysis to Pharmaceutical analysis", *J. Pharm. Biomed.* Annul, vol.40, pp. 16-34

Verbene, A. J. M., Karin, W. S., Sabetghadam, A. and Liewellyn-Smith, I. J. (2016). "Adrenaline: Insights into its Metabolic Roles in Hypoglycemic and Diabetes". *British Journal of Pharmacology*, vol. 173(9), pp. 1425-1437

Vertuani, S., Augusti, A. and Manfredini, S. (2004). "The Antioxidants and Pro-Antioxidants Network: an overview". *Current Pharmaceutical Design*. vol.10, pp. 1677-94

EXTRACTION AND IDENTIFICATION OF SOME CHEMICAL CONSTITUENTS FROM *EULOPHIA CAMPESTRIS* W. (GAMON-THANGA-ZIN) RHIZOME

Myo Min[1], Mon Mon Thu[2], Myint Myint Kyi[3], Saw Hla Myint[4]

Abstract

The present research deals with the isolation and characterization of some chemical constituents of *Eulophia campestris* W. (Gamon-thanga–zin) rhizomes. *Eulophia campestris* W. is widely used in Myanmar as the traditional medicine for the diabetes, heart tonic, and aphrodisiac. Semi-quantitative elemental analysis of *E. campestris* rhizome was carried out by ED-XRF method. From the analysis, the elements of major composition such as K, Fe and Ca and minor composition such as Zn and Cu were observed in the sample. The isolation of some compounds from *E. campestris* rhizome was performed by column chromatographic method. Firstly, the dried powdered sample of *E. campestris* (250 g) was extracted with 70 % EtOH at room temperature. The concentrated extracts were partitioned with Pet-ether (60°-80°C) to remove the fat. The defatted residue was then extracted with ethyl acetate in a separating funnel. Ethyl acetate layer was evaporated to obtain a dry extract (4.0 g). After the extraction with ethyl acetate from *E. campestris* W. crude extract was separated by column chromatographic method on a silica gel column [(Toluene: EtOAc) (95: 5)], as eluent. The eluates were examined under UV lamps (254 nm & 365 nm) and on TLC plates by detecting with anisaldehyde reagent. The fractions with similar R_f values were combined. After combining together similar fractions, the isolated compounds, MM-1, MM-2 and MM-3 were obtained. The isolated compounds were also identified by UV, FT-IR, ^{1}H, ^{13}C NMR and GC-MS method. According to the chemical tests, UV, FT-IR, ^{1}H, ^{13}C NMR, and GC-MS methods, the isolated compounds could be deduced as 1,2-Benzene dicarboxylic acid, diisooctyl ester (MM-1, 0.01%), 3-cyclohexene-1-ol,5-(2-butenylidene)-4,6,6-trimethyl (MM-2, 0.011 %) and Bis -(2-Ethylhexyl) Phthalate ester (MM-3, 0.0075%) respectively.

Keywords: Column chromatographic method, *Eulophia campestris* W., Gamon-thanga-zin, GC-MS method, Spectroscopic method

Introduction

Description of the Plant

Genus *Eulophia* is highly diverse, occurs in a wide range of habitats, and belongs to family Orchidaceae. This plant produces two shoots, reproductive and vegetative, from their underground tubers. The genus *Eulophia* has a wide distribution and comprises over 230 species, which are widespread from tropical and Southern Africa, Madagascar and from neotropics to throughout tropical and subtropical parts of Asia and Australia (Cieslicka, 2006).

A terrestrial orchid *Eulophia campestris* is very common in the beach forests. The genus *Eulophia* species are widely found in the regions which possesses warm and humid, tropical climate with a temperature of 20° to 32°C and a mean relative humidity between 82 to 85% throughout the year. Traditional medicines with therapeutic utility have been used since antiquity and are still contributing a significant role in the primary health-care system. It is estimated that 70-80% of the world's population relies on traditional herbal medicines for their primary health care (WHO, 2008).

[1] Dr, Associate Professor, Department of Chemistry, West Yangon University
[2] Dr, Associate Professor, Department of Chemistry, Pyay University
[3] Dr, Lecturer, Department of Chemistry, West Yangon University
[4] Dr, Professor and Head (Retd.), Department of Chemistry, University of Yangon

Medicinal and Nutritional Uses

In Ayurvedic medicine, *Amarkand* is generally prescribed as expectorant, anabolic, tonic, diuretic, astringent, digestive, and soft purgative, and also recommended for the treatment of ear discharge, blood clotting, joint edema, and debility. In addition, it is also considered as a general tonic to promote strength and alleviates all the three "doshas". These are also used in stomatitis, purulent cough; and in the heart problems, dyscrasia, and scrofulous diseases of the neck; bronchitis, blood diseases, and as a vermifuge (Hossain, 2011). Some of the *Eulophia* species have been studied for their nutritional properties. *E. campestris* Wall. is available as a *salep* (flour of starch) in Indian markets, as food for children and convalescents (Artemas, 1923). Balance between nutrients and anti-nutrients were studied in *E. ochreata* Lindl. It was found that tubers had low values of all free carbohydrates and had a low content of anti-nutrients such as phytic acid and trypsin inhibitors (Aberoumand, 2009). The proximate composition and mineral constituents indicated that these tubers are a good source of plant fibers, proteins, and carbohydrates (Aberoumand and Deokule, 2009).

Figure 1 Leaves, stem and rhizome of *E. campestris* W. (Gamon-thanga-zin)

Materials and Methods

The rhizomes of *E. campestris* were collected from Kyaik-Htiyo hill, Mon State, Myanmar in cold season. Semi-quantitative elemental analysis of *E. campestris* rhizome was carried out by ED-XRF method (Griken, *et al*., 1986). The isolation of some chemical compounds from *E. campestris* rhizome was carried out by solvent extraction and column chromatographic methods (Figure 2). The isolated compounds were confirmed by UV lamp and chemical reagent tests. The isolated compounds were characterized by UV, FT-IR, ^{1}H, ^{13}C NMR and GC-MS methods (Silverstein and Webster, 1998).

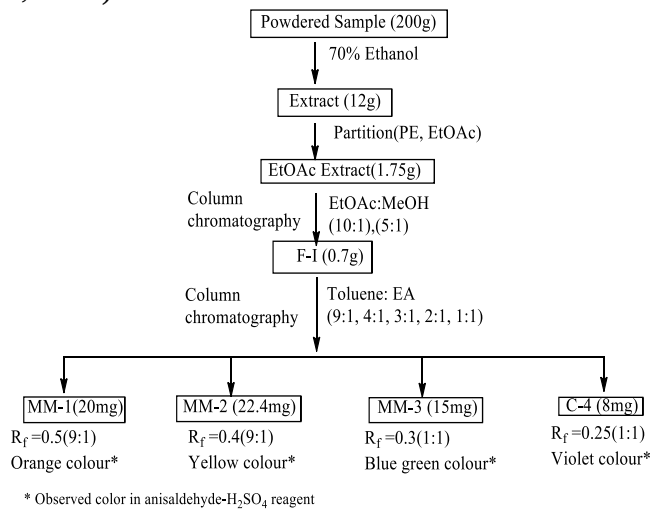

Figure 2 Flow diagram of isolation of compounds from *E. campestris* rhizome

Aim

To identify the isolated compounds of *E. campestris* rhizome by spectroscopic methods

Results and Discussion

Semi-quantitative Elemental Analysis of *E. campestris* Rhizome

Semi-quantitative elemental analysis of *E. camprestris* rhizome was carried out by ED-XRF method (Griken, *et al*., 1986). From the analysis, the elements of major composition such as K (59.75%), Fe (16.89%) and Ca (14.87%) and minor composition such as Zn (4.97%) and Cu (3.52%) were observed in the sample (Figure 3). In human metabolism, potassium reduces the hypertension. Iron helps the function of blood in body. Calcium is very important element for the formation of teeth and bone.

Figure 3 ED – XRF spectrum of *E. campestris* W. rhizome

Isolation and Preliminary Confirmation of the compounds by UV and Reagent Test

Compounds (MM-1, 2 and 3) of EtOAc crude extract from *E. camprestris* rhizome were separated by column chromatographic method on silica gel G adsorbent. The polarity of eluent, toluene and ethyl acetate was successively increased from 9:1 to 1:1. According to the procedure in Figue 2, three compounds (MM-1, 2 and 3) were isolated from EtOAc crude extract. The isolated compounds were UV active (254nm & 365nm) and they were detected by spraying on the TLC chromatograms with anisaldehyde-H_2SO_4 reagent, iodine, 5% $FeCl_3$ and vanillin-sulphuric acid reagent. The results are shown in Figure 4 and Table 1.

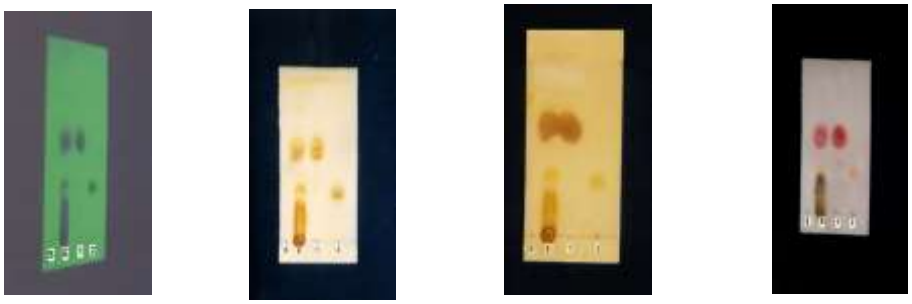

(a) UV_{254}nm (b) I_2 reagent (c) $FeCl_3$ (d) Vanillin & H_2SO_4
(S = Solvent, E = Crude extract, 1 = MM-1, 2 = MM-3)

Figure 4 TLC spot test of isolated compound MM-1 and MM-3

Table 1 Physicochemical Properties of Isolated Compounds by Colour Reaction Tests

Isolated Compound	Solvent System	R_f	UV		Reagent				
			254nm	365nm	Anisal-dehyde	I_2	5%Fe Cl_3	Vanl. & S/A	Liberm.& Burchard
MM-1	Tol.:EA (9 : 1)	0.55	+	+	Orange	Yellow	No colour change	Yellow	-
MM-2	Tol.:EA (9:1)	0.46	+	+	Yellow	Yellow	-	Dark	-
MM-3	Tol: EA (1:1)	0. 3	+	+	Greenis h blue	Yellow	No colour change	Yellow	-

Identification of Chemical Constituents from *E. campestris* Rhizome

Compounds: MM-1, 2 and 3 of EtOAc crude extract from *E. camprestris* rhizome were separated by column chromatographic method. The isolated compound MM-1, MM-2 and MM-3 were identified by UV, FT-IR, ^{1}H NMR, ^{13}C NMR spectroscopic methods and GC-MS method. According to spectroscopic methods, the compound MM-1, MM-2 and MM-3 could be deduced as 1, 2-Benzene dicarboxylic acid, diisooctyl ester (0.01%), 3-cyclohexene-1-ol, 5- (2-butenylidene)-4,6,6-trimethyl (0.011 %) and Bis -(2-Ethylhexyl) Phthalate ester (0.0075%) respectively. The results of isolated compound MM-1 are shown in Figure 5, 6, 7, 8, 9, Table 2, 3, and 4.

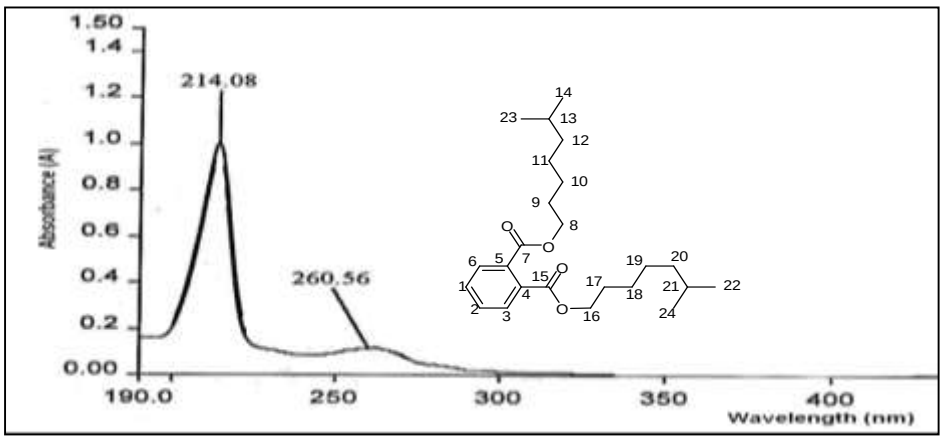

Figure 5 UV spectrum of isolated compound MM-1

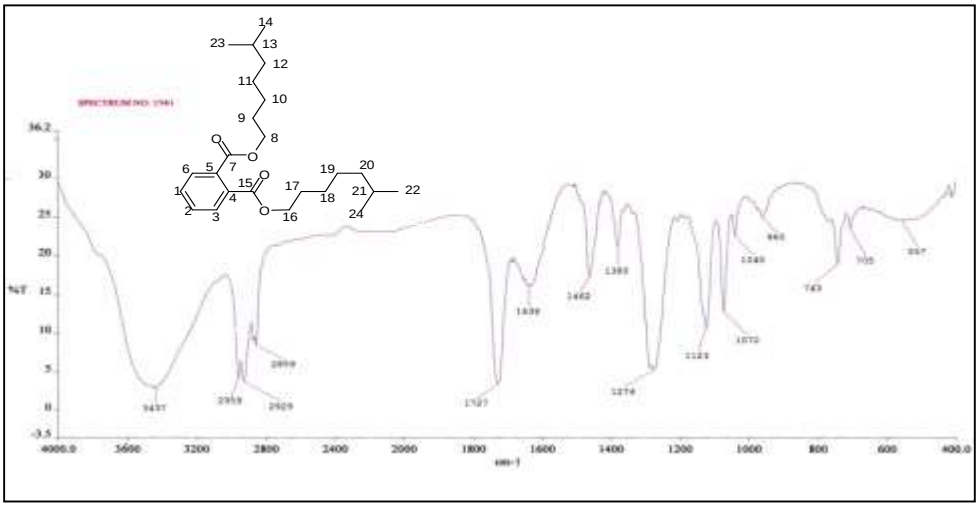

Figure 6 FT-IR spectrum of isolated compound MM-1

Table 2 FT-IR Spectral Data of Isolated Compound MM-1

Frequency Range (cm^{-1})	Mode of Vibration	Assignment
2929	ν_{asym} C-H	- CH_3 and -CH_2
2859	ν_{sym} C-H	- CH_3 and -CH_2
1727	ν C=O	Ester carbonyl
1638 (vw)	ν C=C	Ortho-disubstituted
1462	δ_{oop} -CH_2	-CH_2 group
1380	δ_{oop} -CH_3	-CH_3 group
1274	ν_{asym} C – O – C	Aromatic ester
1123	ν C – O	Alkyl substituent
1072, 1040	$\delta_{in\text{-}plane}$-CH_2 or -CH_3	- CH_2 or -CH_3 group
743 (vs)	ν C = C	Ortho-disubstituted

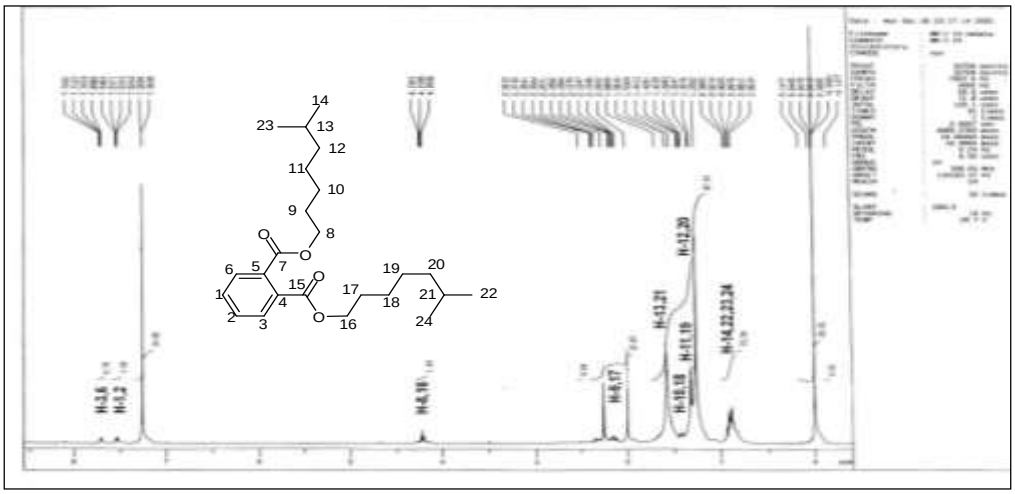

Figure 7 ^{1}H NMR spectrum of isolated compound MM-1 (400 MHz, $CDCl_3$)

Table 3 ^{1}H NMR Spectral Data of Isolated Compound MM-1 (400 MHz, $CDCl_3$)

H – No.	δ_H (ppm)	Type of Proton	H – No.
H – 1, 2	7.53	dd	= CH
H – 3, 6	7.71	d	= CH
H – 8, 16	4.21	t	O – $\underline{CH_2}$- CH_2
H – 9, 17	2.13	m	-CH_2-$\underline{CH_2}$-CH_2
H – 10, 18	1.42	m	-CH_2-$\underline{CH_2}$-CH_2
H – 11, 19	1.30	m	-CH_2-$\underline{CH_2}$-CH_2
H – 12 , 20	1.25	m	-CH_2-$\underline{CH_2}$-CH
H – 13 , 21	1.58	m	CH_2-$\underline{CH}$-
H–14,22,23,24	0.90	m	$\underline{CH_3}$-CH(CH_3)- $\underline{CH_3}$

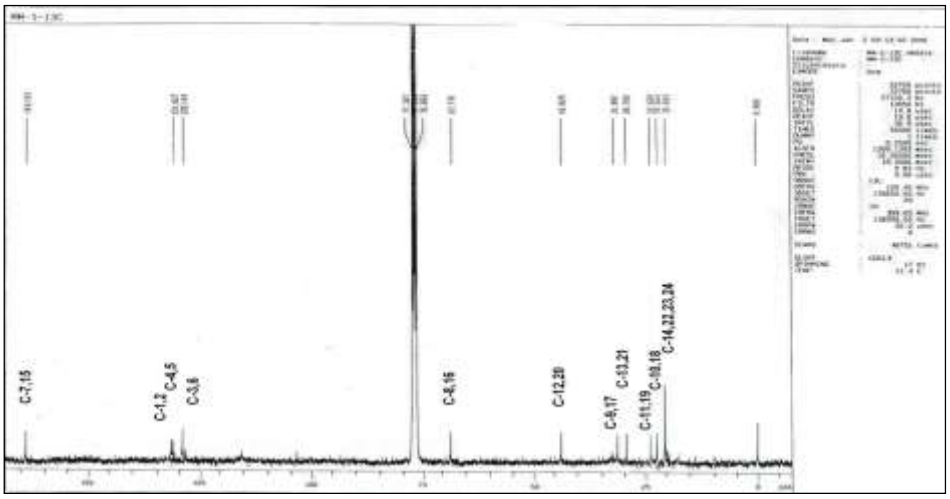

Figure 8 ^{13}C NMR spectral data of isolated compound MM-1(100 MHz, $CDCl_3$)

Table 4 ^{13}C NMR Spectral Data of Isolated Compound MM-1 (100 MHz, $CDCl_3$)

C – No.	δ_C (ppm)	Interpretation
C-7, 15	163.7	Ester carbonyl C
C-4, 5	131.8	Aromatic C (q) with ortho substitution
C-1, 2	132.0	Aromatic methine C
C-3, 6	129.1	Aromatic methine C
C-8, 16	67.7	Oxygenated methylene C
C-9, 17	31.8	Aliphatic methylene C
C-10, 18	22.7	Aliphatic methylene C
C-11, 19	23.6	Aliphatic methylene C
C-12, 20	43.8	Aliphatic methylene C
C-13, 21	29.7	Aliphatic methine C
C-14,22,23,24	20.0	Aliphatic methyl C

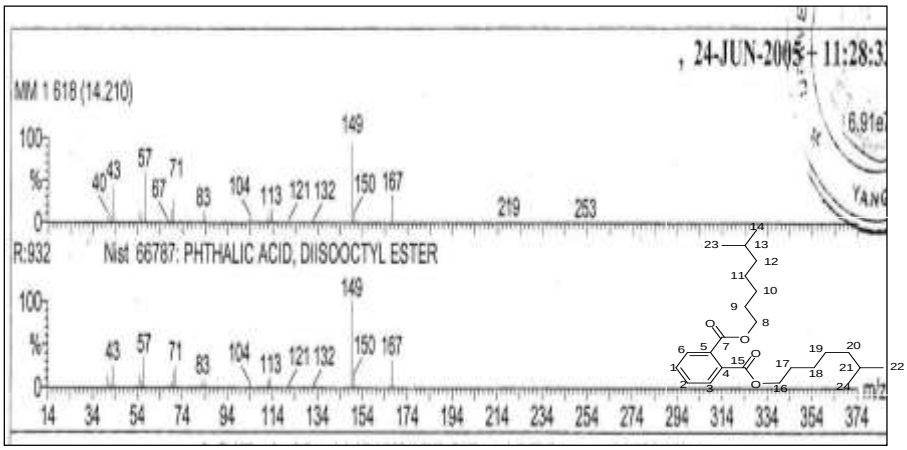

Figure 9 GC-MS spectrum of MM-1 compared with that of 1, 2-benzene dicarboxylic acid diisooctyl ester from GC-MS library data

According to spectroscopic methods, the isolated compound MM-2 was deduced as 3-Cyclohexene-1-ol, 5-(2-Butenylidene)-4,6,6-trimethyl-, (Z, E). The results are shown in Figure 10, 11, 12 and Table 5.

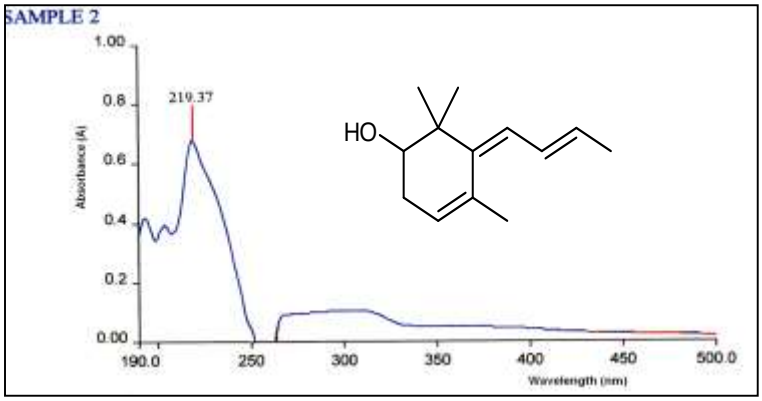

Figure 10 UV spectrum of isolated compound MM-2

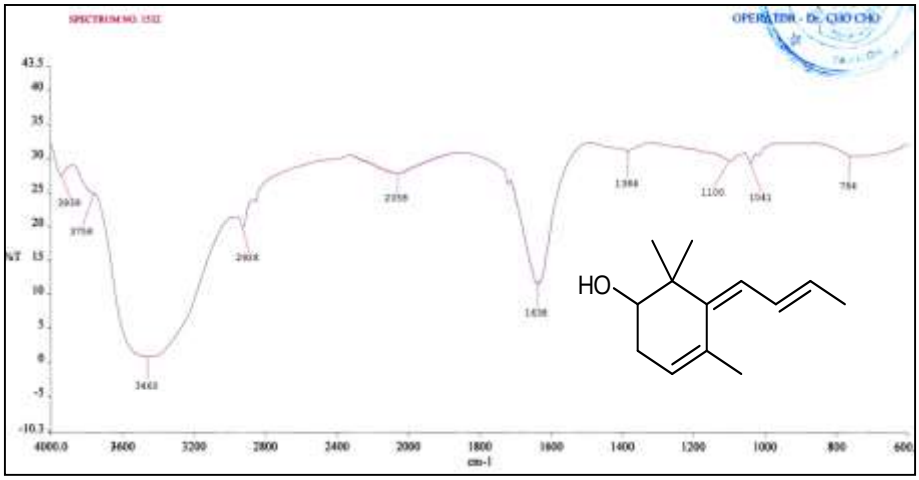

Figure 11 FT-IR spectrum of isolated compound MM-2 (KBr)

Table 5 FT-IR Spectral Data of Isolated Compound MM-2

Frequency Range (cm^{-1})	Mode of Vibration	Assignment
3460	ν_{O-H}	- OH group
2928	ν_{C-H} (asym.)	- CH_2 &CH_3 groups
2870	ν_{C-H} (sym.)	- CH_2 &CH_3 groups
1384	δ –CH_3 (out-of-plane)	Germinal dimethyl group
1638	$\nu_{C=C}$	cyclohexene
1041	ν_{-OH}	Cyclic sec. alcohol group
764	$\nu_{CH=CH}$ (asym.)	Cyclic alkene

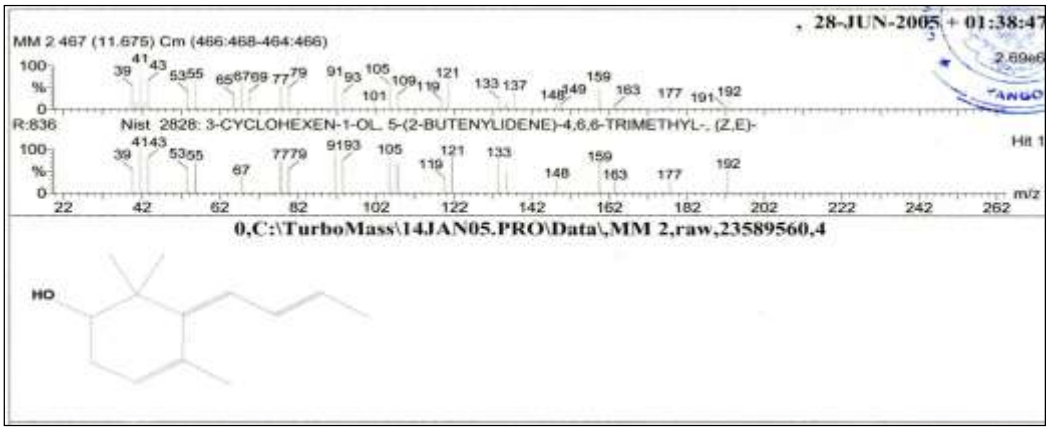

Figure 12 GC-MS spectrum of MM-2 compared with that of 3-cyclohexen-1-ol, 5-(2-butenylidene)-4, 6, 6-trimethyl-,(Z,E) from GC-MS library data

According to spectroscopic methods, the isolated compound MM-3 could be deduced as Bis (2-Ethylhexyl) Phthalate Ester. The results are shown in Figure 13, 14, 15, 16, Table 6 and 7.

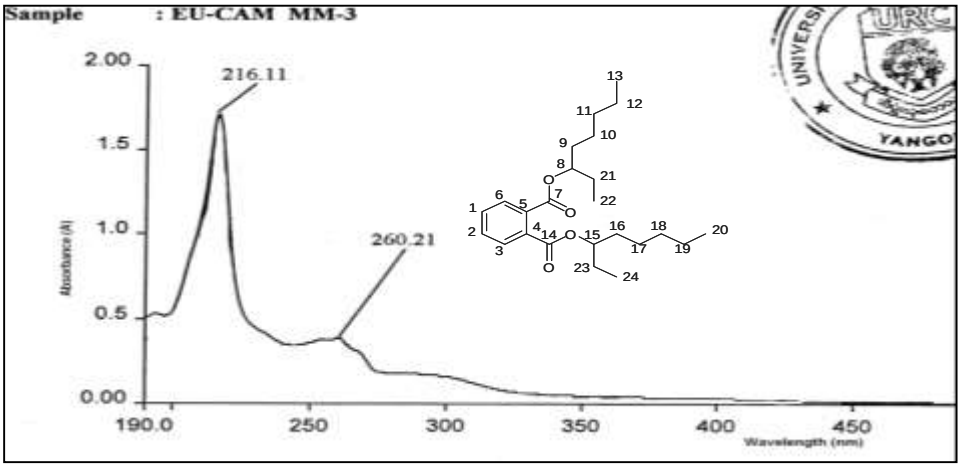

Figure 13 UV spectrum of isolated compound MM-3

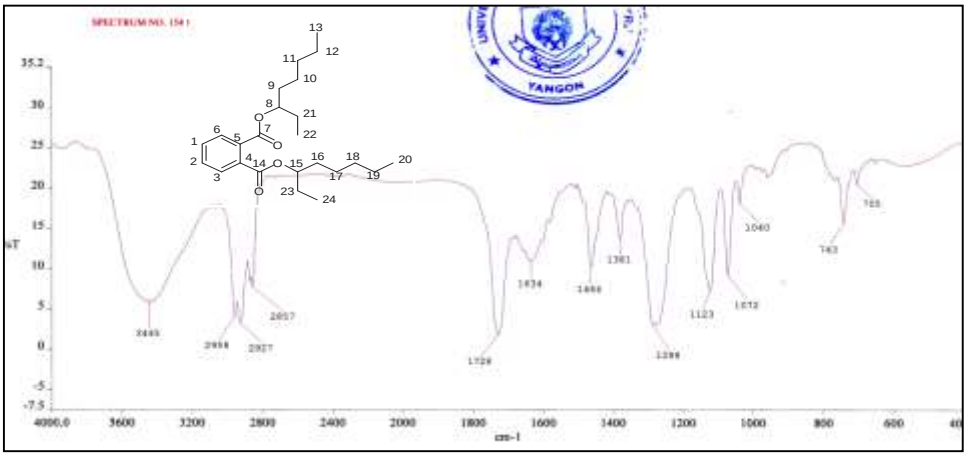

Figure 14 FT-IR spectrum of isolated compound MM-3 (KBr)

Table 6 FT-IR Spectral Data of Isolated Compound MM-3

Frequency Range (cm^{-1})	Mode of Vibration	Assignment
2927	ν_{asym} C-H	- CH_3 and -CH_2 group
2859	ν_{sym} C-H	- CH_3 and -CH_2 group
1728	ν C=O	Ester carbonyl group
1634 (vw), 743(vs)	ν C=C	-C = C-
1464	δ_{oop} -CH_2	-CH_2 group
1381	δ_{oop} -CH_3	-CH_3 group
1288	ν_{asym} C – O – C	Aromatic ester
1123	ν C – O	Alkyl substituent
1072, 1040	$\delta_{in\text{-}plane}$ -CH_2 or -CH_3	- CH_2 or -CH_3 group

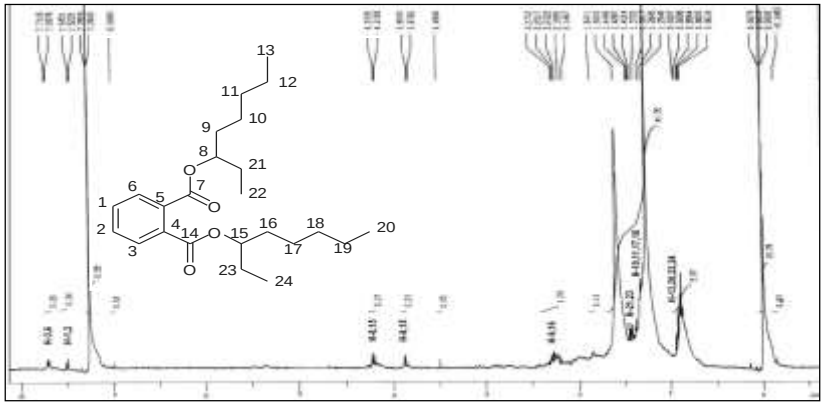

Figure 15 ^{1}H NMR spectrum of isolated compound MM-3 (400 MHz, $CDCl_3$)

Table 7 ^{1}H NMR Spectral Data of Isolated Compound MM-3 (400 MHz, $CDCl_3$)

H – No.	δ_H (ppm)	Multiplicity	Type of Proton
H – 3, 6	7.71	dd	= CH
H – 1, 2	7.53	d	= CH
H – 8, 15	4.21, 3.87	q	O – CH- $(CH_2)_2$
H – 9, 16	2.3	m	-CH-CH_2-CH_2
H – 10, 11, 17, 18	1.25	m	-CH_2-CH_2-CH_2
H – 21, 23	1.4	m	-CH_2-CH_2-CH_2
H–13, 20, 22, 24	0.90	Triplet	-CH_2 – CH_3

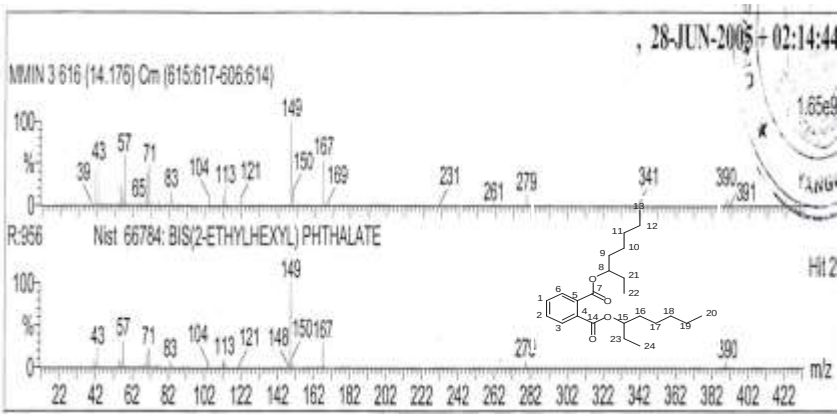

Figure 16 GC-MS spectrum of isolated compound MM-3 compared with that of bis (2-ethylhexyl) phthalate easter from GC-MS library data

Conclusion

This research concerns with the isolation and characterization of some chemical compounds from *E. campestris* (gamon-thanga-zin) rhizome. The rhizome samples were collected from Kyaik-htiyo hill, Mon State, Myanmar. Semi-quantitative elemental analysis of *E. camprestris* rhizome was carried out by ED-XRF method. From the analysis, the elements of major composition such as K (59.75%), Fe (16.89%) and Ca (14.87%) and minor composition such as Zn (4.97%) and Cu (3.52%) were observed in the sample. In human metabolism, potassium reduces the hypertension. Iron helps the function of blood in body. Calcium is very important element for the formation of teeth and bone. The extraction and isolation of *E. camprestris* rhizome were performed by column chromatographic separation method. Form the separation, the pure isolated compounds; MM-1, MM-2 and MM-3 were obtained. The identification of isolated compounds from *E. camprestris* rhizome was carried out by the modern spectroscopic method such as UV, FT-IR, ^{1}H NMR, ^{13}C NMR and GC-MS methods. According to the spectroscopic method, the isolated compounds; MM-1, MM-2 and MM-3 could be deduced as 1,2-benzene dicarboxylic acid diisooctyl ester, 3-cyclohexen-1- ol, 5-(2-butenylidene)-4,6,6-trimethyl-,(Z,E) and bis (2-ethylhexyl) phthalate easter, respectively. According to the experimental results, *E. camprestris* rhizome may be used in the medicinal formulation for human health.

Acknowledgements

The authors would like to express their profound gratitude to the Department of Higher Education (Yangon Office), Ministry of Education, Yangon, Myanmar, for provision of opportunity to do this research and Myanmar Academy of Arts and Science for allowing to present this paper.

References

Aberoumand, A. (2009). "Balance between nutrients and anti-nutrients in some plant food", Asian J Food Agro-Ind., vol. 2, pp. 330–5

Aberoumand, A. and Deokule, S. S. (2009). "Proximate and mineral composition of wild coco (*Eulophia ochreata* L.) tubers in Iran", Asian J Food Agro-Ind., vol. **2**, pp. 203–9

Artemas, W. (1923). "The Encyclopedia of Food", New York: Union Square; 1923.

Cieslicka, D. (2006). "The problems of infrageneric classification of *Eulophia* R. Br. Ex Lindl. (Orchidaceae, Cymbidiinae)", Biodiv Res Conserv. Vol. 3, pp. 210–2

Griken, R. V., Markowicz, A. and Torok, S. (1986). "Energy DispersiveX-ray Spectrometry", Department of Chemistry, University of Antwer (UIA), B-2610, Antwerp-wilrijk, Belgium

Hossain, M. M. (2011). "Therapeutic orchids: Traditional uses and recent advances" - An overview. Fitoterapia. Vol. 82, pp. 102–40

Silverstein, R.M., and Webster, F.X., (1998), "Spectroscopic Identification of Organic Compound", 6th Edition, John Wiley and Sons, Inc., New York

WHO (World Health Organization). (2008). "Traditional Medicines". Media Centre Fact Sheet No. 134. 2015 http://www.who.int/mediacentre/factsheets/fs134/en/2008 .

STRUCTURAL ELUCIDATION OF PALMATINE COMPOUND AND ITS ANTIMICROBIAL ACTIVITY ISOLATED FROM THE TUBER OF *STEPHANIA GLABRA* (ROXB.) MIERS

Khup Lam Tuang[1], Hla Myoe Min[2], Myint Myint Sein[3]

Abstract

The aim of this research was to extract, isolate, determine the structure of isolated compound and its antimicrobial activity from the ethanolic tuber extract of *Stephania glabra* (Roxb.) Miers (Menispermaceae family). The tuber of *Stephania glabra* (Roxb.) Miers, Taung-Kya (Myanmar name) was selected for this present work. It was rinsed with tap water, chopped in to small pieces and dried in air. The prepared dry sample was extracted with 95% of ethanol for one month. After doing filtration and evaporation, the remaining extract mass was further extracted with ethyl acetate and ran by different solvents ratios using thin layer sheet (spot test on TLC plate). A biologically active pure compound (colourless needle shaped crystals) could be isolated from n-hexane and ethyl acetate solvent ratio (n-hex 1:1EtOAc, 400 mg, and R_f value 0.5) by passing through the prepared column chromatogram. The molecular formula of an unidentified palmatine compound was assigned as $C_{21}H_{25}NO_4$ (assumed as glabrine) by using advanced spectroscopic techniques such as FT IR, 1D NMR (^1H, ^{13}C and DEPT), 2D NMR (HSQC, DQF-COSY, HMBC, NOESY) and DART MS spectral evidences. The antimicrobial activity of palmatine compound was examined by agar disc diffusion method against six selected organisms. This compound responds medium inhibition zone (15mm to 18mm) on all tested microorganisms, namely, *Bacillus subtilis* (NCTC 8236), *Staphylococcus aureus* (NCPC 6371), *Pseudomonas aeruginosa* (6749), *Bacillus pumilus* (NCIB 8982), *Candida albicans* and *Escherichia coli* (NCIB 8134). The IUPAC name of palmatine compound was named as (*R*)- 2, 3, 9, 12- tetramethoxy- 5, 8, 13, 13a- tetrahydro-*6H*- isoquinolino [2,1- b] isoquinoline.

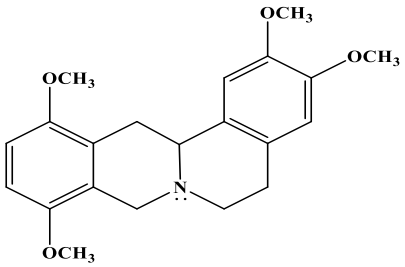

Keywords: *Stephania glabra* (Roxb.) Miers, extraction, isolation, thin layer and column chromatogramphy, palmatine compound, spectroscopic techniques, antimicrobial activity

Introduction

Stephania glabra (Roxb.) Miers (*S. glabra*), Myanmar name Taung-Kya is a species under the genus of climbers belonging to family Menispermaceae. It is a large climbering shrub with greenish yellowish flowers and large tubers (Hemraj *et al.*, 2012). The plant is found in many countries depending on tropical and subtropical regions (Titova *et al*., 2012). The tuber part of *Stephania glabra* (Roxb.) Miers was collected from Kalay Township, Sagaing Region, Myanmar. This plant was identified by Deputy Director General, Dr Soe Myint Aye, Department of Higher Education, Ministry of Education, Naypidaw, Myanmar. The various parts of this plant are also used to treat diabetes, edema, pain, stomach disorders, helminthiasis, malaria, hepatitis, tuberculosis and hypertension (Jahan *et al*., 2010). The plant is extensively used in folk medicine in Asian countries, especially for diabetes (Semwal, D.K and Semwal, R.B. 2015). A dried powder

[1] Dr, Lecturer, Department of Chemistry, Mandalar Degree College
[2] Dr, Professor, Department of Chemistry, University of Mandalay
[3] Dr, Professor and Head (Retd.), Department of Chemistry, University of Mandalay

of the root pulp with tea is used to treat puerperal fever in women (Rahmatullah *et al*., 2014). Until now, *S. glabra* mainly contains over 30 alkaloids classes such as bisbenzylisoquinolines, hasubanalactams, berberines and aporphines have been isolated from its tuber. The palmatine compound has been widely used in pharmaceutical fields such as in pharmacology, toxicity and pharmacokinetics studies (Semwal, D.K. and Semwal, R.B. 2015). Tetrahydropalmatine a class of palmatine compound derived from the tubers of *S. glabra* produces remarkable sedation of the central nervous system (CNS), and also exerts significant effects against dopamine receptors localised in the brain (Semwal, D.K. and Semwal, R.B. 2015). In traditional medicine, *S. glabra* has been used for the treatment of cancer, but no scientific evidence is not yet available (Semwal, D.K. and Semwal, R.B. 2015). The presence of bisbenzylisoquinoline alkaloids in the *S. glabra* plant, which are well known for their anticancer activity (Kuroda *et al*., 1976).

In recent years, the isoquinoline types of a palmatine compound (named as stephanine, $C_{21}H_{25}O_4N$) was elucidated from the rhizome of *Stephania rotunda* lour in Myanmar (Myint Myint Mar. 2007). The molecular formula and structure of an unidentified palmatine compound from the tuber of Myanmar plant *S. glabra* was assigned as $C_{21}H_{25}NO_4$ (assumed as glabrine) by using advanced spectroscopic techniques such as FT IR (Fourier Transform Infrared), ^{1}H NMR (Proton Nuclear Magnetic Resonance), ^{13}C NMR (Carbon Nuclear Magnetic Resonance), DEPT (Distortion Enhancement by Polarization Transfer), HSQC (Heteronuclear Single Quantum Coherence), DART (Direct Analysis of Real Time Mass Spectroscopy) DQF-COSY (Double Quantum Filtered Correlation Spectroscopy), HMBC (Heteronuclear Multiple Bond Coherence) NOESY (Nuclear Overhauser Effect Spectroscopy) spectral evidences. This compound is firstly reported from *S. glabra* tuber in Myanmar, until 2020 year. At present, this isolated palmatine compound (assumed as glabrine), separated from the tuber of *S. glabra* showed the remarkable sedation of the central nervous system (CNS) (Khup Lam Tuang. 2019). Currently, the bioactivity of this compound is determining with the inhibition zone (mm) by agar disc diffusion method against on selected microorganisms.

Figure 1 The Tuber of *Stephania glabra* (Roxb.) Miers (Source by Researcher)

Materials and Mehods

General Experimental Procedure

Commercial grade solvents and analytical grade reagents were utilized throughout this research work. The solvents were purified by distillation method before they were used in experiment. Thin-Layer Chromatographic separation was performed by using aluminum coated sheets silica gel (Merck Co.Inc., Kiesel gel 60 F_{256}) was run for solvents and silica gel (Merck Co.Inc., Kiesel gel 70-230 mesh ASTM) was used for column chromatographic separation. I_2 vapour and UV detector (Lambda-40, Perkin-Elmer Co., England) were used to identify the color of constituent compounds as spot on TLC sheets. The melting point was recorded on a Gallenkamp melting point apparatus (England). Common laboratory tools were used for extraction, isolation and purification of bioactive compound. Shimadzu electronic balance (Japan) was used to determine the weights of substances. The FT IR spectrum was measured by using SHIMADZU

spectrometer. The 1DNMR spectra for ^{1}H NMR (600 MHz), $^{13}CNMR$ (150 MHz), DEPT (150 MHz), DART MS were measured with BRUKER model spectrometry. The ^{2}D NMR spectra for DQF COSY (600 MHz), HSQC, HMBC, NOESY (600 MHz) spectra were also recorded with BRUKER model. All NMR spectra were measured in $CDCl_3$ solvent. Chemical shift scales were expressed in delta (δ/ppm) and solvent peaks were used as internal standards for both ^{1}H (7.28 ppm) and ^{13}C (70.7 ppm) down field from TMS internal reference.

Sample Collection and Preparation

The tuber of *Stephania glabra* (Roxb.) Miers to be analyzed was collected in October, 2015 in Kalay Townships, near Lett-Sey-Kan leak in Myanmar. After washing and cleaning, the tuber was chopped in to small pieces and dried under room temperature using electric fan. The dried tuber was stored in a well stopper bottle for experiment.

Extraction and Isolation

The air dried sample (650 g) was macerated and occasionally percolated with 1000 mL ethanol (95%) for one month. After doing filtration and evaporation, the obtained ethanolic extract (8.5 g) was further extracted with ethyl acetate to isolate pure compound by using column chromatogram over SiO_2 (70-230 mesh) eluting with n-hexane: ethyl acetate in 1:1 ratio. This ratio obtained the colourless crystals (400 mg, R_f = 0.5) having needle shapes. It was showed a yellow spot on TLC and a black spot on UV respectively.

Molecular Formula Determination of Pure Compound

The molecular formula of pure compound (colourless and needle- shaped crystal) could be isolated by column chromatographic method and its structure was elucidated in accordance with ^{1}D and ^{2}D NMR spectral evidence (Silverstein *et al*.,2005).

Antimicrobial Activity of Palmatine Compound

Antimicrobial activity of palmatine compound was tested against microorganisms in ethyl acetate solvent using agar well diffusion method. Agar plug method was adopted for the antimicrobial screening on six selected microorganisms (five bacteria and one fungi) namely, *Bacillus subtilis* (NCTC 8236), *Staphylococcus aureus* (NCPC 6371), *Pseudomonas aeruginosa* (6749), *Bacillus pumilus* (NCIB 8982), *Candida albicans* and *Escherichia coli* (NCIB 8134). 2 mL of the test organisms was aseptically injected into the sterilized plate. 10 mL of the sterilized nutrient agar were poured on top of the test organisms after cooling the disc. Sterilized cork borer of 10 mm diameter was used and made 2 wells on each solidified agar sheet into which 0.5 mL of the prepared palmatine compound were aseptically introduced by the use of sterilized clinical syringe. The plates were incubated at 37°C for 24 hours. Zone of inhibition (mm) were observed around each well after 24 hours (Adewole *et al.*, 2013).

Results and Discussion

Molecular Formula Determination of Pure Compound

According to FT IR spectrum (Figure 2), pure compound consists of sp^3 hydrocarbon carbons (2931.90, 2839.31, 2798.80 and 2752.51 cm^{-1}), sp^2 hydrocarbons (3005.20 cm^{-1}), aromatic benzene ring (1612.54 and 1506.46 cm^{-1}), aromatic amine group (1338.64cm^{-1}), allylic hydrocarbons (1458.23 cm^{-1}), ether group (1139.97, 1078.24, 1033.88, 1273.06 and 1224.84cm^{-1}) and cis or trans alkenic (864.14 and 781.20 cm^{-1}) functional groups respectively (Silverstein *et al*.,2005).

Table 1 ^{1}H NMR (600MHz) Spectrum of Pure Compound in $CDCl_3$

No.	^{1}H (δ/ppm)	Splitting Pattern	J values (Hz)	No. of Proton	Proton Assignment
1	2.65	dd	15.87, 10.23	1	sp^2 methine proton
2	2.68	dd	14.54, 11.33	1	sp^2 methine proton
3	2.83	dd	15.87, 3.86	1	sp^2 methine proton
4	3.15	dd	14.54, 10.23	1	sp^2 methine proton
5	3.20	dd	15.87, 11.33	1	sp^2 methine proton
6	3.27	dd	15.87, 4.25	1	sp^2 methine proton
7	3.53	d	15.87	1	sp^2 methine proton
8	3.55	dd	4.25, 3.86	1	sp^2 methine proton
9	3.85	s	s	3	sp^3 methyl proton
10	3.86	s	s	3	sp^3 methyl proton
11	3.87	s	s	3	sp^3 methyl proton
12	3.89	s	s	3	sp^3 methyl proton
13	4.24	d	15.87	1	sp^2 methylene proton
14	6.62	s	s	1	sp^2 methine proton
15	6.73	s	s	1	sp^2 methine proton
16	6.79	d	8.21	1	sp^2 methine proton
17	6.88	d	8.21	1	sp^2 methine proton
	Total number of protons			=	25

Table 2 ^{1}H-^{13}C NMR (HSQC) and DEPT (150 MHz) Spectral Data of Pure Compound in $CDCl_3$

No	^{1}H (δ/ppm)	^{13}C NMR	DEPT
1	2.65	29.10	sp^2CH
2	2.68	36.33	sp^2CH
3	2.83	51.49	sp^2CH
4	3.15	53.99	sp^2CH
5	3.20	55.86	sp^2CH
6	3.27	55.95	sp^2CH
7	3.53	56.14	sp^2CH
8	3.55	59.30	sp^2CH
9	3.85	60.12	sp^3CH_3
10	3.86	108.66	sp^3CH_3
11	3.87	110.96	sp^3CH_3
12	3.89	111.37	sp^3CH_3
13	4.24	123.80	sp^2CH
14	6.62	126.81	sp^2CH
15	6.73	127.76	sp^2CH
16	6.79	128.69	sp^2CH
17	6.88	129.74	sp^2CH
18	-	145.09	sp^2C
19	-	147.44	sp^2C
20	-	147.49	sp^2C
21	-	150.25	sp^2C
	Total number of carbons		= 21

According to FT IR, ^{1}H NMR, ^{13}C NMR and DEPT spectral data, the complete molecular formula of compound could be deduced (Table 3).

Table 3 Molecular Formula Determination of Pure Compound

Assignments	No. of Carbon	No. of Proton	No. of Oxygen	No. of Nitrogen
From ^{1}HNMR, ^{13}CNMR and DEPT data				
- Four sp^3 methyl	4	12	-	-
- Four sp^2 methylene	4	8	-	-
- Four sp^2 methine	4	4	-	-
- One sp^2 methine	1	1	-	-
- Four methoxy groups	-	-	4	-
- Eight sp^2 quaternary	8	-	-	-
From FT IR data				
- One amine group (tertiary amine)	-	-	-	1
Complete molecular formula	C_{21}	H_{25}	O_4	N

DART MS mass spectrum (Figure 6) of pure compound represented the molecular ion peak at m/z = 356.1844 Da. However, the evaluated mass of molecular formula, $C_{21}H_{25}NO_4$ is 355. Therefore, the actual mass could be match of when only subtracting one unit proton from m/z 356.1844. Hence, the molecular mass of compound is now assigned as 355.1764 Da. This is agreed with the actual mass 355. The molecular mass is also consistent with "Nitrogen rule".

Hydrogen Deficiency Index (HDI) $= 21 - \frac{25}{2} + \frac{1}{2} + 1 = 10$

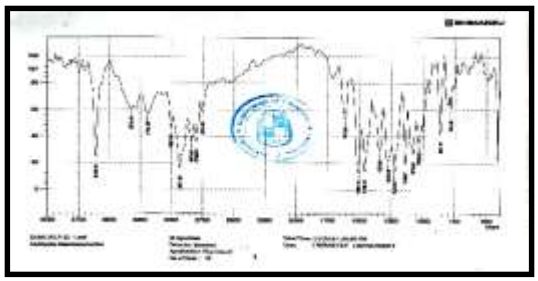

Figure 2 FT IR Spectrum of Pure Compound

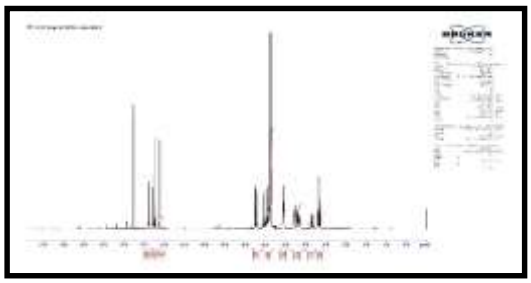

Figure 3 ^{1}H NMR (600MHz) Spectrum of Pure Compound

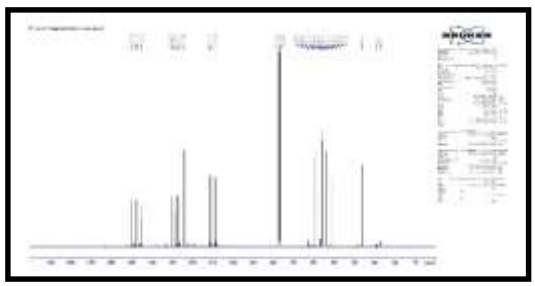

Figure 4 ^{13}C NMR (150MHz) Spectrum of Pure Compound

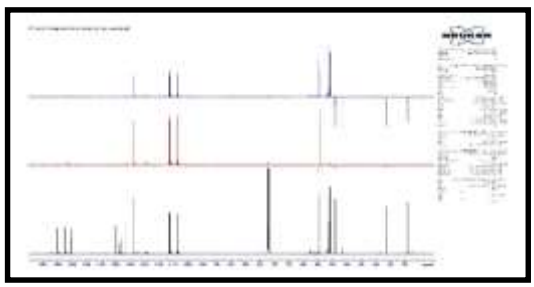

Figure 5 DEPT (150MHz) Spectrum of Pure Compound

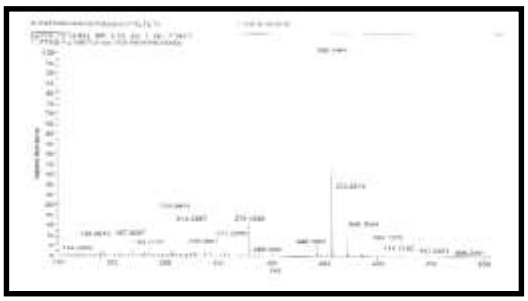

Figure 6 DART MS Spectrum of Pure Compound

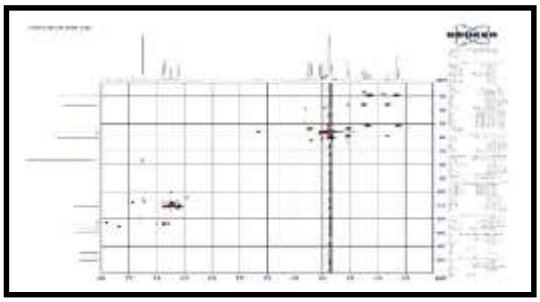

Figure 7 HSQC Spectrum of Pure Compound

Structural Elucidation of Pure Compound

The following fragments (I) to (IV) and fragment (A) could be confirmed by downward appearance of four sp^3 methylene carbons, upward appearance of one sp^3 methine carbon and one sp^3 methylene carbons in DEPT spectrum (Figure 5). Hence, their proton-carbon direct correlation could be observed in HSQC spectrum (Figure 7).

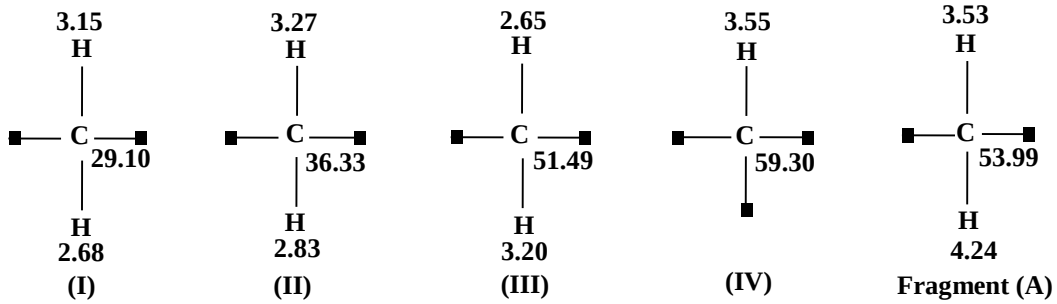

The four set of geminal methylene protons and their spin-spin coupling fragments (I, II, III and IV) in DQF COSY spectrum (Figure 8) are assigned as follow.

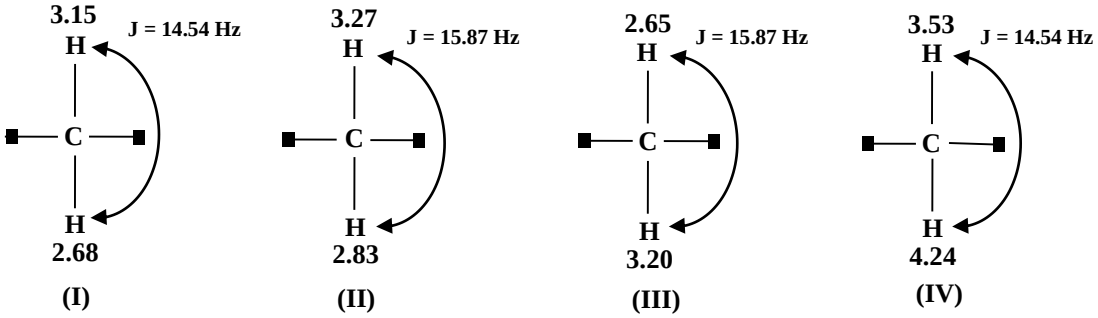

DQF COSY (Figure 8), ^{1}H NMR (Figure 3) and HMBC (Figure 9) spectra show the present of the following fragments (B) and (C).

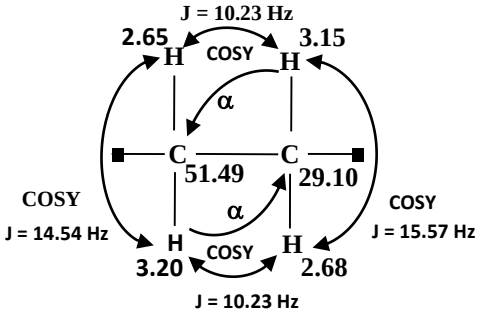

Fragment (B)

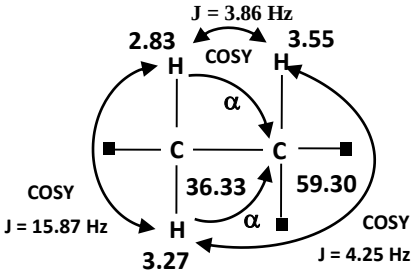

Fragment (C)

In HMBC spectrum (Figure 9), there are proton-carbon long range coupling around methylene and methine groups in fragments (A), (B) and (C) are considered to be connected with N atom. All proton-carbon long range correlation signals are shown in following fragment (D). In accordance with HSQC (Figure 7), ^{1}H NMR (Figure 3) and DEPT (Figure 5) data the four methoxy groups are assigned as below.

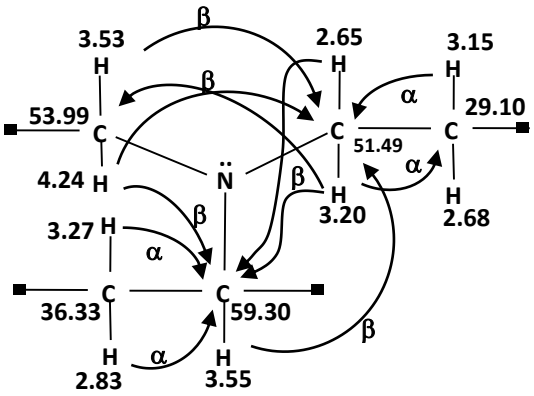

Fragment (D)

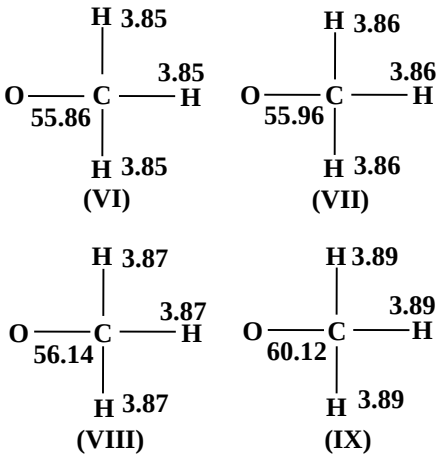

In the ^{1}H NMR spectrum (Figure 3), both of the two aromatic protons of δ 6.88 ppm and δ 6.79 ppm have the splitting patterns and coupling constants (d, J = 8.21 Hz). Hence, the fragments (E) and (F) could be assigned by the observation of proton-carbon direct attachment in HSQC spectrum (Figure 7) and ^{1}H-C long range coupling with both of sp^{2} quaternary carbons in HMBC spectrum (Figure 9).

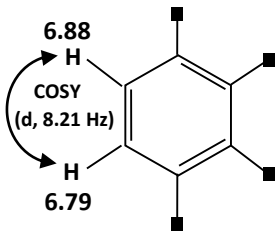

Fragment (E)

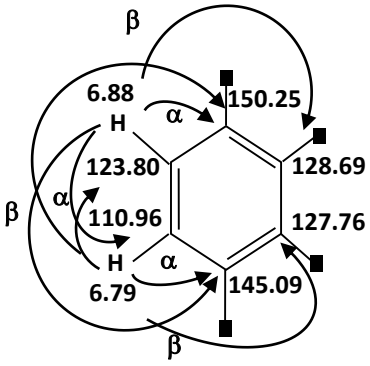

Fragment (E)

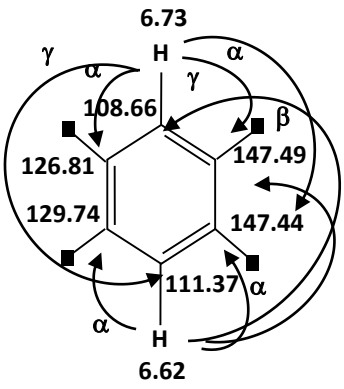

Fragment (F)

In fragments (E) and (F), lower field chemical shift values of sp^2 carbons (150.25 145.09 ppm and 108.66, 111.37 ppm) are considered to be connected with methoxy groups (δ 3.85, 3.86 ppm and δ 3.87, 3.89 ppm) (Figure 9). Methoxy protons (δ 3.85, 3.86 ppm) shows β-correlation cross peak to δ 150.25, 145.09 ppm carbons and similarly, other methoxy protons (δ 3.87, 3.89 ppm) shows β-correlation to 147.44, 147.99 ppm carbons (Figure 9). Therefore, these attachments lead to the following fragments bearing two methoxy groups on benzene ring.

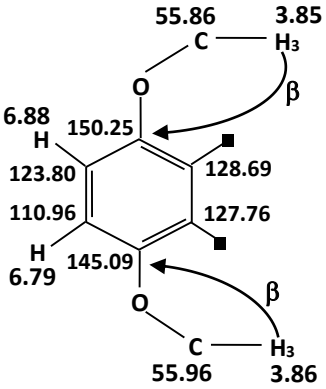

Fragment (E)

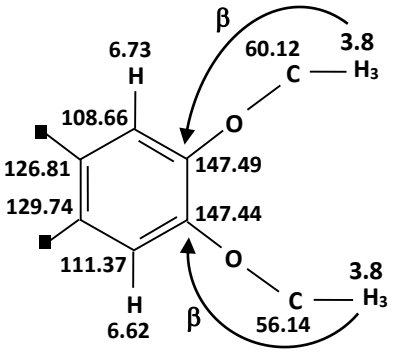

Fragment (F)

Fragments C_5H_9N(D), $C_8H_8O_2$ (E) and $C_8H_8O_2$ (F) could be connected ^{1}H-C long range cross peaks in HMBC spectrum (Figure 9). This correlation gives a good confirmation to be assigned the following fragment (G). Next, the connection between the fragments (G) and (F) could be confirmed by HMBC spectrum (Figure 9). Thus, HMBC correlation confirms the complete structure of pure compound as described below.

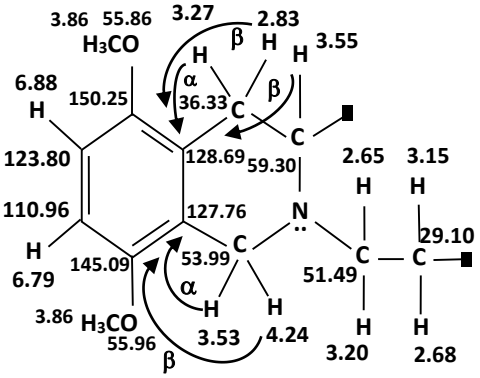

Fragment (G), $C_{13}H_{17}O_2N$

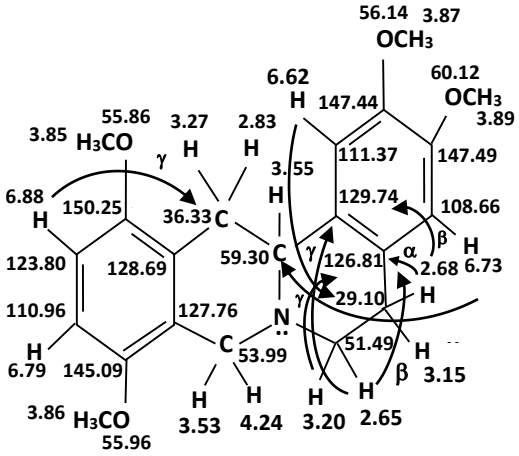

Complete Structure of Pure Compound ($C_{21}H_{25}O_4N$)

The above elucidated structure is also agreed with hydrogen deficiency index (10) calculated from its molecular $C_{21}H_{25}NO_4$ compound having four cyclic ring as describe as follows. In accordance with NOESY spectrum and model analysis (Figure 10), the relative conformation of chiral carbon can be assigned as 'R' configuration.

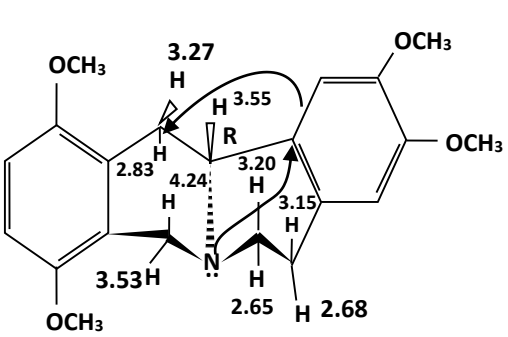

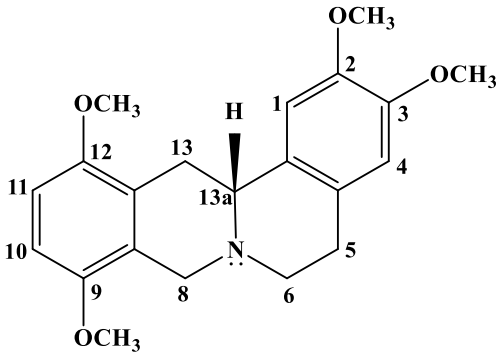

The IUPAC name of palmatine compound is (*R*)- 2, 3, 9, 12- tetramethoxy- 5, 8, 13, 13a-tetrahydro-*6H*- isoquinolino [2,1- b] isoquinoline.

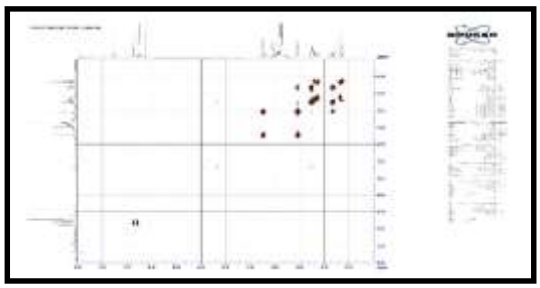

Figure 8 DQF COSY (600MHz) Spectrum of Pure Compound

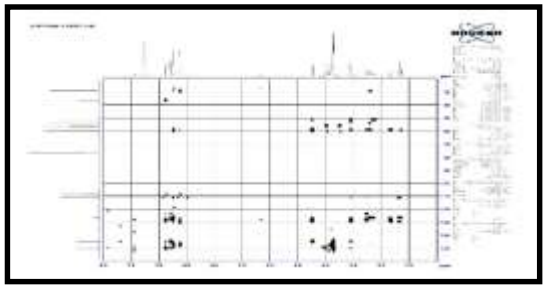

Figure 9 HMBC Spectrum of Pure Compound

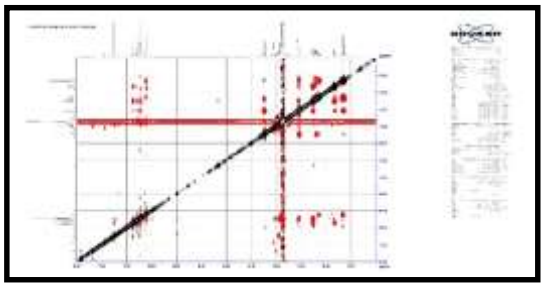

Figure10 NOESY (600MHz) Spectrum of Pure Compound

Antimicrobial Activity of Palmatine Compound

In this study, the palmatine compound preparing with ethyl acetate solvent was tested against microorganisms. The antimicrobial activity of palmatine compound showed medium inhibition zone (mm) on all tested organisms (Table 4).

Table 4 Results of Antimicrobial Activity of Palmatine Compound

Compound	Inhibition Zone (mm)					
	A	B	C	D	E	F
Palmatine	15 (++)	18 (++)	18 (++)	15 (++)	18 (++)	18 (++)

Organisms:

A = *Bacillus subtilis* (NCTC 8236)
B = *Staphylococcus aureus* (NCPC 6371)
C = *Pseudomonas aeruginosa* (6749)
D = *Bacillus pumilus* (NCIB 8982)
E = *Candida albicans*
F = *E.coli* (NCIB 8134)

Inhibition zone diameter of standard Agar Well – 10 mm
(++) Inhibition zone diameter ranging 15mm ~ 19 mm (medium activity)

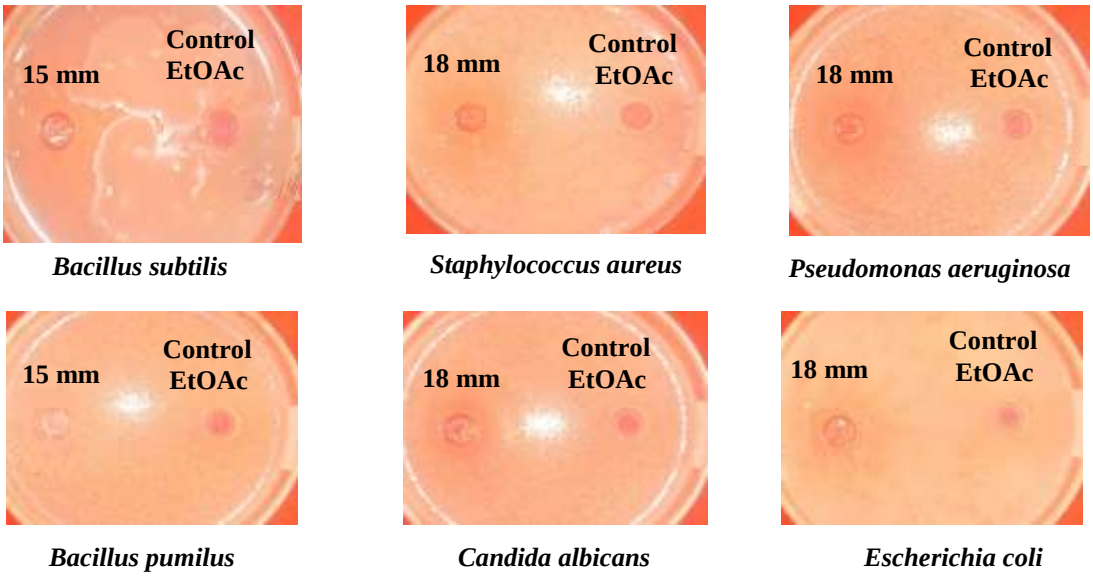

Bacillus subtilis ***Staphylococcus aureus*** ***Pseudomonas aeruginosa***

Bacillus pumilus ***Candida albicans*** ***Escherichia coli***

Figure 11 Antimicrobial Activity of Palmatine Compound by Agar Disc Diffusion Method

Conclusion

A separation method, column chromatography was applied to isolate the palmatine compound depending on different solvent ratios from *S. glabra* tuber. This paper reported the extraction, isolation, structure elucidation, and antimicrobial activity of isoquinoline alkaloid class; an unidentified palmatine, $C_{21}H_{25}NO_4$ compound (named as glabrine). The structure of this compound was done by interpretation of the 1D and 2D NMR and DART MS spectra. Palmatine compound has a wide spectrum of pharmacological effects, including anti-cancer, anti-oxidation, anti-inflammatory, neuroprotection, anti-bacterial, anti-viral and regulating blood lipids. However, palmatine has obvious DNA toxicity, and has a complex effect on metabolic enzymes in the liver (Long *et al* 2019). The present results support that the bioactive palmatine compound isolated from the tuber of *S. glabra* has potent activity against the tested microorganisms. According to the available knowledge about *S. glabra* containing over 30 alkaloids, it has a great potential source of natural health products for pharmaceutical studies.

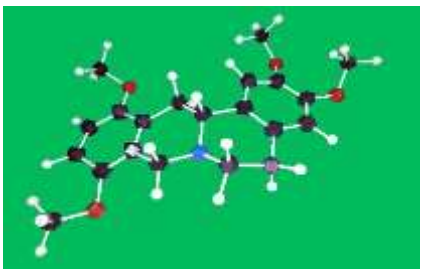

(R)- 2, 3, 9, 12- tetramethoxy- 5, 8, 13, 13a- tetrahydro- 6H- isoquinolino [2,1- b] isoquinoline

Acknowledgements

The authors acknowledge to chairman and all of members of Myanmar Academy of Arts and Science (Department of Higher Education, lower Myanmar, Yangon), Ministry of Education for celebrating the conference and allowing us to publish this paper. We are deeply thankful to Deputy Director General, Dr Soe Myint Aye, Ministry of Education, Naypyidaw, Myanmar for identifying and specifying the research plant species. The authors would like to thank Professor and Head (Rtd.), Dr Saw Hla Myint, Department of Chemistry, University of Yangon, for his invaluable suggestion and advices. The author greatful to Professor and Head, Dr Yi Yi Myint, Department of Chemistry, University of Mandalay, for her permission of doing this research and allowing the writing of this paper. We would like to express special thanks to Associate Professor, Dr Yoshio Takaya, Faculty of Pharmacy, Meijo University, Nayoga, Japan, for his supporting spectral data to carry out the research for this paper.

References

Adewole, E., Olaitan, A.B., Idris, O.O., Ojo, O.A., Onikan, S.A., Ogunmodede, O.T., Adewumi, D.F. (2013). "Phytochemical, Antimicrobial and GC-MS of African Nutmeg (Monodora Myristica)". *International Journal of Pharmaceutical Science Invention,* 2 (5): 25-32

Hemraj., Upmanyu, N., Gupta, A., Jindal, A., Jalhan, S. (2012). "Pharmacological Activities of Stephania glabra, Woodfordia Fruticosa and Cissampelos pareira-A Review". *International Journal of Pharmacy and Pharmceutical Science*, vol. 4(3), pp. 16-23

Jahan, R., Khatun, M.A., Nahar, N., Jahan, F.I., Chowdhury, A.R, Nahar, A., Seraj, S., Mahal, M.J., Khatun, Z., Rahmatullah, M. (2010). "Use of Menispermaceae Family Plants in Folk Medicine of Bangladesh". *Advance of Natural Applied Sciences*, vol. 4, pp. 1-9

Kuroda, H., Nakazawa, S., Katagiri, K., Shiratori, O., Kozuka, M., Fujitani, K. and Tomita, M. (1976). "Antitumor effect of bisbenzylisoquinoline alkaloids". *Jurnal of Chemical Pharmaceutical Bulletin*. Vol. 24, pp. 2413–2420

Khup Lam Tuang. (2019). *Study on Phytochemical Conposition, Antimicrobial Activity, Acute Toxicity, Central Nervous System (CNS) Depressant Activity and Structural Elucidation of Alkaloid and Other Compounds Isolated from The Tuber of Stephania glabra* (Roxb.) Miers. PhD (Dissertation), Department of Chemistry, University of Mandalay, Myanmar.

Long, J., Song, J., Zhong, L., Liao, Y., Liu, L. and Li, X. (2019). "Palmatine: A review of its pharmacology, toxicity and pharmacokinetics". *Journal of Biochimie*, vol. 162, pp. 176-184

Myint Myint Mar. (2007). *Structural Elucidation of a Bioactive Unknown Organic Compound Isolated from Stephania rotunda Lour (Daung-do)*. PhD (Dissertation), Department of Chemistry, University of Yangon, Myanmar.

Rahmatullah, M., Khattun, Z., Saha, S., Tuly, M.a., Hossian, A., Roy, A., Jahan, R. (2014). "Medicinal Plants and Formulations of Tribal Healers of the Chekla Clan of the Patro Tribe of Bangladesh". *Journal of Alternative Complementary Medicine*, vol. 20, pp. 3-11

Semwal, D.K. and Semwal, R.B. (2015). "Efficacy and Safety of *Stephania glabra*: An Alkaloid-rich Traditional Medicinal Plant". *Natural Product Research: Formerly Natural Product letters*, vol. 29, pp. 396-410

Silverstein, R.M., Webster, F.X. and Kiemle, D.J. (2005). *Spectrometric Identification of Organic Compounds*. New York: 7th edition

Titova. M.V., Reshetnyak, O.V., Osipova, E.A., Osip'yants, A.I., Shumilo, N.A., Oreshnikov, A.V. and Nosvo, A.M. (2012). "Submerged cultivation of *Stephania glabra* (Roxb.) Miers Cells in Different Systems: Specific Feature of Growth and Accumulation of Alkaloids Stepharine". *Applied Biochemical of Microbiology*, vol. 48, pp. 645-649

BIOLOGICAL PROPERTIES AND CHEMICAL INVESTIGATION OF MYANMAR FERMENTED TEA LEAF (*CAMELLIA SINENSIS* L.)

San San Aye[1], Ei Ei San[2], Myat Kyaw Thu[3], Ni Ni Than[4]

Abstract

Tea leaves possess many useful biological activities and are consumed in the daily life of the Myanmar people which have been the reason for the selection of this plant for the present paper. Bioassay offers special advantages to know about the biological activity of plant extracts and provide information to isolate active compounds which is a preliminary key step for drug discovery system. Bioassays such as antimicrobial activity, antiproliferative and anti-inflammatory activities were determined. The main aim of the present research was to evaluate the biological properties of *Camellia sinensis* L. leaves. The antimicrobial activity of polar and non-polar extracts of the fermented tea leaves was screened by using agar well diffusion method. Among the tested extracts, flavonoid extract of fermented tea leaves possessed higher antimicrobial activity (30 mm- 35 mm) than the other extracts. *In vitro* antiproliferative activity of ethanol and watery extracts of the fermented tea leaves was investigated against human lung cancer and human cervix cancer by MTT assay. The IC_{50} values of ethanol and watery extracts for human lung cancer were observed 95.34 µg/mL and 123.44 µg/mL, respectively. In the case of human cervix cancer, the IC_{50} values for ethanol and watery extracts were found to be 116.26 µg/mL and 124.39 µg/mL, respectively. No anti-inflammatory activity was found in both water and 70 % EtOH extracts by % NO inhibition assay and there was also no toxicity effect up to >100 µg/mL concentration. The fermented tea leaves were extracted with 70 % ethanol and followed by column chromatographic separation technique. Five compounds were isolated from the ethanol extract. The structures of isolated pure compounds were elucidated by ^{1}H NMR, ^{13}C NMR and ESI-MS spectroscopic methods. In conclusion, 70 % ethanol extracts of the fermented tea leaves possess significantly anticancer activity and antimicrobial activity. Therefore, fermented tea leaves (*C. sinensis* L.) may be used for preventing cancer and used as antimicrobial agent.

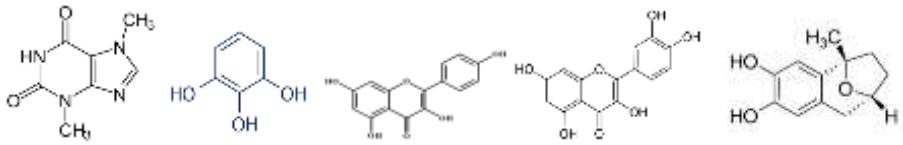

caffeine pyrogallol kaempferol quercetin bruguierol B

Keywords: spectroscopic methods, quercetin, kaempferol, caffeine, pyrogallol, bruguierol B

Introduction

Camellia sinensis L. (Tea Leaf)

Plants have a significant role in maintaining human health and improving the quality of human life. The world health organization (WHO,1999) estimated that 80 % of the people rely on traditional medicine. The medicinal plant (Tea leaf), *C. sinensis* L., belonging to the family, Theaceae, whose leaves and leaf buds are used to produce tea. There are three types of commercially available tea as snack or beverage in Myanmar: fermented tea, black tea, and green tea. Myanmar fermented tea leaf is a common signature and national ancient food that is eaten by all people in the country. Apart from the drinking form of tea, fermented pickled tea, the so- called *lapphet*, is another form of tea leaf. *Lapphet* is of Myanmar origin and not derived from other cultures. It is an essential dish for traditional ceremonies in Myanmar. Because of *Lapphet* is consumed in the daily life of the Myanmar people, *Lapphet* products can be easily found

[1] Dr, Professor, Department of Chemistry, Sittway University
[2] Dr, Lecturer, Department of Chemistry, Bago University
[2] Dr, Professor, Department of Chemistry, University of Yangon
[4] Dr, Professor and Head, Department of Chemistry, University of Yangon

everywhere in Myanmar markets around the country. Most families have a habit, and use *Lapphet* as daily snacks and as a treat for their guests. Tea leaf contains a very large number of polyphenols, which is the most specific feature of tea. *Lapphet* is very unique in the culture of the Myanmar people and habitually consumed as a food in Myanmar. The department of Chemistry the University of Yangon has made much progress in the research on tea leaf "Myat Kyaw Thu (2003) studied on "The Mode of Formation of Myanmar Fermented Tea" and "Myat Kyaw Thu (1993) studied on "Caffeine Contents of Tea Leaves in Various Climates and Ages". In this study, the caffeine contents of various tea samples for tea consumers as beverage were determined. Although many studies relating to the medicinal properties of fermented tea leaves have been made, antiproliferative activity (human cervix cancer and human lung cancer) of fermented tea leave is still lacking. Therefore, it is needed to investigate antimicrobial, anticancer activities and chemical constituents present in Myanmar fermented tea leaves.

Materials and Methods

Plant materials

The fermented tea leaves (*C. sinensis* L.) were procured from local market, Yangon Region. Fermented tea leaves were left in the open air till they were completely dried. The dried sample was ground in a grinding machine. The drug powders were then stored in an air-tight container.

Chemicals

Column chromatography was run on Kiesel gel 60 (Merck) and TLC on Alufolien Kiesel gel 60 GF_{254} (Merck). Other chemicals were procured from the BDH and E. Merck.

Instruments

JEOL, 500 MHz NMR spectrometer, Agilent Technologies 6420 Triple Quad LC/MS spectrometer, autoclave, incubator

Preparation of crude extracts

Dried powdered sample (100 g) was percolated in 500 mL of petroleum ether (PE, 60-80 °C) for one week and filtered. This procedure was repeated for three times. Then the filtrate was concentrated by a vacuum rotatory evaporator to get respective PE extract. Similarly, ethyl acetate and 70 % EtOH extracts of dried powdered sample were prepared according to the above procedure. After removing each solvent by rotary evaporator, crude extract was dried and kept in desiccator. In the preparation of watery extract; 100 g of dried powdered sample was soaked in 500 mL of distilled water into the conical flask. These flasks were boiled on water bath for 6 hours and filtered. This process was carried out for three times. The combined filtrates were to dryness over a water bath at 100 °C to get the corresponding watery extract.

Antimicrobial screening by agar well diffusion method

Antimicrobial activity of the crude extracts was determined by agar well diffusion method. Four small holes of 10 mm diameter each were cut out in the inoculated agar to place samples to be tested. The volume of each sample placed in each hole was 0.1 cm^3. The Petri dish was then incubated at 37 ºC for 48 hours, and the diameters of clear inhibition zones around the holes, if appeared, were measured (Finegold,1982).

Determination of antiproliferative activity by MTT assay

The anticancer or antiproliferative activity of ethanol and watery extracts of ***C. sinensis*** L. leaves samples were determined against two cancer cell lines such as Hela (cervix cancer) and A 549 (lung cancer) by MTT assay (Fatma *et al*., 2015). The sample solution with cell and medium was added with 100 µL MTT reagent. And then the 96 well plates were incubated in an incubator for 3 hours. After the incubation, (100 µL) of DMSO was added in the 96 well plates. After 15 minutes, the absorbance of each solution was measured at 570 nm by using UV-visible spectrophotometer. The percent cell viability activity was calculated by the following equation.

$$\% \text{ Cell viability} = [(\text{Abs (test sample)} - \text{Abs (blank)})/(\text{Abs (control)} - \text{Abs (blank)})] \times 100$$

Where,

$\text{Abs}_{(\text{test sample})}$ = absorbance of test sample solution
$\text{Abs}_{(\text{control})}$ = absorbance of DMSO solution
$\text{Abs}_{(\text{blank})}$ = absorbance of MTT reagent

IC_{50} (50 % inhibitory concentration) values were calculated by linear regressive excel program. The standard deviation was also calculated by the following equation.

$$\text{Standard Deviation (SD)} = \sqrt{\frac{(\bar{X}-X_1)^2+(\bar{X}-X_2)^2+\cdots\cdots(\bar{X}-X_n)^2}{(n-1)}}$$

Where,

$\bar{X}$ = average % inhibition
$x_1, x_2, \ldots, x_n$ = % cell inhibition of test sample solution
n = number of times

Determination of anti-inflammatory and cell viability activity

Anti-inflammatory activity of the ethanol and watery extracts was evaluated by % NO inhibition assay according to the method of (Jin *et al*., 2010) with some modifications. The 100 µL of cells (1×10^4/well) were seeded in the 96-well plates and incubated for 24 h at 37 °C in a humidified atmospheric containing 5 % CO_2. The cells were then treated with 50 µL each of LPS (100 ng/mL) and different doses of samples for 24 h. NO production was monitored by measuring the accumulation of nitrite in the culture supernatant using Griess reagent (Schmidt *et al*., 1996). In brief, 100 µL each of the supernatant from 96-wells was mixed with equal volume of Griess reagent (0.5 % sulfanilamide and 0.05 % naphthylenediamide dihydrochloride in 2.5 % H_3PO_4) in the new 96 well plates and allowed to stand for 15 minutes at room temperature. The absorbance at 540 nm was measured using microplate reader. On the other hand, the effect of the samples on the cell proliferation was evaluated by MTT assay. The remaining medium from the original plate was discarded and 100 µL each of 10 % MTT solution (5 mg/mL) in the medium was added. After 3 h incubation, the medium was discarded and 100 µL each of DMSO was added to dissolve the formazan crystals and the absorbance at 570 nm was recorded by micro plate reader. The percentage of NO inhibition and that of cell viability was calculated as follows:

NO inhibition (%) = $[\text{Abs}_{(\text{control})}-\text{Abs}_{(\text{sample})}/\text{Abs}_{(\text{control})}] \times 100$, where $\text{Abs}_{(\text{control})}$ and $\text{Abs}_{(\text{blank})}$ are the absorbance of the control group treated by LPS alone and the absorbance of the samples

Cell viability (%) = $100 \times [\text{Abs}_{(\text{test sample})} - \text{Abs}_{(\text{blank})}/\text{Abs}_{(\text{control})}-\text{Abs}_{(\text{blank})}]$

Isolation of compounds from *C. sinensis* L. leaves

Dried powered sample of fermented tea leaves (*C. sinensis*) was percolated in 70 % ethanol with occasional shaking for one week and filtered. This procedure was repeated three times. The combined filtrate was concentrated under vacuum evaporator to obtain ethanol crude extract. The ethanol extract was concentrated to dryness and the residue was used for column chromatographic separation. The ethanol extract (15 g) was chromatographed on a silica gel column using $CHCl_3$: EtOAc (9:1, 4:1) solvent mixture. Finally, five pure compounds were obtained.

Results and Discussion

Antimicrobial activity

In the present work, the sample was tested on 6 strains of bacteria which include *Bacillus subtilis, Staphylococcus aureus, Pseudomonas aeruginosa, Bacillus pumilus, Candida albicans* and *Escherichia coli*. The measurable zone diameter, including the agar well diameter, shows the degree of antimicrobial activity. It was found that all the extracts of fermented tea leaves showed antimicrobial activity (12 mm- 35 mm) against microorganisms tested except of *Escherichia coli.* Among the tested extracts, flavonoid extract of fermented tea leaves (30 mm-35 mm) has more pronounced antimicrobial activity than the other extracts (Figure 1 & Table 2).

Antiproliferative activity

The antiproliferative activity of ethanol and watery extracts of fermented tea leaves against human lung cancer and human cervical cancer cell lines were evaluated by using MTT assay. The anticancer effect was expressed as IC_{50} values (50 % inhibitory concentration). The lower the IC_{50} value, the higher is the antiproliferative activity. In the case of human lung cancer cell line, the IC_{50} value of ethanol (95.34 µg/mL) was lower than the watery extract (123.44 µg/mL). The IC_{50} value of ethanol (116.26 µg/mL) was found to be lower than that of the watery extract (124.39 µg/mL) against human cervical cancer. Although the tested extracts were observed to show the antiproliferative activity against both cancer cell lines, the ethanol extract has more antiproliferative activity than the watery extract (Table 3 & 4).

Anti-inflammatory activity

Anti-inflammatory activity of ethanol and watery extracts of fermented tea leaves was determined by % NO inhibition assays. If the extract exhibits only anti-inflammatory effect, the IC_{50} values in % NO inhibition should be less than IC_{50} values in % cell viability. However, the IC_{50} values in % NO inhibition of the tested extracts was found to be higher than 100 µg/mL. Therefore, no anti-inflammatory activity was observed in fermented tea leaves up to 100 µg/mL concentration. Moreover, IC_{50} values of % cell viability were greater than 100 µg/mL. It indicates that no toxicity effect in fermented tea leaves up to 100 µg/mL concentration (Table 5).

Identification of isolated compounds

The isolated compounds were identified by ^{1}H NMR, ^{13}C NMR (Figures 2,3,4,5,6) HMBC and ESI-MS spectroscopic methods. The observed ^{13}C NMR data were compared with the reported data (Table 6).

I (Caffeine): Caffeine is a typical natural alkaloid that can stimulate the nervous system and heart. It is white colourless needles with the melting point of 235-237 ˚C. ESI-MS m/z: 195 $[M+H]^+$, 217 $[M+Na]^+$; ^{1}H NMR (500 MHz, $CDCl_3$) δ (ppm): 7.486 (1H, S, H-8), 3.968 (3H, s, CH_3-7), 3.558 (3H, s, CH_3-3), 3.381 (3H, s, CH_3-1)

II (Pyrogallol): It is white, water soluble solid (m.p. 131-134 ˚C). ESI-MS m/z: 125 [M-H]; ^{1}H NMR (500 MHz, DMSO-D6), δ (ppm): 6.381 (1H, t, J = 8.0 Hz, H-5), 6.214 (2H, d, J = 8.0 Hz, H-4 and H-6), 8.556 (2H, brs)

III (Kaempferol): It is yellow crystalline solid (m.p. 276-278 ˚C). It is slightly soluble in water and well soluble in hot ethanol and diethyl ether. It reduces the risk of chronic diseases especially cancer. ESI-MS m/z: 285 $[M-H]^{+}$; ^{1}H NMR (500 MHz, mthanol-D4) δ (ppm): 8.065 (2H, dd, H-2' and H-6'), 6.883 (2H, dd, H-3' and H-5'), 6.366 (1H, d, H-8), 6.157 (1H, d, H-6)

IV (Quercetin): It is a yellow crystalline powder (m.p. 316-317 ˚C) and is a potent antioxidant flavonoid. It is soluble in ethanol and DMSO. ESI-MS m/z: 301 $[M-H]^{+}$; ^{1}H NMR (500 MHz, methanol-D4), δ (ppm): 7.711 (1H, d, J= Hz, H-2'), 7.618 (1H, dd, H-3'), 6.867 (1H, d, H-5'), 6.382 (1H, d, H-8), 6.155 (1H, d, H-6)

V (Bruguierol B): Bruguierol has the molecular mass of 206 from ESI-MS (m/z 205 for [M-H] peak in the negative ion mode). Four quaternary sp^2 carbons and two methine sp^2 carbons showing two one-proton singlet suggests a 1,2,4,5-tetrasubstituted aromatic ring. Twelve numbers each of protons and carbons were observed in ^{1}H and ^{13}C NMR (C12H12) (Table 1), adding up to mass of 156. This gives the mass balance of 206-156= 50, which suggests presence of 2 OH and an O, and the molecular formula is $C_{12}H_{14}O_3$. The DBE is 6, 4 for benzene ring and 2 for further 2 rings, since no more sp^2 carbons are present. The two OH groups must be logically placed ortho to each other at the two deshielded sp^2 carbons on one side of the benzene ring, while the opposite side is the common bond shared between the aromatic ring and a nonaromatic ring. Another two deshielded sp^3 carbons suggest an oxygen bridge in the nonaromatic ring dividing it into two rings, resulting in a total of DBE 6. The methyl group which appears as a three-proton singlet should be attached to the quaternary bridgehead carbon. The two bridgehead carbons must be chiral centers, which results in the observed three methylene carbons bearing diastereotopic protons. This requires that two of these three methylene groups need to be on either side of one of the bridgeheads. The molecular connectivity/correlation diagrams (MCD) (Soong et al., 2020) were constructed based on the HMBC correlation data (Table 1). In drawing the MCD, Chem Draw Professional 15 software was used, bearing in mind the requirements considered above. Partial molecular connectivity/correlation diagrams (MCD) were constructed. Thus, MCDs for aromatic portion a, for methyl and quaternary sp^3 oxygenated carbon containing portion b and oxygenated sp^3 methine carbon containing portion c were constructed. (In the molecular connectivity/correlation diagram (MCD), the lines represent two bond (2JCH), three bond (3JCH) or four bond (4JCH) correlations. Bold, italic, underlined font is used to represent sp^2 hybridization and normal font is used to represent sp^3 hybridization.

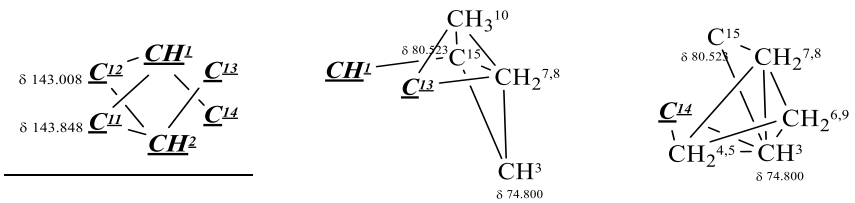

a **b** **c**

From these partial MCDs, the combined MCD d was obtained. The corresponding molecular structure of d was drawn and the two OH and an O were inserted in logical positions to give the deduced structure e of the isolated compound, which is that of bruguierol

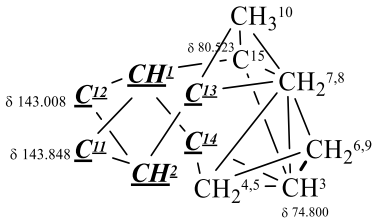

d

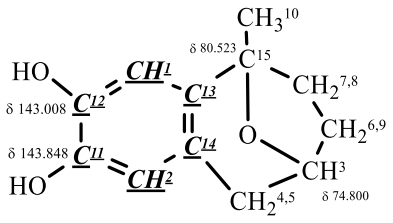

e (bruguierol B)

B. The assignment of the peaks is of the isolated compound and bruguierol B is also compared below using the same numbering system for the position of atoms.

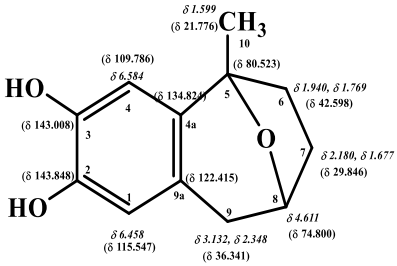

Isolated compound

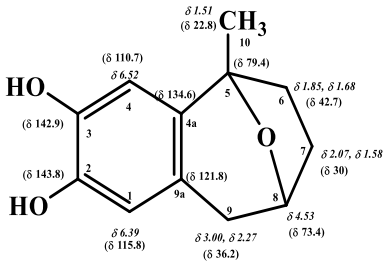

Han *et al.*, 2005

Table 1 NMR Data for the Isolated Compound V (CD_3OD, 500 MHz)

ID	δ [ppm]		# of H	Type	Multiplicity	Connectivity Correlation
	^1H	^{13}C				HMBC (δ [ppm])
1	6.584	109.786	1	CH	s	80.523 ,122.415, 143.008, 143.848
2	6.458	115.547	1	CH	s	134.824, 143.008, 143.848
3	4.611	74.8	1	CH	s br	42.598, 80.523, 122.415
4	3.132	36.341	1	CH_2	dd	29.846, 74.8, 122.415
5	2.348	36.341	1	CH_2	d	29.846, 122.415
6	2.18	29.846	1	CH_2	q	36.341
7	1.94	42.598	1	CH_2	t	74.8
8	1.769	42.598	1	CH_2	m	36.341, 80.523, 134.824
9	1.677	29.846	1	CH_2	m	36.341
10	1.599	21.776	3	CH_3	s	42.598, 80.523, 134.824
4° Cs: 143.848, 143.008, 134.824, 122.415, 80.523 ID: 11,12,13,14,15						

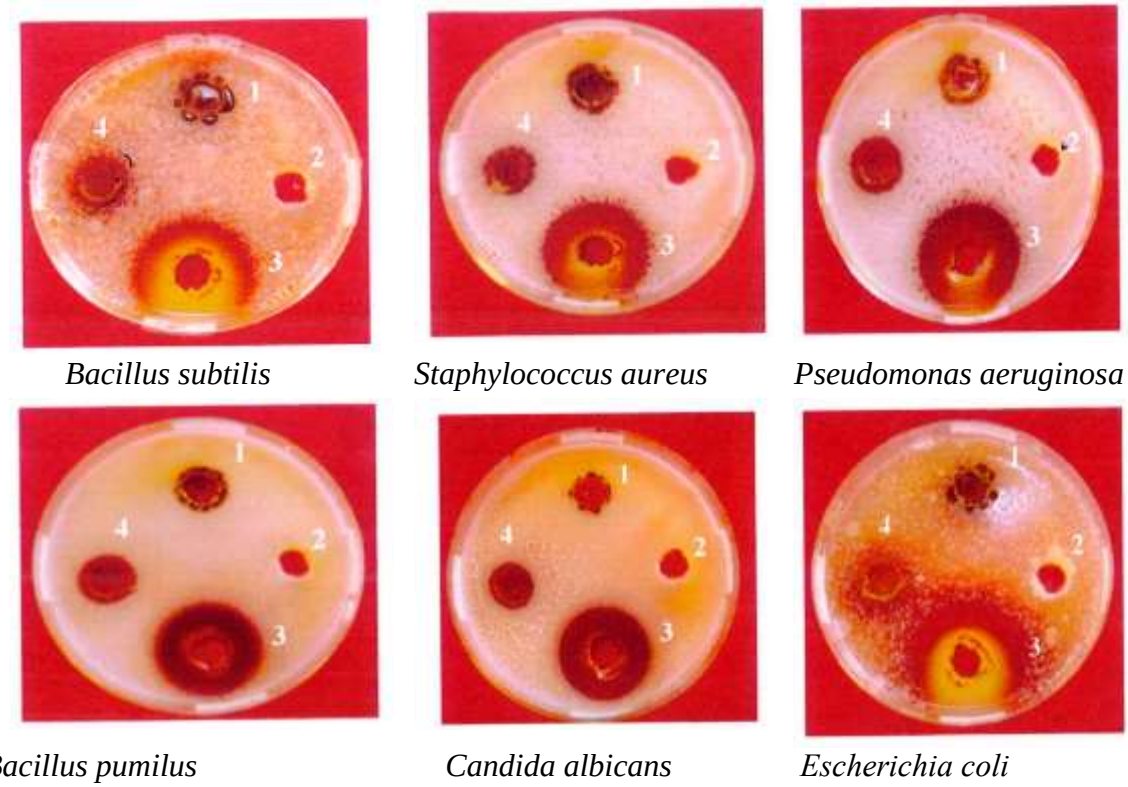

Bacillus subtilis *Staphylococcus aureus* *Pseudomonas aeruginosa*

Bacillus pumilus *Candida albicans* *Escherichia coli*

1= PE, 2= solvent control, 3= Flavonoid extract, 4= 70 % EtOH

Figure 1 Antimicrobial screening of fermented tea leaves on six microorganisms

Table 2 Antimicrobial Screening of Fermented Tea Leaves

	Tested Organisms	Inhibition zone diameter (mm)		
		PE	**70 % EtOH**	**Flavonoid extract**
1.	*Bacillus subtilis*	13	15	30
2.	*Staphylococcus aureus*	15	18	30
3.	*Pseudomonas aeruginosa*	17	20	30
4.	*Bacillus pumilus*	16	17	30
5.	*Candida albicans*	12	17	35
6.	*Escherichia coli*	-	-	-

*Agar well diameter – 10 mm, No activity (-)

Table 3 Antiproliferative Activities of Crude Extracts of the Fermented Tea Leaves against Human Lung Cancer Cell

Extracts	**Human lung cancer cell**		**IC_{50} (µg/mL)**
	20 µg/mL	**200 µg/mL**	
Ethanol	113.90 ± 14.71	13.05± 0.57	95.34
Watery	145.11 ± 22.13	18.59± 0.14	123.44

Table 4 Antiproliferative Activities of Crude Extracts of the Fermented Tea Leaves against Human Cervix Cancer Cell

Extracts	Human cervix cancer cell		IC_{50} (µg/mL)
	20 µg/mL	200 µg/mL	
Ethanol	95.00 ± 17.18	10.85 ± 1.06	116.26
Watery	99.85 ± 11.31	13.84 ± 0.28	124.39

Table 5 Anti-inflammatory and Cell Viability Activities of the Crude Extracts of the Fermented Tea Leaves

Extracts	% NO inhibition		IC_{50} (µg/mL)	% Cell viability		IC_{50} (µg/mL)
	10 µg/mL	100 µg/mL		10 µg/mL	100 µg/mL	
Ethanol	10.33± 0.21	38.53 ± 0.26	>100	81.81 ± 14.35	100.03± 11.17	>100
Watery	9.28 ±0.12	29.07 ± 0.46	>100	77.29 ± 2.97	104.38 ± 2.76	>100
*L-NMMA	18.49 ± 0.1	50.35 ± 0.1	98.25	100.32 ± 12.41	92.01 ± 1.02	>100

*L-*N*MMA(L-*N*-monomethyl-L-arginine) = positive control

Table 6 ^{13}C NMR Data for Isolated Compounds I to V from Fermented Tea Leaves

Position Carbon	I (δ,ppm)		II (δ,ppm)		III (δ,ppm)		IV (δ,ppm)		V (δ,ppm)	
	Obs. (A)	Lit[a] (A)	Obs. (B)	Lit[b] (C)	Obs. (D)	Lit[c] (D)	Obs. (D)	Lit[c] (D)	Obs. (D)	Lit[d] (B)
1	28.0	27.8	146.7	146.2	-	-	-	-	115.5	115.8
2	151.8	151.6	133.5	133.2	146.6	146.8	147.4	147.7	143.8	143.8
3	29.8	29.7	146.7	146.2	135.7	136.6	135.9	135.6	143.0	142.9
4	148.7	148.6	107.6	109.3	176.0	176.6	175.9	176.4	109.7	110.7
4a	-	-	-	-	-	-	-	-	134.8	134.6
5	107.6	107.5	119.0	121.4	161.1	162.3	161.1	161.2	80.5	79.4
6	155.5	155.3	107.6	109.3	97.9	99.2	97.8	98.7	42.5	42.7
7	33.6	33.5			164.2	164.9	164.2	164.4	29.8	30.0
8	141.4	141.5			93.10	94.4	93.0	93.8	74.8	73.4
9					156.9	157.7	156.8	156.1	36.3	36.2
9a					-	-	-	-	122.4	121.8
10					103.1	104.1	103.1	103.0	21.7	22.8
1'					122.3	123.3	120.3	121.9		
2'					129.2	125.9	114.6	115.0		
3'					114.9	116.3	144.8	145.0		
4'					159.2	160.1	146.6	145.8		
5'					114.9	116.3	114.8	115.6		
6'					129.2	125.9	122.7	124.5		
7'										
8'										

a (Sitkowski *et al*, 1995), b (Chemical book.com), c (Natural Product Science, 2017),
d (Han *et al*., 2005)
A (in $CDCl_3$), B (in DMSO-D6), C (in D_2O), D (in Methanol- D4)

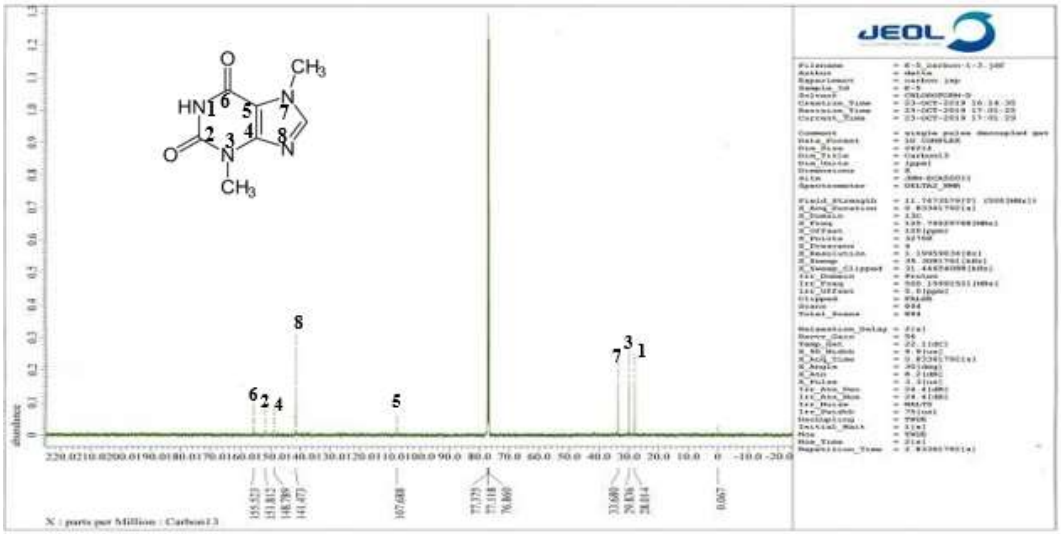

Figure 2 ^{13}C NMR spectrum of caffeine from fermented tea leaves

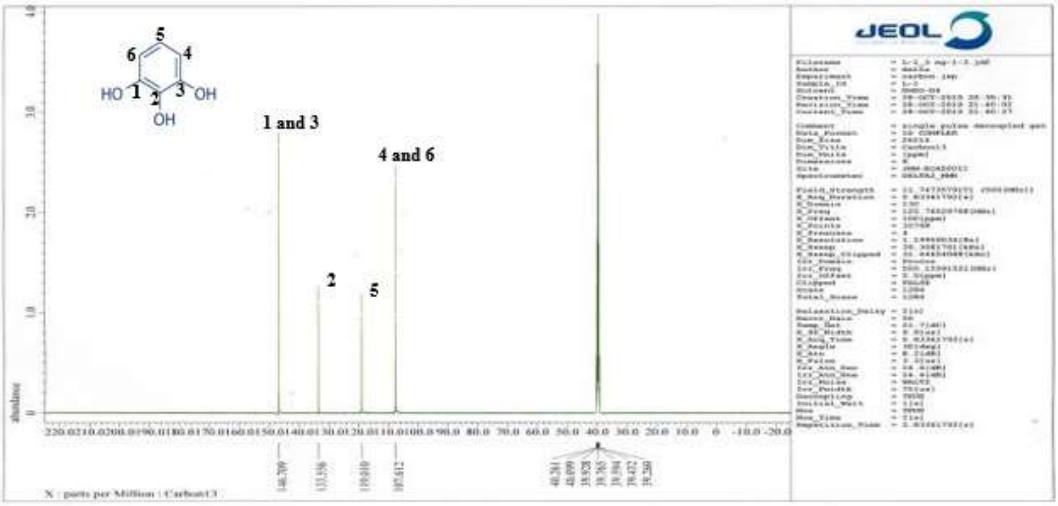

Figure 3 ^{13}C NMR spectrum of pyrogallol from fermented tea leaves

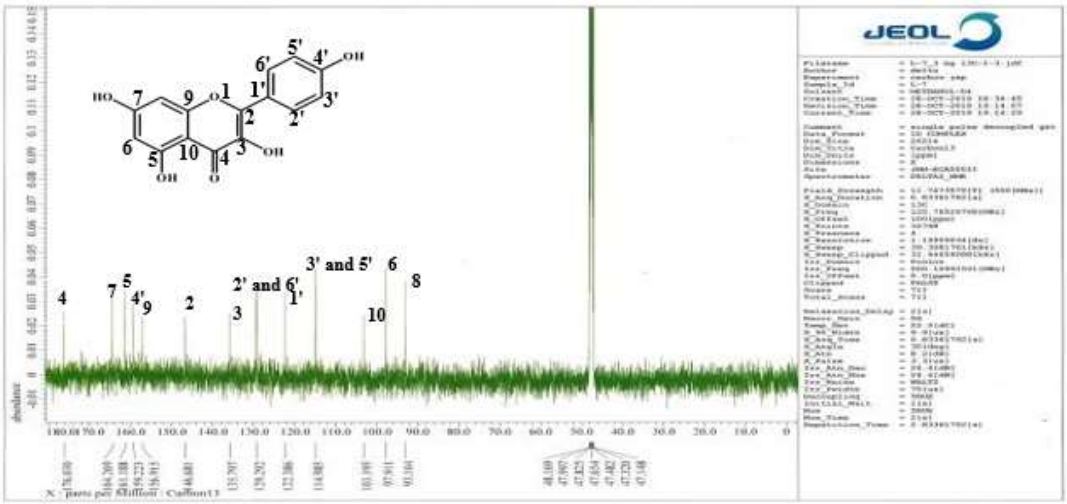

Figure 4 ^{13}C NMR spectrum of kaempferol from fermented tea leaves

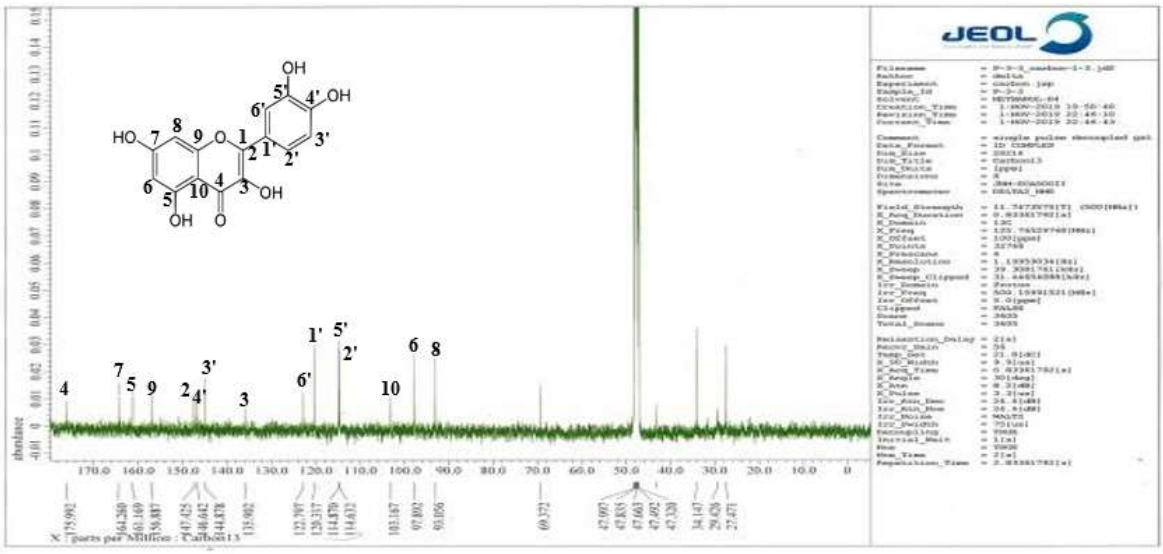

Figure 5 ^{13}C NMR spectrum of quercetin from fermented tea leaves

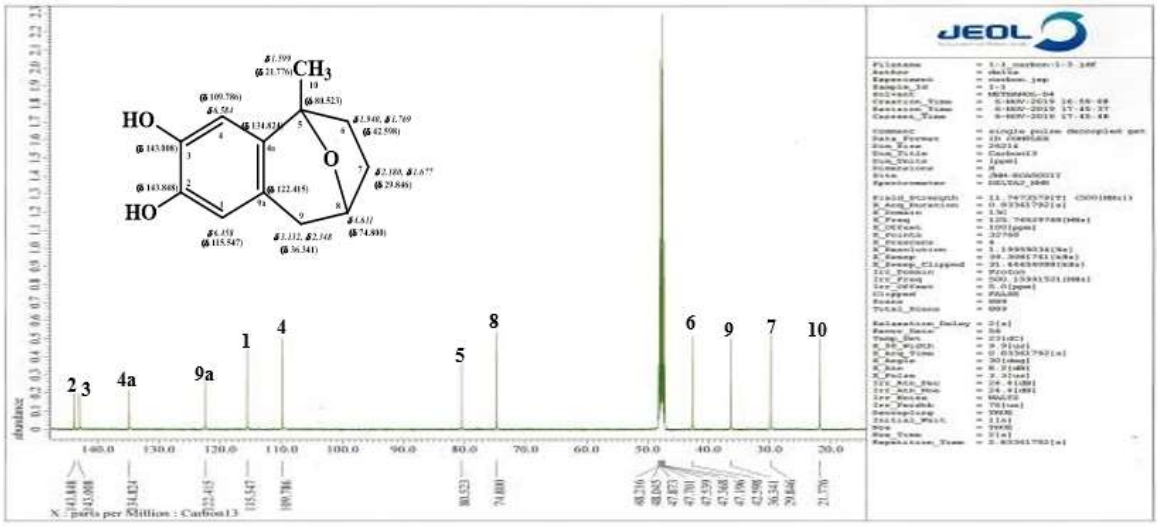

Figure 6 ^{13}C NMR spectrum of kaempferol from fermented tea leaves

Conclusion

From the present research work on "Biological properties and chemical investigation of Myanmar fermented tea leaves (*Camella sinensis* L.)", the following conclusions can be drawn.

The antimicrobial activity of the three crude extracts was screened by *in vitro* method using agar well diffusion technique on six microorganisms. Among the tested extracts, flavonoids extract (35 mm) has more pronounced antimicrobial activity than the other extracts (PE and 70 % EtOH). The ethanol and watery extracts (IC_{50} < 200 µg/mL) had antiproliferative activity against two cancer cell lines (Human lung cancer and Human cervix cancer). Although the tested extracts did not show anti-inflammatory activity by % NO inhibition assay, no toxicity effect was observed in the tested extracts up to 100 µg/mL concentration. Moreover, ethanol extract of fermented tea leaves was separated by column chromatographic method. Five compounds were isolated from fermented tea leaves and identified by ESI-MS and NMR data. The fermented tea leaves, one of the major traditional snacks, can be considered as good sources of natural antioxidant for medicinal uses due to the presence of the isolated flavonoids (quercetin and kaempferol), polyphenol

(pyrogallol) and alkaloid (caffeine). They are strong antioxidants and help to prevent oxidative damage of our cells. Moreover, the isolated bruguierol B has antibacterial activity against mycobacteria and resistant strains. Due to the presence of these active isolated compounds containing fermented tea leaves *Lapphet* definitely provides health benefits such as antimicrobial and anti-cancer to Myanmar people.

Acknowledgements

The authors would like to express their profound gratitude to the Department of Higher Education (Yangon Office), Ministry of Education, Yangon, Myanmar, for provision of opportunity to do this research and Myanmar Academy of Arts and Science for allowing to present this paper.

References

Chemicalbook.com/spectrum, https://www

Fatma, P.K., Yildirim, A.B., Bayram, R., Yavuz, M.Z., Gepdiremem, A. and Arzu, U.T. (2015). "Antiproliferative Activity of Some Medicine Plants on Human Breast and Hepatocellulat Carcinoma Cell Lines and their Phenolic Content". *Tropical Journal of Pharmaceutical Research*, vol. 14(10), pp. 1787-1795

Finegold, S.M. and Martin, W.J. (1982). *Diagnostic Microbiology*. London: The C.V. Mosby Co.

Han, L., Xueshi, H., Isabel, S., Ute, M., Hongzheng, F., Wenhan, L. and Susanne, G. (2005)."New Aromatic Compounds from the Marine Mangrove *Bruguiera gymnorrhiza*", *Planta Med*, vol.71, pp.160-164

Jin, D. and Mumper, R. J. (2010). "Plant Phenolic: Extraction, Analysis and their Antioxidant and Anticancer Properties". *Molecule*, vol. 15, pp. 7313-7352

Lillis, S.A., Yenny, F.Y., Tati, H., Euis, J., Achmad, Z., Ida, N., Ace, T.H., Unang, S. and Yoshihito, S. (2017)."Flavonoid Compounds from the Leaves of *Kalanchoe prolifera* and their Cytotoxic Activity against P-388 Murine Leukemia Cells", vol. 23 (2), pp. 139-145

Myat Kyaw Thu (1993)." Caffeine Contents of Tea Leaves in Various Climates and Ages." MSc *Thesis*, Department of Chemistry, University of Yangon

Myat Kyaw Thu (2003). "The Mode of Formation of Myanmar Fermented Tea". *PhD*, Dissertation, Department of Chemistry, University of Yangon

Ronald Soong, R., Pautler, B.G., Moser, A., Jenne, A., Lysak, D.H., Adamo, A. and Simpson, A.J. (2020). "CASE (Computer-Assisted Structure Elucidation) Study for an Undergraduate Organic Chemistry Class" *J. Chem. Educ*., vol. 97, pp. 855−860

Sitkowski, J., Stefaniak, L., Nicol, L., Martin, M.L., Martin, G.J. and Webb, G.A. (1995). "Complete Assignments of the ^{1}H, ^{13}C and ^{15}N NMR Spectra of Caffeine", *Spectrochimica Acta*, vol.51 (A), No.5, pp. 839-841

World Health Organization. (1999). *W.H.O. Monographs on Selected Medicinal Plants*, Geneva: vol. I, pp.11-14

ANTIMICROBIAL, ANTIOXIDANT PROPERTIES OF *DIOSCOREA BULBIFERA* (AIR POTATO) TUBER EXTRACT AND STRUCTURE ELUCIDATION OF ISOLATED BIBENZYL DERIVATIVE

Khin Hnin Htay[1], Hnin Yu Win[2]*, Myint Myint Sein[3]

Abstract

Chemical investigation of tuber of *Dioscorea bulbifera* Linn. (Local name Put-sar-u) led to the isolation of bibenzyl derivative namely, 3-methoxy-4, 3', 5' -trihydroxybibenzyl (1). The structure of isolated metabolite was elucidated by spectroscopic techniques, particularly by 1D and 2D NMR spectroscopy and mass spectrometry. Antioxidant and antimicrobial properties of various solvent extracts was studied by using DPPH radical scavenging assay and agar-well diffusion method respectively.

Keywords: *Dioscorea bulbifera*, bibenzyl, NMR spectroscopy, DPPH

Introduction

Since ancient times, plants have been used as a source of medicine and a major resource for health care. Nowadays, the modern pharmaceutical industry is paying more and more attention to plants because plant is an almost infinite resource for medicine development (Thomson, 2007). Human beings have depended on nature for their simple requirements especially the sources for medicines, shelters, food stuffs, fragrances, clothing, flavours, fertilizers and means of transportation throughout the ages. In developing countries, medicinal plants show a dominant role in the healthcare system (Dar *et al*., 2017).

The active compounds in medicinal plants have direct or indirect therapeutic effects and are used as medicinal agents. In the body of these plants, certain materials are produced and stored that are referred to as active compounds (substances), which have physiological effects on the living organisms (Phillipson, 2001).

The objective of the present research is to investigate bioactive chemical constituents from *Dioscorea bulbifera*. To achieve this aim, preliminary phytochemical screening, antimicrobial test, antioxidant activity assay, isolation and structure elucidation of selected plant was performed. *Dioscorea bulbifera* tubers have therapeutic benefits as purgative, anthelmintic, diuretic, deflatulent, rejuvenating tonic, aphrodisiac and can also be used for treatment in scrofula, hematological disorders, diabetic disorders, worm infestations and skin disorders (Subasini *et al*., 2013).

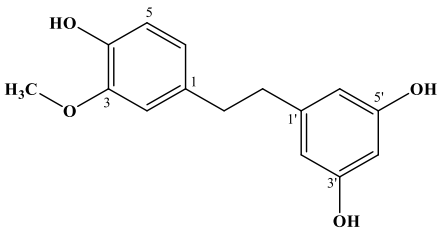

Figure 1 Structure of isolated compound

[1] Lecturer, Department of Chemistry, Yadanabon University
[2] Dr, Associate Professor, Department of Chemistry, University of Mandalay
[3] Dr, Professor and Head (Rtd), Department of Chemistry, University of Mandalay
* Corresponding author: Hnin Yu Win, Department of Chemistry, University of Mandalay, email: snowhninyuwin@gmail.com

Botanical Classification

Figure 2 Plant, flower and tuber of *Dioscorea bulbifera* Linn.

Botanical name	- *Dioscorea bulbifera* L.
English name	- Air potato (or) Yam
Myanmar name	- Put-sar-u
Family name	- Dioscoreaceae
Flowering period	- July-September
Part used	- Tuber

Materials and Methods

General Experimental Procedure

^{1}H NMR spectra: Varian Unity 300 (300.542 MHz), Bruker AMX 300 (300.542 MHz), Varian Inova 500 (499.8 MHz). – ^{13}C NMR spectra: Varian Unity 300 (75.5 MHz), Varian Inova 500 (125.7 MHz). Chemical shifts were measured relatively to tetramethyl silane as internal standard. - 2D NMR spectra: H, H COSY spectra (^{1}H,^{1}H-Correlated Spectroscopy), HMBC spectra (Heteronuclear Multiple Bond Connectivity) and HMQC spectra (Heteronuclear Multiple Quantum Coherence). Thin layer chromatography (TLC): DC-Folien Polygram SIL G/UV$_{254}$ (Macherey-Nagel & Co.). - Column chromatography (CC): MN silica gel 60: 0.05-0.2 mm, 70-270 mesh (Macherey-Nagel & Co). Sephadex LH-20 (Pharmacia) was used for size exclusion chromatography. Commercial grade reagents and solvents were purchased from Super Shell Co. Ltd, Yangon. Common laboratory apparatus were used. PerkinElmer C93927 was used for FT-IR spectra measurement. The antimicrobial activities of plant extracts were measured in Pharmaceutical Research Department, Insein, Yangon.

Plant Material

The tuber of *Dioscorea bulbifera* was collected from Kalay University Campus, Kalay Township, Sagaing Region, Myanmar and identified by Daw Myint Myint Khaing, Department of Botany, Kalay University. The plant material were cut into small pieces and dried at room temperature for about two weeks.

Preliminary Phytochemical Analysis

The preliminary phytochemical screening of *Dioscorea bulbifera* was determined using standard method.

Antimicrobial Assay

Antimicrobial tests were performed at Pharmaceutical Research Department (PRD), Insein Township, Yangon Region. Antimicrobial activities of crude extracts were tested by agar-well

diffusion method on six test microorganisms such as *Bacillus subtilis*, *Staphylococcus aureus*, *Pseudomonas aeruginosa*, *Bacillius pumilus*, *Candida albicans* and *Escherichia coli*.

Antioxidant Activity

The antioxidant activities of the plant extracts were determined by DPPH radical scavenging assay (Yamaguchi *et al*., 1998). The antioxidant activity of sample was expressed in IC_{50}. 1000 µL of test solutions in various concentrations (100 µg/mL, 50 µg/mL, 25 µg/ml, 12.5 µg/ml and 6.25 µg/ml) and 1000 µL of 0.1 M acetate buffer pH 5.5 solutions were mixed in a test tube. 500 µL of $5x10^{-4}$ M DPPH solution was added to the mixture in dark. The mixture was homogenized using a vortex mixer in a dark room (resistant to UV light) and stand for 30 min at room temperature. After that, the absorbance of the solution was measured by a UV spectrophotometer at λ_{max} 517 nm. Vitamin C was used as a reference compound in the same concentration range as the test compound. A control solution was prepared by mixing 1000 µL of buffer (pH 5.5) solution, 1000 µL of ethanol and 500 µL of 5 x 10^{-4} M DPPH solution. Blank solution was prepared by mixing 1000 µL of buffer (pH 5.5) solution with 1500 µL of ethanol. The mean values were obtained from triplicate experiments.

The capability of scavenging DPPH radicals as a percentage of DPPH remaining in the resulting solution was determined using the following equation:

$$\% \text{ inhibition} = \frac{\text{Abs control} - \text{Abs sample}}{\text{Abs control}} \times 100$$

Where $Abs_{control}$ is absorbance of control and Abs_{sample} is absorbance of sample. The antioxidant power (IC_{50}) is expressed as the test substances concentration (µg/mL) that result in a 50% reduction of initial absorbance of DPPH solution and that allows to determine the concentration. IC_{50} (50% inhibition concentration) values were calculated by linear regressive excel program.

Extraction and Isolation of Pure Compound

The air dried sample *of Dioscorea bulbifera* (1000 g) were percolated with methanol for two months. The methanol crude extracts were filtered and evaporated the solvent. The residue was extracted with ethyl acetate to attain 34.13 g of ethyl acetate crude extracts. The crude extract was dissolved in a mixture of n-hexane and EtOAc and 6 g of silica gel were added. The mixture was allowed to dryness under reduced pressure. The obtained crude powder extracts were subjected to silica gel by using various solvent systems of n-hexane and ethyl acetate. 3-methoxy-4,3',5'-trihydroxybibenzyl (1) was isolated as red solid from selected fraction V. It showed UV absorption band at 254 nm.

Results and Discussion

Preliminary Phytochemical Screening

According to preliminary phytochemical test, the crude extracts of *Dioscorea bulbifera* contained flavonoid, glycoside, phenolic compound, polyphenol, reducing sugar, saponin, steroid, tannin and terpenoid.

Antimicrobial Activities of the Tuber of *Dioscorea bulbifera*

The antimicrobial activities of the tuber of *Dioscorea bulbifera* were tested in various solvent systems by using agar-well diffusion method.

Table 1 Antimicrobial Activities of Tuber of Dioscorea bulbifera

Sample	Solvent	Inhibition zone (mm)					
		I	II	III	IV	V	VI
Dioscorea bulbifera	n-hexane	-	-	-	-	-	-
	EtOAc	17 (++)	15 (++)	21 (+++)	15 (++)	18 (++)	17 (++)
	MeOH	15 (++)	18 (++)	18 (++)	15 (++)	15 (++)	15 (++)

Agar Well – 10 mm
(+) ~ 10 mm – 14 mm
(++) ~ 15 mm – 19 mm
(+++) ~ 20 mm above

I = *Bacillus subtilis*
II = *Staphylococcus aureus*
III = *Pseudomonas aeruginosa*
IV = *Bacillus pumilus*
V = *Candida albicans*
VI = *Escherichia coli*

According to antimicrobial tests, the n-hexane extracts did not respond activity on all test microorganisms. The ethyl acetate extracts showed strong activities against *Pseudomonas aeruginosa* and medium activities against other five test microorganisms. The methanol extracts exhibited medium activities on all test microorganisms.

Antioxidant Activity by DPPH Radical Scavenging Assay

The percentage of inhibition in different concentrations of standard ascorbic acid and IC_{50} value was shown in Table 2.

Table 2 % Inhibition in Different Concentrations for Standard Ascorbic Acid and IC50 Value

Concentration (µg/mL)	% Inhibition	IC_{50} (µg/mL)
100	90.9	
50	90.4	
25	59.2	22.14
12.5	19.3	
6.25	4.0	

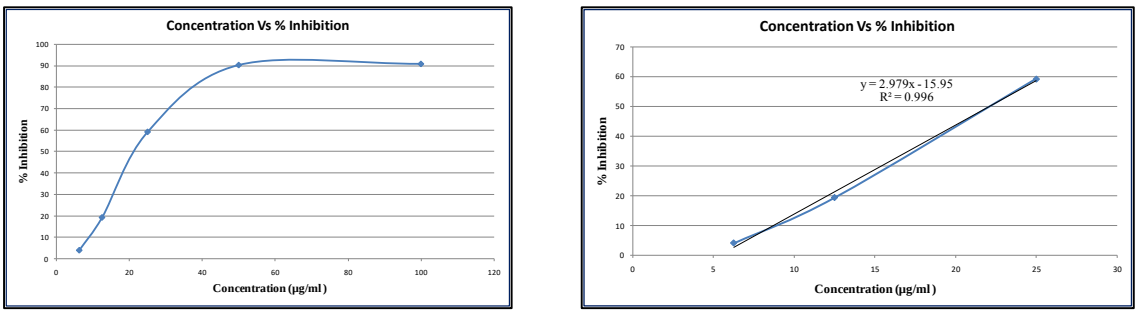

(a) (b)

Figure 3 (a) Standard calibration curve of ascorbic acid (b) Linear graph for calculation of IC_{50} value of standard ascorbic acid solution

Table 3 % Inhibition of Methanolic Extract in Different Concentrations and IC_{50} Value

Concentration (µg/mL)	% Inhibition	IC_{50} (µg/mL)
100.00	81.70	
50.00	63.41	
25.00	38.95	36.23
12.50	27.05	
6.25	12.65	

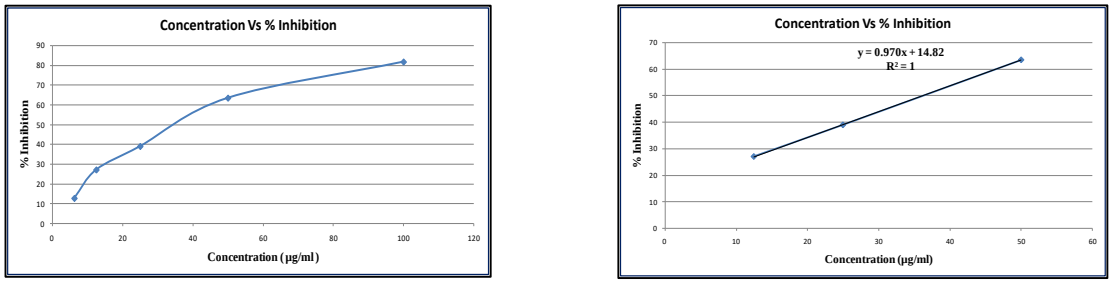

(a) (b)

Figure 4 (a) % Inhibition of methanolic extract of *Dioscorea bulbifera* (b) Linear graph for calculation of IC_{50} value of methanolic extracts

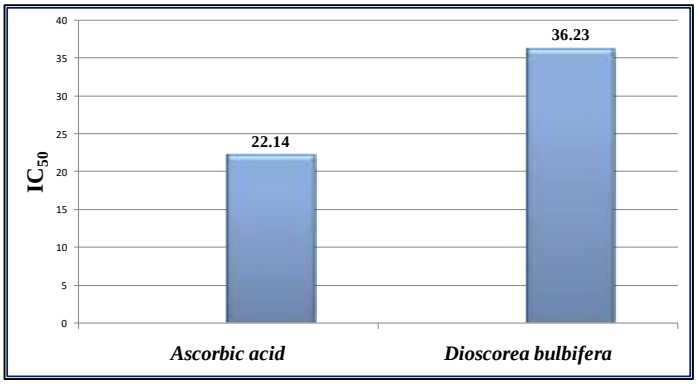

Figure 5 Bar graph of IC_{50} value of ascorbic acid and methanolic extracts of *Dioscorea bulbifera*

DPPH radical scavenging activities of the methanolic extract of *Dioscorea bulbifera* showed significant free radical scavenging activity with IC_{50} value of 36.23 µg/mL.

Structure Elucidation of 3-methoxy-4, 3',5'-trihydroxybibenzyl

Structural elucidation of isolated compound was determined by spectroscopic methods such as FT IR, ^{1}H NMR, ^{13}C NMR, DEPT, DQF-COSY, HSQC and HMBC spectra.

According to the ^{13}C NMR (Figure 8.2) and DEPT (Figure 8.3), total of 15 carbon signals were detected which comprised of six sp^2 quaternary carbons at δ 159.3 (two C_q), 148.6, 145.6, 145.5 and 134.8 ppm, six sp^2 methine carbons at δ 121.9, 115.9, 113.4, 108.2 (2 CH) and 107.1 ppm, one sp^3 methyl carbon at δ 56.3 ppm and two sp^3 methylene carbons at δ 39.5 and 38.4 ppm. Among them, four sp^2 quaternary carbons at δ 159.3, (two C_q), 148.6 and 145.6 ppm were probably attached to oxygen.

In the aromatic region of the ^{1}H NMR spectrum (Figure 8.1), one doublet of doublet methine proton at δ 6.59 ppm (J = 1.76, 7.98 Hz) showed ortho coupling with one doublet methine

proton at δ 6.68 ppm (J = 7.97 Hz) and meta coupling with another doublet methine proton at δ 6.65 ppm (J = 1.69 Hz). Thus, 1, 2, 4-trisubstituted benzene ring could be drawn. In the DQF-COSY spectrum (Figure 8.5), the methine proton at δ 6.59 ppm showed correlation with one methine proton at δ 6.68 ppm as expected. Therefore, fragment (a) could be assigned.

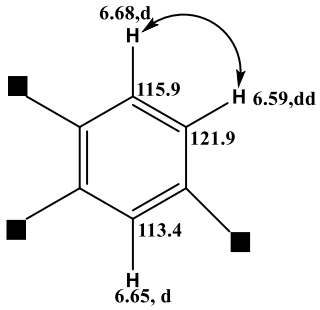

Fragment (a)

In the HMBC spectrum (Figure 8.6), the doublet of doublet methine proton at δ 6.59 ppm showed β-correlation with one sp^2 methine carbon at δ 113.4 ppm, one sp^2 quaternary carbon at δ 145.6 and one sp^3 methylene carbon at δ 38.4 ppm. Therefore, fragment (b) could be drawn. Moreover, one doublet methine proton at δ 6.65 ppm showed β-coupling with one sp^2 methine carbon at δ 121.9 ppm, one sp^2 quaternary carbon at δ 145.6 and one sp^3 methylene carbon at δ 38.4 ppm. Furthermore, in the HMBC spectrum (Figure 8.6), one doublet methine proton at δ 6.68 ppm showed strong correlation with two sp^2 quaternary carbons at δ 134.8 and 148.6 ppm. Therefore, the carbon atoms in the benzene ring could be assigned.

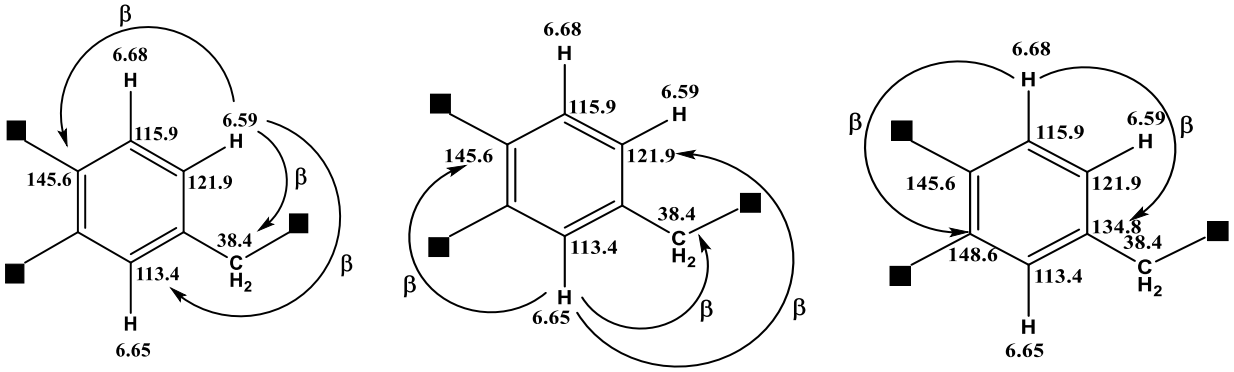

Figure 6 HMBC (→) correlations in fragment (b)

According to the chemical shift, the two quaternary carbons at δ 145.6 and 148.6 could be connected to oxygen. Furthermore, in the HMBC spectrum (Figure 8.6), there was the observation of β-coupling between singlet methoxy group at δ 3.77 ppm and aromatic sp^2 quaternary carbon at δ 148.6 ppm produced fragment (c).

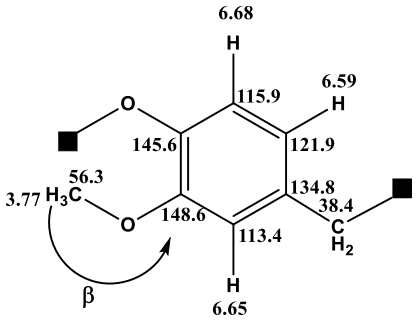

Fragment (c)

In the aromatic region of the ^{1}H NMR spectrum (Figure 8.1), one triplet methine proton at δ 6.09 ppm (J = 2.09 Hz) showed meta coupling with two chemical shift equivalent methine protons at δ 6.12 ppm (J = 2.08 Hz). Thus, 1, 3, 5-trisubstituted benzene ring fragment (d) could be drawn. In the HMBC spectrum (Figure 8.6), the triplet methine proton at δ 6.09 ppm showed strong correlation with two equivalent sp^2 methine carbons at δ 108.2 ppm and two equivalent sp^2 quaternary carbons at δ 159.3 ppm. Moreover, the two chemical shift equivalent methine protons at δ 6.12 ppm showed HMBC correlation with each other. Furthermore, these two protons showed β-coupling with one sp^2 methine carbon at δ 101.1 ppm, two equivalent sp^2 quaternary carbons at δ 159.3 ppm and one sp^3 methylene carbon at δ 39.5 ppm. Therefore, fragment (e) could be assigned.

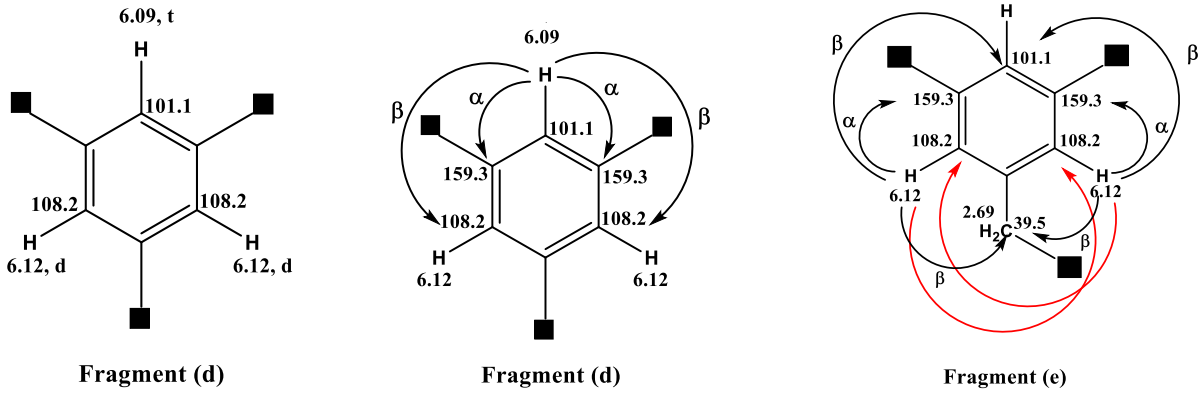

Fragment (d) **Fragment (d)** **Fragment (e)**

Figure 7 HMBC (→) correlations in fragment (d) and (e)

Furthermore, in the HMBC spectrum (Figure 8.6), the doublet of doublet methylene protons at δ 2.69 which is attached to carbon at δ 39.5 ppm showed strong correlation with one sp^2 quaternary carbon at δ 145.5 ppm and two equivalent sp^2 methine carbons at δ 108.2 ppm. Therefore, fragment (e) could be further confirmed.

Moreover, the doublet of doublet methylene protons at δ 2.69 ppm from fragment (e) showed β- correlation with one sp^2 quaternary carbon at δ 134.8 and a-correlation with one sp^3 methylene carbon at δ 38.4 ppm from fragment (c). Similarly, the doublet of doublet methylene proton at δ 2.76 ppm from fragment (c) showed β-correlation with one sp^2 quaternary carbon at δ 145.5 and a-correlation with one sp^3 methylene carbon at δ 39.5 ppm from fragment (e). So the fragment (c) and (e) could be connected as shown in partial structure (I).

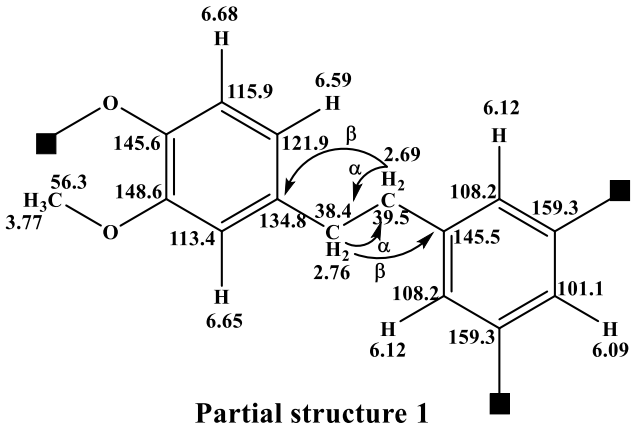

Partial structure 1

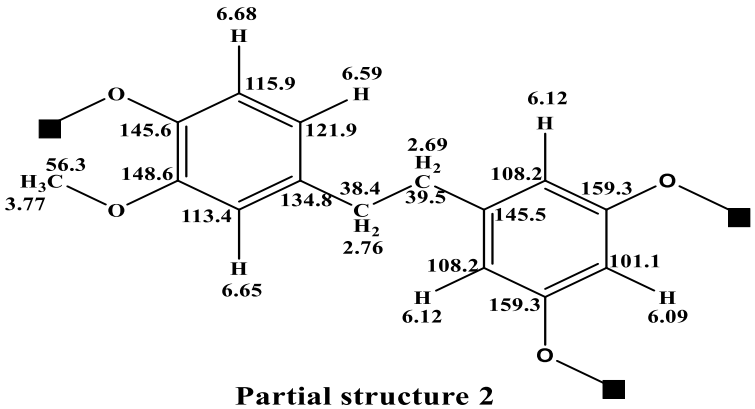

Partial structure 2

According to the chemical shift value, the two equivalent sp^2 quaternary carbons at δ 159.3 ppm could be connected to oxygen and partial structure 2 with the partial molecular mass of 257 could be assigned. Moreover, FT IR spectrum showed the presence of OH group. Therefore, the complete structure of isolated compound could be elucidated as 3-methoxy-4,3',5'-trihydroxybibenzyl. The isolated compound is bibenzyl derivative. Bibenzyl are naturally occurring fungicides. Both natural and synthetic bibenzyls show antifungal activity (Smriti *et al*., 2013). Bibenzyl derivatives constitute a class of stilbenoid compounds with interesting structural scaffolds and biological activities including antioxidant, cytotoxic, antibacterial and antifungal (Osei-Safo *et al*., 2017).

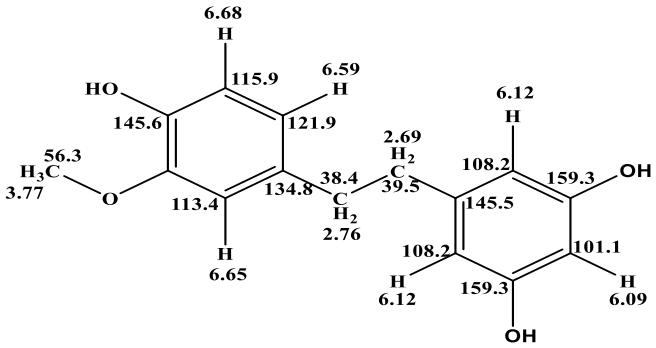

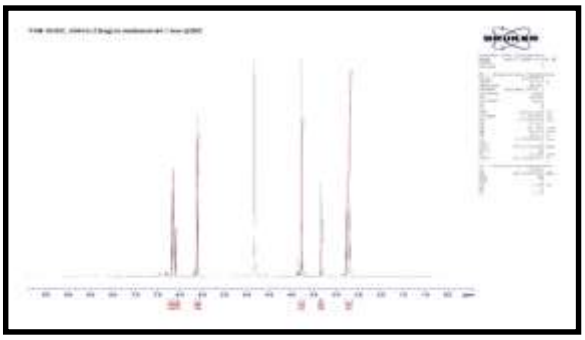

(8.1)

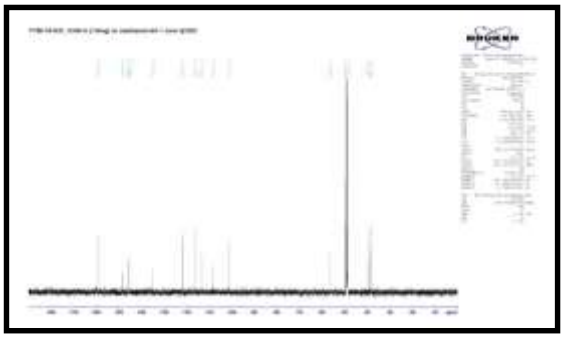

(8.2)

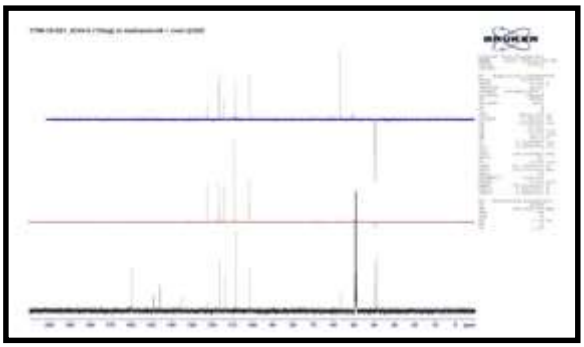

(8.3)

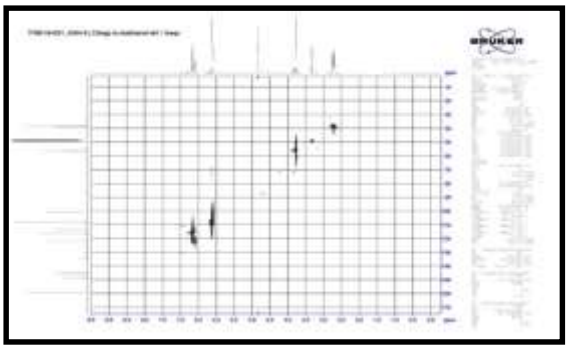

(8.4)

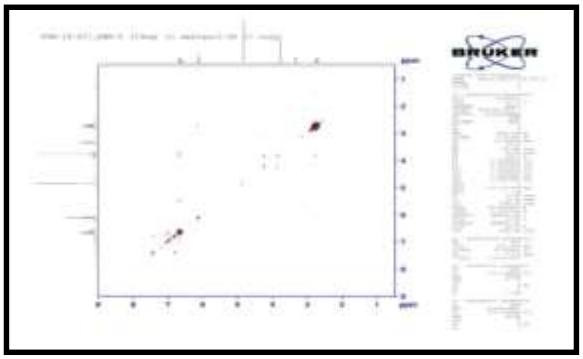

(8.5)

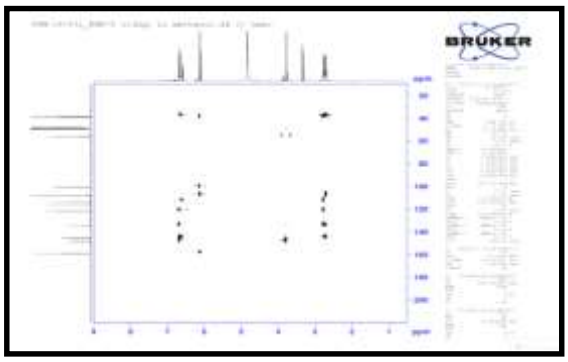

(8.6)

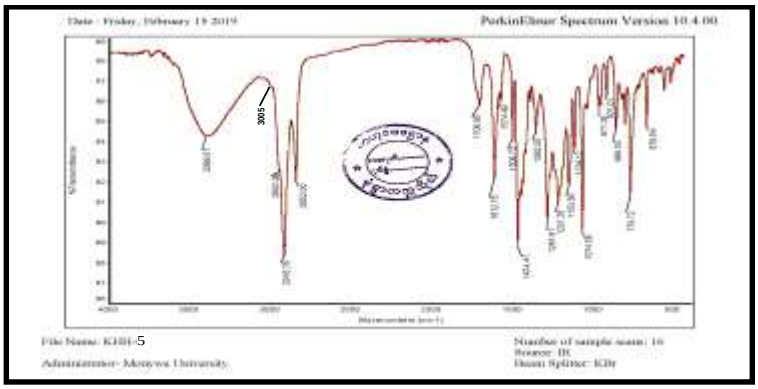

(8.7)

Figure 8 (8.1) ^{1}H NMR, (8.2) ^{13}C NMR, (8.3) DEPT, (8.4) HSQC, (8.5) DQF-COSY, (8.6) HMBC, (8.7) FT-IR of isolated compound

Conclusion

In this research work, *Dioscorea bulbifera* was selected for chemical screening due to its interesting medicinal uses. Preliminary photochemical screening of the crude sample revealed the presence of glycoside, phenolic, reducing sugar, tannin, saponin, flavonoid, steroid, terpenoids and polyphenol respectively. According to antimicrobial assay, the n-hexane extracts did not inhibit the growth of all test microorganisms. The ethyl acetate extracts showed strong activities against *Pseudomonas aeruginosa* and medium activities against other five test microorganisms. The methanol extracts exhibited medium activities on all test microorganisms. Moreover, methanolic extract showed antioxidant activity on DPPH with IC_{50} of 36.23 µg/mL. From ethyl acetate extract, 3-methoxy-4,3',5'-trihydroxybibenzyl was isolated and characterized by FT-IR and NMR studies. The result of the present study suggested that selected plant can be used as a source of antioxidant and antimicrobial for pharmacological preparations which is very well evidenced by the present work.

Acknowledgements

The authors thank Dr Yoshiaki Takaya, Associate Professor, Faculty of Pharmacy, Meijo University for NMR and mass measurements. Sincere thanks are extended to Dr Yi Yi Myint, Professor & Head, Department of Chemistry, University of Mandalay, for her permission to submit the paper.

References

Dar, R.A., Shahnawaz, M., and Qazi, P.H. (2017). "General Overview of Medicinal Plants". *The Journal of Phytopharmacology*, vol. 6, pp. 349-351.

Osei-Safo, D., Dziwornu, G. A., Salgado, A., Sunassee, S. N., and Chama, M.A. (2017). "Bi- and Bisbibenzyls from the Roots of *Dichapetalum heudelotii* and their Antiproliferative Activities". *Fitoterapia*, vol. 122, pp. 95-100.

Phillipson, J.D. (2001). "Phytochemistry and Medicinal plants". *Phytochemistry*, vol. 56, pp. 237-243.

Smriti, D., and Siddiqui, I.R. (2013). "Study of Fungicidal Activity of Synthesized Bio Active 4, 4'-Dihydroxy Bibenzyl Incorporating Various Heterocyclic Moieties". *International Journal of Engineering Science and Innovative Techanology (IJESIT)*, vol.2, pp.342-350.

Subasini, U., Thenmozhi, S., Sathyamurthy, D., Vetriselvan, S., Rajamanickam, G.V., and Dubey, G.P. (2013). "Pharmacognostic and Phytochemical Investigations of *Dioscorea bulbifera* L". *International Journal of Pharmacy & Life Sciences*, vol. 4, pp. 2693-2700.

Thomson, G.E. (2007). "The Health Benefits of Traditional Chinese Plant Medicines: Weighing the Scientific Evidence" Rural Industries Research and Development Corporation (RIRDC Publishing), pp. 1.

Yamaguchi, T., Takamura, H., Matoba, T., and Terao, J. **(**1998**).** "HPLC Method for Evaluation of the Free Radical-scavenging Activity of Foods by Using 1, 1-diphenyl-2-picrylhydrazyl". *Biosci., Biotechnol. Biochem*, vol. 62, pp. 1201-1204.

ISOLATION AND STRUCTURE ELUCIDATION OF PHENYLNAPHTHALENE DERIVATIVE FROM TUBEROUS ROOTS OF *ORTHOSIPHON RUBICUNDUS* (D.DON) BENTH. AND STUDY ON ITS ANTIOXIDANT PROPERTY

Han Su Lwin[1], Hnin Yu Win[2]*, Khaing Khaing Kyu[3]

Abstract

The present study was conducted to investigate bioactive chemical constituent from Myanmar medicinal plant, *Orthosiphon rubicundus* (D.Don) Benth. Firstly, phytochemical screening of the selected medicinal plant was performed according to standard procedure. Then, the antimicrobial assay of various extracts was performed on six test microorganisms. Phenylnaphthalene derivative namely, 1-(4-hydroxy-3,5-dimethoxyphenyl)-2,3-dimethyl-5,6,7-trimethoxynaphthalene (1) was isolated from ethyl acetate extract by using separation techniques such as thin layer and column chromatographic methods. Moreover, the antioxidant activities of crude extract and isolated compound were evaluated using DPPH radical scavenging assay. Furthermore, structure elucidation of isolated compound was performed by spectroscopic techniques, particularly by 1D and 2D NMR spectroscopy.

Keywords: DPPH, phenylnaphthalene, spectroscopic

Introduction

Herbal therapies have played a vital role in the progress of human culture. Medicinal plants are resources of traditional medicines and many of the modern medicines are formed indirectly from plant life. According to WHO, about 80 percent of the world's population rely on traditional medicine and millions of people in the vast rural areas of developing countries use herbal medicines for their health care needs. Meanwhile, consumers in developed countries are becoming disillusioned with modern health care and are seeking alternatives (Hosseinzadeh *et al*., 2015). Although modern medicine may exist side-by-side with such traditional practice, herbal medicines have retained their popularity for historical and cultural reasons (Vishwakarma *et al*., 2013).

The *Orthosiphon* species have widely used in traditional medicines to cure various diseases such as diabetes, kidney stone, edema, rheumatism, hepatitis, hypertensive and jaundice. According to phytochemical investigation, *Orthosiphon* species contain phytoconstituents such as monoterpenes, diterpenes, triterpenes, saponins, organic acid and flavonoid compounds. Antidiabetic, anti-inflammatory, antioxidant, hepatoprotective, analgesic and nephroprotective activities have been reported in the plant extract and phytoconstituents of the *Orthosiphon* genus (Singh *et al*., 2015).

Also in Myanmar, there are many reputed traditional plants in pharmacology. Therefore, the study of traditional indigenous medicinal plants and their usages in therapy play a very important role. In the present work, one Myanmar medicinal plant, *Orthosiphon rubicundus* was selected due to its numerous medicinal properties. It is locally known as Nar-ga-ma. According to personal communication with traditional medicine practitioners, it is used to treat various types of cancer, venom, impetigo and eczema (interviewed with medicinal practitioner, Yesagyo, 2019).

[1] Lecturer, Department of Chemistry, Shwebo University
[2] Dr, Associate Professor, Department of Chemistry, University of Mandalay
[3] Dr, Professor, Department of Chemistry, University of Mandalay
* Corresponding author: Hnin Yu Win, Department of Chemistry, University of Mandalay, email: snowhninyuwin@gmail.com

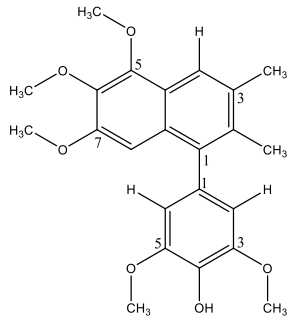

Figure 1 Structure of isolated compound (1)

Botanical Classification

Figure 2 Roots, plants and flowers of *Orthosiphon rubicundus*

Botanical name	-	*Orthosiphon rubicundus* (D.Don) Benth.
Local name	-	Nar-ga-ma
Family name	-	Lamiaceae
Common name	-	Red Java Tea
Part used	-	Tuberous root

Materials and Methods

General Experimental Procedures

^{1}H NMR spectra: Varian Unity 300 (300.542 MHz), Bruker AMX 300 (300.542 MHz), Varian Inova 500 (499.8 MHz). –^{13}C NMR spectra: Varian Unity 300 (75.5 MHz), Varian Inova 500 (125.7 MHz). Chemical shifts were measured relatively to tetramethylsilane as internal standard. - 2D NMR spectra: H, H COSY spectra (^{1}H,^{1}H-Correlated Spectroscopy), HMBC spectra (Heteronuclear Multiple Bond Connectivity) and HMQC spectra (Heteronuclear Multiple Quantum Coherence). Thin layer chromatography (TLC): DC-Folien Polygram SIL G/UV$_{254}$ (Macherey-Nagel & Co.). - Column chromatography (CC): MN silica gel 60: 0.05-0.2 mm, 70-270 mesh (Macherey-Nagel & Co). Sephadex LH-20 (Pharmacia) was used for size exclusion chromatography. Commercial grade reagents and solvents were purchased from Super Shell Co. Ltd, Yangon. Common laboratory apparatus were used. PerkinElmer C93927 was used for FT-IR spectra measurement. The antimicrobial activities of plant extracts were measured in Pharmaceutical Research Department, Insein, Yangon. The antioxidant activity of crude extract and pure compound was analyzed by DPPH radical scavenging method at the Department of Chemistry, Kyaukse University.

Plant Material

The tuberous roots of *Orthosiphon rubicundus* were collected from Shinmadaung, Yesagyo Township, Magwe Region and identified by Dr Khin Myo San, Associate Professor, Department of Botany, Yadanabon University. The root materials were cut into small pieces and dried at room temperature for about two weeks.

Preliminary Phytochemical Analysis

The preliminary phytochemical screening of tuberous roots of *Orthosiphon rubicundus* was determined according to the procedure of Harborne.

Antimicrobial Assays

The antimicrobial activities of crude extracts were tested by agar-well diffusion method on six microorganisms such as *Bacillus subtilis, Staphylococcus aureus*, *Pseudomonas aeruginosa*, *Bacillus pumilus, Candida albicans* and *Escherichia coli*.

Determination of Antioxidant Activities

The antioxidant activities of the methanolic extract and pure compound were determined by DPPH radical scavenging assay. The control solution was prepared by mixing 2 mL of 24 μg/mL DPPH solution and 2 mL of 95% methanol with vortex mixer. Similarly, the blank solution was prepared by mixing 2 mL of test solution and 2 mL of 95% methanol with vortex mixer. The test sample solution was also prepared by mixing 2 mL of 24 μg/mL DPPH solution and 2 mL sample solution in various concentrations (11.25, 22.5, 45, 90, 180 μg/mL for methanolic extract and 25, 50, 100, 200, 400 μg/mL for compound 1). The resulting mixtures were thoroughly homogenized by using vortex mixer. The solutions were allowed to stand at room temperature for 30 mins. After 30 mins, measurements of absorbance at 517 nm were made for these solutions using UV-Vis spectrophotometer. The absorbance values obtained were applied to calculate percent inhibition by % Inhibition = $[A_{control}\text{-}A_{sample}/A_{control}]$ x 100, where, % inhibition = percent inhibition of test sample, $A_{control}$ = absorbance of control (DPPH) solution and A_{sample} = absorbance of test sample solution. The IC_{50} value of the sample, which is the concentration of sample required to inhibit 50% of the DPPH free radical, was calculated using inhibition curve.

Extraction and Isolation of Pure Compound

The air dried samples (1000 g) were percolated with methanol for one month. The methanol crude extracts were filtered and evaporated the solvent. The residue was extracted with ethyl acetate to attain 7 g of ethyl acetate crude extracts. The obtained crude extracts were subjected to silica gel by using stepwise gradients of n-hexane and ethyl acetate. 1 (4-hydroxy-3,5-dimethoxyphenyl) -2,3-dimethyl-5,6,7-trimethoxy naphthalene (1) was isolated as white amorphous from selected combined fraction IV. It showed UV absorbing bands at 254 nm.

Results and Discussion

Phytochemical Analysis

According to preliminary phytochemical test, the crude extracts of *Orthosiphon rubicundus* contained alkaloids, flavonoids, glycosides, polyphenols, steroids, tannins, saponins and reducing sugars respectively.

Antimicrobial Activities

The antimicrobial activities of the roots of *Orthosiphon rubicundus* were tested in various solvent systems by using agar-well diffusion method. These results were shown in Table 1.

Table 1 Antimicrobial Activities of the Roots of *Orthosiphon rubicundus*

Sample	Solvent	Inhibition zone (mm)					
		I	II	III	IV	V	VI
Orthosiphon rubicundus	n-hexane	14	12	-	-	15	15
	MeOH	21	25	25	21	13	22
	EtOAc	15	25	20	-	24	25

Agar well – 8 mm
8 mm ~ 12 mm (+)
13 mm ~ 17 mm (++)
18 mm above (+++)

I = *Bacillus subtilis*
II = *Staphylococcus aureus*
III = *Pseudomonas aeruginosa*
IV = *Bacillus pumilus*
V = *Candida albicans*
VI = *Escherichia coli*

According to antimicrobial tests, the n-hexane extracts responded low activities on *Staphylococcus aureus* and medium activities on *Bacillus subtilis*, *Candida albicans* and *Escherichia coli*. The methanol extracts showed strong activities on all test microorganisms except *Candida albicans*. The ethyl acetate extracts exhibited medium activities on *Bacillus subtilis* and strong activities against other four test organisms except *Bacillus pumilus*.

Determination of Antioxidant Activities of Methanolic Extract and Isolated Compound

The radical scavenging activities of methanolic extract and pure compound (1) were determined by DPPH assay method. The methanolic extract and compound (1) showed the antioxidant activity on DPPH with IC_{50} values of 47.90 µg/ mL and 59.02 µg/mL respectively meanwhile IC_{50} values of standard ascorbic acid was 4.05 µg/mL.

Table 2 % Inhibition of Standard Ascorbic Acid in Different Concentrations and IC_{50} Value

Sample	Concentration (µg/mL)	% Inhibition	IC_{50} (µg/mL)
Standard Ascorbic Acid	1	7.322	4.05
	2	15.27	
	4	40.585	
	8	82.008	
	16	93.93	

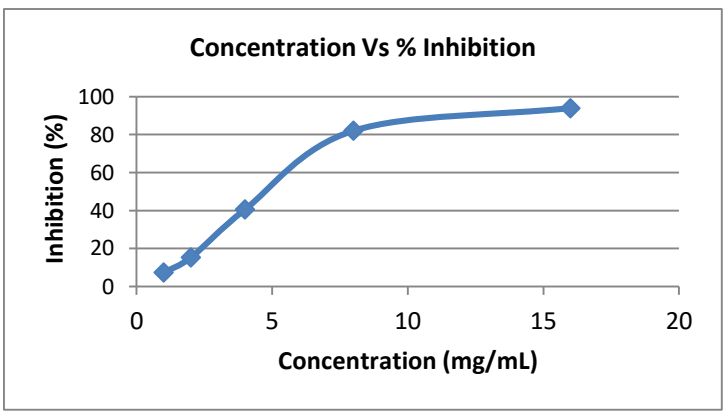

Figure 3 Inhibition percentage of standard ascorbic acid in different concentrations

Table 3 % Inhibition of Methanolic Extract in Different Concentrations and IC_{50} Value

Sample	Concentration (µg/mL)	% Inhibition	IC_{50} (µg/mL)
Methanolic Extract	11.25	25.96	47.90
	22.5	30.7	
	45	47.63	
	90	78.1	
	180	95.26	

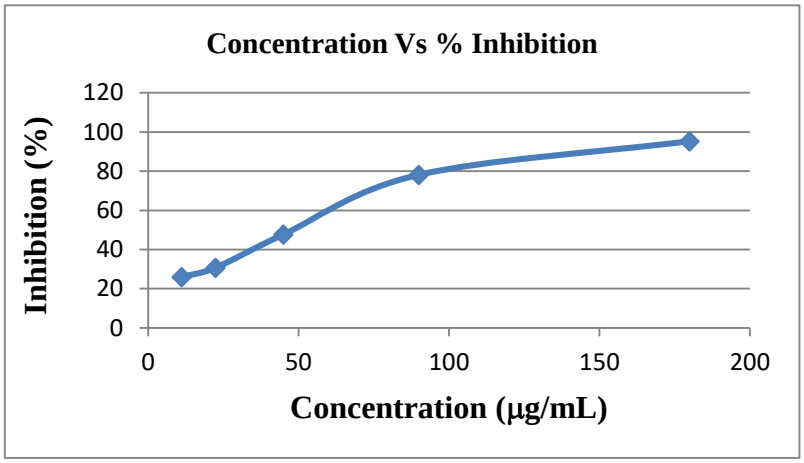

Figure 4 Inhibition percentage of methanolic extract in different concentrations

Table 4 % Inhibition of Compound 1 in Different Concentrations and IC_{50} Value

Sample	Concentration (µg/mL)	% Inhibition	IC_{50} (µg/mL)
Pure Compound (1)	25	29.25	59.02
	50	47.46	
	100	59.26	
	200	77.61	
	400	78.81	

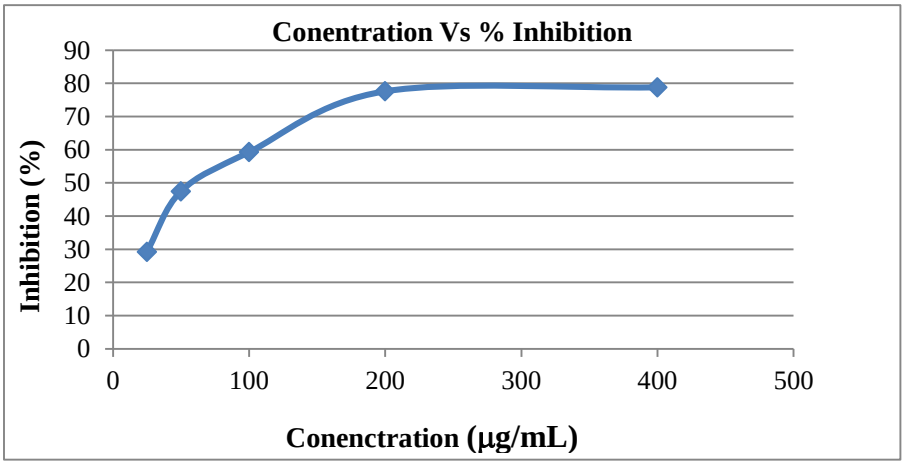

Figure 5 Inhibition percentage of pure compound 1 in different concentrations

Table 5 IC_{50} Values of Standard Ascorbic acid, Methanolic Extract and Compound 1

No.	Sample	IC_{50} (µg/mL)
1	Ascorbic acid	4.05
2	Methanolic Extract	47.90
3	Pure compound 1	59.02

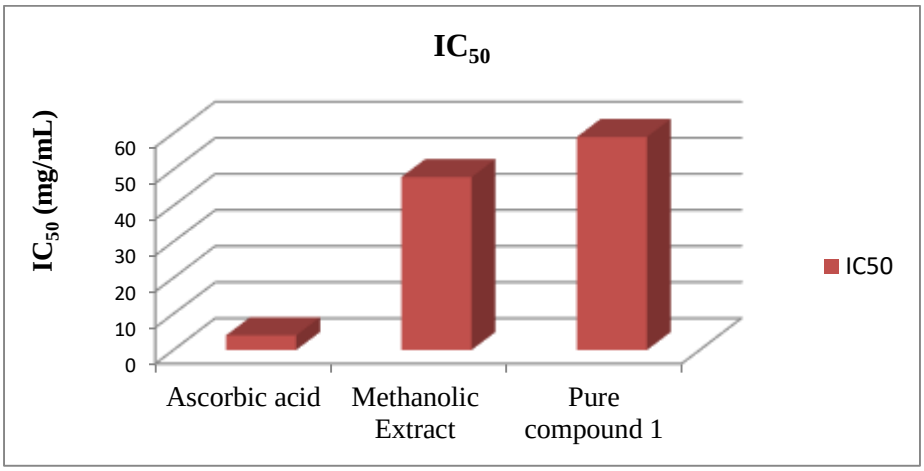

Figure 6 Comparison of IC_{50} values of standard ascorbic acid, methanolic extracts and compound 1

Structure Elucidation

The structure elucidation of compound 1 was determined by spectroscopic methods such as ^{1}H NMR, ^{13}C NMR, DEPT, DQF-COSY, HSQC and HMBC respectively. According to ^{1}H NMR spectrum (Figure 7.1), compound 1 contained 25 protons. By the analysis of ^{13}C NMR (Figure 7.2), together with DEPT (Figure 7.3), total of 23 carbon signals were detected which comprised of twelve sp^2 quaternary carbons at δ 122.7, 129.1, 131.8, 133.1, 133.2, 133.5, 137.3, 140.1, 147.2 (three quaternary carbons), 151.9 ppm, four sp^2 methine carbons at δ 101.6, 106.7 (two equivalent methine carbons), 120.7 ppm, two methyl carbons at δ 17.6, 21.2 and five methoxy carbons at δ 55.7, 56.4 (two methoxy carbons), 61.1 and 61.4 ppm.

In the downfield aromatic region of ^{1}H NMR spectrum, (Figure 7.1), a singlet at δ 7.86 ppm was ascribed to one aromatic methine proton. In the HMBC spectrum, (Figure 7.6), the aromatic methine proton at δ 7.86 ppm showed β-correlation with two sp^2 quaternary carbons at δ 133.1 ppm and 129.1 ppm. Moreover, it showed strong correlation with another sp^2 quaternary carbon at δ 147.2 ppm.

In addition, the aromatic methine proton at δ 7.86 ppm showed HMBC strong correlation with one methyl carbon at δ 21.2 ppm. Moreover, the methyl singlet at δ 2.48 ppm which is attached to carbon at δ 21.2 ppm showed strong correlation with one sp^2 methine carbon at δ 120.7 ppm and one sp^2 quaternary carbon at δ 133.1 ppm. Furthermore, the methyl singlet at δ 2.13 which is attached to carbon at δ 17.6 showed β-correlation with two sp^2 quaternary carbons at δ 133.2 ppm and 137.3 ppm. Therefore, fragment (a) could be assigned.

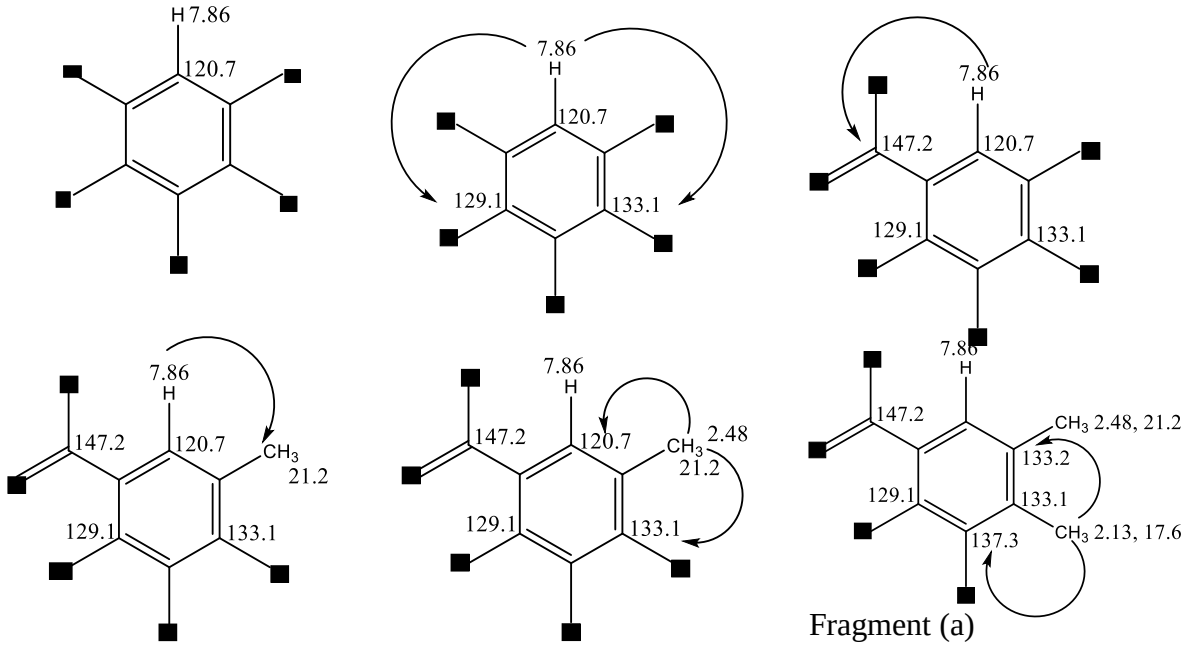

Fragment (a)

In the aromatic region of ^{1}H NMR spectrum (Figure 7.1), a singlet at δ 6.51 ppm was ascribed to another one aromatic methine proton and fragment (b) could be assigned. In the HMBC spectrum, (Figure 7.6), the singlet methine proton at δ 6.51 ppm which is attached to carbon at δ 101.6 ppm showed β-correlation with three sp^2 quaternary carbons at δ 140.1 ppm, 122.7 ppm and 137.3 ppm from the fragment (a). Furthermore, the methine proton at δ 6.51 ppm also showed weak correlation with one sp^2 quaternary carbon at δ 151.9 ppm. Therefore, fragment (a) and (b) could be connected as shown in fragment (c).

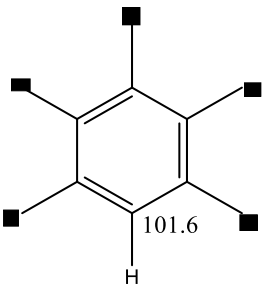

Fragment (b)

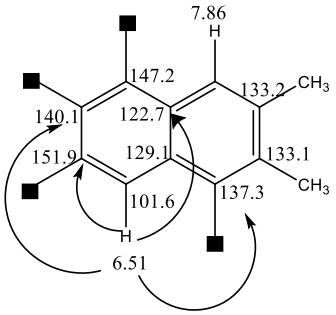

Fragment (c)

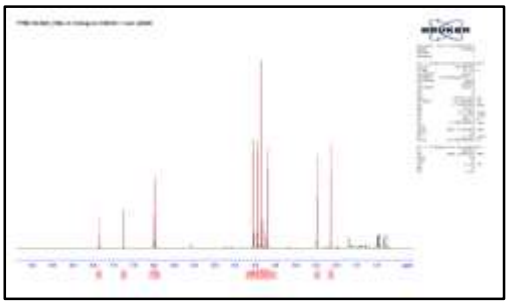

(7.1)

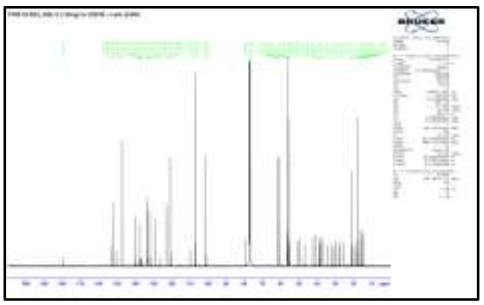

(7.2)

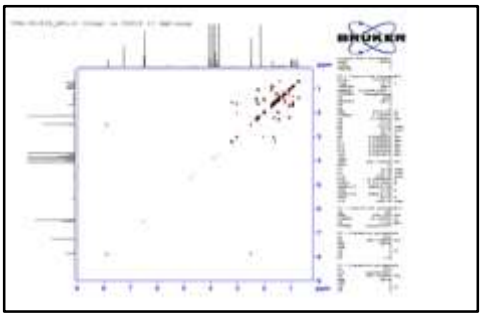

(7.3)

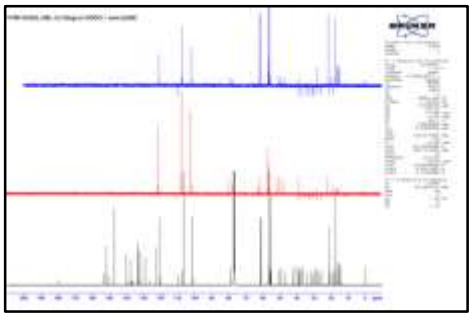

(7.4)

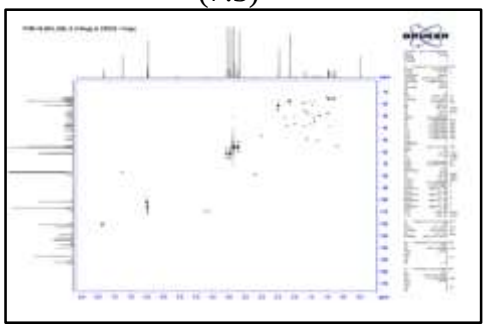

(7.5)

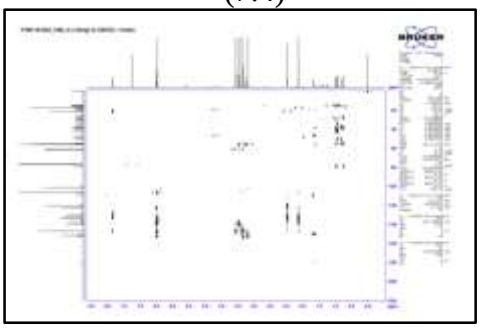

(7.6)

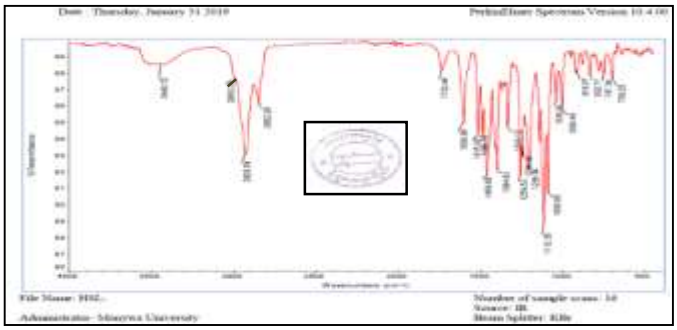

(7.7)

Figure 7 (7.1) ^{1}H NMR, (7.2) ^{13}C NMR, (7.3) DEPT, (7.4) DQF-COSY, (7.5) HSQC, (7.6) HMBC , (7.7) FT-IR of isolated pure compound (1)

Moreover, the three methoxy signals at δ 4.06 ppm (δ_C 61.4), 3.95 ppm (δ_C 61.1) and 3.69 (δ_C 55.7) showed HMBC cross signals to three sp^2 quaternary carbons at δ 147.2, 140.1 and 151.9 ppm respectively. Therefore, fragment (d) could be assigned.

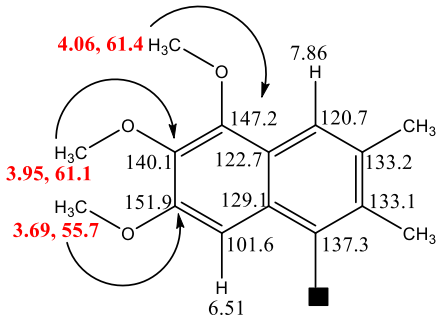

Fragment (d)

Furthermore, in the up field aromatic region of ^{1}H NMR spectrum (Figure 7.1), two chemical shift equivalent methine protons at δ 6.48 ppm (δ_C 106.7) was ascribed to 1, 2, 3, 5-

tetrasubstituted benzene ring. In the HMBC spectrum (Figure 7.6), these two methine protons showed HMBC cross signals between each other and coupled additionally to sp^2 quaternary carbons at δ 131.8, 147.2 and 133.5 ppm. Therefore, the atoms in the benzene ring could be assigned. Furthermore, two methoxy signals at δ 3.86 ppm which are attached to carbons at δ 56.4 showed β-correlation with two sp^2 quaternary carbons at 147.2 ppm. Therefore, fragment (e) could be assigned.

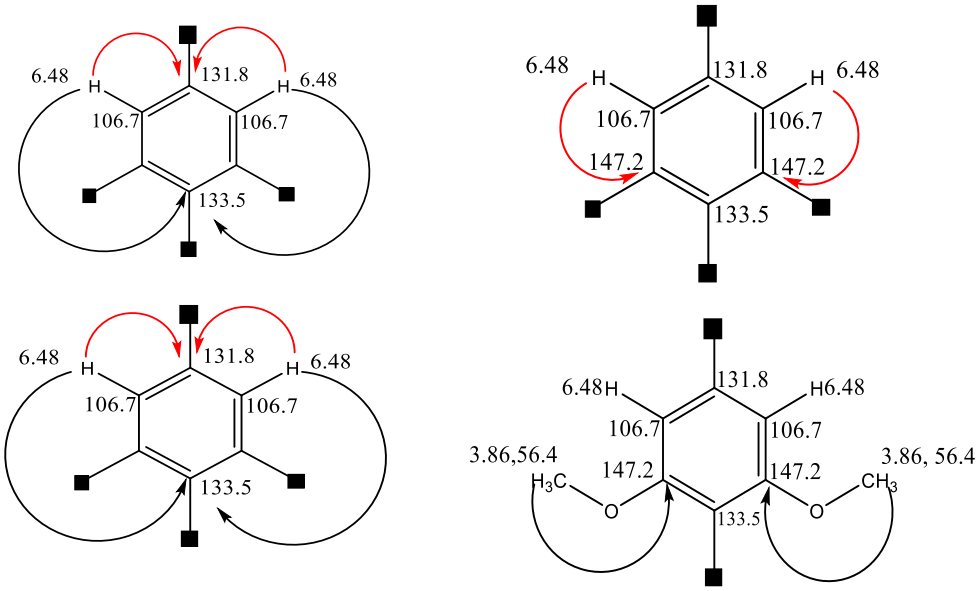

Fragment (e)

Moreover, the two equivalent methine protons at δ 6.48 ppm showed strong correlation with one sp^2 quaternary carbon at δ 137.3 ppm from fragment (d). So, fragment (e) could be connected to fragment (d) as shown in partial structure. Furthermore, FT-IR spectrum displayed the presence of OH group. Therefore, the complete structure of compound 1 could be elucidated with the molecular formula of $C_{23}H_{26}O_6$ and degree of unsaturation was 11.

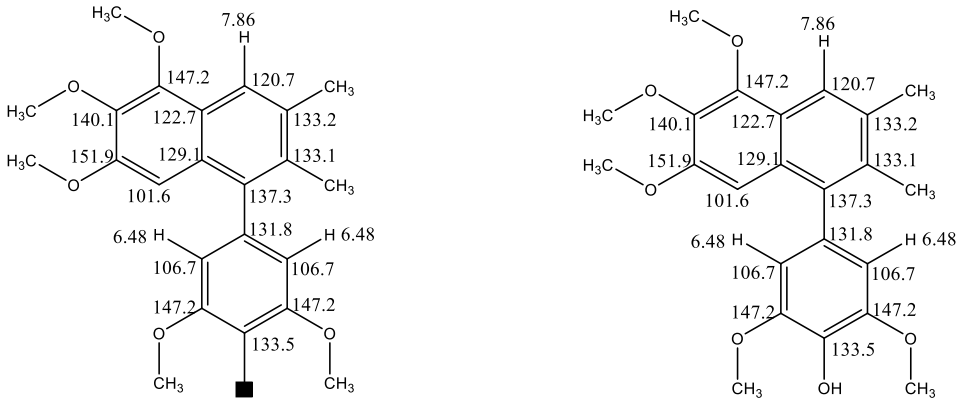

Partial structure of compound 1 Complete structure of compound (1)

The isolated compound was assigned as 1 (4-hydroxy-3,5-dimethoxyphenyl) -2,3-dimethyl-5,6,7-trimethoxy naphthalene (1). According to literature survey and search in database such as Chemspider and Reaxys, the isolated compound was a new phenylnaphthalene derivative.

Conclusion

In this research work, one medicinal plant, *Orthosiphon rubicundus* was selected for chemical and biological characterization. From ethyl acetate extract, phenylnaphthalene derivative, 1-(4-hydroxy-3,5-dimethoxyphenyl)-2,3-dimethyl-5,6,7-trimethoxy naphthalene (1) was isolated and characterized by NMR studies. Moreover, the methanolic extract and compound (1) showed the antioxidant activity on DPPH with IC_{50} values of 47.90 µg/ mL and 59.02 µg/mL, respectively but lower than that of ascorbic acid solution, standard antioxidant. The result of the present study suggested that the selected plant can be used as a source of antioxidant and antimicrobial for pharmacological preparations which is very well evidenced by the present work.

Acknowledgements

The authors thank Dr Yoshiaki Takaya, Associate Professor, Faculty of Pharmacy, Meijo University, Nagoya, Japan, for NMR and mass measurements, Dr Arnt Win, Associate Professor and Dr Kay Thi Win, Lecturer, Department of Chemistry, Kyaukse University for antioxidant tests, Dr Yi Yi Myint, Head of Department of Chemistry, University of Mandalay for research facilities.

References

Hosseinzadeh, S., Jafarikukhdan, A., Hosseini, A., and Armand, R. (2015). "The Application of Medicinal Plants in Traditional and Modern Medicine". *International Journal of Clinical Medicine*, vol.6, pp. 635-642.

Singh, M.K., Gidwani, B., Gupta, A., Dhongade, H., Kaur, C.D., Kashyap, P.P., and Tripathi, D.K. (2015). "A Review of the Medicinal Plants of Genus *Orthosiphon (Lamiaceae)"*. *International Journal of Biological Chemistry*, vol. 9, pp. 318-331.

Vishwakarma, A.P., Vishwe, A., Sahu, P., and Chaurasiya, A. (2013). "Magical Remedies of *Terminalia arjuna* (ROXB.)". *International Journal of Pharmaceutical Archiv*, vol. 2, pp. 189-201.

ANTIOXIDANT AND ANTICANCER ACTIVITIES OF CHEMICAL CONSTITUENTS FROM THE RHIZOMES OF *Geodrum recurvum* (Roxb.)

Hnin Thanda Aung[1], Myint Myint Sein[2]

Abstract

Plants have been used for medicinally since prehistoric period. The rhizomes of *Geodrum recurvum* Roxb. (Orchidaceae) (Myanmar name – Thudar) are used by local people in Lashio Township for cancer treatment, however, it lacks scientific investigation. The purpose of this study is the isolation of bioactive compounds from the rhizomes of *Geodrum recurvum* Roxb. and evaluation of their anticancer and antioxidant activities. The three monophenanthrenes (**1**-**3**) were isolated, during the first investigation of the rhizomes of *Geodrum recurvum* collected in Myanmar by advanced separation techniques. Their structures were determined by ^{1}D and ^{2}D NMR, and FAB-MS spectral data. The anticancer activity of isolated compounds (**1**-**3**) was evaluated in vitro against Hela cells using cell counting kit 8. Compounds (**1**-**3**) showed the potent activity against Hela cancer cells. In addition, compounds (**1**-**3)** exhibited potent antioxidant activity according to DPPH radical-scavenging assay. The present study provides scientific evidence for the use of *Geodrum recurvum* in cancer treatment and as a source of antioxidants for pharmacological preparations by traditional healer.

Keywords: Antioxidant, anticancer, pharmacological, *Geodrum recurvum*, scavenging

Introduction

The phytochemicals with antioxidant and anticancer activities are widely isolated from many plant species. The compounds from the medicinal plants can be further developed into potent drugs against cancers. Recently, many researchers have been interested on bioactive compounds from plants to overcome the burden of chemotherapy related problems. The geneus Geodorum (family Orchidaceae) comprising about ten species is known to distribute in tropical Asia including Myanmar, as far North as South Japan, to Australia and the South-West Pacific Islands (Chen *et al*., 2009). The rhizome of this plant is used in Myanmar traditional medicine for tonics and tumor treatment. As a part of the investigations of the secondary metabolites from medicinal plants used in Myanmar, the constituents of *Geodrum recurvum* rhizomes were studied for the first time. In this paper, the isolation and characterization of three monophenanthrene compounds from the rhizome of *Geodrum recurvum* were described. The antioxidant and anticancer activities of chemically isolated compound were evaluated.

Materials and Methods

Plant Materials

The tubers of *Geodrum recurvum* Roxb. (Myanmar name – Thudar) were collected from Lashio, Eastern Shan State of Myanmar in September, 2015. The plant was identified by Dr Kazumi Fujikawa, Botanist from Makino Botanical Garden. A voucher sample has been deposited in the laboratory of Department of Chemistry, University of Mandalay, Myanmar.

Extraction and Isolation

The tubers of *Geodrum recurvum* (dried 800 g) were extracted with methanol. The methanolic extract was concentrated in vacuo, and dried extract was obtained (30.5 g). The extract was then partitioned with ethyl acetate and 1-butanol against water successively to give ethyl

[1] Associate Professor, Department of Chemistry, University of Mandalay
[2] Dr, Professor (Rtd.), Department of Chemistry, University of Mandalay

acetate (15.3 g), 1-butanol (2.7 g) and water-soluble fractions (12.1 g). The ethyl acetate fraction was partitioned again with acetonitrile and hexane to afford acetonitrile 13.4 g and hexane (1.5 g). The acetonitrile extract (2.67 g) was fractionated by using a silica gel column with mixed solvents of hexane and EtOAc (90:10 to 100 % EtOAc) to give 23 main fractions (A-W). Compound (**1**) (8.2 mg) and compound (**2**) (3 mg) were obtained by purification of fraction L (338.6 mg) using HPLC with octadecylsilanized silica gel (ODS, HG-5) column with methanol–water (1:1) as a mobile phase. Compound (**3**) (2.5 mg) were yielded by purification of sub-fraction K (177.g mg) using HPLC with octadecylsilanized silica gel (ODS, HG-5) column with methanol–water (55:45).

Anticancer Assay

Anticancer effects were measured in vitro in a HeLa (cervix adenocarcinoma) cell line by the colorimetric method using a cell counting kit-8 that was based on the tetrazolium salt/formazan system (Ishiyama *et al*., 1993). HeLa cell (JCRB9004) was obtained from Japanese Collection of Research Bioresources (JCRB) cell bank. Cells were cultured in minimum essential media (MEM) supplemented with 10% fetal bovine serum. For the cytotoxic assay, cells were seeded at a density of 5×10^3 cells/well in 0.2 mL of medium in 96-multiwell plates and adhered. Samples were solved in saline containing 10% DMSO and sterilized by filtration. Series of diluted samples (0.2 mL) were then added to the cells. The plate was incubated at 37 °C under 5% CO_2 atmosphere for 48 h. Twenty microliters of cell counting kit-8 (based on the tetrazolium salt/formazan system) were added to each well, and the microplate was incubated for 1 h, after which cell densities were measured at 450 nm using Bio-RAD Model 550 Microplate Reader. Cisplatin was used as the cytotoxic reference compound.

Antioxidant Activity

The antioxidant activities of the isolated compounds were determined by DPPH scavenging activity assay (Yamaguchi *et al*., 1998). Its reaction principle was based on mechanism of free radicals inhibition by hydrogen transfer, the antioxidant activity of sample expressed in EC_{50}. A total of 500 μL of test solutions in various concentrations (1-100 μM), 500 μL of 0.2 M acetate buffer pH 5.5, and 1000 μL of ethanol are mixed in a test tube for water soluble compounds. For the ethanol soluble compounds, 1000 μL of test solutions in various concentrations (1-100 μM) and 1000 μL of 0.1 M acetate buffer pH 5.5 are mixed in a test tube. 500 μL of $5x10^{-4}$ M DPPH solution was added to the mixture. The mixture was homogenized using a vortex in a dark room (resistant to UV light) and was incubated for 30 minutes. After that, the mixture was measured by a spectrophotometer UV absorbance at this λ_{max} 517 nm. Vitamin C was used as a reference compound in the same concentration range as the test compounds. A control solution was prepared in the same manner as the assay mixture. The capability of scavenging DPPH radicals as a percentage of DPPH remaining in the resulting solution was determined using the following equation: $DPPH\ (\%) = (Abs_{EtOH} - Abs_{sample})/(Abs_{EtOH})$

Results and Discussion

The column chromatography over silica gel and HPLC separation of the MeOH extract of the rhizome of *Geodrum recurvum* afforded three compounds (**1**-**3**). The structures of them are elucidated by ^{1}D, ^{2}D NMR, FAB-MS spectral data and confirmed with previously reported data.

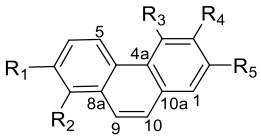

	R_1	R_2	R_3	R_4	R_5
1	OH	H	OMe	OH	OMe
2	OH	OMe	OMe	OH	OMe
3	OH	H	OMe	H	OH

Figure 1 Structures of compounds (**1-3**)

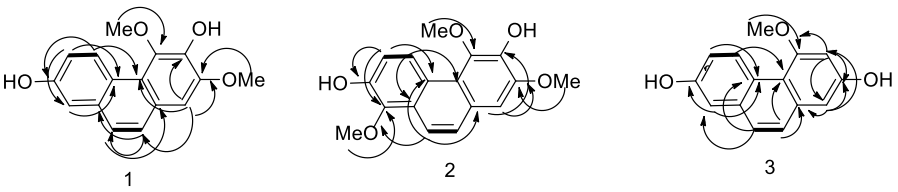

Figure 2 Key COSY (⟝) and HMBC (H↷C) correlations of compounds (**1-3**)

The first compound **1** was obtained as pale brown powder. FAB-MS at m/z 271 $[M+H]^+$, the molecular formula was established as $C_{16}H_{14}O_4$. The ^{1}H NMR and ^{13}C NMR had resonances for six aromatic CH groups [™$_H$ 7.16 (1H, *s*, H-1), ™$_C$ 106.2 (C-1); δ_H 9.33 (1H, *d*, H-5), δ_C 129.2 (C-5); δ_H 7.13 (1H, *dd*, H-6), δ_C 117.4 (C-6); δ_H 7.17 (1H, *d*, H-8), δ_C 112.3 (C-8); δ_H 7.42 (1H, *d*, H-9), δ_C 125.6 (C-9); δ_H 7.56 (1H, *d*, H-10), δ_C 128.2 (C-10)], two hydroxyl protons (3-OH and 7-OH), two methoxyl groups [δ_H 56.5 (3H, *s*, 2-OMe), δ_C 59.8 (3H, *s*, 4-OMe)] and eight tetra-substituted aromatic carbons which constitute a tricyclic system. In this case, the observed COSY, HMBC correlations (Figure 2) were again very valuable in the structure elucidation. Compound **1** was identified as **3,7**-dihydroxy-2,4-dimethoxyphenanthrene and nicely matched with previously reported data (Yuan *et al*., 1997).

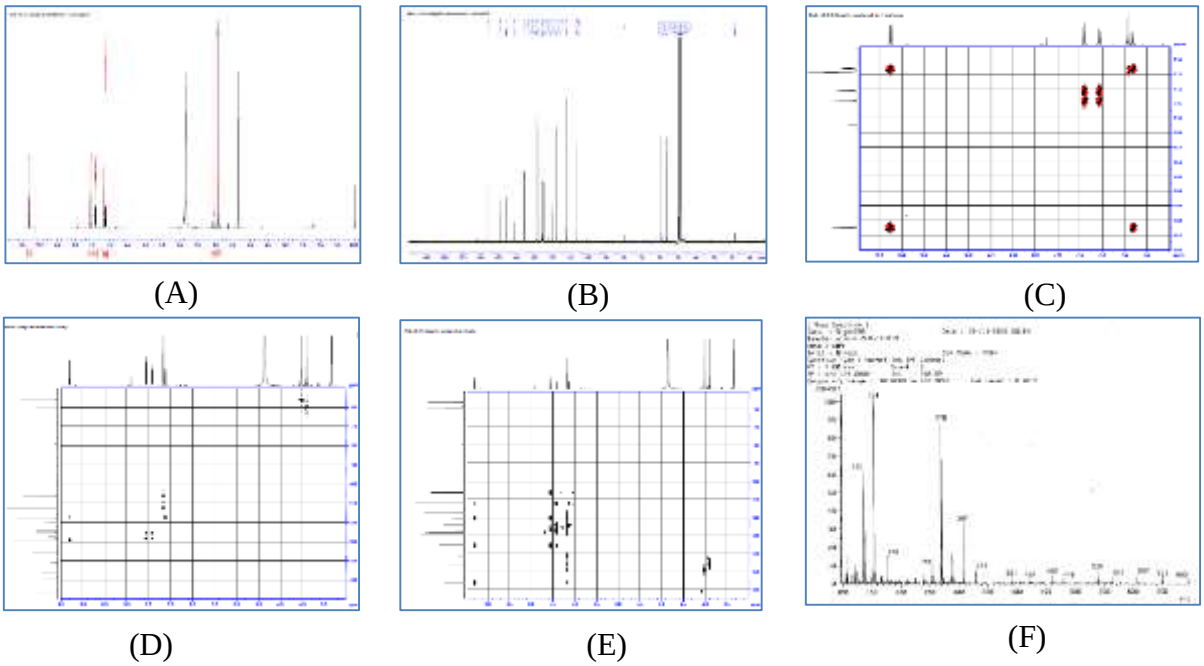

Figure 3 (A) ^{1}H NMR (600 MHz, $CDCl_3$) (B) ^{13}C NMR (150 MHz, $CDCl_3$)
(C) COSY (D) HSQC (E) HMBC (F) FAB-MS spectra of compound **1**

Compound **2** was obtained as pale brown powder. FAB-MS at m/z 301 $[M+H]^+$, the molecular formula was established as $C_{17}H_{16}O_5$. The ^1H NMR spectroscopic data of compound **2** were similar to those of **1** except methoxyl singlet, δ_H 4.01 (3H, *s*, 8-OMe) at C-8 (δ_C 59.8) (Figure 2). Compound **2** was identified as 3,7-dihydroxy-2,4,8-trimethoxyphenanthrene and well matched with previously published data (Sylvie and Roland, 2007).

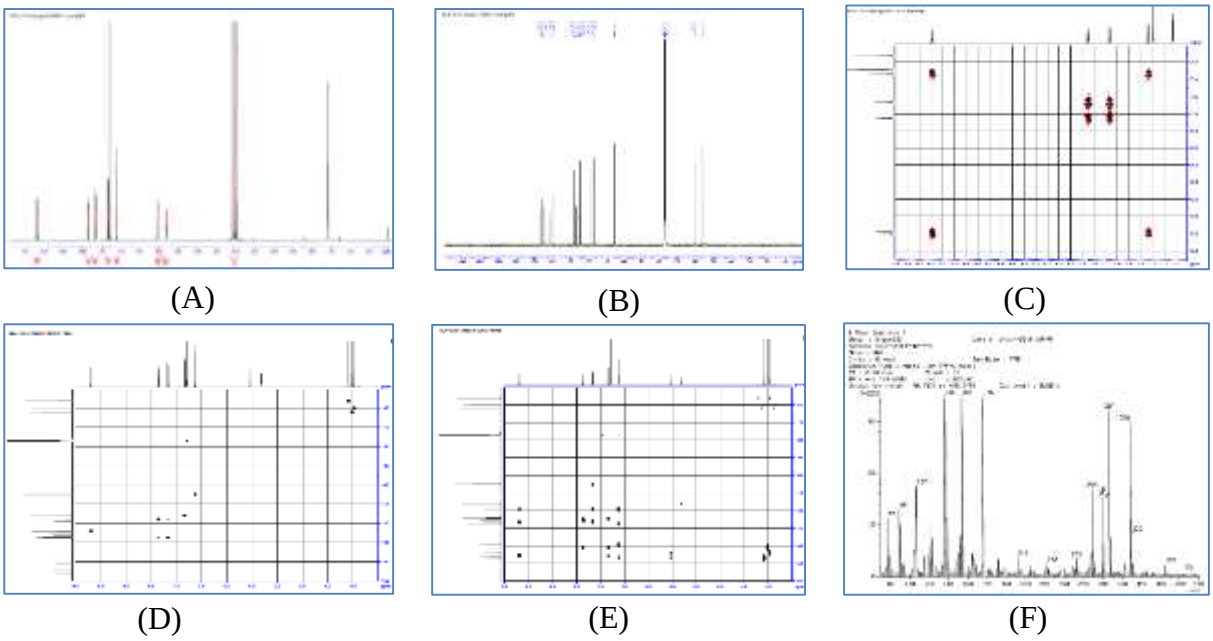

Figure 4 (A) ^1H NMR (600 MHz, $CDCl_3$) (B) ^{13}C NMR (150 MHz, $CDCl_3$)
(C) COSY (D) HSQC (E) HMBC (F) FAB-MS spectra of compound **2**

Compound **3** was obtained as pale brown powder. FAB-MS at m/z 241 $[M+H]^+$, the molecular formula was established as $C_{15}H_{12}O_3$. The ^1H NMR spectroscopic data of compound **3** were also similar to those of compound **1** except the lack of hydroxyl group at C-3 in compound **3** and methoxyl group at C-2 of compound **1** is replaced by a hydroxyl group (Figure 2). Compound **3** was identified as 2,7-dihydroxy-4-methoxyphenanthrene (Yuan *et al*., 1997).

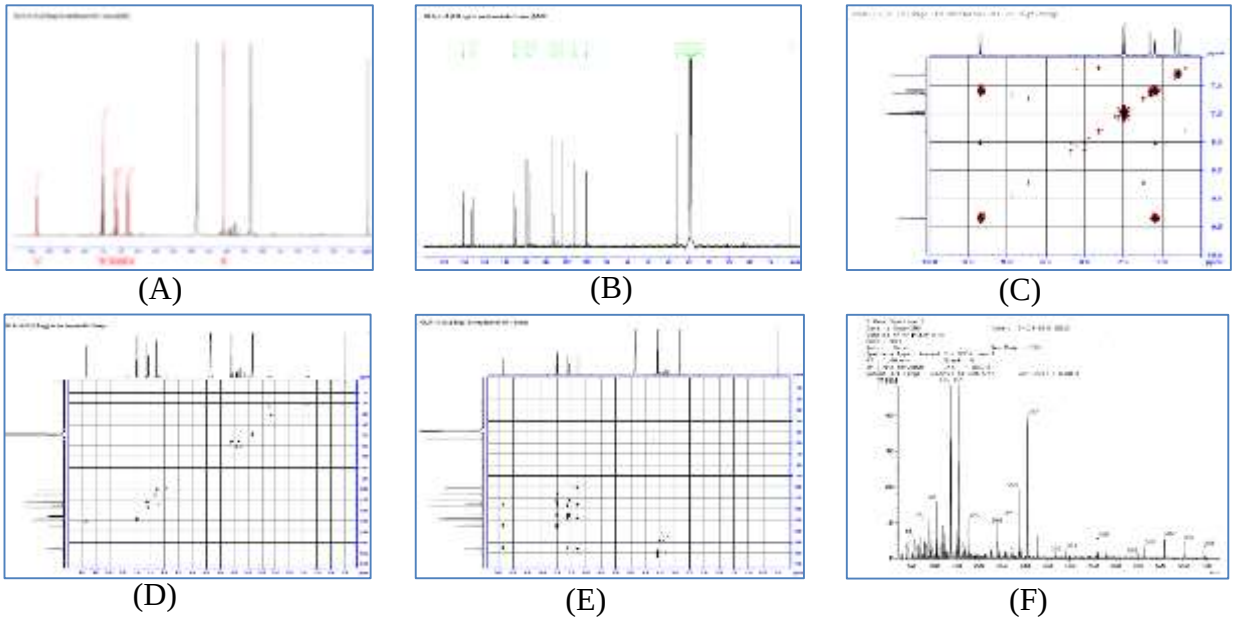

Figure 5 (A) ^1H NMR (600 MHz, $CDCl_3$) (B) ^{13}C NMR (150 MHz, $CDCl_3$)
(C) COSY (D) HSQC (E) HMBC (F) FAB-MS spectra of compound **3**

Table 1 ^{1}H NMR (δH; 600 MHz, $CDCl_3$) and ^{13}C NMR (δC; 150 MHz, $CDCl_3$) Signals of Compounds (1-3)

Position	3,7-dihydroxy-2,4-dimethoxy phenanthrene (1)		3,7-dihydroxy-2,4,8-trimethoxy phenanthrene (2)		2,7-dihydroxy-4-methoxy phenanthrene (3)	
	δ_H	δ_C	δ_H	δ_C	δ_H	δ_C
1	7.16, s	106.2	7.10, s	105.0	6.83, d (*J* = 2.34 Hz)	105.8
2		148.9		146.8		156.3
3		141.2		139.3	6.77, d (*J* = 2.3 Hz)	100.4
4		145.8		144.0		160.7
4a		120.3		119.2		116.1
4b		124.2		124.2		125.5
5	9.33, d (*J* = 9.1 Hz)	129.2	9.18, d (J = 9.3 Hz)	123.9	9.34, d (*J* = 9.3 Hz)	130.2
6	7.13, dd (*J* = 2.8 and 9.1 Hz)	117.4	7.33, (J = 9.3Hz)	116.0	7.09, dd (*J* = 2.8 and 9.3 Hz)	117.3
7		156.0		145.6		155.3
8	7.17, d (*J* = 2.8 Hz)	112.3		140.8	7.15, d (*J* = 2.8 Hz)	112.3
8a		135.4		126.6		134.8
9	7.42 d (*J* = 8.8 Hz)	125.6	7.85, d (J = 9 Hz)	117.9	7.5, d (*J* = 8.8 Hz)	128.5
10	7.56, d (*J* = 8.8 Hz)	128.2	7.66, d (J = 9 Hz)	127.5	7.48, d (*J* = 8.8 Hz)	127.9
10a		126.9		125.7	6.83, d (*J* = 2.34 Hz)	135.9
OMe at C2	4.01, s	56.5	4.08, s	56.1		
OMe at C-4	3.94, s	59.8	3.98, s	61.9	4.1, s	55.9
OMe at C-8			4.01, s	59.8		

Anticancer Activity

The isolated compounds (**1-3**) were tested for their anticancer activities on Hela cell lines using cell counting kit 8. The cell growth-inhibitory potencies of compounds (**1-3**), expressed as IC_{50} values, are shown in Table **2**. Among the tested compounds, compound **1** showed the very potent activity against Hela cancer cell (IC_{50} **7.5** μM respectively). In addition, compound **2** (IC_{50} **13.5** μM) and compounds **3** (IC_{50} 40μM) possessed high inhibitory activity on the proliferation of tested cancer cell lines.

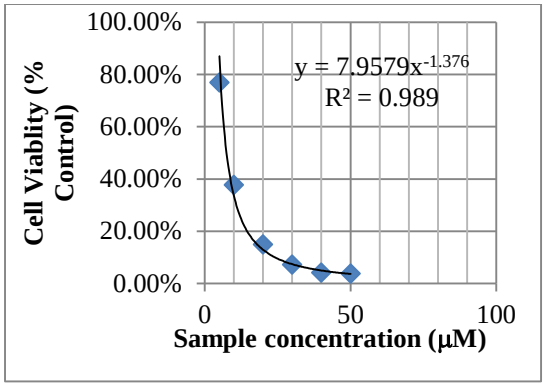

Compound **1** (IC_{50} = 7.5 μM)

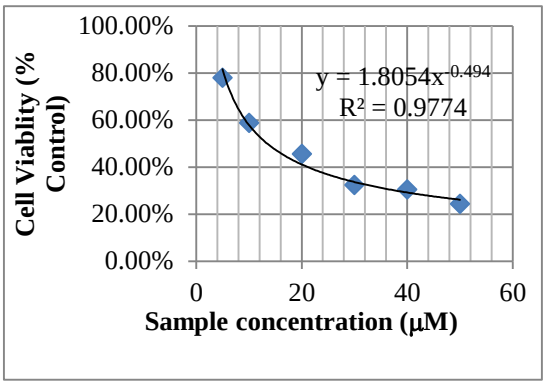

Compound **2** (IC_{50} = 13.5 μM)

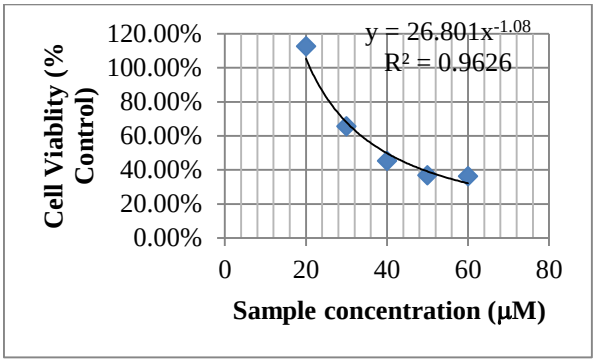

Compound **3** (IC_{50} = 40 μM)

Figure 6 Anticancer activities of compounds (**1-3**) against Hela cell line

Table 2 Anticancer Activities of the Isolated Compounds (**1-3**) on Hela Cells.

Compound	IC_{50} (μM)
1	7.5
2	13.5
3	40

Antioxidant Activity

DPPH assay is used to determine free radical scavenging activity of isolated compounds (**1-3**) by hydrogen transfer mechanism. DPPH scavenging reaction was marked by changes in the solution color from purple to yellow after 30 minutes incubation. Measurements were performed at a maximum wavelength of 517 nm. It is observed that DPPH radical scavenging activities of compound **1** (EC_{50} 26.8 μM) exhibited stronger activity than ascrobic acid (EC_{50} 27.5 μM). In addition, compounds (**2-3)** showed high DPPH radical scavenging activities (EC_{50} 32.1 and 31.2 μM).

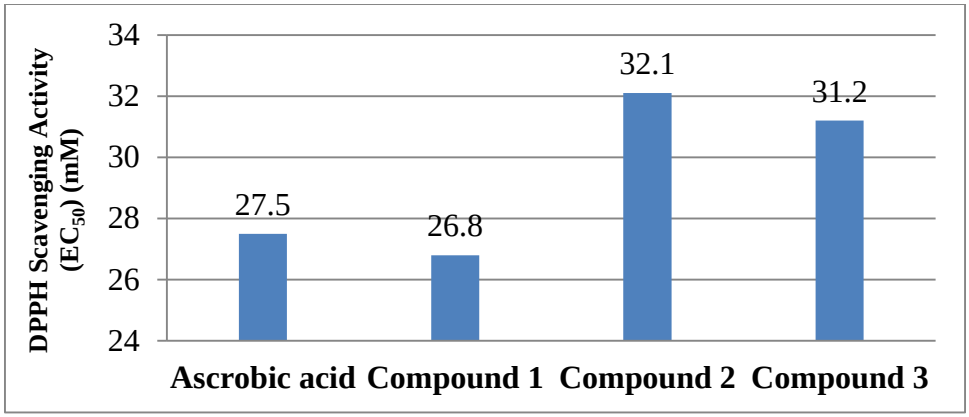

Figure 7 DPPH radical scavenging activity of ascrobic acid (positive control) and isolated compounds (**1-3**)

The isolated compounds (**1-3**) from the rhizomes of *Geodrum recurvum* had an ability to scavenge the free radicals by transferring proton to free radical. The antioxidant capacity of compounds **(1-3)** can be classified as good and potential antioxidant agents. The IC_{50} of pure compounds (**1-3)** on Hela cell lines less than 50 μg/mL is categorized as potential anticancer agents. Compounds (**1-3)** were found to be high antioxidant and anticancer activity. Among the isolated compounds, compound **1** exhibited both the highest antioxidant and anticancer activity in compare to compound **2** and **3**. The anticancer activity can be related to the antioxidant activity. Compounds (**1-3)** have been revealed as a scavenging radical that may be able to inhibit carcinogenesis.

Conclusion

In this study, three monophenanthrene compounds (**1-3**) were isolated from the rhizome of *Geodrum recurvum* for the first time by advanced separation techniques and their structures were elucidated by ^{1}D, ^{2}D NMR and FAB mass spectral data. The present research work suggests that *Geodrum recurvum* possess potent antioxidant and anticancer compounds and these compounds might be applicable for the pharmacological preparations as antioxidant and anticancer agents.

Acknowledgements

The authors would like to express their profound gratitude Myanmar Academy of Arts and Science for allowing to present this paper.

References

Chen, X., J. C. Phillip and G. W. Stephan. (2009) "*Geodorum*. In: Flora of China." *Orchidaceae*, vol.25, pp. 258-260.

Ishiyama, M., M. Shiga, K. Sasamoto, M. Mizogucgi and P. He. (1993). "A new sulfonated tetrazolium salt that produces a highly water-soluble formazan dye." *Chem. Pharm. Bull*., vol.41, pp.1118–1122.

Sylvie, R. and B. Roland. (2007) "Total synthesis of two natural phenanthrenes: confusarin and a regioisomer." *Tetrahedron*, vol.63, pp.12379-12387.

Yuan, W. L., C. K. Chiang., J. H. Leslie and D. P. Andrew. (1997). "Phenanthrenes, dihydrophenanthrenes and bibenzyls from the orchid *Bulbophyllum vadinatum*." *Phytochemistry*, vol.44, pp.157-165.

Yamaguchi T, H. Takamura, T. Matoba and J. Terao. (1998). "HPLC method for evaluation of the free radical-scavenging activity of foods by using 1, 1diphenyl-2-picrylhydrazyl." Bioscience, Biotechnology, and Biochemistry, vol.62, pp.1201-1204.

ISOLATION AND STRUCTURE ELUCIDATION OF ISOFLAVAN DERIVATIVE FROM THE BARK OF *ERYTHRINA CRISTA-GALLI* LINN.

Khaing Yin Mon[1]*, Hnin Yu Win[2]*, Myint Myint Sein[3]

Abstract

Purification of ethyl acetate extract of *Erythrina crista-galli* Linn. led to the isolation of isolflavan derivative, namely, 4', 6', 7-trihydroxy-5'-prenyl isoflavan-4-ol. The structure of isolated compound was elucidated on the basis of 1D and 2D NMR spectral data and mass spectrometry. Moreover, antimicrobial and antioxidant properties of *Erythrina crista-galli* extract were also evaluated by agar-well diffusion method and DPPH radical scavenging assay respectively.

Keywords: isoflavan, 1D and 2D NMR spectral data, DPPH

Introduction

For thousands of years, plant has been used as medical treatments based on experience and folk remedies. In recent time, focus on plant research has increased all over the world and a large body of evidence has been accumulated to highlight the immense potential of medicinal plants used in various traditional systems (Dahanukar *et al.*, 2000). According to the WHO, 80% of the World's population depends on plant derived medicines for their health care. Plants, one of the important sources of natural products have a long history in the treatment of various diseases (Dar *et al*., 2017). Natural products are organic compounds that are intermediates of primary and secondary metabolic pathways. They can be used as pharmacologically active compounds in treating various kinds of diseases (Chintoju *et al*., 2015). In Myanmar, there are many traditional medicinal plants which produce chemical compounds as part of their normal metabolic activities.

Erythrina crista-galli Linn. is widely distributed in tropical and subtropical regions of the American continent and is a popular ornamental plant in subtropical areas. It belongs to the family Fabaceae (Ayoub *et al*., 2017). It is also locally known as Thinbaw-kathit and distributed in Kayah state, Myanmar. The seed extracts of *Erythrina crista-galli* Linn. possess sedative, hypertensive and diuretic activities (Maier *et al*., 1999). The wood of this medicinal plant is used in infusions or decoctions as astringent, narcotic and sedative in Argentina. Antibacterial and anti-inflammatory activities have been reported for this plant (Weber *et al*., 2004). The bark of this plant is used for rheumatism, hepatitis, sedation, and hypnogenesis (Ayoub *et al*., 2017). The present study was conducted to isolate bioactive chemical constituent from the barks of *Erythrina crista-galli* Linn.

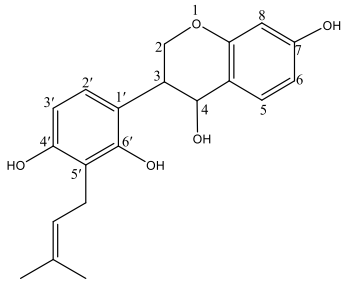

Figure 1 Structure of isolated compound (1)

[1] Lecturer, Department of Chemistry, Taungoo University
[2] Dr, Associate Professor, Department of Chemistry, University of Mandalay
[3] Dr, Professor and Head (Rtd), Department of Chemistry, University of Mandalay
* equally contributed


Figure 2 Plant and flowers of *Erythrina crista-galli* Linn.

Materials and Methods

General Experimental Procedures

NMR spectra were measured on a Varian Inova 600 (599.740 MHz) and a Varian Unity 300 (300.145 MHz) spectrometer. Column chromatography was carried out on MN silica gel 60, 0.05-0.2 mm; TLC was performed on Polygram SIL G/UV_{254}. All silica gel materials were purchased from Macherey-Nagel, Düren, Germany. Size exclusion chromatography was done on Sephadex LH-20 (Lipophilic Sephadex; Amersham Biosciences, Freiburg, Germany, purchased from Sigma-Aldrich Chemie, Steinheim, Germany). Commercial grade reagents and solvents were purchased from Super Shell Co. Ltd, Yangon. Common laboratory apparatus were used. PerkinElmer C93927 was used for FT-IR spectra measurement.

Plant Materials

The barks of *Erythrina crista-galli* were collected from Loikaw Township, Kayah State, Myanmar and identified by Dr Soe Myint Aye, Department of Botany, University of Mandalay. The plant materials were cut into small pieces and dried at room temperature for about two weeks.

Preliminary Phytochemical Analysis

The preliminary phytochemical screening of *Erythrina crista-galli* was determined using standard method of Harbone.

Antimicrobial Assay

Antimicrobial tests were performed at Pharmaceutical Research Department (PRD), Insein Township, Yangon Region. Antimicrobial activities of plant extracts were tested by agar-well diffusion method on six test microorganisms such as *Bacillus subtilis*, *Staphylococcus aureus*, *Pseudomonas aeruginosa*, *Bacillius pumilus*, *Candida albicans* and *Escherichia coli*.

Extraction and Isolation of Pure Compound

The air-dried samples of Erythrina crista-galli (1000 g) were percolated with methanol for two months. The methanol crude extracts were filtered and evaporated the solvent. The residue was extracted with ethyl acetate to attain 7.5 g of ethyl acetate crude extracts. The crude extracts were dissolved in a mixture of n-hexane/EtOAc and silica gel was added. The mixture was allowed to dryness under reduced pressure. The obtained crude extracts were subjected to silica gel by using various solvent systems of n-hexane and ethyl acetate. The obtained fraction was checked by TLC and iodine vapour for purity. Then, the same R_f value fractions were combined. Among them, pure compound (1) was isolated as colorless oil from selected fraction III after purification on Sephadex LH-20 using MeOH only.

Measurement of DPPH Radical Scavenging Activity by UV Spectrophotometric Method

The control solution was prepared by mixing 1.5 mL of 20 µg/mL DPPH solution and 1.5 mL of 95 % ethanol. Similarly, the blank solution was prepared by mixing 1.5 mL of test sample solution and 1.5 mL of 95% ethanol. The test sample solution was also prepared by mixing 1.5 mL of 20 µg/mL DPPH solution and 1.5 mL of sample solution in various concentrations (0.78125, 1.5625, 3.125, 6.250, 12.5, 25, 50, 100, 200 and 400 mg/mL). The solutions were allowed to stand at room temperature for 30 min. After 30 min, measurements of absorbance at 517 nm were made by these solutions using UV-Vis spectrophotometer. The measured absorbance values were applied to calculate percent inhibition by the formula:

$$\%\,\text{inhibition} = \frac{\text{Abs}_{\text{DPPH}} - [\text{Abs}_{\text{sample}} - \text{Abs}_{\text{Blank}}]}{\text{Abs}_{\text{DPPH}}} \times 100\,,$$

where % inhibition = percent inhibition of test sample, Abs_{DPPH} = absorbance of control solution, $\text{Abs}_{\text{sample}}$ = absorbance of test sample solution, $\text{Abs}_{\text{blank}}$ = absorbance of blank solution.

The IC_{50} value of the sample, which is the concentration of sample required to inhibit 50% of the DPPH free radical, was calculated using inhibition curve. Lower absorbance of the reaction mixture indicated higher free radical scavenging activity. Ascorbic acid was used as a reference compound in the same concentration range as the test compound.

Results and Discussion

Phytochemical Analysis

Preliminary phytochemical analysis was performed in order to know different types of organic compounds present in bark of *Erythrina crista-galli*. Analysis of the extract of bark sample revealed the presence of phytochemicals such as alkaloids, flavonoids, phenolic compounds, polyphenols, steroids, tannins, glycoside, and reducing sugars.

Antimicrobial Assay

The antimicrobial activities of plant extracts were tested by applying agar-well diffusion method on six test microorganisms. According to antimicrobial assay, the ethyl acetate extract responded medium activities on *Bacillus subitilis, Pseudomonas aeruginosa*, *Bacillus pumilus* and weak activities on *Staphylococus aureus*, *Candida albicans* and *Escherichia coli*. Ethanol extract showed medium activities on *Escherichia coli* and weak activities on other five test organisms. In addition, n-hexane extract exhibited weak activities on five test organisms. The results were tabulated in Table 1.

Table 1 Results of Antimicrobial Activities of *Erythrina crista-galli* Barks

Samples	Solvents	Inhibition Zone (mm)					
		I	**II**	**III**	**IV**	**V**	**VI**
Erythrina crista-galli	n-hexane	11	13	-	12	12	11
	EtOAc	15	13	18	15	14	13
	EtOH	14	13	12	13	13	15
Control	n-hexane	-	-	-	-	-	-
	EtOAc	-	-	-	-	-	-
	EtOH	-	-	-	-	-	-

Agar-well – 10 mm

10 mm ~14 mm (+) weak active
15 mm ~19 mm (++) medium active
20 mm above (+++) strong active

(I) *Bacillus subtilis*
(II) *Staphylococous aureus*
(III) *Pseudomonas aeruginosa*
(IV) *Bacillus pumilus*
(V) *Candia albicans*
(VI) *Escherichia coli*

Antioxidant Activity

The antioxidant activity of methanolic extracts was analyzed by DPPH (2,2-diphenyl-1-picryl-hydrazyl) method. Mean absorbance values of methanolic extract of *Erythrina crista-galli* barks and ascorbic acid were shown in Table 2. The inhibition percentage of methanolic extracts of *Erythrina crista-galli* barks and standard ascorbic acid in various concentrations were described in Table 3.

Table 2 Absorbance of Standard Ascorbic Acid and Methanolic Extracts of the Barks of *Erythrina crista-galli* at 517 nm by UV Spectrophotometer

No.	Concentration (µg/mL)	Ascorbic acid		*Erythrina crista-galli*	
		Abs_{sample}	Abs_{blank}	Abs_{sample}	Abs_{blank}
1	1.5625	0.283	0.002	0.370	0.003
2	3.125	0.272	0.002	0.289	0.002
3	6.250	0.260	0.003	0.273	0.002
4	12.5	0.259	0.004	0.265	0.001
5	25	0.141	0.005	0.250	0.004
6	50	0.092	0.007	0.248	0.005
7	100	0.072	0.001	0.235	0.006
8	200	0.025	0.009	0.213	0.008
9	400	0.014	0.005	0.139	0.004

Table 3 Percent Inhibition of Methanolic Extracts of *Erythrina crista-galli* Barks and Standard Ascorbic Acid in Various Concentrations

No	Concentration (µg/mL)	% Inhibition	
		Ascorbic acid (Standard)	*Erythrina crista-galli*
1	1.562	34.65	14.65
2	3.125	37.21	33.26
3	6.25	40.23	36.98
4	12.5	40.70	38.64
5	25.0	68.37	42.79
6	50.0	80.23	43.49
7	100	83.49	46.74
8	200	96.28	52.35
9	400	97.91	68.60

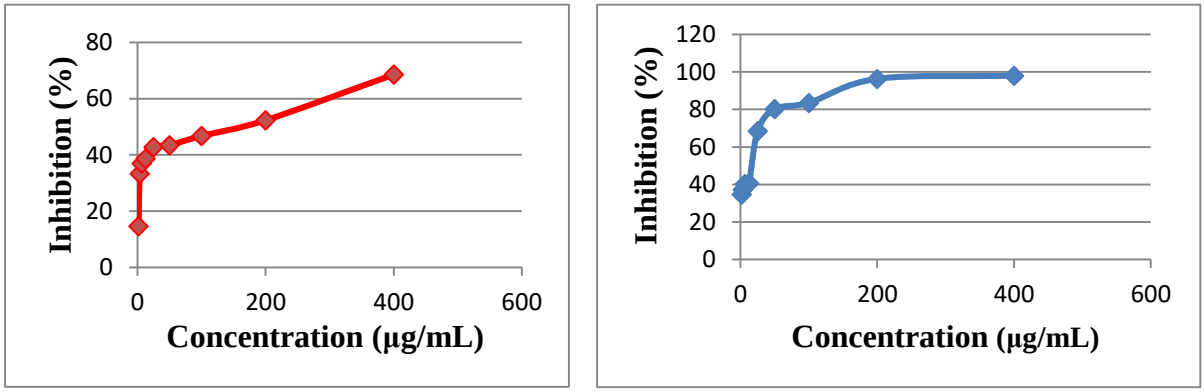

(a) (b)

Figure 3 Percent inhibition of (a) methanolic extracts of *Erythrina crista-galli* barks and (b) standard ascorbic acid in various concentrations

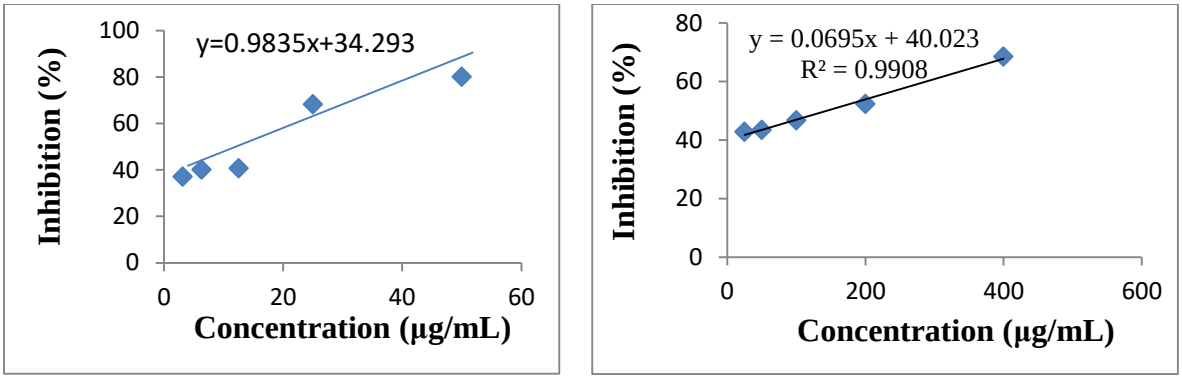

(a) (b)

Figure 4 Linear regression equation for IC_{50} value of (a) *Erythrina crista-galli* bark and (b) standard ascorbic acid

Table 4 The Linear Regression Equations and IC_{50} Values of *Erythrina crista-galli* Bark and Standard Ascorbic Acid

No.	Test Solution	Regression Equations	IC_{50} (ppm)
1	Ascorbic acid	y = 0.9835x + 34.293	15.97
2	*Erythrina crista-galli*	y = 0.0684x + 39.729	143.6

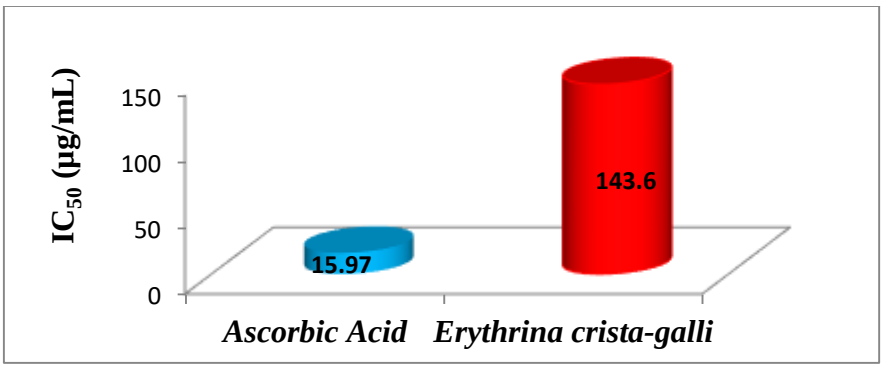

Figure 5 Comparison of IC_{50} values of methanolic extract of *Erythrina crista-galli* and standard ascorbic acid

According to DPPH assay, IC_{50} value of the sample extracts was found to be 143.6 µg/mL. Based on the obtained results, the sample extracts exhibited low antioxidant activity which is comparison with IC_{50} value of standard ascorbic acid (15.97 µg/mL).

Structure Elucidation of Pure Compound

In the aromatic region of the ^{1}H NMR spectrum (Figure 15.b), one doublet of doublet methine proton at δ 6.55 ppm displayed ortho coupling with one doublet methine proton at δ 7.40 ppm (J = 8.35 Hz) and meta coupling with another doublet methine proton at δ 6.41 ppm (J = 2.50 Hz). Therefore, 1, 2, 4-trisubstituted benzene ring (fragment a) could be drawn. Moreover, in the DQF COSY spectrum (Figure 15.f), the methine proton at δ 6.55 ppm showed correlation with another methine proton at δ 7.40 ppm as expected. In the HMBC spectrum (Figure 15.g), the methine proton at δ 6.55 ppm (δ_c 109.6) showed β-correlations with one sp^2 methine carbon at δ 103.6 ppm and one sp^2 quaternary carbon at δ 112.9 ppm. Moreover, one methine proton at δ 7.40 ppm (δ_c 132.3) revealed β-correlations with two sp^2 quaternary carbons at δ 156.7 and

156.9 ppm. Furthermore, the HMBC spectrum (Figure 15.g) showed the observation of β-correlation of the methine proton at δ 6.41 ppm (δ_c 103.6) with one sp^2 methine carbon at δ 109.6 ppm and α-correlations with two sp^2 quaternary carbons at δ 156.7 and 156.9 ppm. According to these correlations, the carbon atoms in the benzene ring could be assigned. Moreover, two sp^2 quaternary carbons at δ 156.7 and 156.9 ppm could be connected to oxygen due to their downfield chemical shifts. Thus, the partial structure (I) could be elucidated.

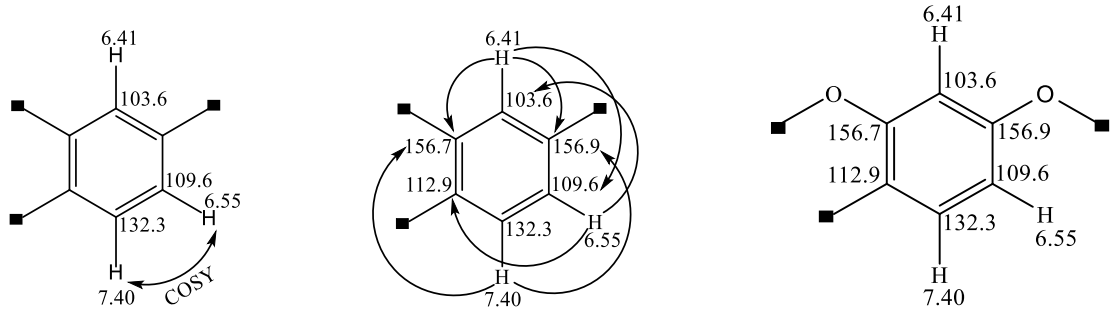

(i) (ii) (iii)

Figure 6 (i) (↔) DQF COSY correlation, (ii) (→) HMBC correlations in fragment (a) and (iii) partial structures (I)

According to the ^{1}H NMR spectrum (Figure 15.b), one doublet methine proton at δ 6.37 ppm (δ_c 108.2) showed ortho coupling with another doublet methine proton at δ 6.95 ppm (δ_c 122.3) with the coupling constant of 7.98 Hz. Therefore, 1, 2, 3, 4-tetrasubstituted benzene ring could be drawn. In the DQF COSY spectrum (Figure 15.f), these two methine protons showed correlation as expected and fragment (b) could be confirmed. The HMBC spectrum (Figure 15.g) revealed β-correlations of methine proton at δ 6.37 ppm (δ_c 108.2) with two sp^2 quaternary carbons at δ 110.3 and 118.6 ppm and α-correlation with one sp^2 quaternary carbon at δ 155.9 ppm. Moreover, in the HMBC spectrum (Figure 15. g), one doublet methine proton at δ 6.95 ppm (δ_c 122.3) gave β-correlations with two sp^2 quaternary carbons at δ 155.9 and 158.4 ppm. According to these correlations, the carbon atoms in the benzene ring could be assigned. According to the downfield chemical shifts of two sp^2 quaternary carbons at δ 155.9 and 158.4 ppm, these carbons could be connected to oxygen. Thus, the partial structure (II) could be assigned.

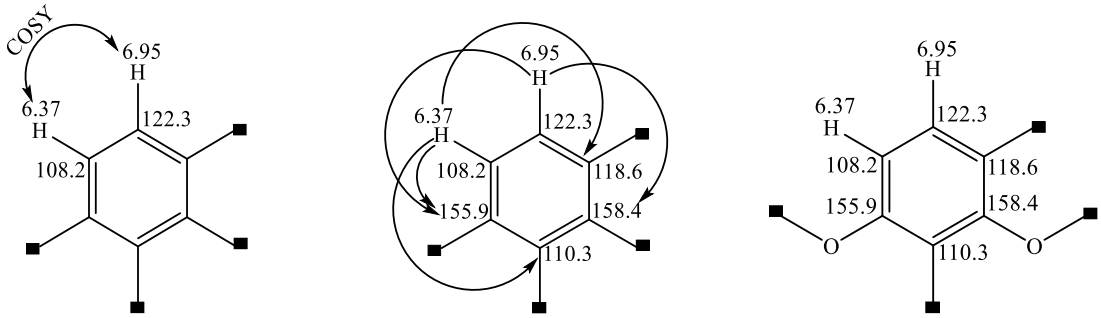

(i) (ii) (iii)

Figure 7 (i) (↔) DQF COSY correlation, (ii) (→) HMBC correlations in fragment (b) and (iii) partial structures (II)

In the DQF COSY spectrum (Figure 15.f), the methine proton at δ 3.51 ppm which is attached to carbon at δ 40.1 ppm showed correlations with the sp^3 methine proton at δ 5.46 ppm (δ_c 78.1) and one of the diastereotopic methylene protons at δ 3.63 ppm (δ_c 66.6). Furthermore, the two diastereotopic methylene protons at δ 3.36 and 4.20 ppm showed correlation with each other.

According to these correlations, the fragment (c) could be assigned. In the HMBC spectrum (Figure 15.g), the doublet methine proton at δ 5.46 ppm (δ_c 78.1) showed β-correlation with the sp^3 methylene carbon at δ 66.6 ppm. Moreover, the two diastereotopic methylene protons at δ 3.63 and 4.20 ppm showed HMBC correlations to the two sp^3 methine carbons at δ 40.1 and 78.1 ppm. Thus, the fragment (c) could be confirmed.

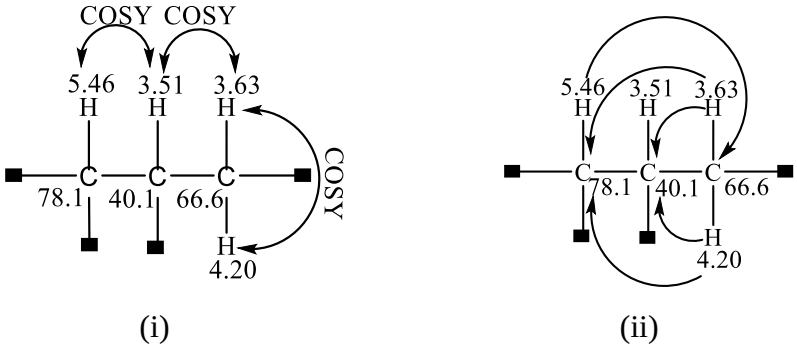

Figure 8 (i) (↔) DQF COSY correlation and (ii) (→) HMBC correlations in fragment (c)

According to the HMBC spectrum (Figure 15.g), the methine proton at δ 5.46 ppm (δ_c 78.1 ppm) showed correlations to two sp^2 quaternary carbons at δ 112.9 and 156.7 ppm and one sp^2 methine carbon at δ 132.2 ppm. Moreover, the methine proton at δ 7.40 ppm (δ_c 132.3) also showed the HMBC correlation to the sp^3 methine carbon at δ 78.1 ppm. Thus, the fragment (c) could be connected to the partial structure (I) as shown in partial structure (III). Furthermore, one of the diastereotopic methylene protons at δ 4.20 ppm which is attached to carbon at δ 66.6 ppm showed the HMBC correlation to the sp^2 quaternary carbon at δ 156.7 ppm.

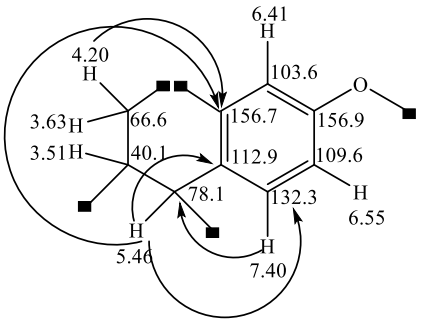

Figure 9 (→) HMBC correlations in partial structure (III)

According to the downfield chemical shifts of sp^3 methylene carbon at δ 66.6 ppm, the sp^3 methine carbon at δ 78.1 ppm and the sp^2 quaternary carbon at δ 156.7 ppm, these carbons could be connected to oxygen and the partial structure (IV) could be elucidated.

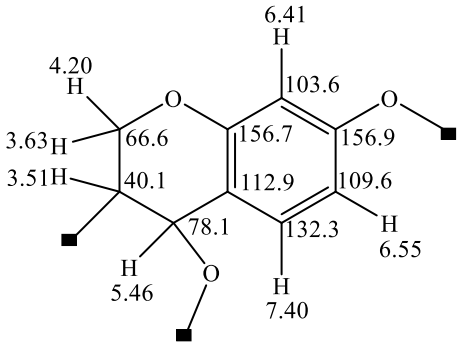

Figure 10 Partial structure (IV)

Furthermore, in the HMBC spectrum (Figure 15.g), the methine proton at δ 3.51 ppm (δ_c 40.1) gave α-correlation with the sp^2 quaternary carbon at δ 118.6 ppm from partial structure (IV). According to this correlation, the partial structure (II) and partial structure (IV) could be connected as shown in partial structure (V).

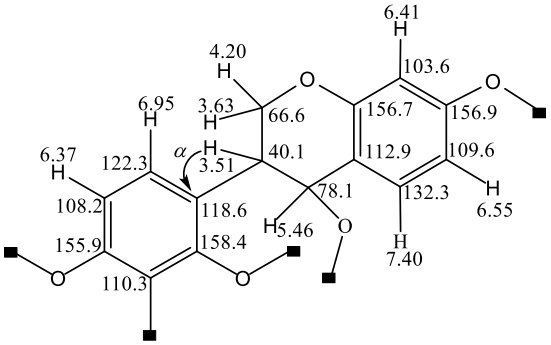

Figure 11 (→) HMBC correlations in partial structure (V)

In the DQS COSY spectrum (Figure 15.f), the sp^2methine proton at δ 5.27 ppm which is attached to carbon at δ 121.3 ppm showed correlation with the doublet methylene protons at δ 3.33 and 3.39 ppm (δ_c 23.2). According to this correlation, fragment (d) could be assigned. Moreover, the HMBC spectrum (Figure 15. g) revealed the observation of β correlation of the methylene protons at δ 3.33 and 3.39 ppm (δ_c 23.2) with the sp^2 quaternary carbon at δ 135.2 ppm and α correlation with the sp^2 methine carbon at δ 121.3 ppm.

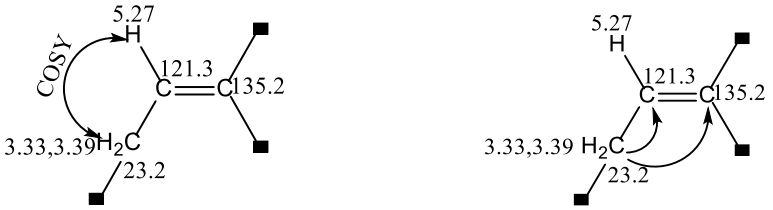

(i) (ii)

Figure 12 (i) (↔) DQF COSY correlation and (ii) (→) HMBC correlations in fragment (d)

In the HMBC spectrum (Figure 15.g), two methyl singlets at δ 1.74 ppm (δ_c 25.8) and 1.80 ppm (δ_c 17.9) showed correlation with each other. Moreover, these two methyl groups showed correlations with one sp^2 methine carbon at δ 121.3 ppm and one sp^2 quaternary carbon at δ 135.2 ppm. Furthermore, the sp^2 methine proton at δ 5.27 ppm (δ_c 121.3) showed HMBC correlation with two methyl carbons at δ 17.9 and 25.8 ppm. Therefore, the fragment (e) could be confirmed.

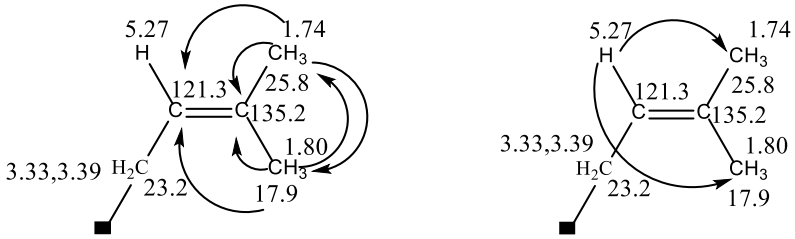

(i) (ii)

Figure 13 (i) and (ii) (→) HMBC correlations in fragments (e)

In the HMBC spectrum (Figure 15.g), the sp^3 methylene protons at δ 3.33 and 3.39 ppm (δ_c 23.2) showed correlations to the sp^2 quaternary carbons at δ 110.3, 155.9 and 158.4 ppm. According to these correlations, fragment (e) could be connected to partial structure (V) as shown in partial structure (VI).

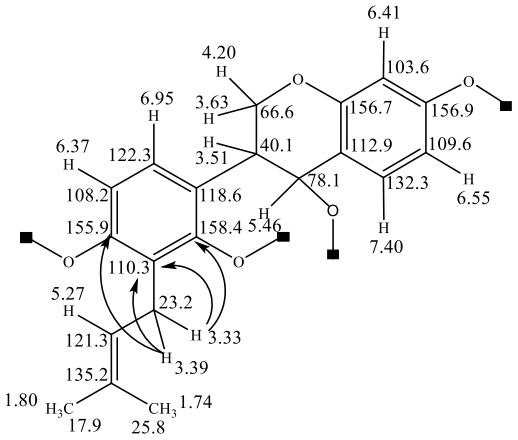

Figure 14 (→) HMBC correlations in partial structure (VI)

The partial molecular formula of compound was $C_{20}H_{18}O_5$ and molecular mass was 338. The (+)-DART mass spectrum (Figure 15.h) showed the peak, $[M+H-H_2O]^+$ at 325. Therefore, the molecular mass was deduced as 342 with the molecular formula of $C_{20}H_{22}O_5$. Thus, the remaining molecular mass was four and it was responsible for four hydrogen atoms. The structure of compound was elucidated 4', 6', 7-trihydroxy-5'-prenyl isoflavan-4-ol (1). Furthermore, the FT IR (Figure 15.a) spectrum of pure compound (1) revealed the presence of -OH group.

(a)

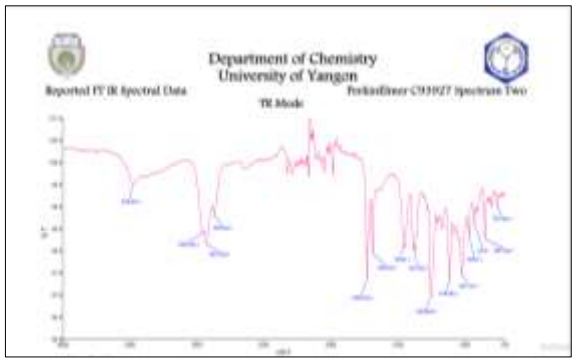

(b)

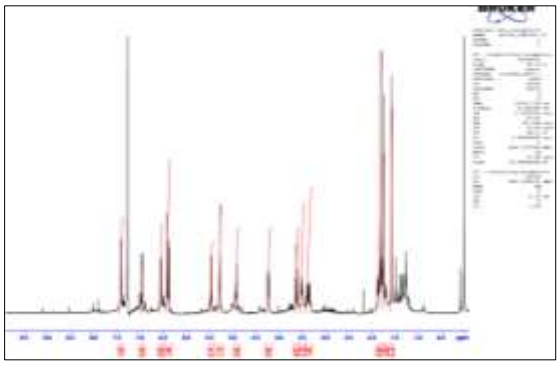

(c)

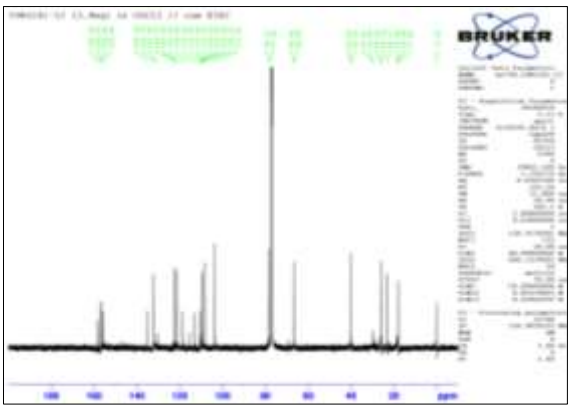

(d)

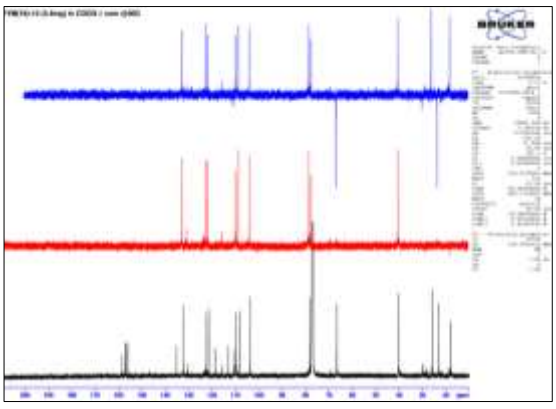

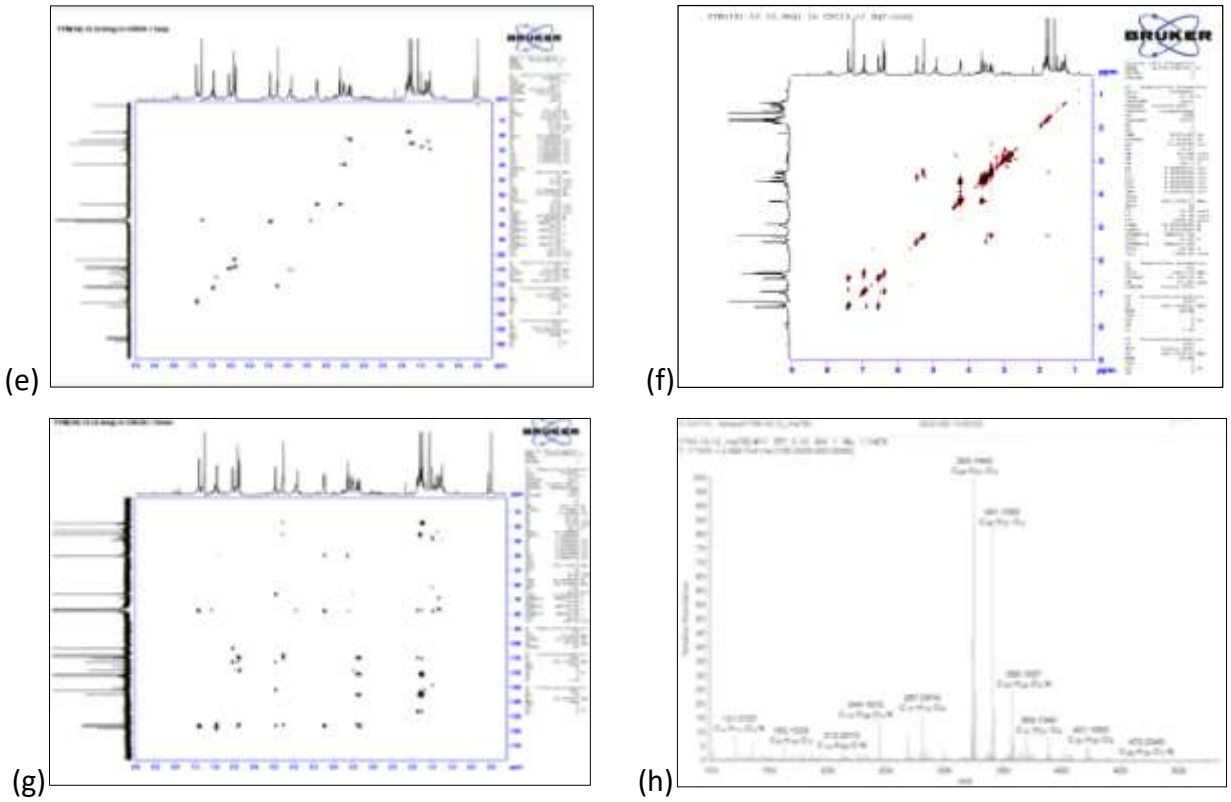

Figure 15 (a) FT IR, (b) ^{1}H NMR (c) ^{13}C NMR (d) DEPT (e) HSQC (f) DQF COSY (g) HMBC and (h) (+) DART mass spectra of 4',6',7-trihydroxy-5'-prenyl isoflavan-4-ol

Conclusion

In this research work, medicinal plant *Erythrina crista-galli* Linn. was selected for chemical screening due to its interesting medicinal uses. From ethyl acetate extract, isoflavan derivative, namely, 4',6', 7-trihydroxy-5'-prenyl isoflavan-4-ol was isolated and characterized. According to DPPH assay, IC_{50} value of methanolic extract was found to be 143.6 μg/mL. Therefore, methanolic extract showed antioxidant activity but less than ascorbic acid (IC_{50} 15.97 μg/mL), standard antioxidant.

Acknowledgements

The authors thank Dr Yoshiaki Takaya, Associate Professor, Faculty of Pharmacy, Meijo University, Japan for NMR and mass measurements. The authors thank Dr Tin Tun, Rector of Taungoo University, Dr Yi Yi Myint, Professor and Head, Department of Chemistry, University of Mandalay and Dr Malar Yi, Professor, Department of Chemistry, Taungoo University for their permission to submit this paper.

References

Ayoub, N.A., Abdel-Naim, A.B., and Ashour, M.L. (2017). "Hepatoprotective Activity of Aerial Parts of *Erythrina crista-galli"*. *Archives of Pharmaceutical Sciences Ain Shams University*, vol. 1, No. 1, pp. 9-15.

Chintoju, N., Konduru, P., Kathula, R. L., and Remella, R. (2015). "Importance of Natural Products in the Modern History". *Journal of Hospital and Clinical Pharmacy*, vol. 1, No. 1, pp. 5-10.

Dahanukar, S.A., Kulkarni, R.A., and Rege, N.N. (2000). "Pharmacology of Medicinal Plants and Natural Products". *Indian Journal of Phytopharmacology*, vol .32, pp. 81-118.

Dar, R.A., Shahnawaz, M., Rasool, S., and Qazi, P.H. (2017). "Natural Product Medicines: A Literature Update". *The Journal of Phytopharmacology*, vol. 6, No.6, pp. 340-342.

Maier, U.H., Rold, W., Deus-Neumann, B., and Zenk, M.H. (1999). "Biosysthesis of *Erythrina* Alkaloids in *Erythrina crista-galli"*. *Phytochemistry*, vol. 52, pp. 373-382.

Weber, D., Sterner, O., Anke, T., Gorzalczancy, S., Martino, V., and Acevedo, C. (2004). "Phomol, a New Antiinflammatory Metabolite from an Endophyte of the Medicinal Plant *Erythgrina crista-galli"*. *The Journal of Antibiotics*, vol. 57, No. 9, pp. 559-563.

ISOLATION, STRUCTURE ELUCIDATION OF FLAVONOID DERIVATIVE FROM THE BARK OF *ALBIZIA PROCERA* (ROXB.) BENTH. AND STUDY ON ITS ANTIMICROBIAL AND ANTIOXIDANT ACTIVITIES

Kyaw Aung[1], Arnt Win[2], Myint Myint Sein[3]

Abstract

In the present research, the bark of *Albizia procera* (Roxb.) Benth. (Local name = Thit-phyu) was selected for chemical investigation. Preliminary phytochemical investigation was carried out according to the standard procedures. Antimicrobial properties was evaluated by using agar-well diffusion method on six test microorganisms such as *Bacillus subtilis, Staphylococcus aureus, Pseudomonas aeruginosa, Bacillus pumilus, Candida albican and Mycobacterium* species. Moreover, a pure compound, pale yellow needled shape crystals, was isolated by using separation techniques such as thin layer and column chromatography. The isolated compound was assigned as flavonoid derivative, namely, 2(R), 3(S)-2-(2, 4-dihydroxy phenyl) chroman-3,5,7-triol by using spectroscopic methods, such as FT-IR, ^{1}H NMR, ^{13}C NMR (125 MHz), DEPT, DQF-COSY, HMQC, HMBC, NOESY, and EI mass spectral data. The isolated compound was further confirmed by phytochemical test which gave rise to positive for flavonoid test. The yield percent was calculated as (33.87 mg), (1.07%) based upon the ethyl acetate crude extract and the melting point was 191°C–192°C. Moreover, the antioxidant activity of isolated flavonoid compound was measured by DPPH (1,1–Diphenyl-2-picryl-hydrazyl) assay. The isolated compound showed the high antioxidant activity.

Keywords: chromatography, flavonoid, DPPH

Introduction

In the last decade, there has been a global upsurge in the use of traditional medicine and complementary and alternative medicines in both developed and developing countries. Hence, the safety and efficacy, as well as the quality control of traditional medicine have become important concerns for both health authorities and the public. Herbal medicines are the most widely used traditional medicines. Before manufactured drugs came into widespread use, herbal medicines played an important role in human health (WHO, 2005). Herbal medicines include herbs, herbal materials, herbal preparations and finished herbal products.

Different medicinal plants and herbs grow in Myanmar as there are different seasons and various geographical features. Among them, one traditional indigenous medicinal plant, *Albizia procera* Benth., which is locally known as Thit-phyu and applying as indigenous medicine (Aye, 2004). No chemical investigation has been done on this plant species in Myanmar. In India, leaves are poultice onto ulcers. Bark is useful in pregnancy and stomachache. Bark extract was given with salt as a medicine for water buffalo. It can prevent the phlegm and the diseases of the bile. So, the bioactive compound from bark of *Albizia procera* Benth. was investigated in the present research work.

[1] Lecturer, Department of Chemistry, Shwebo University
[2] Dr, Associate Professor, Department of Chemistry, Kyaukse University
[3] Dr, Professor and Head (Rtd), Department of Chemistry, University of Mandalay

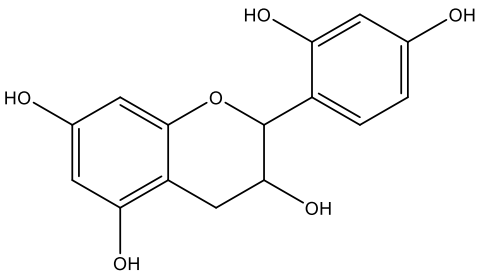

Figure 1 Structure of isolated compound

Figure 2 Plant, stem, leaf and fruit of *Albizia procera* (Roxb.) Benth.

Botanical Classification

Botanical name	- *Albizia procera* (Roxb.) Benth.
Family	- Mimosaceae
Myanmar name	- Sit, Thit-phyu
Distribution	- Native to tropical Asia and Australia

Materials and Methods

General Experimental Procedures

Commercial grade reagents and solvents were used without further purification. Analytical preparative thin layer chromatography was performed by using silica gel. (Merck Co. Inc, Kieselgel 60 F_{254}). Silica gel (60, 70 to 230 mesh ASTM) was used for Column Chromatography. The advanced instruments which were used in the characterization of samples and elucidation of pure compound were shown below.

1. UV lamp (Lamda-40, Perkin-Elmes Co. England)
2. UV 1601 PC (P/N 206.675) spectrophotometer
3. FT-IR spectrometer (Shimadzu, Japan)
4. ^{1}H NMR spectrometer (500MHz)
5. ^{13}C NMR spectrometer (125 MHz)
6. EI-Mass spectrometer

Plant Materials

The bark of *Albizia procera* were collected from Shwebo Township, Sagaing Region, Myanmar. The collected plant materials were screened and taxonomically identified by authorized botanist from Botany Department, University of Mandalay. The plant materials were dried at room temperature and ground into powder.

Preliminary Phytochemical Analysis

The preliminary phytochemical screening of *Albizia procera* was determined using standard method of Harborne (Harborne, 1995).

Antimicrobial Assay

Antimicrobial tests were performed at Pharmaceutical Research Department (PRD), Insein Township, Yangon Region. Antimicrobial activities of plant extracts were tested by agar-well diffusion method on six test microorganisms such as *Bacillus subtilis*, *Staphylococcus aureus*, *Pseudomonas aeruginosa*, *Bacillius pumilus*, *Candida albicans* and *Mycobacterium* species.

Extraction and Isolation of Pure Compound

The air dried bark powder of *Albizia procera* (800 g) was percolated with 95 % ethanol (1500 mL) for two months. The ethanol extract was filtered and evaporated. The residue was dissolved in 500 mL of ethyl acetate. Then, ethyl acetate solution was evaporated and to obtain crude extract (5.64 g). The ethyl acetate crude extract (3.15 g) was chromatographed on a silica gel (70-230 mesh) column, eluting with the solvent system n-hexane: ethyl acetate with various ratios from non-polar to polar. About 1 mL of each portion was collected in a small bottle and followed by TLC detection of each portion. Totally 178 fractions were collected. The fractions with the same R_f value were combined and altogether (11) combined fractions were obtained. The fraction (K) which showed only one spot on TLC, was concentrated and recrystallized by using (50%) ethyl acetate in n-hexane for two times. The pure pale yellow needled shape crystals (33.87 mg) were obtained. The total yield percent of pure compound was (1.07 %) based upon the crude ethyl acetate extract. This pure compound was reconfirmed by phytochemical test which gives rise to positive for flavonoid test.

Determination of Melting Point

A few pale yellow needled shape crystals of pure isolated compound were inserted into the capillary tube and the melting point was determined by using the electric melting point apparatus. The melting point of pure compound was found to be 191°C-192°C.

Measurement of Radical Scavenging Activity by UV Spectrophotometric Method

Preparation of 60 μM DPPH Solution

DPPH powder (2.36 mg) was thoroughly and gently dissolved in 100 mL of 95% ethanol and stored in brown coloured volumetric flask at 5 °C (no longer than 24 hours) before use.

Preparation of Test Sample Solution

Pure isolated compound 2.0 mg and 10 mL of 50% ethanol were gently mixed by vortex mixer to obtain the stock solution. It was diluted with 50% ethanol in various ratios to obtain five ranges of concentrations, such as, 0.625 μg/mL, 1.25 μg/mL, 2.50 μg/mL, 5.0 μg/mL and 10.0 μg/mL respectively. Then, 5.0 mL of ethanol solution was prepared for each concentration.

Preparation of Standard Ascorbic Acid Solution

Furthermore, the solution of standard ascorbic acid was also prepared as the same concentrations of isolated compound in 50% ethanol and the same volume (5 mL) of standard ascorbic solution was prepared for each concentration.

Measurement of DPPH Radical Scavenging Activity by Spectrophotometric Method

The control solution was prepared by mixing 1.5 mL of 60 μM DPPH solution and 1.5 mL of 95% ethanol by vortex mixer. Moreover, the blank solution could be prepared by mixing 1.5 mL of test sample solution and 1.5 mL of 50% ethanol thoroughly in the vortex mixer. Furthermore, the sample solution was also prepared by mixing 1.5 mL of 60 μM DPPH solution and 1.5 mL of test sample solution gently by applying vortex mixer. After that, the solutions were allowed to stand at room temperature for 30 min. Then the absorbance value of each solution was measured at 517 nm by UV-1601 PC (P/N 206-675) spectrophotometer (Kiattsin *et al*., 2016).

These measurements were performed in triplicate for each solution. The absorbance values obtained were applied to calculate percent inhibition by formula:

$$\%\,\text{inhibition} = \frac{\text{Abs}_{\text{DPPH}} - [\text{Abs}_{\text{sample}} - \text{Abs}_{\text{Blank}}]}{\text{Abs}_{\text{DPPH}}} \times 100\,,$$

where % inhibition = percent inhibition of test sample, Abs_{DPPH} = absorbance of control solution, $\text{Abs}_{\text{sample}}$ = absorbance of test sample solution, $\text{Abs}_{\text{blank}}$ = absorbance of blank solution.

Results and Discussion

Phytochemical Analysis

Preliminary phytochemical analysis of the extract of *Albizia procera* bark revealed the presence of phytochemicals such as flavonoid, sugar, glycoside, phenol and polyphenol.

Antimicrobial Assay

The antimicrobial activities of plant extracts were tested by applying agar-well diffusion method on six test microorganisms. According to antimicrobial assay, the n-hexane extract of *Albizia procera* did not inhibit the growth of test microorganisms. But other four solvents extracts (chloroform, acetone, ethyl acetate, ethanol) of *Albizia procera* exhibit the medium activities on five organisms and high activities on *Mycobacterium* species.

Table 1 Antimicrobial Activities of Selected Medicinal Plant

		Organisms/mm					
Samples	**Solvents**	**I**	**II**	**III**	**IV**	**V**	**VI**
Albizia procera Bark	n-hexane	–	–	–	–	–	–
	$CHCl_3$	14	17	13	16	19	20
	Acetone	15	15	14	16	18	20
	EtOAc	15	15	14	16	18	20
	EtOH	13	15	13	15	17	17

Agar-well – 10 mm

10 mm ~14 mm (+) weak active
15 mm ~19 mm (++) medium active
20 mm above (+++) strong active

(I) *Bacillus subtilis*
(II) *Staphylococous aureus*
(III) *Pseudomonas aeruginosa*
(IV) *Bacillus pumilus*
(V) *Candia albicans*
(VI) *Mycobacterium* species

The antimicrobial activities of pure compound were rechecked by using agar-well diffusion method on six organisms. The isolated compound responded medium activities on five test microorganisms except mycobacteria.

Table 2 Antimicrobial Activities of Pure Compound

Name of Organisms	Inhibition Zone (mm)
Bacillus subtilis	15
Staphylococous aureus	15
Pseudomonas aeruginosa	15
Bacillus pumilus	15
Candia albicans	17
Mycobacterium species	-

Antioxidant Activity

The antioxidant activity of isolated pure compound was analyzed by DPPH (2,2-diphenyl-1-picryl-hydrazyl) method. The comparative absorbance values of isolated flavonoid compound and those values of standard ascorbic acid were tabulated in Table 2.

Table 3 Comparative Absorbance Values of Standard Ascorbic Acid Solution and Isolated Compound

No.	Concentration (µg/mL)	Absorbance	
		Ascorbic Acid	Isolated Compound
1	0.625	0.057	0.123
2	1.25	0.031	0.098
3	2.5	0.01	0.078
4	5	0.002	0.063
5	10	0.001	0.033

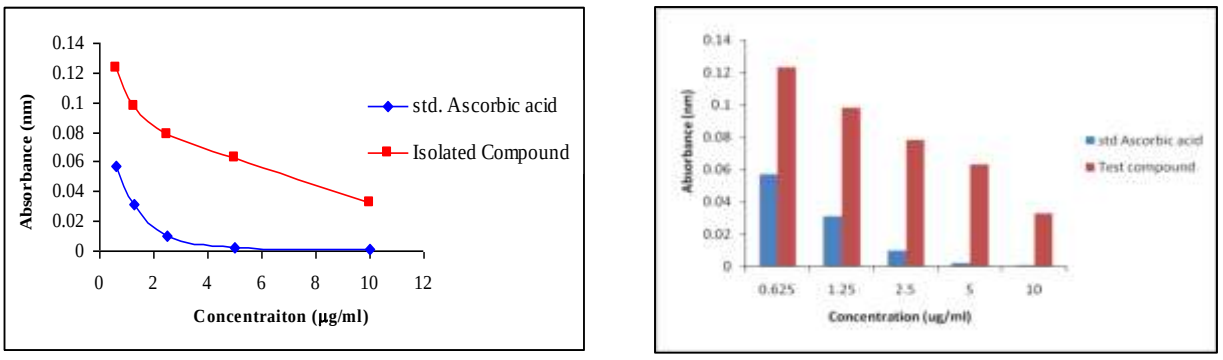

Figure 3 Plot of absorbance vs concentration of isolated compound and standard ascorbic acid

The inhibition percentage of isolated compound and standard ascorbic acid in various concentrations were described in Table 3.

Table 4 %Inhibition of Ascorbic Acid Solution and Isolated Compound in Various Concentrations

No	Concentration (µg/mL)	% Inhibition	
		Ascorbic acid (Standard)	Isolated Compound
1	0.625	69.0	50.2
2	1.25	83.2	60.3
3	2.5	94.6	68.5
4	5	98.9	74.5
5	10	99.5	86.6

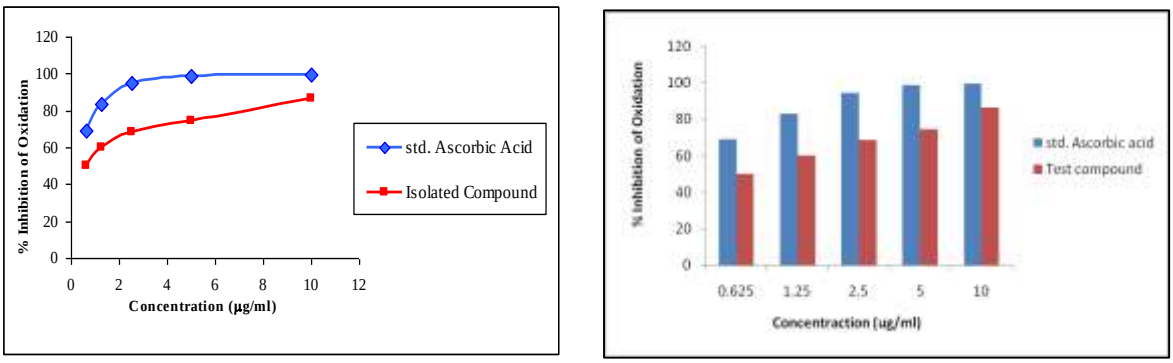

Figure 4 Plot of % inhibition vs concentration of isolated compound and standard ascorbic acid

As indicated in Figure 3, absorbance decreases as concentration increases in both of isolated compound and standard ascorbic acid. Decrease in absorbance implies increase in % inhibition of oxidation. In accordance with these figures, the absorbance values of isolated compound and standard ascorbic acid are considerably different at lower concentration (0.625 µg/mL). But at higher concentration level (10 µg/mL), the differences of absorbance between isolated compound and standard ascorbic acid become smaller. Hence at higher concentration level, the isolate compound responds high antioxidant activity.

Moreover, in Figure 4, % inhibitions of oxidation of isolated compound and standard ascorbic acid increase with the increase in concentrations of both of the two compounds. At higher concentration level (10 µg/mL), the isolated compound responds 85% inhibition of oxidation based upon the standard ascorbic acid.

Structure Elucidation of Pure Compound

In the DQF-COSY spectrum, Figure 5, the observation of the small graphic area between the two aromatic protons at δ 5.69 ppm and 5.89 ppm leads to the following tetra substituted benzene fragment.

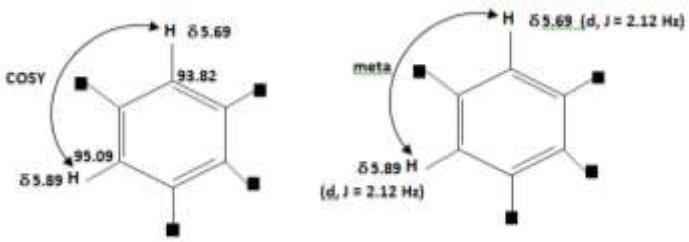

This fragment was supported by the splitting patterns and the coupling constants (J values) of these two aromatic protons at δ 5.69 ppm (d, J = 2.12 Hz) and δ 5.89 ppm (d, J = 2.12 Hz) in ^{1}H NMR spectrum, Figure 5, in which both protons should be oriented at meta position.

Moreover, the proton-carbon orientation of this tetrasubstituted benzene fragment could be determined by HMBC spectrum, Figure 5. In this spectrum, the occurrence of α ^{1}H-C long range signal of both of two aromatic protons at δ 5.69 and 5.89 ppm with the sp^2 quaternary carbon at δ 156.12 ppm and sp^2 quaternary carbons δ 155.32 and 156.41 ppm and indicated the following fragments.

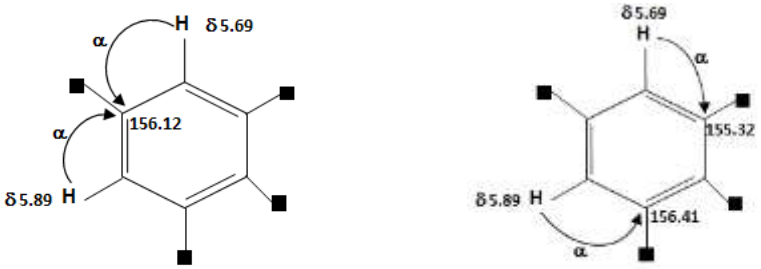

Furthermore, the fragment a could be assigned by the existence of β ^{1}H–C long range signal between both of two aromatic protons (δ 5.69 ppm and δ 5.89 ppm) and sp^2 quaternary carbon (δ 99.02 ppm) in HMBC spectrum, Figure 5, as shown below.

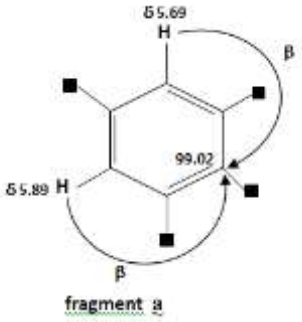

fragment a

On the other hand, the DQF-COSY spectrum, Figure 5, shows a large graphic area between the two geminal methylene protons (δ 2.36 ppm and δ 2.66 ppm) which produces the geminal fragment. In addition, the observation of medium graphic area of these methylene protons (δ 2.36 ppm and δ 2.86 ppm) with their adjacent sp^3 methine proton (δ 3.82 ppm) in the DQF-COSY spectrum, Figure 5, gives rise to the following fragment.

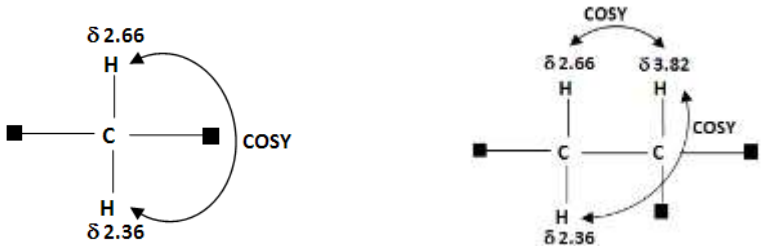

The extended fragment b could be determined by the observation of medium graphic area between sp^3 methine proton (δ 3.82 ppm) and another sp^3 methine proton (δ 4.48 ppm) in DQF-COSY spectrum, Figure 5. Moreover, this fragment b could be confirmed by HMBC spectrum, in Figure 5, in which the two geminal methylene protons (δ 2.36 ppm and δ 2.66 ppm) have α and

β ^{1}H-C long range coupling with sp^3 methine carbon (δ 66.28 ppm) and another sp^3 methine carbon (δ 80.97 ppm). Inversely, the determination of α and β ^{1}H-C long range signal of sp^3 methine proton (δ 4.48 ppm) with sp^3 methine carbon (δ 66.28 ppm) and methylene carbon (δ 27.81 ppm) in this HMBC spectrum.

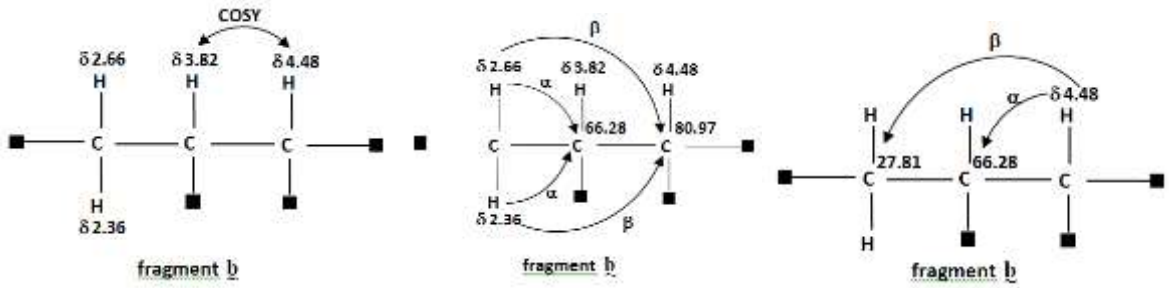

Furthermore, the connection between fragment a and fragment b could be done by HMBC spectrum, Figure 5. In HMBC spectrum, both of the two geminal methylene protons (δ 2.36 ppm and δ 2.66 ppm) have α and β ^{1}H-C long range coupling with three sp^2 quaternary carbons (δ 99.02 ppm, δ 155.32 ppm and δ 156.41 ppm) which leads to the following longer fragment.

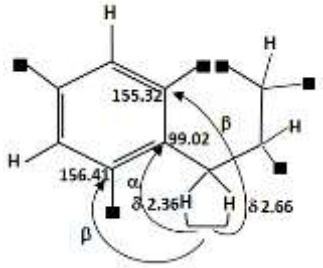

On the other hand, the FT-IR spectrum, Figure 5, give rise to the good evidence for the existence of ether functional group which appears at 1026.1 cm^{-1}. Thus logical correlation of ether oxygen atom to both of down field chemical shift sp^2 quaternary carbon (δ 155.32 ppm) and sp^3 methine carbon (δ 80.97 ppm) produces the most reliable fragment c.

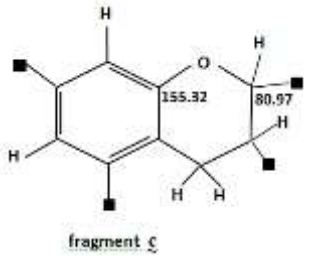

However, in HMBC spectrum, Figure 5, there is β ^{1}H-C long range signal between sp^3 methine proton (δ 4.48 ppm) and sp^2 quaternary carbon (δ 155.32 ppm) which confirms the fragment c as shown below.

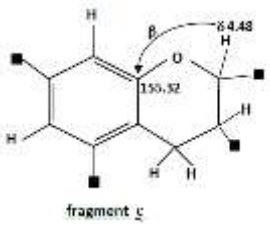

Furthermore, in the DQF-COSY spectrum, Figure 5, the existence of medium graphic area between the two aromatic protons (δ 6.59 ppm and δ 6.68 ppm) implies the following another benzene fragment.

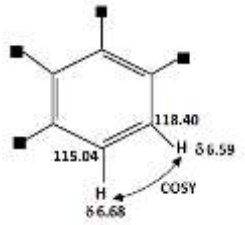

In addition, the occurrence of small graphic area between two aromatic protons (δ 6.59 ppm and δ 6.72 ppm) in the DQF-COSY spectrum, Figure 5, reveals the following trisubstituted benzene fragment d .

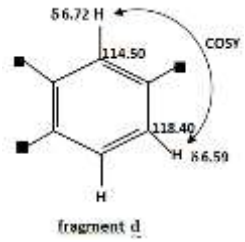

fragment d

The above trisubstituted benzene fragment could be confirmed by the splitting patterns and coupling constants (J values) of these three aromatic protons (^{1}H δ 6.59 ppm, d, d, J = 8 Hz and 1.7 Hz, ^{1}H δ 6.68 ppm, d, J = 8 Hz, and ^{1}H δ 6.72 ppm, d, J = 1.7 Hz) as shown below.

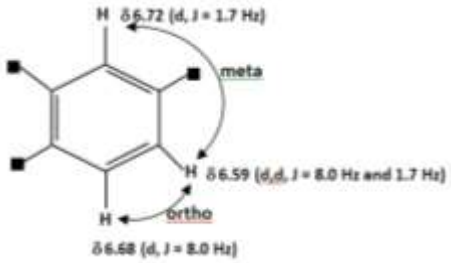

It means that both of these two aromatic protons (δ 6.59 ppm and δ 6.68 ppm) are ortho to each other and the two aromatic protons (δ 6.59 ppm and δ 6.72 ppm) are meta to each other.

The proton-carbon long range coupling of this trisubstituted aromatic benzene ring fragment could be also determined by HMBC spectrum, Figure 5. In this spectrum, the aromatic proton (δ 6.68 ppm) responds α ^{1}H-C long range signal with sp^2 quaternary carbon (δ 130.57 ppm). Moreover, in this spectrum, this methine proton (δ 6.68 ppm) also responds β ^{1}H-C long range signal with the two same chemical shift sp^2 quaternary carbons (δ 144.82 ppm). Furthermore, the HMBC spectrum, Figure 5, displays α ^{1}H-C long range coupling between the aromatic proton (δ 6.72 ppm) and both of two same chemical shift sp^2 quaternary carbons (δ 144.82 ppm) as shown below.

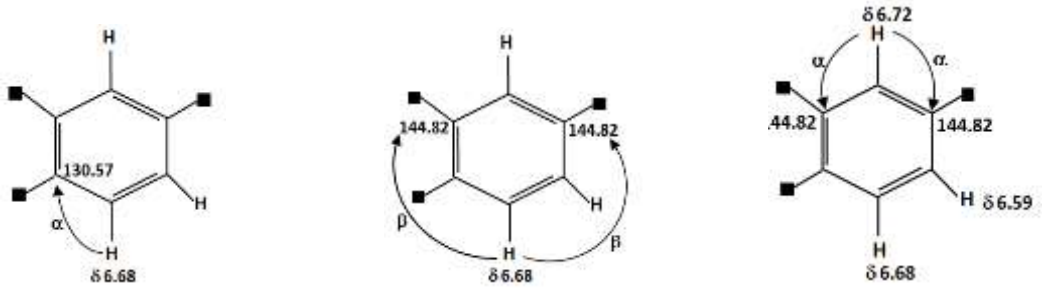

Moreover, the aromatic proton (δ 6.59 ppm) has α and β ^{1}H-C long range coupling with two aromatic carbons (δ 115.04 ppm and δ 114.50 ppm) in HMBC spectrum, Figure 5 which indicates the following fragment ḍ .

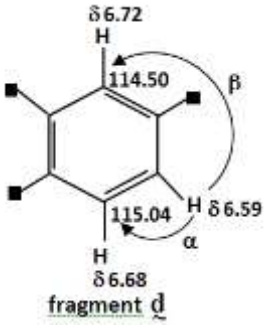

fragment ḍ

Meanwhile, the more longer fragment ḛ could be determined by the connection between fragment ḉ and fragment ḍ according to HMBC spectrum, Figure 5. In this spectrum, there is α and β ^{1}H-C long range signal of sp^{3} methine proton (δ 4.48 ppm) with two sp^{2} aromatic carbons (δ 130.57 ppm and δ 155.04 ppm) which leads to the following more longer fragment ḛ .

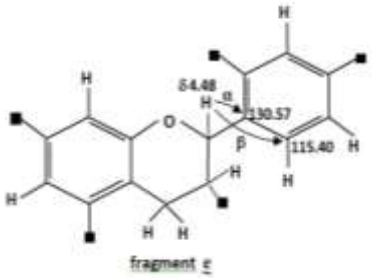

fragment ḛ

However, this HMBC spectrum, Figure 5, also responds the β ^{1}H-C long range coupling between sp^{3} methine proton (δ 3.82 ppm) and sp^{2} quaternary carbon (δ 130.57 ppm) which confirms the above fragment ḛ .

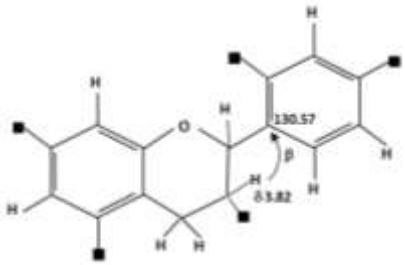

On the other hand, the correlation of β ^{1}H-C long range signal of aromatic proton (δ 6.68 ppm) with sp^{2} methine carbon (δ 80.97 ppm) in HMBC spectrum, Figure 5, also confirms this more longer fragment ḛ .

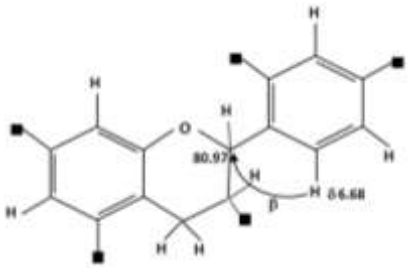

In this fragment ẹ , the remaining partial formula is calculated as H_5O_5, which are assumed to be five hydroxyl groups. It is supported by the FT-IR spectrum, Figure 5.

The complete structure of compound could be elucidated as described below, by the attachment of one –OH group to down field chemical shift of sp^3 carbinol methine carbon (δ 66.28 ppm) and the remaining four phenolic -OH functional groups to down field chemical shift of four aromatic quaternary carbons (δ 144.82 ppm, δ 156.12 ppm and δ 156.41 ppm) in two benzene rings.

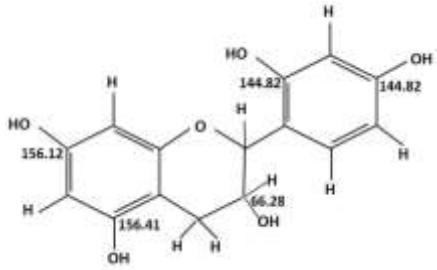

The complete planar structure of pure flavonoid compound could be assigned as follows.

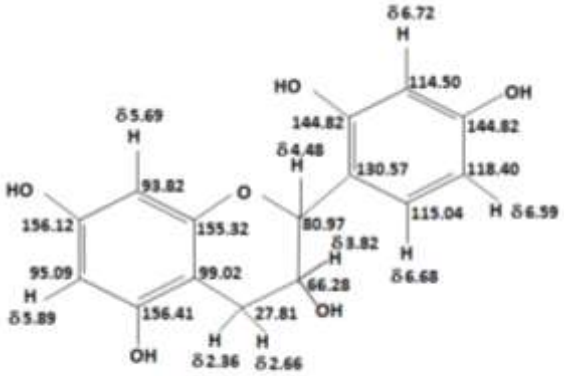

2– (2, 4-dihydroxy phenyl) chroman -3, 5, 7-triol

Confirmation of the Planar Structure of a Pure Flavonoid Compound by the Mass Fragmentation Behaviour

The proposed mechanism for the fragmentation pattern in EI mass spectrum was described below. The homolytic cleavage between $C_2 – C_{1'}$ leads to the fragment ạ and then liberation of carbon monoxide molecule, hydrogen molecule and hydrogen radical can give rise to the most intense base peak, fragment ḅ (m/z – 149).

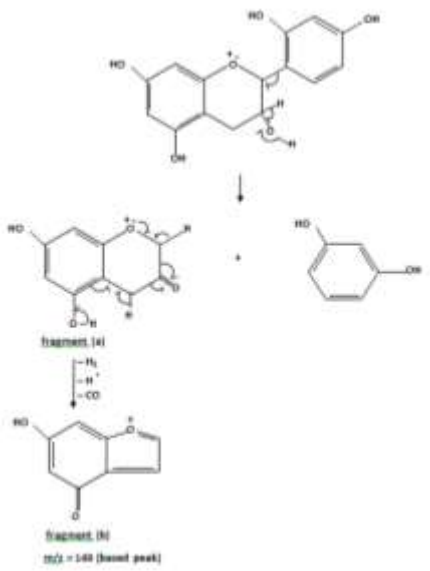

Moreover, the homolytic cleavages between C_2–O produces the intermediate fragment which also occurs the homolytic cleavage between C_2–C_3 give rise to the fragment ç (m/z 167) and the fragment d (m/z 123).

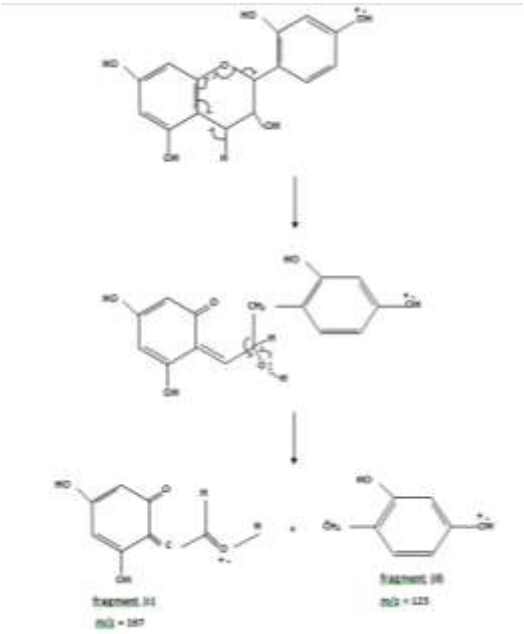

In addition, the abstraction of hydroxyl radical ($OH^{\bullet}$) from based peak, fragment b leads to the fragment e (m/z 152).

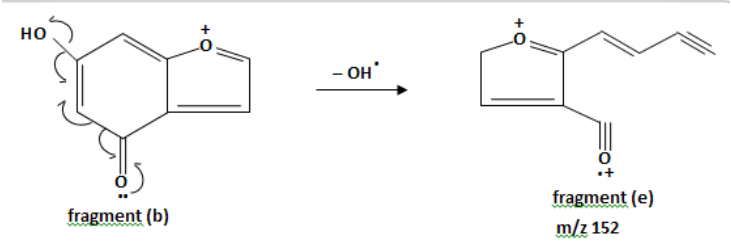

Then the fragment f (m/z 113) and fragment g (m/z 68) could be determined by the fragmentation between the $C_2 - C_{1'}$ and $C_6 - O$ of the molecular ion peak.

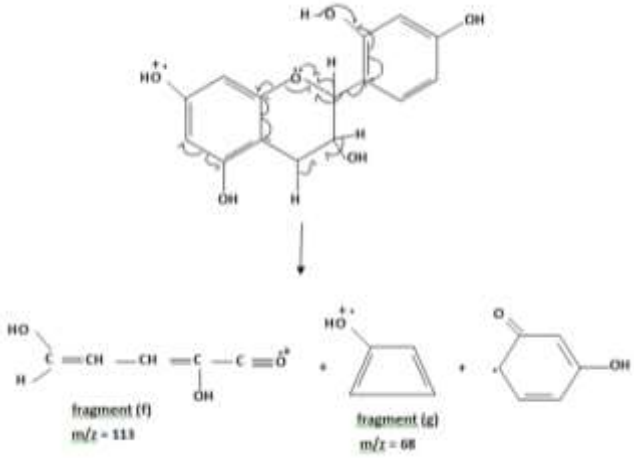

In addition, the fragment h (m/z 71) could be observed by the homolytic cleavages between $C_2 - C_{1'}$, $C_4 - C_{10}$ and $C_9 - O$ and liberation of hydrogen radical from the molecular ion peak.

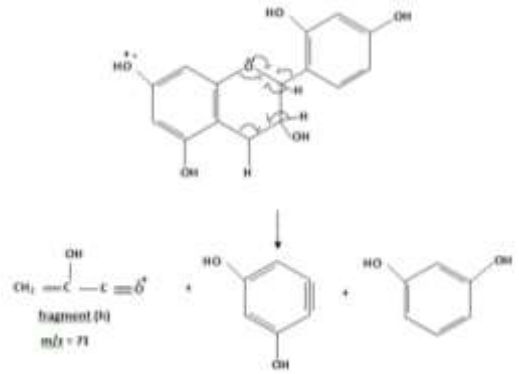

On the other hand, the homolytic cleavages between $C_2 - O$ and $C_2 - C_3$ from the molecular ion peak indicate the fragment i (m/z 84).

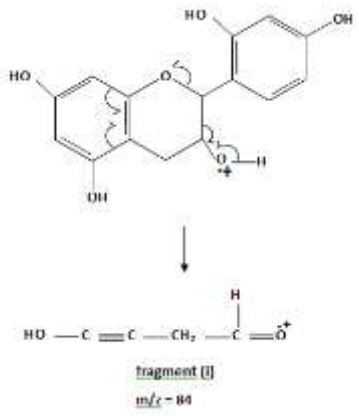

Furthermore, the three fragments j (m/z 123), k (m/z 57) and ℓ (m/z 110) could be observed by the homolytic cleavages between $C_2 - C_{1'}$, $C_4 - C_{10}$ and $C_2 - O$ from the molecular ion peak and then the liberation of hydrogen molecule from fragment k (m/z 57) occurs the fragment m (m/z 55).

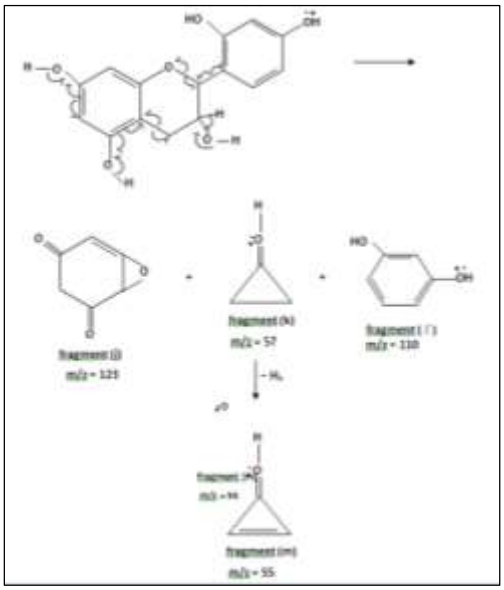

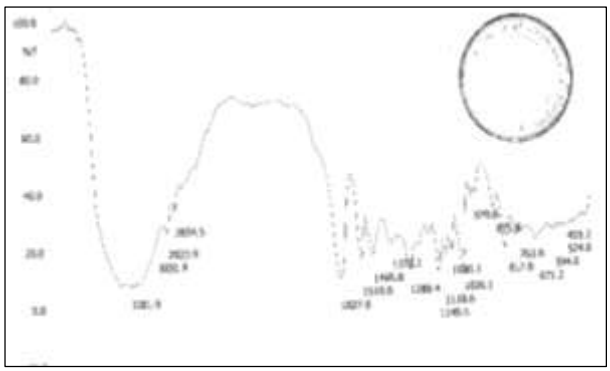

(a)

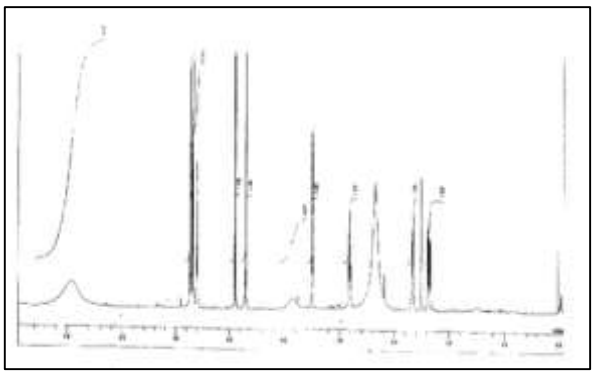

(b)

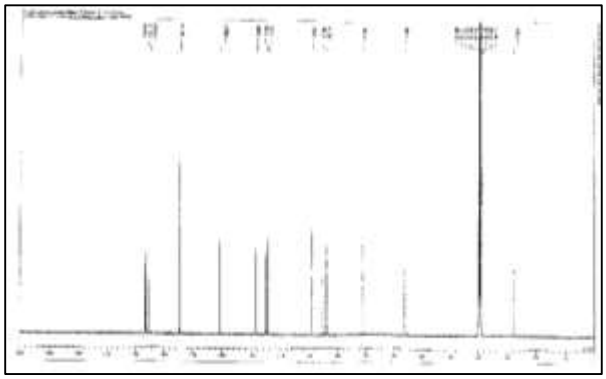

(c)

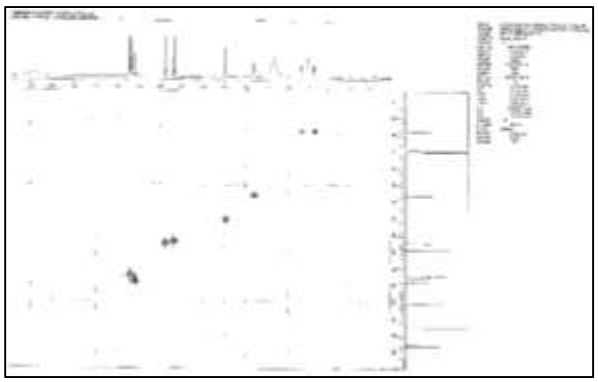

(d)

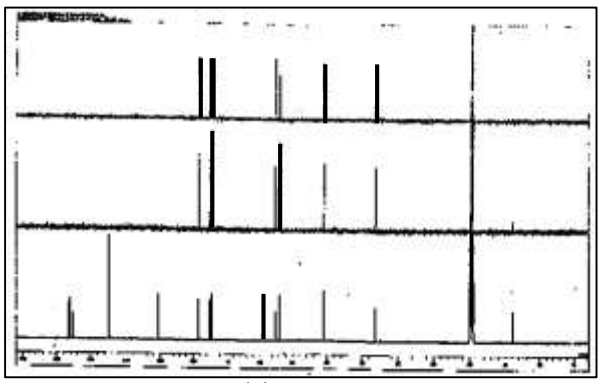

(e)

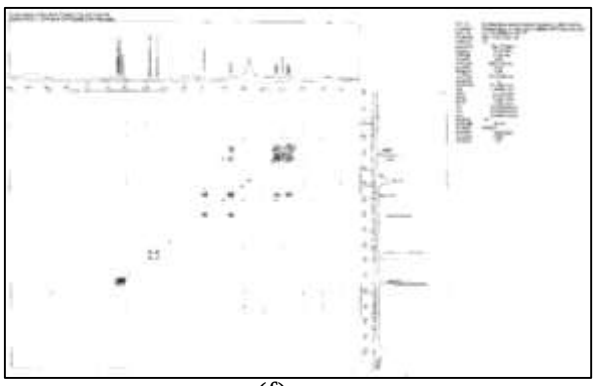

(f)

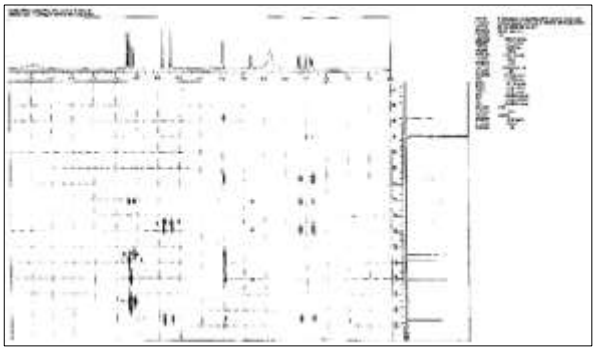

(g)

Figure 5 (a) FT IR spectrum (b) ^{1}H NMR spectrum (c) ^{13}C NMR spectrum (d) HSQC spectrum (e) DEPT spectrum (f) COSY spectrum (g) HMBC spectrum of isolated compound

Conclusion

In this research work, chemical investigation of the bark of *Albizia procera* was carried out. Pale yellow needle-shaped crystals, 2-(2,4-dihydroxy phenyl) chroman-3,5,7-triol was isolated from ethyl acetate extract and characterized spectroscopically. The isolated compound responded medium activities on five test microorganisms except mycobacteria. The isolated compound was further confirmed by flavonoid test. By DPPH assay, the antioxidant activity of isolated flavonoid compound showed the high antioxidant activity.

Acknowledgements

The authors thank Dr Yoshiaki Takaya, Associate Professor, Faculty of Pharmacy, Meijo University for NMR and mass measurements.

References

Aye, S.M. (2004). "Floristic Study and Ethnobotany of Ywa-ngan Area, Shan State in Myanmar." Ph.D Dissertation, Department of Botany, University of Mandalay.

Harbonne, J B. (1982). "Phytochemical Methods: A Guide to Modern Techniques of Plant Analysis". Chapman and Hall Ltd.

Kiattsin, K., Nantarat, T., and Leelapornpisid, P. (2016). "Evaluation of Antioxidant and Anti-tyrosinase Activities as well as Stability of Green and Roasted Coffee Bean Extracts from *Coffea arabica* and *Coffea canephora* Grown in Thailand". *Journal of Pharmacognosy and Phytotherapy*, vol. 8, pp. 182-192.

Porter Q.N. and J.Baldas, (1971). "Mass Spectrometry of Heterocycylic Compound"; Wiley-Inter Science, a Division of John Wiley & Sons, Inc. New York. London. Sydney. Toronto.

Silverstein,R.M. *et al.,* (1998). "Spectrometric Identification of Organic Compound", 6th Edition, John Willy & Sons, Inc. New York.

World Health Organization, (2005). "National Policy on Traditional Medicine and Regulation of Herbal Medicines". Geneva.

STUDY ON ESSENTIAL OIL AND SOME BIOACTIVITIES OF *Citrus hystrix* DC. LEAF

Ei Ei Khaing[1] and Ohn Mar Tin[2]

Abstract

Citrus hystrix DC. (Shout-nu) used in household remedy for medicinal purposes was chosen for present study. Gastrointestinal tract problems and some diseases caused by mosquito become challenges in Myanmar people that many researchers have revealed the finding results of therapeutic properties from natural sources. The aim of this study is to analyze essential oil extracted from *Citrus hystrix* leaf Essential oil (0.02 g, 0.04 %) was extracted from leaf sample by hydro distillation method and was analysed by Fourier transform infrared (FT IR) spectroscopy. The chemical composition with molecular mass in essential oil was then determined by gas chromatography-mass spectrometry (GC-MS). Eight compounds of terpenes: alpha-pinene, D-limonene, beta-ocimene, gamma-terpinene, isopulegol, citronellol, caryophyllene and beta-bisabolene were detected. By solvent extraction method, four crude extracts of *Citrus hystrix* leaf were prepared with various solvents: petroleum ether, ethyl acetate, 96 % ethanol and water. Antimicrobial activity of four crude extracts was investigated against ten microorganisms by paper disc diffusion method. It was found that all tested leaf extracts exhibited ten tested microorganisms with the inhibition zone diameters range between 9~27 mm. Nevertheless, acute toxicity of 96 % EtOH and water extracts from *Citrus hystrix* leaf was evaluated by the method of (OECD) guidelines 423 that all tested *Citrus hystrix* leaf sample showed no toxicity. In addition, larvicidal activity of PE, EtOAc, water extracts and essential oil was studied by WHO standard method. According to larvicidal activity test, PE extract and essential oil have the highest larvicidal activity *in vivo* test larvae model, 3rd and 4th instar *Aede*s larvae. This research can support to the formulation of antimicrobial drugs and can provide on alternative source of mosquito control agents.

Keywords: *Citrus hystrix* leaf, essential oil, terpenes, antimicrobial activity, acute toxicity, larvicidal activity

Introduction

Citrus hystrix DC. derived from the family Rutaceae is famous for household remedy and its edible fruit in Myanmar. It is called Shout-nu in Myanmar, wild lime in English and Nann-non in local name. The fruit and leaf of the plant are well-known in tropical Southeast Asia as their medicinal uses (Okuda, 2005). It is a thorny bush tree, 2 to 11 meters tall with aromatic and distinctively shaped "double leaves" shown in Figures 1(a) and (b). The fruit shown in Figure 1 (c) is rough and green, and ripens to yellow with the size 4 cm wide (Mabberley, 1997). The tree is native to tropical Southeast Asia and widely distributed in Myanmar (Kress, *et al.*, 2003). *C. hystrix* leaf contains high amounts of citronellal, ascorbic acid, limonene, sabinene, comphene, linalool, nerolidal, citronellic acid and terpinolene. In traditional Indian medicine, *C. hystrix* leaf is used for digestion, inflammation, detoxifying the blood, oral health, improving skin, reducing stress and strengthening immune system (Zaibunnisa and Chutima, 2012). The other uses are shampoos, soap, toothpastes, hair oils, body lotion, lipstick, facial makeup, perfume and fingernail polishes. In addition, it is also applied in food industry such as biscuit, juice, cake and candy. The leaf is very popular for ingredients in noodle soup in Thailand (Vermal, *et al.*, 2014). In developing countries, plants are the main source of medicine (Siripongvutikorn, *et al.*, 2014). Today, Myanmar government encourages indigenous forms of medicine. Therefore, this study intends to analyse the extracted essential oil and investigate some bioactivities of *C. hystrix* leaf sample. In the study, the sample collection, extraction and identification of essential oil, preparation of various crude

[1] Dr, Associate Professor, Department of Chemistry, Hinthada University
[2] Dr, Professor (Head), Department of Chemistry, Hinthada University

extracts, screening of antimicrobial activity, determination of acute toxicity and assessment of larvicidal activity from the leaf sample have been carried out.

Figure 1 (a) *C. hystrix* plant (b) *C. hystrix* leaf (c) *C. hystrix* fruit

Materials and Methods

Plant Materials

C. hystrix leaf was collected from Myanaung Township, Ayeyarwady Region. The plant was identified at Department of Botany, Yangon University. The sample was washed, cleaned and dried at room temperature for three weeks. Then the dried sample was powdered and stored in air-tight container.

Extraction of Essential Oil from *C. hystrix* Leaf by Hydro Distillation Method

The fresh *C. hystrix* leaf (50 g) was distilled with deionized water (400 mL) in Clevenger apparatus for 48 h. After the hydro distillation, the essential oil was collected as hydrosol form and then separated two layers of immiscible liquids: water and oil were partitioned with petroleum ether in a separating funnel. The petroleum ether soluble portion was taken and dried with anhydrous sodium sulphate followed by filtration. The yield percent of essential oil was calculated.

Characterization of Essential Oil Extracted from *C. hystrix* Leaf

The functional group of compounds in the essential oil extracted from *C. hystrix* leaf was analyzed by Fourier transform infrared (FT IR) spectroscopy and the chemical composition with molecular mass was determined by gas chromatography mass spectrometry (GC-MS).

Preparation of Crude Extracts of *C. hystrix* Leaf by Direct Extraction Method

The dried powdered sample (50 g) was extracted with petroleum ether (PE), ethyl acetate (EtOAc), 96 % ethanol (EtOH) 500 mL in separate conical flasks for three weeks at room temperature and filtered. Water extract of leaf sample was prepared by boiling 50 g of sample with 500 mL of distilled water for 6 h and filtered. The filtrates were concentrated by rotary evaporator to get crude extracts. The yield % of these extracts were determined and then stored in the refrigerator for the screening of bioactivities such as antimicrobial activity, acute toxicity and larvicidal activity.

In Vitro Study on the Antimicrobial Activity of *C. hystrix* Leaf by Paper Disc Diffusion Method

Paper disc diffusion method was used for the detection of antimicrobial activity of four crude extracts from *C. hystrix* leaf. The test procedure was as follows: the extracts (1 g each) were dissolved in 1 mL of their respective solvents; petroleum ether, ethyl acetate, 96 % ethanol and water, and introduced into sterile petri dishes for testing ten cultural bacterial strains: *Agrobacterium tumefaciens* NITE09678, *Aspergillus parascitius* IFO5123, *Bacillus subtilis*

IFO90571, *Candida albicans* NITE09542, *Micrococcus luteus* NITE83297, *Salmonnella typhi* AHU9743, *Escherichia coli* AHU5436, *Saccharomyces cerevisae* NITE52847, *Pseudomonas fluorescens* IFO94307 and *Staphylococcus aureus* AHU8465. The discs having 8 mm diameter each with 20 µg extract/disc were allowed to dry at 42 ˚C in incubator. The microbial suspension from test broth was streaked evenly into three places on the surface of assay medium agar plates with sterile cotton swab. After inoculation, the assay medium had dried for 5 min, the dried disc impregnated with crude extracts were placed on the agar with flamed forceps and gently pressed down to ensure proper contact. The assay medium in the absence of microorganisms was utilized as negative control, cultured with microorganisms was positive control, and antibiotics chloramphenicol was also used as standard for this study. After overnight incubation at 27 ˚C, the diameters of inhibition zones including 8 mm discs were measured.

In Vivo Study on the Acute Toxicity of *C. hystrix* Leaf on Albino Mice Model

The acute toxicity of 96 % EtOH extract and water extract of *C. hystrix* leaf was done by the method of (OECD) guidelines for Testing of Chemical 423 (OECD, 2001) with albino mice model at Laboratory Animal Services Division, Department of Medical Research (DMR), Yangon. According to the test description, total number of adult female albino mice, weighing (25-30 g) were selected and divided into five groups. Each group contained three animals. They were fasted for 18 h before giving the different doses of *C. hystrix*. Group (1) mice were orally administrated with 96 % EtOH extract of *C. hystrix* 2000 mg/kg dose. Group (2) mice were given orally with 96 % EtOH extract of *C. hystrix* 5000 mg/kg dose. Group (3) mice were also administered with water extract of *C. hystrix* 2000 mg/kg dose. Group (4) mice were orally administrated with water extract of *C. hystrix* 5000 mg/kg dose as shown in Figure 2. Then, Group (5) mice were performed as a control group besides they were treated with clean water and pellet from normal laboratory animal food of Laboratory Animal Services Division, DMR. All groups of mice were kept in the three mice per each cage in the separated room controlling temperature of 26 ± 1º C. After administration of the two extracts of *C. hystrix* on each group of animals were observed first 6 h continuously for mortality and behavior changes. Then, the animals were checked daily for fourteen days of acute oral toxicity experiment. The mortality during this period was noted as nil or percent death.

Figure 2 Acute Oral toxicity test with female albino mice

In Vivo Study on the Larvicidal Activity of *C. hystrix* Leaf on *Aedes aegypti* Mosquito Larvae

Strains of *Aedes aegypti* mosquito larvae and adult *Aedes* mosquitoes emerged from pupae were identified by morphological methods (Rampa and Prachong, 1994). The *Aedes aegypti* mosquitoes were collected from Hlaingthaya Township. Adults were provided with 10 % sucrose solution and 8 weeks old mouse for blood meal. Mosquitoes were held at 26 ± 2 ºC, 65-75 % relative humidity with a photo period of 12 h light and 12 h dark. *Aedes* larvae were used for testing insecticidal properties of *C. hystrix* leaf extracts and essential oil by WHO standard method (WHO, 2005). At first, various concentration of four tested samples: PE extract, EtOAc extract, water extract and essential oil from *C. hystrix* leaf were prepared freshly as 0.1 g, 0.05 g, 0.025 g, 0.0125 g and 0.00625 g in 100 mL each of distilled water in 150 mL plastic cups

respectively. Fifty (50) each 3rd and 4th instars *Aedes aegypti* larvae were put into different concentrations and also negative control (absence of sample) was done simultaneously. Larvae were exposed 24 h for each replication in various concentrations of samples in laboratory at 27-29 ºC and 70 to 80 % relative humidity. Five replicates were carried out and knockdown was checked after 60 min. Then, mortality was recorded after 24 h of exposure period. Knockdown and dead larvae were identified when the larvae failed to move after probing with a needle in the thorax region of the body. Lethal concentration LC_{50} and LC_{90} values for 95 % confidential limits were calculated by the equation of chi-square. Data entry and processing were made by using Microsoft Excel software. The average larval mortality data were subjected to probit analysis for calculating LC_{50} and LC_{90} values and other statistics at 95 % confidence limits of upper confidence limit and lower confidence limit, and chi-square values were calculated using the dose-effect probit analysis (Finney, 1971). Results with probability $p < 0.05$ were considered to be statistically significant.

Results and Discussion

Extraction and Characterization of Essential Oil from *C. hystrix* Leaf by Modern Techniques

The fresh leaf sample of *C. hystrix* was extracted by hydro distillation method with distilled water in Clevenger apparatus and yielded colourless essential oil (0.02 g, 0.04 %). It was identified by modern methods: FT IR spectroscopy and GC-MS spectrometry. According to FT IR spectrum of essential oil, the following groups could be assigned (Figure 3). The O-H stretching vibration for alcohol performed at 3361 cm^{-1}. The absorption bands at 2926 cm^{-1} and 2854 cm^{-1} showed symmetric and asymmetric C-H stretching of aliphatic hydrocarbon due to methyl and methylene group. The stretching vibration of C=O for ester was exhibited at 1728 cm^{-1}. The bending of methylene and asymmetric bending of methyl groups showed at 1456 cm^{-1}. The absorption of 1377 cm^{-1} showed symmetric bending of methyl group. The C-O stretching vibration of alcohol showed in the 1163 cm^{-1} region (Silverstein, 1991). In addition, the GC-MS analysis of essential oil could be deduced as eight compounds with these respective retention times (RT). These compounds could be assigned as alpha-pinene (RT: 3.46 min), D-limonene (RT: 3.97 min), beta-ocimene (RT: 4.11 min), gamma-terpinene (RT: 4.30 min), isopulegol (RT: 5.50 min), citronellol (RT: 6.45 min), caryophyllene (RT: 9.91 min) and beta-bisabolene (RT: 10.11 min) as shown in Figures 4 (a), (b), (c), (d), (e), (f), (g), (h) and Table 1. From the results of GC-MS and FT IR spectral data, it was concluded that extracted essential oil from leaf sample contained monoterpenes and sesquiterpenes.

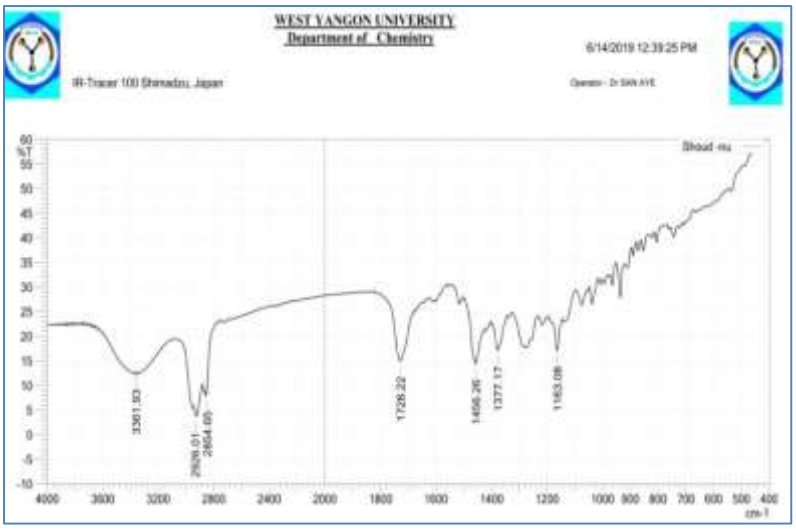

Figure 3 FT IR spectrum of essential oil (leaf oil) from *C. hystrix* leaf

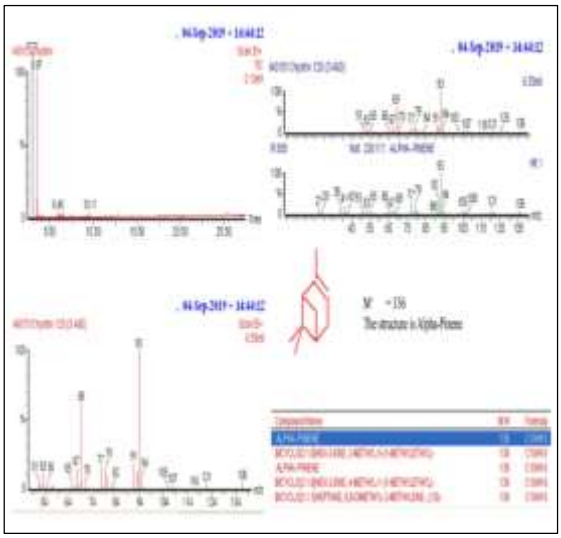

Figure 4 (a) GC- MS spectrum of compound 1from *C. hystrix* leaf at RT 3.46 min

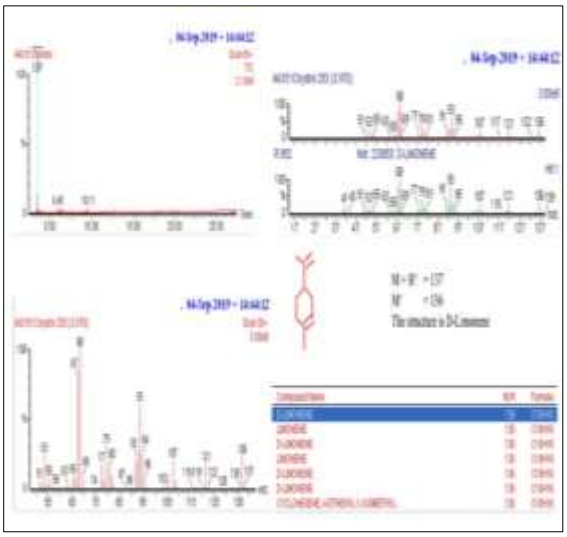

Figure 4 (b) GC- MS spectrum of compound 2 from *C. hystrix* leaf at RT 3.97 min

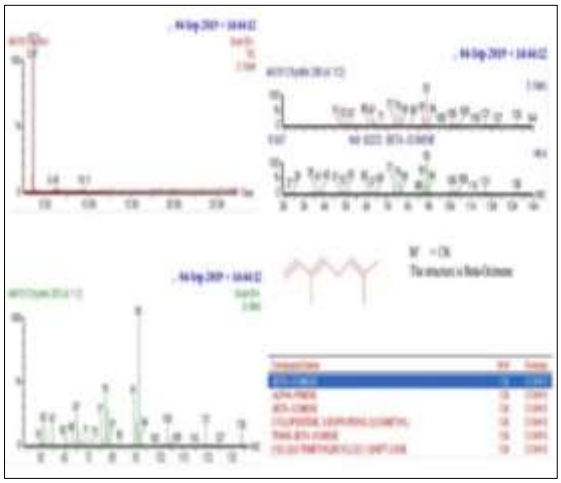

Figure 4 (c) GC- MS spectrum of compound 3 from *C. hystrix* leaf at RT 4.11 min

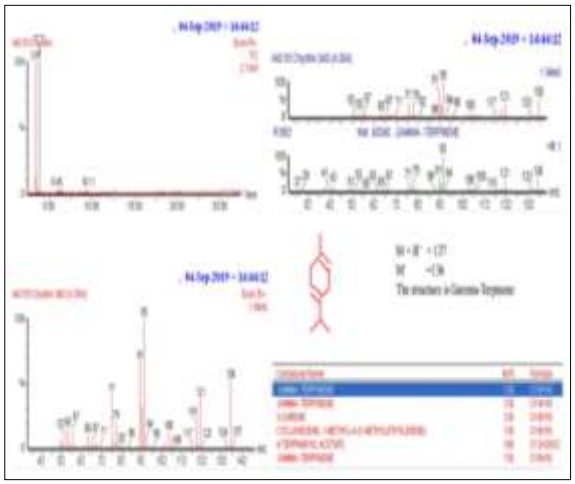

Figure 4 (d) GC- MS spectrum of compound 4 from *C. hystrix* leaf at RT 4.30 min

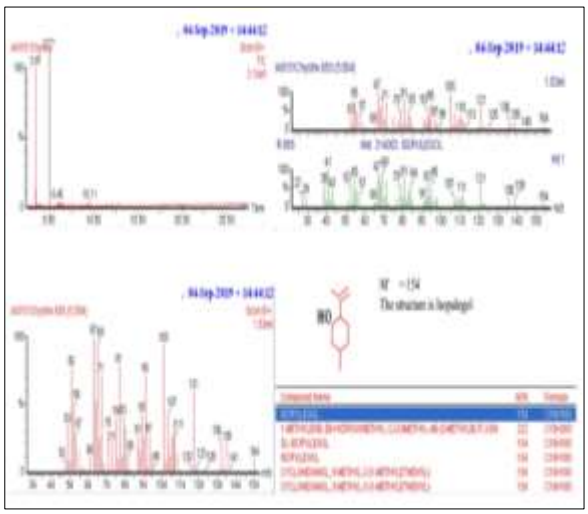

Figure 4 (e) GC- MS spectrum of compound 5 from *C. hystrix* leaf at RT: 5.50 min

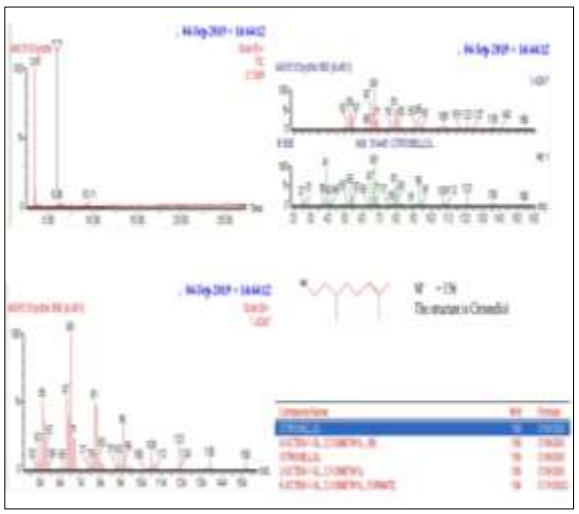

Figure 4 (f) GC- MS spectrum of compound 6 from *C. hystrix* leaf at RT 6.45 min

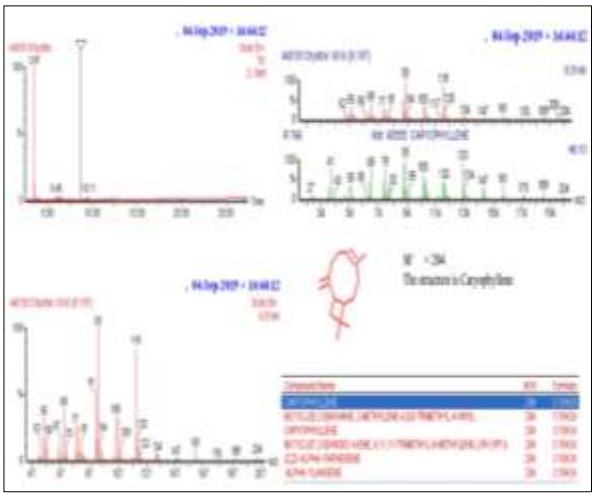

Figure 4 (g) GC- MS spectrum of compound 7 from *C. hystrix* leaf at RT 9.19 min

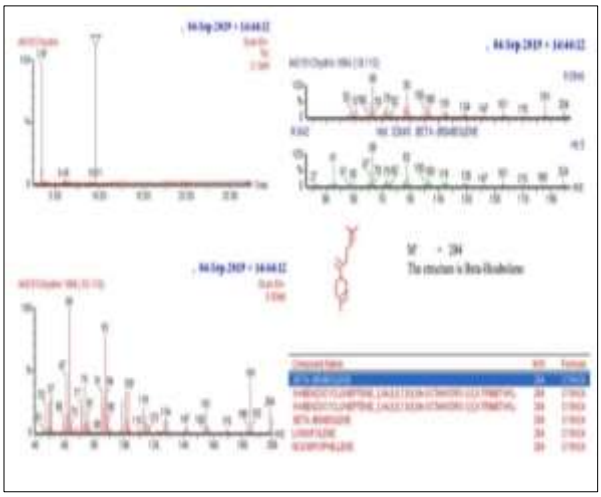

Figure 4 (h) GC- MS spectrum of compound 8 from *C. hystrix* leaf at RT 10.11 min

Table 1 The Nine Compounds detected by GC-MS in Essential Oil from *C. hystrix* Leaf at Different Retention Times (RT)

Compounds	Name	Structure	Molecular weight	Formula	RT (min)
1	alpha-pinene		136	$C_{10}H_{16}$	3.46
2	D-limonene		136	$C_{10}H_{16}$	3.97
3	beta-ocimene	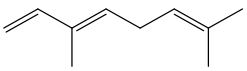	136	$C_{10}H_{16}$	4.11
4	gamma-terpinene	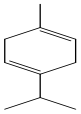	136	$C_{10}H_{16}$	4.30
5	isopulegol	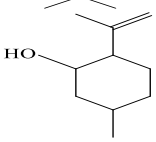	154	$C_{10}H_{18}O$	5.50
6	citronellol	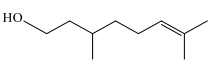	156	$C_{10}H_{20}O$	6.45
7	caryophyllene	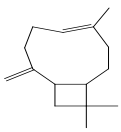	204	$C_{15}H_{24}$	9.19
8	beta-bisabolene	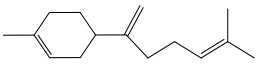	204	$C_{15}H_{24}$	10.11

Screening of Antimicrobial Activity of *C. hystrix* Leaf Extracts by Paper Disc Diffusion Method

The dried leaf powder collected from Myanaung Township, Ayeyarwady Region was extracted with various solvents and the yield % of PE extract (3.40 %), EtOAC extract (7.20 %), 96 % EtOH extract (12.60 %) and water extract (18.20 %) were obtained respectively. These four

crude extracts were tested with ten microorganisms such as *Agrobacterium tumefaciens* NITE09678, *Aspergillus parascitius* IFO5123, *Bacillus subtilis* IFO90571, *Candida albicans* NITE09542, *Micrococcus luteus* NITE83297, *Salmonella typhi* AHU9743, *Escherichia coli* AHU5436, *Saccharomyces cerevisae* NITE52847, *Pseudomonas fluorescens* IFO94307 and *Staphylococcus aureus* AHU8465. The ten tested microorganisms obtained from the source of NITE & Kyowa Hakko Co. Ltd., Japan were cultured at Biological Resources and Biotechnology Development Center (BDC) of Pathein University and then screened at Department of Chemistry, Hinthada University. The microorganism species used in the test are responsible for plant diseases, diarrhea food poisoning, GI tract infection and abscess in skin, nose. The measurable inhibition zone diameter of crude extracts showed the degree of antimicrobial activity (Figures 5 and 6).

From the results given in Table 2, it was observed that all four crude extracts of *C. hystrix* leaf exhibited inhibition zone diameters range between 9-27 mm against ten tested microorganisms. In addition, the inhibition zone diameter (27 mm) of EtOAc extract showed the most potent activity against *Candida albicans* NITE09542. Thus, it may be effectively used as active remedy for this treatment of their related diseases and fungal infection.

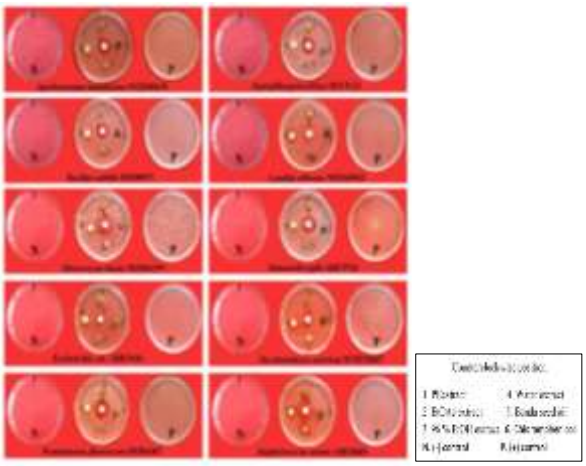

Figure 5 Inhibition zones of various crude extracts from *C. hystrix* leaf against ten species of microorganisms

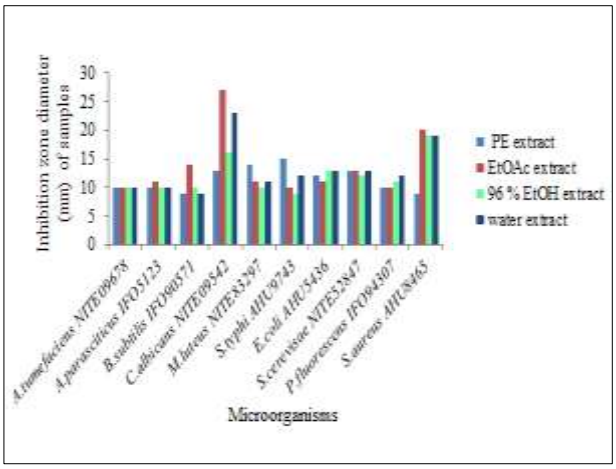

Figure 6 Comparison of inhibition zone diameters for various crude extracts of *C. hystrix* leaf against ten species of microorganisms.

Table 2 Inhibition Zone Diameters of Various Test Samples of *C. hystrix* Leaf Against ten Microorganisms

No	Microorganisms*	Inhibition Zone Diameters (mm) of Test samples				
		PE extract	EtOAc extract	EtOH extract	H_2O extract	Std.
1.	*Agrobacterium tumefaciens* NITE09678	10	10	10	10	26
2.	*Aspergillus parasciticus* IFO5123	10	11	10	10	26
3.	*Bacillus subtilis* IFO90571	9	14	10	9	24
4.	*Candida albicans* NITE09542	13	27	16	23	34
5.	*Micrococcus luteus* NITE83297	14	11	10	11	30
6.	*Salmonella typhi* AHU9743	15	10	9	12	26
7.	*Escherichia coli* AHU5436	12	11	13	13	19
8.	*Saccharomyces cerevisae* NITE52847	15	15	12	13	26
9.	*Pseudomonas fluorescens* IFO94307	10	10	11	12	28
10	*Staphylococcus aureus* AHU8465	9	20	19	19	30

Paper disc diameter– (8mm), 9 mm ~ 14 mm(+), 15 mm ~ 19 mm (+ +), 20 mm ~ above (+ + +)
Tested microorganisms (From the source of NITE & Kyowa Hakko Co. Ltd., Japan *) Std. = Chloramphenico

Study on Acute Toxicity of Ethanol and Water Extracts from *C. hystrix* Leaf

Acute toxicity on 96 % ethanol and water extracts of *C. hystrix* leaf was studied with the dosage of 2000 mg/kg and 5000 mg/kg body weight in albino mice. The condition of mice was recorded after administration for fourteen days. All groups of animals were also observed still alive and did not show any visible symptoms of toxicity like restlessness, respiratory disorders, convulsion, aggressive activities, coma and death. All dosages of *C. hystrix* samples showed no toxicological clinical signs and no mortality of all the groups of mice during fourteen days (Tables 3 and 4).

Table 3 Acute Toxicity Effect of 96 % EtOH and Water Extracts of *C. hystrix* Leaf on Albino Mice Model (after Fourteen Days Administration)

No	Groups of Albino Mice	Administrated Extracts of *C. hystrix* Leaf	Dosages (Single dose) mg/kg	Number of Death	% of Death
1	Group 1	96 % EtOH extract	2000	Nil	0
2	Group 2	96 % EtOH extract	5000	Nil	0
3	Group 3	Water extract	2000	Nil	0
4	Group 4	Water extract	5000	Nil	0
5	Group 5	No administration (Control)	No dosages	Nil	0

Nil = no lethality of the albino mice

Table 4 Observation of Toxic Clinical Signs on 96 % EtOH and Water Extracts *C. hystrix* Leaf in Acute Toxicity Test with Albino Mice

No	Signs of Toxicity	Group 1 2000 mg/kg	Group 2 5000 mg/kg	Group 3 2000 mg/kg	Group 4 5000 mg/kg	Group 5 No administration (Control)
1	Difficult breathing	-	-	-	-	-
2	Restlessness	-	-	-	-	-
3	Convulsion	-	-	-	-	-
4	Coma	-	-	-	-	-
5	Death	-	-	-	-	-

- = did not show any visible symptoms of toxicity

Examination of Larvicidal Activity of *C. hystrix* Leaf Extracts (Crudes) and Essential Oil Against 3rd and 4th Instars *Aedes aegypti* Larvae

From the results of current study, it was noted that the lowest knockdown effect occurred at 0.00625 g/mL dilution of *C. hystrix* leaf extracts such as PE, EtOAc, water and essential oil with the percent knockdown 24.0 %, 10.8 %, 6.0 % and 12.8 % respectively. In addition, the highest knockdown effect of *Aedes aegypti* larvae was observed in 96.0 % knockdown at 0.1 g/mL of PE extract followed by 90.0 % knockdown at 0.1 g/mL of essential oil from *C. hystrix* of leaf sample (Table 5). Furthermore, the percent in the lowest mortality effect for *C. hystrix* leaf extracts such as PE, EtOAc, water extracts and essential oil were 28.40 %, 31.6 %, 10.40 % and 32.8 % respectively at 0.00625 g/mL dilution. And then, the highest mortality effect of *Aedes aegypti* larvae was found out 99.20 % mortality at 0.1 g/mL dilution of essential oil followed by 98.40 % mortality at 0.1 g/mL dilution of PE extract of *C. hystrix* leaf (Table 6). The concentration of 50 % mortality (LC_{50}) value of PE, EtOAc, water extracts and essential oil against 3rd and 4th instars

Aedes aegypti larvae were found in 0.0133 g/mL, 0.0123 g/mL, 0.027 g/mL, 0.0114 g/mL and also 90 % mortality (LC_{90}) value of leaf extracts were found to be 0.0528 g/mL, 0.0697 g/mL, 0.122 g/mL, 0.0452 g/mL respectively as shown in Table 7. In addition, the lowest amount of 0.0114 g/mL of essential oil was needed for 50 % mortality (LC_{50}) and 0.0452 g was needed for 90 % mortality (LC_{90}) of *Aedes* larvae. Out of these tested leaf samples, essential oil was found to be the most active against 3rd and 4th instars *Aedes aegypti* larvae.

Table 5 Knockdown Effect (Within 60 min) on Various Dilutions of *C. hystrix* Leaf Extracts and Essential Oil Against 3rd and 4th Instars *Aedes aegypti* Larvae

Concentrations (g / 100 mL)	Number of Knockdown and % Knockdown of *C. hystrix* Leaf Extracts (Crudes) and Essential oil			
	PE extract	EtOAc extract	Water extract	Essential oil
0.1	240 (96.0)	169 (67.6)	157 (62.8)	225 (90.0)
0.05	201(80.4)	114 (45.6)	57 (22.8)	174 (69.6)
0.025	157 (62.8)	80 (32.0)	41(16.4)	90 (26.0)
0.0125	106 (42.4)	41(16.4)	26 (10.4)	65 (26.0)
0.00625	60 (24.0)	27 (10.8)	15(6.0)	32 (12.8)
Control	0	0	0	0

Total larvae = 250

Table 6 Mortality Effect (Within 24 h) on Various Dilutions of *C. hystrix* Leaf Extracts (Crudes) and Esssential oil against 3rd and 4th instars *Aedes aegypti* larvae

Concentrations (g / 100 mL)	Number of Mortality and % Mortality of *C. hystrix* Leaf Extracts (Crudes) and Essential oil			
	PE extract	EtOAc extract	Water extract	Essential oil
0.1	246 (98.4)	238 (95.2)	221 (88.4)	248 (99.2)
0.05	211 (84.4)	209 (83.6)	162 (64.8)	209 (83.6)
0.025	160 (64.0)	161 (64.4)	121 (48.4)	170 (68.0)
0.0125	124 (49.6)	117 (46.8)	69 (27.6)	149 (59.6)
0.00625	71 (28.4)	79 (31.6)	26 (10.4)	82 (32.8)
Control	0	0	0	0

Total larvae = 250

Table 7 Lethal Concentration (LC) Values of *C. hystrix* Leaf Extracts (Crudes) and Essential oil Against 3rd and 4th Instars *Aedes Aegypti* Larvae

Lethal Concentration (LC)	*C. hystrix* Leaf Extracts (Crudes) and Essential oil			
	PE extract	EtOAc extract	Water extract	Essential oil
LC_{50}	0.0133	0.0123	0.027	0.0114
LC_{90}	0.0528	0.0697	0.122	0.0452
Chi square χ^2	0.0742	0.0191	0.0177	0.1561
D_f	4	4	4	4
P value	0.05	0.05	0.05	0.05

LC_{50} = Lethal Concentration dose 50, LC_{90} = Lethal Concentration dose 90, d_f = *degree of freedom*

Conclusion

Colourless essential oil (0.02 g, 0.04 %) was obtained from the plant, *C. hystrix* leaf by hydro distillation method. In addition, GC-MS analysis of essential oil could be deduced as alpha-pinene (RT: 3.46 min), D-limonene (RT: 3.97 min), beta-ocimene (RT: 4.11 min), gamma-terpinene (RT: 4.30 min), isopulegol (RT: 5.50 min), citronellol (RT: 6.45 min), caryophyllene (RT: 9.91 min) and beta-bisabolene (RT: 10.11 min). Crude extracts were prepared from *C. hystrix* leaf using PE, EtOAc, 96 % EtOH and water as their solvent polarity. These extracts were used to test antimicrobial activity, acute toxicity and larvicidal activity.

Screening of antimicrobial activity of various crude extracts such as PE, EtOAc, EtOH and H_2O extracts from *C. hystrix* leaf sample was also investigated by employing paper disc diffusion method against ten tested microorganisms responsible for plant diseases, diarrhea, typhoid, food poisoning, GI tract infection and abscess in skin, nose. It was observed that all extracts of *C. hystrix* leaf exhibited inhibition zone diameters between 9~27 mm against ten tested microorganisms. Out of these extracts, EtOAc extract of leaf sample was found to be the most potent activity and especially against *Candida albicans* NITE09542 responsible for abscess caused by fungus. By OECD guidelines 423 with albino mice, it was found that there was no acute toxicity in the selected sample. The larvicidal activity of three crudes (PE, EtOAc and water extracts); leaf extracts and essential oil obtained from *C. hystrix* leaf were investigated in the range of 0.00625 to 0.1 g/mL by *Aedes* larvae method at DMR. From the observation, the highest knockdown of *Aedes* larvae was found at the concentration of 0.1 g/mL of PE extract. The highest mortality effect (99.20 %) of *Aedes* larvae was found in the concentration of 0.1 g/mL of essential oil. The lowest mortality effect (10.4 %) of water extract was observed at the concentration of 0.00625 g/mL. Among them, the essential oil showed the highest lethal concentration activity (LC_{50} = 0.0114 g/mL and LC_{90}= 0.0452 g/mL). From larvicidal activity test, the extract provide could an alternative sources of mosquito control agents. In addition, to herbal formulation for maintaining human health.

Acknowledgements

We would like to express our heartfelt gratitude to Dr Nilar Myint, Rector and Dr Mar Lar, Pro-Rector, Hinthada University, for their giving permission to report this research paper. We would also like to extend our gratitude to Dr. Thi Thi Aye, Professor, Department of Chemistry, Hinthada University, for her enthusiastic reading as well as supporting in this research and faculty members of our Department. We deeply thanks to responsible and honorable persons of Myanmar Academy of Arts and Science for giving opportunity to publish this paper.

References

Finney, R. (1971). *Probit Analysis*. Cambridge: 3rd Ed., Cambridge University Press, pp. 9968-9972

Kress, W.J., Defilipps, R.A., Farr, E. and Yin Yin Kyi. (2003). *A Checklist of the Trees, Shrubs, Herbs and Climbers of Myanmar*. Washington, DC, USA: 1st Ed., Department of Systematic Biology- Botany, National Museum of Natural History, p. 87

Mabberley, D.J. (1997). "A Classification for Edible *Citrus* (Rutaceae)". *Telopea*, vol. 7, (2), pp. 167-172

OECD (Organization for Economic Co-operation and Development). (2001). "Guidance Document on Accute Oral Toxicity Testing". OECD Series on Testing and Assessment No. 24, *ENV/JM/MONO*, vol. 4, pp. 8-22

Okuda, T. (2005). "Systematics and Health Effects of Chemically Distinct Tannin in Medicinal Plants". *Phytochemistry*, vol. 66, pp. 2012 – 2031

Rampa, R. and Prachong, P. (1994). "Illustrated Keys to the Medically Important Mosquitos of Thailand". *Southeast Asian Journal of Tropical Medicine and Public Health,* vol .25 (1), pp.1-66

Silverstein, R.M., Bassler, G.C. and Terence, C.M. (1991). *Spectrometric Identification of Organic Compounds*, Singapore: 5th Ed., John Wiley and Sons, Inc., pp. 289-315

Siripongvutikorn, S., Sriket, C. and Sriket, P. (2014). "Phytochemical of Thai Local Edible Herbs". *Inetrnational Food Research Journal,* vol. 21, pp.1009-1011

Vermal, S.C., Vashishth, E., Singh, R., Pant, P. and Padhi, M.M. (2014). "A Review on Phytochemistry and Pharmacological Activity of Parts of *C. hystrix* Used as an Ayurvedic Medicine". *World Journal of Pharmaceutical Research*, vol. 3(5), pp.138-158

WHO (2005). "World Health Organization Guidelines for Laboratory and Field Testing of Mosquito Larvicides". Geneva, *WHO/CDS/WHOPES/GCDPP*

Zaibunnisa, A.H. and Chutima, W. (2012). "Extraction of Volatile Oil from Kaffir Lime Leaves (*Citrus hystrix*) Using Pressurized Liquid Extraction". *International Journal of Food Nutrition and Public Health*, vol. 5, p. 201

ECO-FRIENDLY STARCH SILVER NANOCOMPOSITES FILM FROM *TRITICUM AESTIVUM* L. AND *MANIHOT ESCULENTA* C. AND THEIR ANTIMICROBIAL ACTIVITIES

Nwe Thin Ni[1], Aung Kyaw Moe [2], Aung Than Htwe[3]

Abstract

In this research work, the eco-friendly starch silver nanocomposite films from *Triticum aestivum* L. (Wheat) and *Manihot esculenta* C. (Cassava Roots) were studied. Biosynthesis of starch silver nanoparticles was conducted by using silver nitrate as metal precursor and the starch solution of two plants: *T. aestivum and M. esculenta* as reducing and capping agents. The characterization of prepared starch capped silver nanoparticles and nanocomposite films from Wheat Flour and Cassava Roots were confirmed by XRD, FESEM and FT IR. The average crystallite sizes of prepared silver nanoparticles from *T. aestivum* (Wheat Flour) and *M. esculenta* (Cassava Root) were obtained in the range of 25-30 nm from XRD data. Different ratios of starch silver nanocomposite film were performed by the various concentrations of starch Wheat Flour solution, starch Cassava Root solution, silver nitrate solution, different stirring times and different temperatures. In addition, mechanical properties of prepared nanocomposite films were determined by thickness, tear strength, tensile strength and elongation at break. The swelling [S%] of the prepared nanocomposite films in distilled water was calculated. The antimicrobial activity of prepared nanocomposite film of Cassava Root was higher than those of pure starch extract of wheat flour and Cassava Root against *S. aureus* and *B. subtilis* by agar well diffusion method.

Keywords: biosynthesis, mechanical properties, *Triticum aestivum* L., *Manihot esculenta* C., nanocomposite

Introduction

In the green synthesis method, extracts from biological agents such as microbes and plants can be employed either as reducing or protective agent for the fabrication of metal nanoparticles. In these extracts, various combinations of biomolecules which have the reducing potential can be found such as amino acids, vitamins, proteins, enzymes, and polysaccharides that are environmentally benign, yet chemically complex. For instance, the unicellular green algae *Chlorella vulgaris* extract was utilized to synthesize single-crystalline silver nano-plates at room temperature (Mason *et al.*, 2012). Proteins in the extract were suggested to perform dual function of Ag^+ reduction and shape-control in the synthesis (Annamalai and Nallamuthu, 2016). Organic-inorganic nanocomposites have been studied because of their unique properties for superior to those of individual components (Kusuktham, 2010). Composite materials based on this nature of matrix phase can be divided into polymeric, ceramic and metallic composites (Alves and Mali, 2007). Plastic packaging provides excellent protection for the product and it is cheap to manufacture. But the source of plastics are raising environmental problems in waste for long period of time and that cause a pollution. To prevent the pollution of environment, Wheat Flour silver nanocomposite and Cassava Roots nanocomposite that can be easily degraded in the environment has been focused, (Chivrac *et al*., 2010). The Wheat flour and Cassava Roots are a polymeric carbohydrate consisting of a large number of glucose units joined by glycosidic bonds. It is the most common carbohydrate in human diet (Averous,2004). The physical properties of Wheat Flour and Cassava Roots were possessed hydroxyl groups to form intermolecular hydrogen bonds. From the reported data, Wheat Flour and Cassava Roots have been used as a binder in making paper and

[1] Dr, Professor, Department of Chemistry, Kyaing Tong University

[2] Research Scientist, Chulalongkorn University, Petroleum & Petrochemical College, the Centre of Excellent in Petrochemical and Material Science, Bangkok, Thailan

[3] Assistant Lecturer, Department of Chemistry, University of Yangon

miscellaneous uses including adsorbents, textiles and adhesives and also used in the foodstuff industries, soap, boundary and cosmetic products (Khozemy *et al*., 2018).

Plasticizers are additives that increase the plasticity or decrease the viscosity of a material. These are the substances which are added in order to alter their physical properties (Baharuddin *et al.*,2016). Almost 90% of plasticizers are used in PVC, giving this material improved flexibility and durability and used in films and cables. Glycerol was used as a plasticizer and added in the starch dispersion (Chillo *et al.*, 2008). Nanocomposites (NCs) are wide class of materials that include particulate substances, which have one dimension less than 100 nm at least (Orida and Raji, 2013). Nanocomposites (NCs) showed characteristic colours and properties with the variation of size and shape, which can be utilized in biomedical applications (Dalton *et al.*, 2003). Difficulties have been encountered in preparing composites with very fine particles due to their induced agglomeration and non-homogeneous distribution (Hoiby *et al*., 2010). Composites consist of a metal matrix filled with nanoparticles producing remarkable physical and mechanical properties when compared to those of the matrix, and include several different techniques for characterizing particle size distribution (Fama *et al*., 2007). In this research, the prepared nanoparticles and nanocomposites are characterized by FESEM, XRD, FTIR and their mechanical properties, and swelling properties were conducted.

Materials and Methods

Sample Collection and Scientific Identification of Two Plants

In this present study, the first one of the selected sample of *T. aestivum* L. (Wheat) was collected from Seik Tein Village, Kyaukpadaung Township, Myingyan District, Mandalay Region and the second one of the selected sample of *M. esculenta* C. (Cassava Roots) obtained from Yin Taik Kone Village, Kyauktaga Township, Taungoo District, Bago Region, in the middle of December 2018. These collected samples were identified at the Department of Botany, Taungoo University.

Preparation of Starch and Starch Solution from *T. aestivum* (Wheat) and *M. esculenta* (Cassava Roots)

The collected samples (1 kg each) were washed, peeled and sliced. By using the wet method, the fresh samples were blended with distilled water and the filtrates were decanted and air dried at room temperature for one week and finally starch powdered was obtained. Then, these dried powdered samples of starch were stored in air-tight container to prevent moisture and other contamination. And then, the starch powdered (60 g each) of both *T. aestivum* and *M. esculenta* were weighed in electric balance and placed into a beaker. The distilled water (200 mL) was added to the sample and boiled for one hour at the water bath. Then it was cooled at room temperature and centrifuged at 6000 rpm for 30 min. The water soluble starch was used as a reducing agent as well as stabilizing agent for preparation of NPs (Nanoparticles) and NCF (Nanocomposite Film).

Preparation of Silver Nanoparticles Using Starch Solution of *T. aestivum* and *M. esculenta*

The prepared starch solutions (200 mL each) of *T. aestivum* (Wheat) and *M. esculenta* (Cassava Roots) were added to the 0.001 M of $AgNO_3$ solution (600, 800 and 1000 mL) with the different volume ratios of 1:3, 1:4 and 1:5 v/v in each conical flask under aseptic condition. The flasks were heated and stirred with magnetic stirrer at different temperatures (40 °C, 50 °C and 60 °C) and different stirring times (20 min, 40 min and 60 min). Then, the flasks were placed in a dark place over night. A change in the colour was observed indicating the formation of silver nanoparticles. The solution was centrifuged at 6000 rpm for 20 min to obtain silver nanoparticles

and supernatant was discarded. Then, obtained particles from *T. aestivum* L. (Wheat) and *M. esculenta* C. (Cassava Roots) were washed to purify and dried at 100°C in an oven for 24 h.

Preparation of Starch Silver Nanocomposite Films Using Starch Solution of *T. aestivum* and *M. esculenta*

The starch solution (200 mL) of different sources of *T. aestivum* and *M. esculenta* and 0.001M of $AgNO_3$ solution (600, 800 and 1000 mL) as the different volume ratios of 1:3, 1:4 and 1:5 v/v, respectively, were placed in each conical flask under aseptic condition. These flasks were heated at 60°C and stirred on the magnetic stirrer and cooled for 15 min. A change in colour was observed. Next, sodium hypochlorite (1mL) was added to decolourize the above solution. Then, the plasticizer, glycerin was added to the solutions and stirred continuously throughout the reaction times (20 min, 40 min and 60 min). The solutions were then made into films by pouring onto a melamine shallow plate. Solvent casting methods was used at high temperature (120°C) to obtain the films. Gel of the casted films was allowed to stand at low temperature for more than 12 h for the crystallization to obtain Wheat Flour Starch Silver Nanocomposite Film (WFSSNCF) and Cassava Roots Starch Silver Nanocomposite Film (CRSSNCF).

Characterization of Prepared Silver Nanoparticles and Nanocompostites Film

The prepared starch silver nanoparticles and nanocomposties from *T. aestivum* and *M. esculenta* were characterized by FESEM, XRD, and FTIR. The surface morphology of silver nanoparticles and silver nanocomposites was characterized by field emission scanning electron microscopy FESEM, for external porosity and micro texture. The average crystallite size of prepared silver nanoparticles and nanocomposite film from *T. aestivum* L**.** and *M. esculenta* C. were determined by XRD analysis and calculated by Debye Scherrer's equation.

Determination of thickness of prepared nanocomposite films

The thickness of prepared nanocomposite films (WFSSNCF, CRSSNCF) of different ratios of (Wheat flour: silver nitrate) and (Cassava roots: silver nitrate) were measured using slide clipper by changing different areas of film thickness and also mean values were calculated.

Determination of mechanical properties of prepared nanocomposite films

The prepared nanocomposite films of WFSSNCF and CRSSNCF were cut off and dimension of ended tested film were clamped in the jaws of a testing machine. One jaw was fixed and the other was movable at a rate of 100 mm/min. The tensile strength was recorded in MPa. Then, the percent elongation at break and tear strength were calculated.

Determination of swelling properties of prepared nanocomposite films

The prepared WFSSNCF and CRSSNCF films were cut into (1×1) inches size and dried in vacuum oven for 2 h. Next, the cut films were immersed into distilled water for 20 min, 40 min and 60 min, respectively. Then, the films were removed from distilled water and weighed again. This testing was repeated three times. The percent of swelling was calculated based on the dry weight and wet weight.

Screening of Antimicrobial Activities of Pure Starch, Silver Nanocomposite Film

The inhibitory effect of the wheat flour, Cassava Roots and prepared NCF were evaluated against six microorganisms by using agar well diffusion method. Two small holes of 10 mm diameter each were cut out in the inoculated agar to place samples to be tested. The volume of each sample placed in each hole was 0.1 mL. The starch extract of wheat flour, cassava roots, and silver

NCFs were tested. The petri-dishes were incubated at 37°C for 24 h and the diameters of clear inhibition zone appeared around the holes were measured.

Results and Discussion

Silver Nanoparticles

Starch powder samples were extracted from *T. aestivum* L. (Wheat) and *M. esculenta* C. (Cassava Roots) for the synthesis of NPs and NCF. The yield percents of starch powdered samples were about 8% each from *T. aestivum* L. (Wheat) and *M. esculenta* C. (Cassava Roots). Then, freshly starch solutions were prepared for synthesis of NPs and NCF.

Silver nanoparticles were formed with a colour change from yellow to brownish-black colour during the reaction period of 20 min. The colour change of brownish-black was observed in the formation of silver NPs and it was due to the effect of reducing agent as well as capping agent of starch from *T. aestivum* L. (Wheat) and *M. esculenta* C. (Cassava Roots). The reaction mixture of each starch solution (*T. aestivum* L. and *M. esculenta* C.) and $AgNO_3$ solution with the volume ratio of 1:3 (v/v) at 60 °C and stirring time of 60 min was not in the colloidal state and could be filtered easily than other conditions. The particles obtained were washed and dried at 100 °C in an oven for 24 h. The dried nanoparticles were obtained as 1.215 g from wheat and 1.564 g from cassava roots.

Starch Silver Nanocomposite Film

The starch powdered samples prepared from Wheat Flour and Cassava Roots were used as capping agent as well as reducing agent. The silver nitrate (0.001 M) was used as metal precursor. The nanocomposite film prepared by using starch and silver nitrate with the volume ratio of 1:3 (v/v) was found to have a very smooth surface. Thus, it was chosen for characterization and determination of its mechanical properties.

Characterization of Prepared Silver Nanoparticles

FESEM analysis and XRD analysis

The field emission scanning electron microscopy (FESEM) images of silver NPs prepared by using starch from *T. aestivum* (Wheat) and *M. esculenta* (Cassava Roots) are shown in Figures 1 and 2. The surface morphology of silver NPs showed more spherical and granular nature using *M. esculenta* (Cassava Roots) starch than that of *T. aestivum* (Wheat) starch. In addition, the average particle size of silver NPs using *M. esculenta* (Cassava Roots) starch was 25 nm and that using *T. aestivum* (Wheat) starch was 30 nm by XRD analysis (Figures 3 and 4).

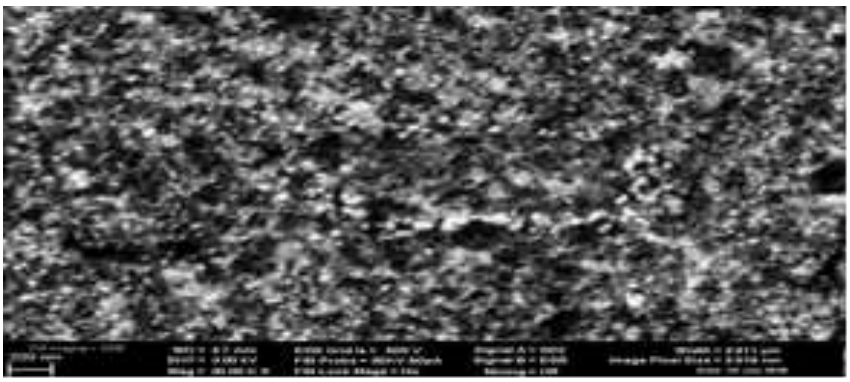

Figure 1 FESEM image of silver NPs using *T. aestivum* (Wheat) starch

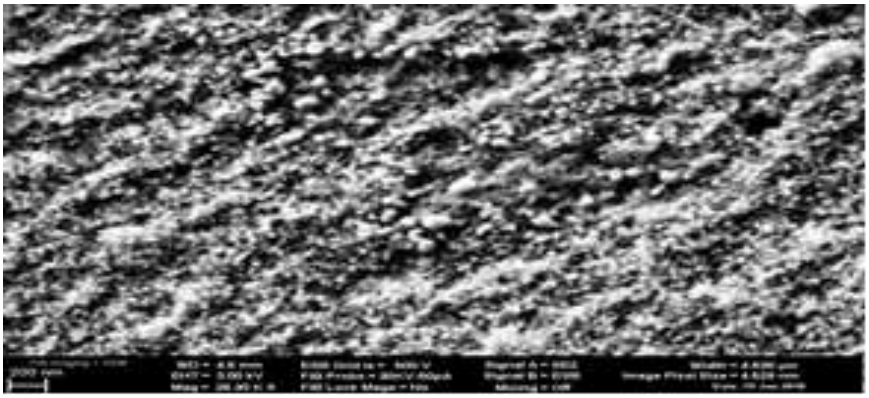

Figure 2 FESEM image of silver NPs using *M. esculenta* (Cassava Roots) starch

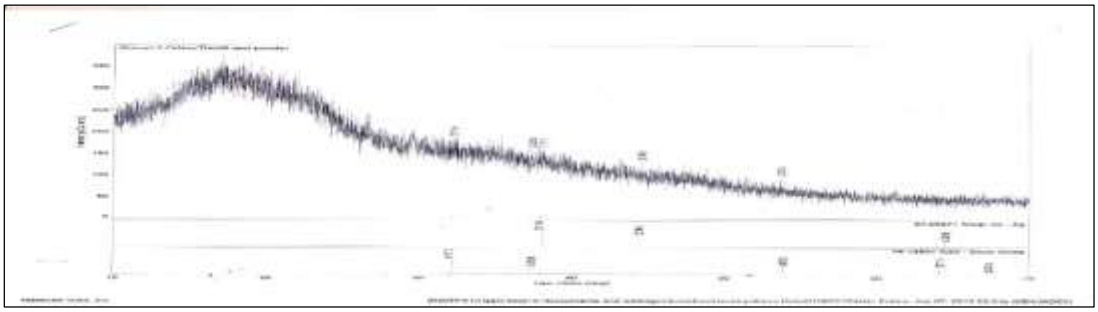

Figure 3 X ray diffractogram of prepared silver NPs using *T. aestivum* (Wheat) starch

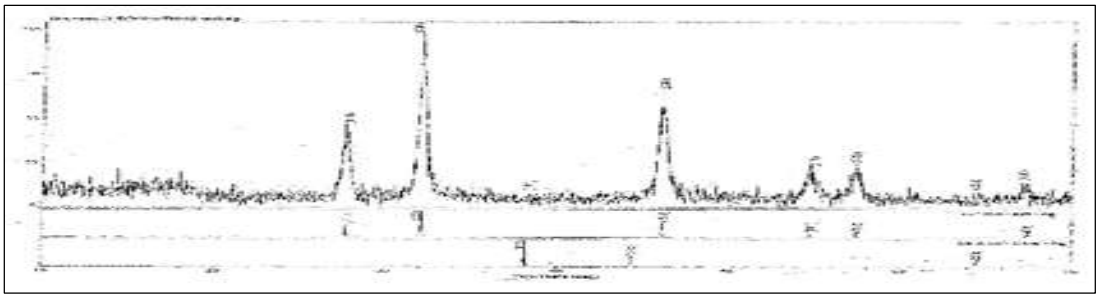

Figure 4 X ray diffractogram of prepared silver NPs using *M. esculenta* (Cassava Roots) starch

Characterization of Starch Silver Nanocomposite Films

FESEM analysis

The scanning electron microscopy images of starch silver nanocomposite films (WFSSNCF and CRSSNCF) from *T. aestivum* (Wheat) starch and *M. esculenta* (Cassava Roots) starch are shown in Figures 5 and 6. The surface morphology of silver nanocomposites film (CRSSNCF) was observed more spherical in nature than (WFSSNCF).

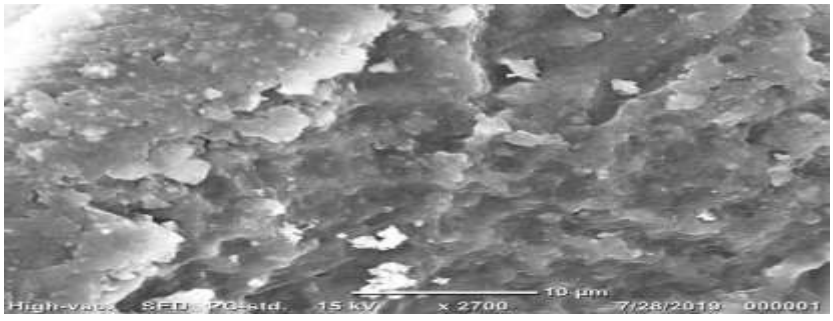

Figure 5 Surface morphology of prepared WFSSNCF from *T. aestivum* (Wheat) starch

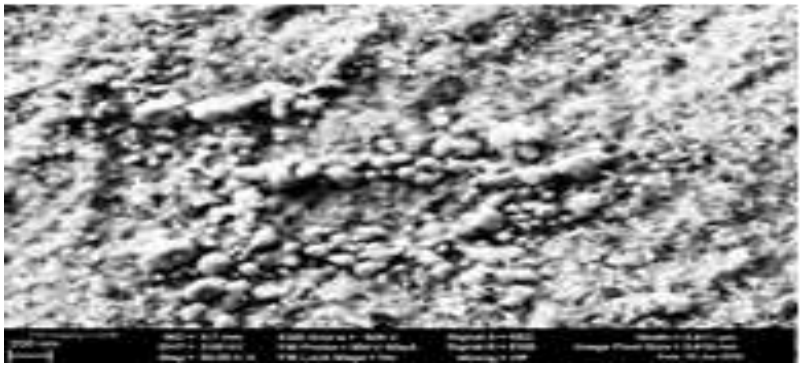

Figure 6 Surface morphology of prepared CRSSNCF from *M. esculenta* (Cassava Roots) starch

XRD Analysis of Prepared Nanocomposite Film

The X ray diffractograms of silver nanocomposites films (WFSSNCF, CRSSNCF) obtained by using starch and $AgNO_3$ solutions with the volume ratio of (1:3) are shown in Figures 7 and 8. The average crystallite size of CRSSNCF using *M. esculenta* C. (Cassava Roots) was observed as 40 nm and that of WFSSNCF using *T. aestivum* L. (Wheat) was 49 nm by XRD analysis data.

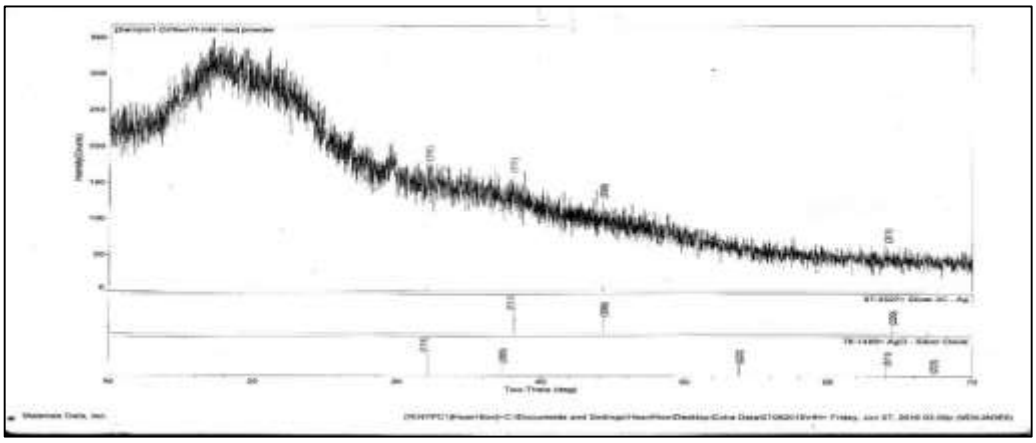

Figure 7 X ray diffractogram of prepared nanocomposite film of WFSSNCF

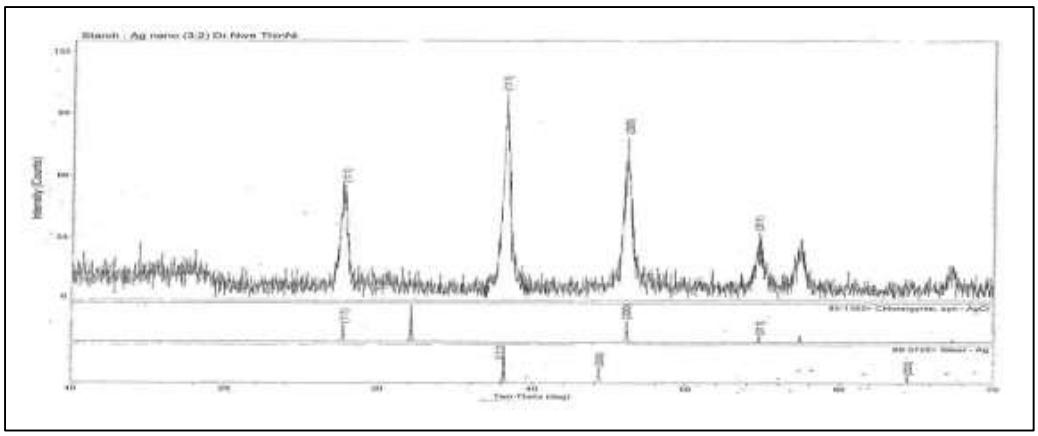

Figure 8 X ray diffractogram of prepared nanocomposite film of CRSSNCF

FTIR analysis

From the observation of surface morphology of prepared nanocomposite film, CRSSNCF was observed as more intense spherical in nature and smaller in particle size than prepared WFSSNCF. Therefore, the prepared nanocomposite film of CRSSNCF was studied by FTIR analysis. The absorption bands of the starch powder of *M. esculenta* (Cassava Roots) and prepared silver nanocomposite film (CRSSNCF) are depicted in Figures 9 and 10. From the FTIR spectrum of pure starch powder of cassava roots, the peaks were observed at 3389 cm^{-1} which may be due to the overlapping of O-H stretching bands. The peak at 2998 cm^{-1} represents aliphatic C-H stretching and that at 1643 cm^{-1} indicates O-H bending. The peak at 1153 cm^{-1} is attributed to C-O stretching vibration and those at 1413 and 1344 cm^{-1} indicate C-H bending. These functional groups may be involved in the formation of (CRSSNCF). Furthermore, in the composite film of CRSSNCF, a new moderate intense peak was observed at 540 cm^{-1} due to silver - oxide stretching vibration.

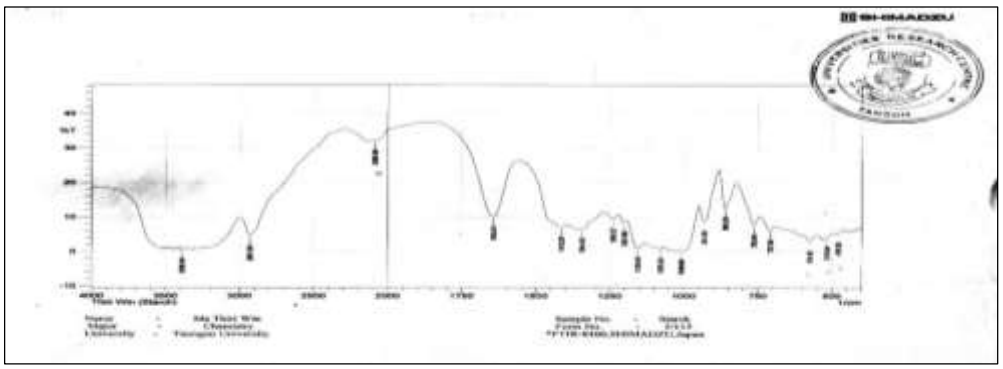

Figure 9 FTIR spectrum of pure starch powdered of *M***.** *esculenta* (Cassava Roots)

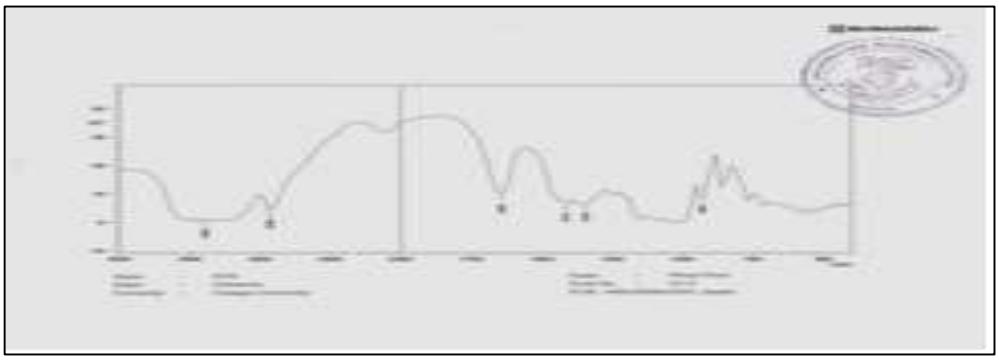

Figure 10 FTIR spectrum of prepared starch silver nanocomposite film of CRSSNCF

Mechanical Properties of Prepared Starch Silver Nanocomposite Film

The mechanical properties such as thickness, tensile strength, percent elongation at break and tear strength of prepared nanocomposites prepared by using starch and $AgNO_3$ with volume ratio of 1:3 are described in Table 1. Among them, higher values of the tensile strength (3.5 MPa), elongation at break (65%) and tear strength (58 kN/m) were observed in CRSSNCF compared to WFSSNCF (2.8 MPa of tensile strength, 43 % of elongation at break and 48 kN/m in tear strength).

Table 1 Mechanical Properties of Prepared Starch Silver Nanocomposite Films

Name of Composite film	Thickness (mm)	Tensile strength (MPa)	Elongation at break (%)	Tear strength (kN/m)
(WFSSNCF)	0.28	2.8	43	48
(CRSSNCF)	0.22	3.5	65	58

Swelling Properties of Prepared Starch Silver Nanocomposite Films

The swelling properties of nanocomposite films prepared by using starch and $AgNO_3$ with volume ratio of 1:3 v/v were determined. From these results, cassava root starch silver nanocomposite film (CRSSNCF) was found to have more swelling percent of 65% than WFSSNCF (52%) after reaction time of 60 min (Table 2).

Table 2 Swelling Properties of Prepared Starch Silver Nanocomposite Films

Time (min)	Swelling Properties (%) Prepared Nanocomposite Film	
	CRSSNCF	WFSSNCF
20	28	38
40	34	45
60	65	52

Antibacterial Activity of Pure Starch and Prepared Nanocomposite Film

For the determination of inhibitory effect, six strains of microorganisms were conducted. Different tested materials of watery extracts of pure starch from wheat flour, cassava roots and prepared silver NCF possessed inhibitory effect by using the agar well diffusion method. According to the experimental results, the prepared nanocomposite film CRSSNCF showed the most potent activity against *Staphylococcus aureus* with the maximum inhibition zone diameter of 20 mm and moderate activity of 19 mm for *Bacillus subtilis*. Moreover, the prepared pure starch and nanocomposite films showed mild antimicrobial activities on the remaining microorganisms. The pure starch powder of wheat flour showed lowest activity of 14 mm against *Candida albicans* (Table 3 and Figure 11).

Table 3 Comparison of Inhibition Zone Diameter of Pure Starch Powder of Wheat Flour, Cassava Root and Prepared Silver Nanocomposite Film

No.	Microorganisms	Inhibition Zone Diameter (mm)			
		Starch (Wheat)	Starch (Cassava)	WFSSNCF	CRSSNCF
1	*B. subtilis*	17 (++)	16 (++)	18 (++)	16 (++)
2	*S. aureus*	16 (++)	17 (++)	16 (++)	20 (+++)
3	*P.aeruginosa*	15 (++)	17 (+)	17 (++)	17 (++)
4	*B. pumilus*	15 (++)	16 (++)	18 (++)	19 (++)
5	*C. albicans*	14 (+)	15 (++)	18 (++)	15 (++)
6	*E. coli*	16 (++)	15 (++)	16 (++)	15 (++)

Agar well -10 mm, 10mm ~ 14 mm (+), 15mm ~19 mm (++), 20 mm above (+++)

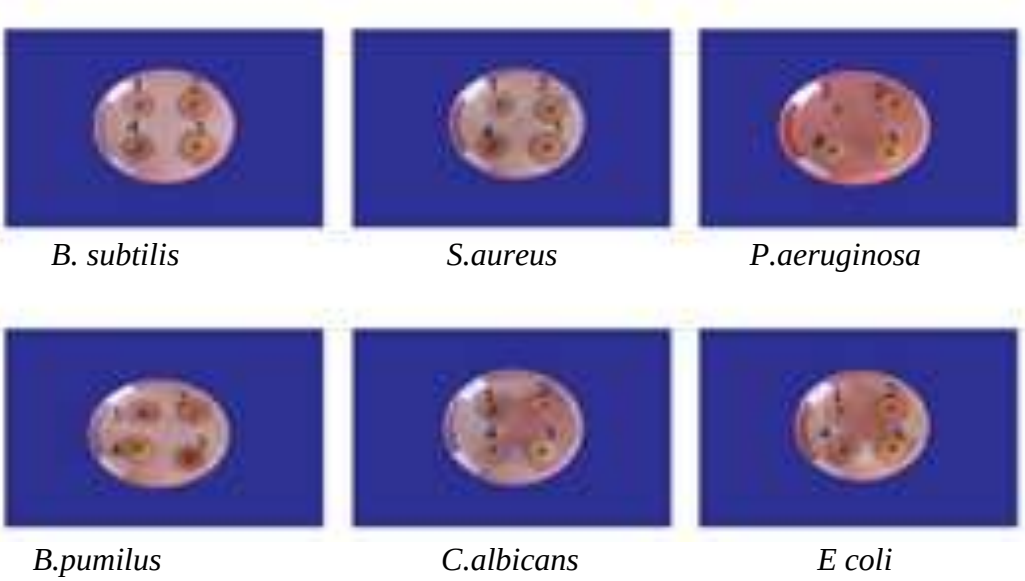

Figure 11 Antimicrobial activities of pure starch of wheat flour and cassava roots and prepared starch silver nanocomposite films against six microorganisms

Conclusion

From this research work, two kinds of selected materials namely, T. *aestivum* L. (Wheat) and *M. esculenta* C. (Cassava Roots) were used as the reducing agent and capping agent for the preparation of eco-friendly nanocomposite film by using the green synthesis. The surface morphology of prepared cassava roots starch silver NPs was observed as spherical in nature from FESEM analysis. XRD analysis showed the average crystallite sizes of silver nanoparticles using wheat and cassava roots were observed within the nano range (25-30) nm. Moreover, the surface morphology of prepared nanocomposite film of (CRSSNCF) was clearly seen as granular shape. The average particle sizes of CRSSNCF and WFSSNCF were found in the nano scale range from 40-50 nm. The stretching band of 3389 cm^{-1} due to the overlapping of O-H stretching was seen in the starch powdered of cassava root from the FTIR spectrum. Silver oxide peak was observed at 540 cm^{-1} in the prepared nanocomposite film of CRSSNCF). The more elongation at break was observed for the nanocomposite film CRSSNCF (65%) compared to WFSSNCF (43%). The swelling property of the prepared nanocomposite film WFSSNCF was lower than that of CRSSNCF. The antimicrobial activity of prepared CRSSNCF film possessed higher potent activity (20 mm) against *S. aureus* by agar well diffusion method. The prepared starch silver nanocomposite films can be used as coatings for food packaging as well as in biomedical applications such as wound healing and inflammation since they have been synthesized using a green synthesis method.

Acknowledgement

We would like to express our sincere thanks to Dr San San Mar, Rector, Kyaing Tong University for her valuable advices and generous support on this paper. Special thanks are due to Dr Tin Tun, Rector, Taungoo University for his kind suggestion and generous encouragements throughout the research work.

References

Alves, B. and Mali. S. (2007). "Effect of Glycerol and Amylose Enrichment on Cassava Starch Film Properties". *Journal of Food Engineering*, vol. 78, pp. 941-946

Annamalai, J. and Nallamuthu, T. (2016). "Green Synthesis of Silver Nanoparticles: Characterization and Determination of Antibacterial Potency". *Applied Nanosci*, vol.6, pp. 259-265

Averous, L. (2004). "Biodegradable Multiphase Systems Based on Plasticized Starch". *Journal of Macromolecular Science*, vol. 44, pp. 231-274

Baharuddin, N. H., Mohamed, M. and Muhammad. N. (2016). "Potential of Cassava Root as Raw Material for Biocomposite Development". *Journal of Engineering and Applied Sciences*, vol. 11(9), pp. 6133-6145

Chillo, S., Mastromatteo, M. and Flores, S. (2008). "Influence of Glycerol and Chitosan on Tapioca Starch-Based Edible Film Properties". *Journal of Food Engineering*, vol. 88, pp.159-168

Chivrac, F., Angellier-Coussy, H., Guillard, V. Pollet, E. and Averous, L. (2010). "How Does Water Diffuses in Starch/Montmorillonite Nano-biocomposite Materials?". *Carbohydrate Polymers*, vol.82, pp.128-135

Dalton, A.B., Collins, S., Munoz, E., Razal, J.M., Ebron, V.H., Coleman, J.P., Kim,B.G. and Baughman R.H, (2003). "Super-tough Carbon-nanotube Fibres". *Nature*, vol. 423 (6941), p.703

Fama, L., Goyanes, S. and Gerschenson, L. (2007). "Influence of Storage Time at Room Temperature on the Physicochemical Properties of Cassava Starch Films". *Carbohydrate Polymers*, vol. 70, pp. 265-273

Hoiby, N., Ciofu, O. and Bjarnsholt, T. (2010). "Pseudomonas Aeruginosa Biofilms in Cystic Fibrosis". *Future Microbiology*, vol. 5(11), pp. 1663-1674

Khozemy, E. E., Nasef, S.M. and Mahmoud, G.A. (2018). "Synthesis and Characterization of Antimicrobial Nanocomposite Hydrogel Based on Wheat Flour and Poly Vinyl Alcohol Using γ-Irradiation". *Adv Polym Technol.*, vol. 37, pp. 3254-3261

Kusuktham, B. (2010). "Surface Modification of Polyester Fabrics with Vinyltriethoxysilane". *Journal of Metals, Materials and Minerals.* vol. 20(2), pp. 85-88

Mason, C., Vivekanandhan, S., Misra, M. and Mohanty, A.K. (2012). "Switch Grass (*Panicum virgatum*) Extract Mediated Green Synthesis of Silver Nanoparticles". *World Journal of Nano Science and Engineering*, vol.2, pp.47-52

Oriola,K. and Raji,A. (2013). "Effects of Tuber Age and Variety on Physical Properties of Cassava [Manihot Esculenta (Crantz)] Roots". *Innovative Systems Design and Engineering*,Special Issue - 2nd International Conference on Engineering and Technology Research, vol.4 (9),pp. 15-24

STUDY ON THE STRUCTURAL, ELECTRICAL AND OPTICAL PROPERTIES OF $LiNi_{1-x}Co_xO_2$ ($0.3 \leq x \leq 0.5$) NANOCRYSTALLINE POWDER BY SOL–GEL METHOD

Naw Mon Thae Oo[1], Hnin Yu Wai[2], KhinThan Yee[3]

Abstract

The main aim of the research is to study structural, electrical and optical properties of $LiNi_{1-x}Co_xO_2$ ($0.3 \leq x \leq 0.5$) nanocrystalline powder. $LiNi_{1-x}Co_xO_2$ ($0.3 \leq x \leq 0.5$) nanocrystalline powders were prepared by a modified sol–gel method using lithium nitrate ($LiNO_3$), cobalt(II) nitrate ($Co(NO_3)_2.6H_2O$) and nickel(II) nitrate ($Ni(NO_3)_2.6H_2O$) as starting materials, de-ionized water as solvent, citric acid ($C_6H_8O_7.H_2O$) as chelating agents and carboxy methyl cellulose as dispersant agent. The prepared samples were calcined at 800 °C. The calcined powder was made as pellet form by using cold pressing method. The pellets were sintered at 900 °C. The pellets of $LiNi_{1-x}Co_xO_2$ were characterized by XRD, FT IR and SEM. Electrical properties were examined by LCR meter in the frequency range 100 kHz – 2 MHz and frequency depended on prepared sample. The optical properties were investigated by UV-Vis spectrophotometer. From XRD data, the observed values of the average crystallite sizes of $LiNi_{0.7}Co_{0.3}O_2$, $LiNi_{0.6}Co_{0.4}O_2$ and $LiNi_{0.5}Co_{0.5}O_2$ sintered at 900 °C were 13.58 nm, 44.31 nm and 48.03 nm, respectively. By increasing Co doping level, the average crystallite size also increased. FT IR spectra indicated the presence of the stretching vibrations of metal-oxygen (Ni-O and Co-O) chemical bonds. The spherical-shaped nanocrystalline powders were observed in SEM images. Electrical measurement revealed that the ac conductivity increased with increase in frequency. The ac conductivity of $LiNi_{0.5}Co_{0.5}O_2$ was lower than those of other two prepared nanopowder samples ($LiNi_{0.7}Co_{0.3}O_2$ and $LiNi_{0.6}Co_{0.4}O_2$). The value of ac conductivity was between 10^{-2} and 10^{-4} S cm^{-1}. Dielectric constants and dielectric loss were found to decrease with increase in frequency. The experimental results indicated that the ac conductivity, dielectric constant and dielectric loss of prepared samples depend on the frequencies. From UV-Vis data, the optical band gap values of $LiNi_{0.7}Co_{0.3}O_2$, $LiNi_{0.6}Co_{0.4}O_2$ and $LiNi_{0.5}Co_{0.5}O_2$ nanopowder samples were found to be 3.2, 3.4 and 3.6 eV, respectively. These band gap values (E_g) are also reliable within semiconductor band gap range.

Keywords: $LiNi_{1-x}Co_xO_2$ crystalline nanopowders, cold pressing method, ac conductivity, optical band gap

Introduction

$LiNi_{0.8}Co_{0.2}O_2$, a nickel-rich phase $LiNi_{1-x}Co_xO_2$ system, crystallizes in R $\bar{3}$ m space group with hexagonal ordering isostructural to $LiCoO_2$ and $LiNiO_2$. Small amount of cobalt in the frame work of $LiNi_{1-x}Co_xO_2$ reduce Jahn-Teller distortion of Ni^{3+} ions and help minimizing structural strain associated with distorted NiO_6 octahedra (Sathiya *et al*., 2011). $LiNi_{1-x}Co_xO_2$ (LNCO) are of great interest for use as positive electrode in rechargeable lithium-ion batteries because of their high specific capacity high voltage and long cycle-life (Baskaran *et al*., 2009). Oxide nanomaterials have been drawing wide attention due to their comparatively excellent electrical, optical or magnetic properties. Their properties such as electrical, optical, etc. can be tuned by engineering size, morphology or composition (Indulal *et al.*, 2017). The aim of this study was to prepare $LiNi_{1-x}Co_xO_2$ ($0.3 \leq x \leq 0.5$) nanocrystalline powders by a modified sol–gel method and to investigate the ac conductivity and dielectric properties of the prepared $LiNi_{1-x}Co_xO_2$, nanopowders.

[1] PhD Candidate, Department of Chemistry, University of Yangon
[2] Dr, Lecturer, Department of Chemistry, University of Yangon
[3] Dr, Lecturer, Department of Chemistry, University of West Yangon

Materials and Methods

Sample Collection

Lithium nitrate, cobalt nitrate, nickel nitrate, citric acid, carboxy methyl cellulose were purchased from BDH Chemicals Ltd., Poole, England. Citric acid was used as a chelating agent and carboxy methyl cellulose as a dispersant agent. Distilled water was used as the solvent in all analyses.

Preparation of $LiNi_{1-x}Co_xO_2$ ($0.3 \leq x \leq 0.5$) Nanocrystalline Powder

$LiNi_{0.7}Co_{0.3}O_2$, $LiNi_{0.6}Co_{0.4}O_2$ and $LiNi_{0.5}Co_{0.5}O_2$ nanocrystalline powders were prepared by sol-gel method using lithium nitrate, cobalt nitrate, nickel nitrate, citric acid and carboxy methyl cellulose (Zhu *et al*., 2010). Firstly, 6.9 g each of lithium nitrate, 20.35 g, 17.44 g and 14.54 g of nickel (II) nitrate and 8.73 g, 11.64 g and 14.55 g of cobalt (II) nitrate salts were added into 100 mL each of deionized water in three separate beakers to obtain molar ratios of 1:0.7:0.3, 1:0.6:0.4 and 1:0.5:0.5, respectively. Next, 42 g of citric acid (the molar ratio of citric acid/ total metal ions = 1) was added into 100 mL of deionized water. The individual solutions were mixed and after that with a small amount of carboxy methyl cellulose (the molar ratio of cellulose to total cations was 5×10^{-6}) was added into this solution. Each mixture solution was heated at 65 °C for 12 h under constant stirring to form the sol. The sol was then evaporated at 120°C in drying oven until the gel was formed. The gel solution was calcined at 800 °C for 4 h. Finally, the samples were finely ground in an agate mortar.

Preparation and Characterization of Pellets

The calcined black powders $LiNi_{1-x}Co_xO_2$ were pressed into pellets with diameter 1.256 cm and thickness 0.3 cm using MAEKAWA Testing machine. The pellets were sintered at temperature 900^0C for 4 h. The resulting pellet was characterized by XRD, SEM, FT IR techniques. The electrical and optical properties were investigated by LCR meter and UV-Vis spectrophotometer, respectively.

X-ray diffraction (XRD) analysis was carried out using Rigaku X-ray Diffractometer, RINI 2000/PC software, Cat. No 9240 J 101, Japan. FT IR spectrum was recorded in the range of 4000-400 cm^{-1} by using Perkin Elmer spectrum Two, FT IR spectrophotometer. The scanning electron microscopy (SEM) images were obtained using JSM-5610 Model SEM, JEOL-Ltd., Japan.

For the electrical conductivity measurements, the obtained samples were pressed in the form of pellet using MAEKAWA Testing machine. The dielectric permittivities such as D, K and tangent loss of composites were determined using LCR-B110G meter (DC 20-10 Hz) in the frequency range of 100 kHz-2 MHz at ambient temperature. Frequency dependent electrical conductivity was evaluated by using dielectric equation (Tharayil *et al*., 2008).

$$C = \frac{K \varepsilon_0 A}{d},\ \tan\delta = D = 1/(2\pi f R_p C_p),\ \omega = 2\pi f',\ \sigma_{ac} = \omega \tan\delta\ K\ \varepsilon_o$$

where, C is capacitance (pF), K is dielectric constant, ε_0 is electrical permittivity in vacuum (8.85×10^{-14} F cm^{-1}), d is sample thickness (cm), ω is circular frequency (MHz), D is dielectric loss factor (D), tan δ is dielectric loss tangent and σ_{ac} is electrical conductivity (S cm^{-1})**.**

Measurement of Optical Properties

Energy band gap of materials is related to absorption coefficient α by the Tauc's relationship. $\alpha h\nu = A\ (h\nu - E_g)^n$ where α is absorption coefficient (α = 2.303 A/t, where A is the

absorbance and t is the denoted thickness of the cuvette), A is constant, hν is photon energy and E_g is band gap (Tharayil *et al*., 2008).

Results and Discussion

XRD Analysis

The XRD patterns of the prepared $LiNi_{0.8}Co_{0.2}O_2$ nanocrystalline powders sintered at 900 °C are shown in Figure 1 and the average crystallite size, crystal system and lattice parameter are listed in Table 1. By increasing Co doping level, it was found that the diffraction peaks of pellet were narrow and more clear sharp peak at this temperature. The crystallite size of $LiNi_{1-x}Co_xO_2$ nanocrystalline powder was calculated by using Scherrer's equation (Ahmed *et al*., 2012).

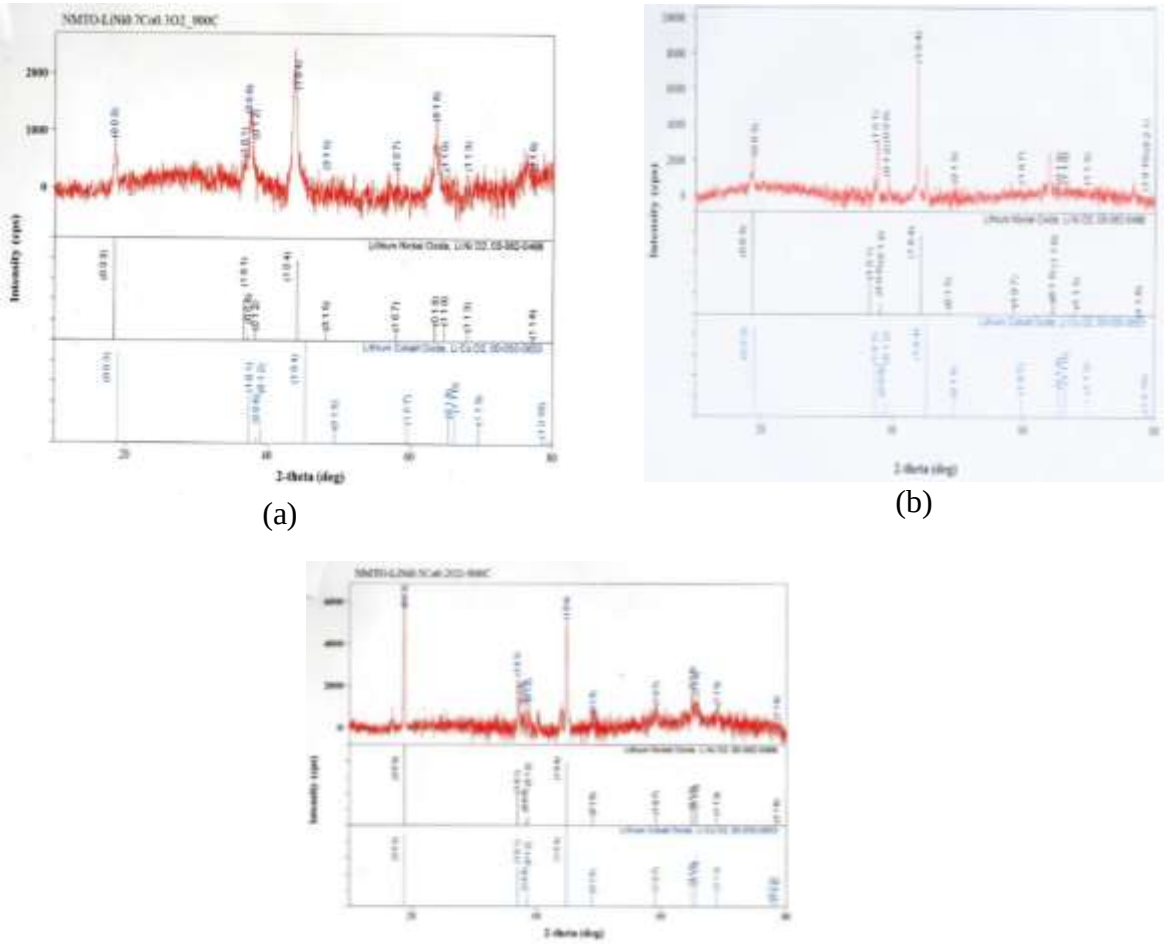

(a) (b)

(c)

Figure 1 X-ray diffraction patterns of (a) $LiNi_{0.7}Co_{0.3}O_2$ (b) $LiNi_{0.6}Co_{0.4}O$ and (c) $LiNi_{0.5}Co_{0.5}O_2$ powders sintered at 900 °C for 4 h

Table 1 Average Crystallite Size of the Prepared $LiNi_{1-x}Co_xO_2$ Powders

Samples	Average crystallite size (nm)	Lattice parameters (Å)		Crystal system
		a	c	
$LiNi_{0.7}Co_{0.3}O_2$	13.58	2.7979	14.1885	Hexagonal
$LiNi_{0.6}Co_{0.4}O_2$	44.31	2.8412	14.0712	Hexagonal
$LiNi_{0.5}Co_{0.5}O_2$	48.03	2.8386	13.9974	Hexagonal

FT IR Analysis

FT IR data indicated the presence of functional groups in the $LiNi_{1-x}Co_xO_2$ powder. The FT IR spectra of the prepared $LiNi_{1-x}Co_xO_2$ powder sintered at 900 °C are shown in Figure 2 and the spectral assignments shown in Table 2. In the spectrum of $LiNi_{1-x}Co_xO_2$ nanocrystalline powder, the peaks indicated the stretching vibration of metal oxygen bond (Nakamoto, 1970).

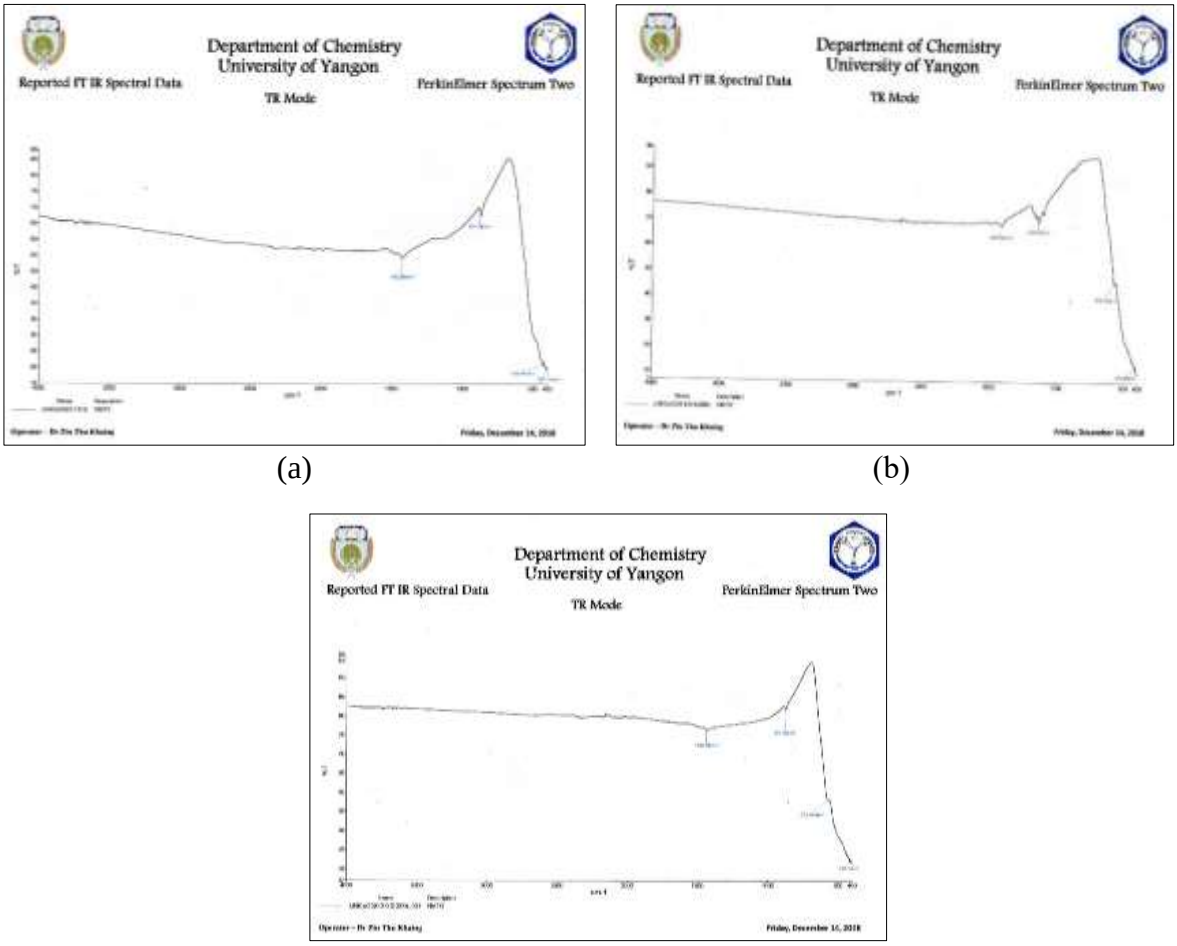

Figure 2 FT IR spectra of (a) $LiNi_{0.7}Co_{0.3}O_2$ (b) $LiNi_{0.6}Co_{0.4}O$ and (c) $LiNi_{0.5}Co_{0.5}O_2$ powders sintered at 900 °C for 4 h

Table 2 Band Assignments of FT IR Spectra of the Prepared $LiNi_{1-x}Co_xO_2$ Powders Sintered at 900 °C for 4 h

Observed wavenumber (cm^{-1})			*Literature wavenumber (cm^{-1})	Band assignments
$LiNi_{0.7}Co_{0.3}O_2$	$LiNi_{0.6}Co_{0.4}O_2$	$LiNi_{0.5}Co_{0.3}O_2$		
-	573	572	650-400	Stretching vibration of Co/Ni-O bond
427 407	416	412		

*Nakamoto, 1970

SEM Analysis

Surface morphology was studied by obtaining micrographs using JOEL-JSM-5610, Japan, Ion sputter-JEC-1600 (Sahoo *et al.*, 2010). The morphology of prepared $LiNi_{1-x}Co_xO_2$ powder was investigated by SEM. The SEM images of all the samples of $LiNi_{1-x}Co_xO_2$ sintered at 900 ºC showed the spherical agglomeration of porous nature and irregular shaped morphology (Figure 3).

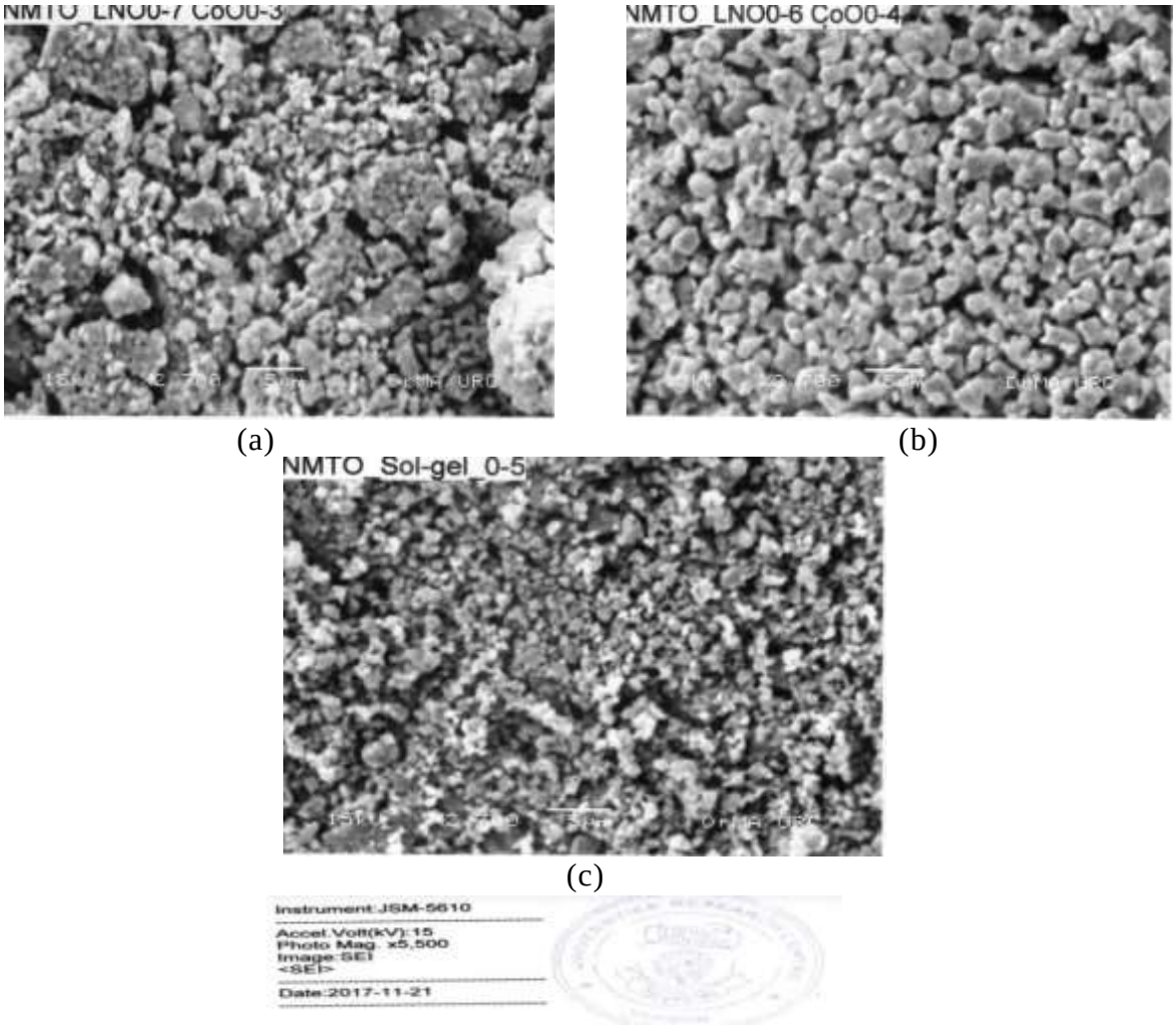

Figure 3 SEM micrographs of (a) $LiNi_{0.7}Co_{0.3}O_2$ (b) $LiNi_{0.6}Co_{0.4}O$ and (c) $LiNi_{0.5}Co_{0.5}O_2$ powders sintered at 900 °C for 4 h

Electrical Properties

Electrical properties were examined by LCR meter in the frequency range 100 kHz –2 MHz. The ac conductivity of $LiNi_{0.5}Co_{0.5}O_2$ was lower than the other prepared samples ($LiNi_{0.7}Co_{0.3}O_2$ and $LiNi_{0.6}Co_{0.4}O_2$) nanopowders as shown in Table 3 and Figure 4. The value of ac conductivity was between 10^{-2} and 10^{-4} S cm^{-1}. The ac conductivity increased with increase in frequency. The dielectric constant decreased with increasing frequency (Table 4 and Figure 5). At higher frequency, dielectric loss Tan δ was also found to decrease as shown in Table 5 and Figure 6.

Table 3 Changes of AC Conductivity of Prepared $LiNi_{1-x}Co_xO_2$ as a Function of Frequency at 2V

Frequency (Hz)	Electrical conductivity (S cm^{-1})		
	$LiNi_{0.7}Co_{0.3}O_2$	$LiNi_{0.6}Co_{0.4}O_2$	$LiNi_{0.5}Co_{0.5}O_2$
100000	1.45E-02	1.06E-02	4.60E-04
400000	1.68E-02	1.22E-02	9.01E-04
800000	2.04E-02	1.48E-02	1.56E-03
1200000	2.35E-02	1.70E-02	2.13E-03
1600000	2.58E-02	1.87E-02	2.61E-03
2000000	2.76E-02	2.01E-02	3.03E-03

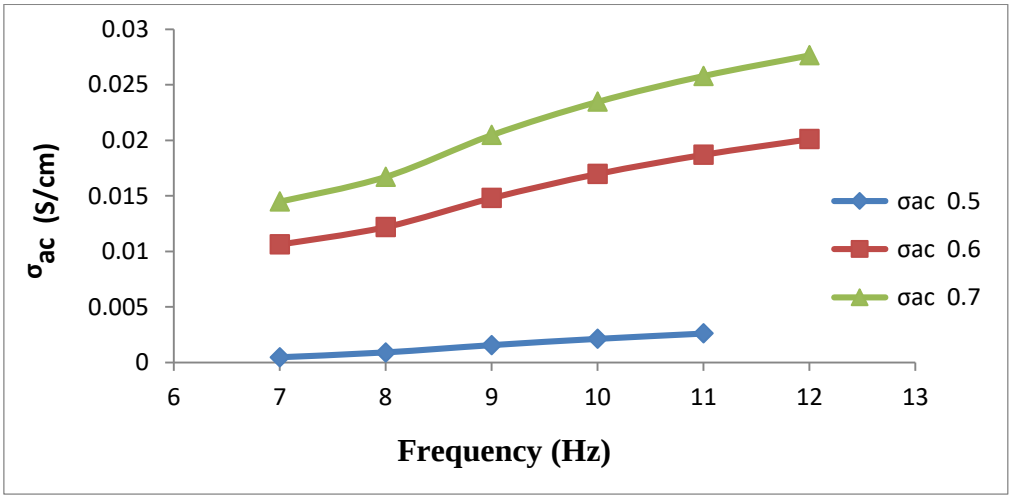

Figure 4 Variation of ac conductivity of prepared $LiNi_{1-x}Co_xO_2$ sintered at 900 °C as a function of frequency at 2 V

Table 4 Dielectric Constant (Tan δ) of Prepared $LiNi_{1-x}Co_xO_2$ as a Function of Frequency at 2V

Frequency (Hz)	Dielectric constant (K)		
	$LiNi_{0.7}Co_{0.3}O_2$	$LiNi_{0.6}Co_{0.4}O_2$	$LiNi_{0.5}Co_{0.5}O_2$
100000	5.42E+13	5.82E+13	1.55E+13
400000	4.77E+13	4.85E+13	1.28E+13
800000	4.27E+13	4.09E+13	1.14E+13
1200000	3.91E+13	3.59E+13	1.06E+13
1600000	3.68E+13	3.26E+13	1.01E+13
2000000	3.52E+13	3.03E+13	9.58E+12

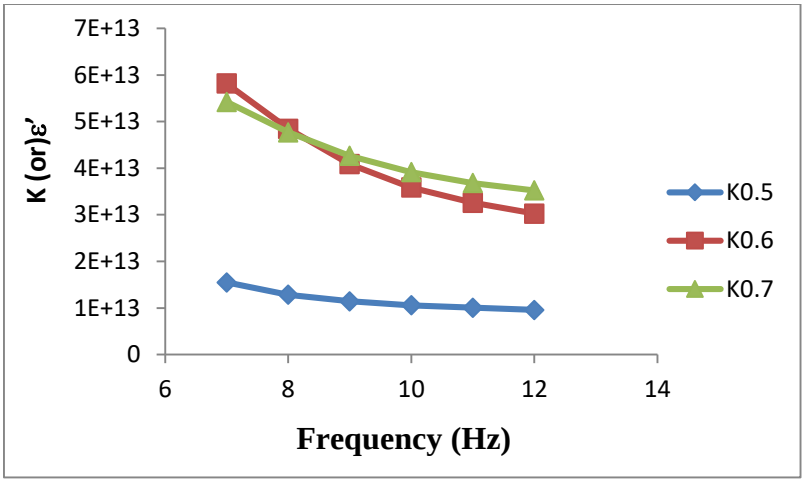

Figure 5 Variation dielectric constant of prepared $LiNi_{1-x}Co_xO_2$ sintered at 900 °C as a function of frequency at 2 V

Table 5 Dielectric Loss (Tan δ) of Prepared $LiNi_{1-x}Co_xO_2$ as a Function of Frequency at 2V

Frequency (Hz)	Dielectric loss (Tanδ)		
	$LiNi_{0.7}Co_{0.3}O_2$	$LiNi_{0.6}Co_{0.4}O_2$	$LiNi_{0.5}Co_{0.5}O_2$
100000	4.48E-09	3.52443E-09	5.35E-10
400000	1.55E-09	1.1492E-09	3.16E-10
800000	1.13E-09	7.7999E-10	3.07E-10
1200000	9.81E-10	6.50425E-10	3.01E-10
1600000	8.9E-10	5.71367E-10	2.92E-10
2000000	8.22E-10	5.13551E-10	2.85E-10

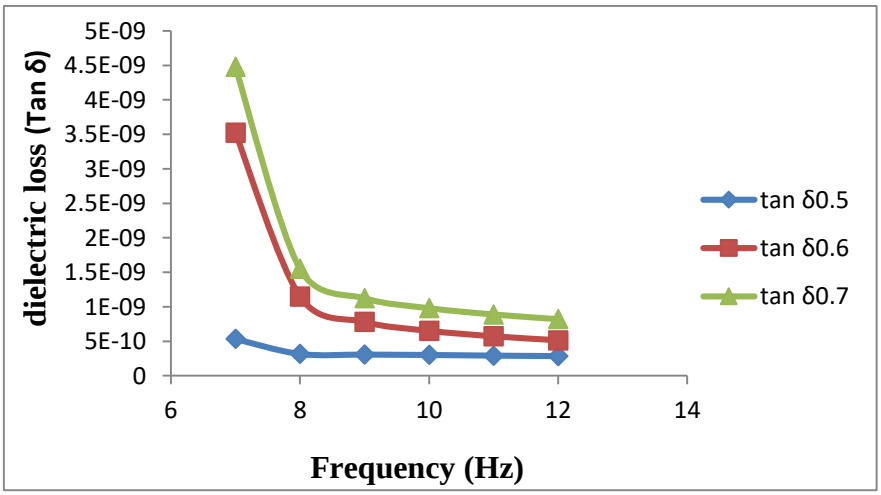

Figure 6 Variation dielectric loss of prepared $LiNi_{1-x}Co_xO_2$ sintered at 900 °C as a function of frequency at 2 V

Optical Properties

Figure 7 shows energy band gap for $LiNi_{0.7}Co_{0.3}O_2$, $LiNi_{0.6}Co_{0.4}O_2$ and $LiNi_{0.5}Co_{0.5}O_2$ nanocrystalline powders. The optical band gap is obtained by Tauc's equation. The band gap values for $LiNi_{0.7}Co_{0.3}O_2$, $LiNi_{0.6}Co_{0.4}O_2$ and $LiNi_{0.5}Co_{0.5}O_2$ powders were found to be 3.2, 3.4 and 3.6 eV, respectively.

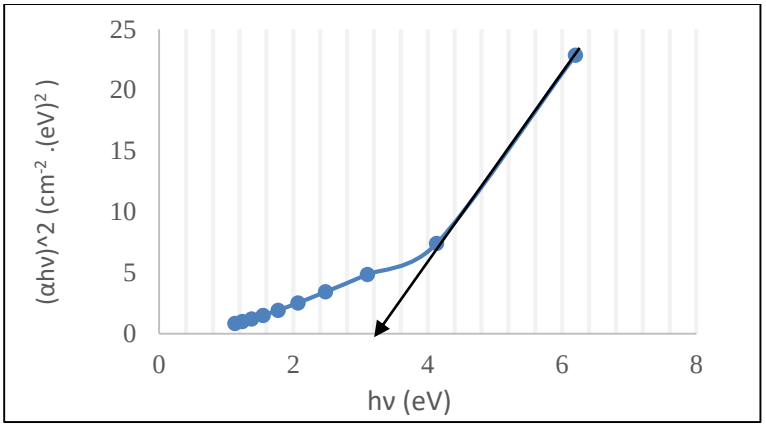

(a)

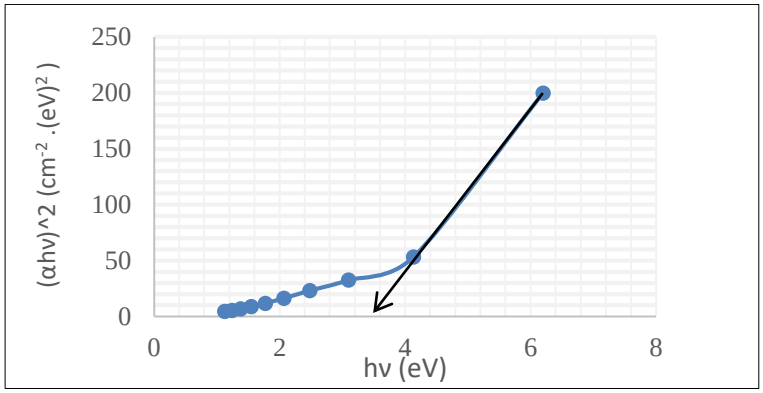

(b)

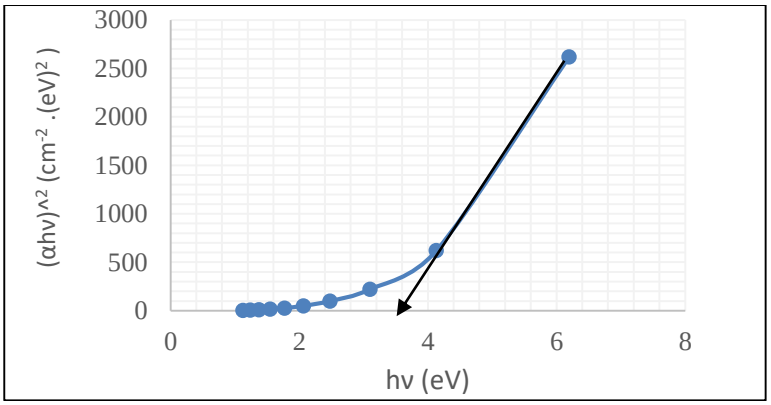

(c)

Figure 7 Tau's plot of (a)$LiNi_{0.7}Co_{0.3}O_2$ (b) $LiNi_{0.6}Co_{0.4}O_2$ and (c)$LiNi_{0.5}Co_{0.5}O_2$ at sintered temperature of 900 °C

Table 6 Optical Band Gap of the $LiNi_{1-x}Co_xO_2$ at Sintered Temperature (900 ˚C)

	Band gap (E_g) (eV)
$LiNi_{0.7}Co_{0.3}O_2$	3.2
$LiNi_{0.6}Co_{0.4}O_2$	3.4
$LiNi_{0.5}Co_{0.5}O_2$	3.6

Conclusion

$LiNi_{1-x}Co_xO_2$ nanocrystalline powder was prepared by using sol-gel method at sintering temperature of 900 °C. The crystallite sizes of $LiNi_{0.7}Co_{0.3}O_2$, $LiNi_{0.6}Co_{0.4}O_2$ and $LiNi_{0.5}Co_{0.5}O_2$ nanocrystalline powders were calculated to be 13.58, 44.31 and 48.03 nm, respectively. By increasing Co doping level, the average crystallite size also increased. $LiNi_{1-x}Co_xO_2$ nanocrystalline powder was indexed as the hexagonal crystal system. FT IR analysis showed the presence of the stretching vibrations of metal-oxygen bonds in $LiNi_{1-x}Co_xO_2$ powders. SEM micrographs exhibited the spherical shape of prepared $LiNi_{1-x}Co_xO_2$ samples sintered at 900 °C. The optical band gap value (E_g) of the Co doped $LiNiO_2$ was calculated from the UV-Vis spectrum by using Tauc's plot relation. By increasing Co doping level, the optical band gap value was slightly increased. The ac conductivity of $LiNi_{0.5}Co_{0.5}O_2$ was lower than those of other prepared samples ($LiNi_{0.7}Co_{0.3}O_2$ and $LiNi_{0.6}Co_{0.4}O_2$) nanopowder. The dielectric studies showed that with decreasing frequency, dielectric constant and dielectric loss were found to increase.

Acknowledgement

The authors would like to express their profound gratitude to the Department of Higher Education, Ministry of Education, Yangon, Myanmar, for provision of opportunity to do this research and Myanmar Academy of Arts and Science for allowing to present this paper.

References

Ahmed, M., Mohammad, R. F. and Reza, M. (2012). "Modified Scherrer Equation to Estimate More Accurately Nano-Crystalline Size Using XRD". *World Journal of Nano Science and Engineering*, vol.2, pp. 154-160.

Baskaran, R., Kuwata, N., Kamishima, O., Kawamura, J. and Selvasekarapandian, S. (2009). "Structural and Electrochemical Studies on Thin Flim $LiNi_{0.8}$. $Co_{0.2}O_2$ by PLD for Micro Battery". *Solid State Ionics*, vol. 15, pp 636-643

Indulal, C.R., Biju, R., Nand, D. and Raveendran, R. (2017). "Dielectric and Optical Band Gap Studies of Nanostructured Manganese Nickel Oxide and Cobalt Nickel Oxide". *Oriental Journal of Chemistry*, vol.33(3), pp 1581-1588

Nakamoto, K. (1970). *Infrad Spectra of Inorganic and Coordination Compounds*. New York: 2nd ed., Wiley Interscience Publication

Sahoo, S. K., Agrawal, K., Polke, B.G. and Raha, K.C. (2010). "Characterization of γ and α-Fe_2O_3 Nanopowders Synthesized by Emulsion Precipitation Calcination Route and Rheological Behaviour of α- Fe_2O_3". *International Journal of Engineering, Science and Technology*, vol.2, pp. 118-126

Sathiya, M., Hemalatha, K., Ramesh, K., Shukla, A.K. and Parkash, A.S. (2011). "Nitrates- melt Synthesized $LiNi_{0.8}Co_{0.2}O_2$ and its Performance as Cathode in Li-ion Cells". *Journal of Material Science*, vol. 34, pp. 1693-1698

Tharayil, N., Raveendran, R., Vaidyan, A. V. and Chitha, P.G. (2008). "Optical, Electrical and Studies of Nickel - cobalt Oxide Nanoparticles". *Indian J. Eng. and Mater. Sci.*, vol.15, pp. 489-49

Zhu, C., Yang,C., Yang,W-D., Wu, M-S., Ysai,H-M.,Hsieh, C-Y. and Fang,H-L. (2010). "Preparation and Electrochemical Characterization of $LiNi_{0.8}$. $Co_{0.2}O_2$ Cathode Material by A Modified Sol–gel Method". *J. Appl. Electrochem.*, vol. 40, pp. 1665–1670

STRUCTURAL AND OPTICAL PROPERTIES OF $LaFeO_3$ AND $La_{0.8}Sr_{0.2}FeO_3$ POWDERS

Mya Theingi[1], Subhajit Nandy[2], Sudakar Chandran[3]

Abstract

$LaFeO_3$ is one of the perovskite structure materials and its optical, electrical and magnetic properties had been frequently investigated. In the present work, nanoparticles of pure $LaFeO_3$ was prepared using the citrate sol-gel method. Sr^{2+} ion doped $LaFeO_3$ or $La_{0.8}Sr_{0.2}FeO_3$ was also synthesized by the same method to study the enhancement of the structural and optical properties. The synthesis involved the sol-gel method, followed by gradual heat treatment for the combustion of organic substances. The resulting powders were characterized by several techniques such as X-Ray diffraction (XRD), scanning electron microscopy (SEM) and Raman spectroscopy to study structure, morphology and the average particle size, phase, and composition. Optical properties were investigated by using the Tauc plot methodology. The optical band gap values were evaluated by diffuse reflectance spectroscopy measurements. The calculated optical band gap were found to be 2.20 eV, 2.37 eV for x = 0.00 and 0.2, respectively. The obtained results show that the structural, morphological and optical properties have affected by the substitution of Sr^{2+} on La^{3+} ion in the crystal lattice of $LaFeO_3$.

Keywords: $La_{0.8}Sr_{0.2}FeO_3$, perovskite, citrate sol-gel method, optical properties

Introduction

Rare-earth orthoferrites, with general formula ABO_3 (A = lanthanide, B = Fe) have become one of the most promising candidates due to their wide range of physical and technological properties, such as ferroelectricity, piezoelectricity, pyroelectricity, high-temperature superconductivity, magnetic behaviour, and catalytic activity (Parida *et al*., 2010; Thirumalairajan *et al*., 2013). $LaFeO_3$ is one of the most promising perovskite materials, which crystallizes in orthorhombic structure with space group P*bnm*. Here the large cations La are located at the unit cell corners while the cation Fe occupies the centre of the distorted octahedron of oxygen anions of the ABO_3 structure where, the degree of distortion depends on the radius of the rare earth ion. The La site doping with other alkaline earth or transition metal ions is believed to be an effective way to alter the properties (Selvadurai *et al*., 2015; Kafa *et al*., 2017). In this regard, a variety of doped $LaFeO_3$ have been reported where doping affects the structural properties and improves its physico-chemical properties.

The easiest route for the preparation of $LaFeO_3$ is the solid-state reaction where the precursor components of metal oxides or carbonates are calcined at a temperature higher than 1273 K. But this process contains several drawbacks such as no control over the particle size, poor homogeneity and high porosity of the samples. To improve the homogeneity and also to lower the preparation temperature several wet chemical methods have been proposed by different reports which include hydrothermal synthesis, solution combustion synthesis, sol-gel, co-precipitation to obtain ultrafine pure powders (Liu *et al*., 2016; Abdallah *et al*., 2019).

In the present work, Sr ion is partially replacing the La ion in the crystal lattice of $LaFeO_3$ prepared by the citrate sol-gel combustion method. In addition, the structural, morphological and optical properties of the prepared nanocrystalline $LaFeO_3$ and $La_{0.8}Sr_{0.2}FeO_3$ powder were also investigated.

[1] Dr, Associate Professor, Department of Chemistry, Taunggoke Degree College
[2] PhD, Multifunctional Materials Lab, Department of Physics, Indian Institute of Technology Madras
[3] Associate Professor, Multifunctional Materials Lab, Department of Physics, Indian Institute of Technology Madras

Materials and Methods

Lanthanum(III) nitrate hexahydrate ($La(NO_3)_3.6H_2O$), iron(III) nitrate nonahydrate ($Fe(NO_3)_3.9H_2O$), strontium nitrate ($Sr(NO_3)_2$), citric acid monohydrate ($C_6H_8O_7.\ H_2O$) were purchased from THE I.L.E. CO. Ltd., Chennai, India. All the reagents are SIGMA-ALDRICH brand and used as received. $LaFeO_3$ and Sr doped $LaFeO_3$ were synthesized from the metal-organic complexes precursor by the citrate sol-gel combustion method. In a stoichiometric ratio of La:Fe is 1:1 mol % for pure $LaFeO_3$ and La : Sr : Fe is (4/5):(1/5):1 mol % for $La_{0.8}Sr_{0.2}FeO_3$ and were dissolved in deionized water, and a citric acid complexing agent was added. The molar amount of citric acid was equal to a total molar amount of metal nitrates in the solution. The mixture was heated under magnetic stirring at a constant temperature of 80 °C to form a sol, and the sol was aged at the same temperature to form a gel. The gel was first pre-calcined in a muffle furnace at 300 °C for 5 h and then ground to a fine powder for further calcination in the furnace. These powders were ground and calcined at the temperature of 600 °C for 5 h in the furnace to make the incompletely combusted part react thoroughly. The prepared Sr doped and undoped $LaFeO_3$ powders were characterized and XRD, SEM, Raman spectroscopy and optical band gap measurements. Phase and structure of the prepared Sr doped and undoped $LaFeO_3$ powders were investigated by Panalytical powder diffractometer with $CuK_{\alpha 1}$ radiation (λ = 1.5405 Å). Field emission scanning electron microscope (Quanta 400, FEI microscope) was employed to observe the morphology determination, and the dispersion of particles. The Raman spectra of all samples were obtained with a 632 nm red excitation line of He–Ne laser using Horiba Jobin-Yvon (HR800 UV) micro-Raman spectrometer in the wavenumber range from 100 to 1000 cm^{-1}. Diffuse reflection spectra were obtained by Perkin Elmer 2 plus UV-Vis-NIR spectrometer for the optical properties study of the samples in the wavelength range from 300 to 1000 nm. Optical band gap of the powder samples were estimated using Tauc plots.

Results and Discussion

X-ray diffraction patterns of Sr doped and undoped $LaFeO_3$ are shown in Figure 1. The diffraction peaks of pure and Sr doped samples were single phase with no trace of impurities. Moreover, the (121) peak drift figure of XRD patterns demonstrated that all the samples were of perovskite orthogonal structure (PDF#37-1493) with P*bmn* space group (No. 62). This volume contraction is expected because of the small difference in ionic radii of Sr^{2+} (1.18 Å) and La^{3+} (1.36 Å) ions.

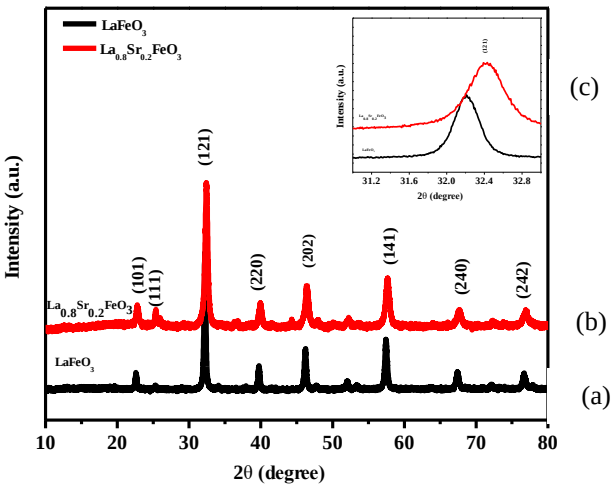

Figure 1 X-ray diffraction patterns of (a) $LaFeO_3$, (b) $La_{0.8}Sr_{0.2}FeO_3$ powder and (c)(inset) their (121) peak figures

The average crystallite sizes of samples were calculated from the dominant peaks of X-ray line broadening planes using Scherrer equation, $D_{Sch} = \frac{0.9\,\lambda}{\beta \cos\theta}$, where D_{Sch} is the average crystallite size, θ is the Bragg angle, λ is the wavelength of the X-ray, β is the full width at half maximum, the constant k is taken as 0.9. The average crystallite sizes are summarized in Table 1. In addition, the crystallite size and the microstrain of samples were also calculated for the comparison by using the Williamson-Hall equation, $\beta_T \,\mathrm{Cos}\,\theta = \varepsilon\,(4\,\mathrm{Sin}\,\theta) + \frac{K\lambda}{D_{WH}}$, where D_{WH} is the average crystallite size, θ is the Bragg angle, λ is the X-ray wavelength, k = 0.9, β is the full width at half maximum of XRD peaks and ε is the microstrain of the lattice (Smirnova, 1999). The plots of β cosθ as a function of sinθ are shown in Figure 2. D_{WH} and ε of samples are determined from the linear extrapolation and slope of these plots, respectively. All of these values are summarized in Table 1. The crystallite size of $La_{0.8}Sr_{0.2}FeO_3$ was 29 nm for Sr doping while those of ε increased from 0.134 % to 0.246 % due to the shrinkage of the lattice parameters.

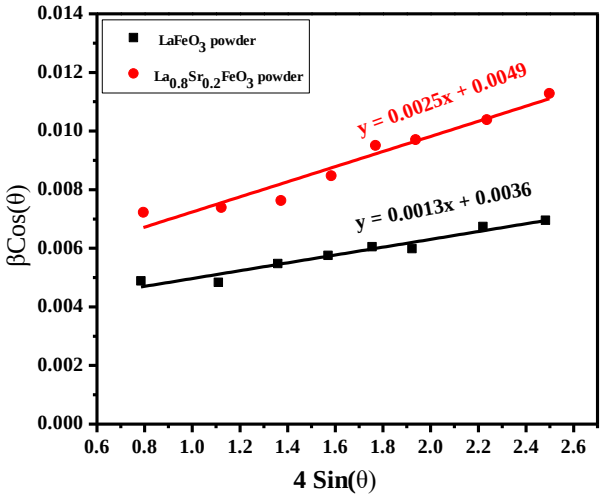

Figure 2 Williamson-Hall plots of β Cosθ against 4Sinθ calculated from XRD spectral data of $LaFeO_3$ and $La_{0.8}Sr_{0.2}FeO_3$ powders

Table 1 Average Crystallite Size, Strain of the Prepared Powder Samples

Samples	Average crystallite size (nm)		Strain (%)
	Scherrer equation	Williamson-Hall Plot	
$LaFeO_3$	24	38	0.134
$La_{0.8}Sr_{0.2}FeO_3$	15	29	0.246

Figure 3 (a), and (b) show Rietveld refined XRD patterns of (a) $LaFeO_3$ and (b) $La_{0.8}Sr_{0.2}FeO_3$ powders that were analyzed by using Fullprof suite software. The observed Residual factors and atomic coordinates of Rietveld refinement of powders samples are listed in Table 2. All the XRD patterns were assigned to orthorhombic structure with a space group P*bnm* (No.62) using CIF file. Furthermore, no other impurity phases were observed from the XRD patterns and it confirmed the single phase formation of samples observed within the detection limit of the XRD. Also, it indicated the absence of biphasic structure such as $LaFeO_3$ and $LaSrO_3$ in doping samples, since both the compound has distinct lattice parameters. Moreover, the peak shift to higher angle 2θ was noted on Sr substitution in $LaFeO_3$. This peak shifting confirms that, there are no biphase present in the samples. Thus, reduction in the lattice parameter observed for Sr may be due to the induced defects, which enhances the physical properties of the prepared samples.

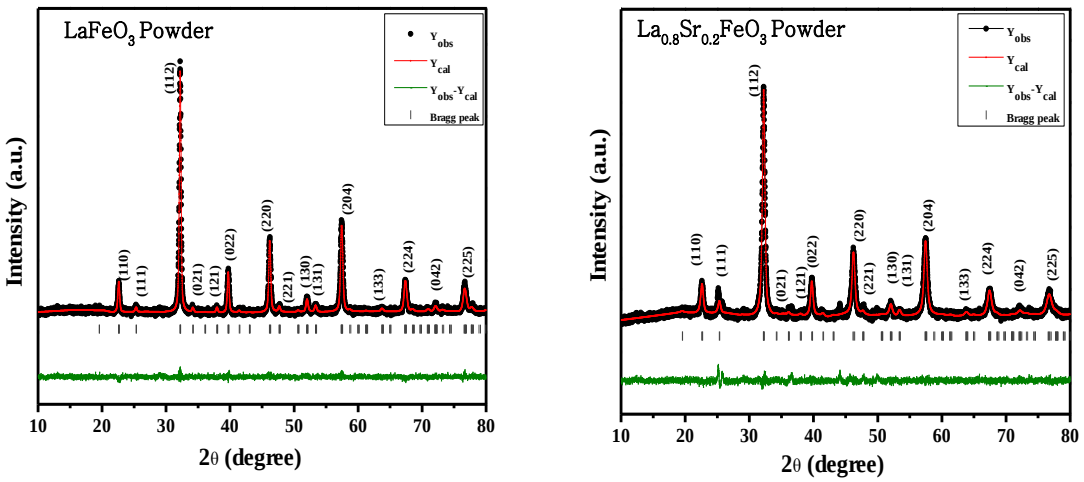

Figure 3 Rietveld refined XRD patterns of (a) $LaFeO_3$ and (b) $La_{0.8}Sr_{0.2}FeO_3$ powders by Fullprof software

Table 2 Structural Parameters and Reliability Factors obtained from Rietveld Analysis of Sr Doped and Undoped $LaFeO_3$ Powders of XRD Patterns

Samples	Lattice Parameters (*Pbnm* setting)				R-factors		
	a (Å)	b (Å)	c (Å)	V (Å^3)	wR_p (%)	R_p (%)	χ^2
$LaFeO_3$	5.5567	5.5618	7.8496	242.631	5.63	3.48	1.11
$La_{0.8}Sr_{0.2}FeO_3$	5.5609	5.5568	7.8388	242.231	4.62	3.52	1.46

The microstructure of the $La_{1-x}Sr_xFeO_3$ (x=0 and 0.2) powder samples was investigated using a scanning electron microscope (SEM) and the recorded SEM micrographs are shown in Figure 4. Powder samples revealed irregular particle shapes with a wide-range of particle size distribution, consisting of nanometer-sized particles and macroplate-like agglomerations. The EDX analysis was employed to determine the element of the synthesized materials. The elemental compositions of powder samples in terms of atomic weight percentages are listed in the Table 3. The elemental composition values are almost in close agreement with the stoichiometry of starting materials used for the preparation of samples.

Table 3 Semiquantitative Chemical Compositions Present in the Powder Samples

Sample	Atomic %			
	La	Sr	Fe	O
$LaFeO_3$	17.7	-	20.1	62.2
$La_{0.8}Sr_{0.2}FeO_3$	11.1	3.5	15.3	70.2

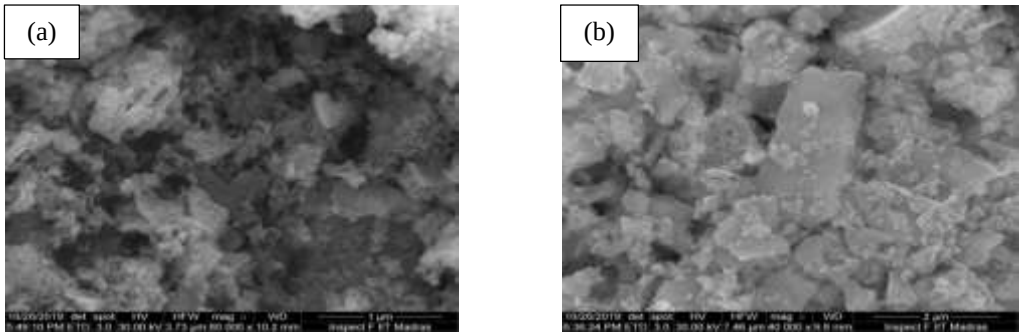

Figure 4 SEM images of the powder samples (a) $LaFeO_3$ and (b) $La_{0.8}Sr_{0.2}FeO_3$

One of the advantages of Raman spectroscopy is that it has a very sensitive to structure distortion and oxygen motion. Therefore, a detailed investigation of electron excitation is very important to understand the doping effect of perovskite-type materials. Room temperature Raman spectra recorded for the prepared samples are shown in Figure 5. According to the group theory analysis that the Brillion zone center normal modes transform according to the representation: $7A_g$ $+8$ $A_u+5B_{1g}+10B_{1u}+7B_{2g}+8B_{2u}+5B_{3g}+10B_{3u}$. The representation A_u + $2B_u$ belongs to three acoustic modes. Modes A_g, B_{1g}, B_{2g} and B_{3g} are Raman active and Modes A_u, B_{1u}, B_{2g}, B_{2u}, B_{3g} and B_{3u} are infrared active (Sharma *et al*., 2017). Raman spectra were recorded using 632 nm laser diode. The modes were measured between the regions of 1000 cm^{-1}-100 cm^{-1}. The modes between 200 and 30 cm^{-1} (denoted as A) are assigned to lattice and La vibrations due to the more mass of the La ion, modes between 350 and 200 cm^{-1} (denoted as T) are assigned to oxygen octahedral tilt modes, and modes between 450 and 350 cm^{-1} (denoted as B) are assigned as bending modes and modes above 500 cm^{-1} (denoted as S) are assigned to oxygen stretching vibrations. The spectra of $LaFeO_3$ and Sr doped samples are distinct from each other. The broaden, appearance and disappearance of phonon modes indicate toward structural rearrangement in the system and such a deviation is considered as a sign of presence of spin-phonon coupling and mixed tendency of Li^{3+} and Sr^{2+} metal ions. No Raman mode above 800 cm^{-1} indicates the absence of impurity phase in doping.

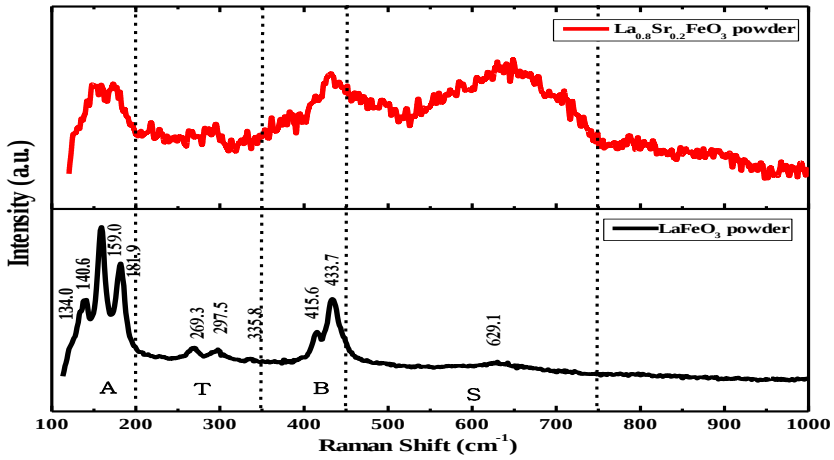

Figure 5 Raman spectra of Sr doped and undoped calcined powders

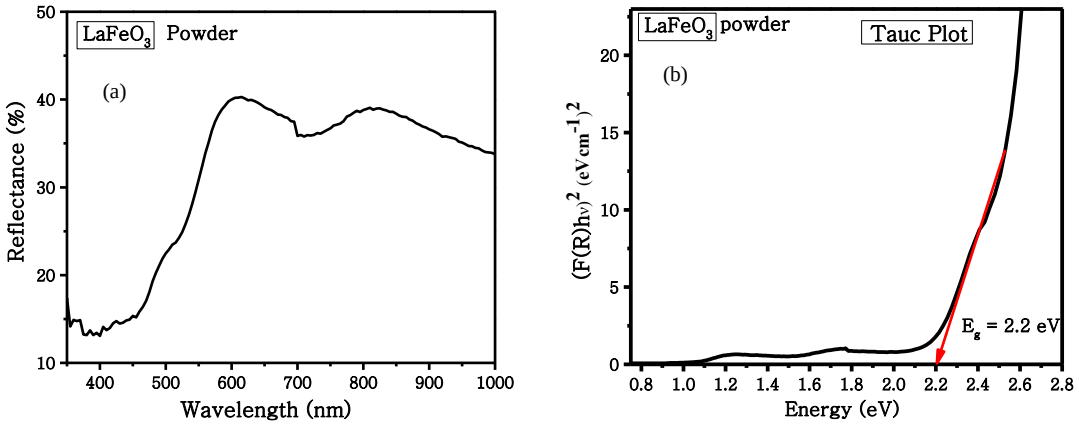

Figure 6 (a) Diffuse reflectance spectrum (b) Plot of (F(R)*hν)^2 vs. the energy in electron volts of $LaFeO_3$ powder

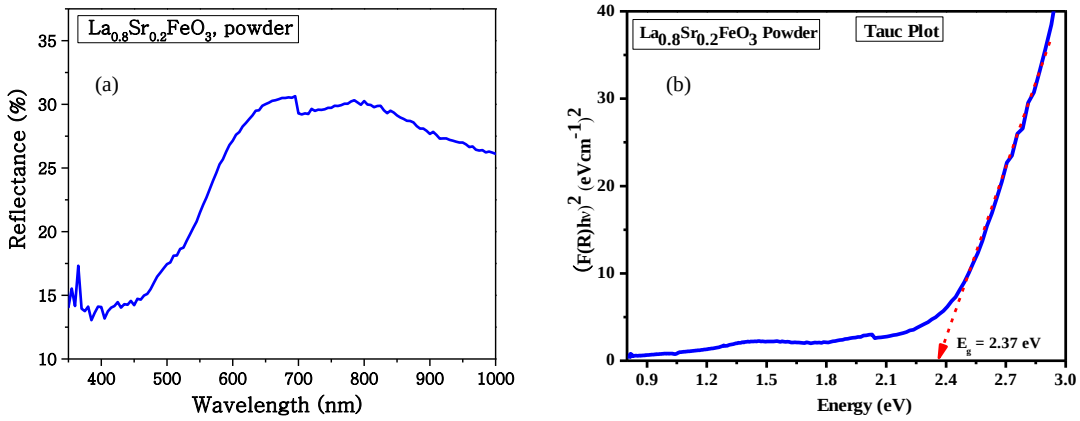

Figure 7 (a) Diffuse reflectance spectrum (b) Plot of (F(R)*hν)^2 vs. the energy in electron volts of $La_{0.8}Sr_{0.2}FeO_3$ powder

Figure 6 and 7 show the diffuse reflectance spectra and Tauc plots of pure $LaFeO_3$, and $La_{0.8}Sr_{0.2}FeO_3$, respectively, and all samples show strong visible-light absorption but by doping Sr on La site it can be seen that decreasing in visible-light absorption. Band gap energy can be determined from Kubelka-Munk equation via a Tauc plot, $\alpha = B\ (h\nu - E_g)^n / h\nu$, where α is the absorption coefficient, ν is the irradiation frequency, E_g is the band gap, B is a constant (being usually 1 for semiconductor), h is the Planck constant and n is a constant depending on the type of semiconductor (direct transition: n = 1/2; indirect transition: n = 2). Diffuse reflectance UV-Vis spectroscopy (DRS) can be mathematically expressed in terms of absorption coefficient through differential equations obtained from Kubelka-Munk theory. Substituting the Kubelka- Munk function ($F(R_\infty)$) in the Tauc equation, the intercept of linear region of $F(R_\infty) = B\ (h\nu - E_g)^n$ curve on the x-axis gives the value of the band gap energy of the sample. $F(R_\infty) = \frac{(1-R_\infty)2}{2R_\infty} = \frac{K}{S}$, R_∞ is diffused reflectance of the powder sample, K is effective absorption coefficient and S is scattering coefficient. The band gap energy can be determined by extrapolating the slope to $F(R) \rightarrow 0$ (Roberto *et al.*, 2013; Schevciw and White, 1983). It is a well-known effect that small particles tend to exhibit increased band gaps and it agrees with Sr doping on $LaFeO_3$. The proper replacement of lanthanum by Sr ion is the best proof for the increase in the band gap energy. This confirms that Sr^{2+} ion can affect the optical transition in $La_{0.8}Sr_{0.2}FeO_3$.

Conclusion

Pure $LaFeO_3$ and Sr doped $La_{1-x}Sr_xFeO_3$ (x=0.2) perovskite powders were synthesized by the citrate sol-gel combustion method. The XRD patterns confirmed the formation of single phase orthorhombic perovskite crystal structure with P*bmn* space group for Sr doped and undoped $LaFeO_3$. The lattice parameters of the synthesized samples were calculated by fullprof retrieved refined method. Morphology of Sr doped $LaFeO_3$ powders differed from those of the pure $LaFeO_3$.This is because the doped ions can cause the disorderness of the atomic configuration in $LaFeO_3$. All the powder sample showed uniform and quite good in grain distribution, with plate form of grains agglomeration in SEM images. The presence of expected elements in the prepared powders was confirmed by EDX analysis. Raman spectra determine the various functional groups present in the prepared $LaFeO_3$ and Sr doped $LaFeO_3$ powder samples. The optical band gap increased with Sr doping in the prepared powder samples. The optical band gap energy of the Sr dopoed $LaFeO_3$ powder is 2.37 eV whereas that of undoped $LaFeO_3$ powder is 2.20 eV. A good correlation between structural and optical properties has been observed for the studied samples. Actually, the distortion of the structure caused by doping leads to a change in optical properties. These interesting properties allow the material to be used in novel applications in the field of science and technology.

Acknowledgements

The authors would like to thank ASEAN- India Research Training Fellowship Program (AIRTF) for providing this Fellowship. The authors express thanks to Dr Sudakar Chandran, Multifunctional Material Laboratory, for guiding in this work. The authors are also thankful to the Indian Institute of Technology Madras (IITM), and Department of Physics IITM, for all the microscopy and research facilities. The authors also would like to express their profound gratitude to the Department of Higher Education, Ministry of Education, Yangon, Myanmar, for provision of opportunity to do this research and Myanmar Academy of Arts and Science for allowing to present this paper.

References

Abdalah, F. B., Benali, A., Triki, M., Dhahri, E., Nomenyo, K. and Lerondel. G. (2019). "Investigation of Structural, Morphological, Optical and Electrical Properties of Double-doping Lanthanum Ferrite". *J. Mater. Sci. Materials in Electronics,* vol. 30, pp. 3349–3358

Kafa, C.A., Triyono, D. and Laysandra, H. (2017). "Temperature-dependent Impedance Spectroscopy of $La_{0.8}Sr_{0.2}FeO_3$ Nano-crystalline Material". *Mater. Sci. and Eng*., vol.188, pp. 012027, 1-5

Liu. Q. S., You, Z., Zeng, S. J. and Guo, H. (2016). "Infrared Properties of Mg-doped $LaFeO_3$ Prepared by Sol–gel Method". *J. Sol-Gel Sci. Technol.*, vol. 80, pp. 860–866

Parida, K.M., Reddy, K.H., Martha, S., Das, D.P. and Biswal, N. (2010). "Fabrication of Nanocrystalline $LaFeO_3$: An Efficient Sol-gel Auto-combustion Assisted Visible Light Responsive Photocatalyst for Water Decomposition". *Int. J. Hydrogen Energy*, vol. 35**,** pp. 12161 - 12168

Roberto, K., Lothar, J. and Stefan, G. E. (2013). "Magnetic and Optical Investigations on $LaFeO_3$ Powders with Different Particle Sizes and Corresponding Ceramics". *Solid State Ionics*, vol. 249–250, pp. 1-5

Schevciw, O. and White, W. B. (1983). "The Optical Absorption Edge of Rare Earth Sesquisulfides and Alkaline Earth -Rare Earth Sulfides". *Mat. Res. Bull.*, vol.18, pp.1059-1068

Selvadurai, A. P. B., Pazhanivelu, V., Jagadeeshwaran, C., Murugaraj, R., Muthuselvam, I. P. and Chou, F.C. (2015). "Influence of Cr Substitution on Structural, Magnetic and Electrical Conductivity Spectra of $LaFeO_3$". *J. Alloys and Compdounds*, vol. 646, pp. 924-931

Sharma, G., Tyagi, S. and Sathe, V. G. (2017). "Raman Spectroscopic Investigation of Spin-Lattice Coupling In $LaFeO_3$". *AIP Conference Proceedings,* vol.1832, pp. 090020, 1-2

Smirnova, I.S. (1999). "Normal Modes of the $LaMnO_3$ Pnma Phase: Comparison with La_2CuO_4 Cmca Phase". *Physica B*, vol 262, pp. 247-261

Thirumalairajan, S., Girija, K., Hebalkar, N. Y., Mangalaraj, D., Viswanathan, C. and Ponpandian, N. (2013). "Shape Evolution of Perovskite $LaFeO_3$ Nanostructures: A Systematic Investigation of Growth Mechanism, Properties and Morphology Dependent Photocatalytic Activities". *RSC Adv.*, vol.3, pp. 7549-7561

ELECTRICAL AND OPTICAL PROPERTIES OF $LaCo_{0.6}Fe_{0.4}O_3$ NANOCRYSTALLINE POWDER BY SOL-GEL METHOD

Zar Chi Myat Mon[1], MyaTheingi[2], Cherry Ohnn[3]

Abstract

A facile transition metal Fe doping has been employed as an effective approach to alter the electrical and optical properties of $LaCoO_3$. The aim of the research work is to study the effect of sintering temperature on structure, electrical and optical properties of the nanocrystalline ceramics. $LaCo_{0.6}Fe_{0.4}O_3$ nanocrystalline ceramics was prepared from constituent metal nitrates, citric acid and ethylene glycol by sol-gel method and sintered at different temperatures. The $LaCo_{0.6}Fe_{0.4}O_3$ powder calcined at 600 ºC were made circular pellets. The pellets were sintered at 800 ºC, 900 ºC and 1000 ºC. The obtained ceramic pellet samples were characterized by X-Ray Diffractometer (XRD), Fourier Transform Infra-Red (FT IR) spectrometer and Scanning Electron Microscopy (SEM). The XRD results show all $LaCo_{0.6}Fe_{0.4}O_3$ samples have hexagonal crystalline structure with R-3c space group and show single phase. The average crystallite size of the pellet samples varied from 20 to 40 nm due to the growth of nanocrystals at higher temperatures. The respective metal-oxygen stretching vibrations of the prepared samples were observed in FT IR spectra. Surface morphology of the prepared ceramics were studied by SEM. The optical properties of $LaCo_{0.6}Fe_{0.4}O_3$ ceramic samples were studied from UV-visible spectrophotometer and the optical band gaps were also estimated by using Tauc's relation. The band gap values of the pellet samples were 2.2 eV, 2.1 eV and 2.0 eV, respectively and these values were within semiconductor band-gap range. The ac conductivities and dielectric properties were studied by LCR meter in the frequency range of 1MHz - 2MHz. The experimental results indicated that the dielectric loss factor (tan δ), dielectric constant (ε′), ac conductivity (σ_{ac}), resistivity (ρ) and dc conductivity (σ_{dc}) were found to depend on the frequency.

Keywords: $LaCo_{0.6}Fe_{0.4}O_3$, nanocrystalline ceramics, sol-gel method, optical properties

Introduction

Perovskite is mixed oxide of transition metals with chemical formula ABO_3 where A is transition metal or lanthanide series cation, B is transition metal cation and O is oxide anion (Farhadi and Sepahvand, 2010). $LaCoO_3$-base material has interesting electrical and electrocatalytic properties owing to their high electronic/ionic conductivity. Lanthanum cobaltite, $LaCoO_3$, belongs to a family of mixed electronic and oxide-ion conducting perovskites that are good materials for catalysts, oxygen separation membranes, solid oxide fuel cell cathodes, and oxygen sensors. Cobalt containing perovskite type oxides have received great attention due to their interesting application properties (Moghadam *et al*., 2012).

Cobalt oxide is well known nanomaterial with enhanced electrocatalytic properties for the development of sensitive, efficient, and effective sensors. The electrochemical properties of cobalt oxide are depending on several parameters such as particle dimension surface morphology and tailored electrocatalytic features. Doping of metal oxide nanostructures with particular element offers a novel way for improving the structural, electrical and optical properties. The doping of transition metals is highly used for various oxides such as Cr, Mn, Fe, Ni and Cu that has shown significant change in the structural and optical properties of metal oxide. Iron (Fe) is one of the doping elements that has tremendous chemical stability and is considered important doping element for the enhancement and tuning the structural properties of cobalt oxide (Tahari *et al*., 2016).

[1] 3PhD Candidate, Department of Chemistry, University of Yangon
[2] Associate Professor, Department of Chemistry, Taunggoke University
[3] Lecturer, Department of Chemistry, West Yangon University

The first description of the tolerance factor for perovskite was made by Victor Moritz Goldschmidt in 1926. Ideal perovskites have the ABO_3 stoichiometry and the ratio of bond length between A-O and B-O maintains a constant value which is equal to $\sqrt{2}$. The deviation from this is taken as the tolerance factor and in terms of ionic radii, it assumes:

$$t = \frac{rA+rO}{\sqrt{2}\,(rB+rO)} \quad (r_{A(la)} = 1.16\text{Å}, r_{B(Co)} = 0.65\text{Å}, r_{B(Fe)} = 0.55\text{Å}, r_O = 1.35\text{Å})$$

Where r_A, r_B and r_O are the ionic radii of A and B cations and oxygen, respectively. If $t > 1$ hexagonal or tetragonal, $0.9 < t < 1$ cubic, $0.71 < t < 0.9$ orthorhombic / rhombohedral, < 0.71 different structures, eg. trigonal (Liu *et al*., 2008).

In the present work $LaCo_{0.6}Fe_{0.4}O_3$ nanocrystalline powder was prepared by citrate sol-gel method. These material have been prepared by many techniques which includes mechanical-synthesis, co-precipitation, solution combustion or thermal decomposition, solid-state reactions, hydrothermal and sol-gel methods. In this paper, $LaCo_{0.6}Fe_{0.4}O_3$ nanocrystalline samples were synthesized via a simple citrate sol-gel method and their structural, optical and electrical properties were investigated for further applications. This synthesis route has several advantages such as simplicity, low cost and no waste compared with other methods.

Materials and Methods

All of the chemicals used were analytical grade. $La(NO_3)_3.6H_2O$ was purchased from Aladdin Industrial Corporation Co., Ltd, Shanghai, China. $Fe(NO_3)_3.9H_2O$, $Co(NO_3)_2.6H_2O$ and citric acid were purchased from Alpha Chemika Co., Ltd, India. Ethylene glycol was purchased from VMP Chemistry Kontor GmbH Co., Ltd, Germany.

Preparation of Nanocrystalline Powders

$LaCo_{0.6}Fe_{0.4}O_3$ nanocrystalline ceramics were prepared by sol-gel method using $La(NO_3)_3.6H_2O$, $Fe(NO_3)_3.9H_2O$, $Co(NO_3)_2.6H_2O$, citric acid and ethylene glycol. The precursor solution was prepared by mixing lanthanum nitrate (4.32 g), cobalt nitrate (1.74 g), iron nitrate (1.61 g), citric acid (8.4 g) and deionized water. The solution was ultra-sonicated for complete dissolution of metal cations in solution. The molar ratio of citric acid to the metal cation was 2:1. The solution was well stirred using magnetic stirrer and heated to about 60 °C. Ethylene glycol (6.7 mL) was added to the above solution in the molar ratio as 3:1 with citric acid. The resultant solution was heated and stirred on the magnetic stirrer to about 90 °C and then transferred to oil bath at 120 °C in order to form gel and finally heated at 300 °C in the furnace. The xerogel was ground in the mortar and pestle. The dried xerogel was calcined at 600 ºC for 4 h. The resulting calcined powders were compacted in a mortar driven uniaxial hydraulic press, using a mould with 10 mm in diameter. The pellet ceramics thus obtained were sintered at 800, 900 and 1000°C for 1 h (Derakhshi *et al*., 2016).

Characterization Techniques

Crystal structure and phase analysis of prepared ceramics were performed by X-ray diffraction (XRD) using XRD-2000 diffractometer, Enraf Nonius Co., Bohemia NY, Physics Department, Yangon University. Morphology of the samples was recorded by scanning electron microscope (SEM) EVO-18, ZEISS, Germany. FT IR transmission spectra in the region from 400-4000 cm^{-1} were measured by using Perkin Elmer GX system FT IR spectrophotometer. The samples were characterized by UV-visible spectrophotometer (SHIMADZU UV-1800) for wavelength dependence absorption spectrum. The electrical properties of the prepared samples were studied by using LCR (Inductance, capacitance and resistance) meter.

Measurement of Electrical Properties

Dielectric properties were studied by LCR meter in the frequency range of 1MHz-2MHz. The ac conductivity was calculated from dielectric data using the following relation.

$$\sigma_{ac} = \varepsilon' \tan\delta \omega \varepsilon_o$$

Where σ_{ac} is ac conductivity of the sample, ε' is the dielectric constant, tan δ is the dielectric loss factor, ω is the angular frequency and ε_o is permittivity of free space.

Results and Discussions

Characterization of the $LaCo_{0.6}Fe_{0.4}O_3$ Prepared Samples

XRD analysis

The XRD patterns of the prepared $LaCo_{0.6}Fe_{0.4}O_3$ ceramic sintered at 800 ºC, 900 ºC and 1000 ºC are shown in Figure 1 and their lattice parameters and average crystallite sizes are summarized in Table 1. It was observed that with an increase in the calcination temperature, the intensity of the peak increased. The crystallite sizes of $LaCo_{0.6}Fe_{0.4}O_3$ nanocrystalline ceramics sintered at 800 ºC, 900 ºC and 1000 ºC were 25.7 nm, 27.6 nm and 32.5 nm, respectively. The diffraction peaks of $LaCoFeO_3$ sintered at 1000ºC, are sharper than those at 800 ºC and 900 ºC. The XRD pattern of each ceramic displayed the reflections corresponding to the trigonal structure of space group hexagonal (R-3c) perovskite $LaCoO_3$ (JCPDS 01-086-1662) and orthorhombic structure of space group Pnma (62) $LaFeO_3$ (JCPDS 00-015-0148). The average particle size of $LaCoFeO_3$ ceramics were found in the range of 20-40 nm. The crystal structure of the prepare samples were matched with those calculated from tolerance factor and they were found to have hexagonal crystal structure.

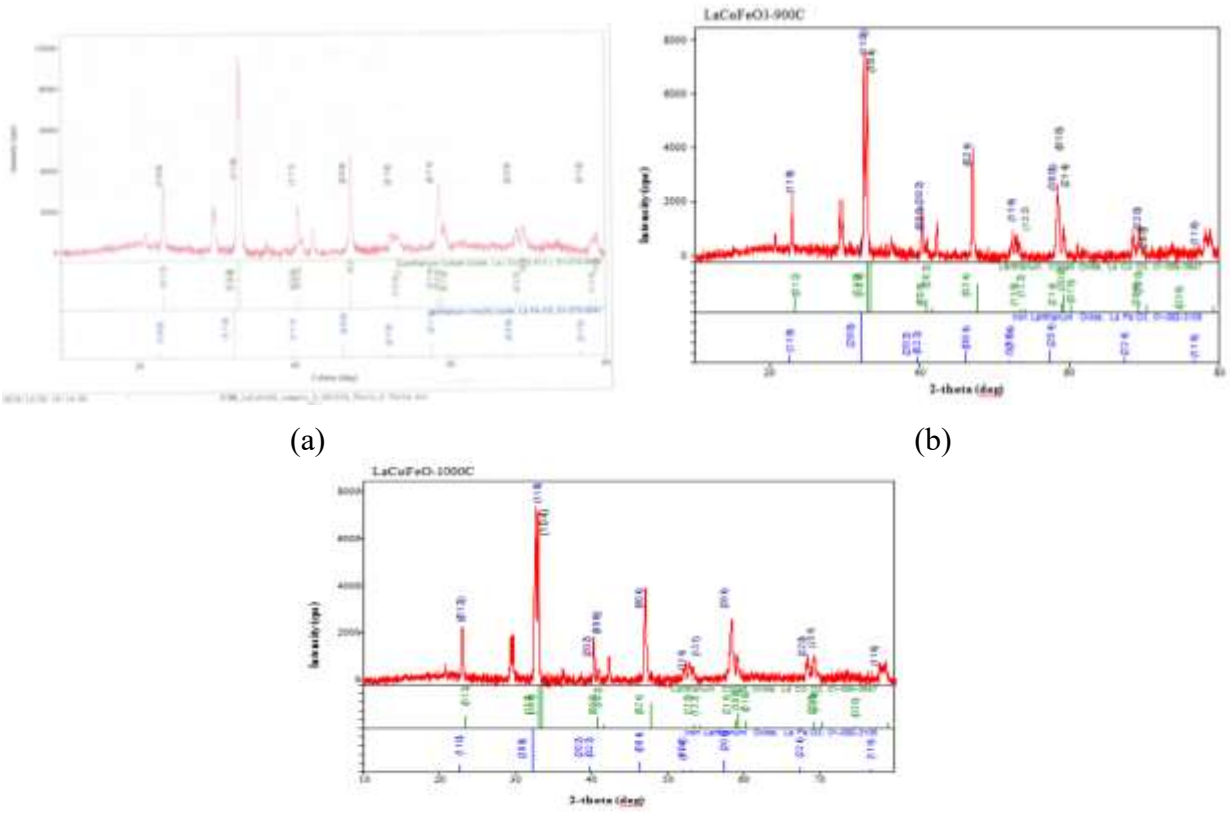

(a) (b)

(c)

Figure 1 XRD patterns of $LaCo_{0.6}Fe_{0.4}O_3$ nanocrystalline ceramics sintered at (a) 800 ºC (b) 900 ºC and (c) 1000 ºC

Table 1 Lattice Parameters (a and c) and the Average Crystallite Size of $LaCo_{0.6}Fe_{0.4}O_3$ Nanocrystalline Ceramics Sintered at Different Temperatures

Temperature (ºC)	Lattice parameter (Å)		Crystal system (XRD)	Crystallite size (nm)
	a	c		
800	5.4740	13.204	Hexagonal	25.7
900	5.4208	13.199	Hexagonal	27.6
1000	5.4811	13.210	Hexagonal	32.5

SEM analysis

SEM micrographs of prepared $LaCo_{0.6}Fe_{0.4}O_3$ nanocrystalline ceramics with different sintering temperatures (800 ºC, 900 ºC and 1000 ºC) for 1 h are shown in Figure 2. As the sintering temperature of $LaCo_{0.6}Fe_{0.4}O_3$ sample increased, the particle sizes were found to become increase and tightly stacked. The compact and dense nature was found at higher temperature the porosity decreased. The high porosity was observed in the sintering temperature 800 ºC due to particle agglomeration.

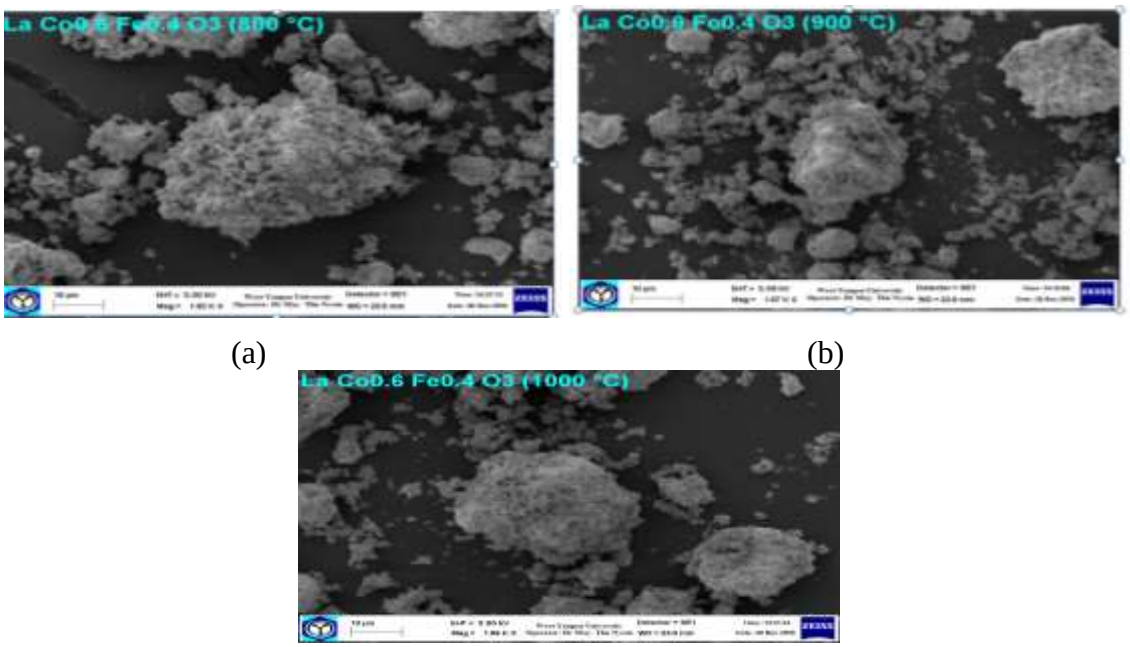

(a) (b)

(c)

Figure 2 SEM microphotograph of $LaCo_{0.6}Fe_{0.4}O_3$ ceramics sintered at (a) 800 ºC (b) 900 ºC (c) 1000 ºC

FT IR analysis

FT IR spectra of $LaCo_{0.6}Fe_{0.4}O_3$ nanocrystalline ceramics are presented in Figure 3 and Table 2. The respective metal-oxygen stretching vibrations are observed in FT IR spectra for all samples sintered at different temperatures (800 °C, 900 °C and 1000 °C). The FT IR spectrum of $LaCo_{0.6}Fe_{0.4}O_3$ has characteristics bands at 408 cm^{-1} and 666 cm^{-1} that ascribed to the vibration of metal oxygen bond. La-O absorption band appeared between 400 cm^{-1} and 450 cm^{-1}. The strong absorption band between 500 cm^{-1}-650 cm^{-1} are assigned to Co-O stretching vibration and that between 550 cm^{-1}-700 cm^{-1} are indicated Fe-O-Fe stretching vibration (Nakamoto *et al*., 1970).

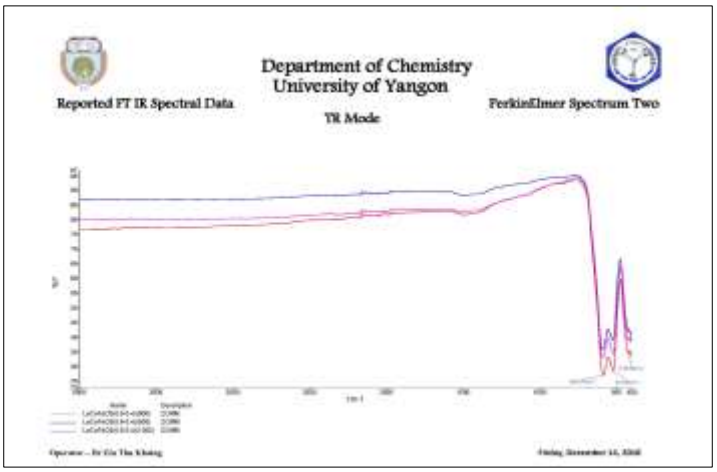

Figure 3 FT IR spectra of $LaCo_{0.6}Fe_{0.4}O_3$ ceramics sintered at (800 ºC, 900 ºC and 1000 ºC)

Table 2 FT IR Spectral Data of the $LaCo_{0.6}Fe_{0.4}O_3$ Ceramics by Citrate Sol-gel Method after Sintering at Different Temperatures

Observed Wavenumber (cm^{-1})	Literature Wavenumber* (cm^{-1})	Band Assignment
416	400-450	Stretching vibration of La-O group
519	500-650	Stretching vibration of Fe-O group
580	550-700	Stretching vibration of Co-O group

*Nakamoto (1970)

Electrical Properties

The electrical properties of the pellet samples of $LaCo_{0.6}Fe_{0.4}O_3$ nanocrystalline ceramics prepared by sol-gel method was studied at different temperatures using LCR (inductance, capacitance and resistance) meter. The dielectric properties and electrical properties of $LaCo_{0.6}Fe_{0.4}O_3$ nanocrystalline ceramics was carried out to determine in the frequency range of 1 MHz-2 MHz. It was observed that the dielectric constant and dielectric loss tangent were found to decrease with increase in frequencies. The dielectric constant was calculated by using the formula $\sigma = Cd/\varepsilon_0 A$ where C is the capacitance of pellet in μF, d is the thickness of the pellet; A is the cross sectional area of the flat surface of the pellet and ε_0 is the permittivity for free space. Thus σ_{ac} depends strongly on the frequency of the applied field (Priyanka *et al*., 2013). At high temperature the dielectric constant and dielectric loss tangent (tan δ) increased significantly as the frequency decreased for the $LaCo_{0.6}Fe_{0.4}O_3$ nanocrystalline ceramics as shown in Figures 4 and 5, and Tables 3 and 4. In the high temperature region, higher value of dielectric constant may be related to polarization which comes from mobility of ions and imperfections from this material. The higher value of dielectric constant measured at low frequencies can also be explained on the basis of interfacial space charge polarization due to inhomogeneous dielectric structure. The dielectric loss indicates the energy dissipation in the dielectric system (Asad *et al*., 2015). Figure 6 and Table 5 show the variation of ac conductivity of $LaCo_{0.6}Fe_{0.4}O_3$ ceramics sintered at different temperatures as a function of frequency. It was noted that σ_{ac} increased with increasing frequency for all the temperatures. AC conductivity indicates that the conduction occurs by the hopping of charge carrier between localized states. It was observed that the ac conductivity of $LaCo_{0.6}Fe_{0.4}O_3$

ceramics increased with an increase in temperatures related to the enormous hopping of charge carriers. The resistivity values of the samples were found to decrease with increase in frequency. The resistivity of $LaCo_{0.6}Fe_{0.4}O_3$ nanocrystalline ceramics at 1000 °C was greater than those of other two temperatures as shown in Figure 7 and Table 6. The resistivity is inversely proportional to dc conductivity. The high value of resistivity has the lower value dc conductivity for all the temperatures as shown in Figure 8 and Table 7. The dc conductivity value of $LaCo_{0.6}Fe_{0.4}O_3$ nanocrystalline ceramics increased when temperature was raised.

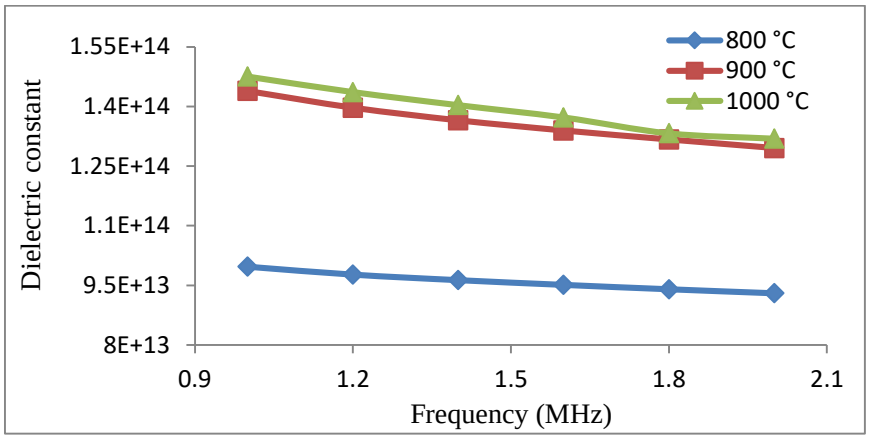

Figure 4 Variation of dielectric constant of $LaCo_{0.6}Fe_{0.4}O_3$ ceramics prepared by sol-gel method sintered at different temperatures as a function of frequency

Table 3 Variation of Dielectric Constant of $LaCo_{0.6}Fe_{0.4}O_3$ Ceramics Sintered at Different Temperatures as a Function of Frequency

Frequency (MHz)	Dielectric constant		
	800 °C	900 °C	1000 °C
1	9.97E+13	1.43E+14	1.48E+14
1.2	9.77E+13	1.39E+14	1.44E+14
1.4	9.63E+13	1.36E+14	1.40E+14
1.6	9.51E+13	1.33E+14	1.37E+14
1.8	9.40E+13	1.31E+14	1.33E+14
2	9.30E+13	1.29E+14	1.32E+14

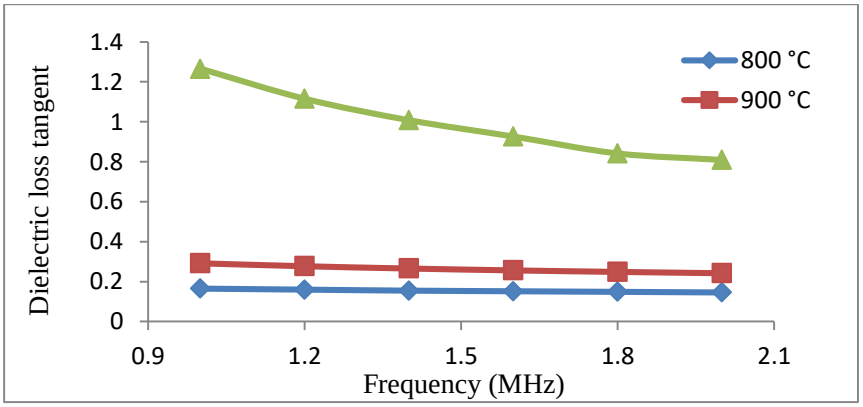

Figure 5 Variation of dielectric loss tangent of $LaCo_{0.6}Fe_{0.4}O_3$ ceramics sintered at different temperatures as a function of frequency

Table 4 Variation of Dielectric Loss tangent of $LaCo_{0.6}Fe_{0.4}O_3$ Ceramics Sintered at Different Temperatures as a Function of Frequency

Frequency (MHz)	Dielectric loss tangent		
	800 °C	900 °C	1000 °C
1	0.165	0.291	1.265
1.2	0.160	0.277	1.115
1.4	0.155	0.265	1.008
1.6	0.152	0.256	0.926
1.8	0.149	0.249	0.841
2	0.146	0.242	0.809

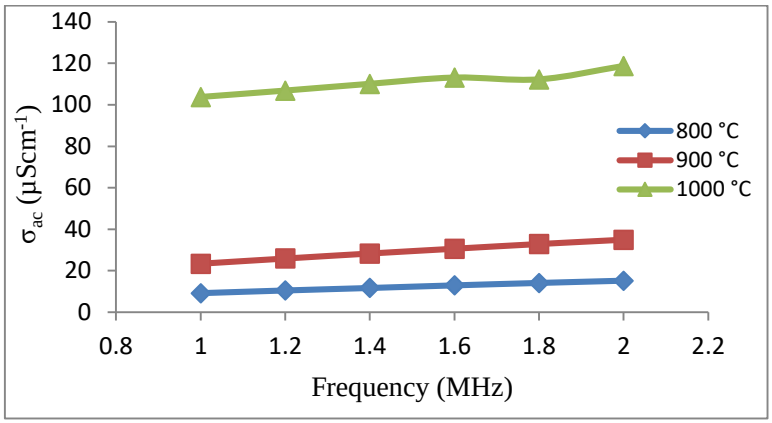

Figure 6 Variation of ac conductivity of $LaCo_{0.6}Fe_{0.4}O_3$ ceramic sintered at different temperatures as a function of frequency

Table 5 Variation of ac Conductivity of $LaCo_{0.6}Fe_{0.4}O_3$ Ceramic Sintered at Different Temperatures as a Function of Frequency

Frequency (MHz)	AC Conductivity (μScm^{-1})		
	800 °C	900 °C	1000 °C
1	9.140	23.329	103.734
1.2	10.424	25.825	106.817
1.4	11.614	28.231	110.082
1.6	12.857	30.549	113.097
1.8	14.015	32.799	112.241
2	15.095	34.882	118.711

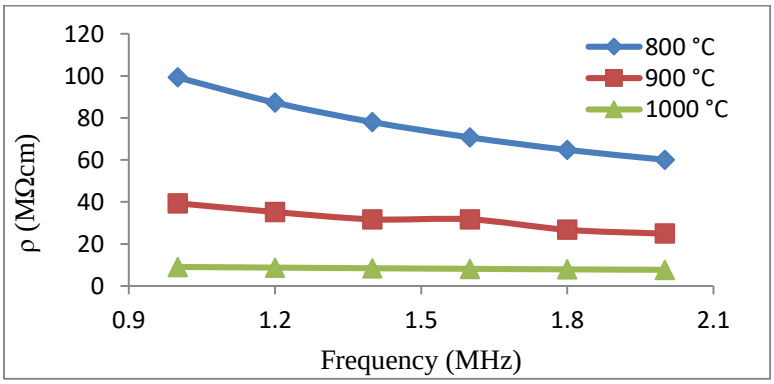

Figure 7 Variation of resistivity of $LaCo_{0.6}Fe_{0.4}O_3$ ceramics sintered at different temperatures as a function of frequency

Table 6 Variation of Resistivity of $LaCo_{0.6}Fe_{0.4}O_3$ Ceramics Sintered at Different Temperatures as a Function of Frequency

Frequency (MHz)	Resistivity (MΩcm)		
	800 °C	900 °C	1000 °C
1	99.28	39.30	8.98
1.2	87.30	35.16	8.67
1.4	78.01	31.73	8.38
1.6	70.73	31.71	8.11
1.8	64.77	26.78	7.87
2	60.08	24.96	7.66

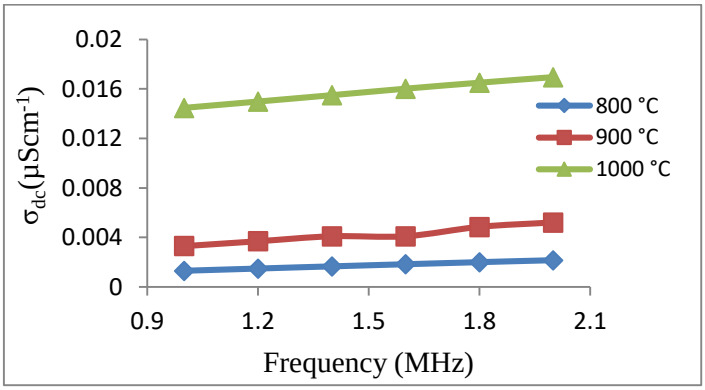

Figure 8 Variation of dc conductivity of $LaCo_{0.6}Fe_{0.4}O_3$ ceramics sintered at different temperatures as a function of frequency

Table 7 Variation of dc Conductivity of $LaCo_{0.6}Fe_{0.4}O_3$ Ceramics Sintered at Different Temperatures as a Function of Frequency

Frequency (MHz)	DC Conductivity (μScm^{-1})		
	800 °C	900 °C	1000 °C
1	0.0013	0.0033	0.0144
1.2	0.0014	0.0036	0.0149
1.4	0.0016	0.0041	0.0154
1.6	0.0018	0.0041	0.0160
1.8	0.0020	0.00481	0.0165
2	0.0021	0.00521	0.0169

Optical Properties

UV-visible absorption spectroscopic method is a powerful technique to explore the optical properties of semiconducting nanoparticles. The optical properties of the prepared $LaCo_{0.6}Fe_{0.4}O_3$ ceramics at different temperatures were studied by UV-visible absorption spectroscopy in the range of 300-700 nm. The absorption coefficient (α) was calculated from the observed absorption spectra and the optical band gaps of $LaCo_{0.6}Fe_{0.4}O_3$ samples were calculated from the Tauc's plots of $(\alpha h\nu)^2$ vs $h\nu$. The optical band gap of the ceramic samples were 2.2 eV for 800 °C, 2.1 eV for 900 °C and 2.0 eV for 1000 °C (Figure 9 and Table 8). These band gap values are also reliable within the semiconductor band gap ranges. The prepared materials can be therefore used as gas sensor, cathode material for solid oxide fuel cell, solar cell and other optoelectronic devices.

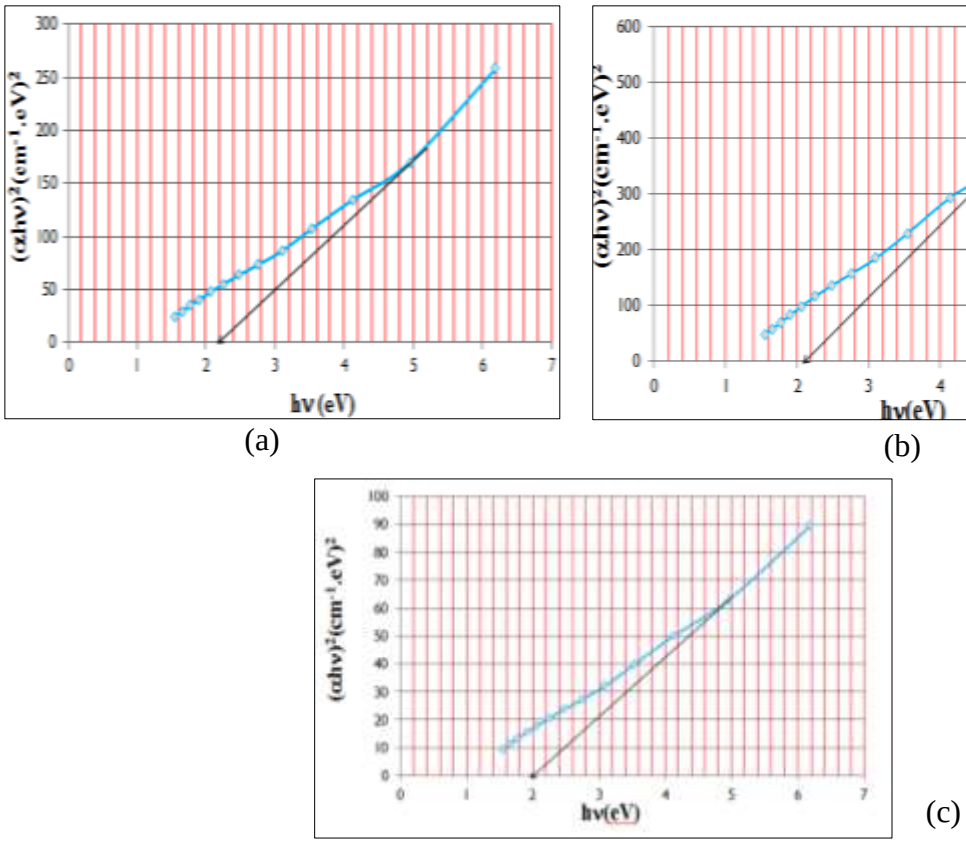

Figure 9 Plot of $(\alpha h\nu)^2$ against $h\nu$ for $LaCo_{0.6}Fe_{0.4}O_3$ ceramics sintered at (a) 800 ºC (b) 900 ºC and (c) 1000 ºC

Table 8 Band Gap Values of $LaCo_{0.6}Fe_{0.4}O_3$ Ceramics Sintered at Different Temperatures

$LaCo_{0.6}Fe_{0.4}O_3$	Band gap values (eV)
800	2.2
900	2.1
1000	2.0

Conclusion

$LaCo_{0.6}Fe_{0.4}O_3$ ceramics were sintered at different temperatures (800 °C, 900 °C and 1000 °C) for 1 h by citrate sol-gel method. The calculated sizes of $LaCo_{0.6}Fe_{0.4}O_3$ ceramics sintered at 800 °C, 900 °C and 1000 °C from Scherrer formula were found to be 25.7 nm, 27.6 nm and 32.6 nm, respectively. In the XRD pattern of the prepared sample after sintering at 1000 ºC, the peaks were sharper than those at 800 ºC and 900 ºC. FT IR spectra showed the presence of the stretching vibrations of metal-oxygen (La-O, Co-O and Fe-O) chemical bonds. From SEM analysis, compact and dense nature was observed. The optical band gap of $LaCo_{0.6}Fe_{0.4}O_3$ ceramic samples were found to be 2.2 eV for $LaCo_{0.6}Fe_{0.4}O_3$ sample at 800 °C, 2.1 eV for 900 °C and 2.0 eV for 1000 °C. The ac conductivity and dielectric properties of $LaCo_{0.6}Fe_{0.4}O_3$ ceramic samples were studied at the frequency range of 1 MHz-2 MHz. The frequency depends of ac conductivity. Both dielectric constant and dielectric loss tangent were found to decrease with increase in frequency and increase with increase in temperature.

Acknowledgments

The authors would like to express their profound gratitude to the Department of Higher Education, Ministry of Education, Yangon, Myanmar, for provision of opportunity to do this research and Myanmar Academy of Arts and Science for allowing to present this paper.

References

Asad A. S., Naseem, S., Khan, W., Sharma, A. and Navqi,A.H. (2015). "Microstructural, Optical and Electrical Properties of $LaFe_{0.5}Cr_{0.5}O_3$Perovskite Nanostructures". *J. Mater. Sci*., vol. 5(16), pp. 1-3

Derakhshi, Z., Tamizifar, M., Arzani, K. and Baghshahi, S. (2016). 'Synthesis and Characterization of $LaCo_xFe_{1-x}O_3$ ($0\leq x \leq 1$) Nano-Crystal Powders by Pechini Type Sol–Gel Method". *Synthesis and Reactivity in Inorganic, Metal-Organic, and Nano-Metal Chemistry,* vol. 46, pp. 25–30

Farhadi, S. and Sepahvand, S. (2010). "Microwave-assisted Solid-state Decomposition of $\{Co(CN)_6\}.5H_2O$ Precursor: A Simple and Fast Route for the Synthesis of Single Phase Perovskite-type $LaCoO_3$ Nanoparticles". *Journal of Alloys Compounds*, vol. 489, pp. 586-591

Liu, X., Hong, R. and Tian, C. (2008). "Tolerance Factor and The Stability Discussion of ABO_3-type Ilmenite". *Journal of Materials Science: Materials in Electronics,* 20(4), pp. 323-327

Moghadam, S. F., Malekzadeh A., Ghiasi1, M., Karimi1, F., Mortazavi,Y. and Khodadadi, A. (2012). "Manganese Oxide Promoted $LaCoO_3$ Nano-Perovskite for Oxidation of a Model Exhaust Gas". *Iranian Journal of Chemical Engineering*, vol. 9(2), pp. 22-33

Nakamoto, K. (1970). *Infrad Spectra of Inorganic and Coordination Compounds.* New York: 2nd Edition, Wiley Interscience Publication

Priyanka, K. P., Joseph, S. and Varghese, T. (2013). "Dielectric Properties and AC Conductivity of Nanocrystalline Titania". *Journal of Basic and Applied Physics*, vol. 2(1), pp. 4-7

Tahira,A., Baloach, Q., Chacha, G.S., Sirajuddin, Willander,M. and Ibupoto,Z.H. (2016). "Fe-Doped Cobalt Oxide Nanostructures for the Development of Sensitive Dopamine Biosensor". *Sensor Letters,* vol. 14, pp 1–5

SYNTHESIS AND CHARACTERIZATION OF CHITOSAN BASED GRAPHENE OXIDE BIONANOCOMPOSITE

Aung Than Htwe[1], Naing Min Tun[2], Myo Min Soe[2], Masao Gohdo[3],Yoichi Yoshida[4], Ni Ni Than[5*]

Abstract

Nowadays, several biomaterials, including natural polymers, are used to solve and reduce the global problem of water pollution and biomedical as cellular interactions. Chitosan (CS) is one of the most studied biocompatible natural polymers. Graphene oxide (GO) is carbon-based nanomaterial capable of imparting desired properties to the scaffolds. In the present study an ecofriendly approach led to the development of biodegradable chitosan based graphene oxide bionanocomposites which have been prepared by the mixing aqueous solution of chitosan and graphene oxide. The synthesized GO and CSGO were characterized by using fourier transform infrared spectroscopy (FT IR), thermogravimetric/differential thermal analysis (TG-DTA), X-ray diffraction (XRD), field emission scanning electron microscope (FE-SEM), UV-Vis spectroscopy. Finally, the synthesized nanoparticles size and surface charge were measured by dynamic light scattering (DLS) and zeta potential analyzer, respectively. The results obtained from those different studies revealed that chitosan and graphene oxide could mix with each other homogeneously. Hence, chitosan based graphene oxide bionanocomposite were successfully synthesized and characterized.

Keywords: chitosan, graphene oxide, bionanocomposite, dynamic light scattering

Introduction

Chitosan (CS), produced from chitin by deacetylation, is an environmentally friendly and renewable natural biopolymer with outstanding properties of non-toxic, biocompatible and biodegradable. Additionally, many amino and hydroxyl groups make CS absorb anionic organic compounds and metal ions efficiently by electrostatic interactions or chelating, which was widely applied in industrial, environment and biomedicine fields (Wu *et al.*,2020). Chitosan, a copolymer of β[1,4]-linked 2-acetamido-2-deoxy-D-glucopyranose and 2-amino-2-deoxy-D-glucopyranose, is generally obtained by deacetylation of chitin, one of the most plentiful natural polymers on earth. Because of its good biocompatibility, biodegradability, and multiple functional groups, chitosan (CS) has attracted significant interest in a broad range of applications such as water treatment, membrane separation, food package, tissue engineering, and drug delivery. However, low mechanical properties of chitosan restrict its use in a wide-range application. (Yang *et al.*, 2010).

Chitosan-based nanomaterials have also been produced using different type of organic and inorganic nanoparticles. Consequently, chitosan has been modified using carbon nanotube, graphene, nanoclay, and metal nanoparticles. The modified chitosan has been reinforced in different polymers to form nanocomposite. These nanocomposites have several improved properties such as porosity, surface area, electrical conductivity, photoluminescence, tensile strength, morphology, and antibacterial and bio-properties (Kausar, 2019).

Graphene, a single layer of carbon atoms in a hexagonal lattice, has recently attracted much attention due to its novel electronic and mechanical properties. Graphene is usually prepared by the reduction of its precursor graphene oxide, a typical pseudo-two-dimensional oxygen-containing solid in bulk form, possesses functional groups including hydroxyls, epoxides, and carboxyls. Both graphene and graphene oxide papers show very high mechanical properties with well

[1] Assistant Lecturer, Department of Chemistry, University of Yangon, Myanmar
[2] Lecturers, Department of Chemistry, University of Yangon, Myanmar
[3] Assistant Professor, The Institute of Scientific and Industrial Research, Osaka University, Japan
[4] Professor, The Institute of Scientific and Industrial Research, Osaka University, Japan
[5] Professor and Head, Department of Chemistry, University of Yangon, Myanmar

biocompatibility, and they have potential application as biomaterials. The chemical groups of graphene oxide have been found to be a feasible and effective means of improving the dispersion of graphene. Additionally, functional side groups bound to the surface of graphene oxide or graphene sheets may improve the interfacial interaction between graphene oxide/graphene and the matrix similarly to that observed for functionalized carbon nanotube-based nanocomposites (Han *et al.*, 2011).

A single layer of carbon atoms constitutes the structure of graphene oxide (GO) packed in a hexagonal arrangement. This is a two-dimensional (2D) nanomaterial having excellent electronic, optical, and mechanical properties. Therefore, it has been able to draw significant interest very recently among the research communities. But strong van der Waals and π–π interactions induce the graphene sheets to agglomerate in aqueous solution. This has posed an enormous problem in the preparation of graphene-based materials for various applications, and thus, an urgent modification toward resolving the issue has been required. To overcome this problem, GOs possessing multiple functional groups such as epoxides, hydroxyls, and carboxyls are prepared. GO along with all these functionalities can be easily exfoliated into monolayer sheets that are capable of forming a stable dispersion in water and in other solvents which are polar. These functional groups facilitate the functionalization through covalent or noncovalent routes. They endow the edges and surfaces of GO to give rise to gels with a higher rate of chemical reactivity having GO and provide them with ample modification potential because of the simple fabrication processes (Nath, 2018).

In the present work, the chitosan based graphene oxide bionanocomposite were prepared by the mixing aqueous solution of chitosan and graphene oxide. The synthesized GO and CSGO were characterized by using FTIR, TG-DTA, XRD, FE-SEM, UV-Vis. Finally, the synthesized nanoparticles size and surface charge were measured by DLS and zeta potential analyzer, respectively.

Materials and Methods

Commercial chitosan from shrimp shell waste was purchased from Asian Technology Groups Co. Ltd., Local Industry, Yangon, Myanmar. Graphite was purchased from Sigma-Aldrich Co., (USA). All other chemicals used were of analytical reagent grade. In all investigations, the recommended standard methods and techniques involving both conventional and modern methods were provided.

Preparation of Graphene Oxide (GO)Powder

Firstly, 3.0 g of graphite powder were placed in beaker and then 90:30 v/v ratio of 98 % of sulphuric acid: 68 % of nitric acid were added. During the reaction, the solution was in exothermic condition so it must be stirred in the ice-bath at 10 °C to maintain temperature while 9 g of $KMnO_4$ was slowly added and stirred at 15 min after the temperature being controlled by the ice bath to 9 ^oC. The mixture was continuously stirred at 300 rpm. Afterward, the solution then was added to 150 mL of distilled water gradually while at the same time it was stirred with 300 rpm at 90 °C for 30 min to achieve neutral conditions. Hence, 30 mL of hydrogen peroxide (H_2O_2 30%) was added into the solution and then stirred with 300 rpm for 1h. The resultant solution was centrifuged and the precipitate was washed with 600 mL hot distilled water. The brown paste was obtained. 100 mL of 10 % hydrochloric acid (10%) was added to the paste and stirred at 30 min. Then, the precipitate was washed with 200 mL distilled water with five times at 7000 rpm for 30 min due to acid free of mixture. The yellow-brown GO mixture was obtained. The obtained GO mixture was sonicated at 2 h and then was centrifuge at 3000 rpm for 30 min. The decant mixture was decanted.

The decanted was centrifuged. The GO dispersed mixture was decanted and dried in oven at 80 °C to obtain GO.

Preparation of Chitosan/Graphene Oxide Bionanocomposite

A 1 g of chitosan was dissolved into 100 mL of 1 % aqueous acetic acid to prepare 1 % (v/v) chitosan (CS) solution. An aqueous dispersion of GO (0.1, 0.2, 0.3, 0.4, 0.5 g) in 50 mL of 1% (v/v) acetic acid was mixed with 50 mL of 1 % CS solution and sonicated for 1 h. The mixture was stirred continuously at 60 °C for 2 h, after which 0.2 mL glutaraldehyde (50 % in H_2O) was added dropwise with constant stirring. A black gel of CSGO solution was cast on glass plate and dried at 60 °C. The different ratios of GO in chitosan/graphene oxide nanocomposite (CSGO0.1, CSGO0.2, CSGO0.3, CSGO0.4 and CSGO0.5) were obtained.

Characterization

The prepared bionanocomposites were characterized by FT IR spectroscopy using PerkinElmer GX instrument. The FTIR spectra were obtained in reflectance mode with a resolution of 4 cm^{-1} over a spectra range of 500-4000 cm^{-1}. Thermogravimetric analysis (TGA) was performed using a DTG-60H, Thermalgravimetric analyzer, Shimadzu, Japan, URC, UY with a nitrogen flow rate of 20 °C/min. The particle size distribution (PSD) of aggregates in GO and CSGO nanocomposites were measured using an optical microscope STZ-171 with Moticam U 2.0 MP, Shimadzu which captured the images. X-ray diffraction (XRD) measurements were performed using a (Rigaku, Japan) with a Cu Kα radiation source (wavelength λ = 0.154 nm) at a voltage of 40 kV and a current of 50 mA. The scanning rate was 3 °/min and the scanning scope of 2θ was from 5° to 40°. The surface morphology was analysed by field- emission scanning electron microscopy (FE-SEM, Hitachi SU8000, Japan). UV-vis absorption spectra were measured on an UVmini-1240, UV-vis Spectrophotometer, Shimadzu, Japan. The particle size distribution and zeta potential of GO and CSGO nanocomposite solutions (0.01 w/v %) were measured using a Zetasizer-Nano ZS (Malvern instruments, UK). Samples were placed into a U-shaped folded capillary cell for zeta potential measurements. Each sample was measured at room temperature (25 °C) in triplicate.

Results and Discussion

Characterization

The CS-GO nanocomposites were successfully prepared by in situ mineralization, where in the CSGO hydrogel was first prepared using GA as a cross-linker. CS is soluble in water at acidic pH, at which amine functional groups of the molecule undergo protonation. The cross-linking treatment with GA was carried out to decrease the degree of swelling and reinforce the mechanical and chemical stability of the composite material in a wide range of solution conditions including an acidic medium.

FT-IR spectroscopy

The FT IR spectra of the CS, GO and CSGO bionanocomposites are shown in Figure 1(a) and (b). The broad peak at 3450 cm^{-1} and the strong absorption peak at 1650 and 1589 cm^{-1} are characteristic of primary amine in chitosan spectrum (Figure 1 a). The broad band at 3000 – 3500 cm^{-1} range is attributed to the OH stretching, which overlaps the NH stretching in the same region. The characteristic chitosan absorption band at 2800 – 2900 cm^{-1} range in spectra of all films represent $>CH_2$ and $–CH_3$ aliphatic groups, respectively. The band at 1560 – 1590 cm^{-1} range presented the –NH bending vibration. The strong peak at 1650 cm^{-1} (amide I) is due to the

vibrations of carbonyl (C=O) groups, which is an evidence of incomplete chitosan deacetylation. A sharp peaks near 1380 and 1420 cm^{-1} correspond to defomation vibrations of OH and CH groups where as the broad peak at 1080 cm^{-1} is due to glycosidic bonds. In Figure 1(b), the FT IR spectrum of GO shows a peak at 3208.43 cm^{-1} that is due to the O-H stretching of the -COOH group. The peak at 1716.6 cm^{-1} and 1620.24 cm^{-1} are characteristics of the C=O stretch of the carboxylic group on the grapheme oxide and deformations of the O-H bond in water. The intense peak occurring at 1391 cm^{-1} is due to O-H deformations of C-OH groups, and the peak at 1039.99 cm^{-1} represents C-O-C stretching. This implies that the sample has strong hydrophilicity. The absorption peak at 1620.24 cm^{-1} can be ascribed to the presence of benzene rings (Konwar *et al.*, 2016; Yang *et al.*, 2010). The characteristic absorption peak of the CSGO nanocomposite at 2869 cm^{-1} which can be assigned to the C-H asymmetric vibration due to chitosan incorporation. The new vibration band appeared at 1541.50 -1560.49 cm^{-1} due to the C=O stretching whereas the carboxylic group bands at 1716.6 cm^{-1} of graphene oxide disappeared (Kumar *et al.*, 2014). According to the FT IR analysis, CSGO shows that the graphene oxide interacts with chitosan through intermolecular hydrogen bonds. So the CSGO nanocomposites should be miscibility between GO and CS.

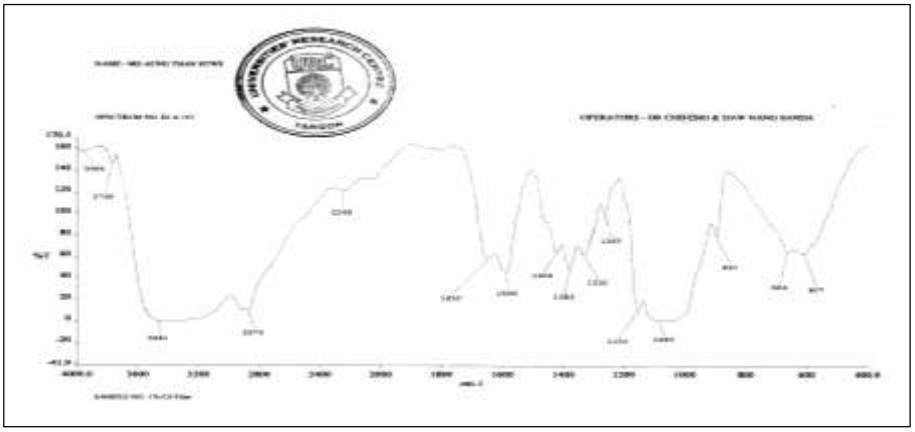

Figure 1(a). FT IR spectrum of pure CS

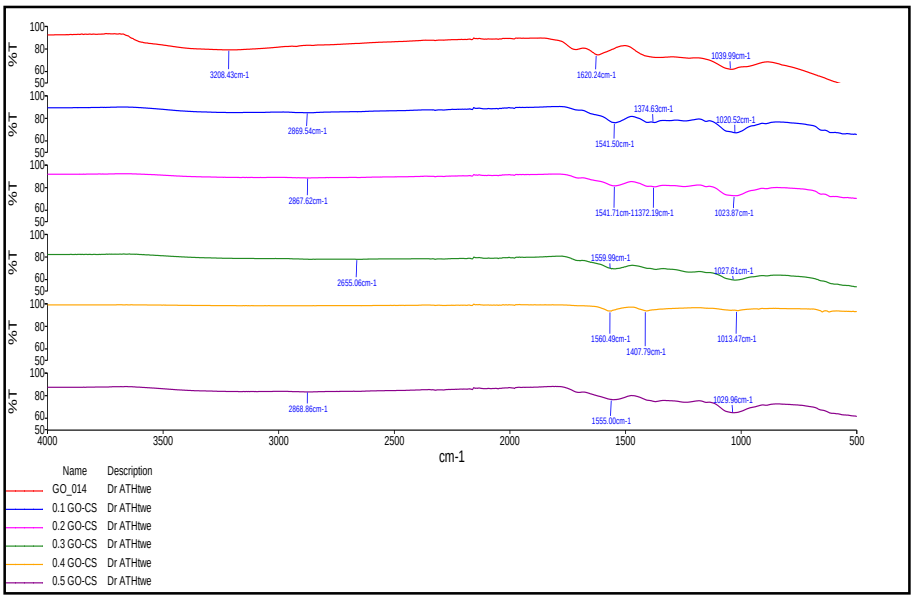

Figure 1(b). FT IR spectra of pure GO and their nanocomposites

Thermogravimetric analysis

The thermal stability of the pure CS, GO and five different ratios of GO in chitosan-graphene oxide nanocomposite particles (CSGO0.1, CSGO0.2, CSGO0.3, CSGO0.4 and CSGO0.5) were studied by thermogravimetric analysis as shown in Figure 2 (a) to (g). According to the TG DTA thermogram profiles, CS showed two decomposition stages. The first stage ranges between about the temperature range is 107.43 °C to 169.30 with 11.40 % of weight loss. There is moisture evaporation upon heating. The second stage is the loss in weight 37.19 % was decomposed within the temperature range of 275.35 °C to 399.33 °C. With reference to the depolymerization and elimination of glycosidic units of CS, the decomposition at 100 °C is clearly observed. Thermal elimination of CS takes place above 200°C after the residual water gets eliminated initially around 100 °C (Aung Than Htwe, 2018).

Thermal stability of GO (Figure 2 (b)) is found to be relatively good. But around 218 °C, there is a decrease in the thermal stability. GO experienced 75.28 % weight loss at this temperature. This attributes to the thermal decomposition of unstable groups containing oxygen and evolution of CO_2 gas. Below 100°C, the TGA curve shows a 21.95 % weight loss, which implies the loss of water molecules bound inside the GO structure. Due to the removal of stable functional groups, mass loss occurs in the range of 250–600 °C (Nath *et al.*, 2018).

The thermogram of all CSGO shown in Figure 2(c to g), having a weight loss in three stages. The first stage ranges between about the temperature range is 36 °C to 187 °C with 18.54 % in CSGO0.1, 13.18 % in CSGO0.2, 14.79 % in CSGO0.3, 10.11 % in CSGO0.4 and 15.58 % in CSGO0.5 of weight loss. There is loss of water molecules bound inside the CSGO structure and evolution of CO_2. The second stage, the temperature range between 187 °C to 365 °C was observed 36.84 % in CSGO0.1, 24.56 % in CSGO0.2, 34.75 % in CSGO0.3, 4.25 % in CSGO0.4 and 35.52 % in CSGO0.5 of weight loss. This is due to the removal of stable function groups and mass loss. The third stage is the loss in weight 36.63 % in CSGO0.1, 26.03 % in CSGO0.2, 43.34 % in CSGO0.3, 9.30 % in CSGO0.4 and 41.86 % in CSGO0.5 was observed to take place within the temperature range of 365 °C to 600 °C. In this stage, weight loss is due to complete degradation of polymer.

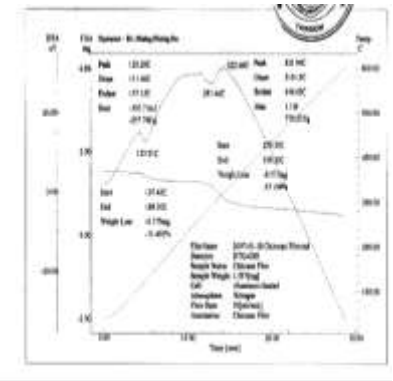

(a) CS

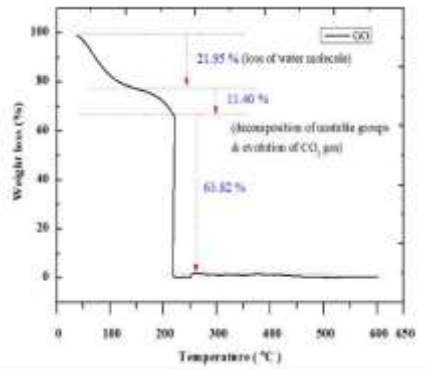

(b) GO

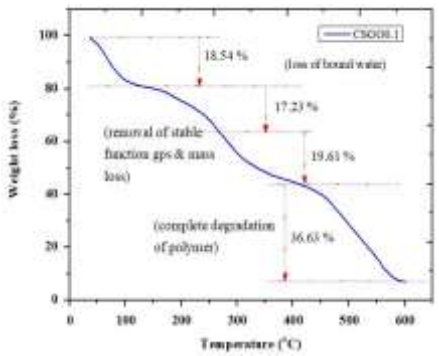

(c) CSGO0.1

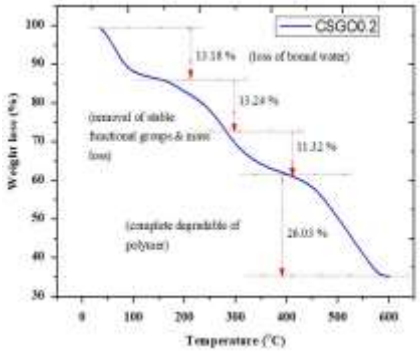

(d) CSGO0.2

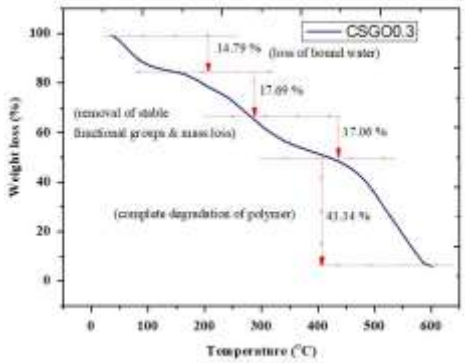

(e) CSGO0.3

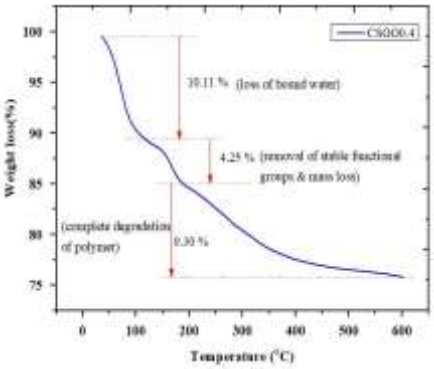

(f) CSGO0.4

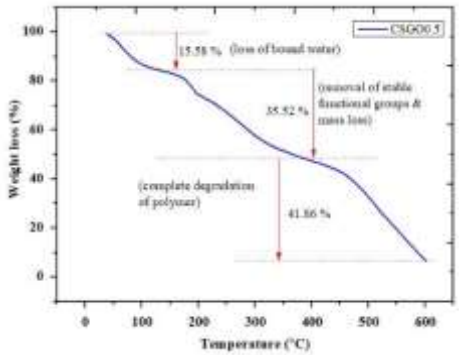

(g) CSGO0.5

Figure 2 TG-DTA thermogram of pure and bionanocomposites

Table 1 The weight loss (%) of GO and CSGO bionanocomposite with different temperature

Temperature (°C)	Weight loss (%)					
	GO	**CSGO0.1**	**CSGO0.2**	**CSGO0.3**	**CSGO0.4**	**CSGO0.5**
0	100	100	100	100	100	100
100	82.72	97.21	88.29	87.36	90.3	86.86
200	71.91	75.42	83.04	79.27	84.56	74.51
300	1.23	55.72	69.53	62.73	80.38	57.76
400	1.28	44.76	61.66	51.52	77.54	47.4
500	0.33	28.79	50.34	35.49	76.53	32.67
600	0.59	7.06	35.27	6.18	75.81	6.99

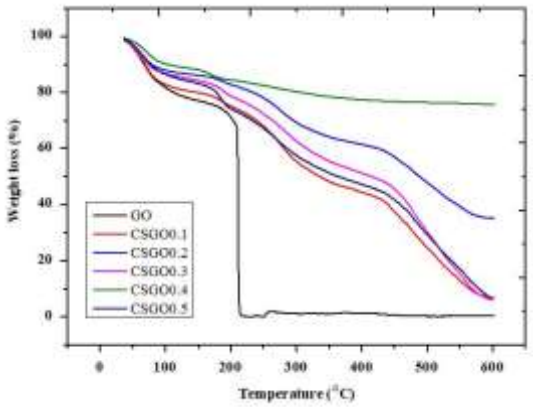

Figure 3 TGA of GO and CSGO bionanocomposite

Compared to the original CS, the decrease in thermal stability for CS/GO hydrogel can be ascribed to the ionically formed bonds among NH_3^+ and $HCOO^-$ groups. Intermolecular hydrogen bonding interaction between amino and hydroxyl groups of CS is destroyed partly by these new ionic bonds. This change eliminates the initial crystallinity of CS, and the rigidity of the CS chains is also weakened. Compared to the TGA of original GO, the hydrogel gains improved thermal stability, which is due to the superior insulation of GO nanosheets and barrier against the mass transport of the volatile compounds generated when the polymer undergoes decay under thermal conditions (Nath *et al.*, 2018).

According to the Table 1 and Figure 3, the results demonstrated that the loading levels of the GO were low so that it can affect the decomposition temperature of the nanocomposite. It also indicates that the weight loss percent of the CSGO is relatively higher than that of GO.

Optical microscope

Figure 4 shows the optical micrographs captured by the camera for resolution 5 mega pixel (MP) samples. In this case, 5 MP of pure GO and CSGO bionanocomposites have a higher quantity of aggregates with fewer fine particles around the large aggregates. Therefore, the image capture must be very fast. The method of measurement for particle size by optical microscopy was also useful for observing the aggregation evolution over time, specifically when fine particles agglomerate to form new, larger aggregates (Quilaqueo *et al.*, 2019).

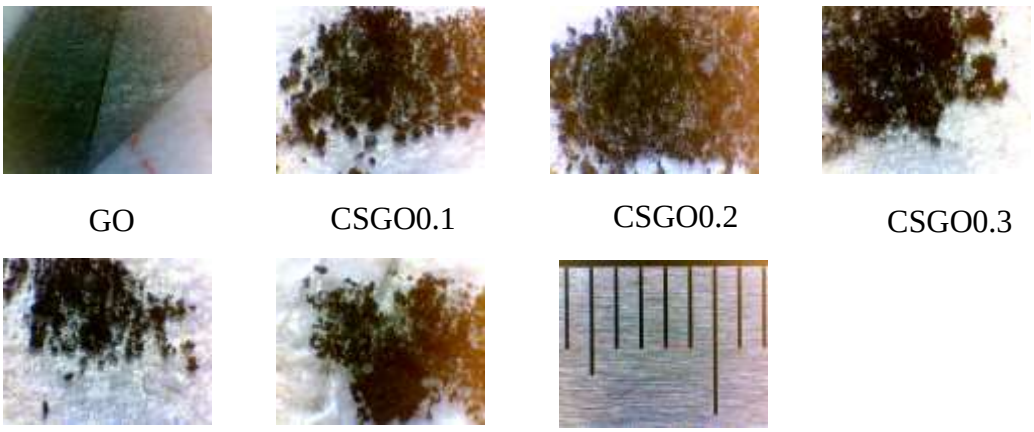

Figure 4 Optical micrographs of pure GO and CSGO bionanocomposite

X-ray diffraction analysis

Figure 5 represents the structural analysis of grapheme oxide, chitosan and chitosan/grapheme oxide bionanocomposites were investigated by X-ray diffraction. X-ray diffraction studies of grapheme oxide exhibits very intense peak at 2θ is 10.58◦. Pure chitosan films showed a characteristic peak at around 2θ is 8.72◦ and sharp peak at 21.74˚. All of the prepared CS-GO bionanocomposite exhibit two broad peaks at 2θ = 9.28° and 21.3° due to the generally amorphous state of the chitosan films. After the formation of CSGO nanocomposite, the intensity of all the reflections decreases. As seen in figure, it is found that the intensity of CS-GO nanocomposite peak are not only lower than GO peak but also higher than CS peak. This is because of the decrease in the degree of crystallinity of CS due to the addition of GO. Formation of new interactions between GO and CS reduces the interactions among CS chains. The peak that appears at 2θ = 8.09° in the hydrogel is attributed to the increased layer spacing in the GO layers (Nath *et al.*, 2018).

The XRD pattern of the CSGO bionanocomposites shows only the CS diffraction peaks from CS and the diffraction peak of GO disappears, which clearly demonstrate the formation of fully exfoliated structure of GO sheets in the polymer matrix (Yang, 2010). When incorporation of graphene oxide in chitosan chemical structure of the chitosan films changes due to the overlap of biopolymer diffraction, it indicates that there were mainly physical interaction but scarcely chemical reaction between chitosan and graphene oxide (Han *et al.*, 2011). In this particular case, the electrostatic interaction and hydrogen bonding may contribute to a relatively ordered arrangement of the attached CS chains along the rigid template offered by GO However, the chemical structure of the chitosan in the composites barely changes with the increasing content of graphene oxide, indicating that there were mainly physical interaction but scarcely chemical reaction between chitosan and graphene oxide (Bissessur *et al.*, 2006 and Han *et al.*, 2011). The CSGO bionanocomposite exhibited a combination of amorphous and crystalline peaks (Kumara *et al.*,2014).

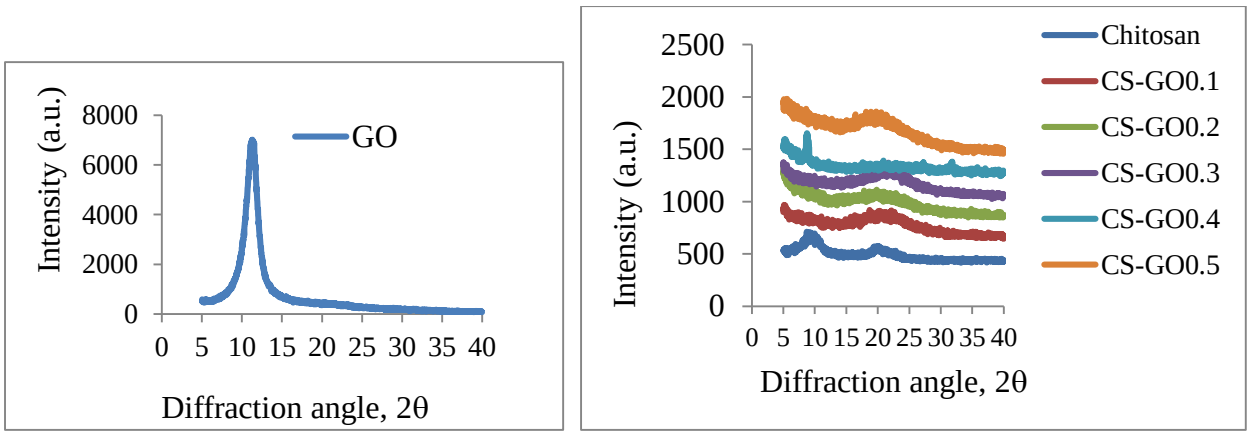

Figure 5 XRD patterns of GO, CS and CSGO bionanocomposite

FESEM-EDS Analysis

The surface morphology and the composition of the synthesized CS-GO nanocomposite samples have been investigated using field-emission scanning electron micrographs (FE-SEM) and the result for CSGO is displayed in Figure 6. The surfaces of CSGO particles with increased GO contents from 0.1 to 0.5 wt % became rough and porous (Figure 6 (a) to (e)). In particular, with an increase of the GO content in the CSGO particles, both the roughness and hole size of the particles increase. The FESEM images showed that bionanocomposite did not show porous structure because the pore sizes were gradually decreasing due to the percentage increase of graphene oxide

stocking on the polymer matrix, which also indicates development of strong hydrogen bond interactions between graphene oxide and polymer. To check the chemical composition of the material, an energy dispersive X-ray (EDX) spectroscopy analysis was also performed. Table 3 shows the elemental composition of CS-GO bionanocomposite samples, which confirms the presence of C, N and O ions in the matrix. The EDS results are also consistent with the weight percentage of C, N and O. From quantitative analysis it is evident that bionanocomposite samples contains approximately 60.68 % C, 3.37 % N and 35.95 % O by weight in CSGO0.1, 60.47 % C, 3.18 % N and 36.36 % O by weight in CSGO0.2, 64.57 % C, 1.85 % N and 33. 58 % O by weight in CSGO0.3, 47.88 % C, 3.75 % N and 48.37 % O by weight in CSGO0.4, and 61.38 % C, 1.94 % N and 36.68 % O by weight in CSGO0.5 respectively. These results were further found consistent with the XRD data.

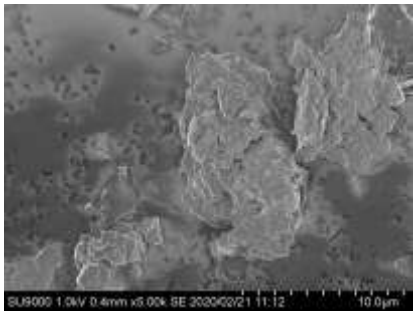

(a)CS-GO0.1

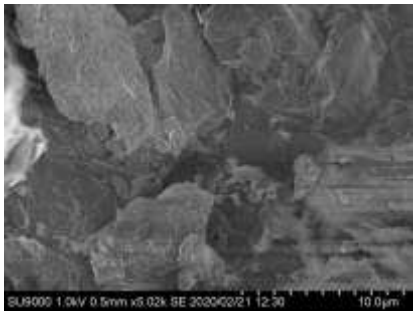

(b)CS-GO0.2

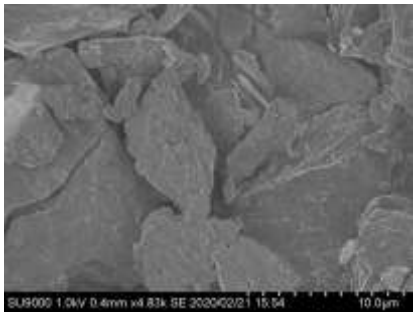

(c)CS-GO0.3

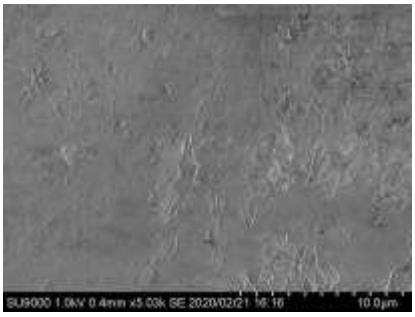

(d)CS-GO0.4

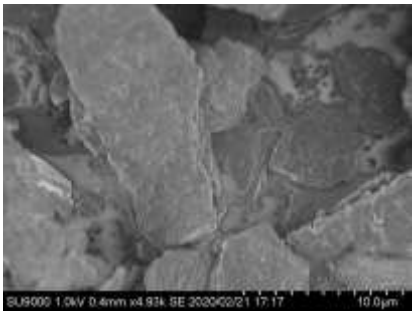

(e)CS-GO0.5

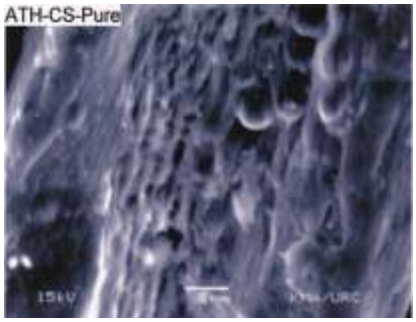

(f) Pure CS

Figure 6 SEM images of chitosan-graphene oxide bionanocomposite

Table 2 Compositional analysis of the CS-GO by EDS

Sample	Atomic % in composites		
	C	N	O
CS-GO0.1	60.68	3.37	35.95
CS-GO0.2	60.47	3.18	36.36
CS-GO0.3	64.57	1.85	33.58
CS-GO0.4	47.88	3.75	48.37
CS-GO0.5	61.38	1.94	36.68

UV-vis absorption spectra

The UV-Vis spectra of the CSGO composite is shown in Figure 7. Pure GO shows the one absorption peaks at 240 nm due to the π-π* transition of C=C (Wong *et al.*, 2015; Xu *et al.*,2013). Emadi *et al.* (2006) presented that the CS peaks are expected at 240 nm. After attachment with CS, the peaks of GO have shown a bathochromic shift. This shift in absorption maxima might be attributed to the formation of particles in the nano scale. This also indicates the strong covalent interaction between GO and CS where the active ester group of GO might have reacted with the amine groups on CS, forming an amide bond between GO and CS. (Suneetha, 2018).

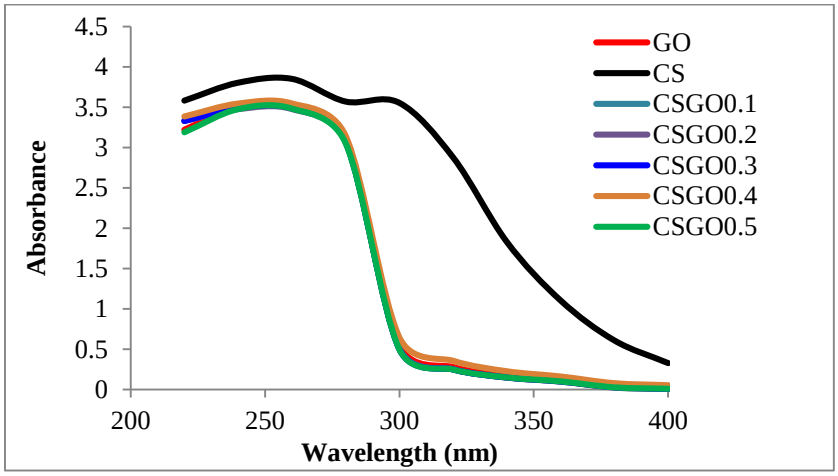

Figure 7 UV-vis spectra of GO and CSGO

Particle Size Study of GO and CSGO by Dynamic Light Scattering

The size of the CSGO is controlled by the parameters influencing the colloidal stability, i.e., ionic strength, pH, charge on the particles, temperature, solvent viscosity, and dielectric constant of the solvent (Sun *et al.*, 2016). The particle size distribution of GO and CSGO nanocomposite were determined using Dynamic Light Scattering (DLS) (Figure 8 (a) to (f)). The average diameter of the GO is 496.7 nm. Due to that, the size is low; the GO do not overlap when dispersed in a solution allowing the construction of scaffolds without GO agglomerations (Valencia, 2018). The average diameter of the prepared CSGO nanocomposites are 999.1 nm for CSGO0.1, 881.1 nm for CSGO0.2, 627.6 nm for CSGO0.3, 628.8 nm for CSGO0.4 and 544.5 nm for CSGO0.5. It was found that the increasing the GO content, the lower will be the average diameter. Therefore, It can be observed that the average diameter of all of the prepared CSGO nanocomposite are higher than that of pure GO.

Zeta Potential Measurement

The zeta potential is an important factor for characterizing the stability of colloidal dispersions and provides a measure of the magnitude and sign of the effective surface charge associated with the double layer around the colloid particle. Changes in the zeta potential in the presence of polymer may be caused by three different effects involving the following: the presence of the charges coming from the polymer dissociated functional groups in the by-surface layer of the solid, the shift of the slipping plane by the macromolecules adsorbed on the metal oxide surface, and the displacement of the counter-ions in the Stern layer as a result of the polymer adsorption (Vincent,1974).

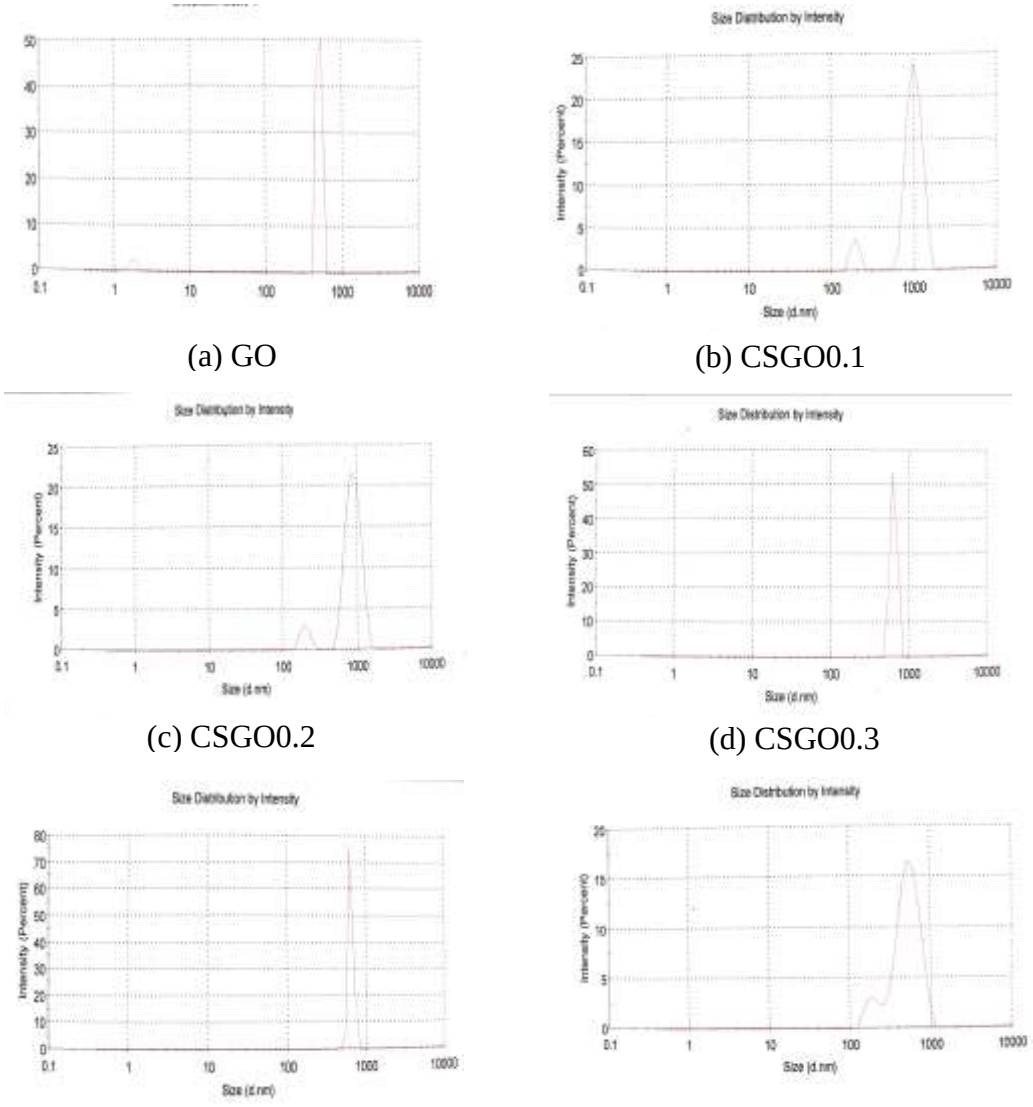

(a) GO (b) CSGO0.1

(c) CSGO0.2 (d) CSGO0.3

(e) CSGO0.4 (f) CSGO0.5

Figure 8 DLS of particles of GO and CSGO nanocomposite

These effects occur simultaneously influencing the obtained zeta potential values. Reduction or increasing the potential is related to the fact which of the above mentioned phenomena predominates. The presence of the dissociated functional groups results in the zeta potential changes depending on the ionic nature of polyelectrolyte; negatively charged groups (e.g., carboxylic groups) cause decrease of ζ, whereas the positively charged groups (e.g., amino groups) contribute to the increase in the zeta potential value. The adsorbed polymer macromolecules are

responsible for the decrease of the zeta potential connected with the shift of the slipping plane from the solid surface. The influence of the counter-ion displacement effect on the zeta potential is more complex and depends on the experiment conditions especially the charge of the colloidal particles (Ostolska, 2014).

The zeta potentials of the obtained pure GO and CSGO in distilled water (pH=7.4) are also showed in Figure 9 and Table 3. As seen in Table 3, the zeta potential and calculated average diameter of the obtained GO and CSGO is suitable range because can be used to evaluate the stability of colloidal systems, zeta potential is very important parameters which reflect their potential as carrier of ultrasound imaging contrast agents, which needs to be inert thus easy to trace and remove during in-vivo using process. It is well known that higher absolute value of zeta potential means higher stable state of colloidal systems, and potential values higher than +30 mV or lower than -30 mV permits a basically stable suspension (Sun *et al.*, 2016).

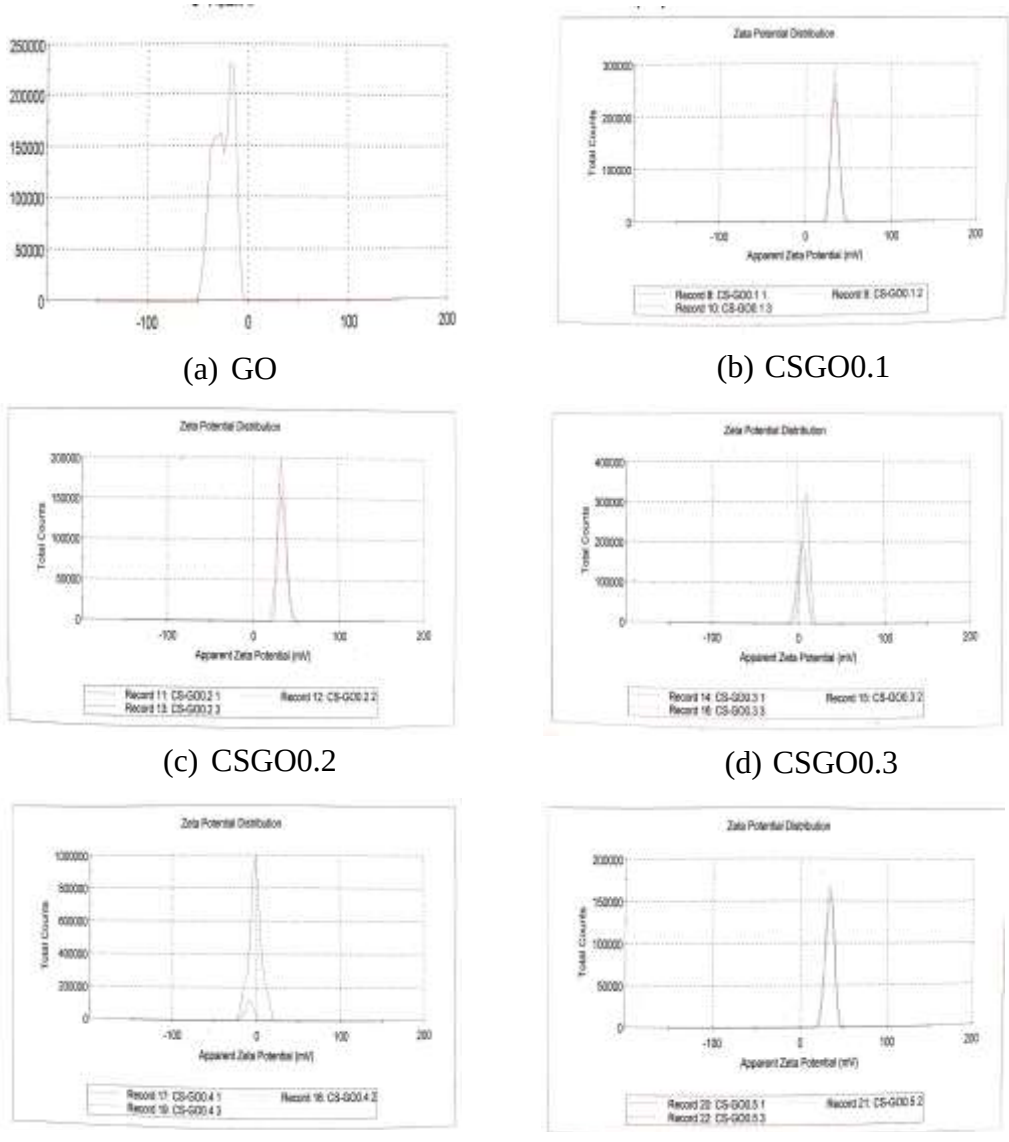

(a) GO (b) CSGO0.1

(c) CSGO0.2 (d) CSGO0.3

(e) CSGO0.4 (f) CSGO0.5

Figure 9 zetapotential measurement of GO and CSGO nanocomposite

Table 3 The zeta potential and calculated average diameter of the GO and CSGO

Sample	Zeta potential (mV)	Average diameter calculated by laser particle size (nm)
GO	- 25.0	249.2
CSGO0.1	+ 33.9	594.6
CSGO0.2	+ 34.1	538.7
CSGO0.3	+ 2.73	627.6
CSGO0.4	-1.38	628.8
CSGO0.5	+ 32.8	369.8

Furthermore, zeta potential data reflect the stability of colloidal systems of the GO and CSGO nanocomposite dispersed in water. The zeta potential values of the GO and CSGO are listed in Table 3. As seen in table, the zeta potential value of pure GO is – 25 mV. All the CSGO nanocomposite except CSGO0.4 obtained show a favorable positive zeta potential value. So, it was found that the zeta potential values of the CSGO increased when particle size increased than that of pure GO due to the amino group related boarded electric double layer surrounding GO. The amide groups act as neutral functional groups to maintain and strengthen the negative charges on the surface of GO, which was the key factor for dispersibility of GO in water. According to DLS results, the advantages for GO reveal their usefulness for size determination in aqueous media for studies related to biological applications, sensing and toxicity.

Conclusion

The biocompatible and biodegradable chitosan based graphene oxide bionanocomposites were prepared by solvent casting method and confirmed by FT IR, TG-DTA, XRD, FE-SEM and UV-vis. The FT IR spectrum suggested that interactions existed between CS and GO as evidenced by the downshift of the C=O stretching vibration of the amide group at 1620.24 cm^{-1}. The thermal studies showed that the loading level of the graphene oxide can affect the decomposition temperature of the bionanocomposites. Optical microscope shows that pure GO and CSGO bionanocomposites have a higher quantity of aggregates with fewer fine particles around the large aggregates in 5 MP. FE SEM micrograph of the nanocomposite showed the presence of the biopolymer chitosan with its porous, rough, granular morphology, the GO with its flat multilayer structure and all of CSGO with rough surface morphology with porous structure. The UV–vis absorption showed optical properties. The bionanoparticles size and surface charge were measured by dynamic light scattering spectroscopy and zeta potential analyzer. According to the results, the synthesized CSGO showed the dispersion peaks, at 594.6 nm with + 33.9 mV in CSGO0.1, at 538.7 nm with + 34.1 mV in CSGO0.2, at 627.6 nm with + 2.73 mV, at 628.8 nm with – 1.38 mV in CSGO0.4 and at 369.8 nm with + 32.8 mV in CSGO0.5, respectively. All the results demonstrated that graphene oxide was well-dispersed in the chitosan matrix, and there are the strong H-bondings between hydroxy groups of the chitosan and hydroxy groups of the graphene oxide. The main contribution of the present work is that the synthesis of chitosan based graphene oxide bionanocomposite may be used for waste water pollution and tissue regeneration.

Author Information

***Corresponding Author**: E-mail: ninithan@uy.edu.mm

ORCID

Aung Than Htwe, http://orcid.org/0000-0002-2937-8117

Acknowledgements

The authors would like to thank the Department of Higher Education, Ministry of Education and University of Yangon for some support to do this research. This research was supported by the KAPLAT program (JSPS Core-to-Core) Japan and Osaka University for intensive 2020. We would like to acknowledge KAPLAT Program Coordinator Professor Dr Hideaki OHGAKI, Institute of Advanced Energy, Kyoto University. Finally, We are also thankful to Nanotechnology Open Facility, Osaka University, for providing zetasizer, XRD, and FESEM facilities.

References

Aung Than Htwe. (2018). "Environmentally Effective Biodegradable and Antimicrobial Properties of Biowaste Chitosan-Polyvinyl Alcohol Hydrogel Composite Film", *International Journal of Scientific and Engineering Research*, vol. 9 (9), pp. 928-934.

Bissessur, R., Liu, P. K. Y., White, W., and Scully, S. F. (2006). "Encapsulation of Polyanilines into Graphite Oxide", *Langmuir*, vol. 22(4), pp. 1729–1734.

Emadi, F., Amini, A., Gholami, A., and Ghasemi Y. (2017). "Functionalized Graphene Oxide with Chitosan for Protein Nanocarriers to Protect Against Enzymatic Cleavage and Retain Collagenase Activity", *Sci. Rep.*, vol. 7(42258), pp. 1-13.

Han, D., Yan, L., Chen, W., and Li, W. (2011). "Preparation of Chitosan/Graphene Oxide Composite Film with Enhanced Mechanical Strength in the Wet State", *Carbohydrate Polymers*, vol. 83, pp. 653–658.

Kausar, A. (2019). "Polymer and Modified Chitosan-Based Nanocomposite: Impending Material for Technical Application", *Polymer-Plastics Technology and Materials*, vol. 158771, pp.1-15.

Konwar, A., Kalita, S., Kotoky, J., and Chowdhury, D. (2016). "Chitosan−Iron Oxide Coated Graphene Oxide Nanocomposite Hydrogel: A Robust and Soft Antimicrobial Biofilm", *ACS Appl. Mater. Interfaces*, vol. 8, pp. 20625−20634.

Kumara, S., Koha, J. (2014). "Physiochemical and Optical Properties of Chitosan Based Graphene Oxide Bionanocomposite", *International Journal of Biological Macromolecules*, vol. 70, pp. 559–564.

Nath, J., Chowdhury, A., and Dolui, S. K. (2018). "Chitosan/Graphene Oxide-Based Multifunctional pH-Responsive Hydrogel with Significant Mechanical Strength, Self-Healing Property, and Shape Memory Effect", *Adv Polym Technol.*, vol. 37, pp. 3665-3679.

Ostolska, I., and Wisniewska, M. (2014). "Application of the Zeta Potential Measurements to Explanation of Colloidal Cr_2O_3 Stability Mechanism in the Presence of the Ionic Polyamino Acids", *Colloid Polym Sci.*, vol. 292, pp. 2453-2464.

Quilaqueo, M., Krumm, M. G., Figueroa, R. R., Troncoso, E., and Esta, H. (2019). "Determination of Size Distribution of Precipitation Aggregates Using Non-Invasive Microscopy and Semiautomated Image Processing and Analysis", *Minerals*, vol. 9 (724), pp. 1-14.

Sun, D., Kang, S., Liu, C., Lu, Q., Cui, L., and Hu, B. (2016). "Effect of Zeta Potential and Particle Size on the Stability of SiO_2 Nanospheres as Carrier for Ultrasound Imaging Contrast Agents", *Int. J. Electrochem. Sci.*, vol. 11, pp. 8520 – 8529.

Suneetha, R. B. (2018). "Spectral, Thermal and Morphological Characterization of Biodegradable Graphene Oxide-Chitosan Nanocomposites", *J. Nanosci. Tech.*, vol. 4(2), pp. 342-344.

Tu, X. Y. Y. F., Li, L., Shang, S., and Tao, X. (2010). "Well-Dispersed Chitosan/Graphene Oxide Nanocomposites", *ACS Applied Materials and Interfaces*, vol. 2(6), pp. 1707–1713.

Valencia, C., Valencia, C. H., Zuluaga, F., Valencia, M. E., Mina, J. H., and Tovar, C. D. G. (2018). "Synthesis and Application of Scaffolds of Chitosan-Graphene Oxide by the Freeze-Drying Method for Tissue Regeneration", *Molecules*, vol. 23(2651), pp. 1-16.

Vincent, B. (1974). "The Effect of Adsorber Polymers on Dispersion Stability", *Adv Colloid Interf*, vol.4, pp.193-277.

Wong, C. P. P., Lai, C. W., Lee, K. M., and Hamid, S. B. A. (2015). "Advanced Chemical Reduction of Reduced Graphene Oxide and Its Photocatalytic Activity in Degrading Reactive Black 5", *Sci. Tech. Adv. Mater.*, vol. 8, pp. 7118-7128.

Wu, K., Liu, X., Li, Z., and Jiao, Y. (2020). "Fabrication of Chitosan/Graphene Oxide Composite Aerogel Microspheres with High Bilirubin Removal Performance", *Materials Science & Engineering*, vol. C 106(110162), pp. 1-10.

Xu, S., Yong, L., and Wu, P. (2013). "One-pot, Green, Rapid Synthesis of Flowerlike Gold Nanoparticles/ Reduced Graphene Oxide Composite with Regenerated Silk Fibroin as Efficient Oxygen Reduction Electrocatalysts", *ACS Appl. Mater. Interf.*, vol. 5, pp. 654-662.

Yang, X., Tu, Y., Li, L., Shang, S., and Tao, X. (2010). "Well-Dispersed Chitosan/Graphene Oxide Nanocomposites", *ACS Applied Materials & Interfaces*, vol. 2(6), pp. 1707-1713.

TAMARINDUS INDICA MEDIATED SYNTHESIS OF COPPER (II) OXIDE NANOPARTICLES AND STUDY ON ITS PHOTOCATALYTIC DEGRADATION OF ALIZARIN AND MALACHITE GREEN DYES

Daisy[1], Ni Ni Sein[2], Daw Hla Ngwe[3]

Abstract

The present study deals with the synthesis of copper(II) oxide nanoparticles (CuO NPs) by using aqueous solution of copper(II) nitrate and leaves extracts of *Tamarindus indica* L. (Ma-Gyi). Characterizations of the CuO NPs were made by Thermogravimetric-Differential Thermal Analysis (TG-DTA), X-ray diffraction (XRD), Fourier Transform Infrared spectroscopy (FT IR), Scanning Electron Microscopy (SEM) and Transmission Electron Microscopy (TEM). CuO nanoparticles were indexed as monoclinic with average crystallite size of 19.9 nm. The presence of characteristic vibration of Cu-O in the range of 430-606 cm^{-1} was confirmed by FT IR analysis. Photocatalytic degradation of alizarin and malachite green dyes by CuO NPs under sunlight was conducted. Highest degradation percentages of alizarin and malachite green were attained at 0.3 g dosage of CuO NPs for 120 min. Treatment of wastewater from textile dye factory with the CuO NPs was performed and 99.13 % of the colour was removed after 8 days.

Keywords: *Tamarindus indica* L., copper(II) oxide nanoparticles, photocatalytic degradation, alizarin, malachite green

Introduction

There are several methods for production of CuO NPs such as chemical, physical and biological processes (Chatterjee *et al*., 2012; Nasrollahzadeh and Sajadi 2015). For example, proton irradiation as physical method and vacuum vapour deposition employed for a wide range of metallic NPs synthesis (Ray *et al*., 2009; Chin *et al*., 2010). However, these methods have several disadvantages since the costs of these methods are higher, the use of toxic chemicals and thus, not environmentally friendly. Therefore, eco-friendly synthesis is essential for production of nanoparticles using biological systems (Lin *et al*., 2011; Honary *et al*., 2012). The use of plant extracts for the synthesis of nanoparticles is a gradually-evolving research area known as green synthesis of nanoparticles (NPs) (Das *et al*., 2013). In green synthesis of metal nanoparticles, the difficult task is to find a suitable and non-toxic natural product, as well as an eco-friendly solvent system (Iravani, 2011). Many researchers have focused on green routes for the synthesis and production of nanoparticles (Sankar *et al.*, 2014).

Organic dyes are extensively used for various industrial applications including textile dyeing, photographic, coating and photochemical industries (Shaabani *et al*., 2014). The presence of these pollutants in the natural environment, particularly in the water surface should be prohibited. Hence, there is a clear need for the development of innovative techniques for the collection, treatment, and storage of water, and the implementation of eco-friendly technology for the effective remediation of water pollutants is highly dedicated. This has inspired the development of photocatalysis, a "catalytic reaction which involves the production of a catalyst by absorption of light" for the treatment of contaminated water. The pollutants can be effectively removed from wastewater by the photocatalytic process using semiconductor photocatalysts like CuO (Narasaiah *et al*., 2017).

[1] Lecturer, Department of Chemistry, Dagon University
[2] Dr, Professor (Retired), Department of Chemistry, University of Yangon
[3] Dr, Professor and Head (Retired), Department of Chemistry, University of Yangon

The aim of this study is the use of environmentally friendly leaf extracts of *Tamarindus indica* L. for the preparation of CuO NPs and to study its photocatalytic activity on degradation of organic dye pollutants.

Materials and Methods

Sample Collection and Sample Preparation

The sample of *Tamarindus indica* L. leaves was collected from Leindaw village, Meiktila Township, Mandalay Region and identified at Department of Botany, Dagon University. The samples were dried under the laboratory condition at room temperature. The dried samples were ground into powder by using grinding machine. The powdered samples were separately stored in air-tight containers.

Preparation of CuO NPs

Leaves extract of *T. indica* was prepared by adding 150 mL of deionized water to 20 g of sample in 250 mL beakers followed by heating the mixtures at 80 ºC for 30 min. Then, the mixture was cooled at room temperature and filtered to obtain leaves extract of *T. indica*. Next, 50 mL of 0.5 M copper(II) nitrate solution was slowly added into 25 mL of leaves extract of *T. indica* in a 250 mL beaker with constant stirring by a magnetic stirrer at 60 ºC. The colour of solution changed from deep blue to dark green and it was heated at 80 ºC. The heated sample was then calcined in a muffle furnace at 500 ºC for 1h. The resulting black coloured powder (CuO NPs) was formed.

Characterization of CuO Nanoparticles

TG-DTA (DTG-60H) Thermal Analyzer, SHIMADZU, Japan was employed for investigation of the thermal property of the prepared sample before calcination. The prepared CuO NPs were analysed by using X-ray diffractometer (Rigaku Co., Tokyo, Japan) using Cu K_α (λ=1.54056 Å) radiation in a scattering range (2θ) of 10° to 70° at an accelerating voltage of 40 kV. The morphology of CuO NPs were characterized by scanning electron microscopy (SEM, JEOL-JSM-5610 LV, Japan) at Universities' Research Center, Yangon and transmission electron microscopy (TEM, JEOL TEM-3010) with an accelerating voltage of 100 kV at State Key Laboratory, College of Science, Beijing University of Chemical Technology, China. The crystallite sizes of CuO NPs were calculated by using Image J software programme. Fourier Transform Infrared (FT IR) spectrum of CuO NPs was recorded on a FT IR spectrometer (FT IR-8400 SHIMADZU, Japan).

Investigation on Photocatalytic Activity of CuO NPs

To study the effect of contact time on degradation of alizarin the following procedure was employed. Briefly, 50 mL of 25 ppm alizarin solution and 0.3 g of prepared CuO NPs were added into 250 mL capacity of clean and dry conical flasks. These solutions were stirred for 15 min in dark for equilibrium of adsorption and desorption processes of alizarin with CuO NPs. After stirring, the conical flasks were placed in sunlight. After every 30 min under sunlight the conical flasks were taken out and centrifuged and decanted. The absorbance values of decantates were measured at 518 nm by using a spectrophotometer. The same procedure was carried out for the degradation study of malachite green and the absorbance values were measured at 617 nm.

To study the effect of dosage of CuO NPs on degradation of alizarin and malachite green dyes, the above mentioned procedure was employed using 0.05, 0.10, 0.15, 0.20, 0.25, 0.30 and 0.35 g of CuO NPs while other factors kept constant.

To study the effect of initial concentrations of alizarin and malachite green dyes, the above mentioned procedure was employed using different concentrations of 15, 25, 35, 45, 55 and 65 ppm while other factors kept constant.

Application of Prepared CuO NPs for Colour Removal of Wastewater Effluent from Textile Factory

Wastewater sample (100 mL each) and prepared CuO NPs (0.5 g each) were added into 250 mL capacity of clean and dry conical flasks. These solutions were stirred for 15 min in dark for equilibrium of adsorption and desorption process of wastewater with nanoparticles. After stirring, the conical flasks were placed in sunlight. After 2 days, 4 days, 6 days and 8 days, the conical flask were taken out and centrifuged and decanted. And then the absorbance values of decantates were measured at 520 nm (wavelength of the maximum absorption of this wastewater) by using a spectrophotometer.

Results and Discussion

Thermogravimetric- Differential Thermal Analysis

Thermal analysis of CuO NPs obtained before calcination was carried out. Figure 1 shows the TG-DTA thermogram of CuO NPs obtained by using leaves extract of *T. indica* and its thermal data are shown in Table 1. The first endothermic peak was due to the removal of physically sorbed water. The second endothermic peak was due to removal of chemisorbed water. The exothermic peak appeared at 329.43 ºC due to conversion of Cu_2O to CuO (Xu *et al*., 2004). It was observed that CuO NPs were almost thermally stable beyond 400 ºC. Thus, according to thermal analysis data the calcination of the residue was calcined at 500 ºC to obtain CuO NPs.

XRD Analysis

CuO NPs prepared by using leaves extract of *T. indica* was characterized by X-ray diffraction analysis. Figure 2 shows the X-ray diffractogram of CuO NPs calcined at 500 ºC. Phase identification by X-ray analysis showed only single phase of CuO. The peaks were well-matched with the standard CuO (89-5899 > CuO). No impurity peaks were observed in the diffractogram. Characteristic diffraction peaks of CuO appeared at 2θ values of 35.308º and 38.518º corresponding to the Miller indices of $(\bar{1}11)$ and (111), respectively. CuO NPs were indexed as the monoclinic structure with a = 4.7093 Å, b = 3.4557 Å and c = 5.1307 Å .The average crystallite size was calculated by Scherrer equation and found to be 19.9 nm (Table 2).

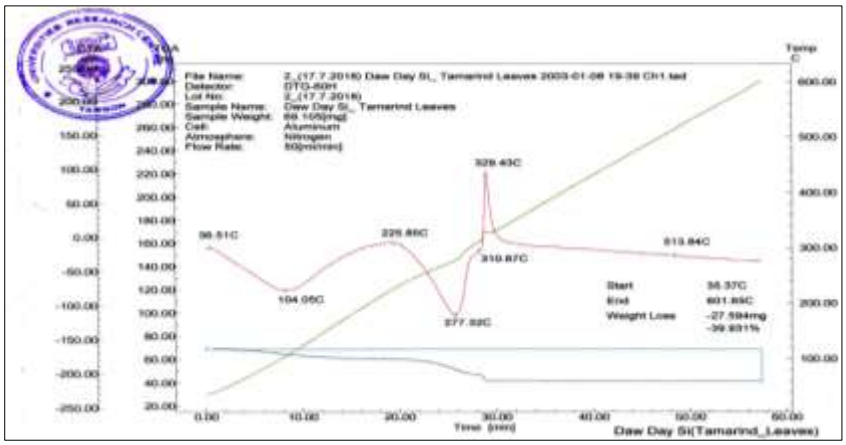

Figure 1 TG-DTA thermogram of the CuO residue by using leaves extracts of *T. indica* at 500 °C

Table 1 TG-DTA Data of the Prepared CuO NPs by Using Leaves Extract of T. indica

No.	Temperature range (°C)	Break in temperature (°C)	Weight loss (%)	Nature of peak	Remark
1	36.51-230	104.05	12.886	Endothermic	Desorption of physically sorbed water molecules
2	230-310	277.32	19.934	Endothermic	Removal of chemisorbed water
3	310-350	329.43	6.639	Exothermic	Conversion of Cu_2O to CuO
4	350-601	-	0.047		Thermally stable

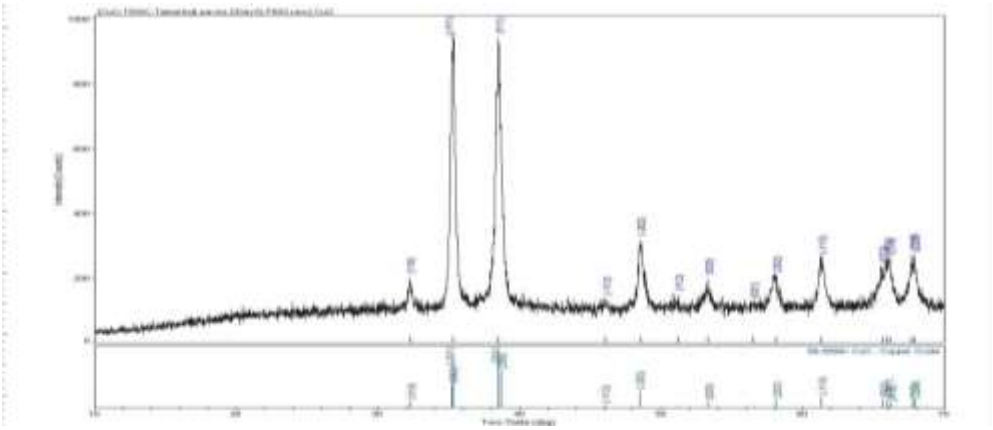

Figure 2 X ray diffractogram of the prepared CuO NPs by using leaves extract of *T. indica*

Table 2 Lattice Constant, Interaxial angle, Crystal Structure and size of the Prepared CuO NPs by Using Leaves Extract of *T. indica* at 500 °C

No.	Lattice constant Axial length (Å)	Interaxial angle (◦)	Crystal structure	Average crystallite size (nm)
1	a=4.7093 b=3.4557 c=5.1307	α,γ=90 β=99.59	Monoclinic	19.9

Scanning Electron Microscopy (SEM) and Transmission Electron Microscopy (TEM) Analysis

SEM and TEM images of prepared CuO nanoparticles by using leaves extract is depicted in Figure 3. A large number of quasi-spherical nanoparticles were observed in SEM image of CuO NPs as shown in Figure 3(a). Furthermore, elongated shapes of CuO NPs were seen in TEM image as depicted in Figure 3(b). It confirmed the monoclinic structure of CuO NPs given by X-ray diffraction analysis. The average crystallite size obtained from TEM was found to be 21.2 nm which was not much different from that calculated from X-ray data.

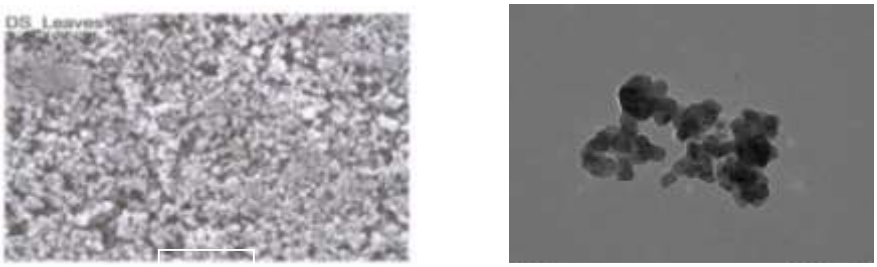

(a) (b)

Figure 3 (a) SEM image and (b) TEM image of CuO NPs by using leaves extract of *T. indica*

Fourier Transform Infrared Analysis

Figure 4 shows FT IR spectrum of CuO NPs. The absorption peaks appeared at 434 cm^{-1} and 511 cm^{-1} were between 430-606 cm^{-1}, the characteristic range of Cu-O stretching vibration (Alizadeh-Gheshlaghi *et al*., 2012).

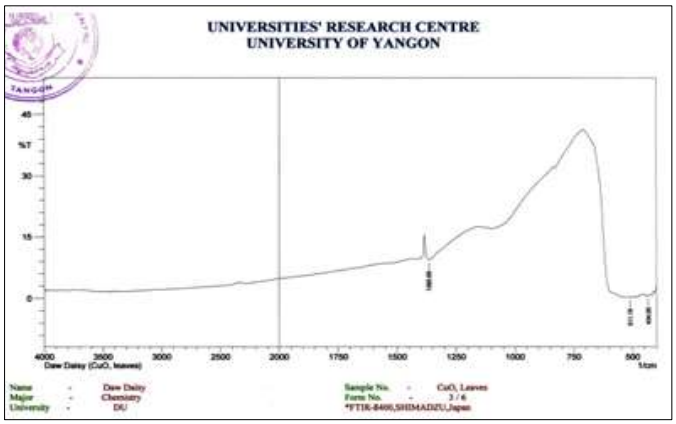

Figure 4 FT IR spectrum of the prepared CuO NPs prepared by using leaves extract of *T. indica*

Photocatalytic Degradation Activity of CuO NPs

Effect of contact time

The photocatalytic degradation experiments were conducted under sunlight by varying the contact time ranging from 30 to 180 min with 30 min interval. After 30 min of contact time, degradation percentage of alizarin was 92.17 % and that of malachite green was 95.76 % (Table 3 and Figure 5). Degradation percentages of alizarin and malachite green dyes solutions increased as the contact time was increased until 120 min at which 97.42 % of alizarin and 98.56 % of malachite dye solutions were degraded. However, beyond 120 min slight changes were observed. The photocatalytic degradation phenomena can be described as follows. First, CuO NPs comes in contact with sunlight, creating a photo-generated electron and a hole (Ijaz *et al*., 2017). The photo-

generated electron reacts with oxygen molecule to form superoxide free radical in the second step. Next, the hole reacts with water and hydroxyl ions to produce highly mercurial hydroxyl radicals. These superoxide free radicals and hydroxyl free radicals degraded the organic dyes and decolourized it. As the time was increased, the surface active sites of CuO NPs was gradually occupied by dye molecules and reached a saturation point. Consequently, less number of surface active sites were available for further adsorption, and followed by photodegradation which was a relatively slow process.

Table 3 Degradation Percent of Dyes by CuO Nanoparticles with Different Contact Times

No	Contact time (min)	Degradation percent (%)	
		Alizarin	Malachite green
1	30	92.17	95.76
2	60	95.47	96.68
3	90	96.91	96.68
4	120	97.42	98.56
5	150	97.32	98.45
6	180	97.37	97.98

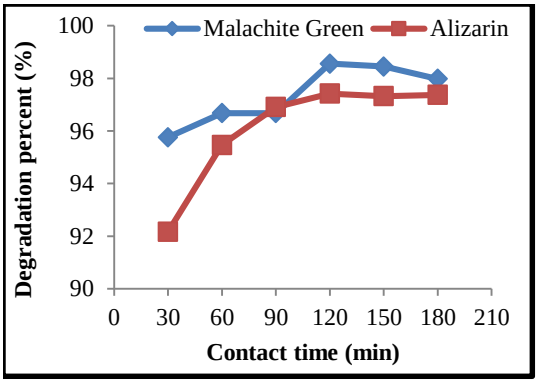

Figure 5 Degradation percentage of dyes solutions as a function contact time

Effect of dosage of CuO NPs

Degradation percentages of alizarin and malachite green dyes using prepared CuO NPs with different dosages (0.05-0.35 g) were studied under sunlight. It was indicated that as the dosage of the sample was increased from 0.05 to 0.3 g, degradation of alizarin increased from 90.11 % to 97.42 % and that of malachite green from 82.69 % to 98.56 % (Table 4 and Figure 6). With the increment of the CuO NPs photocatalyst amount, the quantity of active sites increases on the catalyst surface bringing about the adsorption of more dye particles. Thus, the photocatalytic degradation increased. Further increase of CuO NPs to 0.35 g, degradation percentage of alizarin was found to decrease (96.86 %). After a certain level of catalyst, the degradation percentage decreases because dye molecules are not available for adsorption on active sites of the photocatalyst (Pamecha *et al*., 2016). This reduces the site density for surface holes and electrons and additional catalyst particles, therefore, are not involved in the catalytic activity. Change in degradation percentage of malachite green using 0.035 g CuO NPs was negligible.

Table 4 Degradation Percentage of Dyes by CuO Nanoparticles with Different Dosage

No	Dosage(g)	Degradation percent (%)	
		Alizarin	Malachite green
1	0.05	90.11	82.69
2	0.10	92.73	89.47
3	0.15	95.41	93.51
4	0.20	96.91	95.24
5	0.25	97.73	96.32
6	0.30	97.42	98.56
7	0.35	96.86	98.70

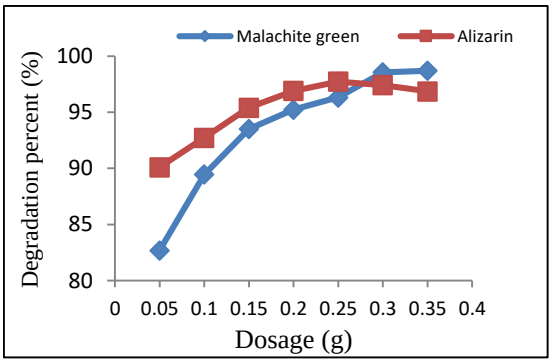

Figure 6 Degradation percentage of dyes solutions as a function of dosage of CuO NPs

Effect of initial concentration of dye solutions

A series of alizarin and malachite green solutions with different concentrations (15 ppm, 25 ppm, 35 ppm, 45 ppm, 55 ppm and 65 ppm) were used to observe the effect of initial dye concentration on the degradation. For 15 ppm concentration of alizarin and malachite green dyes, the degradation percentages were 90.70 % and 91.04 %, respectively (Table 5 and Figure 7). It was observed that the degradation percentages decreased gradually with increasing concentration of dyes. When the initial concentration of the dyes reached 65 ppm, 86.41 % and 87.46 % of alizarin and malachite, respectively, were degraded by CuO NPs obtained from leaves extract of *T.indica*. It is generally noted that increase in dye concentration leads to decrease in the degradation percent. The degradation percent relates to the probability of hydroxyl radicals ($OH^{\bullet}$) formation on the catalyst surface and to the probability of these hydroxyl radicals reacting with dye molecules. Increasing the concentration of dye while keeping the photocatalyst CuO NPs constant, the catalyst surface gets saturated. Simultaneously intense colour of the dye does not permit light to reach photocatalyst (Pamecha *et al*., 2016). The generation of hydroxyl radicals on the surface of catalyst is reduced at high dye concentrations, since the active sites are covered by dye molecules. As a result the degradation percentages decreased.

Table 5 Degradation Percentage of Dyes by CuO NP s with Different Initial Concentration

No	Concentration (ppm)	Degradation Percent (%)	
		Alizarin	Malachite green
1	15	90.70	91.04
2	25	89.01	90.97
3	35	88.26	88.77
4	45	87.87	88.52
5	55	87.10	88.40
6	65	86.41	87.46

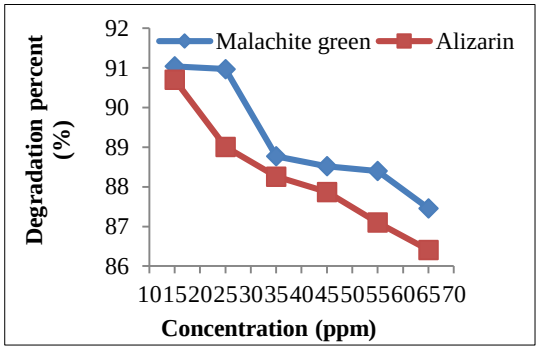

Figure 7 Degradation percentage of dyes solutions as a function of concentration

Application of Prepared CuO NPs for Colour Removal of Wastewater

Wastewater from a textile dye factory (South Okkalapa Township) was firstly determined for its wavelength of maximum absorption and found to be 520 nm. The colour of the effluent from textile dye was reddish brown. After treatment of the wastewater with CuO NPs prepared from leaves extract of *T.indica* for 2 days, 45.07 % of wastewater were decolourized (Table 6 and Figure 8). The percentage of decolourization was observed to be gradually increased and after 4 days, the decolourization percentage was 76.42 %. Increase in decolourization percentage was not noticeable after treatment with CuO NPs for 8 days, i.e., 99.13 %. In this study, higher decolourization percentage of CuO nanoparticles for the treatment of dye effluent was observed.

Table 6 Colour Removal Percentages of Wastewater for Treatment with CuO NPs

No.	Time of treatment (Day)	Absorbance at 520 nm*	Colour removal percent (%)
1	0	2.290	0.00
2	2	1.258	45.07
3	4	0.540	76.42
4	6	0.278	87.86
5	8	0.020	99.13

*λ_{max} of wastewater = 520 nm

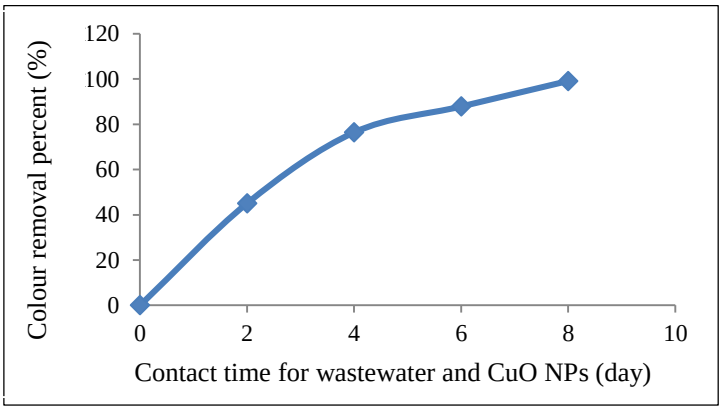

Figure 8 Colour removal percent of wastewater as a function of contact time with CuO nanoparticles

Conclusion

In this study a simple, eco-friendly and efficient preparation of CuO NPs by using leaves extracts of *T. indica* was reported. Aqueous extracts of *T. indica* leaves has been used as reducing agent and also as a capping agent in the CuO NPs preparation. Thermal analysis of CuO nanoparticles showed that CuO was almost thermally stable beyond 400 ºC. The XRD analysis confirmed the crystalline nature of CuO NPs with monoclinic structure and the average crystallite sizes from leaves extracts was found to be 19.9 nm. SEM image showed a large number of quasi-spherical nanoparticles with dense agglomerates. By TEM analysis CuO NPs showed elongated shape and its crystallite size was 21.2 nm. The presence of characteristic vibration of Cu-O in the range of 430-606 cm^{-1} was confirmed by FT IR analysis. The green synthesized CuO NPs showed good photocatalytic activity in the degradation of organic dyes like alizarin and malachite green. Highest degradation percentages of alizarin and malachite green were attained at 0.3 g dosage of CuO and contact time of 120 min. CuO NPs could degrade 99.13 % of the organic dye of the wastewater effluent from the textile factory. The significant catalytic performance of CuO NPs is due to their high surface to volume ratio providing more active sites of the reactant molecules to interact. The photocatalytic results conclude that the prepared CuO nanoparticles have high efficiency to degrade organic dyes under sunlight and thus, they can find applications in textile industry and water treatment plants.

Acknowledgement

The authors would like to express their profound gratitude to the Department of Higher Education, Ministry of Education, Yangon, Myanmar, for provision of opportunity to do this research and Myanmar Academy of Arts and Science for allowing to present this paper.

References

Alizadeh-Gheshlaghi, E., Shaabani, B., Khodayari, A., Azizian-Kalandaragh, Y. and Rahimi, R. (2012). "Investigation of the Catalytic Activity of Nano-sized CuO, Co_3O_4 and $CuCo_2O_4$ Powders on Thermal Decomposition of Ammonium Perchlorate". *Powder Techno,* vol. 217, pp. 330–339

Chatterjee, A. K., Sarkar, R. K., Chattopadhyay, A. P., Aich, P., Chakraborty, R. and Basu, T. (2012). "A Simple Robust Method for Synthesis of Metallic Copper Nanoparticles of High Antibacterial Potency against *E. coli.*". *Nanotechnology*, vol. 23(8), pp. 1-11

Chin, H. S., Cheong, K. Y. and Razak, K. A. (2010). "Review on Oxides of Antimony Nanoparticles: Synthesis, Properties, and Applications". *J Mater Sci*, vol. 45(22), pp. 5993-6008

Das, S. K., Khan, M. M. R., Parandhaman, T., Laffir, F., Guha, A. K., Sekaran, G. and Mandal, A. B. (2013). "Nano-Sillica Fabricated with Silver Nanoparticles: Antifouling Adsorbent for Efficient Dye Removal, Effective Water Disinfection and Biofouling Control". *Nanoscale*, vol. 5(12), pp. 5549-5560

Honary, S., Barabadi, H., Gharaei-Fathabad, E. and Naghibi, F. (2012). "Green Synthesis of Copper Oxide Nanoparticles Using Penicillium aurantiogriseum, Penicillium citrinum and Penicillium waksmanii". *Dig. J Nanomater Biostruct*, vol. 7(3), pp. 999-1005

Ijaz, F., Shahid, S., Khan, S. A., Ahmad, W. and Zaman, S. (2017). "Green synthesis of Copper Oxide Nanoparticles using Abutilon indicum Leaf Extract: Antimicrobial, Antioxidant and Photocatalytic Dye Degradation Activities". *Tropical Journal of Pharmaceutical Research*, vol. 16(4), pp. 743-753

Iravani, S. (2011). "Green Synthesis of Metal Nanoparticles Using Plants". *Green Chem*, vol. 13(10), pp. 2638-2650

Lin, X., Wu, M., Wu, D., Kuga, S., Endo, T. and Huang, Y. (2011). "Platinum Nanoparticles Using Wood Nanomaterials: Eco-Friendly Synthesis, Shape Control and Catalytic Activity for p-Nitrophenol Reduction". *Green Chem*, vol. 13(2), pp. 283-287

Narasaiah, P., Mandal, B. K. and Sarada, N. C. (2017). "Biosynthesis of Copper Oxide Nanoparticles from Drypetes sepiaria Leaf Extract and Their Catalytic Activity to Dye Degradation". *Materials Science and Engineering*, vol. 263, pp. 1-9

Nasrollahzadeh, M. and Sajadi, S. M. (2015). "Green Synthesis of Copper Nanoparticles Using Ginkgo biloba L. Leaf Extract and their Catalytic Activity for the Huisgen [3+ 2] Cycloaddition of Azides and Alkynes at Room Temperature". *J Colloid Interface Sci*, vol. 457, pp. 141-147

Pamecha, K., Mehta, V. and Kabra, B. V. (2016). "Photocatalytic Degradation of Commercial Textile Azo Dye Reactive Blue 160 by Heterogeneous Photocatalysis". *Adv. Appl.Sci.Res*, vol. 7(3), pp. 95-101

Ray, S. C., Saha, A., Jana, N. R. and Sarkar, R. (2009). "Fluorescent Carbon Nanoparticles: Synthesis, Characterization, and Bioimaging Application". *J Phys Chem C*, vol. 113(43), pp. 18546-18551

Sankar, R., Manikandan, P., Malarvizhi, V., Fathima, T., Shivashangari, K. S. and Ravikumar, V. (2014). "Green Synthesis of Colloidal Copper Oxide Nanoparticles Using Carica Papaya and its Application in Photocatalytic Dye Degradation". *Spectrochim Acta Mol Biomol Spectrosc*, vol. 121, pp. 746-750

Shaabani, B., Alizadeh-Gheshlaghi, E., Azizian-Kalandaragh, Y. and Khodayari, A. (2014). "Preparation of CuO Nanopowders and Their Catalytic Activity in Photodegradation of Rhodamine-B". *Advanced Powder Technology*, vol. 25(3), pp. 1043-1052

Xu, C. H., Woo, C. H. and Shi, S. Q. (2004). "Formation of CuO Nanowires on Cu Foil". *Chemical Physics Letters*, vol. 399(1), pp. 62-66

EXTRACTION AND KINETIC PROPERTIES OF PEROXIDASE FROM BITTER GOURD

Khin Sandar Linn[1], Myat Kyaw Thu[2], Thida[3], Ni Ni Than[4]

Abstract

Peroxidase (PODs, E.C.1.11.1.7) catalyzes the oxidation of H_2O_2 and guaiacol forming the product tetraguaiacol and water. In this study partially purified peroxidase enzyme was extracted from fresh bitter gourd by ammonium sulphate precipitation method. Guaiacol was used as a substrate for peroxidase activity determination by using UV-visible spectrophotometer. Protein content of enzyme solution was determined by Biuret method. The specific activity of peroxidase was 0.6361 U mL^{-1} and the enzyme was purified 1.99 fold over its crude extract. The optimum pH of peroxidase was 6.0 in phosphate buffer and optimum temperature was 40 ˚C. The values of K_m and V_{max} treated statistically using the linear regression method were compared with various graphical methods (Michaelis-Menten, Lineweaver-Burk, Eadie-Hofstee and Hanes-Wilkinson). The K_m and V_{max} values of peroxidase were found to be 0.514 x10^{-2} M and 26.853 M min^{-1}, respectively, from Lineweaver-Burk plot. The reaction order for peroxidase-catalyzed reaction of conversion of guaiacol to tetraguaiacol was found to be first order. The activation energy (E_a) of peroxidase-catalyzed reaction was calculated to be 3.592 kcal mol^{-1}. The decolourisation of methyl orange (MO) by crude peroxidase from bitter gourd was studied by using spectrophotometric method.

Keywords: Bitter gourd, peroxidase, guaiacol, ammonium sulphate precipitation method, methyl orange

Introduction

Peroxidase (POD) is an oxidoreductase that catalyzes a reaction in which hydrogen peroxide acts as the acceptor and another compound acts as the donor of hydrogen atoms. Peroxidases have been discovered in various plants and prokaryotic and eukaryotic microbes as well as in mammalian cells. The best characterized plant peroxidase is from horseradish, from which more than 40 isoenzymes have been isolated. In plants, peroxidases have various physiological roles in for example, degradation and synthesis of lignin in cell walls, in the defence mechanism and in cell damage (Vance *et al.,* 1980).

Commercially available peroxidase is widely employed for removal of phenols and amines from industrial wastewater, bleaching of industrial dyestuffs, lignin degradation, fuel and chemical production from wood pulp and in various organic syntheses. Peroxidase act on the removal of hydrogen atom most usually from the alcohol groups, which are combined with hydrogen peroxide in order to form molecules of water and oxidized phenolic compounds, acting as detoxifying enzymes and as a cell wall crossing linked enzyme during wounding stress (Passardi *et al*., 2005).

Several investigations have reported the use of peroxidases for the removal of azo dyes in aqueous phase, obtaining percentages of decolourization ranging from 50 to 90 % using different operating conditions (Nouren and Nawaz, 2015). In the literature several studies employing soybean peroxidases (SBP) for the decolouration of azo dyes can be found.

The aim of this research was to study the extraction and biochemical characterization of peroxidase from bitter gourd.

[1] Dr, Lecturer, Department of Chemistry, University of Yangon
[2] Dr, Professor, Department of Chemistry, University of Yangon
[3] Dr, Associate Professor, Department of Chemistry, University of Yangon
[4] Dr, Professor and Head, Department of Chemistry, University of Yangon

Materials and Methods

Sample Collection

Bitter gourd samples were purchased from local shop, Kyeemyindaing Township, Yangon Region. Bovine Serum Albumin (BSA) was purchased from Sigma-Aldrich, England. All other chemicals used were of analytical reagent grade. In all investigations, the recommended standard methods and techniques involving both conventional and modern methods were provided.

Solution Preparation

Guaiacol (0.12 mL) was dissolved in phosphate buffer (pH 7) and the volume made up to the mark in a 50 mL volumetric flask. Hydrogen peroxide (0.128 mL of 50 % v/v) was dissolved in phosphate buffer (pH 7) and the volume made up to the mark in a 100 mL volumetric flask. Bovine Serum Albumin 0.2 g was dissolved in a small amount of distilled water, then 1mL of 10 % sodium hydroxide was added and the volume made up 20 mL with distilled water.

Extraction and Partial Purification of Peroxidase from Bitter Gourd

The fresh bitter gourd was washed with tap water, chopped and mixed with phosphate buffer pH 7.0 solution. It was stirred in ice for 2 h and filtered. Solid ammonium sulphate was slowly added to this extract to obtain 20 % first and then 70 % saturation and stirred for 2h in an ice bath (Koktepea *et al*., 2017). After standing overnight, the precipitated protein containing peroxidase enzyme was collected by centrifugation at 5000 rpm for 30 min.

Peroxidase Assay, Protein Determination and Kinetic Studies of Peroxidase from Bitter Gourd

For enzyme assay the peroxidase activity of bitter gourd was determined by the spectrophotometric method at 470 nm using guaiacol as a substrate in the presence of hydrogen peroxide (Koktepea *et al*.,2017). Substrates were mixed with different concentrations of enzyme and then the absorbance values were observed at 470 nm. Peroxidase activity assay was based on the measurement of tetraguaiacol formation in the presence of guaiacol and H_2O_2 within 2 min. The final mixture contained 0.1 mL enzyme sample, 20 mM guaiacol (1.0 mL), 22.5 mM H_2O_2 (0.1 mL), and 2.7 mL phosphate buffer (0.1 M, pH 6.0).

Protein content was determined by Biuret method using Bovine Serum Albumin (BSA) as standard at 550 nm. In brief, 4 mL of Biuret reagent solution was added to 1 mL of protein solution in a test tube. The solution mixture was stored at room temperature for 30 min and the absorbance measured (Stoscheck, 1990).

Effects of enzyme concentration, pH, temperature, reaction time and substrate concentration were studied by spectrophotometric method. The enzyme kinetic parameters of K_m, V_{max}, activation energy, and reaction order of peroxidase-catalyzed reaction were determined by spectrophotometric method.

Decolourization of Azo Dye by Peroxidase

The decolourization of methyl orange (MO) by partially purified peroxidase from bitter gourd was studied by using spectrophotometric method. Methyl orange (20 ppm) was incubated with bitter gourd peroxidase in 0.1 M citrate buffer, pH 4.0 at 30 ^oC in the presence of 2 mM hydrogen peroxide for 4 h (Ambatkar and Mukundan, 2015). Dye decolourization was monitored at 464 nm and the percent decolourization was calculated by taking untreated dye solution as control 100 % (Verma and Madamwar, 2002).

Results and Discussion

Effect of Enzyme Concentration on Peroxidase-catalyzed Reaction

Increasing the amount of enzyme increases the frequency of with which the enzyme and substrate collide. As a result, enzyme-substrate complexes form more quickly and the rate of reaction increases. The validity of enzyme assay method was tested using different concentrations of enzyme.

In this experiment guaiacol was used as substrate. Oxidized guaiacol (yellowish-brown colour) was observed (Figure 1). The absorbance of the oxidized guaiacol was found to have a linear relationship with different enzyme concentration ranging between 11.94 to 59.70 mg/mL of enzyme (Table 1 and Figure 2). The velocity of an enzymatic reactions was found to vary directly with the enzyme concentration, i.e., the more the enzyme, the faster the reaction. If the amount of is doubled the reaction rate will also be doubled generally.

(a) (b) (c) (d) (e) (f)

Figure 1 Mixture of 20 mM guaiacol and 22 mM H_2O_2 solutions (a) without enzyme (control) and with (b) 11.94 mg mL^{-1}, (c) 23.88 mg mL^{-1}, (d) 35.82mg mL^{-1} (e) 47.76 mg mL^{-1} and (f) 59.70 mg mL^{-1} enzyme solutions

Table 1 Relationship between Absorbance and Enzyme Concentration

No	Enzyme concentration (mg mL^{-1})	Absorbance at 470 nm
1	59.70	0.865
2	47.76	0.678
3	35.82	0.502
4	23.88	0.357
5	11.94	0.193

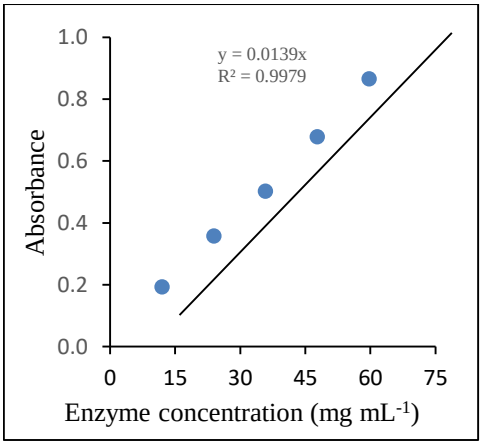

Figure 2 Plot of absorbance as a function of enzyme concentration

Calibration Curve for Protein Determination by Biuret Method

In the present work, bovine serum albumin (BSA) was used as a standard protein (Savary *et al.*, 1969). The determination of protein concentration was done using a calibration curve created using samples of known concentrations. The different absorbance values were obtained for various standard protein solutions by using a UV-visible spectrophotometer. The absorbance of protein treated with Biuret reagent was measured at 550 nm after the purple product formed.

It was found that the nature of the plot of absorbance at 550 nm *vs.* concentration of protein (mg mL^{-1}) (Table 2 and Figure 3), was a straight line passing through the origin showing that Beer's Law was obeyed.

Table 2 Relationship Between Absorbance and Concentration of Bovine Serum Albumin (BSA) Solutions

No.	Protein Concentration (mg mL^{-1})	Absorbance at 550 nm
1	2.0	0.147
2	4.0	0.283
3	6.0	0.405
4	8.0	0.524
5	10.0	0.630

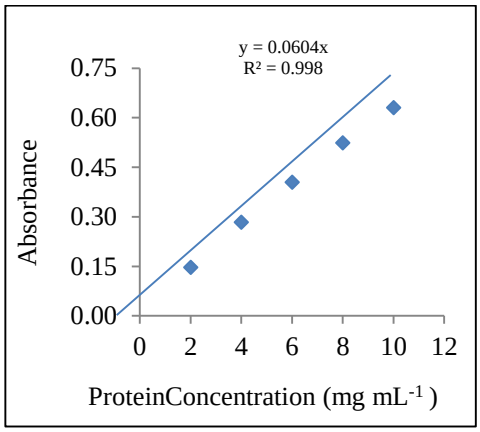

Figure 3 Calibration curve for standard protein solution

Peroxidase Activity, Protein Content and Specific Activity of Peroxidase

Enzyme activity was tested using guaiacol as substrate where the effect of peroxidase enzyme on guaiacol in the presence of hydrogen peroxide was tested (Lakshmi *et al*., 2018). Spectrophotometric method of analysis was used at a wavelength of 470 nm to quantify the activity on the basis of the production of coloured complex due to the action of the enzyme. One unit of peroxidase was defined as the amount of enzyme that caused the formation of 1 mM of tetraguaiacol per minute.

The protein content was determined by Biuret method and it was observed to be 10.8702 mg mL^{-1} (Table 3). Specific enzyme activity is the number of enzyme units per mL divided by the concentration of protein in mg mL^{-1}. The specific activity was calculated to be 0.6361 U mg^{-1}. After 70 % ammonium sulphate precipitation, peroxidase was purified to 1.99 fold over crude extract.

Table 3 Peroxidase Activity, Protein Content and Specific Activity of Bitter Gourd in Different Purification Steps

Fraction	Total activity (U)	Total protein (mg)	Specific activity (U mg^{-1})	Purification fold
Crude	21.9286	68.4252	0.3204	1.0
After precipitation with 20 % ammonium sulphate	31.1102	66.3363	0.4689	1.46
After precipitation with 70 % ammonium sulphate	6.9154	10.8702	0.6361	1.99

Optimum pH of Peroxidase Activity

The enzyme activity is affected by pH due to changes in the ionization pattern of ionic groups located in the lateral chains of amino acids constituents of the protein primary structure. The bell-shaped activity versus pH curve is an indication of pH influence on the enzyme molecular structure conformation (*Vitolo*, 2010).

In this work, different buffers of pH values 5.0 to 8.0 were used to determine the activity of the prepared peroxidase sample. The nature of the activity *vs.* pH curve of the enzyme (Table 4 and Figure 4) was obviously found to be unsymmetrical and the optimum pH was obtained at pH 6.0 with guaiacol as substrate.

Table 4 Relationship between Peroxidase Activity and pH of Phosphate Buffer Solution

Phosphate Buffer	pH	Peroxidase activity (U mL^{-1})
1	5.0	5.692
2	5.5	6.354
3	6.0	7.146
4	6.5	6.662
5	7.0	5.723
6	7.5	5.500
7	8.0	4.962

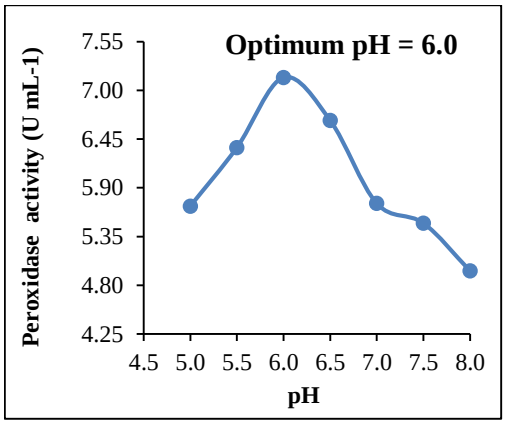

Figure 4 Plot of peroxidase as a function of pH solutions

Optimum Temperature of Peroxidase Activity

The optimum temperature of an enzyme is a temperature at which the greatest amount of substrate changes in time units (*Vitolo*, 2010). Temperature affects the **reaction rate of enzymes**, as do pH, substrate concentration and enzyme concentration. The optimum temperature for any enzyme not only changes in relation to time, but may also change in relation to changes in pH, concentration and purity of enzyme preparation.

In this study, the effect of the temperature on the peroxidase activity was investigated in the temperature range from 10 to 70 ºC. The optimum temperature for peroxidase was found to be 40 ºC in phosphate buffer pH 6.0 (Table 5 and Figure 5). The activation energy E_a of peroxidase-catalyzed reaction was calculated by Arrhenius equation, log k = -E_a/ (2.303 RT) (Whitaker, 1996). Table 6 shows the relationship between temperature and velocity of peroxidase-catalyzed reaction. Figure 6 shows the graph for determination of activation energy and Arrhenius constant. By using the constant substrate concentration throughout the experiment, rate constant (K) in Arrhenius equation can be substituted by velocity of the peroxidase-catalyzed reaction. The activation energy (E_a) was determined to be 3.592 kcal mol^{-1} from linear regression method.

Table 5 Relationship between Peroxidase Activity and Temperature of the Solution at pH 6.0

No.	Temperature (°C)	Peroxidase Activity (U mL^{-1})
1	10	2.792
2	20	3.908
3	30	5.223
4	40	6.741
5	50	5.769
6	60	5.346
7	70	3.246

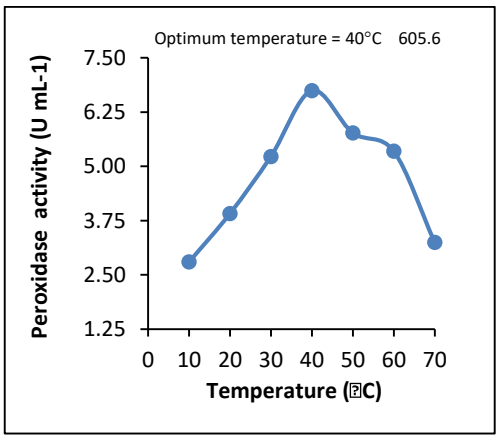

Figure 5 Plot of peroxidase activity as a function of temperature of the solutions at pH 6.0

Table 6 Relationship between Temperature and Velocity of the Peroxidase-catalyzed Reaction

Temperature (°C)	Temperature (K)	1/T (10^3 K^{-1})	Velocity (M min^{-1})	Log V
10	283	3.534	9.308	0.9689
20	293	3.413	13.026	1.1148
30	303	3.300	17.410	1.2408
40	313	3.195	22.487	1.3519

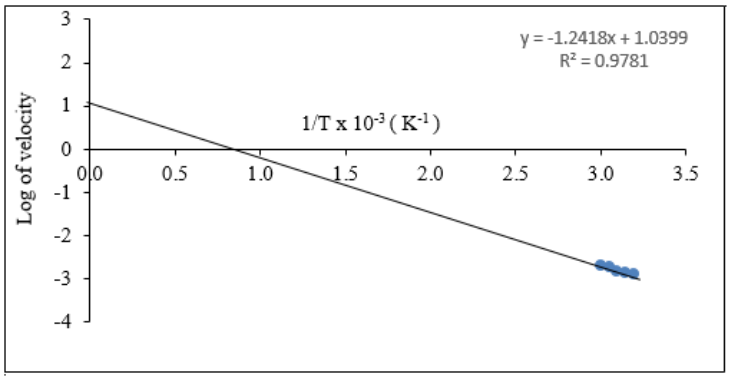

Figure 6 Plot of log of velocity as a function of 1/T for peroxidase

Effect of Reaction Time on Peroxidase-catalyzed Reaction

The activity of the enzyme is determined by the enzyme concentration, substrate concentration, pH, temperature and reaction time (Wiseman, 1985). In this work, the action of the peroxidase on guaiacol was studied in phosphate buffer of pH 6.0. The amount of tetraguaiacol liberated during the various reaction time of 1, 2, 5, 8, 11, 14, 17 and 20 min were determined by spectrophotometric method (Table 7). Figure 7 shows the plot of velocity of peroxidase reaction as a function of reaction time. At the beginning of the reaction (during 5 min), the reaction was very fast. Then, velocity decreased steadily. Therefore, in sequence studies, reaction time of 2 min was used for initial velocity measured in enzyme kinetic.

Table 7 Relationship between Reaction Time and Velocity of Peroxidase - catalyzed Reaction

No	Reaction Time (min)	Velocity (M min^{-1})
1	1	19.795
2	2	14.256
3	5	3.487
4	8	2.718
5	11	2.581
6	14	2.205
7	17	2.103
8	20	1.915

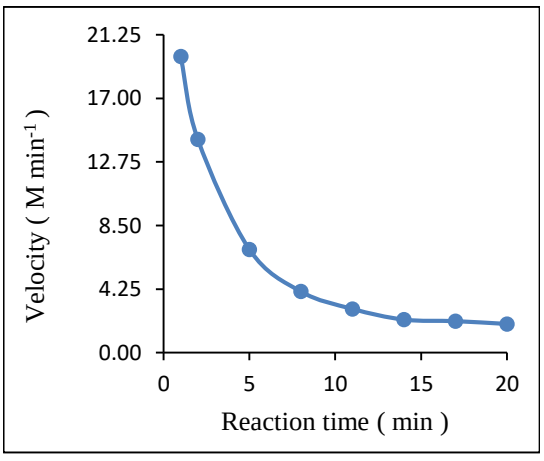

Figure 7 Plot of velocity of peroxidase-catalyzed reaction as a function of reaction time

Effect of Substrate Concentration on Peroxidase-catalyzed Reaction

The effect of substrate concentrations on peroxidase-catalyzed reaction is shown in Table 8. Each enzyme has a characteristic substrate concentration (K_m, the Michaelis-Menten constant) at which the reaction velocity is one-half maximal (Sawhney and Singh, 2000). Michaelis-Menten equation, ($V=V_{max}[S]/K_m+[S]$) explains kinetics but, because it is nonlinear, is a little hard to deal with real practical data. K_m and V_{max} were found to be 0.472 x 10^{-2} M and 23.205 M min^{-1}, respectively, from Michaelis-Menten plot (Figure 8).

Most common transform is the Lineweaver-Burk plot which is also called double reciprocal plot 1/V *vs* 1/[S]) plot. The reciprocal transformation distorts the error in the measurements as shown in Table 9 and Figure 9. The noisiest data are too heavily weighted when linear regression (Paradine and Rivert, 1970) is used to determine the best straight line. Figures 10 and 11 show Eadie-Hofstee and Hanes-Wilkinson plots, respectively, for evaluation of K_m and V_{max} values. The values of K_m and V_{max} treated statistically using the linear regression method were compared with various graphical methods. From the Lineweaver-Burk plot K_m and V_{max} value were found to be 0.515× 10^{-2} M and 26.831 M min^{-1}, respectively, by graphical method and 0.514 × 10^{-2} M and 26.853 M min^{-1} by linear regression method.

Table 8 Relationship between Substrate Concentration and Velocity of Peroxidase-Catalyzed Reaction

No	[S]×10^3 (M)	-[S]×10^3 (M)	1/[S]×10^{-3} (M^{-1})	V (M min^{-1})	1/V×10^1 (M^{-1}min)	V/[S] ×10^{-3} (min^{-1})	[S]/V×10^3 (min)
1	5	-5	0.2000	12.9487	0.7723	2.5897	0.3861
2	10	-10	0.1000	18.8462	0.5306	1.8846	0.5306
3	15	-15	0.0667	20.6923	0.4833	1.3795	0.7249
4	20	-20	0.0500	21.5128	0.4648	1.0756	0.9297
5	25	-25	0.0400	22.1282	0.4519	0.8851	1.1298
6	30	-30	0.0333	22.4359	0.4457	0.7479	1.3371
7	35	-35	0.0286	22.7179	0.4402	0.6491	1.5406
8	40	-40	0.0250	23.2051	0.4309	0.5801	1.7238

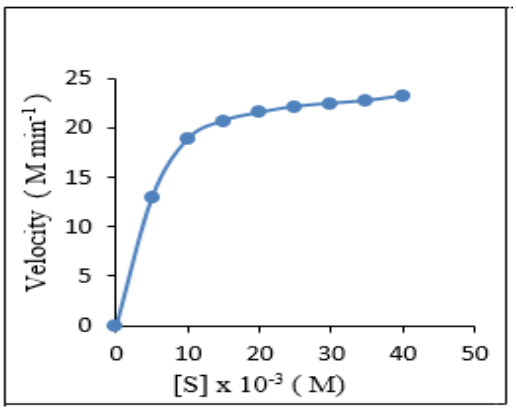

Figure 8 Michaelis-Menten plot used for graphic evaluation of V_{max} and K_m for crude peroxidase

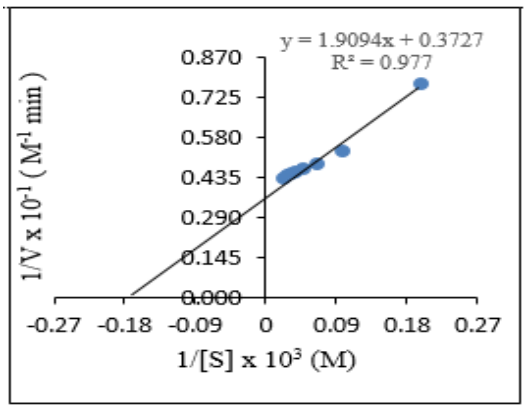

Figure 9 Lineweaver-Burk plot of 1/V *vs.* 1/[S] used for graphic evaluation V_{max} and K_m for crude peroxidase

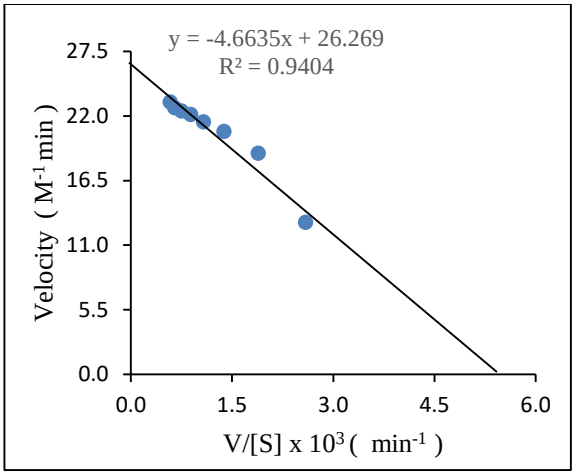

Figure 10 Eadie-Hofestee plot of V *vs.* V/[S] used for graphic evaluation of V_{max} and K_m for crude peroxidase

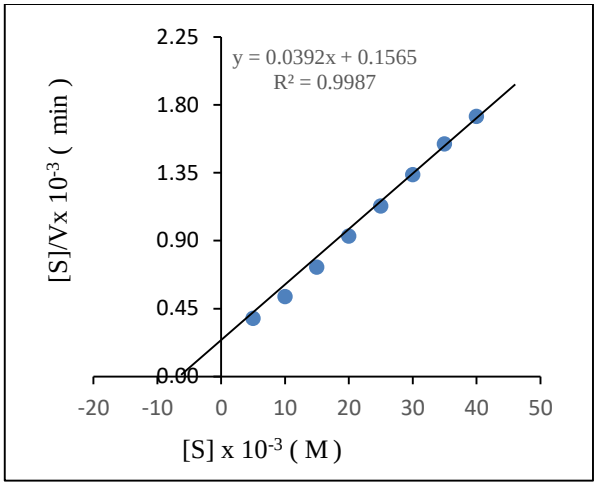

Figure 11 Hanes-Wilkinson plot of [S]/V *vs.* [S] used for graphic evaluation V_{max} and K_m for crude peroxidase

Table 9 Comparison of Kinetic Parameters of the Peroxidase Enzyme from Different Methods

No.	Methods	Graphical method		Linear regression method	
		V_{max} (M min^{-1})	$K_m \times 10^2$ (M)	V_{max} (M min^{-1})	$K_m \times 10^2$ (M)
1.	Michaelis-Menten	23.205	0.472	-	-
2.	Lineweaver-Burk	26.831	0.515	26.853	0.514
3.	Eadie-Hofstee	26.269	0.469	26.269	0.466
4.	Hanes-Wilkinson	26.837	0.421	25.510	0.397

Effect of Reaction Order on Peroxidase-catalyzed Reaction

The order of a chemical reaction with respect to the individual components is defined as power of the component concentration included into the rate equation. Depending on the substrates concentrations, the kinetic of an enzyme-catalyzed reaction may be described by the first-order rate equation (Bergmeyer, 1983).

The plot of Log $V/(V_{max}–V)$ *vs*. Log [S] will give a straight line from which reaction order (n) value can be computed from the slope (Table 10 and Figure 12). The reaction order (n) for peroxidase was calculated to be 1.22 proving that the reaction order was first order.

Table 10 Reaction Order for Peroxidase-catalyzed Reaction

No.	Log [S]	Log $V/(V_{max}-V)$
1	-2.3010	0.0462
2	-2.0000	0.5160
3	-1.8239	0.7250
4	-1.6989	0.8446
5	-1.6021	0.9537
6	-1.5229	1.0177
7	-1.4559	1.0841
7	-1.3979	1.2243

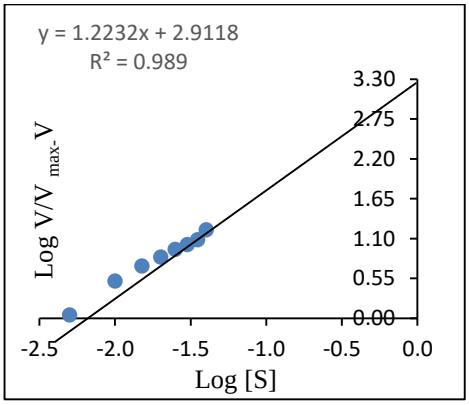

Figure 12 Plot of V/V_{max}-V as a function of log [S] of peroxidase-catalyzed reaction

Enzymatic Dye Decolourization

The decolourization of methyl orange (MO) by partially purified peroxidase from bitter gourd was studied by using spectrophotometric method. MO is a pH sensitive dye, red–orange under acidic conditions and yellow in neutral and alkaline conditions. Decolourization caused a change in colour from orange to yellow (Figure 13). Bitter gourd peroxidase was demonstrated a maximum dye decolourization efficiency of 80.42 % under the conditions of 4 h incubation at 30 °C using 2 mM of hydrogen peroxide, 0.2 mL crude bitter gourd peroxidase and 20 ppm methyl orange at pH 4.0.

The decolourization of MO may be thought to occur by the oxidation of the molecule by the partially purified peroxidase with H_2O_2. This oxidation is brought about by the enzyme by two sequential one-electron transfers (Veitch, 2004). This oxidation causes the formation of dye radicals and related chemical species that comprise the decolourized or bleached form of the dye (Coen *et al*., 2001). The susceptibility of the MO molecules to enzymatic oxidation would also depend on the pH of the reaction mixture.

Figure 13 (a) Methyl orange solution containing H_2O_2 (2 ppm) without enzyme (control) after 4 h
(b) Decolourized methyl orange solution containing H_2O_2 solution (2mM) using with peroxidase after 4 h

Conclusion

In this research, partially purified peroxidase enzyme was extracted from fresh bitter gourd by ammonium sulphate precipitation (20-70 %) method. The specific activity of peroxidase was 0.6361 U mg^{-1} and the enzyme was purified 1.99 fold over its crude extract. The optimum pH was 6.0 in phosphate buffer and optimum temperature of peroxidase was 40 ˚C. The activation energy for peroxidase-catalyzed reaction was calculated to be 3.592 kcal mol^{-1} between 10 and 40 ˚C and thus at lower temperatures, peroxidase enzyme will be relatively stable. K_m and V_{max} for guaiacol by Lineweaver-Burk was 0.515 x 10^{-2} M and 26.831 M min^{-1}, respectively, by graphical method and 0.514 x 10^{-2} M and 26.853 M min^{-1} by linear regression method. K_m and V_{max} values by other methods such as Eadie-Hofstee and Hanes-Wilkinson were also determined and found to agree with each other. The reaction order for peroxidase-catalyzed reaction of conversion of guaiacol to tetraguaiacol was found to be first order. Bitter gourd peroxidase was demonstrated a maximum dye decolourization efficiency of 80.42 % under the conditions of 4 h incubation at 30 °C using 2 mM of hydrogen peroxide, 0.2 mL crude bitter gourd peroxidase and 20 ppm methyl orange at pH 4.0.

Acknowledgement

The authors would like to thank the Myanmar Academy of Art and Science for allowing to present this paper and Professor Dr Myint Myint Khaing, Department of Chemistry, University of Yangon, for her kind encouragement.

References

Ambatkar, M. and Mukundan, U. (2015). "Enzymatic Decolourisation of Methyl Orange and Bismarck Brown using Crude Peroxidase from Armoracia rusticana". *Appl. Water Sci*., vol.5, pp.397- 406

Bergmeyer, H. U. (1983), "Methods of Enzymatic Analysis". *Braz. Arch. Biol. Technol.*, vol 54(1), pp.125-132

Coen, J. J. F., Smith, A. T., Candeias, L. P. and Oakes, J. (2001). "New Insights into Dye Degradation Mechanisms by One-electron Oxidation Processes". *J. Chem. Soc.*, vol.2, pp.2125–2129

Koktepea, T., Altına, S., Tohmaa, H., Gulçinb, I. and Koksa, E. (2017). "Purification, Characterization and Selected Inhibition Properties of Peroxidase from Haricot Bean (*Phaseolus vulgaris* L.)". *International Journal of Food Properties*, vol. 20(2), pp.1944-1953

Lakshmi, G. M., Shashidhara, G. M., Madhu, R., Muthappa, R., Vivek, H. K. and Prasad, M. N. N. (2018). "Characterization of Peroxidase Enzyme and Detoxification of Phenols Using Peroxidase Enzyme Obtained from *Zea Mays* L. Waste". *Applied Water Science*, vol.8 (7), pp.1-7

Nouren, S. and Nawaz, B. A. (2015). "Mechanistic Study of Degradation of Basic Violet 3 by Citrus Limon Peroxidase and Phytotoxicity Assessment of its Degradation Products". *Biochem. Eng. J.*, vol.95, pp.9-19

Paradine, C. G. and Rivert, B. H. P. (1970). *Statistical Methods for Technologists.* London: The English Universities' Press Ltd

Passardi, F., Cosio, C., Penel, C. and Dunand, C. (2005). "Peroxidases have More Functions than a Swiss Army Knife". *Plant Cell Reports*, vol.24, pp. 255-265

Savary, J., Pu, P. H. and Sunderman, F. W. (1969). "A Biuret Method for Determination of Protein in Normal Urine". *Clinical Chemistry*, vol 14(12), pp. 1160-1171

Sawhney, S. K. and Singh, R. (2000). *Introductory Biochemistry*. New Delhi: Narosa Publishing House

Stoscheck, C. M. (1990). "Quantitation of Protein Method in Enzymology". *J. Biol. Chem*., vol.182, pp.69-73

Vance, C. P., Kirk, T. K. and Sherwood, R. T. (1980). "Lignification as a Mechanism of Disease Resistance". *Annu. Rev. Phytopathol.*, vol.18, pp.259–288

Veitch, N. C. (2004). "Horseradish Peroxidase: A Modern View of a Classical Enzyme". *J. Phytochem*., vol.65 (3), pp.249-259

Verma, P. and Madamwar, D. (2002). "Decolorization of Synthetic Textile Dyes by Lignin Peroxidase of *Phanerochaete chrysosporium*". *Folia Microbiol*. vol.47, pp.283–286

Vitolo, M. (2010). "Brief Review on Enzyme Activity". *World Journal of Pharmaceutical Research*, vol.9 (2), pp.60-76

Whitaker, J. R. (1996). *Enzymes*, *Food Chemistry.* New York: 3rd Edition, Marcel Dekker, Inc., pp.431-530

Wiseman, A. (1985). *Handbook of Enzyme Biotechnology*. Sydney: John Wiley and Sons, Inc., p.12

GREEN SYNTHESIS AND CHARACTERIZATION OF TIN(IV) OXIDE NANOPARTICLES AND STUDY ON ITS ANTIMICROBIAL ACTIVITY

Khine Yee Htoo[1], Yee Mun Than[2], Khin Mar Cho[3]

Abstract

The tin oxide nanoparticles (SnO_2 NPs) were fabricated via eco-friendly process using lime (*Citrus aurantifolia*) peels extract as reducing agent. The main phytochemicals present in aqueous peels of lime are α–amino acid, carbohydrates, organic acids, glycosides, phenolic compound, reducing sugar, saponins, steroids and starch are responsible for bio-reduction of nanoparticles. The crystalline nature and lattice parameter was studied by x-ray diffraction (XRD) which confirmed the formation of tetragonal rutile SnO_2 NPs with average crystallite size of 40.8 nm. The functional groups present in prepared SnO_2 NPs were identified by using fourier transform infrared (FTIR) spectroscopy. Surface morphology of prepared nanoparticles was studied with the help of scanning electron microscopy (SEM). The percentage composition and purity of the SnO_2 NPs was determined by energy dispersive x-ray (EDS). SnO_2 NPs was screened against the selected microorganisms and the order of antimicrobial activities given as; C*andida albicans* > *Bacillus subtilis* > *Escherichia coli.*

Keywords: tin oxide nanoparticles, lime, *Citrus aurantifolia*, bioreduction, antimicrobial activities

Introduction

Numerous efforts have been made to development of semiconductor nanoparticles (NPs) in the last two decades due to their novel optical, chemical, photo-electrochemical and electronic properties which are different from that of bulk (Fu *et al*., 2015). Tin(IV) oxide (SnO_2) is a well know n-type wide band gap (E_g = 3.6 eV) semiconductor (Celina *et al*., 2017). Nano-sized SnO_2 is regarded as a highly preferred multitasking metal oxide, such as gas sensors and lithium rechargeable batteries (Fu *et al*., 2015). SnO_2 nanoparticles are commonly synthesized by wet chemical route, vapour phase process, hydrothermal method, precipitation, electrode position and sonochemical methods. However, chemical methods lead to the presence of some toxic chemicals adsorbed on the surface that may have adverse effects in applications and environment. Thus, to design a simple and green route to synthesize SnO_2 nanoparticles is of considerable necessary. Recently, development of an eco-friendly method for the synthesis of nanoparticles via biological methods has been attracted lots of attentions. Using bacterial, fungi and plant extract are three main routes for biosynthesis of nanomaterials (Sudhaparimals *et al*., 2014) Among them, synthesis of nanomaterials using plant extract attracted lots attention due to its lower cost and simplicity. The biosynthesis of SnO_2 was only conducted by using aqueous peels extract of lime (*Citrus aurantifolia*). The *Citrus aurantifolia* (green source) used in the present work for the environment-friendly preparation of SnO_2 nanoparticles, belongs to the family Rutaceae and its peels are of medicinal importance. The lime is small, densely and irregular branched tree with short, sharp spains (Kose *et al*., 2014). For the synthesis of metal/metal oxide nanoparticles, plant biodiversity has been broadly considered due to the availability of effective phytochemicals in various plant extracts, such as α – amino acid, carbohydrates, organic acids, glycosides, phenolic compound, reducing sugar, saponins, steroids and starch. These components are found in peels of lime and capable of reducing metal salts into metal nanoparticles. Synthesized green SnO_2 nanoparticles was carried out using aqueous peels extracts of lime (*Citrus aurantifolia*) as reducing agent. The surface and structural properties of the prepared SnO_2 nanoparticles were studied by XRD, TG-DTA, FTIR, SEM-EDS and TEM. The SnO_2 nanoparticles were also screened for the antimicrobial

[1] 2 PhD Candidate, Department of Chemistry, University of Yangon
[2] Dr, Lecturer, Department of Chemistry, University of Yangon
[3] Dr, Associate Professor, Department of Chemistry, University of Yangon

activity against *Bacillus subtilis* as Gram Positive Bacteria, *Escherichia coli* as Gram Negative Bacteria, *Candida albicans* as fungi. The biological synthesis especially from bacteria, provides advancement over chemical and physical method as it is cost effective, environmentally friendly, easily scaled up for large scale synthesis and there is no need to use high pressure, energy, temperature and toxic chemicals.

Materials and Methods

Phytochemical Analysis of *Citrus aurantifolia* Peels Extract

The preliminary phytochemical screening of *C. aurantifolia* aqueous peel extracts were detected by qualitative assay. The more well-prepared aqueous peels essence was qualitatively proven for the existence of tannin, saponin, flavonoids, terpenoids, alkaloids, cardiac glycosides and anthraquinones using the standard protocol reported formerly.

Preparation of Tin Oxide Nanoparticles

A 30 g of lime (*C. aurantifolia*) peels were washed with distilled water and cut into small pieces. Then, it was blended with 100 mL of double distilled water, and filtered. A 40 mL of this extract was mixed with 0.02 M tin(II) chloride dihydrate solution with constant stirring. During mixing, the colour of mixture solution was found to be changed greenish yellow to pale yellow. Then the precipitate was washed with distilled water and dried in oven at 80 ºC. The obtained dried power was tin oxide nanoparticles and carefully stored in air-tight container (Junjie, 2015).

Characterization of Synthesized SnO_2 Nanoparticles

The SnO_2 nanoparticles were synthesized by using aqueous peels extracts of lime (*C. aurantifolia*). The crystal structure and crystallite size were determined by X- ray Diffraction technique. The FT IR spectrum was used to identify the functional groups presents in the sample. Surface morphology was analyzed by SEM and TEM and the nanoparticles purity was checked by energy - dispersive X- ray analysis.

Determination of Antimicrobial Activity

The crude extracts were screened for antimicrobial activity by determination the zone of inhibition against the test organisms using agar-well diffusion method. Sterile Mueller- Hinton agar plates were inoculated with prepared inoculum with sterile cotton swab. Then with the help of sterile cork borer, wells were made in the inoculated media plate. Next, 50 µL each of the working solutions were transferred into the wells with the help of micropipette. The control was also placed in the separate well at the same time. After proper incubation, the plates were viewed for the zone of inhibition, which is suggested by clear areas without growth around the well (Haq *et al*., 2020).

Results and Discussion

Preliminary phytochemical screening

The green synthesis of SnO_2 nanoparticles from *Citrus aurantifolia* aqueous peels extract was carried out successfully. Lime peels extract contained the phytochemicals present in the extract are presented in Table 1.

Table 1 Phytochemical Constituents of Lime (*C. aurantifolia*) Aqueous Peels Extract

No.	Test	Extract	Test Reagents	Observation	Results
1.	Alkaloids	1% HCl	Dragendorff's reagent	No orange ppt	-
			Sodium picrate	No yellow ppt	-
			Wagner's reagent	No reddish brown ppt	-
			Mayer's reagent	No white ppt	-
2.	α-amino acids	H_2O	Ninhydrin reagent	Purple spot	+
3.	Carbohydrates	H_2O	10 % α-naphthol and conc.H_2SO_4	Red ring	+
4.	Cyanogenic glycosides	H_2O	Sodium picrate solution and conc. H_2SO_4	No brick red ppt	-
5.	Flavonoids	EtOH	Mg turning and onc.HCl	No pink colour	-
6.	Glycosides	H_2O	10% Lead acetate	White ppt	+
7.	Phenolic compounds	EtOH	5% $FeCl_3$	Deep blue colour	+
8.	Organic acids	H_2O	Bromocresol green indicator	Blue colour	+
9.	Reducing sugars	H_2O	Benedict's solution	Brick red ppt	+
10.	Saponins	H_2O	Distilled water	Frothing	+
11.	Starch	H_2O	1 % Iodine solution	No deep blue colour	-
12.	Steroids	PE	Acetic anhydride and conc. H_2SO_4	Blue or green colour	+
13.	Terpenoids	$CHCl_3$	Acetic anhydride and conc. H_2SO_4	No pink colour	-
14.	Tannins	H_2O	5% $FeCl_3$	No green ppt	-

Biosynthesis of Tin(IV) Oxide nanoparticles

The SnO_2 nanoparticles obtained through *Citrus aurantifolia* were white in colour, powdery, crystalline and insoluble in water Figure 1.

Figure 1 Green synthesized tin(IV) oxide nanoparticles

Characterization of Prepared SnO_2 Nanoparticles

X-ray diffraction analysis

The phase purity and levels of crystallinity of the prepared SnO_2 nanoparticles were analyzed by the X-ray diffractometer. Figure 2(a) shows the XRD pattern of SnO_2 nanoparticles obtained at 80 ºC. It was observed that noise peaks and some impurities were present in the SnO_2 sample.

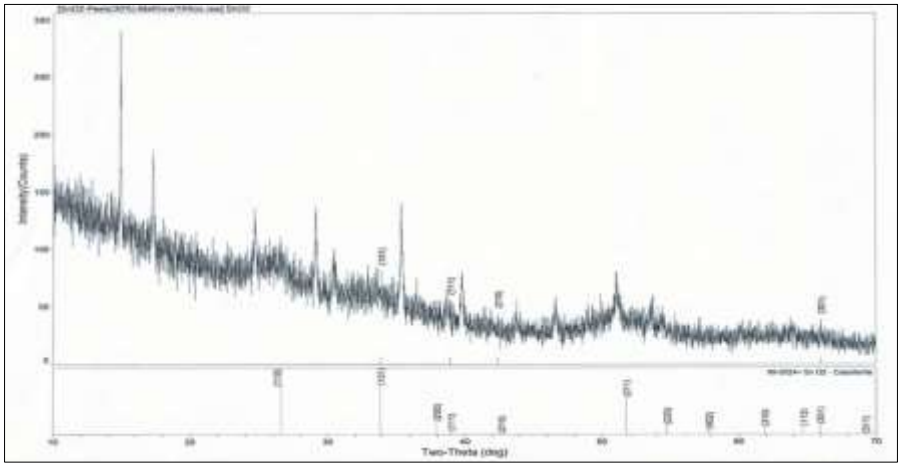

Figure 2(a) XRD pattern of prepared SnO_2 nanoparticles using aqueous peels extract of lime before calcination at 80 ºC

Figure 2(b) shows the XRD pattern of prepared SnO_2 nanoparticles using aqueous peels extracts of lime after calcination at 600 ºC. The peaks at 2θ values of 47.9º, 45.8º, 44.6º, 47.8º, 39.9º, 32.2º, 43.1º, 34.8º, 32.6º, 15.1º, 38.7º and 41.6º associated with (110), (100), (200), (111), (210), (211), (220), (002), (010), (221), (112) and (001), respectively, indicated the formation with tetragonal structure according to JCPDS File No. 99-0024. By using Scherrer equation, the average crystallite sizes of SnO_2 nanoparticles were found to be 40.8 nm by using aqueous peels extracts of lime at 600 ˚C. According to XRD, pure and crystallite SnO_2 nanoparticles with smaller size was obtained after calcination at 600 ˚C. On annealing the sample at higher temperature, the peak broadening decreased and the sharpness of the peak increased which clearly denoted the reduction of lattice strain and increased in crystallinity of the sample.

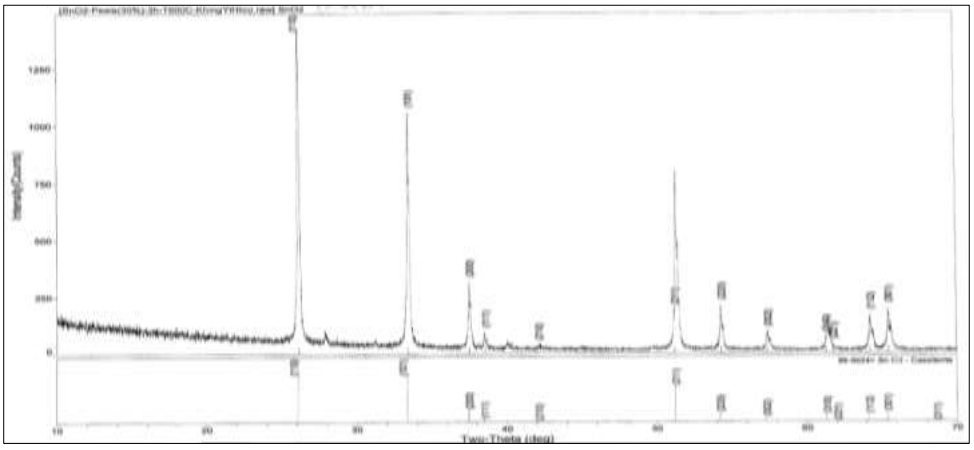

Figure 2(b) XRD pattern of prepared SnO_2 nanoparticles using aqueous peels extract of lime after calcined at 600 ºC

TG-DTA analysis

The TG-DTA thermogram of prepared powder (Figure 3) indicated an endothermic peak at 101.54 ºC which was due to the loss of water from the sample surface. The peak at 494.58 ºC was due to decomposition of hydroxide groups and phase transition from $Sn(OH)_2$ to SnO_2 (Jejenija and Damian, 2017). SnO_2 nanoparticles were found to be thermally stable beyond this temperature in this study.

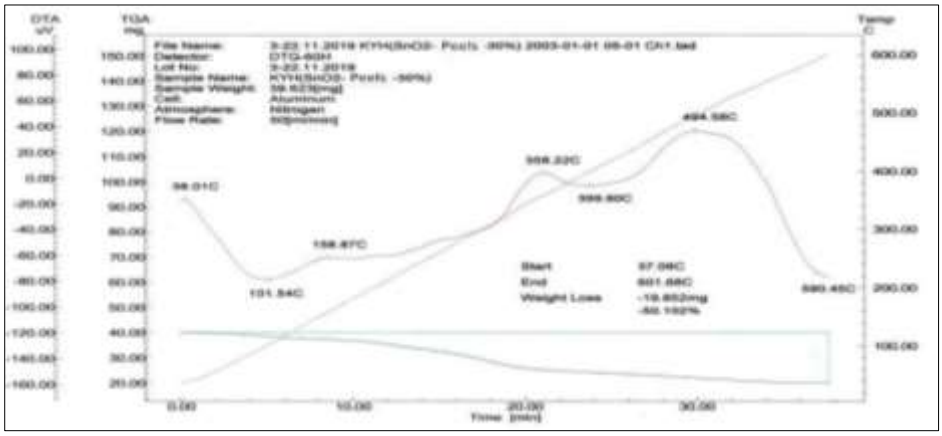

Figure 3 TG-DTA thermogram of green synthesized SnO_2 nanoparticles using aqueous peels extract of lime prepared at 80 ºC

FT IR analysis

Figure 4 shows FT IR spectrum of the prepared SnO_2 nanoparticles using aqueous peels extract of lime after calcination at 600 ºC. From this spectrum, it can be observed a strong band at 607 cm^{-1} associated with the anti- symmetric O-Sn-O stretching mode of the surface-bridging oxide formed by condensation of adjacent surface hydroxyl groups. This band confirms the presence of SnO_2 as crystalline phase formed at 600 ºC for 3 h.

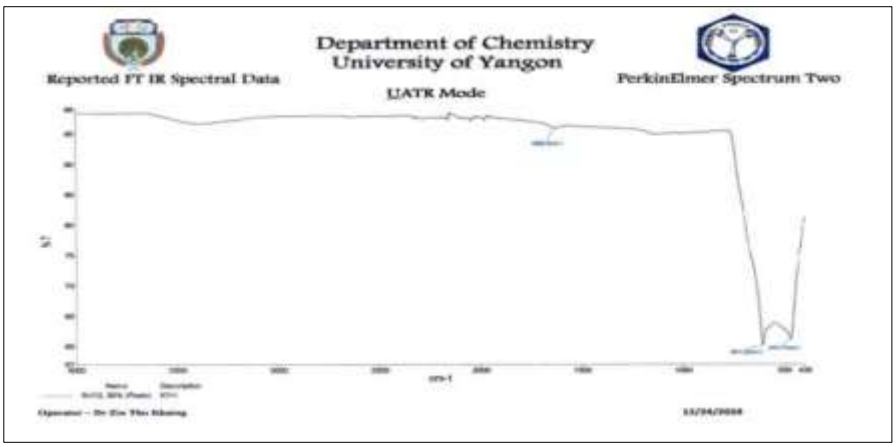

Figure 4 FT IR spectrum of the green synthesized SnO_2 nanoparticles using aqueous peels extract of lime after calcined at 600 ºC

SEM-EDS analysis

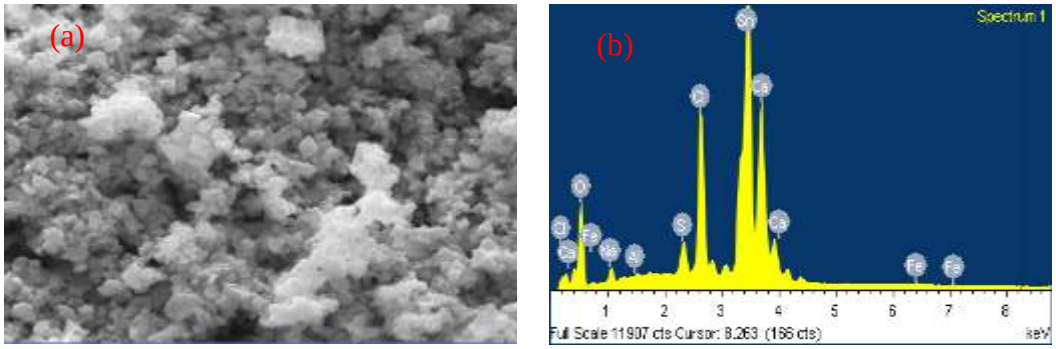

Figure 5 (a) SEM image, (b) EDS spectrum of green synthesized SnO_2 nanoparticles using aqueous peels extract of lime after calcined at 600 ºC

Figure 5(a) shows the SEM image of green synthesized SnO_2 nanoparticles. Small crystals of SnO_2 nanoparticles crystallized in tetragonal shape with slight agglomeration. This photograph indicated the porous nature of the surface. The elemental composition of fabricated SnO_2 nanoparticles was evaluated using EDS analysis as shown in Figure 5(b). The EDS spectrum showed the intense peaks of Sn which confirmed the formation of SnO_2 nanoparticles. The spectrum also showed the peaks of Na, Al, S, Cl, Ca and Fe in addition to Sn. The oxygen peaks were mainly due to the polyphenol groups present in *C. Aurantifolia* aqueous peels extract that could reduce and stabilize SnO_2 nanoparticles, while the Na, Al, S, Cl, Ca and Fe peaks were attributed to the impurities involved in synthesis process. The elemental weight percentage of the sample showed that 57.83% of samples consisted of Sn, 27.65% of O and small amount of impurities such as 2.76% of Na, 0.24% of Al, 0.82% of S, 8.27% of Cl 2.13% of Ca and 0.30% of Fe.

TEM Analysis

The TEM image of prepared SnO_2 nanoparticles after calcination at 600 ˚C is shown in Figure 6. It can be seen that SnO_2 nanoparticles consist of tetragonal structure with the particles size 37.5 nm. The small aggregations arise in synthesized nanoparticles are due to the hydrogen bonding between biomolecules used as reducing agents. The aggregations in the particles are dependent on the nature of the extracts and the biomolecules present in the extracts.

Figure 6 TEM image of SnO_2 NPs using aqueous peels extract of lime

Antimicrobial Behaviour of SnO_2 nanoparticles

The antimicrobial effects of SnO_2 nanoparticles was investigated using Gram positive, Gram negative and fungus strains such as, *Bacillus subtilis, Candida albicans, Escherichia coli, Pseudomonas fluorescens, Sacchromyces cerevisiae and Salmonella typhi*, respectively, by agar well diffusion method. Due to the large surface area the activity of the nanoparticles increases, therefore SnO_2 nanoparticles react efficiently with the cell membrane and inactivate the bacteria. The bactericidal efficacy for tin oxide nanoparticles against *B. subtilis, E. coli* and *C. albicans* were 17.93 mm, 17.73 mm and 19.12 mm, respectively. In Figure 7, it was observed that *C albicans* showed more significant activity than *B subtilis* and *E coli*. Other three microorganisms was not detected activity. Moreover, electrostatic interactions are directly responsible for the attachment of nanoparticles to bacteria. These interactions changes the integrity of cell membrane of bacteria and toxic free radicals are released which induce oxidative stress on bacteria (Khin Cho Khat, 2014).

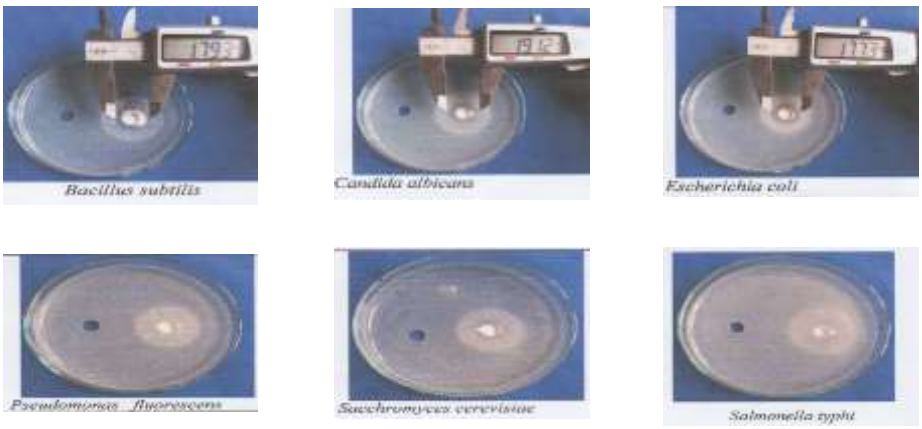

Figure 7 Antimicrobial activity of SnO2 nanoparticles

Conclusion

The green synthesis method is an economically beneficial and easy process which could eliminate several problems associated with the use of toxic reagents in the chemical synthesis procedure for SnO_2 nanoparticles. The phytochemicals act as good reducing agents in the formation of nanoparticles from aqueous peels extract. The XRD pattern of the SnO_2 nanoparticle indexed as tetragonal rutile structure. The peak at 494.58 ºC from TG-DTA curve indicated the formation of crystalline phase SnO_2. FT IR spectral data of SnO_2 nanoparticles related to the stretching vibration of O-Sn-O group. Based on SEM-EDS analysis, the small crystal of SnO_2 nanoparticles with porous and cluster structure with intense peak of Sn and O. By TEM analysis, SnO_2 nanoparticles obtained at 600 ºC showed tetragonal structure and the particles size distribution of SnO_2 nanoparticles was found to be 37.5 nm. The higher antimicrobial activity of SnO_2 nanoparticles was observed against *C. albican*, a fungus as compared to *B subtilis*, Gram positive bacteria and *E coli*, Gram negative bacteria. Therefore, the prepared SnO_2 nanoparticles can be used for the wastewater treatment. The eco-friendly green chemistry approach by the use of these peels extracts for the synthesis of nanoparticles will increase their economic viability and sustainable management. The potential nanofactories has heightened interest in the biological synthesis of nanoparticles.

Acknowledgement

The authors are thankful to Department of Chemistry, University of Yangon for providing the research and analytical instrument facilities. Special thanks are also due to Defense Services Science and Technology Research Center, Pyin Oo Lwin for SEM-EDS imaging and Science and Technology Research Equipment Centre in Chulalongkorn University for TEM imaging.

References

Celina, J. S., Ahila, M., Malligavathy. M and Pacliyan, D. P. (2017). "Structural, Morphological and Optical Properties of Tin(IV) Oxide Nanoparticles Synthesized using *Camellia sinensis* Extract: A Green Approach". *J.of Mineral, Metallurgy and Materials,* vol. 24 (9), pp 1043.

Fu, L., Zheng. Y., Ren, Q., Wang, A and Deng, B. (2015). "Green Biosynthesis of SnO_2 Nanoparticles by Plectrathus amboinicus Leaf Extract Their Photocatalytic Activity toward Rhodamine B Degradation". *J. of Ovonic Research,* vol. 11 (1), pp 21-26

Haq,S. , Rehman,W. , Waseem,M., Shah,A. , Khan, A.R. , Rehman,M.U., Ahmad,P. , Khan,B. and Ali,G. (2020). "Green Synthesis and Characterization of Tin Dioxide Nanoparticles for Photocatalytic and Antimicrobial Studies". *Material Research Express.* vol. 7, p 025012

Jejenija, O and Damian, C. (2017). "Biosynthesis and Photocatalytic Properties of SnO_2 Nanoparticles Prepared Using Aqueous Extract of Cauliflower". *J. Cluster Science.* vol 4, pp 1883-1896

Junjie, H. (2015). "Biosynthesis of SnO_2 Nanoparticles by Fig (*Ficus Carica*) Leaf Extract for Electrochemically Determining Hg (II) in Water Samples". *J. Electrochem. Sci*. vol 10, pp 10668-10676

Khin Cho Khat. (2014). *Magnesium Hydroxide, Magnesium Oxide and Magnesium Ferrite Nanoparticles: Synthesis, Characterization and Application,* Yangon. PhD Dissertation, Department of Chemistry, University of Yangon

Kose, H., Aydin, A. O and Akbulut, H. (2014). "The Effect of Temperature on Grain Size of SnO_2 Nanoparticles Synthesized by Sol-Gel Method". *Acta Physica Polonica A.* vol.125, p 345-347

Sudhaparimals, S., Arumugam, G. A and Asit, B. M. (2014). "Green Synthesis of Tin Based Nano Medicine: Assessment of Microstructure and Surface Property". *J. of Nanoscience and Nanotechnology*, vol. 2 (4), pp 75-83

INFLUENCE OF THERMOPLASTIC WASTES ON THE PROPERTIES OF BETEL NUT SHELL FIBER (*ARECA CATECHU* L.) PARTICLEBOARDS

Saw Win[1], Win Win Nu[2], Nwel Nwel Myint[3]

Abstract

This study aimed to prepared particleboards using bio-waste Betel Nut Shell Fiber (BNF) and resinous materials recycled thermoplastics polyethylene (RPE), polypropylene (RPP) and reused polystyrene (RPS) obtained from plastic wastes. The particleboards were prepared by mixing the fibers and plastics followed by hydraulic hot press molding method. The fibers and plastics (1:1) by weight ratio were pressed under 2200 psi with pressing temperature 170 ºC for 15 min. The properties of prepared particleboards were measured according to BS -1811, IS-3087 and ASTM D – 412 and ASTM D- 256 standard methods. The results obtained were compared with FAO (2013) and JSA (2003) standard values. The surface morphological characters of prepared particleboards were recorded by Digital Microscope. It was found that the properties of particleboards were in agreement with the standard values. The obtained properties convincingly indicate high bonding ability of the recycled and reused plastics. The reused polystyrene was the most suitable for particleboard production among two recycled and one reused plastics due to the particleboard made with reused polystyrene possess the highest bending strength 232.70 kg/cm^2, the lowest water absorption (9.31%) and swelling thickness (11.47%) even though it had the lowest thickness value of 0.35 cm.

Keywords: Betel nut shell fiber, recycled and reused plastics, hydraulic hot press molding method, particleboards, bonding ability

Introduction

Today, the construction industry is rapidly growing at an enormous pace due to the increasing population around the world. Presently, particleboard is one of the most popular construction materials commonly used for interior and exterior applications such as walls, ceiling panels office dividers, bulletin boards, cabinets, furniture, countertops and desktops (Guru *et al*., 2008).The most common type of particleboard is made from wood chips which came from timber waste, shavings and mill waste (Odozi *et al*., 1986).The increase in the demand for wood products led to the depletion of timber resources. Thus, the depletion of wood resources promotes the use of alternative raw materials for wood products. Agricultural residues comprise an alternative source for wood which would otherwise be used. Many types of natural fibers have been investigated for use in plastics including straw, wood fiber, rice husks, grass reeds, coir, banana fiber, pineapple leaf fiber, etc. Natural fibers have the advantage that they are renewable resources and have commercial and marketing appeal (Baccay, 2017). In this study, the potential of thermoplastics resins RPE, RPP and RPS as substitute for urea or formaldehyde-based resins that are known to emit carcinogenic gases. The recycling presents advantages such as reduction of environmental problems and saving both material and energy (Francis, 2016).

Thermoplastics are made up of linear molecular chains and this polymer softens on heating and hardens when cooled (Amin and Amin, 2011). The crystalline thermoplastics (RPE, RPP) have more mechanical impact resistance. The melting points and densities of RPE and RPP are 120 - 130 ℃, 160 - 171 ℃ and 0.93 - 0.97 g cm^{-3}, 0.89 - 0.92 g cm^{-3} (Van de Velde and Kiekens, 2001). The amorphous thermoplastic (RPS) has melting point 210 - 249℃ but they begin to flow at their

[1] Dr, Associate Professor, Department of Engineering Chemistry,West Yangon Technological University
[2] Dr, Associate Professor Department of Botany, Myeik University
[3] Lecturer, Department of Engineering Chemistry, Technological University (Maubin)

glass transition point 100 ℃ and density of 0.96 - 1.05 g cm^{-3}. The density is a very important parameter because its purpose is to produce a composite that is as light as possible.

The betel nut palm is believed to have originated in the Philippines which grown in much of the tropical pacific, Asia and parts of East Africa (Heatubun *et al.*, 2012). The betel nut palms have been cultivated as gardens and hedges in Thaninthayi Region, Bago Region, Mon State, Kayan State and Rakhine State in Myanmar. They have been grown for its commercially important seed crop. The betel nut shell fiber is composed of cellulose (53.20 %) with varying proportions of hemicelluloses (32.98 %), lignin (7.2 %) and other materials (Ramachandra and Ashok, 2011). The betel nut shell fiber appears to be a promising material because of low cost, less weight, extremely strong, abundantly available and also biodegradable. It is also used as reinforcement in polymer composite particleboard (Hodzic *et al*., 2006).

Materials and Methods

Sample Preparation

The recycled plastics polyethylene, polypropylene and reused polystyrene were obtained from Polymer Department in Department of Research and Innovation (DRI), Ministry of Education, Yangon, Myanmar. The recycled and reused plastics were made into powder by Refiner Machine before blending with fibers. The three types of recycled and reused plastics are shown in Figure 1 (a-c). The betel nut shell fibers (*Areca catechu* L.) were gathered from betel nut plantation in Myeik Township, Thaninthayi Region.

Betel nut shell fibers (BNF) were soaked in water at ambient temperature for 2 days to loosen fibers. The fibers were washed with water 3 - times to remove impurities. The fibers were dried in air at ambient temperature for 3 days. The dried fibers were soaked in a 3 % NaOH solution at ambient temperature for 1 h to modify the fiber strength.

The fibers were then soaked in very dilute acetic acid for 1 h to neutralize the excess NaOH. The fibers were washed with water 2 times and dried in air at ambient temperature for 7 days. The modified dry fibers with 9.27 % moisture content were ground in Hensel Mixer for 7 min and screened into 1 mm particle size and dried again at 100 ℃ in air oven for 30 min to reduce moisture content. The modified betel nut shell fiber particles are shown in Figure 1(d).

(a) (b) (c) (d)

Figure 1 (a) Recycled polyethylene (b) polypropylene (c) reused polystyrene and (d) betel nut shell fiber particles

The modified dry betel nut shell fiber particles were blended with RPE, RPP and RPS separately in the weight ratio of (1:1) in Hensel Mixer for 5 min. Three different samples of particleboards were manufactured as indicated in Table 1. The target size of the particleboard was 15 cm × 15 cm with a thickness of 0.5 cm. After blending, the mats of the particles were formed manually by placing the blend in a mould and lightly press for 5 min at ambient temperature. Oil was used as a releasing agent on mould surface to achieve easy particleboard removal from the mould after formation. After being lightly pressed, the mats of particles were pressed under hydraulic hot press machine (LJT- 815566, APEX CONSTRUCTION) with

2200 psi at 170 °C for 15 min. The pressed particleboard was transferred to cool press and pressed the boards for 5 min to cure sides and surface of boards. The produced particleboards were subjected to physical and mechanical tests with their respective methods after successful curing.

Table 1 Composition of the Particleboards

Particleboards	Compositions (w/w)
RPEPB	50 %BNF + 50 % RPE
RPPPB	50 %BNF + 50 % RPP
RPSPB	50 % BNF + 50 % RPS

All tests were carried out in accordance with ASTM, IS and BS standard methods. At least three specimens were selected for each type of panel for testing the physical and mechanical properties. Density of boards (BS: 1811-1961), water absorption (IS: 3087 – 1965), swelling thickness (IS : 3087 -1965), moisture content (MOC - 63U), modulus of rupture (ASTM D- 412), impact strength (ASTM D - 256) and hardness (ASTM D - 2240) were determined by their respective methods. To obtain water absorption and swelling thickness, samples were fully immersed in water at ambient temperature for 24 h.

Results and Discussion

Effect of Thermoplastic Types on the Physical and Mechanical Properties of Particleboards

The three type of particleboards (RPEPB, RPPPB, RPSPP) were produced by using betel nut shell fibers and (RPE, RPP, RPS) in the ratio of (1:1) by weight. The physical and mechanical properties of prepared particleboards are shown in Table 2.

Table 2 Physical and Mechanical Properties of Prepared Particleboards

Properties	RPEPB	RPPPB	RPSPB	Reference** (Reported)
Thickness(cm)	0.40	0.50	0.35	-
Density (g/cm^3)	0.90	0.83	0.94	0.4 – 0.9 (JSA,2003)
Water absorption*(%)	10.65	16.23	9.31	20 -75
Swelling thickness* (%)	12.63	14.06	11.47	5 – 15
Moisture content (%)	2.34	2.33	2.41	5- 13 (JSA,2003)
Modulus of rupture (kg/cm^2)	163.21	108.41	232.70	100-500
Impact strength (kJ/m^2)	128.73	171.27	42.60	-
Hardness (Shore A)	88.90	92.75	94.95	-

* = after soaking period 24 h
** = FAO (2013), JSA (2003)
FAO = Food and Agriculture Organization
JSA = Japanese Standard Association
Pressing Temperature = 170 ℃
Pressing Pressure = 2200 psi
Pressing Time = 15 min

Fiber type = Betel Nut Shell Fiber (BNF)
Resin type =Recycled plastics polyethylene (RPE), polypropylene RPP), reused polystyrene (RPS)
RPEPB = recycled polyethylene particleboard made by RPE and BNF (1:1) by weight
RPPPB = recycled polyethylene particleboard made by RPP and BNF (1:1) by weight
RPSPB = reused polyethylene particleboard made by RPS and BNF (1:1) by weight

Physical Properties of Produced Particleboards

Thickness and density

As shown in Table 2, thickness of three prepared particleboards, RPEPB, RPPPB, and RPSPB were 0.40, 0.50 and 0.35 cm, respectively. The particleboard (RPSPB) was found to have the lowest thickness value of 0.35 cm due to the usage of RPS which had the greatest adhesive property. Polystyrene (PS) is amorphous thermoplastic, usually transparent with the molecules arranged randomly (Francis, 2016). It was found that the resin type is one of the essential parameters for good binding capacity of fibers.

Density is the most important gauge of particleboards performance, which mostly affects all other properties and considerations (Abdutkareem and Adeniyl, 2017). The densities of the particleboards (RPEPB, RPPPB and RPSPB) made from betel nut shell fiber waste at 50 % each of RPE, RPP and RPS were 0.90, 0.83 and 0.94 g/cm^3, respectively. According to JISA 5908 – 2003 standard (JSA, 2003), the densities of prepared particleboards were in the range 0.40-0.90 g/cm^3. Hence, the densities of all the produced particleboards fulfilled to the universal standard for the particleboards. Several factors that influencing of board density were wood density, pressing pressure, particle quantity in mat, resin content and other additive (Kelley, 1997).

Water absorption and swelling thickness

According to Table 2, the water absorption (WA) capacity of prepared particleboards were found to be in the range of 9.31-16.23 % (Figure 2). The standard range of particleboards was 20-75 % (FAO, 2013). Hence WA values of prepared particleboards were less than that of standard particleboards. The resultant particleboard (RPSPB) from the usage of RPS resin as binder is excellent water repellent. The higher density board absorbed less water than a lower density board.

The swelling thickness (ST) values of particleboards, RPEPB, RPPPB and RPSPB were 12.63, 14.06 and11.47 %, respectively (Figure 2). According to standard, ST values of prepared particleboards were found to be in the range of 5-15 % (FAO, 2013). Hence the ST values of prepared particleboards met the requirement of the universal standard value for particleboard. The density and WA capacity have more effect on ST and linear expansion of particleboard (Abdulkareem and Adeniyl, 2017). Guler *et al.* (2008) reported that ST of wood panels were influenced by quantity and distribution of adhesive, moisture content of furnish, furnish compatibility, chemical composition of furnish etc.

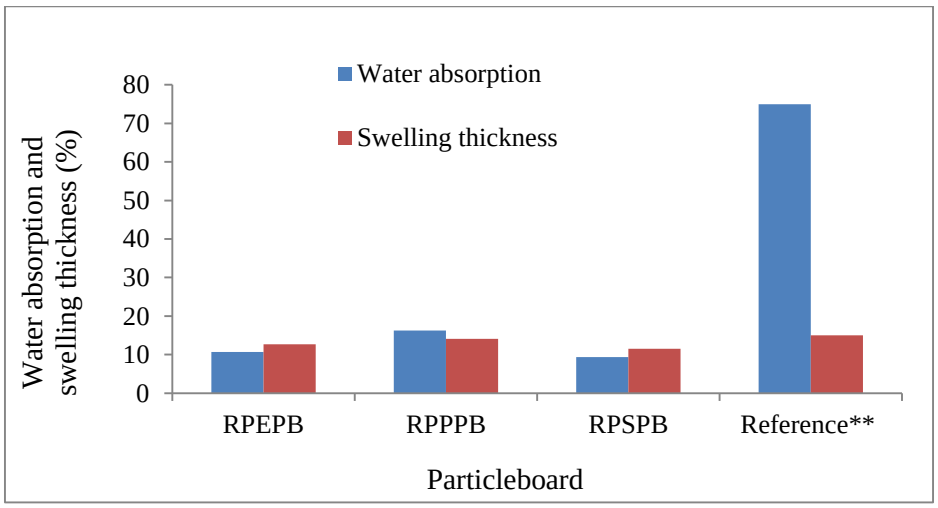

Figure 2 Water absorption and swelling thickness of particleboards

Moisture content

As shown in Table 2, the moisture content of prepared particleboards were found to be in the range of 2.33- 2.41 %. According to standard JISA 5908 - 2003, moisture content of prepared particleboards was in the range between 5 and 13 % (JSA, 2003). Maloney (1993) stated that initial moisture content of raw material is one of the important factors to determine of moisture content in particleboard produced. It was expected that possessing of low moisture content (ca 2 %) is due to the usage of hydrophobic plastics. It was expected that the fungi could not grow on the surface of board by using recycled and reused plastics.

Mechanical Properties of Prepared Particleboards

Modulus of rupture

The modulus of rupture (MOR) of prepared particleboards were in the range of 108.41 - 232.70 kg/cm^2 (Figure 3). Modulus of rupture is a measure of the ability of a sample to resist a transverse (bending) force perpendicular to its longitudinal axis. Table 2 also shows the modulus of rupture of particleboards with different resin type to betel nut shell fiber content. The result showed that particleboard with reused polystyrene (RPSPB) gave the highest value of MOR with 232.70 kg/cm^2. It is established that RPSPB with RPS content can withstand more force than the other samples before failure and therefore represents the optimum resin type. According to (FAO, 2013) standard, the MOR value of prepared particleboards were found to be in the range of 100 - 500 kg/ cm^2. It is noted that the MOR values obtained for the particleboards (RPEPB, RPSPB) were higher than the standard minimum value of 100 kg/cm^2. The MOR value of particleboard (RPPPB) with 108.41 kg/cm^2 also met the requirement of the standard value with 100-500 kg/cm^2.

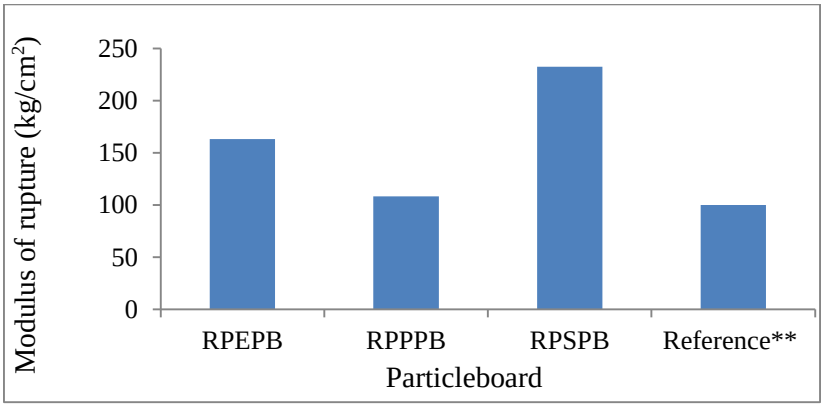

Figure 3 Modulus of rupture for particleboards

Impact strength

Impact Strength is the ability of a material to resist breaking under a shock loading or the ability to resist the fracture under stress applied at high speed. The impact strength of prepared particleboards were in the range of 42.60 - 171.27 kJ/m^2 as shown in Table 2. This indicates that the impact strength of particleboard (RPSPB) was the lowest value of 42.60 kJ/m^2 among them. It was expected that RPSPB had the lowest thickness 0.35 cm which is directly proportional to its lowest impact strength with 42.60 kJ/m^2.

Hardness property

Hardness property means a resistance to penetration, wear or a measure of low stress and resistance to cutting and scratching (Westbrook and Conrad, 1973). The hardness value of prepared particleboards RPEPB, RPPPB and RPSPB were 88.90, 92.75 and 94.95 Shore A, respectively.

Shore A is unit of Hardness value. The particleboard RPSPB had the highest hardness value of 94.95 Shore A which was the best particleboard in this study. This is because hardness is a function of the relative fiber content and modulus of rupture.

Surface Morphological Study of Prepared Particleboards

The surface micrographs of over view and side view of prepared particleboards are shown in Figure 4.

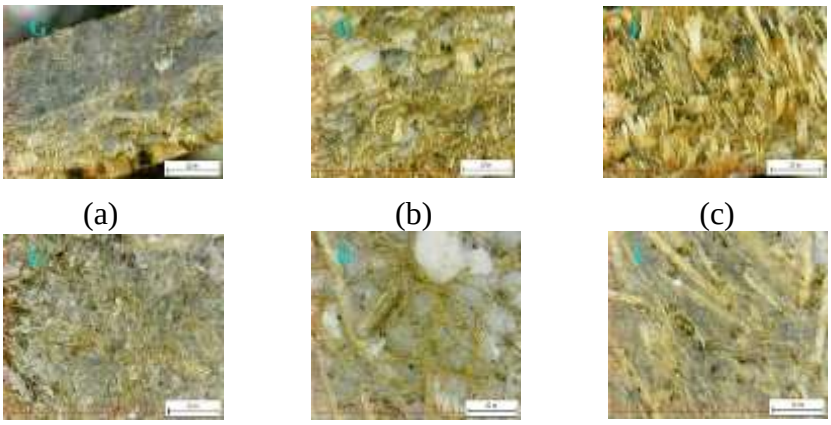

(a) (b) (c)

(d) (e) (f)

Figure 4 Surface micrographs of prepared particleboards
(a) side view of RPSPB (b) side view of RPPPB (c) side view of RPEPB
(d) over view of RPSPB (e) over view of RPPPB (f) over view of RPEPB

The surface morphologies of the prepared particleboards were studied by Digital Microscope (50 x-500 x). The micrographs were recorded at (300 x) magnification to ensure clear images. The surfaces of board (RPSPB) were the smoothest in all of three boards i.e. the fibers and plastics were not pulled out from the surfaces. In other word, the surfaces of the boards had less micropores and microcracks on it. This tends to increases MOR value and decreases WA and ST values of the boards. The surfaces from over and side views of RPEPB was more uniform than that of RPPPB but not than RPSPB. The properties of RPEPB were better than that of RPPPB. The surfaces of RPPPB were the roughest in all of them which tend to decrease the properties. It can be seen clearly that RPP resin was not completely soft and melt. The distribution of resinous plastics between the fibers was not enough to form uniform board. So, the surface structure of particleboards is related to the properties of particleboards.

Conclusion

Based on the results of the present work conducted, the density test results recorded the extreme value of 0.83, 0.90 and 0.94 g/cm^3 for the RPPPB, RPEPB and RPSPB respectively. The particleboard RPSPB recorded the least water absorption value of 9.31% while exhibiting the least swelling thickness value of 11.47 %. The moisture content range of all particleboards was (2.33 – 2.41 %). This very low moisture content value of prepared board is due to usage of plastics resin having hydrophobic property.

In the bending strength test, two types of particleboard RPSPB and RPEPB exhibited the large modulus of rupture (bending strength) values 232.70 kg/cm^2 and 163.21 kg/cm^2. The particleboard RPPPB had modulus of rupture value (108.41 kg/cm^2). The impact strength of particleboard RPSPB showed the lowest value of 42.60 kJ/m^2 with the lowest thickness value of 0.35 cm. The hardness value of particleboard RPSPB had the largest value of 94.95 Shore A. The surfaces from over view and side view of particleboard RPSPB were the most uniform. It was

found that the particleboards prepared using betel nut shell fibers and RPS was the best particleboard due to the highest MOR, lowest WA and ST values. This research work will encourage in waste materials being efficiently utilized as a sustainable resource for the industrial manufacture of particleboards thus reducing the amount of wastes and eliminating the environmental pollution occasioned by the burning of such residues.

Acknowledgements

The authors are deeply grateful to all persons from Department of Engineering Chemistry, West Yangon Technological University, West Yangon University and Department of Research and Innovation (DRI) for their kind encouragement, helpful suggestions and supporting research facilities. We also would like to express our profound gratitude to the Department of Higher Education, Ministry of Education, Myanmar for provision of opportunity to do this research.

References

Abdulkareem, S. A. and Adeniyl, A. G. (2017). "Production of Particleboards Using Polystyrene and Bamboo Wastes". *Nigerian Journal of Technology (NIJOTECH),* vol. 36 (3), pp.788-793

Amin, S. and Amin, M. (2011). "Thermoplastic Elastomeric (TPE) Materials and their Use in Outdoor Electrical Insulation". *Rev. Adv. Mater.Sci*, vol. 29, pp. 15-30

Baccay, M. A. (2017). "Influence of Varying Mix Design and Fiber Length on the Properties of Water Hyacinth Particleboard". *PUP J. Sci. Tech*. vol. 7 (1), pp. 1-17

FAO. (2013). *Characteristic Mechanic of Polyester Composite Particleboard with Filler Particle of Areca Nut Fiber*, http://www.fao.org/3/a-i 4441e. pdf (Accessed 8 June 2013)

Francis, R. (2016). *Recycling of Polymers: Methods, Characterization and Application.* NJ, USA**:** John Wiley and Sons

Guler, C., Copur, Y. and Tascioglu, C. (2008). "The Manufacture of Particleboards Using Mixture of Peanut Hull and European Black Pine Wood Chips". *Bioresource Technology*, vol. 99, pp. 2893-2897

Guru, M., Atar, M. and Yildirim. R. (2008). "Production of Polymer Matrix Composite Particleboard from Walnut Shell and Improvement of its Requirements". *Materials and Design*, vol. 29 (1), pp. 284-287

Heatubun,C.D., Dransfield, J., Flynn,T., Tjitrosoedirdjo, S. S.,Mogea, J.P. and Baker,W. J. (2012). "A Monograph of the Betel Nut Palms (Areca: Arecaceae) East Malesia". *Botanical Journal of the Linnaean Society*, vol. 168 (2), pp. 147-173

Hodzic, A., Curro, R., Britton, P., Shu, L., Berndt, C.C. and Shanks, R. A. "Mechanical Properties of PHB-Bagasse Composites". ACUN: *International Composites Conference*, pp. 156-161

JSA. (2003). *Japanese Industrial Standard Particleboard JISA-5908*.Tokyo: Japanese Standard Association

Kelley, M. W. (1977). *Critical Literature Review of Relationship between Processing Parameter and Physical Properties of Particleboard.* Wisconsin: General Technical Report FPL -10, US. Department of Agriculture Forest Service Forest Products Laboratory University of Wisconsin

Maloney, T. M. (1993). *Modern Particleboard and Dry-Process Fiberboard Manufacturing.* San Francisco: Miller Freeman

Odozi, T.O., Akaranta, O. and Ejike, P. N. (1986). "Particleboards from Agricultural Wastes". *Agricultural Wastes*, vol. 16, pp. 237-240

Ramachandra, R. G. and Ashok, K. M. (2001). "Fabrication and Performance of Hybrid Betel Nut Short Fiber Sansevieria Cylindrical Epoxy Composites". *International Journal of Materials and Biomaterials Applications,* vol.1(1), pp. 6-13

Van de Velde, K. and Kiekens, P. (2001). "Thermoplastic Polymers: Overview of Several Properties and Their Consequences in Flax Fibre Reinforced Composites". *Polym. Test*. vol. 20, pp. 885-893

Westbrook, J. H. and Conrad, H. (1973). *The Science of Hardness Testing and Its Research Applications*. Ohio: American Society for Metals

SYNTHESIS OF 2D g-C_3N_4/BiOCl HETEROJUNCTION WITH MIXED SOLVENTS TO ENHANCE VISIBLE-LIGHT PHOTOCATALYTIC PERFORMANCE

Aung Khaing[1,4], Dong Yang[2,3], Yao Chen[3], Zhongyi Jiang*[4]

Abstract

Visible-light response and highly effective charge separation are the vital factors to improve the photocatalytic performance of photocatalysts. In this study, two-dimensional (2D) graphitic carbon nitride/bismuth oxychloride (g-C_3N_4/BiOCl) heterojunctions were synthesized by one-pot ethanol-assisted solvothermal process in the presence of ionic liquid 1-butyl-3-methyl imidazolium chloride ([Bmim]Cl). The ionic liquid acts as solvent, and electrically conducting fluids in the synthesis process, contributing to the uniform dispersion of g-C_3N_4 on the BiOCl surface. The nanostructured heterojunction was formed with g-C_3N_4 covering the surface of BiOCl nanosheets uniformly. 2D g-C_3N_4/BiOCl heterojunctions showed higher photocatalytic performance for Rhodamine B (RhB) under visible-light irradiation compared with pure g-C_3N_4 and BiOCl. The mechanism of synthesized sample g-C_3N_4/BiOCl-4 showed that $^{\cdot}O^{2-}$ and h^+ plays an active role in the degradation process and the separation of photo induced charges transversely the heterostructure boundary reversed electron-hole recombination. This study provides a new insight into the development of high efficient and stable catalyst with tunable catalytic activity.

Keywords: g-C_3N_4/BiOCl, heterojunction, phytocatalyst, ionic liquid, Rhodamine B

Introduction

In recent years, there is an increasing interest in the study of photocatalysis technology applications for water/air purification (Fujushima *et al*., 2000; Sharma *et al*., 2015), hydrogen production (Yamasita *et al.*, 2004), self-cleaning coatings (Zhang *et al.*, 2005) and solar cells (Regan *et al.*, 1991). Taking advantage of inexhaustible solar energy as the driving source, the photocatalytic technology has been regarded as a "green" method to deal with environmental pollution and energy shortage alongside (Yan *et al.*, 2009). Recently, the varieties of inorganic semiconductors and molecular assemblies have been developed as photocatalysts under visible-light (Akhavan and Ghaderi, 2013; Weng *et al.*, 2013; Wang *et al.*, 2009; Hou *et al.*, 2014). However, most of them lack the ability of directly utilizing visible-light, which seriously hinders their further development in environment remediation.

Graphite-like carbon-nitride (g-C_3N_4), a metal-free photocatalyst has shown great photocatalytic performance due to its visible-light response (Kang *et al.*, 2013). Moreover, g-C_3N_4 is recognized to be the more stable derivative of carbon with high stability and moderate band gap of ~2.7 eV (Regan *et al.*, 1991). The most distinct feature of the layered g-C_3N_4 from other common layered compound is the presence of abundant hydrogen bonds, which dominate the intra-layered framework due to the incomplete polymerization of the precursors containing amine groups (Cai *et al.*, 2015). However, the photocatalytic performance of g-C_3N_4 is strongly hindered by the fast recombination of photogenerated electrons and holes in a very short time. Thus, several strategies such as constructing heterojunction structure, regulating surface morphology and compositing carbon material, have been applied to promote the separation efficiency of photogenerated carriers. Among them, constructing type II or Z-scheme heterojunction structure can effectively separate

[1] Lecturer, Department of Chemistry, University of Yangon
[2] Key Laboratory of System Bioengineering of Ministry of Education, School of Chemical Engineering and Technology, Tianjin University, 300072, China
[3] School of Environmental Science and Engineering, Tianjin University, 300072, China
[4] Collaborative Innovation Center of Chemical Science and Engineering (Tianjin), Tianjin 300072, China
* Corresponding author, Zhongyi Jiang, zhyjiang@tju.edu.cn Tel: +86-22-27406646

electrons and holes to different materials due to the inequality of energy bands. To date, a variety of metal composite materials have been utilized as the second component, in which the bismuth-based semiconductors, such as $BiErWO_6$ (Di *et al.*, 2014), Au-Bi_2S_3 (Du and Luan, 2012), and $BiNbO_4$ (Manna *et al.*, 2014), is one of the optimal choices for its feasibility of constructing Z-scheme heterojunction with g-C_3N_4. Bismuth oxyhalide (BiOX), which is a kind of the layered ternary oxide semiconductors, has arisen much attention due to its high-photocatalytic efficiency for eliminating toxic textile dyes and other organic pollutants (Zhai *et al.*, 2013). Based on the recent reports, the BiOX compound like BiOCl is more effective than TiO_2 for methyl orange (MO) degradation under UV light illumination. However, BiOCl can only use the photons in the ultraviolet region (3% of the solar energy) and the rapid recombination of photogenerated charge carriers considerably restricts its quantum efficiency. Therefore, taking the advantages of pure BiOCl and g-C_3N_4 to construct the heterojunction structure can be a feasible way to improve the visible-light response and charge separation efficiency simultaneously.

In this work, considering the suitable conduction and valence bands level between BiOCl and g-C_3N_4, a novel visible-light driven g-C_3N_4/BiOCl heterojunction photocatalyst was designed and synthesized. The schematic formation process of 2D g-C_3N_4/BiOCl heterojunctions is shown in Figure 1.

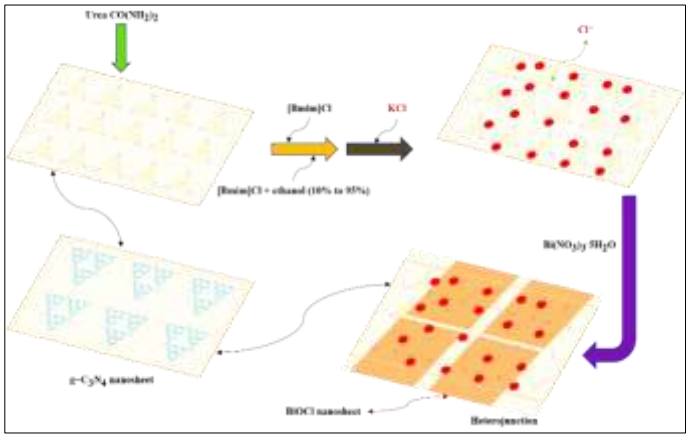

Figure 1 Schematic demonstration of the formation process for 2D g-C_3N_4/BiOCl heterojunctions in mixed polar solvent.

Materials and Methods

Chemicals and Reagents

Urea (CH_4N_2O) was purchased from Aladdin Industrial Corporation, Shanghai, China. Bismuth(III) nitrate pentahydrate was purchased from Tianjin Chemical Reagent Technology Co. Ltd. Tianjin, China. Potassium Chloride (KCl) was purchased from Tianjin Kermel Chemical Reagent Co. Ltd. Tianjin, China. The ionic liquid 1-butyl-3-methyl imidazolium chloride [Bmim]Cl was purchased from Shanghai Macklin Biotech Chemical Co. Ltd., Shanghai, China. Ethanol (EtOH) was purchased from Rionlon Bohua Pharmaceutical Chemical Co. Ltd. Tianjin, China. All chemicals were of analytical grade and used directly without further purification. Deionized water was used throughout all the experiments.

Synthesis of g-C_3N_4 /BiOCl/Heterojunctions

The pristine g-C_3N_4 was prepared by the thermal polymerization of urea (Kang *et al.*, 2013). Briefly, 20 g of urea was put into a porcelain crucible with a cover to prevent the

sublimation of urea, and then heated at 510 ˚C for 4 h with a ramping rate of 2.5˚C min^{-1} in a muffle furnace. The naturally-cooled resulting yellow product was ground to obtain a powder sample. Moreover, to prepare the carbon nitride product with broken hydrogen bonds, the pristine g-C_3N_4 was annealed at 580˚C for 2 h with a ramping rate of 5˚C min^{-1} in a tube furnace under nitrogen atmosphere.

The samples of g-C_3N_4/BiOCl composites were synthesized using different ratios of solvents between water ($s \leq 10^{-8}$ Ω cm^{-1}) and ethanol. Different samples with solvent ratio using 10%-95% ethanol for the g-CN/BiOCl-1, 100 mL of 10% EtOH solution containing 1 mmol of ionic liquid (1-butyl-3-methyl imidazolium chloride) was sonicated for half an hour and then further stirred another 2 h to obtain a uniform suspension. After that, 0.75 g of KCl was dissolved in 50 mL of deionized water under sonication for half an hour. The ionic liquid solution was added into KCl solution and it was stirred for another half hour. Next, 4.85 g $Bi(NO_3)_3.5H_2O$ was dissolved in 50 mL of deionized water, ultrasonicated for 0.5 h, then stirred on a magnetic stirrer for 2 h and added into the above solution dropwise with the flow rate at 2.5 $mLmin^{-1}$ under stirring. The heterogeneous solution was precipitated using 3-4 mL of 25% aqueous NH_3 solution and pH of the mixture was maintained at 2.0 and stirred continuously for another 15 h to get suspension of g-C_3N_4/BiOCl. Then, the resulting suspension was collected by filtration and washed five times with ethanol and water for complete removal of undesirable water-soluble products. Finally, solid powder sample was obtained by drying at 60ºC in an oven for overnight. A series of samples were prepared using same procedure by varying the ethanol compositions of 25%, 50%, 75%, and 95% which are noted as CN/BiOCl-X (X=1,2,3,4 and 5).

Characterization

The crystal phases of the material was analyzed using powder X-ray diffractometer (XRD) at a scanning rate of 5 º min^{-1}. The surface morphology of as-synthesized samples was observed with a field emission scanning electron microscope (FE-SEM) (JEOL JSM-7001F) equipped with an energy-dispersive X-ray spectroscopy (EDX) operated at an acceleration voltage of 10 kV. The morphology and structure of the synthesized samples were further examined by the transmission electron microscopy (TEM). Fourier transform infrared spectroscopy (FTIR) was measured for functional group estimation using a Nicolet-560F Fourier transform infrared spectrometer. The diffuse reflectance spectrum (DRS) was recorded with a UV-Vis spectrophotometer (U-3010, Hitachi) equipped with an integrating sphere, using $BaSO_4$ as the reference.

Photocatalytic Activity

In brief, 20 mg of photocatalyst was dispersed into 30 mL of 10 mgL^{-1} RhB. Prior to the irradiation, the suspension was magnetically stirred for 30 min in the dark to ensure the adsorption-desorption equilibrium. Then 2.0 mL suspension was collected and centrifuged and the dye concentration was analyzed with a UV-Vis spectrophotometer (Hitachi-3900) at 553 nm for RhB.

Results and Discussion

Morphology and Structure of g-C_3N_4/BiOCl Heterojunctions

X-ray power diffraction peaks were analyzed to investigate phase structures of pure BiOCl, g-C_3N_4 and g-C_3N_4/BiOCl composites as shown in Figure 2a. The diffraction peaks of synthesized samples appear at 2θ values which match with (hkl) values according to JCPDS card No. 85-0861 for g-C_3N_4 and No. 06-0249 for BiOCl. However, the typical (002) plane peak of g-C_3N_4 does not appear in the composites, probably low concentration and relatively low diffraction intensity of g-C_3N_4 in the g-C_3N_4/BiOCl (Xiong *et al.*, 2011). The results suggest that the coupling of BiOCl and g-C_3N_4 should take place between (001) plane of BiOCl and (002) plane of g-C_3N_4. The mutual

covering of BiOCl (001) plane and g-C_3N_4 (002) plane would lead to the decrease in the diffraction intensity. The weak peak around 27° (2θ) is a characteristic interlayer stacking peak of aromatic system, which indexes the (002) plane of graphitic materials. No impurity was observed from the patterns. Moreover, sharp and clear diffraction peaks illustrate that all composites have good crystallinity.

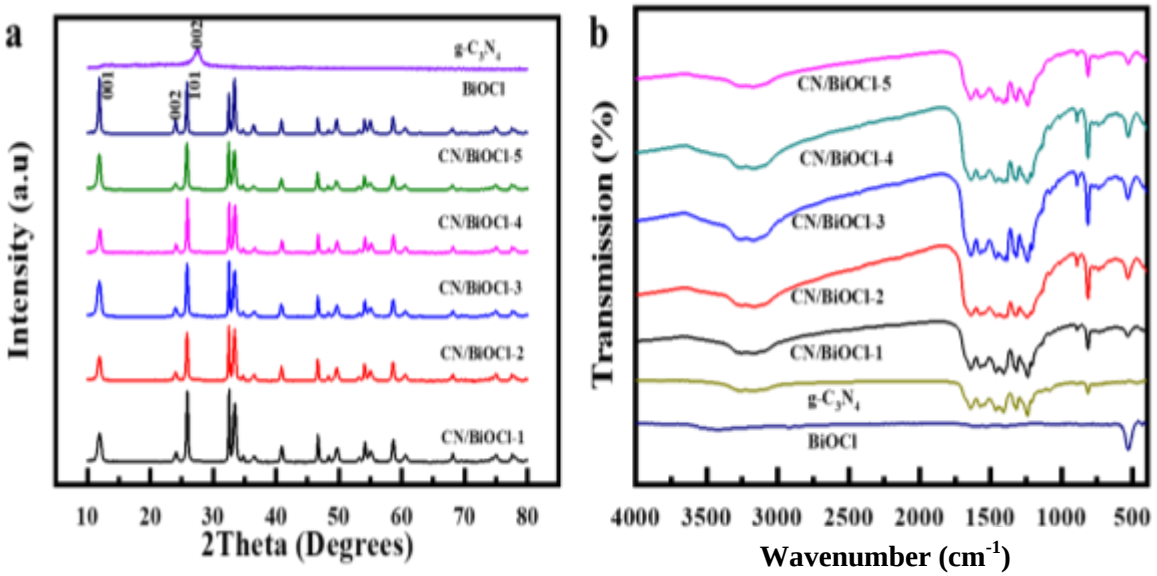

Figure 2 (a) XRD patterns and (b) FT IR spectra of pure g-C_3N_4, BiOCl and 2D g-C_3N_4/BiOCl heterojunctions prepared in different solvents

The results of FT IR spectra analysis of the composite samples are displayed in Figure 2b. In the composites, the broad absorption band at 3209 cm^{-1} is attributed to the stretching vibration mode of N-H on the g-C_3N_4 surface due to the surface defective sites. Additionally, the broad absorption band at 1644, 1577, 1465, 1402, and 1242 cm^{-1} can be assigned to the typical skeletal stretching modes of C-N heterocycles and tris-s-triazine. These absorption peaks indicate the maintenance of g-C_3N_4 basic structure after hybridization. With regard to the composites g-C_3N_4/BiOCl-1 to 5, the sharp peak at 512 cm^{-1} in the spectrum can be assigned to the stretching vibration mode of Bi-O in a tetragonal phase of the BiOCl crystal. Moreover, a characteristic breathing mode of s-triazine at 813 cm^{-1} is observed. To sum up, the coupling of composites is attributed to the intense interaction between g-C_3N_4 and BiOCl phases with the increase of ethanol concentration.

Figure 3 shows the SEM images of the as-prepared samples in different solvents. It is clear that the composites consist of a large number of irregular nanosheets. Although the morphology of as-prepared samples is uniform, the separated bulk nanosheets provide more active sites for the interaction with pollutant molecules. In fact, by using the lower concentration of ethanol, the structures of well-defined flake-like nanosheets with round corners can be observed. Moreover, one can see that with the increase of the ethanol concentration, the sample size becomes larger. It can be concluded that there are distinct differences in platelet shape suggesting that the two-dimensional bulky flake-like nanosheets morphology can be adjusted using different solvent ratios by different attractive forces in the reaction system (Ye *et al.*, 2013; Xiong *et al.*, 2011). As shown in Figure 3g, several g-C_3N_4 spread the surface of BiOCl nanosheets uniformly. The dense structure can be attributed to the localization of electrons and stronger binding between the layers. For pure BiOCl, the flower-shape irregular nanosheets were observed as shown in Figure 3b. After combining with two composites, as-prepared samples changed to bulky and smooth flake-like nanosheets.

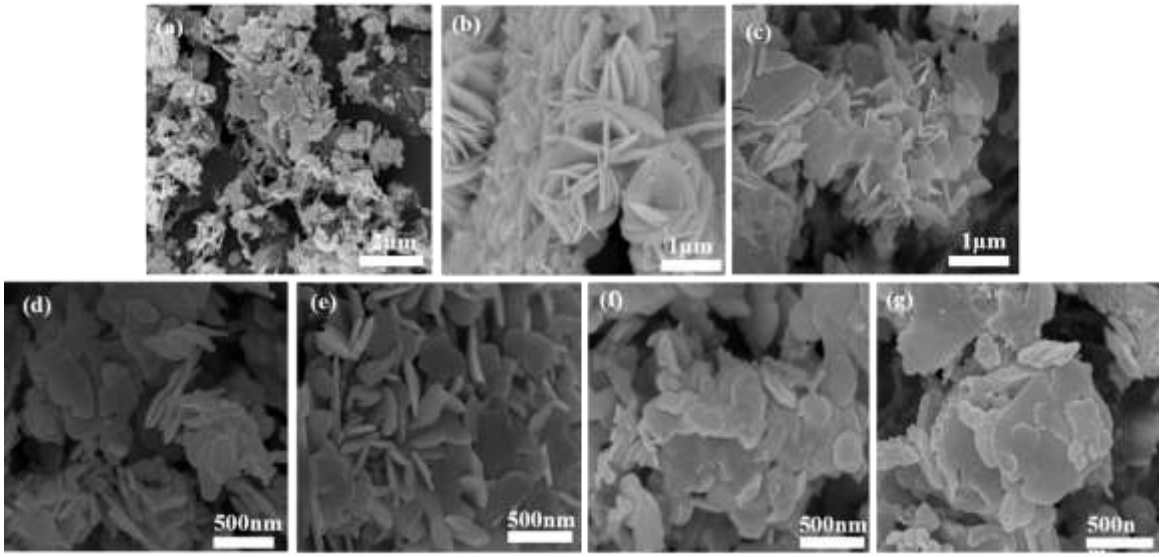

Figure 3 SEM images of 2D g-C_3N_4/BiOCl heterojunctions: (a) pure g-C_3N_4, (b) pure BiOCl, (c) g-C_3N_4/BiOCl-1, (d) g-C_3N_4/BiOCl-2, (e) g-C_3N_4/BiOCl-3,(f) g-C_3N_4/BiOCl-4 and (g) g-C_3N_4/BiOCl-5

Figure 4 shows the TEM images of several composites with polycrystalline structures and agglomerate. All composites consisting of numerous uniform nanosheets and tiny nanosheets of g-C_3N_4, which can be seen on the surface of BiOCl. Due to the presence of tiny nanosheets in the composites, the photocatalytic activity of composites can be enhancing under visible-light irradiation based on more active sites.

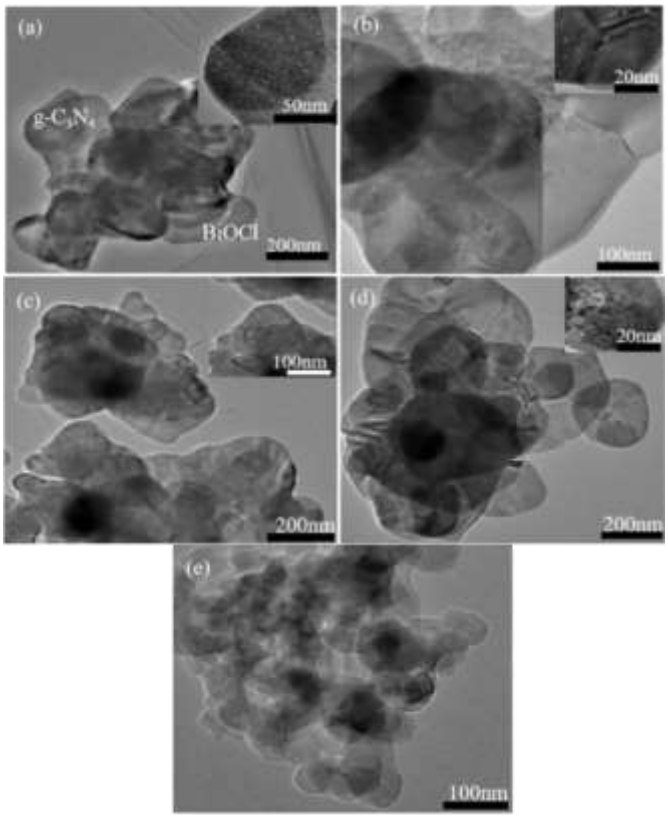

Figure 4 TEM images of as-prepared g-C_3N_4/BiOCl heterojunctions: (a) g-C_3N_4/BiOCl-1, (b) g-C_3N_4/BiOCl-2, (c) g-C_3N_4/BiOCl-3, (d) g-C_3N_4/BiOCl-4 and (e) g-C_3N_4/BiOCl-5

Optical Properties of g-C_3N_4/BiOCl Heterojunctions

The optical absorption and energy band feature of the semiconductors are important for determining its photocatalytic performance. The DRS of the as-prepared samples is shown in Figure 5a. It can be seen that the main absorption edge of pure BiOCl is located around 360 nm, while pure g-C_3N_4 can absorb the light from UV through the visible range up to 462 nm. The g-C_3N_4/BiOCl heterojunction (1 to 5) exhibit the adsorption edges in the visible-light absorption region, indicating the combination of the optical property of g-C_3N_4 with that of BiOCl. As the concentration of ethanol solvent increases to 75%, the absorption wavelength of g-C_3N_4/BiOCl-4 heterojunction at 468 nm for g-C_3N_4 increases, while that at 405 nm for BiOCl simultaneously decreases. Moreover, the absorption edge of g-C_3N_4/BiOCl samples exhibits a red shift in comparison with those of pure g-C_3N_4 and BiOCl with increasing the ethanol concentration. The band gap energy of semiconductors can be calculated approximately based on the following equation:

$$\alpha h\nu = A\left(h\nu - E_g\right)^{n/2} \quad (1)$$

Where α, h, ν, E_g and A are the absorption coefficient, Planck's constant, light frequency, band gap energy and constant respectively; n is determined by the type of optical transition of a semiconductor (n=1 for direct transition and n=4 for indirect transition) (Jiang *et al*., 2012; Xiao *et al.*, 2012). As can be seen in Figure 5b, E_g values of pure g-C_3N_4 and BiOCl are estimated to be 2.65 eV and 3.44 eV, respectively. The band gaps of g-C_3N_4/BiOCl composites gradually decrease with increasing the ethanol ratio to 95%, i.e. changing from 2.70 eV to 2.65 eV. Then, the band gaps of BiOCl in g-C_3N_4/BiOCl composites gradually decrease with increasing the ethanol solvent ratio up to 95%, changing from 3.44 eV to 3.06 eV determined from a plot of $(\alpha h\nu)^{1/2}$ versus $h\nu$. From these results, it can be deduced that all of the g-C_3N_4/BiOCl-1 to 5 have suitable band gaps to be activated by visible-light for photocatalytic decomposition of organic contaminants

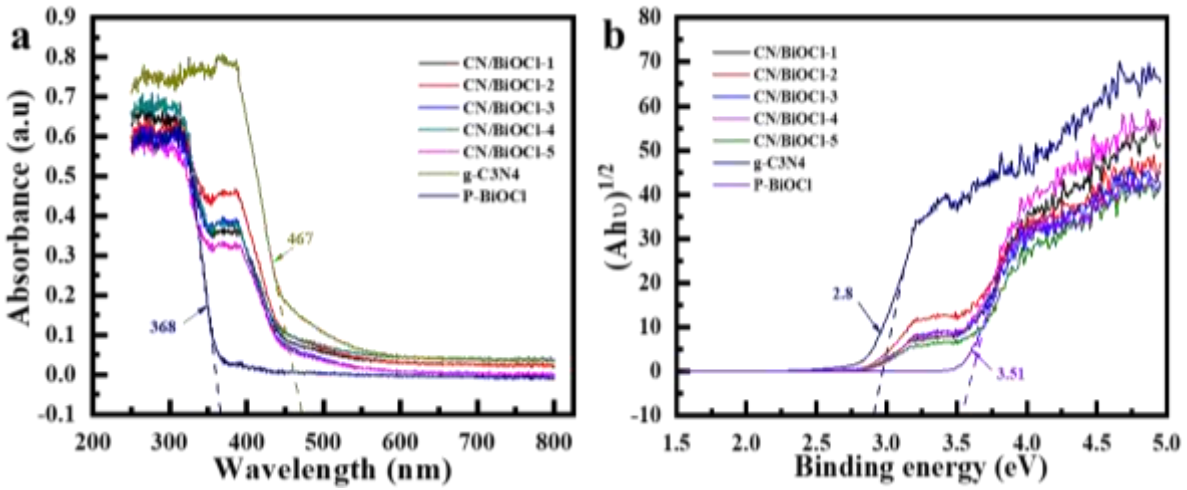

Figure 5 (a) UV-Vis diffuse reflectance spectra (b) Band gap plot of $(\alpha h\nu)^{1/2}$ vs. hν(eV) curves for pure g-C_3N_4, g-C_3N_4/BiOCl samples and BiOCl

The band edge position of conduction band (CB) and valence band (VB) for a semiconductor can be calculated according to the following theoretical empirical formulae (Zhang *et al.*,2005),

$$E_{CB} = \chi - E^e - 0.5E_g \quad (2)$$

$$E_{VB} = E_{CB} + E_g \quad (3)$$

where E_{CB} is the conduction band (CB) edge potential; χ is the absolute electronegativity of the constituent atoms, expressed as the arithmetic mean of the atomic electron affinity and the first ionization energy; E^e is the energy of free electrons on the hydrogen scale (~4.5 eV); E_g is the band gap energy of the semiconductor; E_{VB} is the valence band (VB) edge potential. The absolute electronegativity values for BiOCl and g-C_3N_4 are 6.36 and 4.73 eV, respectively. As can be seen in Figure 5b for CN/BiOCl-4, g-C_3N_4 has an electronic structure with an appropriate band gap energy of 2.65 eV, corresponding to an optical wavelength of 468 nm. The conduction band and valence band values of g-C_3N_4 in CN/BiOCl-4 are at -1.09 eV and 1.56 eV, respectively. BiOCl has an electronic structure with an appropriate band gap energy of 3.06 eV, corresponding to an optical wavelength of 468 nm. Then, the conduction band and valence band edge values of BiOCl in composite CN/BiOCl-4 are 0.33 eV and 3.39 eV, respectively, as can be seen in Table 2. These electronic structures of g-C_3N_4 and BiOCl possess good photo-response, which can be easily excited thus engendering the photogenerated electron-hole pairs under visible-light irradiation. The layer structure of g-C_3N_4 is beneficial for the transformation of the electron to BiOCl in CN/BiOCl-4. Indeed, their layered structure feature endows those self-built internal static electric fields, which can improve the effective separation of the photo induced electron-hole pair.

Table 2 Absolute Electronegativity, Calculated CB Edge, Calculated VB Position and Band Gap Energy for C_3N_4 and BiOCl in g-C_3N_4/BiOCl Heterojunction at the Point of Zero Charge

Semiconductors	Absolute electronegativity (χ) (eV)	Calculated CB position (eV)	Calculated VB position (eV)	Band gap energy, E_g (eV)
g-C_3N_4	4.73	-1.09	1.56	2.65
BiOCl	6.36	0.33	3.39	3.06

Photocatalytic Performance of g-C_3N_4/BiOCl Heterojunctions

To prove the photocatalytic activity of g-C_3N_4/BiOCl heterojunctions, RhB was chosen as the target organic dye pollutant. The characteristic absorption band of RhB at 553 nm is employed to monitor the degradation process under visible-light irradiation. As shown in Figure 6a, RhB self-photolysis without catalyst is not observable, indicating that RhB is stable under visible-light irradiation. For composites, the photocatalytic performance is gradually enhanced with the ethanol ratio increases from 10% to 75% in the presence of ionic liquid. The catalytic efficiency can achieve ~100 % removal within 1 h. Furthermore, the ethanol ratio was increased to 95% ethanol, contrarily leading to the increase of photocatalytic degradation activity. It can be seen that both g-C_3N_4 and BiOCl behave the important function in g-C_3N_4/BiOCl for improving the photocatalytic efficiency at 75% of ethanol ratio. The g-C_3N_4/BiOCl heterojunctions are 2D-2D layered composites, which enhance the photocatalytic performances due to the increased contact surface area and charge transfer rate. Furthermore, compared with other 2D material-based composites (i.e. 0D-2D and 1D-2D composites), 2D-2D layered nanosheets composite can achieve a solid construction due to the large contact surface area between two sheets, and exhibit greater stability than 0D-2D and 1D-2D composites (Low *et al.*, 2014).

In order to understand the reaction kinetics of dye degradation, the pseudo-first-order rate constant was expressed according to the following equation:

$$-\ln\frac{C}{C_0} = kt$$

In the above equation, *k* is the kinetic constant. C_0 and *C* are the initial and final concentration of RhB in solution at time 0 and t, respectively. g-C_3N_4/BiOCl composites exhibit the higher rate constants than pure g-C_3N_4 and BiOCl. It can be seen that the rate constant values of g-C_3N_4/BiOCl composites changed distinctly (Figure 6 b). The maximum value of k is 0.046 min^{-1} for CN/BiOCl-4, which is three times as high as that of pure BiOCl under visible-light illumination over RhB. Therefore, the modification of g-C_3N_4 with BiOCl could effectively enhance the photocatalytic activity by using high polar solvent ratio. Moreover, the kinetic constant values of as-prepared g-C_3N_4/BiOCl (1 to 5) follows the decreasing rate of CN/BiOCl-4 > CN/BiOCl-5 > CN/BiOCl-3> CN/BiOCl-1 > CN/BiOCl-2> BiOCl > g-C_3N_4.

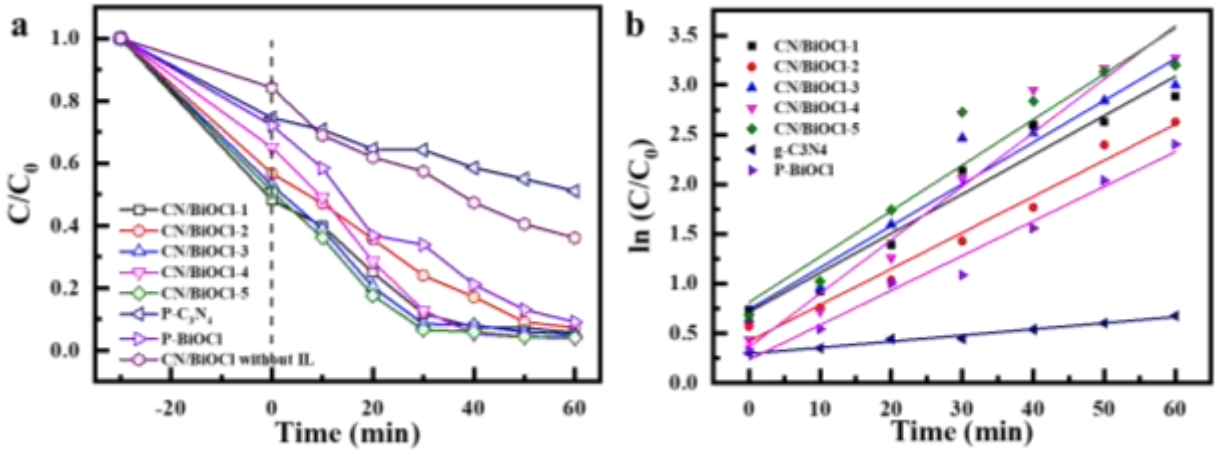

Figure 6 Photocatalytic activity of (a) RhB dye degradation; (b) pseudo-first-order kinetics plot of for RhB with pure g-C_3N_4, pure BiOCl, and g-C_3N_4/BiOCl composites under visible-light irradiation

Photocatalytic mechanism of g-C_3N_4/BiOCl-4 heterojunction

The enhancement of the photocatalytic activity of the g-C_3N_4/BiOCl-4 composite is mainly attributed to the effective separation of the photogenerated electron-hole pairs. As shown in Figure 7, both g-C_3N_4 and BiOCl are easily excited thus engendering the photogenerated electron-hole pairs. Unlike the traditional model, the Z-scheme mechanism photocatalysts retain stronger redox abilities, contributing to the improvement of photocatalytic performance.

g-C_3N_4 has an electronic structure with an appropriate band gap of 2.65 eV, corresponding to an optical wavelength of 468 nm. The estimated CB and VB of g-C_3N_4 material are -1.09 eV and 1.56 eV, respectively. The CB and VB edge potentials of BiOCl were at 0.33 eV and 3.39 eV. Here, the CB value of g-C_3N_4 (-1.06 eV) is more negative than that of BiOCl (0.18 eV), while the VB of BiOCl (3.54 eV) is more positive than that of g-C_3N_4 (1.52eV). The g-C_3N_4 and BiOCl semiconductors belong to overlapping bond potentials, suggesting that the band potential of g-C_3N_4 and BiOCl can be matched to fabricate the effective heterojunction. In general, the charge separation occurs in a heterojunction with different band gaps and edge positions. In this study, the dissolved O_2 in the aerated solutions act as an electron acceptor and the E_{CB} of g-C_3N_4 is more negative than the standard redox potential of $E(O_2/\cdot O_2^-)$. Furthermore, the VB of g-C_3N_4 and CB of BiOCl are close to each other. Therefore, the photo-excited electrons in the CB of BiOCl rapidly transfer to VB of g-C_3N_4, leading to the combination of photogenerated electrons in the CB of BiOCl with photogenerated holes in the VB of g-C_3N_4. Then, these accumulating electrons in the CB of g-C_3N_4 and holes in the VB of BiOCl participate in the dye degradation. Consequently, the more negative potentiated electrons in the CB of g-C_3N_4 reduce the molecular oxygen to yield. O_2^-, which induces the RhB degradation. Meanwhile, the more positive potentiated holes in the VB of BiOCl produce active $\cdot OH$ with powerful oxidation. In addition, the holes in the VB of BiOCl can

directly oxidize the organic dyes. Therefore, the charge transfers of the g-C_3N_4/BiOCl-4 composite may follow a direct Z-scheme route, which can improve the photogenerated electron-hole pair separation efficiency and enhance the photocatalytic activity for the degradation of organic pollutants.

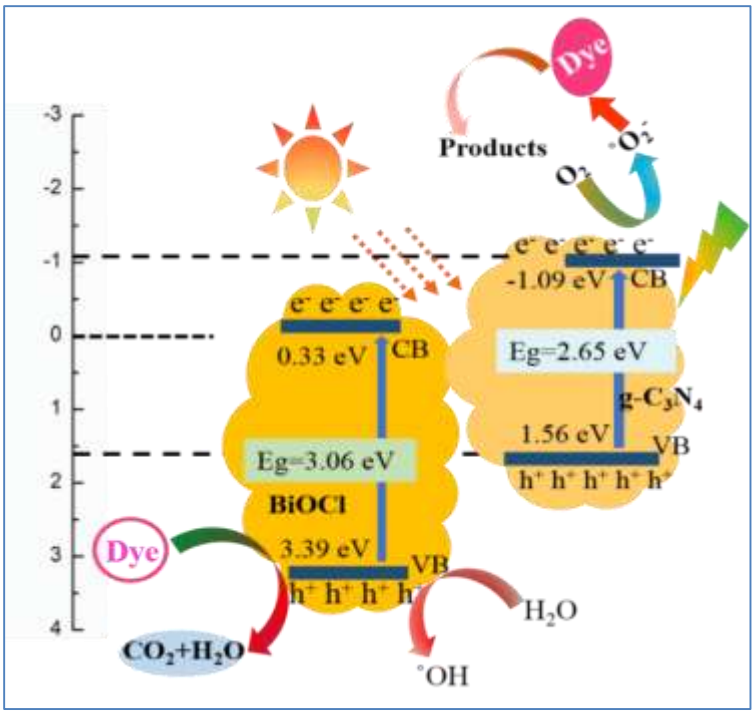

Figure 7 Schematic illustration of the photocatalytic mechanism for the dye degradation by using g-C_3N_4/BiOCl-4 heterojunction under visible-light.

Conclusion

The novel 2D g-C_3N_4/BiOCl heterojunctions were prepared by using a one-pot ethanol-assisted solvothermal method in the presence of ionic liquid [Bmim]Cl. The morphology characterization indicated that the g-C_3N_4 nanosheet covers the surface of flake-like BiOCl uniformly and the heterostructures formed when the ethanol ratio is in the range of 10-95%. Their band gap energies were lower than pure g-C_3N_4 and BiOCl as the ethanol ratio increased. The as-synthesized g-C_3N_4/BiOCl heterostructures display enhanced degradation performance in comparison with pure g-C_3N_4 and BiOCl, which can be attributed to the favorable optical property and suitable energy band gap potential. Among all the samples, CN/BiOCl-4 showed the highest photocatalytic activity. The heterojunction formed between g-C_3N_4 and BiOCl enhanced electron-hole recombination and photocatalytic activity. These results indicated that the g-C_3N_4/BiOCl nanosheet is a promising candidate photocatalyst for wastewater treatment and textile dyes degradation due to its enhanced photocatalysis properties.

Acknowledgements

The authors thank the financial support from the National Natural Science Foundation of China (21621004, 91534126), National Science Fund for Distinguished Young Scholars (21125627), Natural Science Foundation of Tianjin (18JCYBJC21000) and Program of Introducing Talents of Discipline to Universities (B06006). Also, the authors would like to express their profound gratitude to the Department of Higher Education, Ministry of Education, Yangon, Myanmar, for provision of opportunity to Myanmar Academy of Arts and Science for allowing to present this paper.

References

Akhavan, O. and Ghaderi, E. (2013). "Differentiation of Human Neural Stem Cells on Graphene/TiO_2 Heterojunction for Differentiation into Neurons". *Nanoscale*, vol. 5, pp. 10316-10326

Cai, L. (2015). "Enhanced Visible Light Photocatalytic Activity of BiOCl by Compositing with g-C_3N_4". *Mater. Research Innovations*, vol.19(5), pp. 392-396

Di, J., Xia, J., Yin, S., Xu, H., Xu, L., Xu, Y., He, M. and Li, H. (2014). "Preparation of Sphere-Like g-C_3N_4/BiOI Photocatalysts via Reactable Ionic Liquid for Visible-Light-Driven Photocatalytic Degradation of Pollutants". *J. Mater. Chem. A*, vol.2, pp. 5340-5351

Du, H.Y. and Luan, J. F. (2012). "Synthesis, Characterization and Photocatalytic Activity of New Photocatalyst $CdBiYO_4$". *Solid State Sci.*, vol.14, pp. 1295-1305

Fujushima, A., Tata, N. R. and Donald, A. T. (2000). "Titanium Dioxide Photocatalysis". *J. Photochemistry and Photobiology C*, vol. 1(1), pp. 1-21

Hou, Y. F., Liu, S. J., Zhang, J. H., Cheng, X., Wang, Y. (2014). "Facile Hydrothermal Synthesis of TiO_2-Bi_2WO_6 Hollow Superstructures with Excellent Photocatalysis and Recycle Properties". *Dalton Trans.*, vol. 43, pp. 1025-1031

Jiang, J., Zhao, K., Xiao, X. Y. and Zhang, L. Z. (2012). "Synthesis and Facet-Dependent Photoreactivity of BiOCl Single-Crystalline Nanosheets". *J. Am. Chem. Soc.*, vol.134(10), pp. 4473-4476

Kang, Y. Y., Yang, Y. Q., Yin, L. C., Kang, X. D., Wang, L. Z., Liu, G., Cheng, H. M. (2013). "Selective Breaking of Hydrogen Bonds of Layered Carbon Nitride for Visible Light Photocatalysis". *Adv. Mater.*, vol.28, pp. 6471-6477

Low, J., Cao, S., Yu, J., Wageh, S. (2014). "Two-Dimensional Layered Composite Photocatalysts". *Chem. Commun.*, vol.50(74) pp. 10768-10777

Manna, G., Bose, R. and Pradhan, N. (2014). "Photocatalytic Au-Bi_2S_3 Heterostructures. *J. Angew. Chem. Int. Ed.*, vol.53(26), pp. 6743-6746

Regan, B. O. and Gratzel, M. (1991). "Low-Cost High Efficiency Solar Cell Based on Dye-Sensitized Colloidal TiO_2 Films". *Nature*, vol.353, pp. 737-740

Sharma, I.D., Tripathi, G.K., Sharma, V.K., Tripathi, S. N., Kurchania, R., Kant,C., Sharma, A.K.and Sain,K.K.(2015). "One-pot Synthesis of Three Bismuth Oxyhalides (BiOCl, BiOBr, BiOI) and Their Photocatalytic Properties in Three Different Exposure Conditions". *Cogent Chem.*, vol. 1(1), pp. 1-15

Wang, X. C., Maeda, K., Thomas, A., Takanabe, K., Xin. G., Carlsson, J. M., Domen, K. and Antonietti. M. (2009). "A Metal-Free Polymeric Photocatalyst for Hydrogen Production from Water Under Visible Light". *Nature Materials*, vol.8, pp.76-80

Weng, S. X., Chen, B., Xie, L., Zheng, Z. and Liu, P. (2013). "Facile *in Situ* Synthesis of a Bi/BiOCl Nanocomposites with High Photocatalytic Activity". *J. Mater. Chem. A*, vol.1, pp. 3068-3075

Xiao, X., Hao, R., Liang, M., Zuo, X. X., Nan, J. M., Li, L. S. and Zhang, W. D. (2012). "One Pot Solvothermal Synthesis of Three-Dimensional (3D) BiOI/BiOCl Composites with Enhanced Visible-Light Photocatalytic Activities for the Degradation of Bisphenol-A". *J. Hazard. Mater.*, vol. 233, pp. 122-130

Xiong, J. Y., Cheng, G., Li, G. F., Qin, F. and Chen, R. (2011). "Well-Crystallized Square-like 2D BiOCl Nanoplates: Mannitol-Assisted Hydrothermal Synthesis and Improved Visible-Light-Driven Photocatalytic Performance". *RSC. Adv.*, vol.1, pp. 1542-1553

Yamasita, D., Takata, T., Michikazu, H., Junko, N. K. and Domen, K. (2004). "Recent Progress of Visible-Light-Driven Heterogenous Photocatalyst for Overall Water Splitting". *Solid State Ionics*, vol.172, pp.591-595

Yan, S. C., Li, Z. S.and Zou, Z. G. (2009). "Photodegradation Performance of g-C_3N_4 Fabricated by Directly Heating Melamine". *Langmuir Article*, vol.25(17), pp. 10397-10401

Ye, L., Liu,J.Y., Jiang, Z., Peng, T. Y. and Zan, L. (2013). "Facets Coupling of BiOBr-g-C_3N_4 Composite Photocatalyst for Enhanced Visible Light-Driven Photocatalytic Activity". *Appl. Catal. B*, vol.142-143, pp. 1-7

Zhai, H. F., Li, A. D., Kong, J. Z., Li, X. F., Zhao, J., Guo, B. L., Yin, J., Li, Z. S. and Wu, D. (2013). "Preparation and Visible Light Photocatalytic Properties of $BiNbO_4$ and $BiTaO_4$ by a Citrate Method". *J. Solid State Chem.*, vol.202, pp. 6-14

Zhang, K. L, Liu, C. M, Haung, F. Q, Zheng, C. and Wang, W. D. (2006) "Study of the Electronic Structure and Photocatalytic Activity of the BiOCl Photocatalyst". *Appl. Catalysis B. Environ.*, vol.68(3-4), pp.125-129

Zhang, X. T., Sato O., Taguchi, M., Einaga, Y., Murakami, T.and Fukishima, A. (2005). "Self-Cleaning Particle Coating with Antireflection Properties". *Chem. Mater.*, vol.17(3), pp. 696-700

PREPARATION OF BIOPLASTICS FROM POTATO STARCH

Khin Mar Cho[1], Lae Lae Myo[2], Aung Than Htwe[3]

Abstract

This research concerns with preparation of bioplastics from starch (S*olanum tuberosum* L.). The aim of this work is to prepare biodegradable plastics from potato starch and to study the swelling and water uptake properties, physicomehanical properties, antimicrobial activity and biodegradability of the prepared bioplastics. The potato samples were purchased from Maydawee Market in North Okkalapa Township, Yangon Region, Myanmar. Starch was extracted from potato by cold extraction method. The extracted potato starch was characterized by FT IR technique. FT IR spectrum of extracted potato starch was compared with that of commercial starch. Bioplastic films SG-a, SG-b, SG-c, SGV-a, SGV-b and SGV-c were prepared from extracted potato starch using plasticizer as glycerol (4 %, 6 % and 10 %) with and without vinegar. All bioplastic films are clear and flexible. The degree of swelling and water uptake of prepared bioplastic films were determined. The physicomechanical properties (thickness, tensile strength, percent elongation at break and tear strength) of prepared bioplastic films were measured. The morphology of prepared bioplastic films was studied by SEM technique. In addition, the antimicrobial activities of all sample films were tested by agar well diffusion method against six microorganisms. Moreover, the biodegradability of prepared bioplastic films was evaluated by soil burial method. The prepared bioplastic samples were applied for food packaging.

Keywords: potato, bioplastics, physicomechanical properties, starch, plasticizers

Introduction

The major disadvantages of petro-based plastics are non-biodegradable and result in environmental pollution. The petrochemical plastics have been largely used as packaging material due to economical abundance and their desirable properties of good barrier properties towards O_2, aroma compounds, tensile strength and tear strength (Jabeen, *et al*., 2015). Bioplastics of renewable origin are compostable or degradable by the enzymatic action of micro-organisms. There has been an increased interest in the last few years from the food packaging industry towards the development and application of bioplastics for food packaging. The bioplastics nowadays have found applications for both short-shelf life products like fresh fruits and vegetables and long-shelf life products. Two major advantages to bio-based plastic products: they save fossil resources by using biomass and provide the keenly sought-after possibility of carbon neutrality (Özdamara and Ateşb, 2018). Food packaging as a vital part of the subject of food technology is involved with protection and preservation of all types of foods (Jabeen *et al*., 2015). Bioplastic development efforts have focused predominantly upon starch, which is a renewable and widely available raw material. Starch as biodegradable polymer becomes reasonable material for the production of bioplastics because of its low cost (Maulida *et al*., 2016). Edible film made from starch is less elastic and is hydrophilic, and to cope with this, another additional material needs to be added to improve its mechanical characteristic. The addition of glycerol as the plasticizer, is intended to improve its elasticity and to weaken the stiffness of the polymer, and to improve the flexibility of the polymers. Glycerol has the ability to decrease the internal hydrogen bond in the intermolecular bond (Asria, 2016). This paper illustrates the preparation of edible bioplastic film made from potato starch with glycerol as its plasticizer for food packaging purpose.

[1] Dr, Associate Professor, Department of Chemistry, University of Yangon
[2.] MSc Candidate, Department of Chemistry, University of Yangon
[3.] Dr, Assistant Lecturer, Department of Chemistry, University of Yangon

Materials and Methods

Extraction and Characterization of Potato Starch

Firstly, the potato (500 g) was washed with tap water, cleaned and dried. Samples were peeled and then, grated using a grater. The grated potatoes were mixed with distilled water and sieved with metal strainer. It was transferred to a beaker and filtered. The residue was washed with distilled water two times and dried at room temperature for 24 h. The dried insoluble starch was crushed into powder by mortar and pestle. Finally, the potato starch powder was obtained and calculated the yield percent. The extracted starch powder was characterized by FT IR technique.

Preparation of Bioplastic Films from Potato Starch Powder

The three bioplastic films with 5 mL of vinegar (SGV-a, SGV-b and SGV-c) were prepared by thoroughly mixing 10 g each of potato starch powder with 2 mL, 3 mL and 5 mL of glycerol and 50 mL each of distilled water in separate 250 mL beakers. The starch solution was placed on a hot plate set at 70 ºC and was continued to stir until the mixture became thick and almost transparent. The solution was poured onto a melamine plate and allowed to dry at room temperature for three days. Similarly, another three bioplastic films samples (SG-a, SG-b and SG-c) were prepared without vinegar. The ratios of starch: glycerol: water were (10:2:50, 10:3:50 and 10:5:50 w/v) in each three bioplastic samples (Arıkan and Bilgen, 2019).

Determination of Chemical and Physicomechanical Properties

The chemical properties (degree of swelling and water uptake) and the physicomechanical properties (thickness, tensile strength, percent elongation at break and tear strength) of prepared bioplastic films were determined.

Determination of Morphology, Antimicrobial activity and Biodegradability

The surface morphology of the bioplastic films was investigated by SEM. The study of antimicrobial activity was performed by agar-well diffusion method. The inhibition zone (clean zone) appeared around the agar-well indicating the presence of antimicrobial activity. The extent of antimicrobial activity was measured from the zone of inhibition diameter. To investigate the biodegradability of the prepared bioplastic samples, the prepared samples (equal dimensions) were buried under a soil tray (2' × 2' × 2') at a depth of 1 ft. The the films were taken out from the soil at 24 h interval and degradation were monitored and recorded in physical features by photograph.

Results and Discussion

Extraction of Starch Powder from Potatoes

The potato starch was extracted from potato (S*olanum tuberosum* L.) by cold extraction method and the percent yield of extracted potato starch powder was calculated to be 6.1296 %. The potato and extracted potato starch powder are shown in Figure 1.

(a) (b)

Figure 1 (a) Potatoes (b) The extracted potato starch powder

Characterization of Extracted Potato Starch by FT IR Analysis

Potato starch powder was characterized by FT IR technique to identify the corresponding functional group compared with that of commercial potato starch (Figure 2 and Table 1). The peaks at 3263 cm^{-1} and 2929 cm^{-1} of extracted starch are due to stretching vibration of -OH and -CH groups. The absorption band at 1643 cm^{-1} is related to C-O bending associated with -OH groups of starch. Moreover, the absorption band at 1157 cm^{-1} and 1016 cm^{-1} are attributed to C-O-C asymmetric stretching vibration and C-O stretching vibration of saccharides molecules present in starch, respectively. The characteristic C-O-C ring vibration of starch appeared at 929 and 856 cm^{-1}. It was found that FT IR spectrum of extracted potato starch is matched with that of commercial starch.

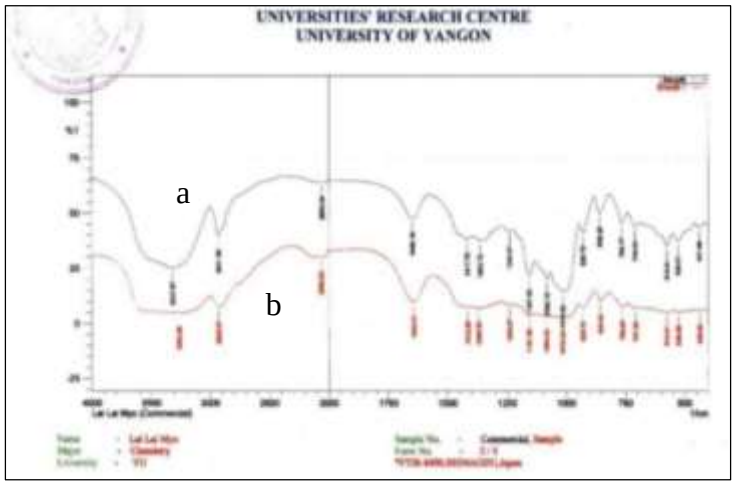

Figure 2 FT IR spectra of the (a) extracted potato starch and (b) commercial potato starch

Table 1 FT IR spectral Data of Extracted and Commercial Potato Starch

No	Wavenumber (cm^{-1})			Interpretation
	Extracted Starch	Commercial Starch	Reported Value *	
1	3263	3317	3600-3300	ν_{OH} groups
2	2929	2931	2931	$\nu_{as\ CH}$ groups
3	1643	1649	1637	C-O bending associated with OH group
4	1157	1157	1149	C-O-C asymmetric stretching
5	1016	1016	1200-800	C-O stretching
6	929,856	929,858	920,856,758	C-O-C ring vibration of carbohydrate

(*Abdullah *et al*., 2018)

Bioplastic Films from Potato Starch Powder

All prepared bioplastic films were clear, transparent and flexible. The prepared bioplastics samples are shown in Figure 3.

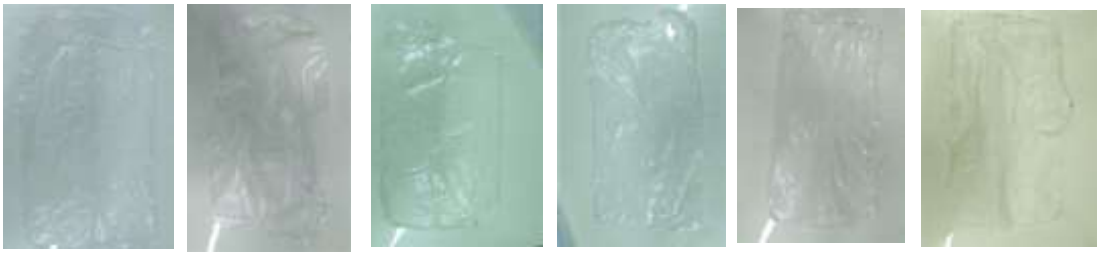

SG-a SG-b SG-c SGV-a SGV-b SGV-c

Figure 3 The prepared bioplastic films

Degree of Swelling and Water Uptake

Degree of swelling and water uptake are important properties of membrane. Table 2 shows the percent degree of swelling of bioplastic films with respect to the time-frame presented in minutes. The degree of swelling of all of prepared bioplastic samples decreased with increase in glycerol composition and increased with time. Bioplastic films prepared with vinegar showed higher swelling power than those without vinegar. It was observed that SG-c has lowest swelling power among all samples. The percent water uptake of bioplastic films with respect to the time frame presented in minutes is also shown in Table 2. It was found that, in general, water uptake percent decreased with increase in glycerol concentration in the bioplastic films without and with vinegar. Generally, the bioplastic films prepared with vinegar, SGV-a, SGV-b and SGV-c showed higher water uptake than those without vinegar except SG-a.

Table 2 Variation in Degree of Swelling and Water Uptake of Prepared Bioplastic Films

Samples	5 min		10 min		15 min		20 min		25 min	
	swelling (%)	water uptake (%)	swelling (%)	water uptake (%)	swelling (%)	Water uptake (%)	swelling (%)	Water uptake (%)	swelling (%)	Water uptake (%)
SG-a	22.72	29.40	28.26	39.40	31.03	45.00	32.61	48.40	32.61	48.40
SG-b	23.67	31.00	21.40	27.20	25.05	33.40	17.36	21.00	19.21	23.80
SG-c	10.55	11.80	15.11	17.80	12.58	14.40	11.03	12.40	10.70	12.00
SGV-a	25.70	34.60	27.50	38.00	27.20	37.40	26.70	36.60	27.50	37.20
SGV-b	25.37	34.00	27.22	34.40	29.07	41.00	25.60	34.40	27.11	37.20
SGV-c	33.24	49.80	22.96	29.80	21.75	27.80	19.35	24.00	19.35	24.00

Physicomechanical Properties of Prepared Bioplastic Films

The physicomechanical properties of the prepared bioplastic films were determined at the Myanmar Scientific and Technological Research Department. Tansometer (Monsanto T0212) was used to determine for the tensile strength and elongation at break of the prepared bioplastic films. Although SGV-a and SGV-b films have same thickness, the tensile strength of SGV-a film was higher than that of SGV-b film. It was found that bioplastic film SG-c has lowest in tensile strength among the bioplastic films prepared without vinegar. Similarly, bioplastic film SGV-c has the lowest in tensile strength among the bioplastic films prepared with vinegar. Although having lower elongation at break the bioplastic films SG-a and SVG-a have higher tensile and tear strengths (Table 3).

Table 3 Physicomechnical Properties of Prepared Potato Bioplastic Films

Sample	Thickness (mm)	Tensile Strength (MPa)	Elongation at break (%)	Tear Strength (kN/m)
SG-a	0.91	2.2	17	31.9
SG-b	0.61	2.1	40	15.0
SG-c	0.31	0.7	35	4.70
SGV-a	0.52	3.3	15	34.2
SGV-b	0.52	2.8	45	19.6
SGV-c	0.75	0.9	28	3.90

Morphology of Prepared Bioplastic Films by SEM Analysis

SEM is a type of electron microscope that produces the image of a sample by scanning it with a focused beam of electrons. In this present work, morphological features of the prepared bioplastic (SG-a, SG-b, SG-c) without vinegar and (SGV-a, SGV-b and SGV-c) films with vinegar were examined by SEM. The surface structures of the materials had lost their evenness (Figure 4). The samples exhibited a substantial variation in the structure as reported by Marichelvam *et al*. (2019).

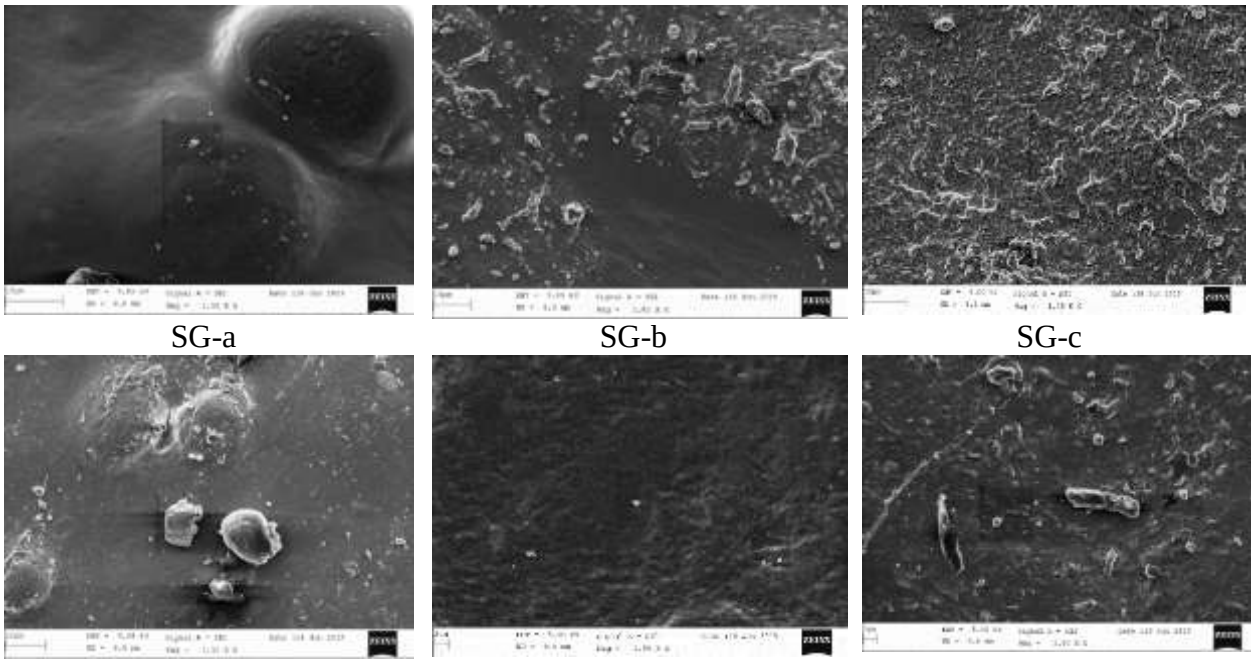

SG-a SG-b SG-c

SGV-a SGV-b SGV-c

Figure 4 SEM images of prepared bioplastic films

Antimicrobial Activity of Prepared Bioplastic Films

Antimicrobial activities of all bioplastic films were examined against six microorganisms: *Bacillus subtilis, Staphylococcus aureus, Pseudomonas aeruginosa, Bacillus pumilus, Candida albicans* and *Escherichia coli* by agar well diffusion method (Figure 5 and Table 5). All samples (SG-a, SG-b, SG-c, SGV-a, SGV-b and SGV-c) showed antimicrobial activities on *B. pumilus*. SG-a and SG-c showed antimicrobial activity on three microorganisms (*S. aureus, B. pumilus* and *E. coli.*) whereas the other samples did not. Only the SGV-a inhibited three microorganisms (*P. aeruginosa, B. pumilus* and *C. albicans*). SGV-b and SGV-c inhibited two bacteria (*B. pumilus* and *E. coli*).

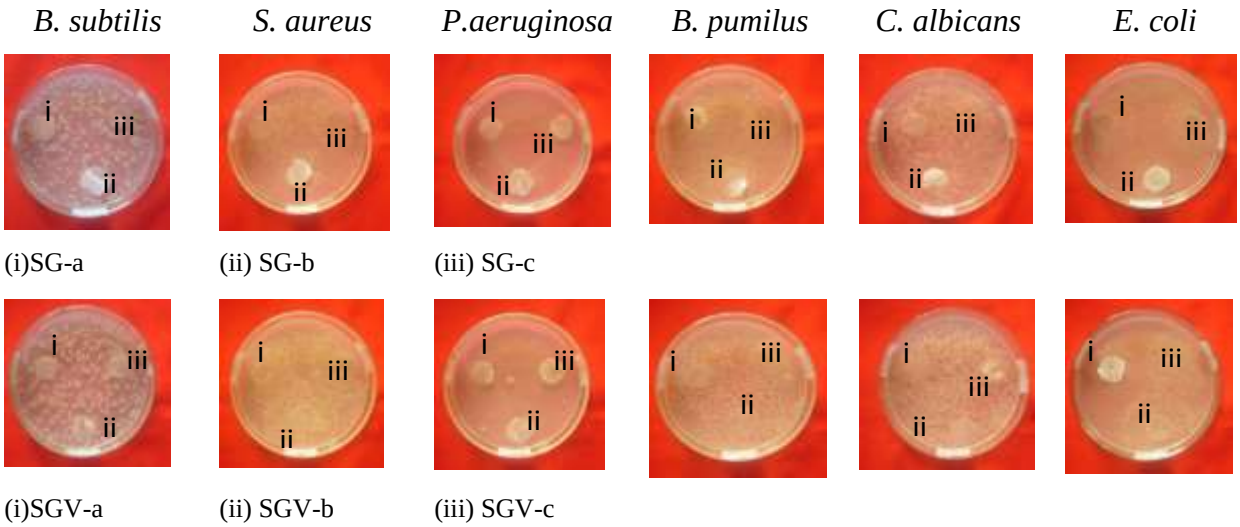

Figure 5 Zone inhibitions of the biodegradable plastic films against six microorganisms

Table 5 Antimicrobial Activities of Bioplastic Films against Six Microorganisms

Sample	*B.subtilis*	*S.aureus*	*P.aeruginosa*	*B.pumilus*	*C.albicans*	*E.coli*
SG-a	–	+	–	+	–	+
SG-b	–	–	–	+	–	–
SG-c	–	+	–	+	–	+
SGV-a	–	–	+	+	+	–
SGV-b	–	–	–	+	–	+
SGV-c	–	–	–	+	–	+

Acceptance criteria (+) inhibited, (-) un-inhibited
Susceptible ≥ 21 mm (+++) Intermediate 17.20 mm (++) Resistant ≤ 16 mm (+)

Biodegradability of Prepared Bioplastic Films

One of the objectives of developed bioplastic film is to make easy throw away materials from degradable plastic to alternative waste disposal problems by means of environmental degradation. Biodegradation is degradation caused by living organisms such as fungi and bacteria (Folino *et al.*, 2020).

In this work, biodegradation of all sample films was tested by soil burial method. Environmental effects mentioned in this work are moisture and soil which may be favourable conditions for the microbial growth. Soil burial is a traditional way to test samples for degradation because of its actual condition of waste disposal. Uniformly sized samples were buried in the soil from waste disposal. The physical appearance of films before and after in the soil buried are shown in Figure 6. The figure clearly showed significant deforming of films at each investigation period. The biodegradation of all sample films was found to be degraded after 5 days. Samples SG-a, SVG- and SGV-b were highly degraded within 5 days according to physical appearances.

Samples	Before test	After test				
	0 day	1 day	2 days	3 days	4 days	5days
SG-a						
SG-b	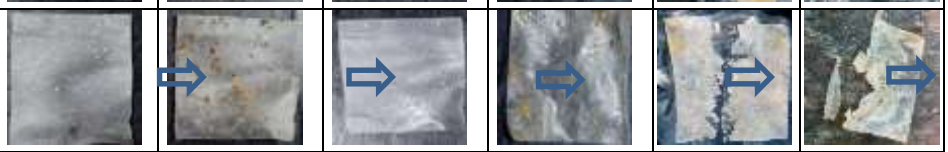					
SG-c	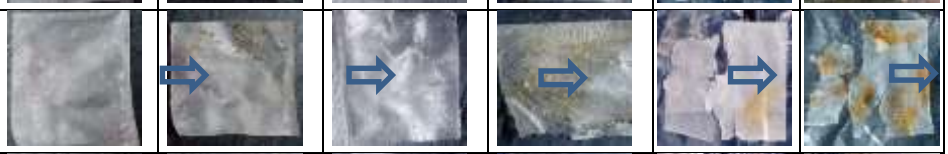					
SGV-a	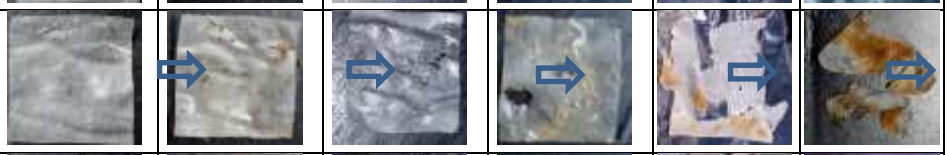					
SGV-b						
SGV-c	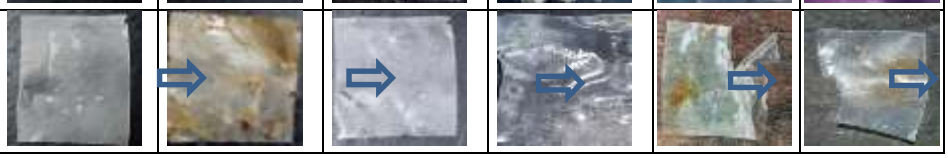					

Figure 6 Physical appearance of bioplastic films by soil burial test

Application of Bioplastic Films

In this research, the prepared bioplastics do not contain any chemicals, toxins and thus are safe. So, it can be applied for food packaging. According to water uptake and mechanical properties, both of the bioplastic films SG-a and SGV-a have good water retainability, high tensile and tear strengths and it can be applied for packaging of tea leaves and coffee mix. The bioplastic bags were made by packing tea leaves and coffee mix in the bioplastic film SGV-a and closed the edges by heating. Boiling water was added into a glass which contained tea leaves bioplastic bag and allowed to infuse for 3 minutes. Yellowish brown coloured tea was obtained.The applications of prepared bioplastics are shown in Figure 7.

(a) (b) (c)

Figure 7 Application of bioplastic film SVG-a in food packaging (a) tea leaves in prepared bioplastic bag (b) coffee mix in prepared bioplastic bag and (c) tea leaves bag in hot water

Conclusion

Potato starch is a feasible component in the preparation of bioplastic films and glycerol is a plasticizer that is compatible with starch. Percent yields of extracted potato starch was found to be 6.1296 % based on wet sample. All prepared bioplastic film samples are clear and flexible. Functional groups shown in FT IR spectrum of the extracted potato starch were matched with those of commercial starch. SEM images showed all samples had rough surface and lost their evenness. The antimicrobial activities of all bioplastic films were investigated by agar well diffusion method using six microorganisms. All bioplastic films showed the antimicrobial activity on *Bacillus pumilus*. It was found that higher levels of glycerol decreased both tensile strength and tear strength. Variable elongation at break for plastic films with and without vinegar may be due to unequal thickness. In soil burial method, biodegradation of all sample films was degraded after 5 days. From the study of water uptake, antimicrobial activity and mechanical properties, both of the bioplastic films SG-a and SGV-a have good water retainability, can resist on *Bacillus pumilus*, high tensile and tear strengths so that they can be applied for food packaging. It is clear that bio-based packaging materials offer a versatile potential in case of packaging industry, however, there is need of certain storage tests to be performed on packaging machinery in order to certify the use of these packaging films on a commercial scale. A critical evaluation is required to access the functionality of bio-based packaging materials before they are launched into the market as sole substitutes for conventional packaging materials.

Acknowledgement

The authors would like to mention their sincere thanks to Dr Ni Ni Than, Professor of Head of Department of Chemistry from University of Yangon for providing research facilities and Myanmar Academy of Arts and Science Association for submission of this research paper.

References

Abdullah, A. H. D., Chalimah, S., Primadona, I. and Hanatyo, M. H. G. (2018). "Physical and Chemical Properties of Corn, Cassava, and Potato Starchs". *IOP Conference Series Earth and Environmental Science,* vol.160 (1), pp. 1755-1315

Arıkan, E. B. and Bilgen, H. D. (2019). "Production of Bioplastic from Potato Peel Waste and Investigation of Its Biodegradability". *International Advanced Researches and Engineering Journal,* vol. 3(2), pp. 093-097

Asria, M. (2016). "Preparation and Characterization of Edible Film from The Belitung Taro Starch (*Xanthosoma sagitifolium*) and Chitosan". *Journal of Chemical and Pharmaceutical Research*, vol. 8(6), pp. 57-62

Folino, A., Karageorgiou, A., Calabrò, P. S. and Komilis. D. (2020). "Biodegradation of Wasted Bioplastics in Natural and Industrial Environments: A Review". *Sustainability*, vol. 12 (15), pp. 1-37

Jabeen, N., Majid, I. and Nayik, G.A. (2015). "Bioplastics and Food Packaging: A Review", *Cogent Food & Agriculture*, vol. 1, pp. 1-7

Marichelvam M. K., Jawaid, M. and Asin, M. (2019). "Corn and Rice Starch-Based Bio-Plastics as Alternative Packaging Materials". *Fibers,* vol. (7), 32, pp. 1-14

Maulida, Siagian,M. and Tarigan, P. (2016). "Production of Starch-based Bioplastic from Cassava Peel Reinforced with Microcrystalline Cellulose Avicel PH101 Using Sorbitol as Plasticizer". *Journal of Physics Conference Series,* vol. 710 (1), pp. 1-7

Özdamara, E. G. and Ateşb, M. (2018). "A Research on Starch Based Bioplastic". *J Sustain. Construct. Mater. Technol.*, vol. 3(3), pp. 249-260

PREPARATION AND CHARACTERIZATION OF CHITOSAN-POLYVINYL ALCOHOL-GRAPHENE OXIDE COMPOSITE MEMBRANE AND THEIR MECHANICAL PROPERTIES

Aung Paing[1], Khin Than Yee[2], Mya Theingi[3]

Abstract

In this study, the composite membrane forming ability of chitosan (CS), polyvinyl alcohol (PVA) and graphene oxide were prepared. The graphene oxide was prepared from graphite powder. The graphite powder (GP) and prepared graphene oxide (GO) samples were characterized by the X-ray diffraction (XRD), Scanning electron microscopy (SEM), Fourier transform infrared spectroscopy (FT IR) and Thermogravimetric- Differential thermal analysis (TG-DTA). The XRD pattern of graphite powder and exhibited a strong peak at 2θ of 26.4° corresponding to a basal spacing of d_{002} 0.336 nm and that of graphene oxide at 2θ of 9.79° corresponding to a basal spacing of d_{002} 0.901 nm. The composite membranes were prepared by 1.5 % (w/v) chitosan, 4 % (w/v) PVA and modified with variable loadings of graphene oxide (GO) ranging between 0.2 g to 0.5 g wt. percent. The criteria ratio was investigated using mechanical properties such as tensile strength, elongation at break and tear strength. According to the mechanical properties of composite membranes, CS-PVA-GO2, results revealed that the incorporation of graphene oxide into the CS-PVA polymer matrix lead to the improvement of tensile strength and percent of elongation of break. FT IR analysis, indicated that the characteristic absorption peak of CS-PVA-GO2 composite membrane confirmed the polymer blended with GO. SEM micrograph of CS-PVA-GO2 composite membrane exhibited homogeneous and smooth texture. TG-DTA analysis showed that CS-PVA-GO2 composite membrane exhibited the major thermal stability reflected in lower loss of weight with increasing temperature that led to the delay of decomposition.

Keywords: Graphene oxide, chitosan, polyvinyl alcohol, composite membrane

Introduction

Two-dimensional (2D) graphene oxide has a unique properties and wide range of applications, since the awarded of Nobel prize in physics for the discovering of graphene, it has large effect in the natural science communities. Nanocomposites of graphene due to the improvement in physical properties like electrical, thermal and mechanical as it compared with other nanocomposites and pure polymer. Graphene is an ideal nano filler for function composite due to exceptional properties likes, high surface area, along with its electrical, thermal and mechanical (Tagreed and Mustafa, 2015). GO can be easily dispersed in water; thus, hydrophilic polymer, or water-soluble polymers matrices for polymer/graphene nanocomposite, due to their dispersion properties. Polyvinyl alcohol (PVA) is a hydroxyl-rich, water-soluble, biocompatible and non-toxic polymer that is commonly used in fuel cells, drug delivery, coating material, and adhesives (Ye *et al.*, 2012).

Chitosan (CS) is the product of chitin deacetylation and contains a large quantity of hydrophilic groups (e.g., amino carboxyl groups). Thus, CS molecules are easily protonated. It has been widely used in medicine and has many excellent biological properties, such as biocompatibility, biodegradability and coagulation activity (Lu *et al.*, 2013). Not only does GO contain carboxyl and epoxy groups, it is also possible to insert small molecules or polymers between its layers. The surface anionic groups of GO are able to interact with the CS matrix via hydrogen bonding and electrostatic interactions, to achieve good dispersion (Yuan *et al.*, 2016). As the combination of properties of chitosan such as water binding capacity, fat binding capacity,

[1] PhD Candidate, Department of Chemistry, University of Yangon
[2] Dr, Lecturer, Department of Chemistry, West Yangon University
[3] Dr, Associate Professor, Department of Chemistry, Sittwe University

bioactivity, biodegradability, nontoxicity, biocompatibility and antifungal activity, chitosan and it modified analogs have shown many applications (Yang and Chiu, 2012).

Polyvinyl alcohol (PVA) is an inexpensive semi-crystalline polyhydroxy polymer, and has also excellent film-forming properties and a high density of reactive chemical functions (Feketefoldi *et al.,* 2016). The addition of graphene to polymeric matrices has been recently studied in which pristine CS and PVA, and hybrid CS:PVA membranes have been modified by means of the addition of graphene oxide (GO), providing an increase in tensile strength and at the glass transition temperature (Acurio *et al.,* 2017).

A vast number of studies have reported the incorporation of graphene oxide into biocompatible, eco-friendly and cheap polymers for instance, chitosan and polyvinyl alcohol in order to synthesize enhanced nanocomposite material for a wide number of applications (Jiang *et al.,* 2010). Membrane manufacture and performance are attracting great attention in academia and industry in a wide variety of industrial applications. The development of new membranes requires the materials has advanced for the last years, allowing the development of highly featured carbon nanostructures with properties that offer unexpected opportunities in many fields such as adsorption application (Garcia-Cruz *et al.,* 2016).

In this study, the composite membrane was prepared based from CS, PVA and doped with GO as a carbon filler. An intensive physicochemical characterization of this membrane was carried out by FT IR, SEM, TG-DTA and mechanical properties of these membranes were also studied.

Materials and Methods

Sample Collection

Chitosan, graphite powder, sulphuric acid (H_2SO_4), sodium nitrate ($NaNO_{3)}$, potassium permanganate ($KMnO_4$) and hydrogen peroxide (H_2O_2) were purchased from Academy Chemical shop (Yangon, Myanmar). Polyvinyl alcohol was purchased from First Prime Co. Ltd. Distilled water was used as the solvent in all analyses.

Preparation of Graphene Oxide from Graphite Powder

Graphene oxide (GO) was prepared starting with graphite powder by modified Hummer's Method (Shahriary and Athawale, 2014). Firstly, 3 g of graphite powder and 1.5 g of sodium nitrate and 69 mL of concentrated sulphuric acid were mixed under constant stirring for about 1 h in an ice bath. After stirring, 9 g of potassium permanganate was added gradually to the above mixture solution while keeping the rate of addition carefully controlled the reaction temperature below 20 °C to prevent overheating and explosion. At this state, the mixture solution was gradually becoming dark brown. The mixture was stirred at 35 °C for 12 h and then 1500 mL of deionized (DI) water was added under vigorous stirring. To ensure the completion of reaction of potassium permanganate, 15 mL of 30 % hydrogen peroxide was added to reduce the residual potassium permanganate. And then, dark brown coloured mixture solution gradually changed into bright yellow. Finally, the resulting mixture solution was washed by rinsing with 5 % (v/v) hydrochloric acid and then deionized (DI) water for several times until neutral pH. After centrifugation, the filtrate was dried in oven at 70 °C and graphene oxide (GO) was obtained as shown in Figure 1 (a) and (b).

(a) (b)

Figure 1 (a) Graphene oxide solution and (b) graphene oxide powder (GO)

Preparation of Chitosan (CS)-Polyvinyl Alcohol (PVA)-Graphene Oxide (GO)(CS-PVA-GO) Composite Membrane

CS-PVA-GO composite membrane were prepared from a blend of 1.5 wt. % of CS and 4 wt. % of PVA homogenous solution. Firstly, CS powder was added to the acidic aqueous solution (1 % (v/v) acetic acid) and stirred at room temperature for 12 h. Separately, PVA powder was added to distilled water and stirred at 70 °C for 2 h. Then, CS and PVA solution were filtered by vacuum filtration to remove impurities. The blend membrane was prepared with CS-PVA ratio of 50:50 (v/v %) by mixing the appropriate amounts of the single polymer solutions and stirring for 24 h. Then, a certain amount of GO (0.2, 0.3, 0.4, and 0.5 wt.%) was added into polymers mixture and stirred for three days until a brownish homogenous mixture was achieved. Finally, the CS-PVA-GO mixture solutions were kept for sufficient times to remove any bubble formation and were cast onto a cleaned and dried melamine plate at room temperature. The prepared CS-PVA-GO composite membranes were neutralized with 0.1M NaOH solution and the membranes were washed with water for several times and dried in air. All of the prepared CS-PVA-GO membranes (Figure 2) were kept under dry condition for further use.

(a) (b) (c) (d)

Figure 2 (a) CS-PVA-GO1 (b) CS-PVA-GO2 (c) CS-PVA-GO3 and (d) CS-PVA-GO4 composite membranes

CS-PVA-GO1 = 1.5 % CS - 4 % PVA – 0.2 % GO composite membrane
CS-PVA-GO2 = 1.5 % CS - 4 % PVA – 0.3 % GO composite membrane
CS-PVA-GO3 = 1.5 % CS - 4 % PVA – 0.4 % GO composite membrane
CS-PVA-GO3 = 1.5 % CS - 4 % PVA – 0.5 % GO composite membrane

Characterization of the Prepared Samples

X-ray diffraction (XRD) analysis was carried out using Rigaku X-ray Diffractometer, RINI 2000/PC software, Cat. No 9240 J 101, Japan. Copper tube with nickel filter was used. The diffraction pattern was recorded in terms of 2θ in the range of 10-70 °. FT IR spectrum was recorded in the range of 4000-400 cm^{-1} by using 8400 SHIMADZU, Japan FT IR spectrophotometer. The scanning electron microscopy (SEM) images were recorded by using JSM-5610 Model SEM, JEOL-Ltd., Japan. Thermogravimetric and differential thermal analysis was carried out using (TG-DTA-BAHR-Thermoanalyse GmbH (Germany).

Results and Discussions

Characterization of Graphite Powder (GP) and Graphene Oxide (GO)

XRD analysis of graphite powder and graphene oxide

In XRD measurements, the peaks indicated with Miller indices in the graphite precursor were well matched with the standard graphite diffraction peaks. The smaller peaks are likely originated form impurities in the material. The X-ray diffraction profiles of GP and prepared GO samples are shown in Figure 3. The GP powder exhibited a strong and sharp peak at 2θ of 26.44° as shown in Figure 3 (a), indicating a higher ordered structure corresponding to a basal *d*-spacing d_{002} of 0.336 nm. The crystallite site calculated using the diffraction peak of (002) plane was 58.8 nm. Figure 3(b) shows the XRD pattern of GO which exhibited a strong peak with reflection at 2θ of 9.79° corresponding to a basal *d*-spacing d_{001} of 0.901 nm. The crystallite site of GO was 8.15 nm. This value is higher than interlayer spacing of prepared GO, due to the presence of oxygenated functional groups and intercalated water molecule. The addition of the oxygen-containing groups converted regions of the graphite to amorphous material, reducing the size of the crystalline regions.

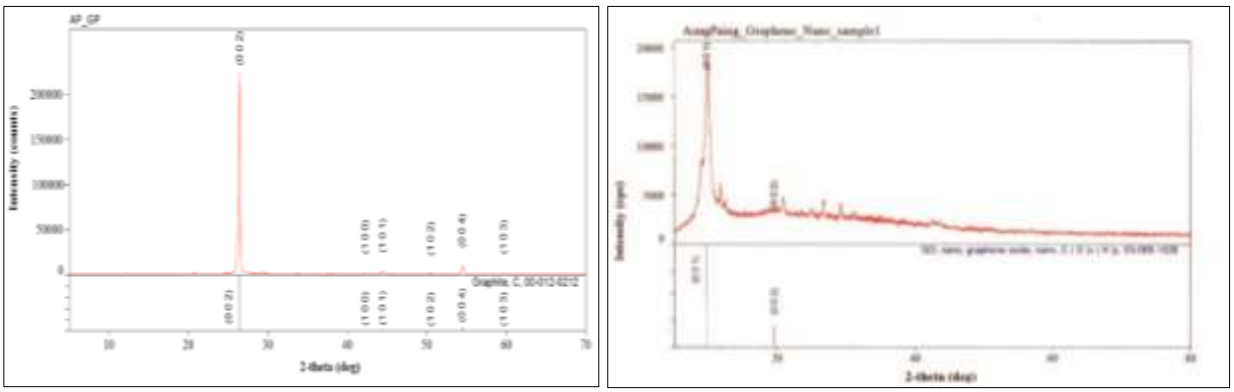

(a) (b)

Figure 3 XRD diffractograms of (a) graphite powder (GP) and (b) prepared graphene oxide (GO)

FT IR analysis graphite powder and graphene oxide

The functional groups of GP and prepared GO were studied by Fourier Transform Infrared Spectrophotometer and the results are presented in Figure 4 and Table 1. From the FT IR data of GP, the band observed at 3703 cm^{-1} was attributed to O–H stretching group. The bands appeared at 2883 cm^{-1} and 1022 cm^{-1} were related to C–H stretching vibration and C–O–O stretching vibration, respectively. In FT IR spectrum of GO, the bands observed at 1716 cm^{-1} was due to C–O stretching group, that at 1626 cm^{-1} was due to the presence of C=O stretching group and the band at 1124 cm^{-1} was related to the C–OH stretching group present in prepared GO.

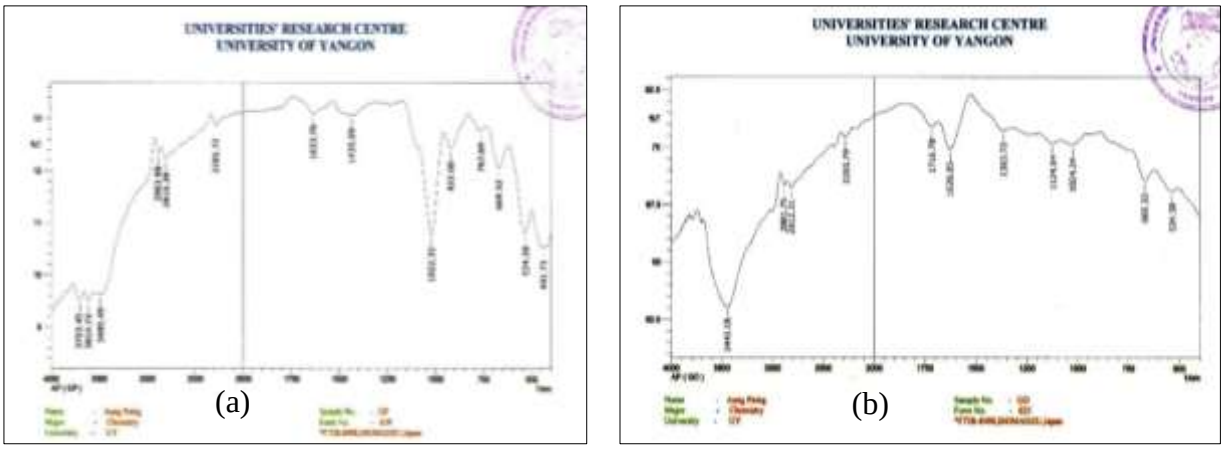

Figure 4 FT IR spectra of (a) graphite powder (GP) and (b) prepared graphene oxide (GO)

Table 1 FT IR Band Assignments for Graphite Powder (GP) and Prepared Graphene Oxide (GO)

Observed Wavenumber (cm^{-1})		Literature* Wavenumber (cm^{-1})	Band Assignment
GP	GO		
3703	3443	3700-3400	O – H stretching
2883	2881	2980-2850	C – H stretching
	1626	1665 - 1620	C = O stretching
	1363	1450 - 1350	C = C stretching
	1716	1870 - 1650	C – O stretching
	1124	1210 - 1120	C – OH stretching
1022	1024	1050 - 1000	C – O – O stretching
767		770 - 690	C – H bending
669	669	680 - 620	C - HO stretching

***** Silverstein *et al*. (2003)

SEM analysis of graphite powder and graphene oxide

The SEM images show surface morphology of GP and prepared GO samples. It can be seen that the different surface morphology was observed. The GP particle showed plate like layer and the prepared GO particle showed both plate and nano-rod like surface morphology as shown in Figure 5.

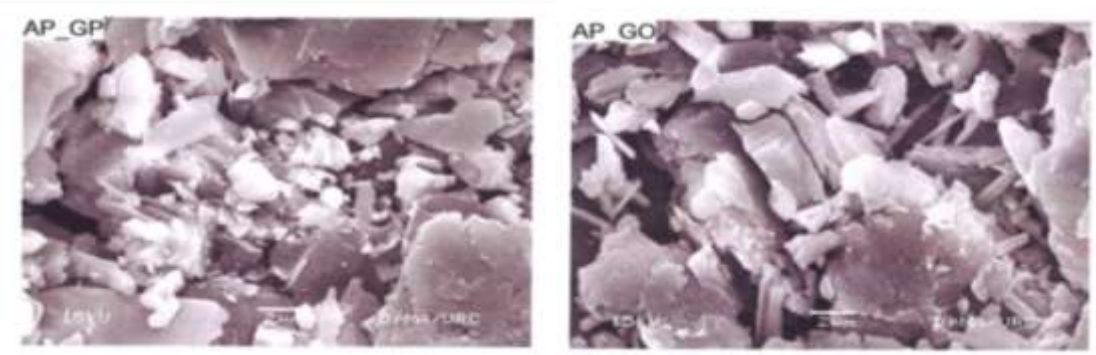

Figure 5 SEM images of (a) graphite powder (GP) and (b) prepared graphene oxide (GO)

TG-DTA analysis of graphite powder and graphene oxide

The TG-DTA thermogram of the GP is presented in Figure 5 (a). According to the TG-DTA thermogram profiles of GP, two steps of weight loss were observed. In the first step, the temperature range between 38 °C and 120 °C accompanied with 1.26 % weight loss was due to the removal of moisture and absorbed surface water. The weight loss approximately1.55 % was observed in the temperature range between 120 °C and 600 °C. In this state, the weight loss was due to the combustion of impurity compound.

The TG-DTA thermogram of the GO is presented in Figure 5 (b). Four steps or weight loss was occurred. In the first step, GO was decomposed (18.77 %) at 40 °C until 200 °C, showing the elimination of water molecule and unstable oxygen functional group.

In the second step, the decomposition was occurred at 200 °C until 430 °C (81.23 %). This decomposition was caused by elimination of more stable oxygen functional group as well as burning of ring carbon. Then, small endothermic and exothermic peaks occurred at 472 °C and 536 °C. The total weight loss was about 100.00%. The GP and prepared GO samples are thermally stable and decrease in weight loss when increasing temperature.

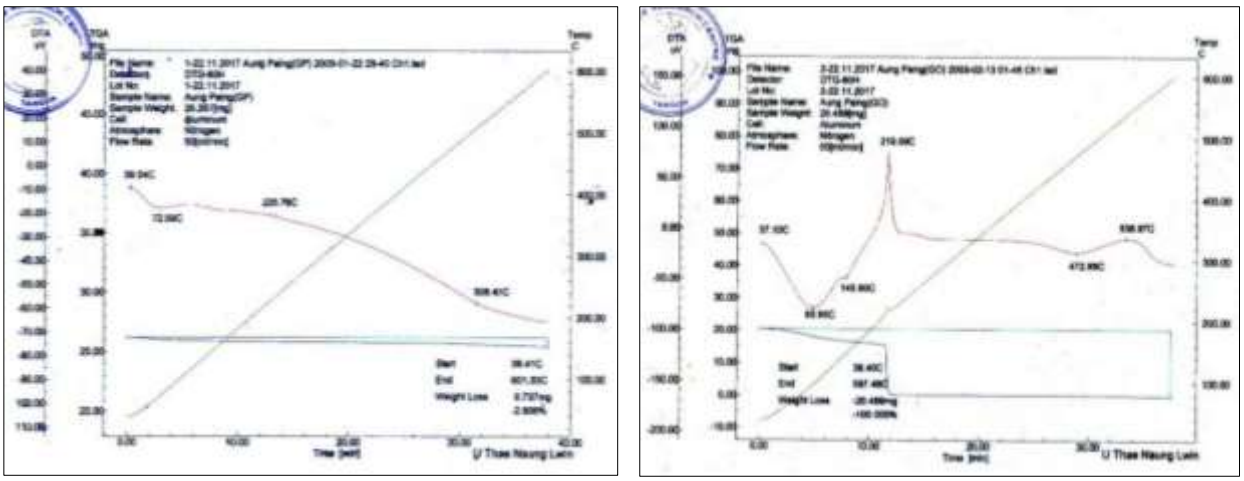

(a) (b)

Figure 6 TG-DTA thermograms of (a) graphite powder (GP) and (b) prepared graphene oxide (GO)

Physicomechanical Properties of Chitosan-Polyvinyl Alcohol-Graphene Oxide (CS-PVA-GO) Composite Membranes

The physicomechanical properties of CS-PVA-GO composite membranes are shown in Table 2 and Figure 7. The thicknesses of CS-PVA-GO composite membranes are approximately ~ 0.24 mm. The composite membranes were prepared from 1.5 wt. % of chitosan, 4 wt. % of polyvinyl alcohol and different weights of graphene oxide. In the concentration range of graphene oxide 0.2 g to 0.5 g, the tensile strength was found to increase to 17.3 MPa with graphene content up to 0.3 g for CS-PVA-GO2 composite membrane. Further increase in graphene oxide content to 0.4 g and 0.5 g, the temsile strength slightly decreased. The percent elongation at breaks slowly decreased with increase in graphene oxide content and the percent elongation value reached to 86 % when the graphene oxide content was 0.3 g. Thus, the maximum tensile strength and percent of elongation values are flexible in CS-PVA-GO2 composite membrane. Thus, CS-PVA-GO2 composite was selected for further investigation.

Table 2 Physicomechanical Properties of CS-PVA-GO Composite Membranes

CS-PVA-GO Composite Membranes (wt. %)	Tensile Strength (MPa)	Elongation at Break (%)	Tear Strength (kNm^{-1})
CS-PVA-GO1	13.8	104	64.7
CS-PVA-GO2	17.3	86	58.6
CS-PVA-GO3	16.7	66	39.7
CS-PVA-GO4	16.3	83	55.3

Membrane Thickness = ~ 0.24 mm

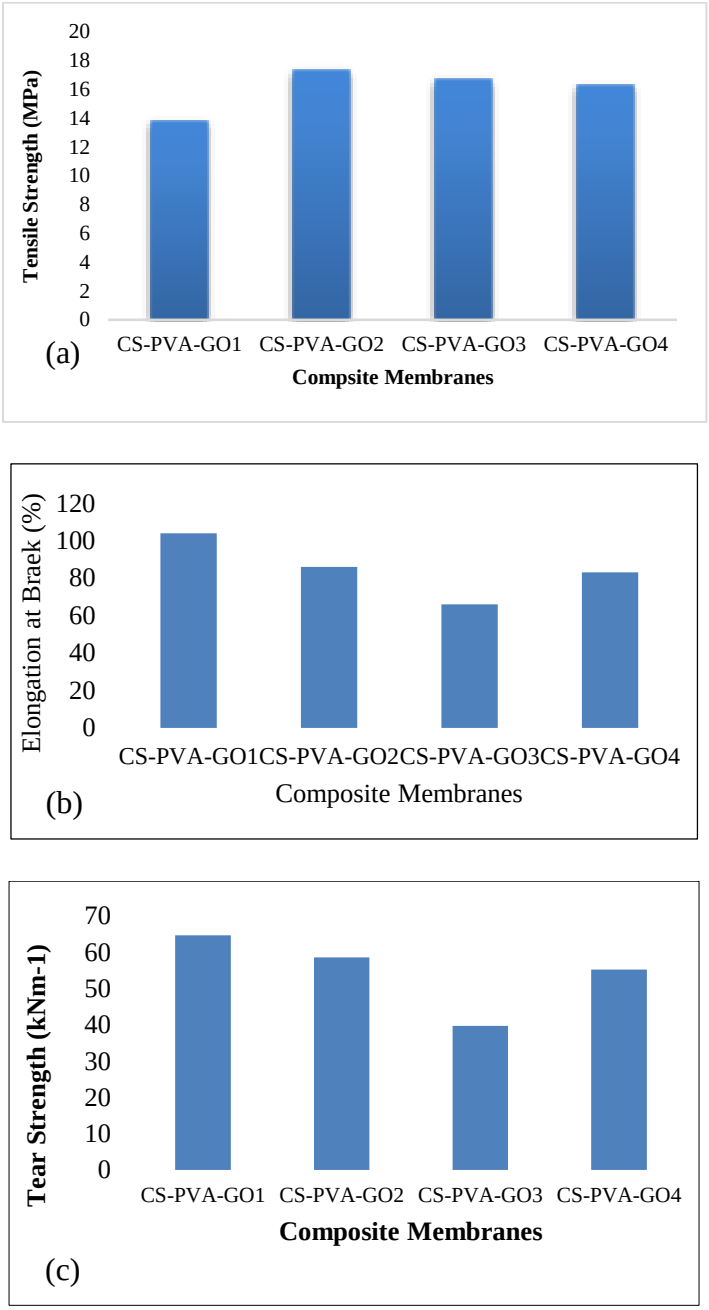

Figure 7 (a) Tensile strength (b) elongation at break and (c) tear strength of CS-PVA-GO composite membranes

Characterization of CS-PVA-GO2 Composite Membrane

FT IR analysis of CS-PVA-GO2 composite membrane

The chitosan and polyvinyl alcohol molecule are able to form hydrogen bonds. It is expected that some of the special interactions between different molecular groups influence the sample spectrum as shown in Figure 8 and Table 3. The band at 1075 cm^{-1} was related to C – O – C stretching groups. The peak at 1587 cm^{-1} was concerned with the symmetric deformation of $– NH_2$ resulting from ionization of primary amino groups in the acidic medium whereas the peak at 1419 cm^{-1} related to the C – N stretching vibration. The strong broad peak at 3461 cm^{-1} was caused by amine N – H symmetric vibration and – OH stretching vibration. When the addition of GO, the spectra did not show obvious changes.

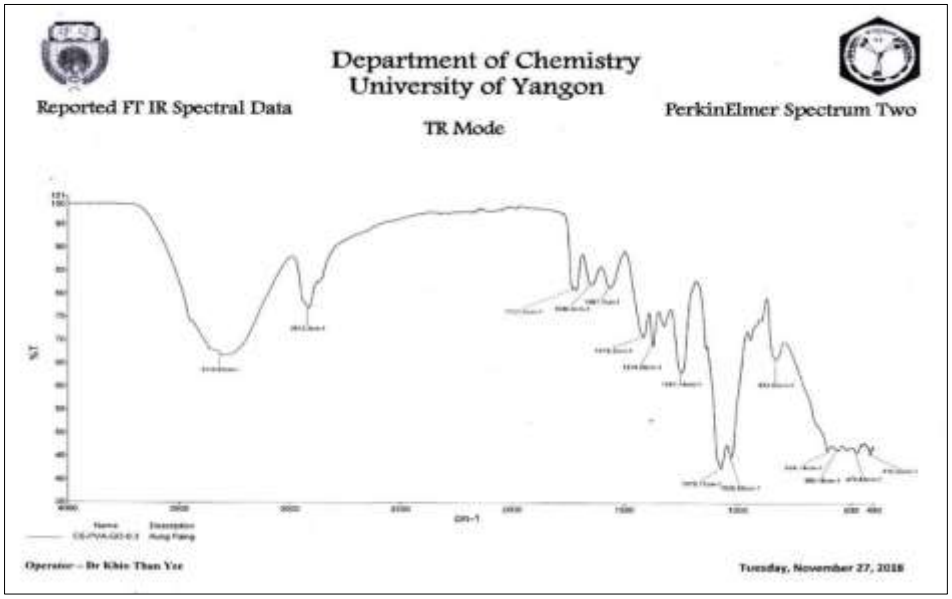

Figure 8 FT IR spectra of CS-PVA-GO2 composite membrane

Table 3 FT IR Band Assignment of CS-PVA-GO2 Composite Membrane

Observed Wavenumber (cm^{-1}) CS-PVA-GO2 Composite Membrane	*Literature Wavenumber (cm^{-1})	Band Assignment
3310	3400-3200	O – H stretching and N – H stretching
2913	2940-2915	C – H stretching of $– CH_3$ group
1731	1765-1725	C = O stretching
1646, 1587	1650-1580	NH_2 deformation
1419	1420-1400	C – N stretching
1247	1285-1240	C – O Stretching
1075	1240-1070	C – O – C stretching

*Silverstein *et al*. (2003)

SEM analysis of CS-PVA-GO2 composite membrane

The scanning electron micrograph of CS-PVA-GO composite membrane is shown in Figure 9. From the SEM analysis, it was observed that the small loading of 0.3 wt. % of GO provides a homogenous surface where the GO sample were not distinguishable from the polymer membrane indicating that the dispersion step through stirring of GO in CS-PVA mixture ratio of (50:50 v/v) was sufficient upon membrane solution.

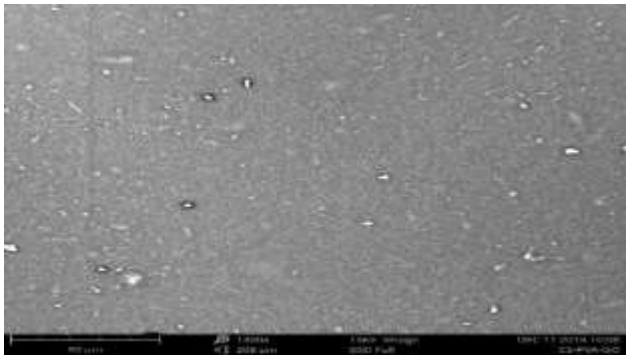

Figure 9 SEM micrograph of CS-PVA-GO2 composite membrane

TG-DTA analysis of CS-PVA-GO composite membrane

Thermal stability of prepared CS-PVA-GO2 composite membrane was investigated by TG-DTA analysis under nitrogen atmosphere and heating rate of 20 °C min^{-1} from 40 °C to 600 °C. The degradation peak value and weight loss of CS-PVA-GO2 composite membrane were presented in Figure 10. According to the TG-DTA thermogram of composite membrane, three steps of weight loss were observed. In the first step, the temperature range between 37 °C to 120 °C, the weight loss was 12.54 % which attributed to the release of the moisture preferentially absorbed by the polymer. The second weight loss started at 120 °C and 430 °C during which the polymer decomposition and elimination of the volatile products occurred. In the third step (from 430 °C to 600 °C) the weight loss about 25.73 % was actually observed due to the decomposition of the polymer matrix. According to the degradation results, the CS-PVA-GO2 composite membrane was found to retain its thermal stability.

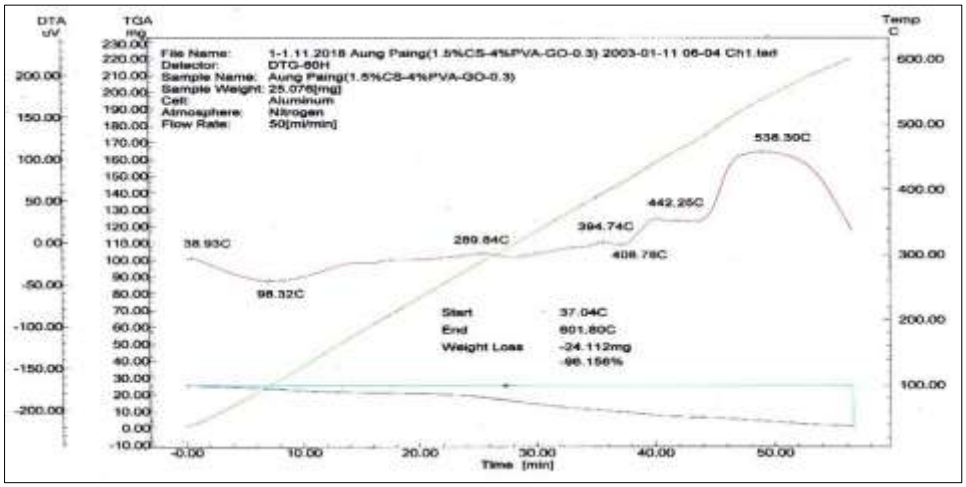

Figure 10 TG-DTA thermograms of CS-PVA-GO2 composite membrane

Conclusion

In this study, the graphene oxide was prepared by oxidizing graphite powder using modified Hummer's method. The XRD results demonstrated that the GP showed 2θ of 26.4° and the prepared GO showed 2θ of 9.79° with interlayer spacing equal to 0.901 nm. FT IR spectrum indicated that the graphite powder was oxidized and the oxygen atoms replaced into the graphite layers forming C=O, C–O and C–OH bonds in graphene oxide. SEM images showed that GP was found to be relatively the plate like layer and GO showed the mix plate and nano-rod like surface morphology. From the TG-DTA analysis, the total weight loss of GP was less than the prepared GO. The polymer composite membranes were prepared from chitosan, PVA and different weight percents of graphene oxide. According to the mechanical properties, CS-PVA-GO2 composite membrane was found to have optimum tensile strength and elongation at break. FT IR analysis showed that CS-PVA-GO2 composite membrane exists intermolecular interaction between CS, PVA and GO. From SEM analysis the surface morphology of CS-PVA-GO2 composite membrane exhibited homogenous nature and smooth surface texture. Thermal stability of CS-PVA-GO2 composite membrane was observed since the significant weight loss did not occur in the polymer matrix backbone.

Acknowledgement

The authors would like to express their profound gratitude to the Department of Higher Education, Ministry of Education, Yangon, Myanmar, for provision of opportunity to do this research and Myanmar Academy of Arts and Science for allowing to present this paper.

References

Acurio, E., Garcia-Cruz, L., Montiel, V. and Iniesta, J. (2017). "Preparation and Poly (Vinyl) Alcohol/Chitosan Hybrid Membranes Doped with Graphene Nanosheets". *J. Advance Mate. and Technol*., vol. 1, pp. 9-19

Feketefoldi, B., Cermenek, B., Sprik, C., Schenk, A., Grimmer, C., Bodner, M., Koller, M., Ribitsch, V. and Hacker, V. (2016). "Chitosan-Based Anion Exchange Membranes for Direct Ethanol Fuel Cells". *J. Membra. Sci. Technol.,* vol 6 (1), pp. 1-9

Garcia-Cruz, L., Casado-Coterillo, C., Irabien, A. and Montiel, V. (2016). "High Performance of Alkaline Anion-Exchange Membrane Based on Chitosan/Poly (Vinyl) Alcohol Doped with Graphene Oxide for the Electrooxidation of Primary Alcohols". *J. Carbon Res.,* vol. 2 (10), pp. 1-19

Jiang, L., Shen, X. P., Wu, J. P. and Shenk, K. C. (2010). "Preparation and Characterization of Graphene/Poly (Vinyl Alcohol) Nanocomposites". *J. Appl. Polm. Sci.,* vol. 118, pp. 275-279

Lu, J. J., Feng, M. and Zhang, H. B. (2013). "Preparation and Adsorption of the Graphene Oxide/Chitosan Composite Films and Investigations on their Nanolinear Optical Limiting Effect". *Acta. Phys. Scn*., vol. 62 (1), pp. 11-17

Shahriary, L. and Athawale, A. A. (2014), "Graphene Oxide Synthesized by Using Modified Hummers Approach". *International J. of Renewable Ener. and Envir. Eng.*, vol. 2 (1), pp. 58-63

Silverstein, R. M., Webster, F. X. and Kiemle, D. J. (2003). *Spectrometric Identification of Organic Compounds*. New York: 7th Edition, John Wiley and Sons, Inc. 216

Tagreed, M. A., and Mustafa, A. K. (2015). "Preparation and Characterization of Graphene/PMMA". *International J. of Adv Res. In Sci., Eng. and Tech.*, vol. 2 (10), pp. 902-909

Yang, J. Y. and Chiu, H.C. (2012). "Preparation and Characterization of Polyvinyl Alcohol/Chitosan Blend Membrane for Alkaline Direct Methanol Fuel Cells". *J. Membrane Sci.,* vol. 15, pp. 65-71

Ye, Y. S., Rick. J. and Hwang, B. J. (2012). "Water Soluble Polymers as Proton Exchange Membranes for Fuel Cells". *J. Polymers*, vol. *4* (2), pp. 913-963

Yuan, H., Meng, L. Y. and Park, S. J. (2016). "Synthesis and Application of Graphene/Chitosan Nanocomposites". *J. Carbon*, vol. 17 (1), pp. 11-17

STUDY ON THE ADSORPTION OF SURFACTANT WITH AND WITHOUT ELECTROLYTES ON ACTIVATED SEASHELL SORBENT

Myint Myint Than[1], Nwe Nwe Aung[2], Aye Thant Zin[3], Su Su Aung[4]

Abstract

In this study, waste seashell was used as biosorbent for the adsorption of surfactant with and without electrolytes from model aqueous solution at pH 6. Surfactant, Sodium Dodecyl Sulphate (SDS) was used as modifier. The Critical Micelle Concentration (CMC) value of SDS decreased with mixing electrolytes (Na_2SO_4 and Na_3PO_4). Therefore, upon addition of Na_2SO_4 and Na_3PO_4 in SDS, Na_3PO_4 decreased the CMC value of SDS more than Na_2SO_4. Adsorption of SDS on Heat Activated Sea Shell Powder (HASSP-7) sample by batch operations were conducted with different operation parameters such as initial concentration of adsorbate and dosage of adsorbent. The optimum dosage was 0.1 g and initial concentration was 100 ppm. Sorption of SDS on HASSP-7 was conducted with and without electrolytes. The adsorbed amount of SDS was found more with electrolytes than without electrolytes. Moreover, the amount of SDS adsorption with Na_2SO_4 was high in comparison with Na_3PO_4. The outcome of the present research is the surfactant consumption can be reduced by adding small amount of electrolytes to the surfactant solutions. It is expected that they can be used in the treatment of paper industrial wastewater containing surfactant (SDS).

Keywords: seashell, sodium dodecyl sulphate, critical micelle concentration, electrolytes, adsorption

Introduction

Surfactants have two main features, i.e. surface activity and the ability to form micelles in solutions which in turn affects the functionality of surfactants (Caron *et al*., 1995). One of the main characteristics of surfactants is their tendency, in dilute aqueous solutions, to self-assemble and form aggregates by exposing polar head groups to water and segregating hydrophobic tails from water (Antonello *et al*., 2016). The monomers combined in aqueous solution to form big molecules depend on the molecular structures of the surfactant, concentration, temperature and different electrolyte which are added (Lindman and Wennerstrom, 1980). The opposite charged groups of the electrolyte and the surfactant are attracted electrostatically. So, electrolyte works as a pattern for the aggregation of the surfactants, which finally results in the reduction of the repulsive interaction among surfactant head group which facilitate the aggregation behaviour (Neumann and Tiera, 1997). Electrolyte decreases the surface activity of surfactants (Pethica *et al*., 1954) and the CMC and surface tension of aqueous solution decrease in presence of electrolyte.

The critical micelle concentration (CMC) is defined as the concentration above which micelles form. At low surfactant concentration the surfactant molecules arrange on the surface. When more surfactant is added the surface tension of the solution starts to rapidly decrease since more and more surfactant molecules will be on the surface. When the surface becomes saturated, the addition of the surfactant molecules will lead to formation of micelles. This concentration point is called critical micelle concentration. The effect of ionic strength or electrolytes can significantly influence the critical micellar concentration (CMC), surface tension value at CMC and adsorption densities at air-liquid and solid-liquid interfaces which may have great importance in many applications. Electrolyte decreases the value of CMC; because the ions of the electrolytes neutralized the charge on the micelle surface thus decreasing the thickness of ionic compound

[1] Lecturer, Department of Chemistry, Banmaw University
[2] Dr, Lecturer, Department of Chemistry, Yangon University
[3] Dr, Associate Professor, Department of Chemistry, Mandalar Degree College
[4] Dr, Associate Professor, Department of Chemistry, Banmaw University

around the surfactant and electrostatic repulsion between them helping in this way to micellization process (Paredes *et al*., 1984).

Sodium dodecyl sulphate has the chemical formula $C_{12}H_{25}NaO_4S$ or CH_3-$(CH_2)_{11}$-O-SO_3-Na^+. SDS is a high production volume chemical. In solution, the sodium cation (Na^+) dissociates from the anionic part of the compound (lauryl or dodecyl sulphate), and this anionic compound is the active chemical. SDS is an anionic surfactant, which is a class of chemicals used for their detergent properties. SDS is a highly effective surfactant and is used in the removal of oily stains and residues. SDS also takes part in an essential function in commerce as leather softening and wool cleaning, metal processing, emulsifier, penetrant in glaze, paint remover and antifoaming agent in solid rocket propellants. It may also use as penetrant, flocculating and de-inking agent in paper industry.

Seashell, crab carapace, palm shell and others have been discovered as a natural biosorbent to remove heavy metal (Kadir *et al*., 2013; Pavan *et al*., 2006). Biosorption process is nonpolluting, easy to operate, offers high efficiency of treatment of wastewaters containing low metal concentrations and possibility of metal recovery (Febrianto *et al*., 2009). The objective of this paper is to study the adsorption behaviour of surfactants in the presence of electrolytes to reduce the surfactant consumption. The presence of electrolyte along with the surfactants in the cleaning process may reduce the consumption of surfactant along with the increase in adsorption and wetting properties. In many cases, after the cleaning process surfactants are disposed in the environment; in this situation, less consumption of surfactant may also reduce environmental problems.

Materials and Methods

Sample Collection

Mussel shell was obtained from fish market in Pathein Township, Ayeyarwady Region.

Preparation of Heat Activated Seashell Powder (HASSP)

The mussel shell was washed with distilled water and dried at room temperature for 2 d. It was also dried in an oven at 105 °C for 2 h. The dried sample was ground with blender and the pulverized shell was sieved through 80 mesh size to achieve Raw Sea Shell Powder (RSSP) (Srividya and Mohanty, 2009). RSSP was calcined in furnace at (400 °C to 1000 °C) for 2 h to get heat activated seashell powder (HASSP) and these were designed as HASSP 1-7. Finally, heat activated seashell powder (HASSP 1-7) were obtained.

Determination of Critical Micelle Concentration (CMC) of Sodium Dodecyl Sulphate (SDS) with and without Electrolytes

Different concentrations of sodium dodecyl sulphate solution (1×10^{-3} M to10×10^{-3} M) was prepared with 0.001 M of electrolytes solutions (Na_2SO_4 and Na_3PO_4). These solutions were adjusted at pH 6. Then, 1 mL each sodium dodecyl sulphate solution was placed into the beaker and 2 drops of 0.005 M acridine orange, 2 drops of acetic acid and 5 mLof toluene were added. Then, it was shaken with a separating funnel for 1 min and allowed to stand for 5 min. The aqueous layer was discarded. The toluene layer was collected and measured by UV-Visible spectrophotometer at λ_{max} 498 nm and 25 °C. The absorbance and concentration of sodium dodecyl sulphate was plotted and the CMC value was determined from the breaking point of the CMC.

Sorption Studies of More Activated Seashell Sorbent

For the adsorption experiment, sodium dodecyl sulphate solution (100 ppm) was mixed with 0.001 M of electrolyte solution (Na_2SO_4 and Na_3PO_4). All the measurements were carried out at pH 6. Then, 0.1 g of heat activated seashell powder at 1000 °C (HASSP-7) was added into the

100 mL of above the mixture solution. It was shaken with electric shaker for 1 h and filtered. Then, 10 mL of filtrate solution was taken and added 2 drops of 0.005 M acridine orange, 2 drops of glacial acetic acid and 5 mL of toluene. The contents were shaken with separating funnel for 1 min and allowed to stand for 5 min. The aqueous layer was discarded. The toluene layer was collected and measured by UV-Vis spectrophotometer at λ_{max} 498 nm and adsorption data were computed. Similarly,the above procedure was carried out using 25,50,75,125 and 150 ppm sodium dodecyl sulphate solutions to study the effects of initial concentration solutions. To investigate the effect of dosage of HASSP on the removal of SDS, the different amounts of HASSP-7 (0.1,0.2,0.3,0.4 and 0.5 g) were used.

Results and Discussion

Critical Micelle Concentration (CMC) of SDS with and without Electrolytes

The critical micelle concentration (CMC) values of sodium dodecyl sulphate (SDS) with and without electrolytes (Na_2SO_4 and Na_3PO_4) are shown in Table 1 and Figure 1. Here, the CMC value of SDS decreased with mixing electrolytes. It may be due to partial neutralization of anionic head group negative charge by electrolyte cations (Berr and Jones, 1988). Therefore, upon addition of Na_2SO_4 and Na_3PO_4 in SDS, Na_3PO_4 is more effective in reducing the CMC value of SDS. In this research, Na_3PO_4 decreased the CMC value of SDS more than Na_2SO_4.

Table 1 Critical Micelle Concentration (CMC) of SDS with and without Electrolytes

Concentration (10^{-3}M)	Absorbance*		
	SDS without electrolytes	SDS with Na_2SO_4	SDS with Na_3PO_4
1	0.286	0.277	0.263
2	0.275	0.264	0.248
3	0.286	0.273	0.261
4	0.268	0.259	0.231
5	0.215	0.204	0.173
6	0.262	0.235	0.222
7	0.296	0.288	0.258
8	0.283	0.261	0.247
9	0.317	0.295	0.275
10	0.296	0.266	0.242

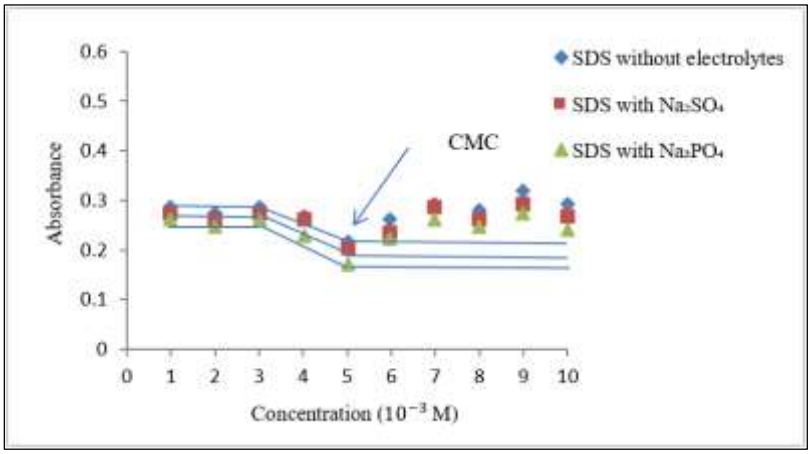

Figure 1 Critical micelle concentration (CMC) of SDS with and without electrolytes Electrolytes = Na_2SO_4 and Na_3PO_4, pH = 6, SDS = sodium dodecyl sulphate

Effect of Initial Concentration of SDS on the Adsorption of SDS by HASSP-7

In this research, the effect of initial concentration of SDS was studied by varying SDS concentrations (25 ppm to 150 ppm) for the removal of SDS. It was found that the highest adsorbed amount of SDS by HASSP-7 was 51.25 mg/g in 100 ppm concentration of SDS. The results are shown in Table 2 and Figure 2.

Table 2 Effect of Initial Concentration of SDS on the Adsorption of SDS by HASSP-7

No	Initial concentration of SDS (ppm)	q_e (mg/g)
1	25	5.11
2	50	12.29
3	75	37.92
4	100	51.25
5	125	38.47
6	150	27.29

HASSP-7 = Heat Activated Seashell Powder at 1000 ºC, Shaking time = 60 min
SDS = Sodium Dodecyl Sulphate, Dosage = 0.1 g, pH = 6, λ_{max} = 498 nm

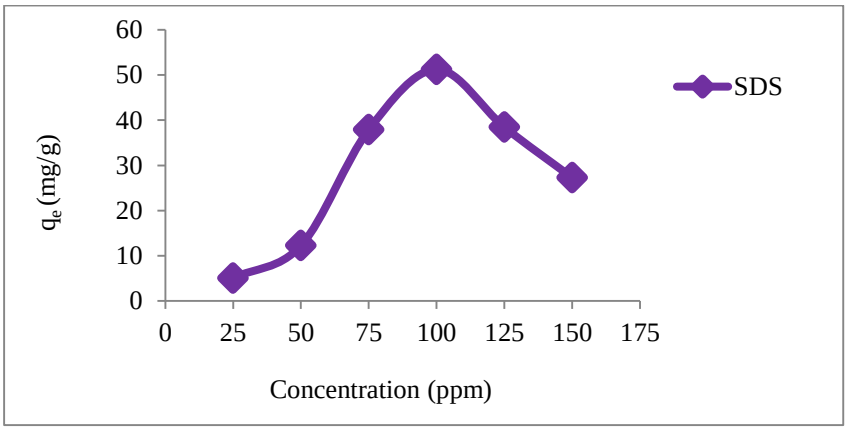

Figure 2 Effect of initial concentration of SDS on the adsorption of SDS by HASSP-7

Effect of Dosage of HASSP-7 on the Adsorption of SDS

In this research work, the different dosage amounts of HASSP-7 (0.1 g to 0.5 g) was carried out for the removal of SDS. It was observed that the optimum dosage was 0.1 g. In the case, the adsorbed amount was decreased with increasing adsorbent mass. Therefore, it was indicated that the increase in SDS adsorption efficiency is not directly proportional to adsorbent mass. The results are shown in Table 3 and Figure 3.

Table 3 Effect of Dosage of HASSP-7 on the Adsorption of SDS

No.	Dosage of Adsorbent (g)	q_e (mg/g)
1	0.1	60.55
2	0.2	25.82
3	0.3	17.13
4	0.4	12.61
5	0.5	9.33

HASSP-7 = Heat Activated Seashell Powder at 1000 ºC, Shaking time = 60 min
Initial concentration = 100 ppm, Stirring rate = 200 rpm, pH = 6, λ_{max} 498 nm

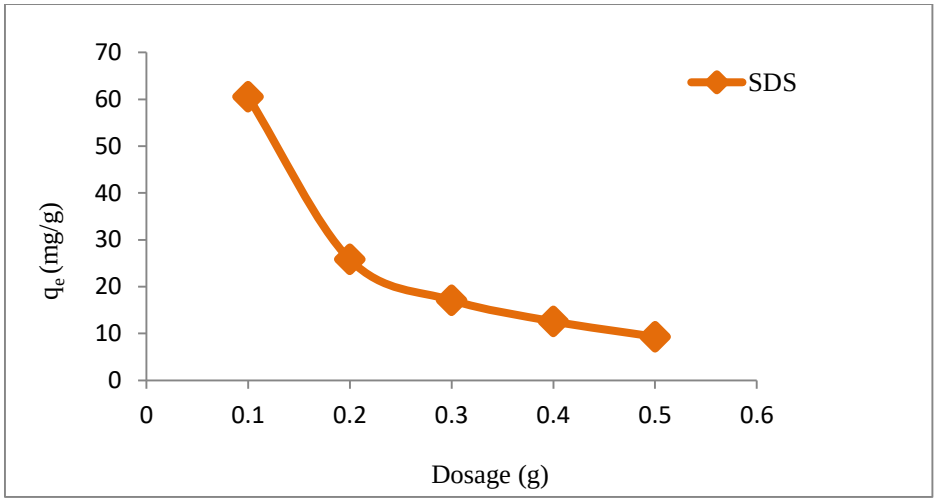

Figure 3 Effect of dosage of HASSP-7 on the adsorption of SDS

Adsorption of SDS with and without Electrolytes on HASSP-7

The adsorption efficiencies of HASSP-7 were determined on the adsorption of SDS with and without electrolytes (Na_2SO_4 and Na_3PO_4) at the optimum condition. It was indicated that the adsorbed amount of SDS without electrolytes was 51.29 mg/g. The amount of SDS adsorption with Na_2SO_4 and Na_3PO_4 were 75.62 mg/g and 65.63 mg/g, respectively. Here, the adsorption of SDS with electrolytes was found to be higher than that without electrolytes. Furthermore, the adsorption capacities of SDS with Na_2SO_4 was high in comparison with Na_3PO_4. The results are shown in Table 4 and Figure 4.

Table 4 Adsorption of SDS with and without Electrolytes on HASSP-7

No	HASSP-7	q_e (mg/g)
1	SDS without electrolytes	51.29
2	SDS with Na_2SO_4	75.62
3	SDS with Na_3PO_4	65.63

Electrolytes = Na_2SO_4 and Na_3PO_4 (0.001M), SDS = Sodium dodecyl sulphate

HASSP-7 = Heat activated seashell powder at 1000˚C, λ_{max} = 498 nm

SDS concentration = 100 ppm, Dosage = 0.1 g, Shaking time = 60 min

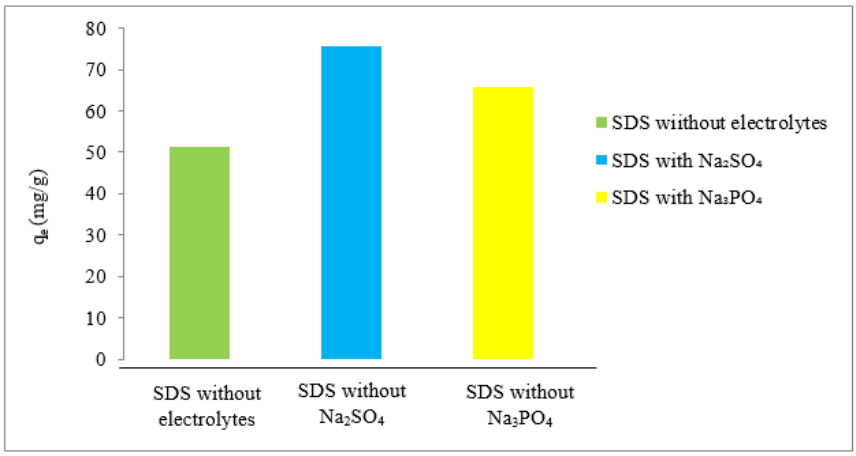

Figure 4 Adsorption of SDS with and without electrolytes on HASSP-7

Conclusion

In this research work, the critical micelle concentration (CMC) values of SDS with electrolytes (Na_2SO_4 and Na_3PO_4) were more effectively reduced than without electrolytes. Moreover, the CMC value of SDS in the presence of Na_3PO_4 decreased more than Na_2SO_4. For the adsorption of HASSP-7 the optimum conditions were initial concentration of SDS as 100 ppm and dosage as 0.1 g. Sorption of SDS on HASSP-7 sample was conducted with and without electrolytes. The amount of SDS adsorption without electrolytes was 51.29 mg/g and those with Na_2SO_4 and Na_3PO_4 were 75.62 mg/g and 65.63 mg/g, respectively. The adsorption of SDS with electrolytes was more than without electrolytes. Furthermore, the adsorbed amount of SDS on HASSP-7 was found to be more than those in the presence of Na_2SO_4 than Na_3PO_4. The contribution of this study is that the surfactant consumption can be reduced by adding small amount of electrolytes to the surfactant solutions and they can be used in the treatment of paper industrial wastewater containing surfactant (SDS).

Acknowledgement

The authors would like to express their profound gratitude to the Myanmar Academy of Arts and Science for giving permission to submit this paper and to Professor and Head, Dr Daw Ni Ni Than, Department of Chemistry, University of Yangon, for her kind encouragement.

References

Antonello, D.C., Pietro, D.P., Gabriella, S., Romina, Z. and Antonella, F. (2016). "Optimizing the Interaction of Surfactants with Graphitic Surfaces and Clathrate Hydrates". *Journal of Langmuir*, vol. 32, pp. 6559-6570

Berr, S.S. and Jones, R.R.M. (1988). "Effect of Added Sodium and Lithium Chlorides on Intermicellar and Micellar Size of Aqueous Dodecyl Sulphate Aggregates as Determined by Small-Angle Neutron Scattering". *Journal of Langmuir*, vol. 4, pp. 1247–1251

Caron, J.E.G., Beaulieu, S. and Perron, G. (1995). "Thermodynamic Micellar Properties of N-Octyldimethylamine Oxide Hydrochloride in Water", *Journal of Langmuir*, vol. 11, pp. 1905- 1911

Febrianto, J., Kosasih, A.N., Sunarso, J., Ju, Y.H., Indraswati, N. and Ismadji, S. (2009). "Equilibrium and Kinetic Studies in Adsorption of Heavy Metals Using Biosorbent: A Summary of Recent Studies". *Journal of Hazardous Materials*, vol. 162(2-3), pp. 616-645

Kadir, A.A., Abdullah, A. and Wal, L.K. (2013). "Study on Ferum (Fe) and Zinc (Zn) Removal by Using Rice Bran at Sungai Pelepah, Kota Tinggi, Johor". *Journal of Advances in Environmental Biology*, vol. 7(12), pp. 3580-3586

Lindman, B. and Wennerstrom, H. (1980). "Micelles. Amphiphile Aggregation in Aqueous Solution". *Journal of Topics in Current Chemistry*, vol. 87, pp. 1-87

Neumann, M.G. and Tiera, M.J. (1997). "Photochemical Determination of the Interactions between Surfactants and Polyelectrolyte", *Journal of Pure & Applied Chemistry*, vol. 69(4), pp. 791-795

Paredes, S., Sepulveda, L. and Tribout, M. (1984). "Enthalpies of Micellization of the Quaternary Tetradecyl- and -Cetyl Ammonium Salts". *Journal of Physical Chemistry*, vol. 88, pp. 1871-1875

Pavan, F.A., Lima, I.S., Lima, E.C., Airoldi, C. and Gushikem, Y. (2006). "Use of Ponkan Mandarin Peels as Biosorbent for Toxic Metals Uptake from Aqueous Solutions". *Journal of Hazardous Materials*, vol. 137(1), pp. 527–533

Pethica, A. (1954). "Surface Tension of Aqueous Solutions of Dodecyldimethylammonium Chloride, and Its Adsorption on Aqueous Surfaces". *Journal of Trans Faraday Society*, vol. 50, pp. 412-419

Srividya, K. and Mohanty, K. (2009). "Biosorption of Hexavalent Chromium from Aqueous Solutions by Catla Catla Scales: Equilibrium and Kinetics Studies". *Journal of Chemical Engineering*, vol. 155(3), pp. 666–673

PREPARATION AND CHARACTERIZATION OF NANOSIZED ULTRAMARINE BLUE PIGMENT FROM NATURAL KAOLIN SAMPLE

May Myat Nwe[1], Yu Yu Myo[2], Chit Chit Nyo[3]

Abstract

The aim of this research is the preparation of nanosized Ultramarine blue pigment for the production of pozzolanic cement. Ultramarine blue pigment was made from natural kaolin which was collected from Kyaukpataung Township, Mandalay Region, Myanmar. pH of natural kaolin sample was determined and then was characterized by EDXRF, XRD, SEM, FT IR and TG-DTA techniques. All of the results showed that natural kaolin sample had appropriate properties for the preparation of nanosized Ultramarine blue pigment. The procedure for the preparation of Ultramarine blue pigment involved the heat activation of kaolin. The activated kaolin was then characterized by XRD and SEM techniques. The comparison of XRD patterns of activated kaolin with natural kaolin sample showed that most peaks of the kaolinite mineral disappeared in activated kaolin. The average crystallite size of activated kaolin was 35.86. The comparison of SEM images of activated kaolin with natural kaolin sample showed that smaller aggregates were closer to one another in activated kaolin. Therefore, the natural kaolin sample was transformed into nano metakaolin state during calcination. The yield percent of the prepared Ultramarine blue pigment was 49.32 %. The Ultramarine blue pigment was characterized by XRD, SEM, and FT IR techniques. From analyzed data, Ultramarine blue pigment has cubic crystal form and has cohesive agglomerated structure.

Keywords; Natural kaolin, activated kaolin, Ultramarine blue pigment, calcination

Introduction

Rocks that are rich in kaolinite are known as kaolin or china clay. Kaolin is also known as white clay. Kaolinite clay is a clay mineral, part of the group of industrial minerals, with the chemical composition $Al_2Si_2O_5(OH)_4$ (Fadzil *et al*., 2017). Kaolinite clay occurs in abundance in soils that have formed from the chemical weathering of rocks in hot, moist climates, for example in tropical rain forest areas (Thet Thet Han, 2014). Kaolin clay or white clay is rich in kaolinite mineral and also classified as layered silicate mineral. Due to endothermic process or dihydroxylation process, which involves heat, Kaolin particles can easily transform into other shape or particles (Morsy, 2012). The reaction of endothermic process will create kaolin into metakaolin, nano metakaolin and nano metaclay and slight increment of silica content were produced (Fadzil *et al*., 2017).

In literature, the chemical composition weight % of natural kaolin are SiO_2-48.5, Al_2O_3-38, Fe_2O_3-1.1, TiO_2-0.03, CaO-0.10, MgO-0.30, K_2O-1.85, Na_2O-0.10. The silicon and aluminium ratio in china kaolin is 1.13. China kaolin has as minority minerals illite and orthoclase and the activation temperature of kaolin was 700 ºC (Sancho *et al*., 2008). The primary use of kaolin is the paper industry. Kaolin has a variety of other uses in products including paint, rubber, cable insulation, specialty films and fertilizers (Lvorkin, 2012).

The history of Ultramarine blue goes back to Bible times, being still used widely today. The natural material with the typical colour is the mineral lazurite (Sancho *et al.*, 2008). Lazurite or natural Ultramarine is arguably the most expensive source of blue pigment. Natural Ultramarine was undoubtedly the most favoured blue colour: the pigment worked well in water and oil, did not fade, and gave a very consistent shade (Hamerton *et al*., 2013).

[1] PhD candidate, Department of Chemistry, University of Yangon
[2] Dr, Professor, Department of Chemistry, Yangon University of Distance Education
[3] Dr, Lecturer, Department of Chemistry, University of Yangon

The applications of Ultramarine are diverse and include the production of plastics, paints and powder coatings, printing inks, paper and paper coating, rubber and thermoplastic elastomers, latex products, detergents, cosmetics and soaps, artists′ colours, toys and educational equipment, lather finishes, powder markers, roofing granules, synthetic fibers, theatrical paints and blue mattes, cattle salt licks and white enhancer (Buxbaum and Pfaff, 2005).

Materials and Methods

All chemicals used in this work consist of the product from British Drug House (BDH). Chemicals are stated in each of the experiment. The apparatus used in this paper include a Balance (E Mettler, Switzerland), pH meter (Jenway 4330, Labquip, England), Scanning Electron Microscope (JEOL JSM - 5610 series), Energy Dispersive X–Ray Fluorescence Spectrometer (NEXCG-Rigaku), X–Ray Diffractometer (XRD-Regaku-D-Max-2200, Japan), Thermo Gravimetric Analyzer (Model –Universal V 2.5 H. Hi–Res TGA 2950, TA Instrument, Japan) and Reflection Transmission Color Densitometer (Noritsu DM 1).

Sample Collection and Characterization of Natural Kaolin Sample

Natural kaolin sample was collected from Kyaukpataung Township, Mandalay Region, Myanmar. Qualitative elemental composition of natural kaolin sample was determined by EDXRF technique. Natural kaolin sample was characterized by XRD, SEM, TG-DTA and FT IR techniques at Universities' Research Centre, University of Yangon.

Preparation and Characterization of Activated Kaolin Samples

Natural kaolin sample was pulverized in a ball mill and sieved (240 mesh) to obtain the powdered sample. pH of powder sample was determined. The powder sample was then calcined at 600 °C for two hours and activated kaolin sample was obtained. Activated kaolin sample was characterized by XRD, SEM, TG-DTA and FT IR techniques at Universities' Research Centre, University of Yangon.

Preparation and Characterization of Ultramarine Blue Pigment

A mixture of 3.0 g of activated kaolin sample, 3.2 g of anhydrous sodium carbonate, 3.0 g of sulphur, 0.4 g of silica and 0.4 g of charcoal were pulverized in a mortar and pestle. It was placed in a crucible with lid and sealed tight using wet fire clay. Crucible with mixture was calcined at 700 °C, 750 °C, 800 °C, 850 °C and 900 °C for three and half hours, Ultramarine blue pigment was obtained. It was stored in a desiccator for further characterization.

The solubility of Ultramarine blue pigment was tested with various solvents and colour density was also determined. Ultramarine Blue pigment was characterized by XRD, SEM, TG-DTA and FT IR techniques at Universities' Research Centre, University of Yangon.

Results and Discussion

The photograph of natural Kyaukpataung kaolin sample is shown in Figure 1. pH value of natural kaolin sample is presented in Table 1.

Figure 1 The photograph of natural kaolin sample

Table 1 pH Value of Natural Kaolin Sample

Sample	pH	*Literature pH
Natural kaolin	4.05	4-5

*Keller, 1990

Characterization of Natural Kaolin Sample

EDXRF analysis

The mineral oxide composition of collected natural kaolin sample is presented in Table 2. Natural kaolin is rich in aluminium oxide and silicon dioxide. Theoretical ratio of Si: Al in pure kaolin is 1.04 (Lvorkin, 2012). The ratio of Si: Al in collected natural kaolin sample was found to be 1.67. The collected natural kaolin sample has a bit less alumina and more silica. It was not detected the oxide of magnesium, manganese and sodium as reported by Sancho *et al.* (2008).. Moreover, it was found to have less potassium, iron, titanium and calcium.

Table 2 EDXRF Analysis for Natural Kaolin Sample

Metal Oxide	Mass (%)	Reported value*(%)
MgO	-	0.30
Al_2O_3	33.800	38.00
SiO_2	64.100	48.50
P_2O_5	0.134	-
K_2O	0.054	1.85
CaO	0.041	0.10
TiO_2	0.453	0.03
Fe_2O_3	0.682	1.10
Na_2O	-	0.10
MnO	-	-

*Sancho *et al.,* 2008

XRD analysis

The X-ray diffractogram of natural kaolin sample is presented in Figure 2. According to XRD analysis,the diffraction pattern was well-matched with kaolinite $Al_4(OH)_8(Si_4O_{10})$, aluminium silicate hydroxide. From X-ray diffractogram of natural kaolin sample, the average crystallite size can be calculated. According to Debye Scherrer Equation, the average crystallite size of natural kaolin sample was found to be 27.95 nm.

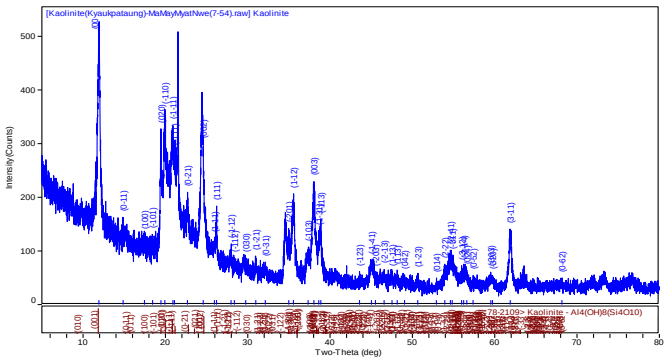

Figure 2 X-ray diffractogram of natural kaolin sample

SEM analysis

The SEM image of natural kaolin sample is presented in Figure 3. In SEM micrograph of sample, shape and surface texture can be seen. From literature, the shape of kaolin is flaky and platy form and whitish layer represent by alumina system (Fadzil *et al*., 2017). From the SEM micrograph of natural kaolin sample it was in layer or flakes with spherical particles.

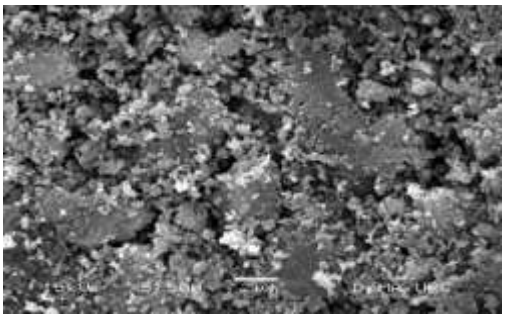

Figure 3 SEM image of natural kaolin sample

FT IR spectrum and band assignments

FT IR spectrum of the studied sample is presented in Figure 4. Kaolinite has absorption bands between 3500 cm^{-1} and 3750 cm^{-1} correspond to stretching frequencies of OH groups (Wilson, 2003) where three characteristic bands (3693 cm^{-1}, 3653 cm^{-1} and 3619 cm^{-1}) are defined. If the band at 3670 cm^{-1} disappears, Kaolinite structure is disordered and easier to dehydrate (Bich *et al*., 2009). But kaolinite present in the analyzed sample has an ordered structure, since the three bands are defined (Vaculíková *et al*., 2011). The FT IR spectrum of natural kaolin sample showed band at 3693 cm^{-1}, 3653 cm^{-1} and 3619 cm^{-1} indicate partial ordered structure of this sample Figure 4. Diffused bands observed at about 3473 cm^{-1} and 1631 cm^{-1}, which are attributed to the stretching and deformation vibrations of the physically adsorbed water (O-H) molecules at the surface, respectively. The most pronounced OH stretching bands in Kaolinite are the inter hydroxyl bands 3620 cm^{-1}, and the most intense band is located at 3693 cm^{-1}(Fernandez, 2005). The next three bands in the spectrum of kaolinite (1114 cm^{-1}, 1031 cm^{-1} and 1008 cm^{-1}) also have a consensual assignment by the different literature sources (Fernandez, 2005). These are the most intense Si-O stretching modes, and can be observed in most of the silicate minerals. According to the literature, two bands at 777 cm^{-1} and 713 cm^{-1} could be attributed to asymmetric stretching in Si-O-Al bonds (Fernandez, 2005). And then, low intensity peaks at about 530 cm^{-1} and 450 cm^{-1} appeared; the bands at 792 cm^{-1}, 752 cm^{-1}, 694 cm^{-1}, 534 cm^{-1}, 466 cm^{-1} and 430 cm^{-1} were assigned to quartz. The observed quartz peaks were weak in this FT IR spectrum. Selective kaolin has very similar with the literature value of kaolinite sample.

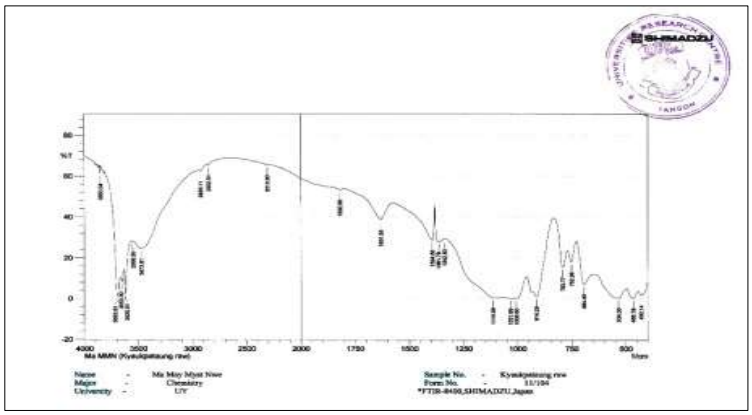

Figure 4 FT IR spectrum of natural kaolin sample

Thermal analysis for natural kaolin sample

TG-DTA thermogram of natural kaolin sample is presented in Figure 5. Thermogram was found to have two endothermic peaks at 63.18 °C and 574.4 °C. First peak was observed due to the dehydration of natural sample and second endothermic peak was attributed to the decomposition of organic compounds and removal of structural water (Vahideh, 2014). Because of high decomposition temperature for organic compounds and structural water, they were tightly bound in systematic arrangement of natural kaolin sample. The small amount of reliable weight loss was observed 12.89 % in the TGA. Thus, the natural kaolin sample contains low impurities and organic compounds. Therefore, the calcination temperature for the natural kaolin sample was chosen as 600 °C for activation.

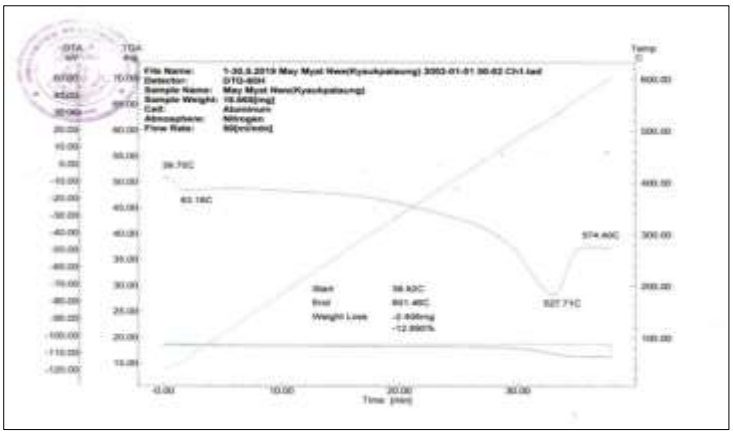

Figure 5 TG-DTA thermogram of natural kaolin sample

Characterization of Activated Kaolin Sample

X-ray diffractogram of activated kaolin sample obtained by calcination of natural kaolin at 600 °C for 2 h is presented in Figure 6. The comparison of XRD pattern of activated kaolin with natural kaolin sample revealed that most peaks of the kaolinite mineral disappeared at the 600 °C. Therefore, dehydroxylation and transformation of kaolinite into metakaolin have been performed completely as described by Moodie et al. (2011). The average crystallite size of activated kaolin after calcination was calculated. According to Debye Scherrer Equation, the average crystallite size of activated kaolin was 35.86 nm. The average crystallite size of activated kaolin was larger than natural kaolin and it was assumed to be accumulated nature of particles.

The SEM image of activated kaolin sample is presented in Figure 7. The comparison of SEM images of activated kaolin with natural kaolin sample showed that flakes with spherical form as well as agglomerates, smooth surface and uniform texture were observed in the former. Smaller aggregates were closer to one another, similar to nano metakaolin. That is, shape and surface texture were similar to metakaolin. The flakes form was similar to nano metakaolin (Fadzil *et al*., 2017). Therefore, meta or nano metakaolin may be formed after calcination.

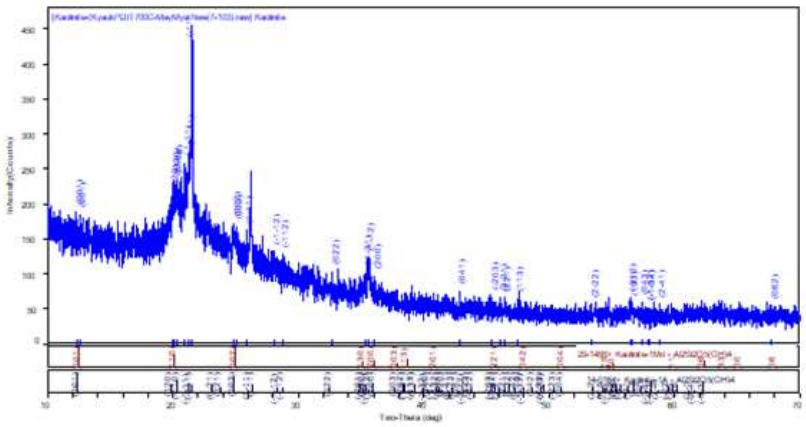

Figure 6 X-ray diffractogram of activated kaolin sample

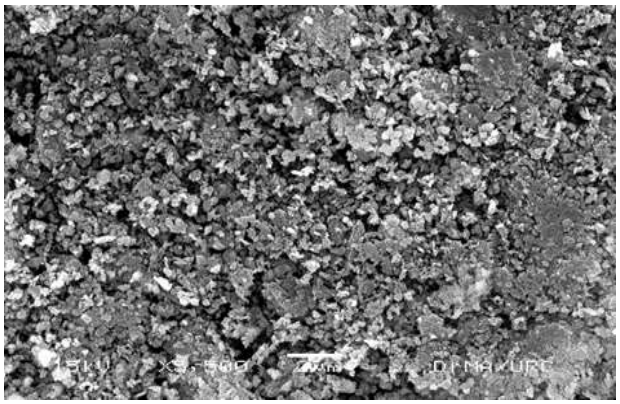

Figure 7 SEM image of activated kaolin sample

Colour Density and Solubility Test of Ultramarine Blue Pigment

The photograph of Ultramarine blue pigment prepared using natural kaolin sample (850 ℃ and 3:30 h) is shown in Figure 8. The yield percent of the prepared Ultramarine blue pigment from Natural kaolin sample was observed as 49.32%.

Figure 8 The photograph of the prepared Ultramarine blue pigment

Colour density

The colour observation obtained in final calcination step are presented in Table 3. It was observed that the colour observations vary with different calcination temperatures. In this table, it was found that 850 ℃ temperature gave mature navy blue colour for Ultramarine blue pigment. Colour density of Ultramarine blue pigment was observed as 1.14D.

Table 3 Colour Observation of Prepared Pigment Using Different Temperatures

No.	Temperature(℃)	Colour	Remark
1	700	Light coca brown	
2	750	Rosy brown	
3	800	Slate blue	
4	850	Navy blue	Optimum colour
5	900	Burned blue	

Solubility tests

Solubility of Ultramarine blue pigment in different solvents is presented in Table 4. Ultramarine blue pigment was soluble in inorganic acids, moderately soluble in sodium hydroxide and water, and insoluble in organic solvents. Ultramarine blue pigment is polar inorganic compound due to the metal and oxygen linkage (Sancho, 2008).

Table 4 Solubility of Ultramarine Blue Pigment in Different Solvents

No.	Solvents	Results
1	Nitric acid	+
2	Sulphuric acid	+
3	Hydrochloric acid	+
4	Sodium hydroxide (0.1 M)	±
5	Sodium hydroxide (0.01 M)	±
6	Petroleum ether	-
7	Chloroform	-
8	Ethanol	-
9	Ethyl acetate	-
10	Water	±

(+) = soluble (-) = insoluble (±) = moderately soluble

Characterization of Ultramarine Blue pigment

X-ray diffractogram of Ultramarine blue pigment is presented in Figure 9 and Table 5.

XRD results showed the cubic crystal form with axial length 9.2866 Å and the average crystallite size of Ultramarine blue pigment was 36.1 nm. The SEM image of Ultramarine blue pigment is presented in Figure 10. SEM micrograph of Ultramarine blue pigment showed cohesive agglomerated nature, larger and loose cluster. FT IR spectrum of Ultramarine blue pigment is presented in Figure 11. The FT IR band assignments of Ultramarine blue pigment, stretching and bending vibrations of aluminosilicate (Al_2SiO_5) and stretching vibration of S^{3-} ion were observed.

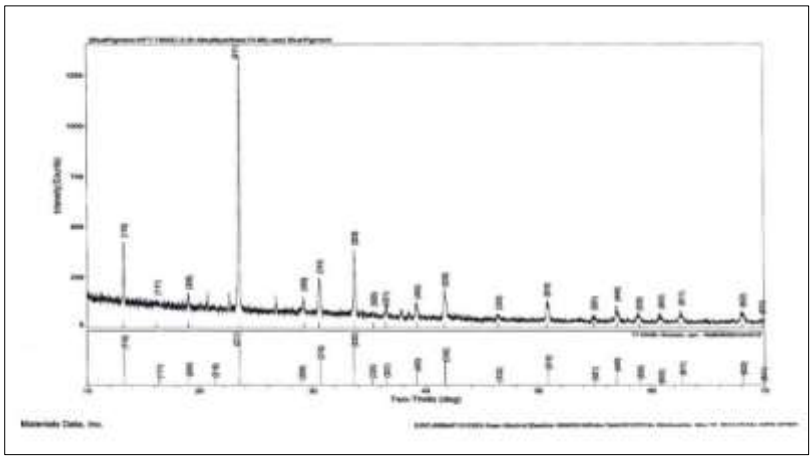

Figure 9 X-ray diffractogram of Ultramarine blue pigment

Table 5 Some Parameters of Ultramarine Blue Pigments Using XRD Analysis

Parameters	Results
Crystal form	Cubic
Lattice constant (Å)	9.2866
Average crystallite size (nm)	36.1

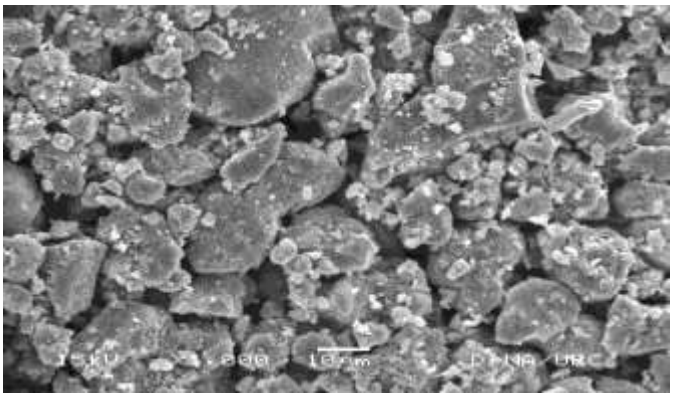

Figure 10 SEM image of Ultramarine blue pigment

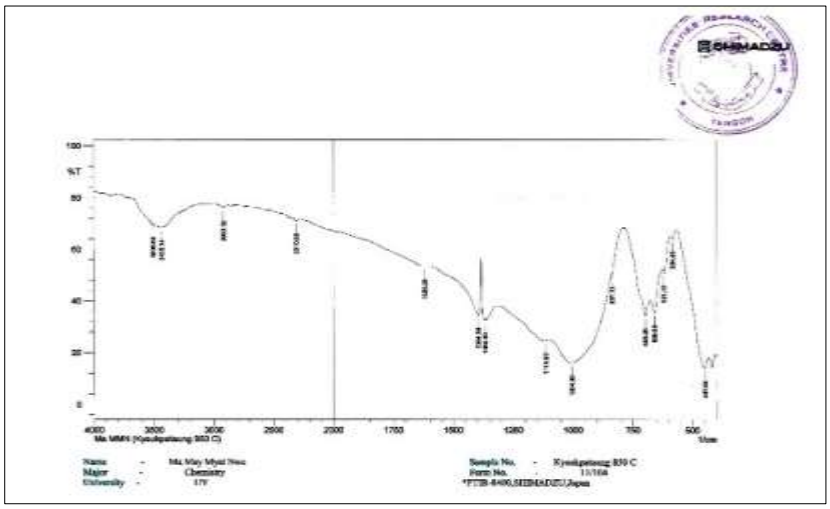

Figure 11 FT IR spectrum of Ultramarine blue pigment

Table 6 FT IR Band Assignment of Ultramarine Blue Pigment

Experimental Frequency (cm^{-1})	Literature Frequency* (cm^{-1})	Band Assignment
3508 3405	3750-3500	stretching vibration of OH group
1394 1396	1500-1000	stretching vibration of aluminosilicate (Al_2SiO_5)
698 659	950-650	bending vibration of OH group
584	582-547	stretching vibration of S^{-3} ion
447	550-400	bending vibration of Si-O-Si or Si-O-Al

*Sancho *et al*., 2008; Vahideh, 2014

Conclusion

This paper revealed that Ultramarine blue pigment can be prepared by using activated kaolin from natural kaolin sample. According to EDXRF analysis, mineral oxide composition of natural kaolin sample is kaolinite. The ratio of silicon and aluminium is 1.67, higher than theoretical ratio (1.04). From the study of characterization of natural and activated kaolin, it can be proved that the qualified kaolin sample is available as natural abundance in Myanmar. Therefore, the natural kaolin sample from Kyaukpataung Township, Mandalay Region, Myanmar, has appropriate properties for the preparation of Ultramarine blue pigment. From analyzed data, the prepared Ultramarine blue pigment has cubic crystal form and has cohesive agglomerated structure.

Acknowledgement

The authors are thankful to Chemistry Post-Graduate Steering Committee of Yangon University for their helpful suggestions and advices. Special thanks are extended to the Myanmar Academy of Arts and Science.

References

Bich Ch., Ambroise,J. and Péra,J. (2009). "Influence of Degree of Dehydroxylation on the Pozzolanic Activity of Metakaolin". *Applied Clay Science*, vol.44 (3–4), pp. 194–200

Buxbaum, G. and Pfaff, G. (2005). *Industrial Inorganic Pigments.* Berlin: Germany, 3rd ed., Wiley-VCH, Weinheim.

Fadzil, M. A., Muhd Nurhasri, M. S., Norliyati, M. A., Hamidah, M. S., Ibrahim, M. H. W. and Assrum, R.Z. (2017). "Characterization of Kaolin as Nano Material for High Quality Construction". *MATEC Web of Conferences*, vol. 103, pp. 1-9

Fernandez. A. (2005). "Mid-infrared Spectroscopic Studies of Alkaline Activated Fly Ash Structure". *Microporous*, vol. 86, pp. 207-214

Hamerton, I., Tedaldi, L. and Eastaugh,N. (2013). "A Systematic Examination of Colour Development in Synthetic Untramarine According to Historical Methods". *Faculty of Engineering and Physical Sciences*, vol. 8(2), pp. 1-16

Keller, W. D. (1990). "The pH of Clay Suspensions in the Field and Laboratory, and Method of Measurement of their pH". *Applied Clay Science*, vol. 5(2), pp. 123-133

Lvorkin, D. (2012). "Using Mathematical Modeling for Design of Self Compacting High Strength Concrete with Metakaolin Admixture". *Construction and Building Materials*, vol. 37, pp. 851-864

Moodi,F., Ramezanianpour, A. A. and Safavizadeh, A.Sh.(2011). "Evaluation of the Optimal Process of Thermal Activation of Kaolins". *Scientia Iranica, Transactions A: Civil Engineering* vol.18, pp.906–912

Morsy, M.S. (2012). "Behavior of Blended Cement Mortars Containing Nano-metakaolin at Elevated Temperatures". *Construction and Building Meterials*, vol. 35, pp. 900-905

Sancho, J. P., Restrepo, O. J., Garcia, P., Ayala, J., Fernandez, B. and. Verdeja, L. F. (2008). "Ultramarine Blue from Asturian 'Hard' Kaolins". *Applied Clay Sciences*, vol. 41, pp. 133-142

Thet Thet Han. (2014). *Kinetic and Equilibrium Studies:Sorption of Heavy Metals B Modified Kaolinite Clay*. PhD (Dissertation). Department of Chemistry, University of Yangon

Vaculíková,L.,Plevová,E., Vallová,S. and Koutnik,I. (2011). "Characterization and Differentiation of Kaolinites from Selected Czech Deposites Using Infrared Spectroscopy and Differential Thermal Analysis." *Acta Geodyn. Geomater*, vol.8(1), pp. 59-67

Vahideh, T.K. (2014). "Replacing Nano-clay for Kaolin in Ultramarine Pigment". *Pigment & Resin Technology*, vol. 43(1), pp. 1-7

Wilson, M. J. A., (2003). *Handbook of Determinative Methods in Clay Mineralogy.* USA: Chapman and Hall

OPTIMIZATION FOR COLOUR REMOVAL PROPERTY OF PREPARED GRAPHENE OXIDE (GO)

Su Myat Htay[1], Khin Mar Cho[2], Thazin Nyo[3]

Abstract

In this research work, graphene oxide (GO) was prepared from graphite powder by Modified Hummer's method. Layers of graphene oxide consist of various oxidizing groups like hydroxyl, epoxides, carbonyl and carboxyl at the basal planes as well as at the edges. Prepared GO were characterized by XRD, FT IR, UV-visible, SEM and EDX techniques. To investigate the colour removal property of GO, malachite green (MG) was used as model dye contaminant. Firstly, wavelength of maximum absorption (λ_{max}) of malachite green was investigated at different dye concentrations in the wavelength range of 400-800 nm. Malachite green was found to have λ_{max} of 617 nm. To investigate the optimum conditions for colour removal, effects of concentration, pH, contact time and dosage on removal of malachite green dye using prepared GO were carried out. The optimal conditions were found to be 10 ppm of MG concentration, pH 4, 60 min of contact time and 0.08 g of adsorbent dosage for colour removal of malachite green by using prepared GO.

Keywords: graphite, graphene oxide, Modified Hummer's Method, malachite green

Introduction

Graphite, one of many allotropes of carbon, can provide great potential in many applications such as in electronic and functional nanocomposites (Hidayah *et al.,* 2017). Single atomic plane layer of graphite is called graphene. Graphene can produce from graphite using by chemical vapour deposition (CVD), mechanical or chemical methods (Zaaba *et al.,* 2017). Both graphite and graphene have unique properties (Hidayah *et al.,* 2017). Graphene Oxide (GO) is prepared from oxidation of graphite powder by Modified Hummer's Method (Mindivan, 2016). The oxidation of graphite in protonated solvents leads to graphite oxide, which consists of multiple stacked layers of graphene oxide. GO has a similar hexagonal carbon structure to graphene but also contains hydroxyl, alkoxy, carbonyl, carboxylic acid and other oxygen-containing functional groups (Smith *et al.,* 2019). GO was synthesized and characterized using various analytical techniques and exploited as adsorbent for rapid removal of malachite green dye from the aqueous solution (Mohamadi *et al.,* 2016).

Materials and Methods

Sample Collections

In this research, graphite powder (extra pure purchased from China Aladdin Industry Corporation), sodium nitrate($NaNO_3$), sulphuric acid (H_2SO_4), potassium permanganate ($KMnO_4$), hydrogen peroxide(H_2O_2) and hydrochloric acid(HCl) were purchased from local chemical shop. All chemicals used were of analytical reagent grade.

Preparation of Graphene Oxide

Graphene oxide was prepared from graphite powder using Hummer's Method. Firstly, 5g of graphite and 5 g of $NaNO_3$ were added to 120 mL of concentrated sulphuric acid (H_2SO_4). The mixture was ultrasonicated for 1 h and maintained the temperature approximately 5 ºC using ice bath. After that, 15 g of $KMnO_4$ was added slowly. Then a mixture was stirred by ultrasonication

[1] Assistant Lecturer, Department of Chemistry, Panglong University
[2] Dr, Associate Professor, Department of Chemistry, University of Yangon
[3] Dr, Lecturer, Department of Chemistry, Dagon University

using ultrasonic bath for 1 h for a homogeneous mixture. After that, 250 mL distilled water was added gradually to mixture followed by ultrasonication for 1 h. The brown colour of the mixture was observed. The colour of the mixture changed to light brown. Subsequently, another 100 mL deionized water was added to the mixture and the temperature was increased to 90 ^{o}C while stirring for 1 h. Finally, 50 mL of hydrogen peroxide and 100 mL of distilled water were added to obtain a light yellow suspension. When hydrogen peroxide was added, the residual $KMnO_4$ and MnO_2 formed in the solution was also reduced to colourless soluble salts and the colour changes from brown to light yellow.

Characterization of Graphene Oxide

The prepared graphene oxide was characterized by using modern techniques. X-ray Diffraction (XRD, Rigaku, /max 2200, Japan) examined the crystalline phase present in the sample. Fourier Transform Infra-Red (FT IR, spectrometer) was used to investigate the presence of functional groups in the sample. For morphological analysis, Scanning Electron Miscroscopy (SEM, JOEL-JSM-5610, Japan, Ion Sputter-JEC-1600) was used. The relative abundance of element in graphene oxide was detected by Energy Dispersive X-Ray Fluorescence (EDXRF) method. The absorbance of sample solution was measured by UV-visible Spectrophotometer (Shimadzu: UV-1800).

Colour Removal of Malachite Green Dye Solution by the Prepared Graphene Oxide

In this research, prepared graphene oxide was used for investigation of colour removal efficiency. The stock solution of malachite green (MG) (1000 mg/L) was prepared in distilled water. Series of standard MG solution were prepared by serial dilution. The absorbance values of standard solutions were measured at the wavelength range of 400-800 nm by means of a spectrophotometer. The standard calibration curve was constructed by plotting the absorbance versus concentration of the malachite green solution.

Determination of the Optimum Conditions for Colour Removal of MG Dye

For the determination of the optimum conditions for colour removal of MG dye by using prepared GO, effects of initial dye concentration, pH, contact time, dosage of adsorbent were carried out.

Effect of initial concentration of malachite green

Accurately weighed samples (0.06 g each) were placed in separate conical flasks. Then 50 mL each of dye solution was added into each conical flask. The mixtures were shaken for 120 min and the sampling mixture was centrifuged immediately at 200 rpm for 20 min to obtain a clear solution. After sampling out 10 mL of clear solution the residual content of malachite green in the solution was determined by a spectrophotometer at 617 nm.

Effect of pH on the colour removal of malachite green

Accurately weighed samples (0.06 g each) were placed in separate conical flasks. Then, 50 mL each of dye solution was added into each conical flask. The initial pH value of the solution was previously adjusted with 0.1 M HCl or NaOH using a pH meter and shaken with electric shaker at room temperature for 1 h and the sampling mixture was centrifuged immediately at 200 rpm for 20 min to obtain a clear solution. After sampling out 10 mL of clear solution the residual content of malachite green in the solution was determined by a spectrophotometer at 617 nm.

Effect of contact time on the colour removal of malachite green

Accurately weighed samples (0.06 g each) were placed in separate conical flasks. Then 50 mL each of dye solution was added into each conical flask and was shaken with electric shaker. The contact time was varied at interval of 30 min, 60 min, 90 min, 120 min and 150 min. The sample solution was centrifuged immediately at 200 rpm for 20 min to obtain a clear solution. The residual content of malachite green in the solution was determined by a spectrophotometer at 617 nm.

Effect of dosage of graphene oxide for the colour removal of malachite green

The samples of various masses (0.02, 0.04.0.06,0.08 and 0.10) g were separately placed in the conical flask and 50 mL each of standard dye solutions was added into each conical flask. In order to attain complete equilibrium, the solutions were shaken with electric shaker for 1 h at room temperature. The sample solutions were removed from the sorbent by centrifugation at 200 rpm for 20 min. The residual content malachite green in the solution was determined by a spectrophotometer at 617 nm.

Result and Discussions

X-ray Diffraction (XRD) Analysis

A sharp diffraction peak of graphite powder was observed at 2θ, 26.609^{o} (002) and d-spacing (interplanar spacing) was 0.334 nm (Figure 1). For graphene oxide its diffraction peak appeared at 2θ 10.557^{o} with d-spacing of 0.850 nm (Figure 2). The characteristic (001) crystal plane of GO was evident. The increased distance in GO was due to the introduction of a number of oxygen-containing groups on the edge of each layer, which increased the distance between the layers.The crystallite size of graphite was calculated based on the (002) plane, using the Scherrer' equation and found to be 40.3 nm whereas that of the prepared GO was 4.1 nm.

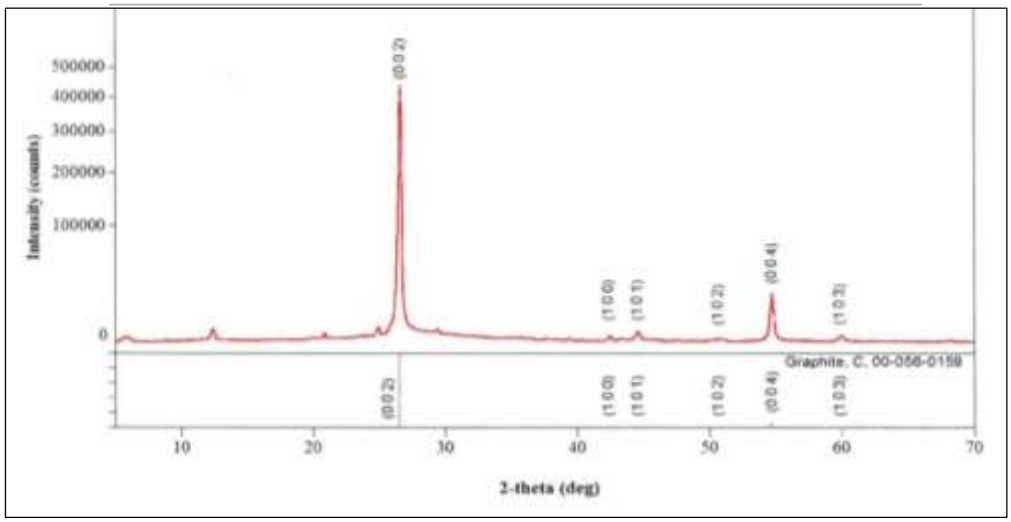

Figure 1 X-ray diffractogram of graphite powder

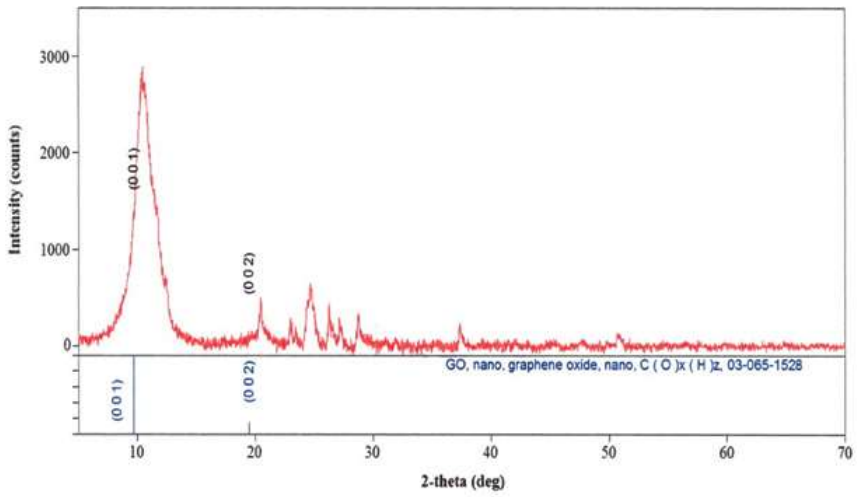

Figure 2 X-ray diffractogram of prepared GO

Characterization of Prepared GO

FT IR analysis

The FT IR spectrum of GO (Figure 3) shows the intense and broad peak that appeared at 3581 cm^{-1} due to the presence of (O-H) bond, the stretching vibration of hydroxyl group. Moreover, C=O carbonyl stretching (COOH) group at 1722 cm^{-1} and the C-O epoxy group stretching at 1039 cm^{-1}. With the presence of all these carboxylic, hydroxyl and epoxide groups oxygen molecules were confirmed to be highly occupied at the edge and the basal plane of GO which can be concluded that GO was synthesized successfully.

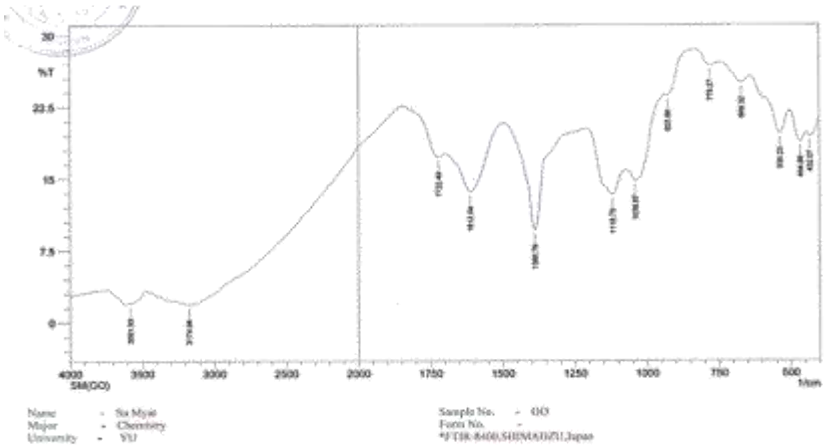

Figure 3 FT IR spectrum of graphene oxide

Optical property

The UV spectroscopic measurement was carried out in the range of 200-400 nm to monitor the optical property of graphene oxide (Figure 4). The π -π^* absorption peaks of graphene oxide appeared at λ_{max} = 238 nm which was in agreement with the reported value of Hidayah *et al.* (2017). The absorption peak at 238 nm in the UVspectrum of GO corresponds to $\pi \rightarrow \pi^*$ transitions of the aromatic sp^2 C = C bonds.

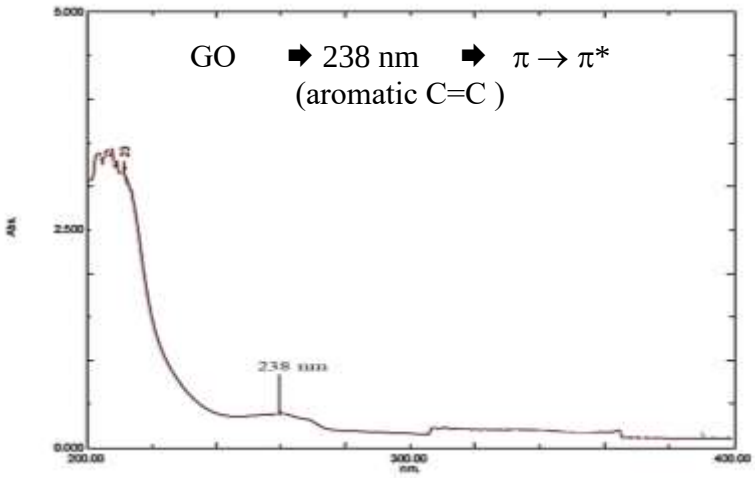

Figure 4 UV absorption spectrum of GO

Scanning electron microscopic (SEM) analysis

The SEM measurement was carried out to investigate the morphology of prepared GO (Figure 5). In SEM micrograph, platelet-like morphology was observed in GO crumpled morphology.

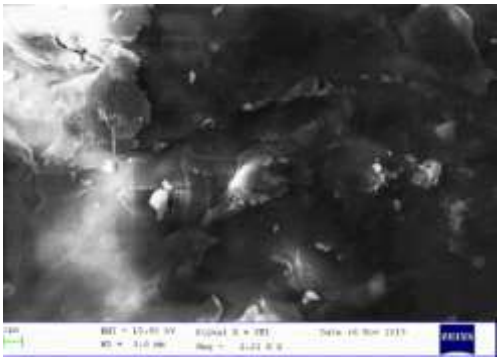

Figure 5 SEM micrograph of graphene oxide (GO)

Energy Dispersive X-Ray (EDX) Analysis

The elemental composition of prepared GO was analyzed by Energy Dispersive X-Ray (EDX) spectrometer (Figure 6 and Table 1). EDX analysis pointed out that elemental composition of carbon and oxygen in GO was found to be 53.82% and 41.84%. According to the literature (Mindivan, 2016) oxygen percent 41.84% in GO can be confirmed the formation of GO.

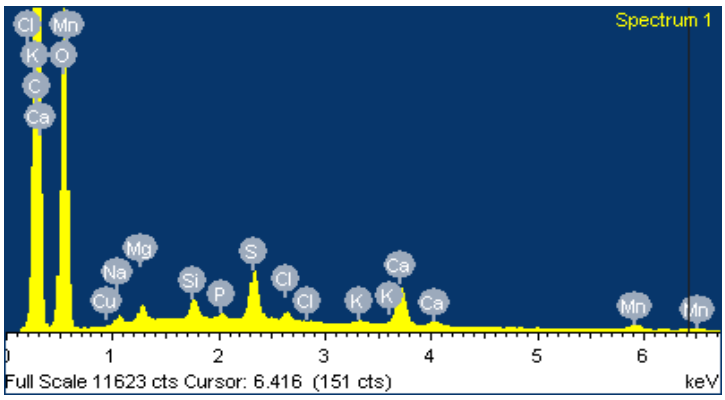

Figure 6 EDX spectrum of graphene oxide (GO)

Table 1 Relative Abundance of Elements in Graphene Oxide

No.	Elements	Weight (%)
1	C	53.82
2	O	41.84
3	Na	0.28
4	Mg	0.39
5	Si	0.36
6	P	0.12
7	S	1.11
8	Cl	0.21
9	K	0.10
10	Ca	1.23
11	Mn	0.38
12	Cu	0.16
13	Total	100.00

The Wavelength of Maximum Absorption of Malachite Green

In this work, the absorption spectra of MG Dye with various concentrations were recorded in the wavelength range of 400-800 nm. It was observed that the wavelength of maximum absorption was 617 nm (Figure 7).

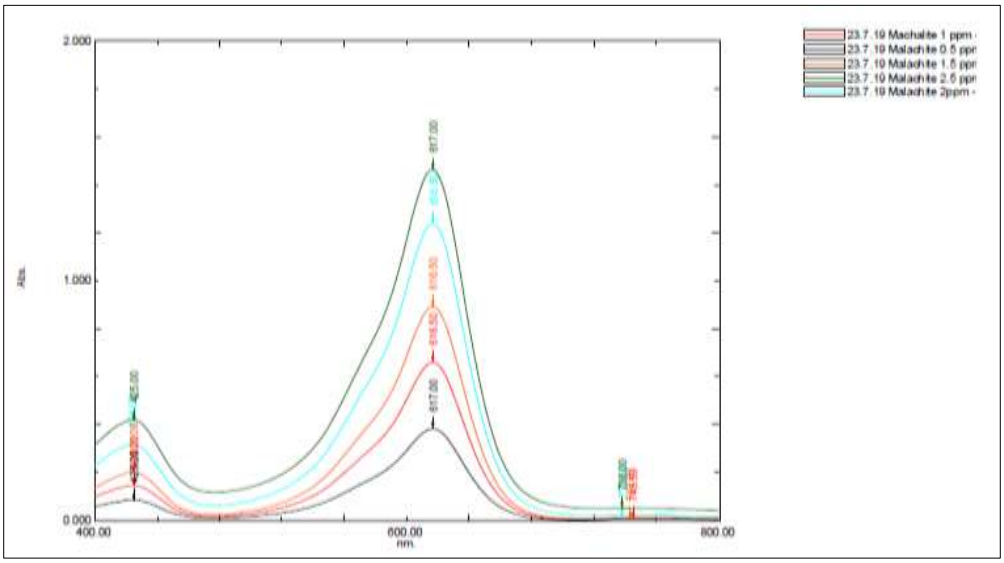

Figure 7 Wavelength of Maximum Absorption of Malachite Green at Various Concentrations

Construction of Standard Calibration Curve

Standard calibration curve for malachite green dye at various concentrations was constructed. At a wavelength of maximum absorption (λ_{max}) of 617 nm, a plot of absorbance vs. concentration was also drawn by plotting six different concentrations (0.312, 0.625, 1.250, 2.500, 5.00 and 10.000 ppm) of MG dye. The curve was straight line and passed through the origin indicating that Beer's Law was well obeyed (Table 2 and Figure 8).

Table 2 Changes of Absorbance with Concentration of Malachite Green

Concentration (ppm)	Absorbance at 617 nm
0.312	0.0052
0.625	0.0701
1.250	0.18884
2.500	0.4457
5.000	1.0176
10.000	2.0101

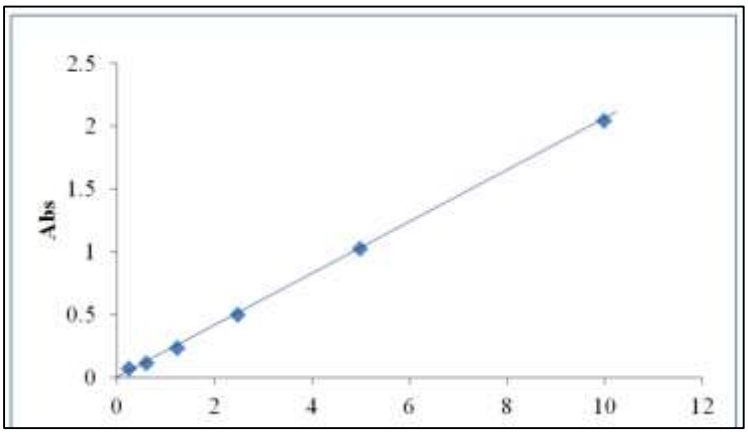

Figure 8 Calibration curve for malachite green

The Optimum Conditions for Colour Removal of MG Dye using Prepared GO

Effect of initial concentration

The effect of initial concentration of dye on adsorption capacity was well studied and elicited. The initial concentrations of MG dye in solution were varied as 10, 20, 30, 40 and 50 ppm at pH 7 by using 0.06 g of prepared GO. The maximum colour removal efficiency was obtained at initial concentration of MG dye (10 ppm). The highest colour removal percent was 95.73% as shown in Table 3 and Figure 9. With increase in initial dye concentration the available adsorption sites became saturated and insufficient to accommodate the increasing amount of dye molecules.

Table 3 Effect of Initial Concentration of Malachite Green

No.	Concentration (ppm)	Percent Removal (%)
1	10	95.73
2	20	94.73
3	30	94.52
4	40	91.57
5	50	87.12

Volume of dye solution = 50 mL
Weight of sample (GO) = 0.06 g
Contact Time = 60 min
Temperature = room temperature
pH = 7

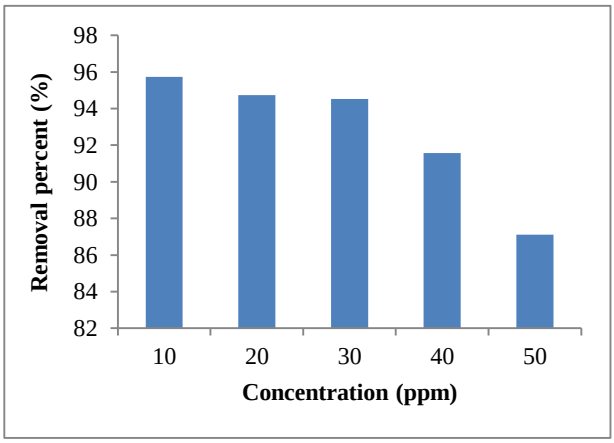

Figure 9 Effect of initial concentration of malachite green

Effect of pH

The effect of pH (2, 4, 6, 8 and 10) on removal of MG dye by using prepared GO was carried out for 60 min at room temperature. The maximum colour removal efficiency of 99.30 % was obtained at pH 4 by using 0.06 g of prepared GO (Table 4 and Figure 10).

Table 4 Effect of pH on the Removal of Malachite Green

No.	pH	Percent Removal (%)
1	2	98.08
2	4	99.30
3	6	96.83
4	8	85.71
5	10	79.02

Volume of dye solution = 50 mL
Concentration = 10 ppm
Weight of sample = 0.06 g
Contact Time = 60 mins
Temperature = room temperature

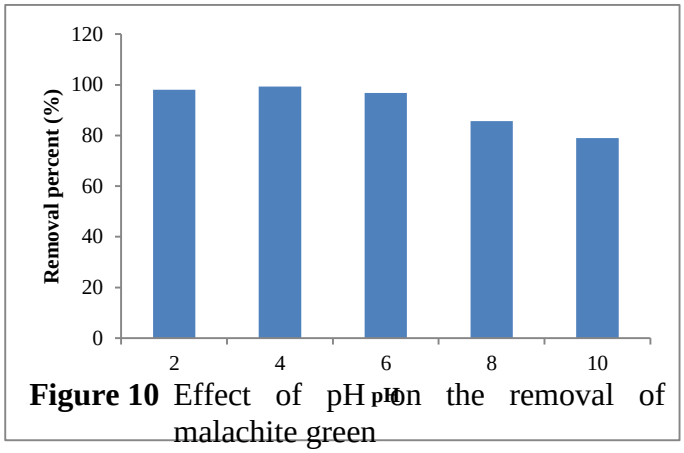

Figure 10 Effect of pH on the removal of malachite green

Effect of Contact Time

The effect of contact time between the adsorbent and adsorbate was varied as (30, 60, 90, 120 and 150 min) on rotary shaker. After 60 min of contact time, the highest colour removal percent (98.05 %) was obtained using 0.06 g of prepared GO at RT and pH 7 (Figure 11 and Table 5).

Table 5 Effect of Contact Time on the Removal of Malachite Green

No.	Time (min)	Percent Removal (%)
1	30	91.88
2	60	98.05
3	90	92.41
4	120	94.53
5	150	95.23

Volume of dye solution = 50 mL
Concentration of dye solution = 10 ppm
Weight of sample = 0.06 g
Temperature = room temperature
pH = 7

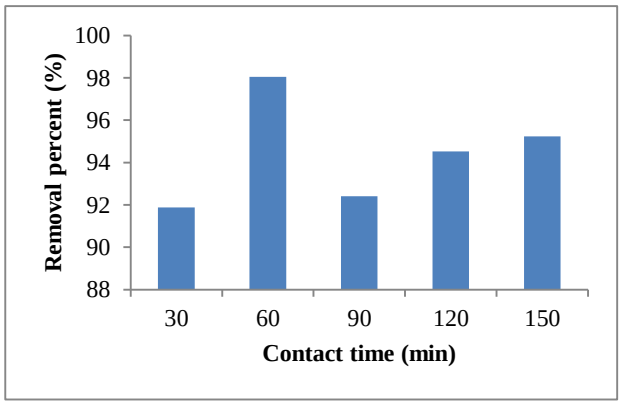

Figure 11 Effect of contact time on the removal of malachite green

Effect of Dosage

The dosage of adsorbent was varied in the range of 0.02 to 0.10 g (0.02, 0.04, 0.06, 0.08 and 1.00) g while keeping contact time and concentration of MG at 60 min and 10 ppm respectively. The maximum colour removal percent was observed at the dosage of 0.08 g of prepared GO (Figure 12 and Table 6). When the amount of dosage of GO was increased, the total surface area of the adsorbent became larger. Subsequently, the available adsorption sites also increased, which in turn improved the dye adsorption process. However, as the dosage amount further increased to 0.10 g the colour removal percent slightly decreased due to the desorption of dye molecules.

Table 6 Effect of Dosage of Graphene Oxide for Removal of Malachite Green

No.	Dosage (g)	Percent Removal (%)
1	0.02	89.38
2	0.04	96.35
3	0.06	97.84
4	0.08	97.92
5	0.10	95.78

Volume of dye solution = 50 mL
Concentration of dye solution = 10 ppm
Time = 60 mins
Temperature = room temperature
pH = 7

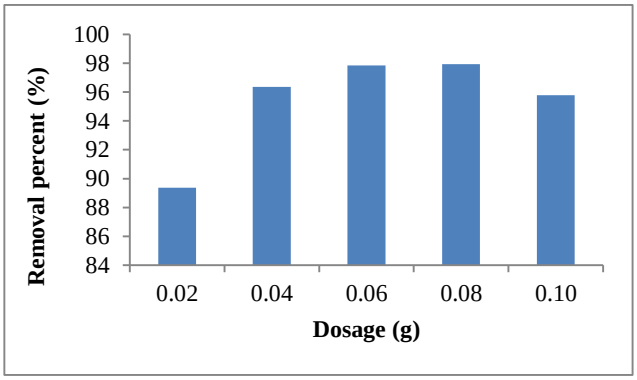

Figure 12 Effect of dosage of graphene oxide for removal of malachite green

Conclusion

Graphene oxide was successfully prepared by oxidizing graphite by a Modified Hummer's Method. Chemical method results as an efficient method for the synthesis of GO as required for various applications. The prepared GO was confirmed by XRD, FT IR, SEM, UV-visible spectroscopy and EDX result. The optimized values of initial concentration of MG dye, pH, contact time and adsorbent dose were found to be 10 ppm, 4, 60 min and 0.08 g, respectively, for colour removal using prepared GO. These unique properties possessed by graphene oxide could open up possibilities to satisfy the needs in various applications.

Acknowledgements

The authors would like to thank the Myanmar Academy of Art and Science for allowing to present this paper. We are extremely grateful to Rector Dr Khin May Aung, Head of Department Professor Dr Nyun Tun, and Professor, Dr Myat Sandar Hla, Department of Chemistry, Panglong University, for their valuable advice to do this research.

References

Hidayah, N. M. S., Liu, W.W., Lai, C.W., Noriman, N. Z., Khe, C.S., Hashiman, U. and Lee, H. C. (2017). "Comparison on Graphite, Graphene Oxide and Reduced Graphene Oxide: Synthesis and Characterization". *AIP* Conference Proceeding, vol. 1892(1), p. 150002

Mindivan, F. (2016). "The Synthesis and Characterization of Graphene Oxide (GO) and Reduced Graphene Oxide (RGO)". *Machines, Technologies, Materials*, vol. 2, pp.51-54

Mohamadi, A. S., Skrkhosh, M., Atafar, Z., Avazpour, M., Nazari, S., Rezaei, S., Mohseni, S. M. and Baziar, B. (2016). "Removal of Malachite Green, a Hazardous Dye using Graphene Oxide as an Adsorbent from Aqueous Phase". *Journal of Chemical and Pharmaceutical Research*, vol. 8 (3), pp. 624-633

Smith, A. T., Lachance, A. M., Zeng, S., Liu, B and Sun, L. (2019). "Synthesis, Properties and Applications of Graphene Oxide/Reduced Graphene Oxide and Their Nanocomposites". *Nano Materials Science*: vol. 1, pp. 31-47

Zaaba, N. I., Foo, K. L., Hashim, U., Tan, S. J., Liu, W and Voon, C. H. (2017). "Synthesis of Graphene Oxide Using Modified Hummers Method: Solvent Influence". *Advances in Material & Processing Technologies Conference*: vol. 184, pp. 469-477

REMOVAL OF PHOSPHATE FROM NATURAL WATER RESOURCES USING ACID TREATED COAL FLY ASH

Ohn Mar Khin[1], Hlaing Hlaing Oo[2] , Ni Ni Than[3]

Abstract

The excess of phosphorus (P) in the environment can promote chemical pollution and harm ecosystems, especially water. The protection and restoration of natural lakes is increasingly important in countries with limited water resources in the world. The increasing release of phosphate-containing wastewater to natural water bodies such as natural lakes have caused eutrophication, which has become a globally concerning problem. In order to overcome accelerating eutrophication, therefore, there is a need to control and reduce the level of phosphate in water resources. The aim of this research was to detect the phosphate-uptake capacity from five eutrophic lakes at Yangon urban region using low cost of sorbents like modified coal fly ash. This research work conducted during August 2018 to April 2020. The amount of phosphate ion in water bodies was determined by using standard spectrophotometric method. According to the investigated data, phosphate-uptake capacity of acid treated coal fly ash was 97.86 percent, which was obtained by batch tests in laboratory. The results of this study showed that acid treated coal fly ash was effective in removal of phosphate ions in water bodies of natural lake. Thus, the results allow to evaluating the chances of successful lake restoration by applying acid treated coal fly ash to natural water bodies.

Keywords: Acid treated coal fly ash, eutrophication, phosphate ion, natural lakes

Introduction

Water is essential to life, the pollution of the lakes and rivers has become an international problem that has reached crisis proportions in many regions. In developing countries, human sewages and animal wastes often enter streams and lakes from restaurants, hotels, food shops and sport activities; it causes increasing nitrates and phosphates levels into surface water bodies. The phosphates stimulate the growth of aquatic algae, causing sudden spurts growth called algae blooms. Excess concentrations of phosphate ion in water cause eutrophication. There are two types of eutrophication: natural and cultural. Natural eutrophication is a natural aging process for most lakes and ponds. Cultural eutrophication happens when the amount of nutrients in the water and the water temperature are changed due to human activity and the eutrophication process begins to run at high speed. It is not only destroyed the aquatic life but also disrupts the balance of the aquatic ecosystem (Mustafa *et al.,* 2008). To control eutrophication, James (1997) has recommended that total phosphate should not exceed 0.025 mg per liter in lakes and reservoirs, and should not exceed 0.1 mg/L in streams and reservoirs. Therefore, it is necessary to remove the phosphate ion, before discharged wastes from water resources into natural water environment. During the past decades, various techniques, including biological treatment and chemical precipitation have been reported for phosphate removal. Adsorption is one of the techniques, which is comparatively more useful and economical for such removal (Ragheb, 2013). Sorption technique is an effective, reliable, and environmentally friendly treatment process for the removal of phosphorus from wastewater sources which otherwise can cause eutrophication of receiving waters.The principle of phosphorus removal from water consists in the formation of insoluble metal phosphates, namely calcium, iron and aluminum that influence concentrations of phosphorus in water (Benito *et al.,* 2001). The coal fly ash consists of Si, Al, Fe, Ca, and Mg, and therefore a good candidate material for phosphate

[1] Lecturer, Department of Chemistry, Defence Services Medical Academy
[2] Dr, Professor, Department of Chemistry, West Yangon University
[3] Dr, Professor and Head, Department of Chemistry, University of Yangon

removal from water (Mikendova *et al.,* 2010). Recently, the acid treated coal fly ash has been used for the removal of phosphate ion.

Materials and Methods

Materials

The chemicals used were procured from British Drug House (BDH), England, Wako Co. Inc., Tokyo, Japan and Sigma-Aldrich, USA. The apparatus and instruments are conventional labware, glassware and modern equipment**.**

Sample Preparation of Coal Fly Ash

Coal fly ash sample was collected from Tigyit power plant located in South-west Shan State in Myanmar (PYO, 2011). It was taken systematically from a large number of material bags. Sampling was carried out by cone and quartering method. Sample was homogenized into small particles using a grinding mill and then made to obtain 250 μm mesh size. The obtained coal fly ash sample was dried at 105 °C in an oven for an hour. The samples were kept in plastic bags and placed in cold and dried place.

Preparation of Acid Treated Coal Fly Ash

The coal fly ash was treated with hydrochloric acid and optimal conditions were found to be 2 M HCl solution, the ratio of coal fly ash and acid solution is 1:2 (w/v) and 2 h for acid treated time at ambient temperature.

Sample Collection

The lake water samples were collected for three seasons and in the mornings from August 2018 to April 2019. The water samples were collected in clean new 1 L plastic bottles. The bottles were placed in a dark ice box and immediately taken to the laboratory. The water samples of five lakes were collected in Yangon urban region, Myanmar. The satellite data and townships of selected eutrophic lakes were shown in Table 1. The study duration of phosphate ion removal for eutrophic lakes is shown in Table 2.

Table 1 The Satellite Data and Townships of Selected Eutrophic Lakes

Sr. No	Samples	Latitude (N)	Longitude (E)	Lake	Townships
1	S_1	16.929678	96.119856	DSMA Campus Lake	Mingaladon
2	S_2	16.943986	96.105544	Inn Pounk Su Lake	Shwepyitha
3	S_3	16.841060	96.138428	Inya Lake	Kamayut
4	S_4	16.796817	96.161935	Kandawgyi Lake	Mingala Taungnyunt
5	S_5	16.793479	96.148985	Kan Taw Min Lake	Dagon

Table 2 Study Duration of Phosphate Ion Removal for Eutrophic Lakes

Study duration		
Year	**Season**	**Sampling date**
2018	Rainy	16.8.2018
	Cold	5.12.2018
2019	Hot	3.4.2019
	Rainy	11.8.2019
	Cold	15.12.2019
2020	Hot	4.4.2020

Standard Calibration Curve for Phosphate Ion by Using Spectrophotometric Method

The amount of phosphate ion in water bodies was determined by using standard spectrophotometric method at a wavelength of 880 nm. Ammonium molybdate and potassium antimonyl tartrate react in acid medium with orthophosphate to form a heteropolyacid-phosphomolybdic acid- that is reduced to intensely coloured molybdenum blue by ascorbic acid. The primary stage of the work, include the evaluation of calibration curve by using absorbance and concentration of standard phosphate solution (Arnold *et al*., 1992). The standard solutions of phosphate in different concentrations range between 0.2 mg L^{-1} to 1.2 mg L^{-1} were chosen. Standard solution (50 mL) was pipetted into a clean and dry beaker. A mixed reagent was prepared by adding 5 mL of ammonium molybdate solution, 50 mL of 2.5 M sulphuric acid, 5 mL of potassium antimonyl tartrate solution and 30 mL of ascorbic acid solution. Mixed reagent (8 mL) was added and the solution was then allowed to stand for 10 min. The absorbance of blue colour solution was measured by UV-visible spectrophotometer at 880 nm against a blank of distilled water.

Phosphate Sorption

A spectrophotometer was used to measure the intensity of residual colour of solutions after sorption. The residual colour index is expressed as absorbance.

Acid treated coal fly ash (0.1 g each) was added to 100 mL each of collected lake water samples and adjusted the pH at 5.5. The samples were equilibrated by continuous shaking on a rotating shaker (150 rpm) at ambient temperature for 90 min. The suspensions were filtrated. Mixed reagent (8 mL each) was added and the solutions were then allowed to stand for 10 min.

The absorbance of blue colour solution was measured by UV-visible spectrophotometer at 880 nm against a blank of distilled water

Results and Discussion

To determine phosphorus by a spectrophotometric method a calibration curve of standard phosphorus solution was constructed.The data for absorbance values for different concentration of potassium dihydrogen phosphate solution are shown in Table 3 and the corresponding calibration curve is shown in Figure 1. The calibration curve was used to calculate the amount of phosphate in water bodies against a series or standard phosphate concentrations.

Table 3 Absorbance vs Concentration of Potassium Dihydrogen Phosphate Solution

Concentration (mg L^{-1})	Absorbance at 880 nm
0.2	0.12
0.4	0.25
0.6	0.37
0.8	0.50
1.0	0.62
1.2	0.75

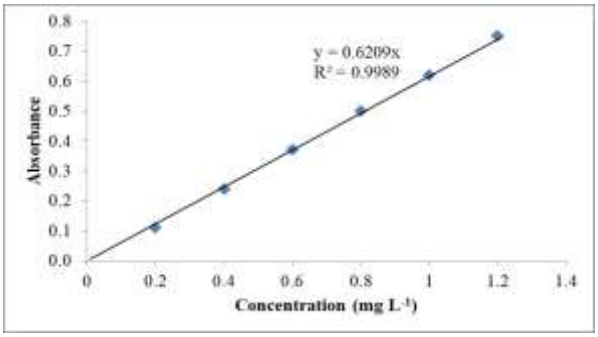

Figure 1 Calibration curve for potassium dihydrogen phosphate solution

The protection and restoration of lakes is increasingly important in countries with limited water resources. Eutrophication conditions of five lakes at Yangon urban region are presented in Figure 2. In this study, initial phosphate ion concentration of five lake water samples collected from different locations of Yangon urban region were determined. The initial phosphate concentrations are shown in Table 4. The phosphate concentrations after discharged with acid treated coal fly ash and percent removal of phosphate in selected lake waters are described in Tables 5 to 6 and Figures 3 to 8.

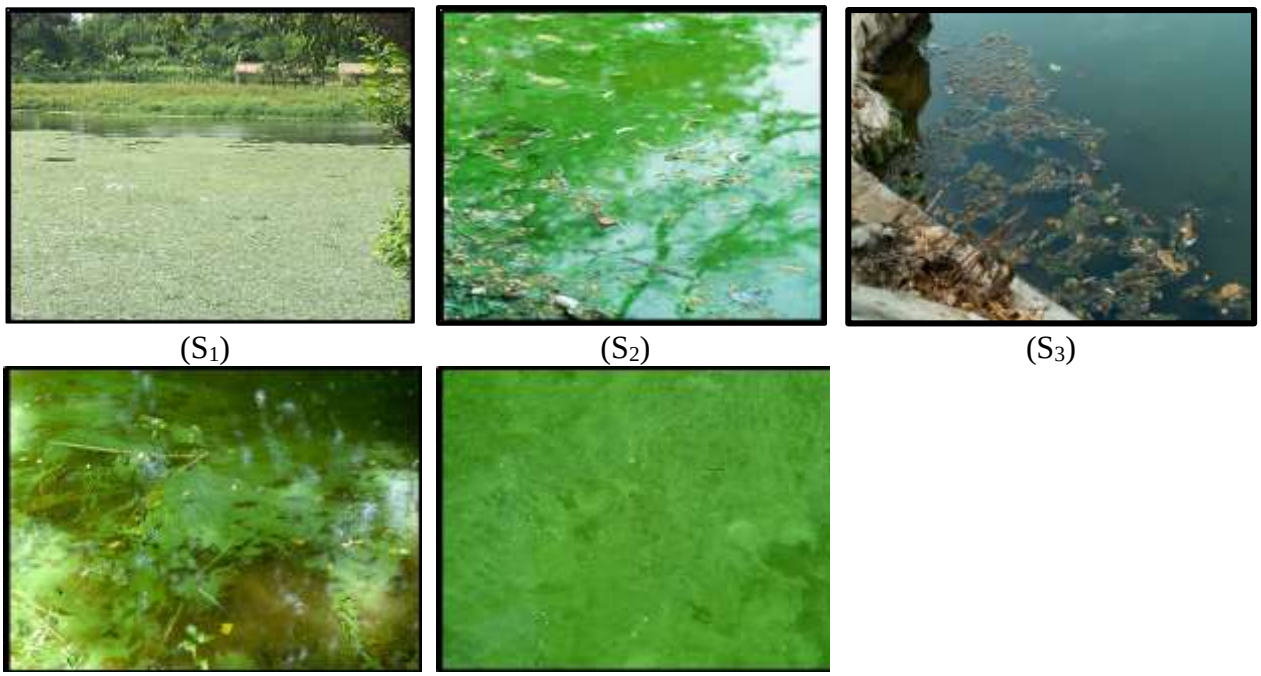

(S_1) (S_2) (S_3)

(S_4) (S_5)

Figure 2 Eutrophication conditions of five lakes at Yangon urban region

Table 4 Initial Phosphate Ion Concentration of Lake Water Samples from Rainy Season (2018) to Hot Season (2020)

Sr. No	Lake water samples	Initial phosphate ion concentration (mg L^{-1})					
		Rainy season (2018)	Cold season (2018)	Summer season (2019)	Rainy season (2019)	Cold season (2019)	Summer season (2020)
1	S_1	0.2271	0.6732	0.9518	0.4123	0.2674	0.1917
2	S_2	0.1659	0.0548	0.0370	0.0605	0.0322	0.0515
3	S_3	0.0193	0.0338	0.0290	0.0596	0.0966	0.0970
4	S_4	0.0451	0.0531	0.1884	0.1514	0.1933	0.1966
5	S_5	0.1450	0.1498	0.7537	0.4107	0.6845	0.8117

$>$ 0.025 mg L^{-1} eutrophication level, James, 1997

From the resulting data, in sampling site S_1 (Defence Service Medical Academy), initial phosphate ion concentration significantly increased from rainy season (2018) to summer season (2019). It is because wastewater discharged from farming sites existed near the lake. And then, it decreased from rainy season (2019) to hot season (2020) because of the sustainability of lake during this period.

In sampling site S_2, initial phosphate ion concentration of Inn Pounk Su Lake water sample in rainy season (2018) significantly increased due to flooding. Here an urban sewer overflow due to heavy rain causing runoff likely containing phosphorus, nitrogen, ammonia, nitrates, and raw sewage into the lake nearby waterways.

In sampling site S_3, initial phosphate ion concentration of Inya Lake water sample gradually increased from rainy season (2018) to hot season (2019). And then, it significantly increased from rainy season (2019) to hot season (2020). Because popular recreational center, many restaurants and food shops at lake side of Inya Lake, and a new hospital and hotels were recently constructed.

In sampling site S_4, initial phosphate ion concentration of Kandawgyi Lake water sample significantly increased from rainy season (2018) to hot season (2020). At the Kandawgyi Lake (recreation center of Yangon) environment, existing hotels, restaurants, shopping mall, amusement arcade, health club and playground exist at the lake side of Kandawgyi.

In sampling site S_5, initial phosphate ion concentration of Kan Taw Min Lake water sample significantly increased from rainy season (2018) to hot season (2020) due to the fact that some restaurants were located at the lake side of Kan Taw Min.

Environmental degradation due to the release of different pollutants into receiving lake waters has become of great importance. Thus, to maintain our environment in a good condition, lake waters must be treated. In this research work the removal of phosphate ion from lake waters was carried out by using acid treated coal fly ash. Acid treated coal fly ash was more favourable for phosphate adsorption onto the surfaces of aluminum and iron phases (Pengthamkeerati *et al.*, 2008). The acid treated coal fly ash generally showed larger specific surface area and higher pore volume. The sorption mechanism is formation of a variety of Al-, and Fe-phosphate minerals and sorbed phases of acid treated coal fly ash. The results of this study show that acid treated coal fly ash is effective in removal of phosphate ion contained in lake water samples. High phosphate removal rates greater than 90 % were obtained.

Table 5 Residual Phosphate Ion Concentration of Lake Water Samples during 2018 to 2020

Sr. No	Lake water samples	Residual phosphate ion concentration ($mg\ L^{-1}$)					
		Rainy season (2018)	Cold season (2018)	Summer season (2019)	Rainy season (2019)	Cold season (2019)	Summer season (2020)
1	S_1	0.0129	0.0433	0.0725	0.0258	0.0145	0.0048
2	S_2	0.0048	0.0016	0.0016	0.0016	0.0016	0.0016
3	S_3	0.0016	0.0016	0.0016	0.0032	0.0048	0.0048
4	S_4	0.0016	0.0016	0.0145	0.0097	0.0129	0.0113
5	S_5	0.0048	0.0032	0.0515	0.0306	0.0483	0.0644

Table 6 Percent Removal of Phosphate Ion in Lake Water Samples during 2018 to 2020

Sr. No	Lake water samples	Percent removal of phosphate ion (%)					
		Rainy season (2018)	Cold season (2018)	Summer season (2019)	Rainy season (2019)	Cold season (2019)	Summer season (2020)
1	S_1	94.32	92.82	92.38	93.74	94.58	97.49
2	S_2	97.11	97.08	95.68	97.36	95.03	96.89
3	S_3	91.71	95.27	94.48	94.63	95.03	95.05
4	S_4	96.45	96.99	92.30	93.59	93.33	94.25
5	S_5	96.69	97.86	93.17	92.55	92.94	92.07

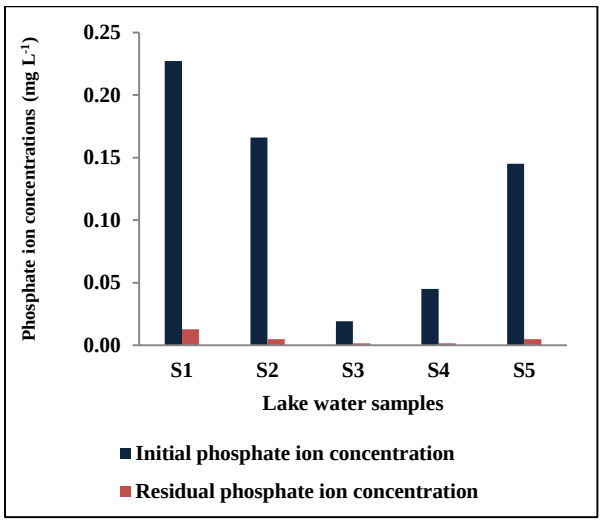

Figure 3 Graphical presentation of phosphate ion concentration before and after treated with acid treated coal fly ash in the lake waters samples during rainy season (2018)

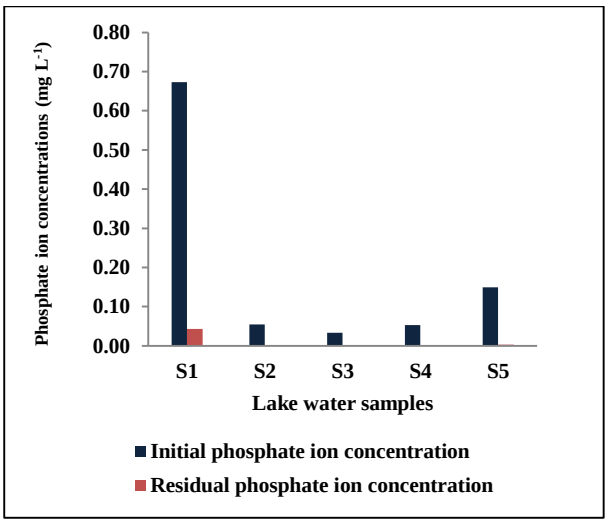

Figure 4 Graphical presentation of phosphate ion concentration before and after treated with acid treated coal fly ash in the lake waters samples during cold season (2018)

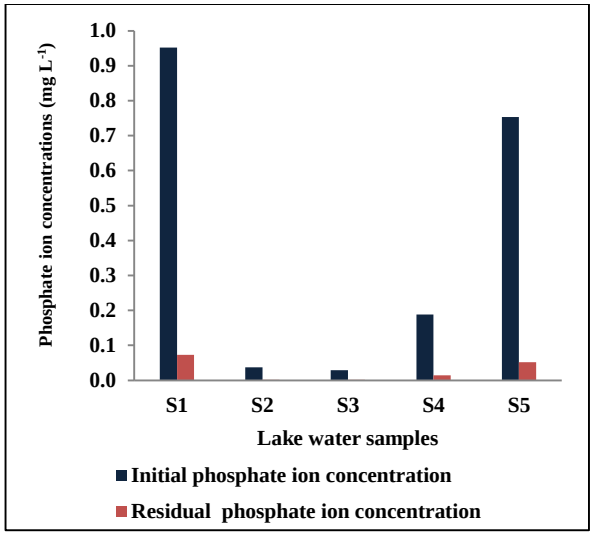

Figure 5 Graphical presentation of phosphate ion concentration before and after treated with acid treated coal fly ash in the lake waters samples during hot season (2019)

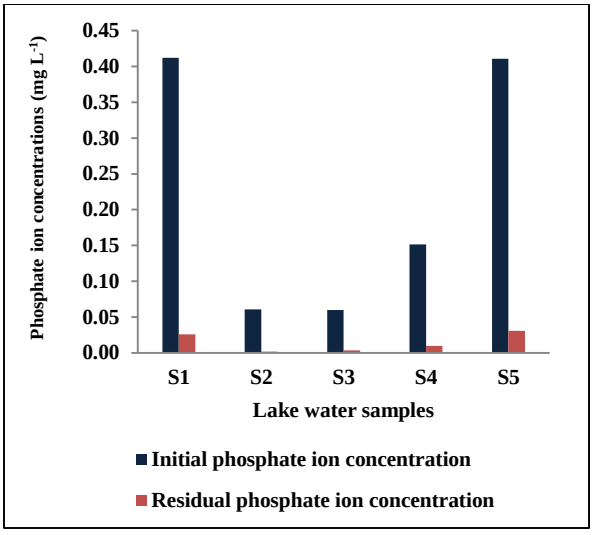

Figure 6 Graphical presentation of phosphate ion concentration before and after treated with acid treated coal fly ash in the lake waters samples during rainy season (2019)

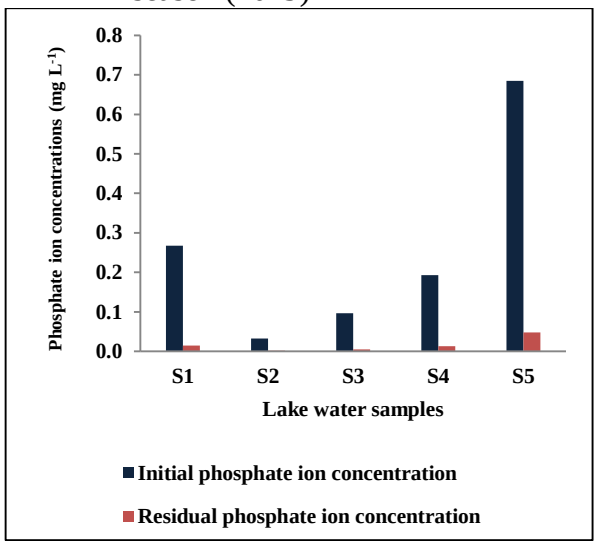

Figure 7 Graphical presentation of phosphate ion concentration before and after treated with acid treated coal fly ash in the lake waters samples during cold season (2019)

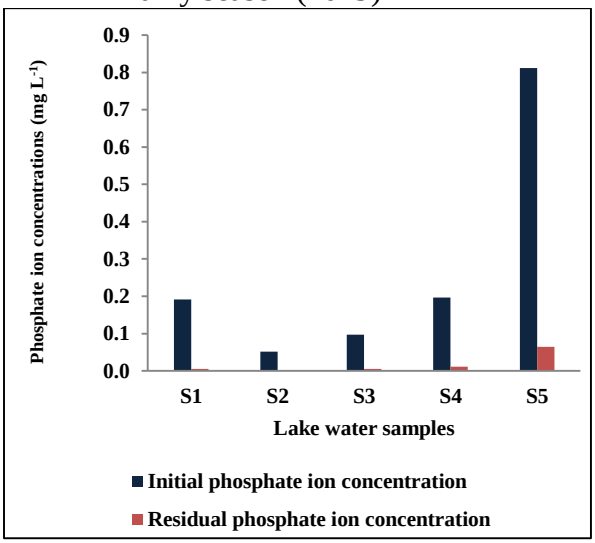

Figure 8 Graphical presentation of phosphate ion concentration before and after treated with acid treated coal fly ash in the lake waters samples during hot season (2020)

Conclusion

In this research, the process of sorption and precipitation is the main mechanism for using fly ash to remove phosphate ion from the lake waters. The sorption behaviours of the maximum percent removal of phosphate ion in lake waters were found to be 97.86 % by acid treated coal fly ash at 0.1 g/100 mL of dosage, pH 5.5 and 90 min of contact time at ambient temperature. Acid treated coal fly ash showed promising potential for controlling water bodies because of its low cost and high efficiency. Therefore, acid treated coal fly ash on the treatment of lake waters was obviously improved. The prevention of eutrophication requires the cooperation of different parts of our society including experts and scientists, farmers, environmental organizations, politicians and even the public.

Acknowledgement

The authors would like to thank the Department of Higher Education, Ministry of Education, Yangon, Myanmar for giving us the opportunity to do this research.

References

Arnold, E., Lenore, S. and Andrew, D. E. (1992). *APHA Method 4500-P; Standard Methods for the Examination of Water and Waste Water*. Washington, DC: American Public Health Association, pp.108-116

Benito, Y., Ruiz, M., Cosmen, P. and Merino, L. J. (2001). "Study of Leaches Obtained from the Disposal of Fly Ash from PFBC and AFBC Processes". *Chem. Eng. J.*, vol.84, pp.167-171

James, E. K. (1997). *Information on Phosphorus Amounts & Water Quality*. http://osse.ssec.wisc.edu/curriculum/earth/Minifact2_Phosphorus.pdf (Accessed 20 September 2019)

Mikendova, B., Thomas, J. and Danek, T. (2010). "Phosphorus Removal from Water Using Fly Ash and Modificated Fly Ash - Comparison of X-Ray Fluorescence Spectrometry and Standard Spectrophotometric Methods". *Geosci.Eng*., vol 1(6), pp. 22-31

Mustafa, S., Zaman, M. I. and Khan, S. (2008). "Temperature Effect on the Mechanism of Phosphate Anions Sorption by β-MnO_2". *Chem. Eng. J.*, vol.141 (1-3), pp.51-57

Pengthamkeerati, P., Satapanajaru,T. and Chularuengoaksorn,P. (2008). "Chemical Modification of Coal Fly Ash for the Removal of Phosphate from Aqueous Solution". *Fuel*, vol.87 (12), pp. 2469 - 2476

PYO, Pa-Oh Youth Organization. (2011). *Poison Clouds: Lessons from Burma's Largest Coal Project at Tigyit* http://burmacampaign.org.uk/media/PoisonClouds.pdf (Accessed 14 October 2016)

Ragheb, S. M. (2013). "Phosphate Removal from Aqueous Solution using Slag and Fly Ash". *HBRC Journal*, vol. 9, pp. 270-275

PREPARATION OF GELATIN DERIVED FROM FISH SKINS OF FISH SPECIES, CIRRHINUS MRIGALA (NGA-GYIN) AND NOTOPTERUS CHITALA (NGA-PHE) AND THEIR CHARACTERIZATION

Chang Myaw[1], Thinzar Nu[2], Khin Than Yee [3]

Abstract

The aim of the research work is the isolation of gelatin powder from *Cirrhinus mrigala* (Nga-gyin) and *Notopterus chitala* (Nga-phe) fish skin. Gelatin was derived from the thermal degradation of collagen, which is the principal protein found in skin and bones. Gelatin was extracted by acid treatment and confirmed by FT IR analysis. The physicochemical properties of prepared gelatin such as moisture content, ash content, pH and solubility in water, colour appearance, odour description, viscosity, gelling and melting temperatures were also determined. The yield percent of prepared gelatin from Nga-phe skin was greater than that of Nga-gyin skin. The prepared gelatin was characterized by Fourier Transform Infrared (FT IR) spectrophotometer, Scanning Electron Microscopy (SEM) and Thermogravimetric-Differential Thermal Analysis (TG-DTA). FT IR analysis showed the chemical bond formation of gelatin. Morphological investigation showed that the Nga-gyin skin (Ngy) exhibited sponge or coral structure and the surface of Nga-phe skin (Nph) had denser strand with small pores. TG -DTA data showed three steps of degradation. The initial degradation was due to moisture, the second was due to thermal degradation of composite and the third was denaturing of protein. Therefore, the use of fish skin waste as raw material in the gelatin production is quite potential and plays a major role in recycling of waste.

Keywords: *Cirrhinus mrigala, Notopterus chitala,* gelatin, thermal degradation, collagen, acid treatment

Introduction

Gelatin, a protein with the molecular formula $C_{102}H_{151}N_{31}O_{39,}$ derived from collagen is the major structural protein in connective tissue of animal skin and bone (Cho *et al*., 2004). It is an important constituent in a number of food and non-food products due to its multi-functional properties, thermal stability, digestibility, solubility and its biological characteristics.

In the food industry, it serves primarily as a gelling agent, but it is also used as a thickener, film former, stabilizer, emulsifier, adhesive agent, foaming agent, protective colloid and as a beverage fining agent (Johnston-Barks *et al*., 1990). The quality of gelatin for a particular application therefore depends largely on its rheological properties that are desirable for that application (Gomez- Guillen *et al*., 2002).

Commercially, two main types of gelatin are used: Type A and Type B gelatins (Ward and Courts, 1977). Type A gelatin results from acid process and Type B gelatin results from alkaline process. Dry commercial gelatins for the food industry usually contain about 88% protein, 10% water and 1 – 2% salts (GME, 1990).

Gelatin is being widely used in food, drug and cosmetic industries as stabilizing, thickening and gelling agent (Kittiphattanabawon *et al.*, 2010). The quality of gelatin is largely determined by its gelling strength and thermal stability. This is dependent on the amino acid composition which is species specific and molecular weight distribution as influenced by processing conditions (Gomez-Guillen *et al.*, 2002).

Fish by-products are seldom used as a source of raw materials for gelatin extraction. They are mainly used for animal feed supplements due to their small size. However, some studies have

[1] PhD Candidate, Department of Chemistry, University of Yangon
[2] Dr, Lecturer, Department of Chemistry, University of Yangon
[3] Dr, Lecturer, Department of Chemistry, West Yangon University

ascertained freshwater and marine water fish to have vast amounts of waste after removal of useful edible parts and high gelatin yield being expected from them. Additionally, most findings suggest that gelatin from these species has an advantage over those extracted from cold water species, providing better rheological properties nearly similar to mammalian gelatins.

Fish skin contains large amounts of collagen and can be considered as a potential source of gelatin. One major advantage of gelatin from aquatic sources is that it is not associated with the risk of Bovine Spongiform Encephalopathy and is acceptable to most religious groups. Further, the utilization of fish skin for the extraction of gelatin can significantly address the problem of waste disposal in the fish processing industry. Although fish gelatin will be unable to completely replace mammalian gelatin, in future it might become a niche product offering unique and competitive properties to other biopolymers, as well as meeting the demand of global halal market (Karim and Bhat, 2009).

In the present paper, gelatin was extracted from nga-gyin and nga-phe fish skin used by acid treatment. The physicochemical properties of extracted gelatin were investigated. Moreover, the extracted gelatin was characterized by modern techniques such as FT IR, SEM and TG-DTA analysis.

Materials and Methods

Raw Materials and Chemicals

Nga-gyin (NGY) fish skin and Nga-phe (NPH) fish skin were collected from Hlaing Yadanar Market, Hlaing Township Yangon. Other requiring chemicals were purchased from chemical store. Distilled water was used as the solvent in all analyses.

Extraction of Gelatin

Fish skins stored at -20°C were thawed and cut it into small size of about 1 cm^2. The fish skins were thoroughly rinsed with limewater to remove superfluous materials. The samples (100 g) were rinsed and soaked in 1 % (w/v) citric acid (1:3 w/v) for 12 h. The samples were neutralized by washing several times until the pH of the washing water was faintly at basic pH (pH 6-7).

The fish skins were extracted in distilled water at 60°C for 6 h. The solubilized gelatin was separated from residual skin fragments by filtration through a fabric filter followed by Whatman No. 1. The mixture was cooled until gelatin gel was formed, and then dried using an oven at 60°C for 24 h. The dried gelatin was ground and sieved to produce gelatin powder (Gomez-Guillen *et al*., 2002).

Yield of gelatin

Yield percent of gelatin was calculated by the following equation:

$$\% \text{ yield (wet weight basis)} = \frac{\text{dried weight of gelatin (g)}}{\text{wet weight of fish skin waste (g)}} \times 100$$

Determination of Viscosity

Gelatin solutions at the concentration of 6.67% (w/v) were prepared by dissolving the dry powder in distilled water and heating at 60°C for the determination of viscosity. The viscosity (cP) of 10 mL of the solution was determined using Atago digital viscometer equipped with a No.2 spindle.

Determination of Gelling temperature and Melting temperature

Briefly, 20 mL of gelatin extracts were taken onto test tubes keep in freezer (- 4°C). The gelling temperature was noted. The freezed gelatin kept in water bath at 40°C and the time period corresponding to the melting temperature was recorded.

Characterization of the Prepared Samples

The physicochemical properties (moisture, ash, pH, solubility in water, colour appearance, odour description, viscosity, gelling and melting temperature) of gelatin prepared from nga-gyin (NGY) fish skin gelatin and nga-phe(NPH) fish skin gelatin were determined. The structural characterization of gelatin extracted from NGY and NPH fish skins were characterized using FT IR. The morphological structure of prepared samples were characterized by SEM. Thermal stability of prepared samples were characterized by TG-DTA. FT IR spectrum was recorded in the range of 4000-400 $cm^{-1}$by using 8400 SHIMADZU, Japan FT IR spectrophotometer. The scanning electron microscopy (SEM) images were recorded by using JSM-5610 Model SEM, JEOL-Ltd., Japan. Thermogravimetric analysis of samples were performed using TG-DTA apparatus, (Hi-TGA 2950 model) at the temperature range between 0 and 600°C under nitrogen gas flushing (at a rate of 50 mL/min).

Results and Discussion

Physicochemical Properties of Nga-gyin and Nga-phe gelatin

Table 1 shows the physicochemical properties (moisture, ash, pH and solubility in water, colour appearance, odour description, viscosity, gelling and melting temperature) of gelatin obtained from nga-gyin fish skin and nga-phe fish skin. In this table, nga-gyin gelatin was found to have a significant higher content of moisture and yield percent than those of nga-phe gelatin. The value obtained for the moisture content of gelatin was within the acceptable range (9–12 %) for high quality gelatin giving an indication of good shelf life. The ash content of nga-gyin gelatin and nga-phe gelatin were 2.56 % and 4.88 %, respectively. The value of nga-gyin gelatin is less than the recommended maximum limit of 2.6 % (Jones, 1977) and the limit given for edible gelatin i.e. 2 %. Low ash content suggested that the extracted gelatin was of high quality, as the ash content for a high quality gelatin should be lower than 2 % (Ockerman and Hansen, 1988). The high content of ash for nga-phe gelatin is due to improper washing method during extraction. The pH of nga-gyin gelatin and nga-phe gelatin were 4.21 and 5.48 respectively. pH values are variable and dependent on the gelatin extraction process; thus, different pH ranges can be observed. Jamilah and Harvinder (2002) reported pH values for extracted from the skin of black tilapia (3.81) and red tilapia (3.05). Both of gelatin are soluble in water.

Colour appearance of nga-gyin gelatin and nga-phe gelatin were white and dark yellow colour. Both of gelatin had less fishy odour. Low viscosity of nga-gyin and nga-phe gelatin might be due to over hydrolysis of the collagen during the pretreatment steps. The viscosity of most of the commercial gelatins also have been reported to be in the range of 2.0 to 7.0 cP and upto 13.0 cP for specialized ones (Johnston-Barks *et al*., 1990), Significant differences were observed in the melting temperature of the nga-gyin and nga-phe fish skin gelatin samples. Gelatin with high melting temperature formed stronger gel, and it was also observed that nga-gyin which had higher melting temperature formed stronger gel than nga-phe gelatin. Setting (gelling) temperature denotes the gelling process which involves the transition from random coil to triple helical structure of gelatin.

Table 1 Physicochemical Properties of Nga-gyin and Nga-phe gelatin

Physicochemical Properties	NGY-GLT	NPH-GLT
moisture (%)	11.70	5.24
ash (%)	2.56	4.88
pH	4.21	5.48
solubility in water	soluble	soluble
yield percent (%)	10.08	9.18
colour appearance	white	dark yellow
odour description	less fishy odour	less fishy odour
viscosity (cP)	3.8	3.0
gelling temperature (℃)	10	9
melting temperature (℃)	32	23

NGY-GLT = Nga-gyin fish skin gelatin
NPH-GLT = Nga-phe fish skin gelatin

FT IR Analysis

FT IR spectroscopy has been used to monitor the functional groups and secondary structure of gelatin. Proteins are comprised of amino acids joined together by amide bonds. The polypeptide and protein repeat units give rise to nine characteristic infrared (IR) absorption bands, namely; amide A, B, and I – VII. Amide bands represent different vibration modes of the peptides bond. The absorption bands of gelatin in the IR spectra are situated in the amide band region; Amide-I represents C=O stretching/hydrogen bonding coupled with COO, Amide-II represents bending vibration of N-H groups and stretching vibrations of C-N groups, Amide-III is related to the vibrations in plane of C-N and N-H groups of bound amide (Nur Hanani *et al*., 2011). Figure 2 shows the result of the FT IR analysis of NGY-GLT and NPH-GLT. Based on the FT IR spectra, the peaks of the gelatin at 3400-3200 cm^{-1} attributed to the presence of hydrogen bond water and amide-A, 1660-1580 cm^{-1} peaks were due to the occurrence of amide-I, 1550-1510 cm^{-1} indicated amide-II, band at 1275-1200 cm^{-1} indicated the amide-III, peaks range from 1460cm^{-1} to1380cm^{-1} were attributed to the symmetric and assymmetric bending vibrations of methyl group.

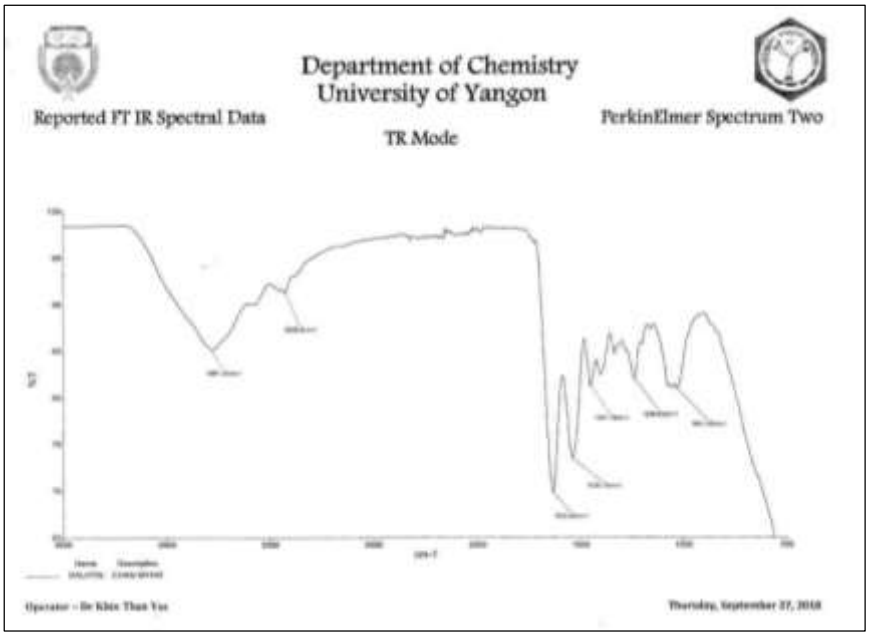

(a)

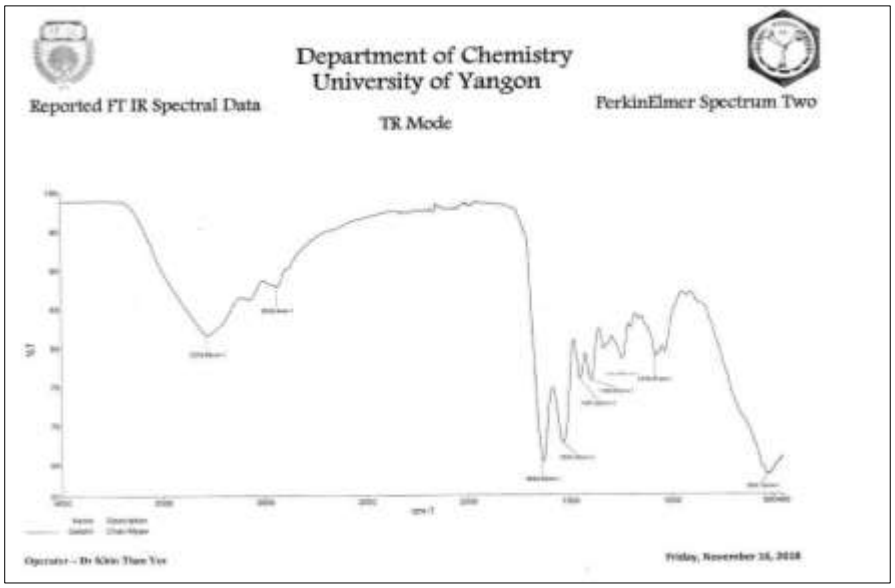

(b)

Figure 2 FT IR spectra of prepared (a) nga-gyin skin gelatin powder and (b) nga-phe skin gelatin powder

Table 2 FT IR Band Assignments of the Prepared Gelatin from Nga-gyin and Nga-phe Skin Gelatin Powder

Observed wavenumber (cm^{-1})		* Literature wavenumber (cm^{-1})	Band Assignments
Nga-gyin	**Nga-phe**		
3281	3278	3400-3200	O-H stretching
2926	2936	2940-2915	C-H stretching in -CH_2 group
1633	1630	1660-1580	C=O stretching (amide I)
1538	1535	1550-1510	C-N stretching
1451	1451	1485-1455	C-H bending (asym:) in alkane
-	1395	1395-1365	C-H bending (symm:)
1238	1242	1275-1200	C-O-C asym: stretching
1031	1079	1055-1028	C-O stretching

***** Silverstein *et al.*, 2003

SEM Analysis

In order to further investigate the structural changes in the gelatins, SEM micrographs of the NGY-GLT and NPH-GLT are shown in Figure 3. Benjakul *et al* (2009) noted that the arrangement and combination of protein molecules in gel matrix contributes to the gel strength. According to the SEM image, NGY-GLT powder had sponge or coral structure. The structure of the NPH-GLT powder had rather thick, clear and uniform tissue.

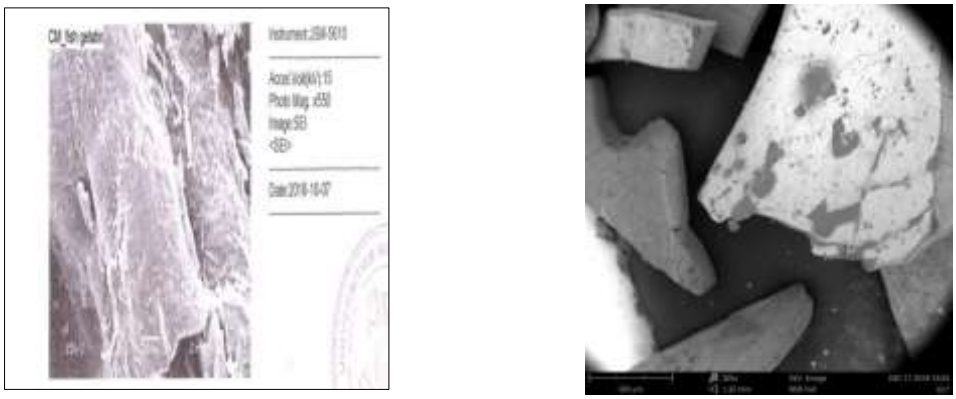

(a) (b)

Figure 3 SEM micrographs of (a) nga-gyin fish skin gelatin (NGY-GLT) and (b) nga-phe fish skin gelatin (NPH-GLT)

TG-DTA Analysis

TG-DTA analysis was carried out by heating the sample at 20°C/min in the temperature range 0-600°C in nitrogen atmosphere and the flow rate 50 mL/min. TG-DTA curve showed the change in mass with the increase of temperature. The results of NGY-GLT and NPH-GLT are shown in Figure 4 and Tables 3 and 4. In this analysis actual weight losses were observed in three steps degradation and the related temperature range was 35-600°C. The initial weight losses were due to the dehydration of adsorbed water and moisture, the second degradation resulted from dehydration of absorbed water and burning of organic compounds in the samples and third losses were denaturing and decomposition of protein in gelatin samples.

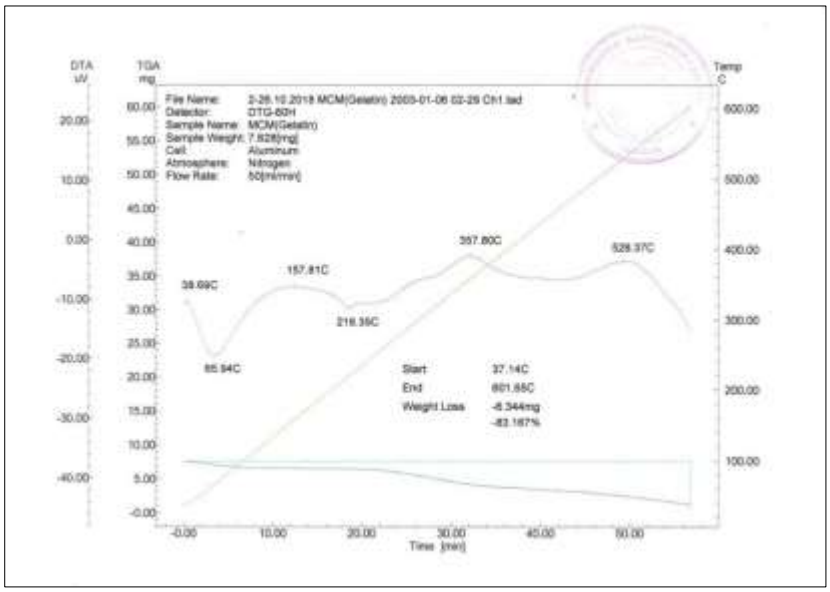

(a)

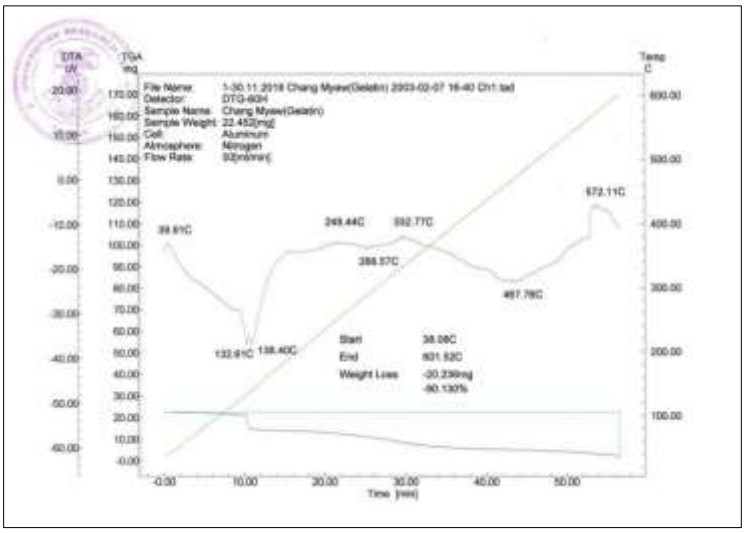

Figure 4 TG-DTA thermograms of prepared gelatin from (a) nga-gyin skin and (b) nga-phe skin

Table 3 TG-DTA Thermogram of Prepared Gelatin from Nga-gyin Skin

Temp: range (ºC)	Weight loss (%)	Peak's Temp: (ºC)	Nature of Peak	TG Remark
37-130	13.66	66	endothermic	due to the dehydration of adsorbed water and moisture
130-365	30.04	357	exothermic	due to the decomposition of volatile materials
365-600	39.47	528	exothermic	due to the decomposition and degradation of gelatin

***** Chen *et al*., 2005

Table 3 (b) TG-DTA Thermogram of Prepared Gelatin from Nga-phe skin

Temp: range (ºC)	Weight loss (%)	Peak's Temp: (ºC)	Nature of Peak	TG Remark
38-130	7.85	133	endothermic	due to the dehydration of adsorbed water and moisture
130-250	37.76	249	exothermic	due to the dehydration of absorbed water and burning of organic compounds
250-600	44.52	333 572	exothermic exothermic	due to the denaturing and decomposition of protein in gelatin

***** Chen *et al*., 2005

Conclusion

In this study, gelatin was extracted from Nga-gyin and Nga-phe by acid treatment. Nga-gyin gelatin was a significant higher content of moisture and yield percent than that of nga-phe gelatin. The value obtained for the moisture content of gelatin was within the acceptable range (9 – 12 %) for high quality gelatin giving an indication of good shelf life. Low ash content suggested that the extracted gelatin was of high quality. The high content of ash for nga-phe gelatin is due to improper washing method during extraction. Significant differences were observed in the

melting temperature of the nga-gyin and nga-phe fish skin gelatin. Nga-gyin which had the higher melting temperature formed the stronger gel than nga-phe gelatin. FT IR spectroscopy has been used to monitor the functional groups and secondary structure of gelatin. The peaks of the gelatin at 1238 cm^{-1} is due to the the presence of functional group (-O- CH_3) and 2926 cm^{-1} is related with the symmetric and asymmetric stretching vibration of the aliphatic group (CH_2). According to the SEM image, NGY-GLT powder had sponge or coral structure. The structure of the NPH-GLT powder had rather thick, clear and uniform tissue. TG-DTA analysis showed three steps degradation due to the dehydration of adsorbed water, burning of organic compounds in the samples and denaturing and decomposition of protein in gelatin samples.

In this study, the physicochemical properties of nga-gyin and nga-phe fish skin gelatin had illustrated the potential of high quality of gelatins that could be used in food applications to replace mammalian gelatin. Therefore, the use of fish skin waste as raw material in the gelatin production is quite potential and plays a major role in recycling of waste.

Acknowledgement

The authors would like to express their profound gratitude to the Department of Higher Education, Ministry of Education, Yangon, Myanmar, for provision of opportunity to do this research and Myanmar Academy of Arts and Science for allowing to present this paper.

References

Benjakul, S., Oungbho, K., Visessanguan, W., Thiansilakul, Y. and Roytrakul, S. (2009). "Characteristics of Gelatin from the Skins of Bigeye Snapper, *Priacanthus tayenus* and *Priacanthus macracanthus*". *Food Chemistry*, vol. 116 (2), pp. 445-451

Chen, P. R., Kang, P. L., Su, W. Y., Lin, F. H. and Chena, M. H. (2005). The Evaluation of Thermal Properties and in Vitro Test of Carbodiimide or Glutaraldehyde Cross-linked Gelatin for PC 12 Cells Culture. *Biomedical Engineering Application, Basis and Communication*, vol. 17 (2), pp. 41-47

Cho, S. M., Kwak, K. S., Park, D. C., Gu, Y. S., Ji, C. I., Jang, D. H., Lee, Y. B. and Kim, S. B. l. (2004). "Processing Optimization and Functional Properties of Gelatin from Shark (Isurus oxyrinchus) Cartilage". *Food Hydrocolloid*, vol. 18(4), pp. 575–579

GME. (1990). Gelatin Manufacturer of Europe. http://www.gelatin.org. Accessed: 30 May 2020

Gomez-Guillen, M.C., Turnay, J., Fernandez-Diaz, M.D., Ulmo, N., Lizarbe, M.A. and Montero, P. (2002). "Structural and Physical Properties of Gelatin Extracted from Different Marine Species: A Comparative Study". *Food Hydrocolloids*, vol. 16, pp. 25-34

Jamilah, B. and Harvinder, K. G. (2002). "Properties of Gelatins from Skin of Fish-Black Tilapia (Oreochromis mossambicus) and Red Tilapia (Oreochromis nilotica)". *Food Chemistry*, vol. 77 (1), pp. 81-84

Johnston-Barks, F.A. (1990). *Gelatin*. In Food Gels. Harris, P. (Ed.). London: Elsevier Applied Food Science Series, pp. 150

Jones, N.R. (1997). *Uses of Gelatin in Edible Products*. In The Science and Technology of Gelatin. Ward, A. G. and Courts, A. (Eds). London: Academic Press Inc. pp. 366-394

Karim, A.A. and Bhat, R. (2009). "Fish Gelatin: Properties, Challenges, and Prospects as an Alternative to Mammalian Gelatins". *Food Hydrocolloids*, vol.23, pp. 563-576

Kittiphattanabawon, P., Benjakul, S., Visessanguan, W. and Shahidi, F. (2010). "Effect of Extraction Temperature on Functional Properties and Antioxidative Activities of Gelatin from Shark Skin". *Food and Bioprocess Technology*, vol. 5(7), pp.1-9

Nur Hanani, Z.A., Beatty, E., Roos, Y.H., Morris, M.A. and Kerry, J. P. (2012). "Manufacture and Characterization of Gelatin Films Derived from Beef, Pork and Fish Sources using Twin Screw Extrusion". *Journal of Food Engineering*, vol. 113, pp. 606–614

Ockerman, H. W. and Hansen, C. L. (1988). "Animal By-product Processing". *Ellis Horwood Series in Food Science and Technology*, pp. 366

Silverstein, R. M., Webster, F. X. and Kiemle, D.J. (2003). *Spectrometric Identification of Organic Compounds*. New York: 7th ed., John Wiley and Sons, Inc.

Ward, A.G. and Courts, A. (1977). *The Science and Technology of Gelatin*. New York: 2nd Edition, Academic Press Inc.

OPTICAL PROPERTIES OF UNDOPED ZINC OXIDE AND NICKEL DOPED ZINC OXIDE

Ei Ei Hpoo[1], Khin Than Yee [2], Cho Cho[3]

Abstract

The main aim of the research work is to study the optical properties of undoped ZnO and Ni doped ZnO. Undoped ZnO and Ni doped ZnO were prepared by using a co-precipitation method. The prepared undoped ZnO and Ni doped ZnO were characterized by Thermogravimetric-Differential Thermal Analysis(TG-DTA), X-ray Diffraction (XRD), Fourier Transform Infra-red (FT IR) spectroscopy, Energy Dispersive X-ray (EDX) spectrometry and Scanning Electron Microscopy (SEM) analyses.TG-DTA analysis of the synthesized undoped ZnO and Ni doped ZnO were carried out to determine the appropriate calcination temperature. From XRD analysis, it was observed that the average crystallite sizes of the prepared undoped ZnO and Ni doped ZnO were 28 and 22 nm, respectively. In FT IR spectra of undoped ZnO and Ni doped ZnO powder, the prominent peak of OH stretching, H-O-H bending and M-O stretching vibrations were observed. Morphological studies were conducted using SEM to confirm the uniform distribution of particles. UV-Visible spectrum showed the absorbance peaks in the 200-800 nm region. From UV-Visible spectral data, it was found that the band gap values of undoped ZnO and Ni doped ZnO are 2.7 and 2.8 eV, respectively.

Keywords: co-precipitation, optical properties, Ni doped ZnO, band gap

Introduction

Semiconductor nanoparticles are gaining much attention due to its peculiar physical and chemical properties. Metal oxide are widely used in commercial products such as catalysts, cosmetics, microelectronic devices, semiconductors, sporting goods, and textiles.

The optical properties of nanocrystalline semiconductors have been studied extensively in recent years. As the size of the material becomes smaller and the band gap becomes larger, this changes the optical and electrical properties of the material, making it suitable for new applications and devices. Among them, the widely accepted method to modify the electrical and optical properties of a semiconductor is the addition of impurity atoms, or doping (Devi and Velu., 2015).

Nanoparticles of ZnO are used in a variety of applications. They can be used as UV absorbent, antibacterial treatment material, catalytic agent and as an additive material in several industrial products. It is currently being used in the fabrication of solar cells, gas sensors, luminescent materials, transparent conductors, heat mirrors and coatings (Ghosh *et al*., 2015).

ZnO nanoparticles can be prepared on a large scale at low cost by simple solution based method, such as chemical precipitation, sol-gel synthesis, and hydrothermal reaction. Many of the earliest synthesis of nanoparticles were achieved by co-precipitation of sparingly soluble products from aqueous solution followed by thermal decomposition of those products to oxides. Co-precipitation method is a promising alternative synthesis method because of the low process temperature and easy to control the particle size. Some of the most commonly substances used in coprecipitation operations are hydroxides, carbonates, sulphates and oxalates.

The aim of this study is to investigate optical properties of undoped ZnO and Ni doped ZnO by using the co-precipitation method.

[1] PhD Candidate, Department of Chemistry, University of Yangon
[2] Dr, Lecturer, Department of Chemistry, West Yangon University
[3] Dr, Professor, Department of Chemistry, University of Yangon

Materials and Methods

Sample collection

Zinc sulphate heptahydrate, nickel (II)sulphate hexahydrate, ethylene glycol and sodium hydroxide were procured from BDH. Distilled water was used as the solvent in all analyses.

Preparation of Undoped Zinc Oxide and Nickel Doped Zinc Oxide by Co-Precipitation Method

The common salts $ZnSO_4.7H_2O$ (0.97 mol) and $NiSO_4.6H_2O$ (0.03 mol) were used as zinc and nickel precursors. Zinc sulphate was dissolved in distilled water. Next, the nickel sulphate for a final composition of NiO to ZnO were calculated and added to the solution. Then these solutions were mixed during continuous stirring. Next, 100 mL of 1 M NaOH solution was slowly added to the mixture under constant stirring until the pH of the solution reached to 10. During addition of NaOH solution, precipitates were started to appear. After addition of NaOH, 10 mL ethylene glycol was added immediately. The final solution was then stirred for 20 h at room temperature, so that homogeneity could be maintained. Then the sample was washed with distilled water several times until the pH was 7. After washing the sample was dried at 120 °C. The sample obtained was ground to make fine particles and it was calcined at 500 °C for 4 h in the muffle furnace. Finally, Ni doped ZnO powder was obtained. For the preparation of undoped ZnO, the same procedure as above was applied **(**Chauhan *et al.,* 2017**).**

Characterization of the Prepared Undoped ZnO and Nickel Doped Zinc Oxide Samples

Thermal properties of the prepared undoped ZnO and Ni doped ZnO were investigated by TG-DTA. The powder X-ray diffraction method was used to study the structural properties and the phase purity of the samples. The functional group of prepared undoped ZnO and Ni doped ZnO were identified using FT IR. The elemental composition of the prepared undoped ZnO and Ni doped ZnO were studied by using EDX analysis. The surface morphology of the prepared undoped and Ni doped ZnO were examined by SEM. The optical properties of prepared undoped ZnO and Ni doped ZnO were studied by UV-vis spectrophotometer in the range of 200 to 800 nm. Thermogravimetric analysis of sample was performed by using TG-DTA analyzer, (Hi-TGA 2950 model). The temperature was the range between 0 °C and 600 °C under nitrogen gas (at a rate of 50 mL/min). X-ray diffraction (XRD) analysis was carried out using Rigaku X-ray Diffractometer, RINI 2000/PC software, Cat.No 9240 J 101, Japan. Copper tube with nickel filter was used. The diffraction pattern was recorded in terms of 2θ in the range of 10-70 °. FT IR spectrum was recorded in the range of 4000-400 cm^{-1} by using 8400 SHIMADZU, Japan FT IR spectrophotometer. The scanning electron microscopy (SEM) images were obtained by using JSM-5610 Model SEM, JEOL-Ltd., Japan. The energy dispersive X-ray analysis was carried out using Phenom, Pro-X. The UV-Visible spectra of powder samples are observed in the 200-800 nm range by using UV-Visible spectrophotometer. The energy band gap was determined by using the relationship;

$$\alpha = A\,(h\upsilon - E_g)^n$$

"Where," $h\upsilon$ is photon energy, α is Absorption coefficient ($\alpha = 4\pi k/\lambda$), k is the absorption index or absorbance, λ is wavelength in nm, E_g is energy band gap, A is constant and the exponent n depends on the transition. The value of (n = 1/2, 3/2, 2, or 3 depends on the nature of the electronic transition (1/2 for allowed direct transition, 2 for allowed indirect transition, 3/2 and 3 for forbidden direct and forbidden indirect transitions, respectively).

Results and Discussion

Undoped ZnO and Ni doped ZnO powder were prepared by using co-precipitation method. The resultant prepared samples were characterized by modern techniques (TG-DTA, XRD, FT IR, EDX and SEM).

Thermal Analysis of the Prepared Undoped ZnO and Ni Doped ZnO

Thermogravimetric analysis (TGA) and differential thermal analysis (DTA) thermograms of prepared undoped ZnO and Ni doped ZnO are shown in Figure 1. Weight loss percent of undoped ZnO and Ni doped ZnO are listed in Table 1. TGA curve of prepared undoped ZnO and Ni doped ZnO indicated the two stages of decomposition (Figure 1). Endothermic peaks observed at 91 °C and 150 °C for undoped ZnO and Ni doped ZnO with 1.96 and 2.82 % weight loss were due to the evaporation of loosely bound water of the samples. Endothermic peaks observed at 288 °C and 268 °C for undoped ZnO and Ni doped ZnO with 10.20 and 15.66 % weight losses, respectively, were due to the decomposition of $Zn(OH)_2$, which was formed by absorption of water, and then was converted to ZnO and Ni doped ZnO. Total weight loss of undoped ZnO and Ni doped ZnO were given in Table 1.

XRD Analysis of the Prepared Undoped ZnO and Ni Doped ZnO

The powder x-ray diffraction methods are used to study the structural properties and the phase purity of the samples. Figures 2 shows the XRD pattern of prepared undoped ZnO and Ni doped ZnO. The average crystallite sizes of prepared samples were calculated using the Debye Scherrer equation.

$$D = k\lambda/\beta Cos\theta$$

Where k is constant equal to 0.94, D and λ are the crystallite size in nanometers and wavelength of the radiation (1.54056 Å for Cu K_α radiation), respectively. B and θ are the peak width at half-maximum intensity (FWHM) and peak position, respectively. The volume of unit cell for hexagonal system has been calculated from the following equation.

$$V = 0.866a^2c$$

The bond length L for Zn-O is given by $L = \sqrt{(\frac{a^2}{3} + \left(\frac{1}{2} - u\right)^2 c^2)}$. The parameter *u* in the Wurtzite structure is given by $u = \frac{a^2}{3c^2} + 0.25$.

The average crystallite size of undoped ZnO is found to be 28 nm. The average crystallite size for Ni doped ZnO was found to be 22 nm which is lower than 28 nm for undoped ZnO. Interestingly, doping of Ni^{2+} shows no additional peaks, which confirms no additional impurity phase formation. The lattice parameters a and c for undoped ZnO and Ni doped ZnO are presented in Table 2. The change in a and c lattice parameters are observed due to Ni- doping. The decrease in lattice parameters can be attributed to the replacement of larger Zn^{2+} ions with smaller Ni^{2+} ions.

The wurtzite structure attained from the diffraction peaks indicate that Ni^{2+} is successfully incorporated into the ZnO lattice, which further means no changes in the crystal lattice by the Ni doping.

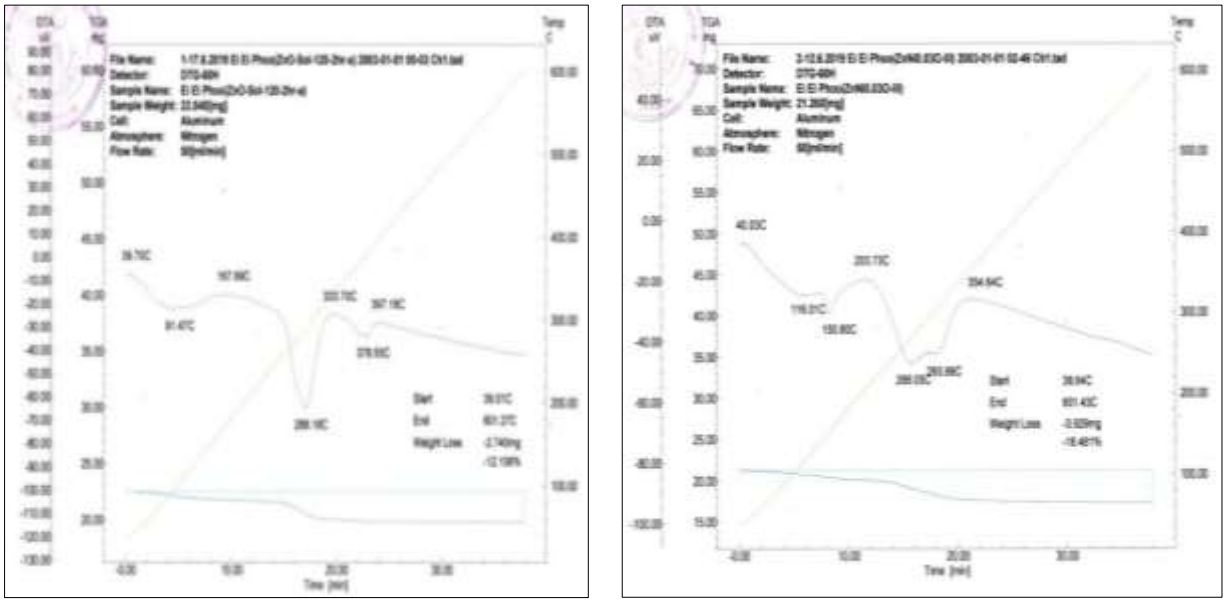

(a) (b)

Figure 1 TG-DTA thermograms of prepared (a) undoped ZnO and (b) Ni doped ZnO

Table 1 Total Weight Loss Percent of Prepared Undoped ZnO and Ni Doped ZnO from TG-DTA Analyses

Sample	Temperature Range(°C)	Nature of Peak	Weight Loss (%)	Total Weight Loss (%)
Undoped ZnO	38-170 170-450	endothermic	1.96 10.20	12.16
Ni doped ZnO	38-170 170-450	endothermic	2.82 15.66	18.48

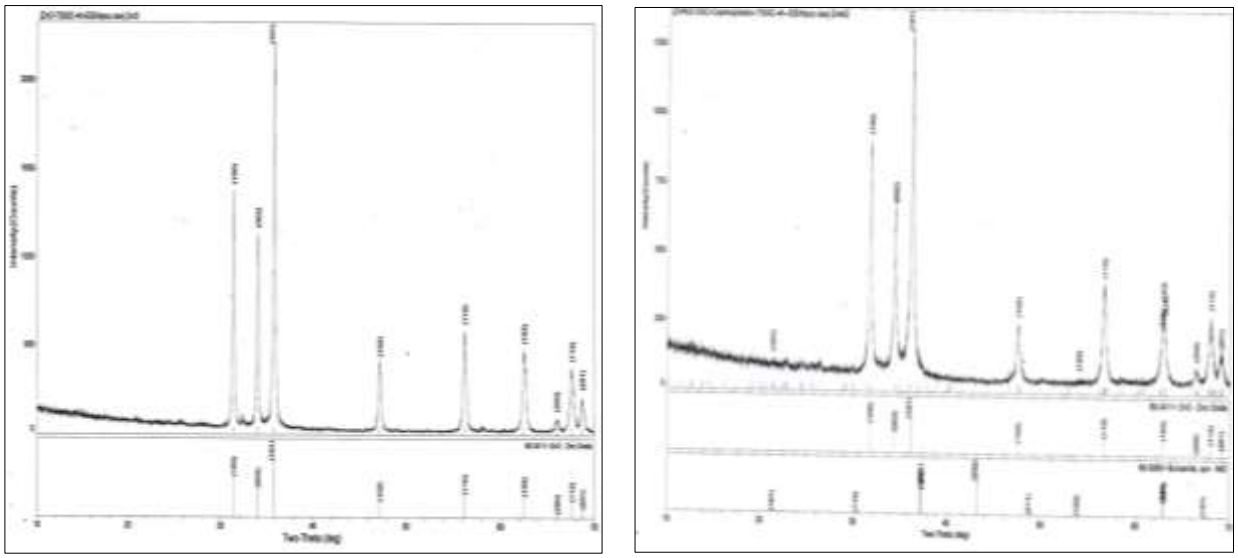

(a) (b)

Figure 2 XRD patterns of prepared (a) undoped ZnO and (b) Ni doped ZnO

Table 2 XRD Analyses of Prepared Undoped ZnO and Ni Doped ZnO

Samples	c	a=b	c /a	Crystallite Sizes from XRD (nm)	Crystallite Sizes from Debye- Scherrer formula (nm)	Volume (Å)^3	Zn-O bond length (Å)
Undoped ZnO	5.2345	3.2852	1.5934	30	28	48.92	1.99
Ni doped ZnO	5.2051	3.2494	1.6019	23	22	47.59	1.98

FT IR Analysis of the Prepared Undoped ZnO and Ni Doped ZnO

Figure 3 shows the FT IR spectra of prepared undoped ZnO and Ni doped ZnO. The assignment data is summarized in Table 3. In the spectra of prepared undoped ZnO and Ni doped ZnO, the peak observed at 3439 cm^{-1} and 3404 cm^{-1} for undoped ZnO and Ni doped ZnO, respectively, correspond to O-H stretching vibration and the peak at 1628 cm^{-1} and 1631 cm^{-1} for undoped ZnO and Ni doped ZnO, repectively, correspond to H-O-H bending vibration which are related to the absorbed water on the surface of nanomaterial. Another intense absorption peak at 435 cm^{-1} and 445 cm^{-1} for undoped ZnO and Ni doped ZnO, respectively are related to the stretching vibrations of the Zn-O bond (Table 3) (Silverstein *et al*., 2003; Nakamoto, 1970).

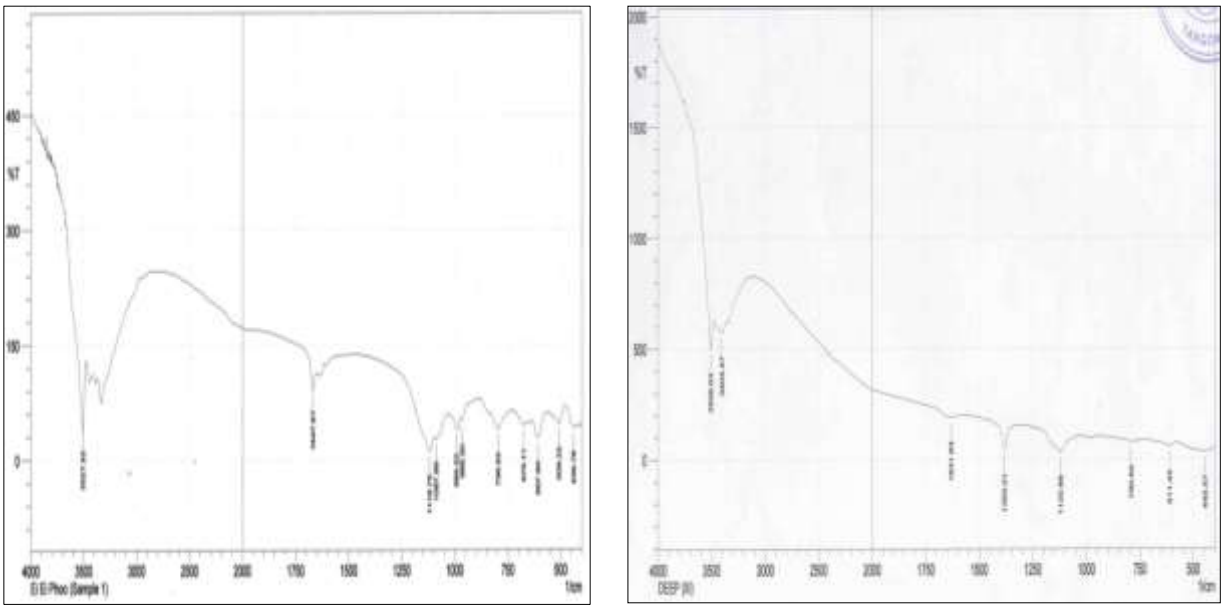

(a) (b)

Figure 3 FT IR spectra of the prepared (a) undoped ZnO and (b) Ni doped ZnO

SEM Analysis of the Prepared Undoped ZnO and Ni Doped ZnO

Figure 4 shows the morphological differences between the prepared undoped ZnO and Ni doped ZnO. The SEM images reveal the formation of homogeneous and uniformly distributed particles. The average crystallite size was found to decrease by doping Ni into the ZnO matrix. The decrease in the crystallite size is mostly ascribed to the formation of Ni-O-Zn on the surface of the doped nanoparticles, which prevents the growth of crystal grains and assists separation of particles.

EDX Analysis of the Prepared Undoped ZnO and Ni Doped ZnO

The chemical compositions of prepared undoped ZnO and Ni doped ZnO were measured by EDX spectra and shown in Figure 5. The EDX shows signals of all the expected elements Zn, O and Ni, which confirms the presence of Ni^{2}+ ions which are substituting the Zn^{2+} ions in the Zn matrix.

Table 3 FT IR Band Assignments of the Prepared Undoped ZnO and Ni Doped ZnO

Observed wavenumber (cm^{-1})		*Literature wavenumber (cm^{-1})	Band Assignment
Undoped ZnO	Ni doped ZnO		
3439	3404	3500-3200	O-H stretching
1628	1631	1655-1630	H-O-H bending
607	611	650-420	Zn-O stretching (or)
435	445		Ni-O stretching

*(Silverstein *et al*., 2003; Nakamoto, 1970)

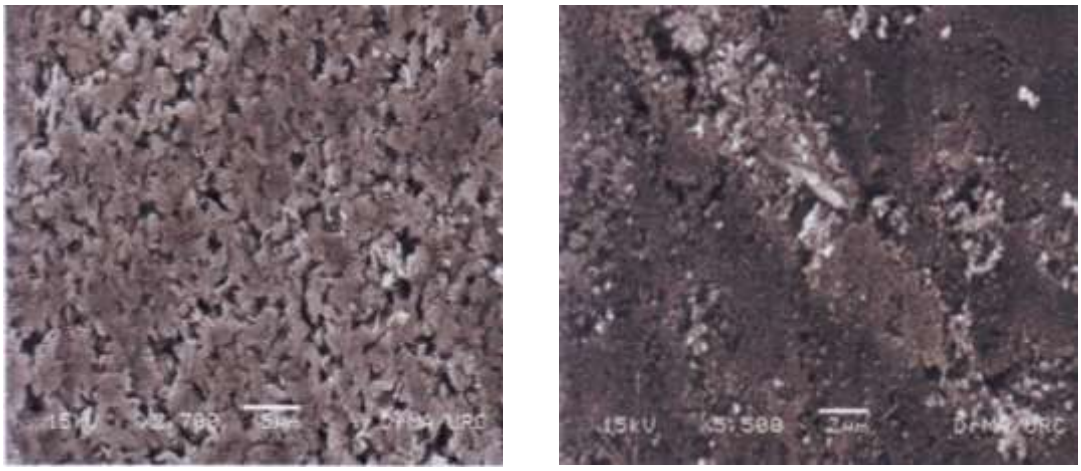

(a) (b)

Figure 4 SEM micrographs of the prepared (a) undoped ZnO and (b) Ni doped ZnO

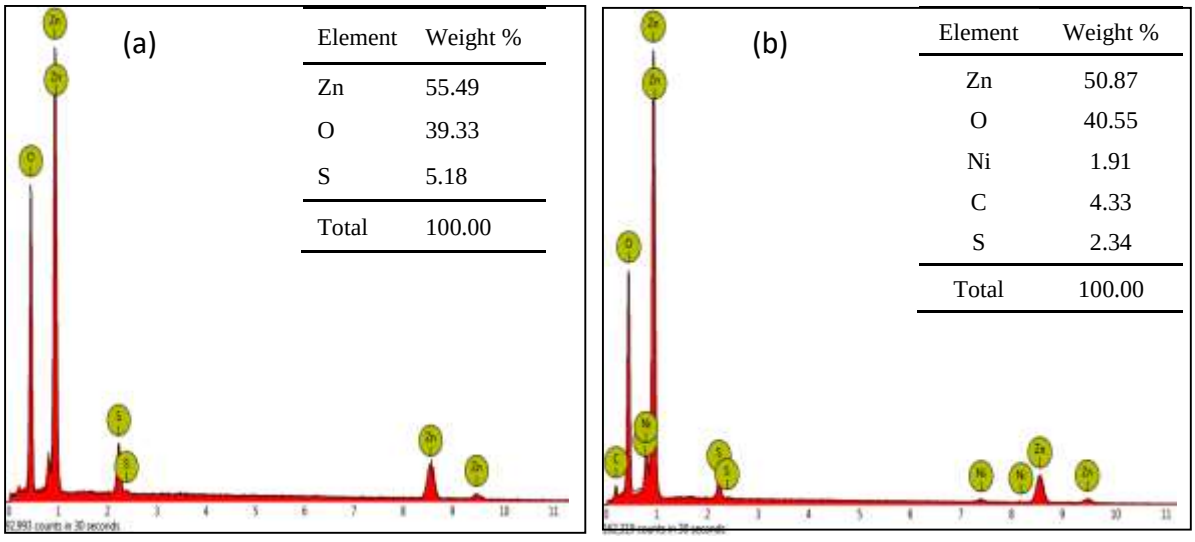

Figure 5 EDX spectra of the prepared (a) undoped ZnO and (b) Ni doped ZnO

UV-vis Analysis of the Prepared Undoped ZnO and Ni Doped ZnO

In UV-vis absorption spectra, peaks are found at 382 and 370 nm for undoped ZnO and Ni doped ZnO, respectively, as shown in Figures 6 (a) and (b). The position of the absorption spectra was observed to shift toward the shorter wavelength side for Ni doped ZnO. This indicates that the band gap of ZnO material increases with the doping Ni^{2+} ions.

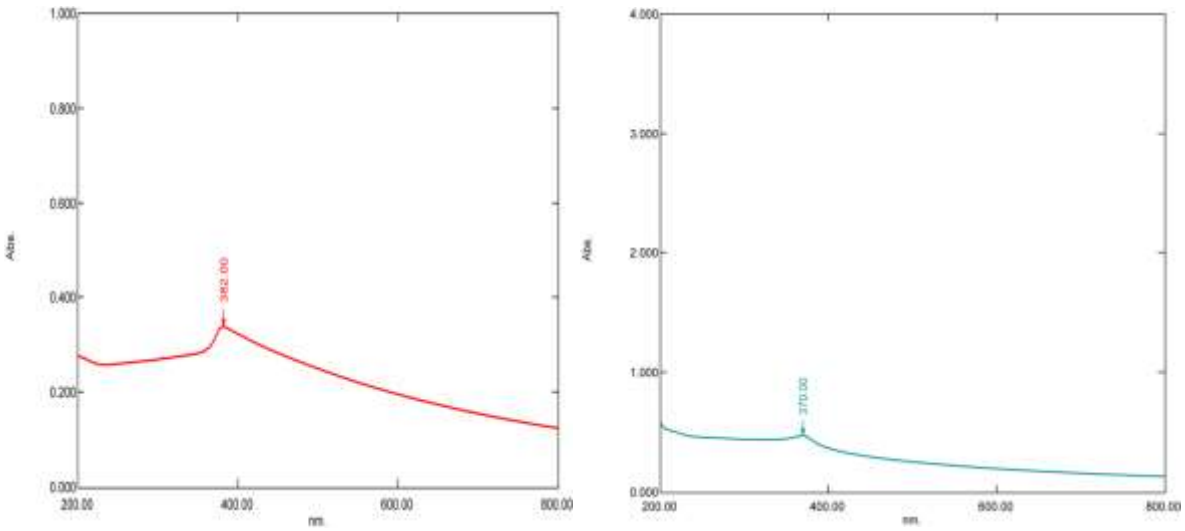

Figure 6 UV-visible spectra of the prepared (a) undoped ZnO and (b) Ni doped ZnO

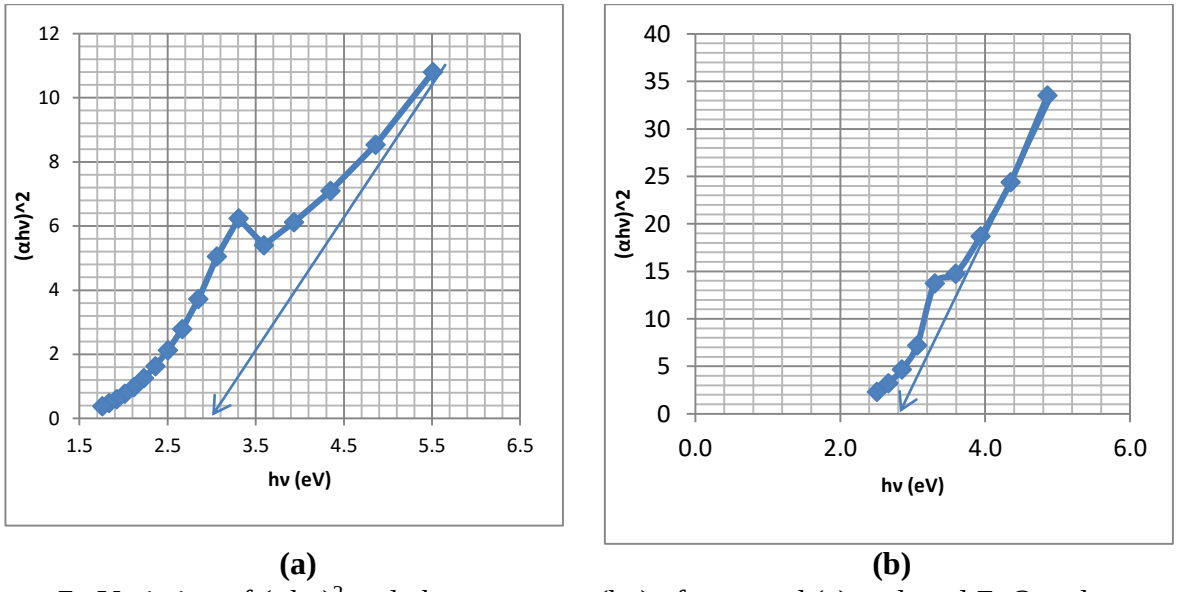

(a) **(b)**

Figure 7 Variation of $(\alpha hv)^2$ and photon energy (hv) of prepared (a) undoped ZnO and (b) Ni doped ZnO

Optical Properties

The relationship between absorption coefficient, the energy of the incident photon (hv) and near absorption edge of semiconductors is given by the Taucs' relation. The electronic transition is represented in Figure 7. The optical energy band gap E_g is determined by extrapolating the straight portion of this plot to the photon energy in x-axis and it reveals that the value of band gaps were found to be 2.7 eV and 2.8 eV for undoped ZnO and Ni doped ZnO. The decrease in the band gap may be due to the sp-d exchange interaction present between the band electrons and the localized d electrons of the substituted divalent ions (Abood *et al*., 2017).

Conclusion

In this study, the structural and optical properties of prepared undoped ZnO and Ni doped ZnO were prepared by using chemical co-precipitation method. Structural investigation of the undoped ZnO and Ni doped ZnO showed a decrease in lattice parameter. Optical properties and band gap were determined by UV-Visible spectra. The energy band gap values for prepared undoped ZnO and Ni doped ZnO were found to be decreased from 2.7 to 2.8 eV. The observations of Ni doped ZnO reveal that this sample can be chosen as a semiconductor material to be used as photocatalyst.

Acknowledgement

The authors would like to express their profound gratitude to the Department of Higher Education, Ministry of Education, Yangon, Myanmar, for provision of opportunity to do this research and Myanmar Academy of Arts and Science for allowing to present this paper.

References

Abood, I., Gadalla, A. A. and Elokr, M. M. (2017). "Structural, Optical and Magnetic Properties of Ni-Doped ZnO Synthesized by Co-Precipitation Method". *Journal of Nanotechnology Material Science*, vol. 4(1), pp. 19-26

Chauhan, J., Shrivastav , N., Dugaya, A. and Pandey, D. (2017). "Synthesis and Characterization of Ni and Cu doped ZnO". *MOJ Polymer Science*, vol. 1, pp. 26-34

Devi, P. G. and Velu, A. S. (2015). "Synthesis by Coprecipitation Method, Structural and Optical Properties of ZnO and Nickel Doped ZnO Nanoparticles". *Journal of Advanced Applied Scientific Research*, vol.1, pp.130-137

Ghosh, A., Kumari, N. and Bhattacharjee, A. (2015). "Influence of Cu Dopping on the Structural, Electrical and Optical Properties of ZnO". *Journal of Physics*, vol. 84, pp.621-635

Nakamoto, K. (1970). *Infrared Spectra of Inorganic and Coordination Compound*. New York: 2nd Edition, Wiley Interscience Publication

Silverstein, R. M., Webster,F. X.and Kiemle,D. J. (2003). *Spectrometric Identification of Organic Compounds*. New York: 7th Edition, John Wiley and Sons, Inc.

ASSESSMENT OF HEAVY METALS POLLUTION AND DEGREE OF CONTAMINATION IN THE HEINDA MINING AREA, DAWEI TOWNSHIP

Myo Than[1], Soe Soe[2], Phyu Phyu Myint[3], Saw Hla Myint[4]

Abstract

In this research, five soil samples from the mining sites and one from control site from mining works were collected from Heinda mining areas in Dawei Township, Tanintharyi Region in March, 2019. Physicochemical properties of collected soil samples (S_1, S_2, S_3, S_4, and S_5 from the industrial mining sites and undisturbed site (S_0) were determined. All soil samples were nearly neutral in the pH range of 6.32-7.03. Moisture of soil samples were in the range of 0.11- 0.40. Soil types of soil samples were found to be loamy sand for S_0, and sand for S_1, S_2, S_3, S_4 and S_5. In addition, the concentrations of some heavy metals (Pb, Cd, Mn, Zn, Fe, Cu) contents in soil samples were analysed by Atomic Absorption Spectrophotometric method. According to AAS method, Pb contents of soil samples (S_0, S_1, S_2, S_3, S_4, S_5) were not detected. However, Cd contents were observed as 0.05, 0.04, 0.04, 0.07, 0.04, and 0.03 ppm, respectively. Moreover, 6.04, 54.26, 31.42, 19.76, 40.10, and 36.86 ppm of Mn, 0.35, 0.65, 0.69, 0.67, 0.77, and 0.62 ppm of Zn, 39.02,48.02, 49.76, 45.41, 48.06 and 44.46 ppm of Fe and then, 0.50 ppm of Cu was observed for S_0, but not detected for S_1, S_2, S_3, S_4 and S_5. The contamination factor (C_f), degree of contamination (C_d) and pollution load index (PLI) were used to assess the degree of heavy metal pollution in soil. According to PLI, the sites were classified as moderately contaminated with Zn, considerably contaminated with Fe, and highly contaminated with Mn compared to control site.

Keywords: Heinda mining areas, heavy metals, contamination factor, degree of contamination, pollution load index

Introduction

Some heavy metals are either essential nutrients (such as iron, cobalt and zinc), or relatively harmless (such as ruthenium, silver, and indium), but can be toxic in larger amounts (Moe Thu Zar Lwin, 2012). Due to the many anthropogenic activities in industrial areas, soil may get polluted which may cause major heavy metal contaminations and which is more responsible for increasing the pollutants in the soil (Alessio *et al*., 2007). Other heavy metals, such as cadmium, mercury, and lead are highly poisonous. Potential sources of heavy metal poisoning include mining, tailings, industrial-wastes, agricultural-runoff and treated timber (Miller *et al*.,1965).

With the rapid development of mining activities landscape changes as well as environmental pollution have become still more serious (Yao *et al*., 2003). The intense mineral extraction has produced a large amount of waste material accumulated on the heaps or tailings (Ashraf and Ali, 2007). In Myanmar, Heinda Mine is a large old tin mine in the northern part of the Great Tanintharyi River Basin in Tanintharyi Region. The mine is in the proximity of Myitta town and around 45 km away from Dawei city. Current concession area of the tin mine covers around 2,110 acres of land. The area includes three open-pit placer mines Around 2 km downstream from the mining site located "Myaung Pyo" village which is the community most directly and adversely affected by the mining operation.

The Heinda mine is tin ore mine, the pollution from the Heinda mine and wastewater from the mine's overflowing tailing ponds have contaminated the Myaung Pyo creek, the source of the surrounding communities' water for drinking, domestic use and irrigation. The wastewater also

[1] Lecturer, Department of Chemistry, Dawei University
[2] Lecturer, Department of Chemistry, Dawei University
[3] Dr, Professor, Department of Chemistry, Loikaw University
[4] Dr, Professor (Retd.), Department of Chemistry, University of Yangon

impacts farmland, reportedly damaging the quality of soil. These changes have allegedly caused health problems and disrupted the livelihoods of communities in the area. The communities rely on agriculture, cultivating betel nut, rubber, durian, coconut, vegetables, cashews and bananas to sell. Though the project affected over a dozen villages, one of the most impacted was Myaung Pyo village, located 2 km from the mining site (Gardiner *et al*., 2015). The aim of the study was to determine the level of contamination with heavy metals in this area and to assess the level of contamination using the contamination factor, degree of contamination, and pollution load index.

Materials and Methods

Sample Collection and Sample Preparation

Soil sampling from six sampling sites of Heinda mining area were carried out in March, 2019. Heinda mine is located at 14°7' 52.048" N latitude and 98°26' 12.825" E longitude, Dawei Township, Tanintharyi Region. The total area of Heinda mine is about 2110 acres. The study area and study stations are given in Figure 1.

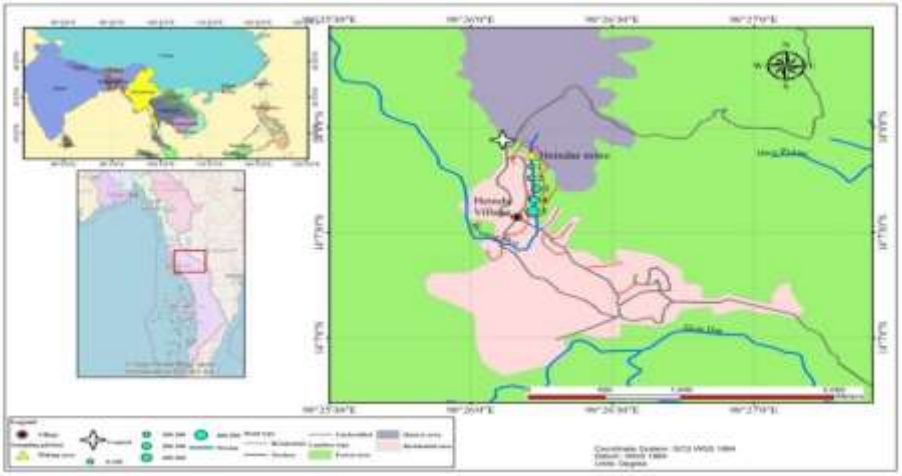

Figure 1 Location of sampling sites on the Heinda mine area

Soil samples were collected from six different stations situated in mining sites and control site of the mining works of Heinda mine. Sampling stations (S_1) was selected within 100 m from the mine and (S_2, S_3, S_4 and S_5) were selected within 100 m of each other. The station, S_0 is the control station, 285 m away, in the north east side of the mining site, and is in a benign environment. The description of the sampling stations is given in Table 1.

Soil samples were taken about 20 cm depth from the surface of the soil. From each sampling site five samples were collected within (2 m × 2 m) square and the collected soil samples were dried in the shade before sieving. Afterwards, the impurities such as gravel, roots, were discarded. Then, these soil samples were ground into fine powder and passed through a 0.2 mm sieve. The soil samples were stored in polyethylene bags and clearly labeled before measurement.

Table 1 GPS and Altitude Information of Sampling Sites on Heinda Mine Area

Sampling Sites	Description	GPS Coordination		Altitude above sea level (m)
		Latitude (N)	Longitude (E)	
S_0	285 m up from work site	14° 7' 56.453"	98° 26' 4.492"	332
S_1	100 m (S) down from site	14° 7' 48.793"	98° 26' 12.833"	267
S_2	200 m (S) down from site	14° 7' 45.538"	98° 26' 12.826"	265
S_3	300 m (S) down from site	14° 7' 42.486"	98° 26' 13.986"	260
S_4	400 m (S) down from site	14° 7' 39.274"	98° 26' 13.446"	258
S_5	500 m (S) down from site	14° 7' 36.035"	98° 26' 13.119"	256

Physicochemical Analysis of Soil Samples

Six soil samples were obtained from six sampling sites of Heinda mine. Some physicochemical parameters of soil samples were determined by using the following procedures. An appropriate clean porcelain crucible was dried and then weighed. A 1 g of accurately weighed air-dried sampling soil was placed in the crucible. The crucible and contents were weighed. Then, it was heated in the oven at 105-110 °C for 3h. Just after removal from the oven, it was allowed to cool in a desiccator. The crucible and dried sample were weighed again. The process of heating, cooling and weighing was repeated until a constant weight was obtained (Hinojosa *et al*., 2004). To a 5 g of soil sample in a 50 mL beaker, 50 mL of deionized water was added to the sample. Then, the electrode of pH was placed in the slurry, swirled carefully and measured the pH with a pH meter.

To determine the composition of soil, a 50 g of soil sample was weighed and placed in a 500 mL conical flask. Then 125 mL of distilled water and 50 mL of 10 % sodium pyrophosphate solution were added to disperse the soil colloids and heated for 15 min and cooled down and the solution were made up to the mark with distilled water and then kept overnight to allow the soil colloids to settle. Then, the contents were stirred for about 4 min. From the residue, the percentage of clay, silt and sand were calculated (Jackson, 1958).

Determination of Heavy Metal Contents (Pb, Cd, Mn, Zn, Fe, Cu) by AAS

A 1 g of soil sample was accurately weighed and placed in a 250 mL beaker and then treated with 10 mL aliquots of high purity concentrated nitric acid. The mixture was heated to dry on a sand bath and then cooled. This procedure was repeated with another 10 mL concentrated nitric acid followed by 10 mL of concentrated hydrochloric acid. The digested soil samples were then warmed in 20 mL of 2 M hydrochloric acid to re-dissolve the metal salts. Extracts were filtered through Whatman No. 40 filter paper and the volume was then adjusted to 40 mL with deionized water. The heavy metal concentrations in the above solutions were determined by Atomic Absorption Spectrophotometeric (AAS) method.

Assessment of soil contamination

The contamination factor (C_f) was used to assess the enrichment of trace metals in the soils and to measure the pollution levels. The C_f of individual metal is the ratio of metal concentration in the soil (C_i) and the background value of the same metal (concentration of the metal in undisturbed soil, C_0). The C_f is computed using the following equation.

$$C_f = C_i/C_0$$

The degree of contamination, C_d, is defined as the sum of all contamination factors for various heavy metals. In order to facilitate the pollution control "degree of contamination (C_d)" was proposed by Hakanson which is obtained as follows:

$$C_d = \sum C_{fi}$$

Pollution load index (PLI) is an index for evaluation of contamination status of soil samples to heavy metals. PLI is defined as follows:

$$PLI = (C_{f1} \times C_{f2} \times C_{f3} \times \ldots \times C_{fn})^{1/n}$$

Results and Discussion

Some Characteristics of Soil Samples from Heinda Mine Area

Some properties of six soil samples from Heinda mining areas such as pH, moisture and texture values were determined. pH of the undisturbed site (S_0), was 6.32. The soil from this control site was acidic. Moreover, it was found that other five sites, S_1, S_2, S_3, S_4, and S_5 have nearly neutral of pH 7. The moisture percent of control site (undisturbed soil) was the lowest, i.e., 0.11%. The location of other sites, S_1 through S_5 were in the middle of the small stream. This stream dried up in summer season, however, there were a little of water in some sites of S_1 and S_4. So these sites were found to have higher moisture percent than the others. The textural type of control site was loamy sand and those of other sites of S_1 through S_5. were sand. Table 2 shows some characteristics of soil samples from Heinda mine area.

Table 2 Some Characteristics of Soil Samples from Heinda Mine Area

Sampling Sites	pH	Moisture (%)	Texture
S_0	6.32	0.11	loamy sand
S_1	6.77	0.24	sand
S_2	6.71	0.13	sand
S_3	6.93	0.16	sand
S_4	6.91	0.40	sand
S_5	7.03	0.15	sand
Min-max	6.32- 7.03	0.11- 0.40	

Heavy Metals (Pb, Cd, Mn, Zn, Fe, Cu) Contents in Soil Sample from Heinda Mine Area

In this study, the heavy metal contents (Pb, Cd, Mn, Zn, Fe, Cu) of the six soil samples from Heinda mine area in Dawei Township, Tanintharyi Region were determined. Table 3 and Figure 2 show the levels of heavy metals in six soil samples from Heinda mine. Pb content was not detected in these six soil samples. Cd content of S_3, 0.07 ppm was the highest content, however, Cd contents in other sites, S_0, S_1, S_2, S_4 and S_5 were nearly the same i.e., 0.05 ppm, 0.04 ppm, 0.04 ppm, 0.04 ppm and 0.03 ppm, respectively. Cd contents were below the allowable limit of 0.8 ppm. Although Mn content was observed as the highest in S_1 (54.26 ppm), it was found within the allowable limit of 300 ppm. Zn contents were also found within the allowable limit of 50 ppm. The highest content of Zn, 0.77 ppm was observed in S_4 and the lowest content of Zn, 0.35 ppm was found in S_0. Fe content in S_0, 39.02 ppm, was the lowest in all soil samples, because this site is situated in undisturbed area of mining works. Cu content was observed in S_0, 0.50 ppm, but Cu content was not detected in other sites of S_1, S_2, S_3, S_4 and S_5. Pb, Cd, Mn, Zn, Fe, and Cu contents were within the allowable limits of WHO (1996).

Table 3 Heavy Metal Contents of Soil Samples from Heinda Mine Area

Sampling Sites	Heavy Metal Contents (ppm)					
	Pb	**Cd**	**Mn**	**Zn**	**Fe**	**Cu**
S_0	ND	0.05	6.04	0.35	39.02	0.50
S_1	ND	0.04	54.26	0.65	48.02	ND
S_2	ND	0.04	31.42	0.69	49.76	ND
S_3	ND	0.07	19.76	0.67	45.41	ND
S_4	ND	0.04	40.10	0.77	48.06	ND
S_5	ND	0.03	36.86	0.62	44.46	ND
Min- max	ND	0.03- 0.07	6.04-54.26	0.35-0.77	39.02-49.76	ND- 0.50
*Permissible limit	85	0.8	300	50	300	36

*WHO (1996)

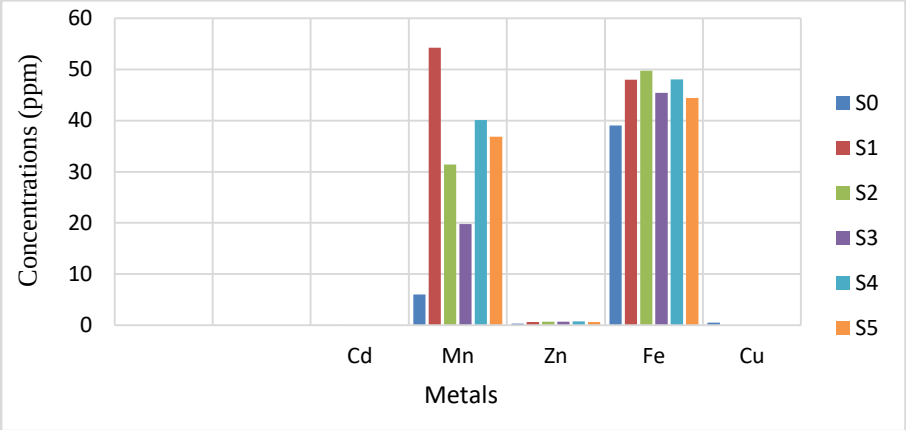

Figure 2 Heavy metal contents of soil samples in Heinda mine area

Contamination Factor (C_f), Degree of Contamination (C_d) and Pollution Load Index (PLI) for Each Sampling Site in Heinda Mine Area

For determination of metal pollution in soils, contamination factor (C_f) and degree of contamination (C_d) were used. The C_f was classified into four levels of pollution: $C_f < 1$ represents no or minimal pollution; $1 < C_f < 3$ indicates moderate pollution; $3 < C_f < 6$ indicates considerable pollution; and $C_f > 6$ indicates very high pollution (Zaigham *et al*., 2012). The range of C_f values were 0.65-1.44 for Cd, 3.27-8.99 for Mn, 1.77-2.21 for Zn and 1.14-1.28 for Fe. The results indicated that the surface soil in the Heinda mining area were moderately polluted by Zn and Fe. In contrast, Cd exhibited low concentration. However, it is noteworthy that several sampling sites showed considerable contamination of Mn and moderate contamination of Zn and Fe.

The C_d was also divided into four groups as follows: (i) low degree of contamination $C_d < 8$), (ii) moderate degree of contamination ($8 \leq C_d < 16$), (iii) considerable degree of contamination ($16 \leq C_d < 32$), and (iv) very high degree of contamination ($C_d \geq 32$) (Zorpas *et al*., 2002). The calculated C_d range of soil samples were in the range of 7.79-12.83. The results indicated that the surface soils of site 1, site 2, site 4 and site 5 in the Heinda mining area were found to be moderately contaminated. In contrast, site 3 exhibited low concentration. Pollution load index (PLI) is an empirical index that comparatively assesses the level of heavy metal pollution for each sampling site (Aydinalp and Marinova, 2004). Site 1 was the highest degree of

contamination degree and highest pollution load index. The results are shown in Table 4 and Figure 3.

Table 4 The Values of Contamination Factor (C_f), Degree of Contamination (C_d) and Pollution Load Index (PLI) for Sampling Sites in Heinda Mine Area

Sampling Sites	C_f						C_d	PLI
	Pb	Cd	Mn	Zn	Fe	Cu		
S_1	ND	0.85	8.99	1.85	1.23	ND	12.83	2.04
S_2	ND	0.73	5.20	1.96	1.28	ND	9.17	1.76
S_3	ND	1.44	3.27	1.92	1.16	ND	7.80	1.80
S_4	ND	0.85	6.61	2.20	1.23	ND	10.93	1.98
S_5	ND	0.65	6.11	1.77	1.14	ND	9.66	1.68
Min-max	ND	0.65- 1.44	3.2- 8.99	1.77-2.20	1.14-1.28	ND	7.80 -12.83	1.68-2.04

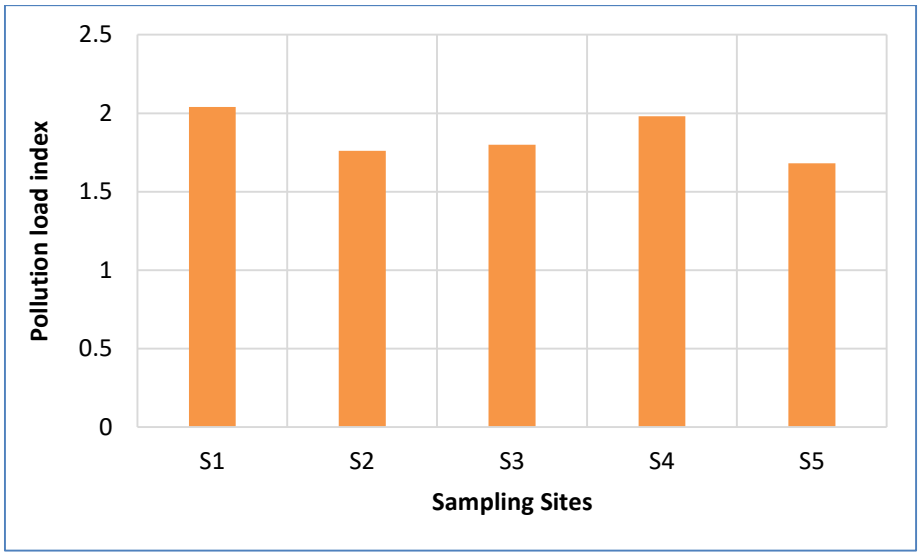

Figure 3 Pollution load index of each sampling site in Heinda mine area

Conclusion

In this research work, six soil samples were collected from Heinda mine area in March, 2019. According to the physicochemical analysis, the moisture percent of S_4, 4.4%, was the highest content. The pH values for S_0, S_1, S_2, S_3, S_4, and S_5 were 6.32, 6.77, 6.71, 6.93, 6.91 and 7.03 respectively. Soil types of S_1, S_2, S_3, S_4, and S_5 were found to be sand and S_0 was found to be loamy sand. According to the AAS results, Pb was not detected for all sampling sites. Minimum and maximum contents were observed to be 0.03 and 0.07 ppm of Cd, 6.04 ppm and 54.26 ppm of Mn, 0.35 ppm and 0.77 ppm of Zn, 39.02 ppm and 49.76 ppm of Fe and ND and 0.50 ppm of Cu. The degree of contamination (C_d) of soil samples showed site 3 < site 2 < site 5 <site 4< site 1. The pollution load index (PLI) of soil samples showed site 5< site 2 < site 3 < site 4<site 1. Based on results, site 1 and site 4 have higher C_d and higher PLI than other sites due to the accumulation of mine waste near these sites. However, the heavy metals in soil samples were under the permissible contamination levels.

Acknowledgement

The authors would like to express their profound gratitude to the Department of Higher Education, Ministry of Education, Yangon, Myanmar, for provision of opportunity to do this research and to Myanmar Academy of Arts and Science for allowing to present this paper.

References

Alessio, L., Compagna, M. and Lucchini, R. (2007). "From Lead to Manganese through Mercury: Mythology, Science and Lessons for Prevention". *American Journal of Industrial Medicine,* vol. 50(11), pp.779 - 787

Ashraf, R. and Ali, T. A. (2007). "Effect of Heavy Metals on Soil Microbial Community and Mung Beans Seed Germination". *Pakistan Journal of Botany*, vol. 39 (2), pp. 629- 636

Aydinalp, C. and Marinova, S. (2004). "Lead in Particulate Deposits and in Leaves of Road-side Plants". *Pol. J. of Environ Studies,* vol. 13, pp. 233-235

Gardiner, N., Sykes, J. Trench, A. and Robb, L. (2015). "Tin Mining in Myanmar''. *Production and Potential. Resources Polic*y, vol. 46 (2), pp. 219-233

Hinojosa, M.B., Carreira, J.A. Ruız R.G.and Dick, R.P. (2004). "Soil Moisture Pre-treatment Effects on Enzyme Activities as Indicators of Heavy Metal Contaminated and Reclaimed Soils". *Soil Biology and Biochemistry*, vol. 36, pp. 1559-1568

Jackson, M. L. (1958). *Soil Chemical Analysis*. New Jersey: Prentice Hall Inc., pp. 214-221

Miller, C. E., Truk, L. M. and Foth, H. D. (1965). *Fundamentals of Soil Science*. 4th Edn., New York: John Wiley and Sons Inc., pp. 101-103

Moe Thu Zar Lwin. (2012). *Environmental Study on Heavy Metals (Pb, Cd, Cu, Zn) Contamination in Roadside Soil and Plant Samples at Phayathonzu Village on Yangon-Bago Highway*. PhD Dissertation, Department of Chemistry, University of Yangon, Myanmar

WHO. (1996). *Permissible Limits of Heavy Metals in Soil and Plants*. Geneva: World Health Organization, Switzerland.

Yao, H., Xu J. and Huang, C. (2003). "Substrate Utilization Pattern, Biomass and Activity of Microbial Communities in A Sequence of Heavy Metal Polluted Paddy Soils". *Geoderma,* vol. 115, pp. 139-148

Zaigham, H. A., Zubair, U.K. Khalid, I. Mazhar, U. Rizusan K. and Jabar, Z. K. (2012). "Civic Pollution and Its Effect on Water Quality of River Toi at District Kohat, NWFP". *Research Journal of Environmental and Earth Sciences,* pp. 4,5

Zorpas, A.A., Vassilis, I. Loizidou, M. and Grigoropoulou, H. (2002). "Particle Size Effects on Uptake of Heavy Metals from Sewage Sludge Compost Using Natural Zeolite Clinoptilolite". *Journal of Colloid and Interface Science,* vol. 250, pp.1– 4

PREPARATION AND CHARACTERIZATION OF ZINC SULPHIDE NANOPARTICLES USING HONEY AS CAPPING AND STABILIZATION AGENTS

Phyu Phyu Zan[1], Yee Mun Than[2], Myat Kyaw Thu[3]

Abstract

Zinc sulphide (ZnS) nanoparticles were successfully prepared by using Zn $(NO_3)_2.6H_2O$ and Na_2S as precursors and different volumes of honey as capping and stabilizing agents. The structural, morphological, thermal and optical properties of as synthesized nanoparticles were investigated using x-ray diffraction (XRD), transmission electron microscopy (TEM), scanning electron microscopy- energy dispersive x-rays spectroscopy (SEM-EDX), Fourier transform infrared spectroscopy (FT IR), thermogravimetric differential thermal analysis (TG-DTA) and UV-visible spectroscopy. ZnS nanoparticles were indexed as hexagonal crystal structure with particles size ranging from 12.9 to 17.2 nm. The average particle size was also measured by TEM using image J software. EDX analysis revealed the high purity of synthesized zinc sulphide nanoparticles. From TG-DTA analysis and FT IR, biomolecules were involved in synthesis of ZnS nanoparticles because of the presence of organic compounds. *The ultraviolet absorption spectra showed the blue shift in absorption maxima due to the quantum effect.* The results revealed the direct relationship between volume of honey while the reverse relation were observed for absorption wavelength, crystallite size and refractive index of ZnS nanoparticles.

Keywords: zinc sulphide nanoparticles, honey, capping and stabilizing agents, hexagonal

Introduction

Honey mediated synthesis is a relatively novel concept used during the past few years to synthesize metal nanoparticles (Balasooriya *et al.*, 2017). It provides a simple, cost effective, biocompatible, reproducible, rapid, and safe method and also offers several advantages over the microorganism mediated synthesis. Honey acts as both a stabilizing and a reducing agent in nanoparticle synthesis. Honey can be produced by bees using nectar from flowers and hence, is a natural sweetener. It contains several biomolecules responsible for the reduction and stabilization of nanoparticles from metal salts precursors and has been exploited by several groups for the synthesis of metal nanoparticles and semiconductor nanoparticles (Buba *et al.*, 2013). Nanoparticles refers to objects that are sized on a nanometer scale where at least one of the dimensions of a particle must be less than 100 nm. Nanomaterials as promising in many fields including cosmetics, healthcare, biomedical, food and feed, environment, health, mechanics, optics, chemical industries, electronics, industries, energy science, catalysis, light emitters, single electron, transistors, nonlinear optical devices and photoelectron chemical application (Thangam *et al*., 2012). ZnS crystallizes as two allotropic forms; zinc blende which can exist in cubic form and wurtzite which can exist in hexagonal close packing form (Hedayati *et al*.,2016). Zinc sulphide is a semiconductor material of the II–VI group and it can be widely utilized in photonics, optical devices, such as ultraviolet light emitting diodes, flat panel displays, optical coatings, field effect transistors, sensors, solar cells and optical sensors (Chaliha *et. al*., 2019).

The main aim of this study is to prepare zinc sulphide by using honey as capping and stabilization agent and to characterize the prepared zinc sulphide.

[1] 3PhD Student, Department of Chemistry, University of Yangon & Lecturer, Engg/Chemistry Department, Technology of University (Maubin)
[2] Lecturer, Department of Chemistry, University of Yangon
[3] Professor, Department of Chemistry, University of Yangon

Materials and Methods

Samples Collection

In the present work, honey samples were collected from Mrauk-Oo Township in Rakhine State. Honey samples were stored in clean air-tight bottles at an ambient temperature to avoid moisture absorption. Honey samples were later taken to the Laboratory of the Department of Chemistry, Yangon University. The chemicals used in this research work were the products from British Drug House (BDH), London and Kanto Chemical Co., Japan.

Preparation of Zinc Sulphide Nanoparticles

ZnS nanoparticles were prepared by homogeneous chemical co-precipitation method using $Zn(NO_3)_2.6H_2O$ and Na_2S precursors and honey was applied as stabilizer and capping agent. Aqueous solution of zinc nitrate hexahydrate (3g in 25 mL of distilled water) and sodium sulphide (1.3 g in 25 mL of distilled water) were freshly prepared. Into the mixture aqueous solution of zinc nitrate hexahydrate and 25 mL of honey, sodium sulphide solution was added drop-wise with continuous magnetic stirring at 2000 rpm. After the formation of white precipitate, stirring was continued for 30 min for the completion of the reaction. The product obtained in the form of white precipitate was centrifuged and washed with distilled water and dried at room temperature (Dilpazir *et al*., 2015).

The above procedure was repeated with 50 mL and 75 mL of honey. The ZnS precipitate obtained were designated as S1, S2 and S3, respectively, for using 25 mL, 50 mL and 75 mL of honey. The chemical equation for the formation of ZnS is given as below:

$$Zn(NO_3)_2 + Na_2S \xrightarrow{\text{honey}} ZnS + 2NaNO_3$$

Characterization of Zinc Sulphide Nanoparticles

Prepared zinc sulphide nanoparticles were characterized by XRD technique using as X-rays diffractometer (D-max 2200, Rigaku Co., Tokyo, Japan) of the wavelength 0.154 nm. The morphology of the ZnS sample was studied using a scanning electron microscope (SEM) and the purity and elemental analysis was carried out using energy dispersive X-ray spectrscopy (EDX) by Shimadzu Super Scan SSX-550. The crystal structure and size of ZnS were obtained by TEM image using TEM (JEOL TEM-3010) with an accelerating voltage of 100 kV at State Key Laboratory, College of Science, Beijing University of Chemical Technology, China. The crystallite sizes of ZnS NPs were calculated by using Image J software. TG-DTA analysis was carried out by (DTG-60H) Thermal Analyzer, Shimadzu, Japan. FT IR spectra were recorded by FT IR spectrophotometer, Perkin Elmer. UV-Visible spectra were recorded in a Thermo Scientific Evolution 201 Spectrometer.

Results and Discussion

XRD Analysis

Figure 1 shows the x-ray diffractograms of ZnS nanoparticles obtained by using 25 mL, 50 mL and 75 mL honey, respectively. All the peaks in the XRD patterns are well matched with the standard diffraction pattern of zinc sulphide. No other impurity peaks were observed. Three dominant peaks were observed in the diffractogram of S1 at 2θ values of 28.6°, 47.5° and 56.7° corresponding to the Miller indices of (006), (108) and (116) planes, respectively. For S2 and S3 these dominant peaks appeared around the above mentioned 2θ values. ZnS nanoparticles were

indexed as hexagonal packed wurtzite structure. Phase identification by XRD results showed that only single phase of zinc sulphide with no other phase was found in each XRD pattern (Table 1).

The average crystallite size (t) of the ZnS sample was calculated using the Scherrer formula:

$$t = 0.9\lambda / \beta \cos \theta$$

Where, t is thickness of the crystallites (nm), λ= 1.54056 Å is wavelength of X –ray, θ is diffraction angle of the Bragg peak and β is the full width at half maximum (FWHM) of that peak in radian. Table 2 shows the crystallite sizes of ZnS nanoparticles obtained by using three different volumes of honey. The calculated average crystallite size of zinc sulphide nanoparticles was estimated to be 17.2 nm, 15.6 nm and 12.9 nm by using 25mL, 50 mL and 75 mL of honey, respectively. The calculated values were not much different from the data obtained by XRD. The average crystallite size was found to vary in the range of 12 nm -18 nm for the samples with decreasing trend as the amount of honey was increased. It was observed that by using higher volume of honey smaller crystallite sizes of ZnS nanoparticles were obtained.

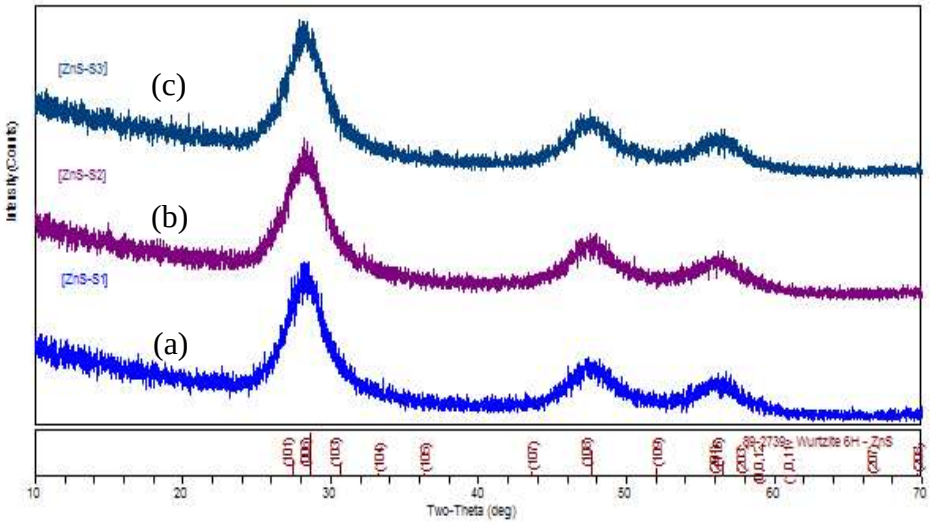

Figure 1 XRD pattern of zinc sulphide nanoparticles using (a) 25 mL of honey (S1) (b) 50 mL of honey (S2) and (c) 75 mL honey (S3)

Table 1 Phase Identification of Zinc Sulphide Nanoparticles Using Different Volumes of Honey

Samples	Diffraction Angle '2θ'(°)	Interplanar Spacing d(Å)	Miller Indices (h k l)	Remark
S1	28.6	3.11	006	ZnS
	47.5	1.91	108	
	56.4	1.62	116	
S2	28.6	3.11	006	ZnS
	47.7	1.91	108	
	56.6	1.63	116	
S3	28.6	3.12	006	ZnS
	47.8	1.90	108	
	56.9	1.63	116	

Table 2 Crystallite Sizes of Zinc Sulphide Nanoparticles using Different Volumes of Honey

No.	Diffraction Angle '2θ'(°)	FWHM 'β' (°)	FWHM 'β' (radian)	Calculated Crystallite Size (nm)	Crystallite Size from XRD (nm)
S1	28.6	0.94	0.016	17.2	18.5
	47.5	0.54	0.009		
	56.4	0.23	0.004		
S2	28.6	0.64	0.011	15.6	17.4
	47.7	0.58	0.010		
	56.6	0.38	0.017		
S3	28.6	0.54	0.019	12.9	14.8
	47.8	0.66	0.012		
	56.9	0.67	0.011		

TEM Analysis

Crystallite size of ZnS nanoparticles (S1) obtained by using 25 mL honey was also studied by transmission electron microscopy. Figure 2 shows the TEM image of ZnS nanoparticles. TEM image of sample indicated the evident morphology and regular (spherical) shape. The average particle size measured by using image J software which was nearly the same as that measured by XRD of 17.2 nm.

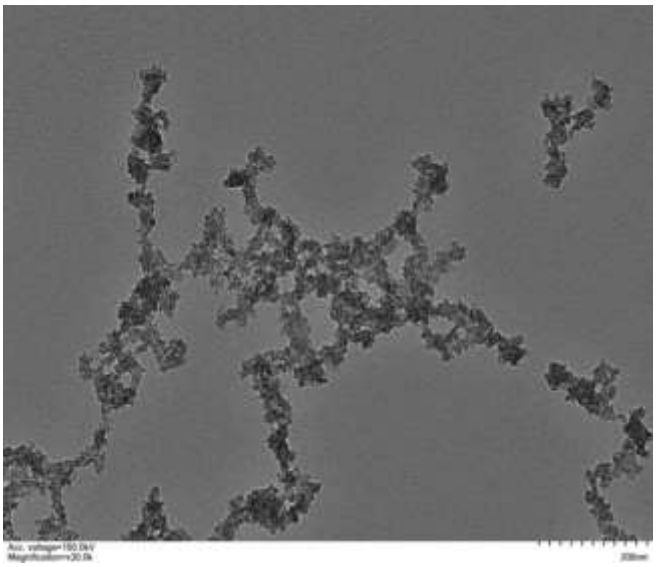

Figure 2 TEM image of zinc sulphide nanoparticles using 25 mL of honey (S1)

SEM –EDX

The morphology as well as the composition of the prepared ZnS nanoparticles were investigated by SEM-EDX.

Morphological analysis

Figure 3 shows the SEM images of ZnS nanoparticles. The image for the samples depicts the homogeneous plate-like form. The SEM also produces images of high resolution, which means

that closely features can be examined at a high magnification. However, the actual size cannot be determined by SEM due to the limitation of the resolution of the instrument

Element analysis

The EDX spectra of as synthesized zinc sulphide samples are shown in Figure 4. The clear peaks of Zn and S confirmed the presence of zinc and sulphur. Other element oxygen was also recorded possibly due to the elements from honey. The average atomic percentages of zinc and sulphur were found to be 65.08: 33.02 in S1, 63.81: 31.32 in S2 and 62.08: 31.02 in S3. These ratios of Zn and S atoms are very close to the theoretical expectation of 1:1 for the atom ratio in ZnS nanoparticles. Similarly, the weight ratios of Zn and S in all sample particles were also found to be nearly 2:1 of zinc sulphide nanoparticles.

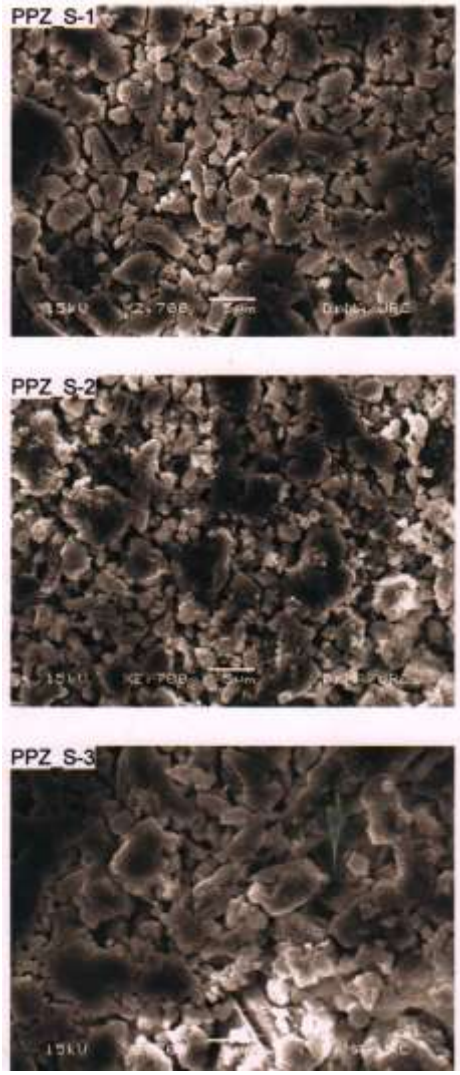

Figure 3 SEM images of zinc sulphide nanoparticles using (a) 25 mL of honey (S1), (b) 50 mL of honey (S2) and (c) 75 mL of honey (S3)

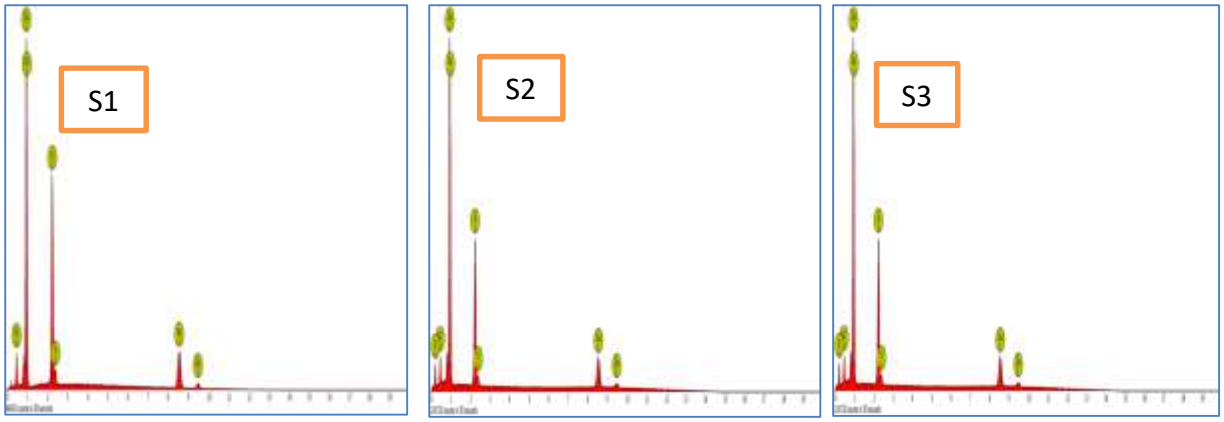

Figure 4 EDX spectra of zinc sulphide (S1, S2 and S3) nanoparticles

Table 3 EDX Spectral Data of Zinc Sulphide Nanoparticles Using Honey

Samples	Element Number	Element Symbol	Element Name	Atomic (%)	Weight (%)
S1	30	Zn	Zinc	65.08	62.74
	16	S	Sulphur	33.02	34.95
	8	O	Oxygen	1.90	1.31
S2	30	Zn	Zinc	63.81	62.87
	16	S	Sulphur	33.32	30.50
	8	O	Oxygen	2.87	5.63
S3	30	Zn	Zinc	62.08	60.73
	16	S	Sulphur	34.68	34.85
	8	O	Oxygen	2.24	3.42

Thermogravimetric -Differential Thermal Analysis

Figure 5 shows the thermograms of ZnS nanoparticles **(**samples S1, S2 and S3). In each thermogram, one endothermic peak and one exothermic peak were observed. The endothermic peak was due to the evaporation of residual moisture on the surface of the samples and the exothermic peak was attributed to the combustion of residual organic compounds from honey. The TGA showed significant weight losses arising from desorption of water below 200 ºC and the decomposition of organic components occurred between 250–320 ºC. The weight losses were 23.3 % for sample (S1), 24.4 % for sample (S2) and 31.3 % for sample (S3), and the results were described in Table 4.

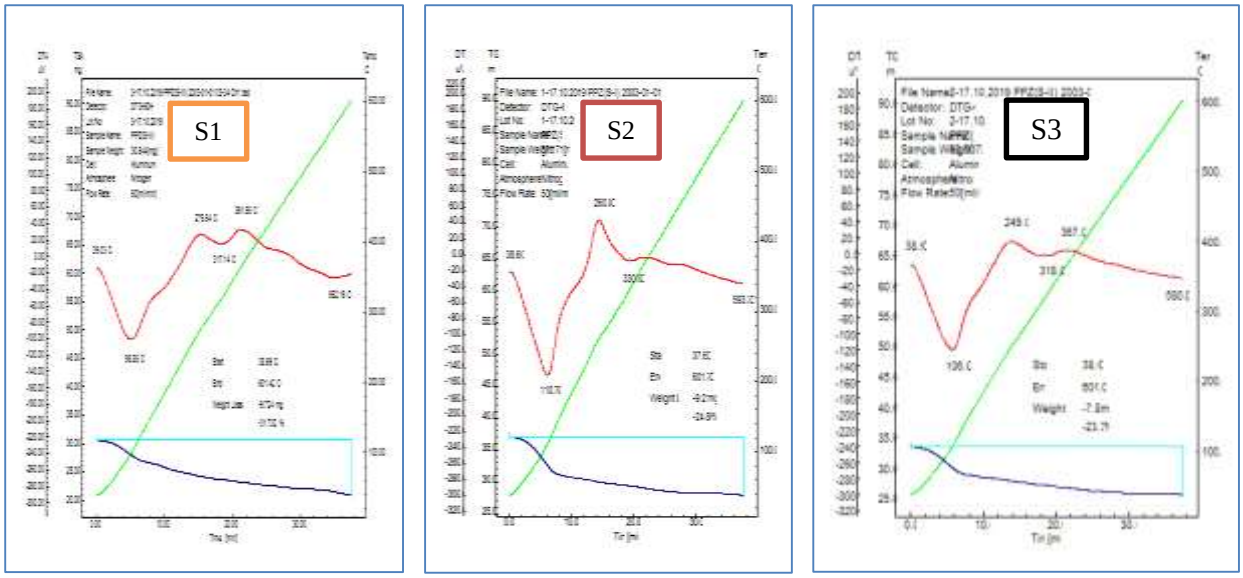

Figure 5 TG-DTA thermogram of zinc sulphide nanoparticles (S1, S2 and S3)

Table 4 TG-DTA Data of the Prepared Zinc Sulphide Nanoparticles using Honey

Samples	Temperature Range (°C)	Break Temperature (°C)	Weight Loss (%)	Nature of Peak	Remarks
S1	38 -135	98.8	11.3	Endothermic	Removal of water
	135-380	361.5	9.5	Exothermic	Combustion of organic compound
	380- 601		2.5	---	Thermally stable
S2	37 -180	110.8	11.5	Endothermic	Removal of water
	180-290	260.9	9.5	Exothermic	Combustion of organic compound
	290- 601		3.4	---	Thermally stable
S3	38 - 200	106.2	14.2	Endothermic	Removal of water
	200-300	249.3	12.5	Exothermic	Combustion of organic compound
	300-601		4.5	---	Thermally stable

FT IR Study

The FT IR spectra of zinc sulphide nanoparticles were recorded between 400-4000 cm^{-1} as shown in Figure 6. The peaks were observed at 459 cm^{-1} for the sample (S1), 435cm^{-1} for the sample (S2) and 552cm^{-1} for the sample (S3) due to Zn-S stretching vibration. The characteristic major peak of ZnS was reported to be 464 cm^{-1} (Ummartyotin *et al.*,2012). The broad bands between 3200cm^{-1}- 3400cm^{-1} are assigned to the O-H stretching vibration. The absorption peaks of 1617cm^{-1}, 1629 cm^{-1} and 1625 cm^{-1} are assigned to the O-H bending of water molecules. The

vibration bands in the range of 1332cm^{-1} - 1350 cm^{-1} are assigned to the -O-H bending in C-O-H vibration and the bands between 1009 and 1119 cm^{-1} are stretching of C-O in C-O-C group.

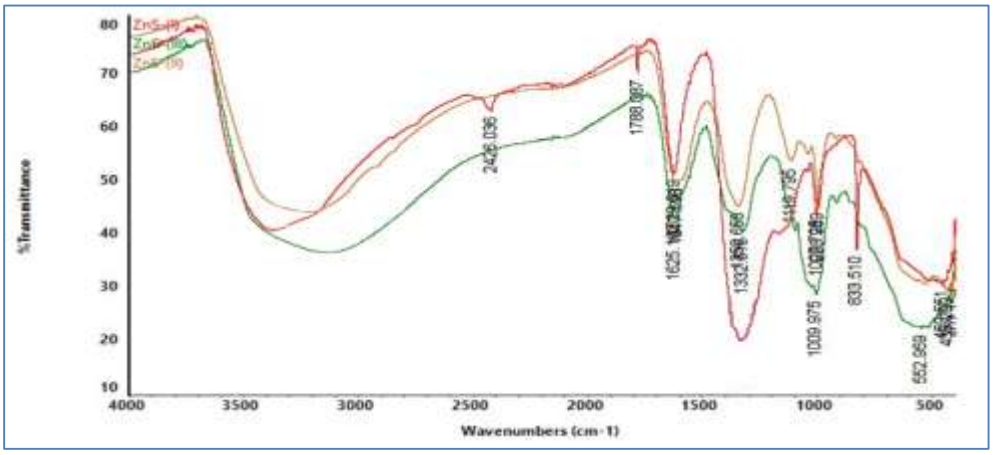

Figure 6 FT IR spectra of zinc sulphide nanoparticles (S1, S2 and S3)

Table 5 FT IR Spectral Data of Zinc Sulphide Nanoparticles using Honey

Wavelength (cm^{-1})				Assignment
S1	**S2**	**S3**	**Reported values**	
3200-3400	3200-3400	3200-3400	3200-3400*	-O-H stretching vibration
1629	1617	1625	1640-1646*	O-H bending of H_2O
1332	1350	1339	1342-1347*	O-H bending in -C-OH
1119	1007	1009	1101-1105*	(C-O) in C-O-C group
459	435	552	464**	Zn-S Stretching

***** Kędzierska-Matysek *et al*.,2018
** Ummartyotin *et al*., 2012

Optical study

The absorption spectra of ZnS nanoparticles are shown in Figure 7. The strongest absorption peak of zinc sulphide nanoparticles appear at λ_{max} of 329 nm for the sample (S1), 315 nm for the sample (S2) and 308 nm for the sample (S3) using different volumes of honey. The ultraviolet absorption spectra showed the blue shift *in absorption maximum, i.e., moved to shorter wavelength* due to the quantum effect.

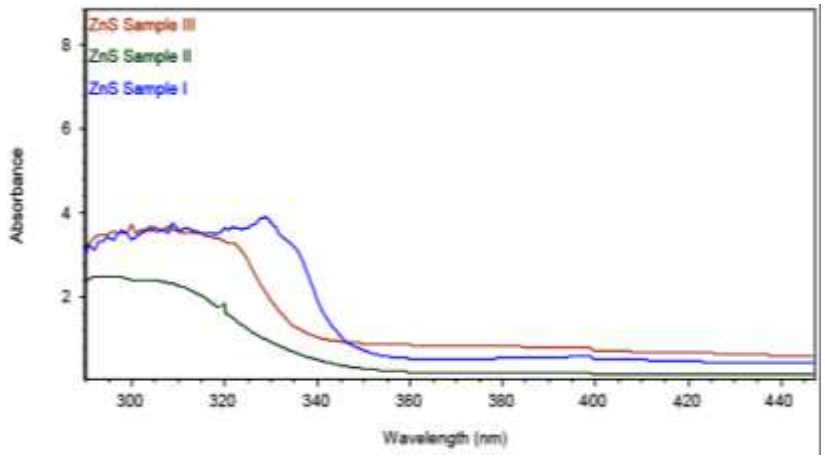

Figure 7 Absorption spectra of zinc sulphide nanoparticles (S1, S2 and S3)

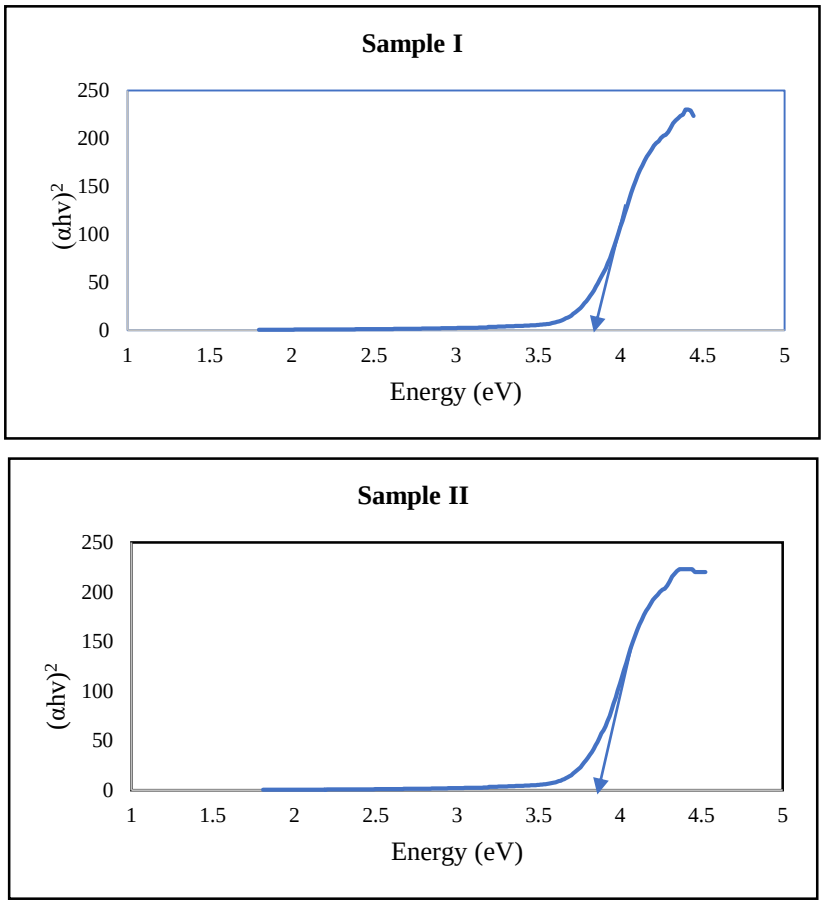

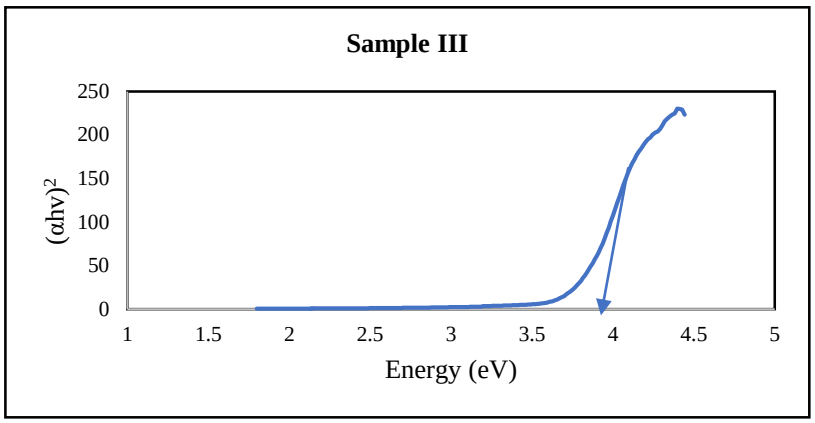

Figure 8 Tauc plots for calculation of band gap energy values of zinc sulphide nanoparticles (S1, S2 and S3)

The optical band gap energy of the ZnS nanoparticles was calculated from the UV absorption study using the following equation;

$$\alpha\, h\nu = A(h\nu - E_g)^n$$

where, α is the absorption coefficient,

$h\nu$ is the incident photon energy,

A is a constant, and

E_g is the optical band gap energy of the material.

Figure 8 shows the Tauc plots of ZnS nanoparticles to calculate the band gap energy. The optical band gap energy data of the all samples are found to lie in the range of 3.7 – 3.9.eV (Table 6). The band gap was found to increase from 3.7 eV to 3.9 eV as the λ_{max} of ZnS nanoparticles decreased . The obtained band gap values were higher than that of the bulk value (3.7 eV) owing to the quantum confinement effect. The refractive index of the ZnS nanoparticles S1, S2 and S3 were calculated using the relation:

$$n^4\, E_g = 59\ eV$$

where, n is the refractive index

E_g is the band gap of the sample.

The refractive indices were in the range of 1.9 to 1.7 for ZnS nanoparticles (S1, S2 and S3). It was found that as the λ_{max} decreased, the band gap increased and the refractive index decreased.

Table 6 Wavelength of Maximum Absorption, Band Gap and Refractive Index of ZnS Nanoparticles Using Honey

Sample	Wavelength of maximum absorption (nm)	Band gap (eV)	Refractive Index
S1	329	3.7	1.9
S2	315	3.8	1.8
S3	308	3.9	1.7

Conclusion

ZnS nanoparticles were successfully synthesized using three different volumes of honey as capping and stabilizing agents. ZnS nanoparticles in this study were indexed as hexagonal structure with the average crystallite size between 12.9 to 17.2 nm. TEM image of sample indicated the evident morphology and regular shape. SEM images for the samples showed homogeneous plate-like form. EDX analysis confirmed the presence of Zn and S with correct atomic and weight ratios. TG-DTA analysis showed endothermic and exothermic peaks due to loss of moisture and combustion of organic compounds from honey. The FT IR study showed the characteristic peak of zinc sulphide. ZnS nanoparticles exhibited the absorption maximum in the range of 329 nm and 308 nm. From this study it was found that when the volume of honey was increased, the band gap energy of ZnS nanoparticles increased but particle size and refractive index decreased.

Acknowledgement

The authors would like to thank the Myanmar Academy of Arts and Science for allowing to present this paper and Professor and Head Dr Ni Ni Than, Department of Chemistry, University of Yangon, for the permission of doing this research.

References

Balasooriya, E.R., Jayasinghe, C.,Jayawardena,U. and Ranasinghe, D.R. (2017). "Honey Mediated Green Synthesis of Nanoparticles: New Era of Safe Nanotechnology". *Journal of Nanomaterials*,vol. 2017(3), pp. 1-10

Buba, F., Gidado, A. and Shugaba, A. (2013). "Analysis of Biochemical Composition of Honey Samples from North-East Nigeria". *Biochem. Anal. Biochem*., vol. 2(3), pp. 1-7

Chaliha, **C**., Nath, B. K., Verma, P. K. and Kalita, E. (2019). "Synthesis of Functionalized Cu: ZnS Nano Systems and its Antibacterial Potential". *Arab. J. of Chem.***,** vol. 12, pp. 515- 524

Dilpazir, S., Siddiq, M. and Iqbal, A. (2015). "Synthesis of Zinc Sulphide Nanostructures by Co-precipitation: Effects of Doping on Electro-optical Properties". *Ken. J. of Nanotech and Nanosci*., vol. 1, pp 34-39

Hedayati, K., Zendehnam, A. and Hassanpour, F. (2016). "Fibration and Characterization of Zinc Sulphide Nanoparticles and Nanocomposites Prepared via a Simples Chemical Precipitation Method". *J. Nano*., vol. 6(3), pp. 207-212

Kędzierska-Matysek, M., Matwijczuk, A., Florek,M., Barłowska,J., Wolanciuk, A., Matwijczuk, A.,Chruściel, E.,Walkowiak, R., *Dariusz* Karcz, D. and Gładyszewska, B. (2018). "Application of FTIR Spectroscopy for Analysis of the Quality of Honey". *BIO Web of Conferences, Contemporary Research Trends in Agricultural Engineering*, vol.10, pp. 1-8

Thangam, Y. Y., Anitha, R. and Kavitha, B. (2012). "Novel Method to Synthesize and Characterize Zinc Sulfide Nanoparticles". *Int. J. of App. Sci. and Engg. Rese.*, vol. 1(2), pp. 282- 286

Ummartyotin,S., Bunnak , N., Juntaro, J., Sain, M. and Manuspiya, H. (2012). "Synthesis and Luminescence Properties of ZnS and Metal (Mn, Cu)-doped-ZnS Ceramic Powder". *Solid State Sciences*, vol.14, 299-304

PREPARATION AND CHARACTERIZATION OF MAGNESIUM FERRITE ($MgFe_2O_4$) NANOPARTICLES

Toe,[1] Yi Yi Myint,[2] Kyaw Soe[3]

Abstract

The materials with porous structure and high surface area are very popular for several applications in nanotechnology in the current years. The present research deals with a study on the synthesis and characterization of (spinels) nanoparticles ($MgFe_2O_4$). Two types of $MgFe_2O_4$ nanoparticles were synthesized by sol-gel method using two different acids such as acetic acid and formic acid. The metal nitrates such as magnesium nitrate and ferric nitrate were used as oxidizers. The gels were dried in the oven at temperature of 105°C to obtain constant weights. The resulting samples were thermally treated in the muffle furnace at temperature of 400 ºC for four hours to get required $MgFe_2O_4$ nanoparticles. The prepared samples were characterized by X-ray powder diffraction (XRD), Fourier transform Infrared spectroscopy (FTIR) and Energy Dispersive X-ray fluorescence (EDXRF).

Keywords: Magnesium ferrite, nanoparticles, spinels, sol-gel method

Introduction

Gradually, primary energy resources such as fossil fuel, coal and natural gas are depleting, while the global energy consumption is increasing. Solar energy, wind energy, biomass, tidal and geothermal sources is emerging as an answer to the energy starved planet. These renewable energy resources which are freely available in nature are non-polluting and help in reducing global CO_2 emissions. Out of the available sources of energy, solar energy is the cleanest and the most abundant. Second part of the series challenges in the quest for clean energies is focused on different solar technologies and materials that can be used to make an efficient photovoltaic cell. Available photovoltaic cells can be broadly classified into first, second and third generation solar cells. First generation cells are basically silicon based crystalline cells while second generation cells are thin film based and third generation cells comprise new emerging technologies. Solar cells used for power generation must possess certain characteristics like high efficiency, low cost of materials, simple fabrication technique, ease of solar panel installation and long term stability. Unfortunately, there is not yet a device that can simultaneously meet all the above requirements. First and second generation solar cells have high efficiency and stability except for the amorphous silicon solar cells. However, they also possess some disadvantages. Majority of these solar cells employ high efficiency silicon based materials which are expensive. The scarcity of indium which is used in copper indium gallium silicon (CIGS) solar cells is a potential challenge for the widespread use of these cells. The toxicity of cadmium and the low earth abundance of tellurium (CdTe) solar cells.

In the recent years, researchers have focused on the development of cost-effective and feasible non-silicon solar cell technologies. Polycrystalline ferrites are optimal structural materials in high frequency circuits, owing to their excellent electrical and magnetic properties. Moreover, they are more stable than other competing materials and able to fulfill a range of applications in radio frequency circuits, operator devices (Schmid, 2010).

[1] Lecturer, Department of Chemistry, University of Magway
[2] Dr, Professor and Head, Department of Chemistry, University of Mandalay
3 Dr, Lecturer, Department of Chemistry, University of Magway

Materials and Methods

All chemicals were analytical grade. Magnesium nitrate ($Mg(NO_3)_2.6H_2O$), iron nitrate ($Fe(NO_3)_3.9H_2O$), formic acid(CH_2O_2), and acetic acid($C_2H_4O_2$) were Merck product with a purity of 99.99%. Ethylene glycol was product from Applichem, Germany. All solutions were prepared using distilled water during preparation procedures. Various conventional and modern instrumental techniques were used throughout the experimental procedure. These include X-ray Diffraction (XRD), Fourier Transform Infrared Spectroscopy (FT-IR) and Energy Dispersive X-ray Fluorescence (EDXRF).

Preparation of Magnesium Ferrite ($MgFe_2O_4$) Nanoparticles by Sol-Gel Method

Magnesium nitrate, iron nitrate, acetic acid, formic acid, ethylene glycol and distilled water were used as starting materials to synthesize two types of $MgFe_2O_4$ nanoparticles.

Preparation of $MgFe_2O_4$ Nanoparticles using Acetic Acid by Sol-Gel Method

Magnesium nitrate and iron nitrate were dissolved in distilled water to obtain solution (I). Acetic acid was dissolved in distilled water and solution (II) was obtained. The solutions (I) and (II) were mixed as molar ratio of acetic acid and metal ion was 1:2 and then 5 mL of ethylene glycol was added to the mixture solution. The mixture solution was stirred with magnetic stirrer and heated at 70 ºC-80 ºC for 7 h to get $MgFe_2O_4$ gels. The gel was dried at 105 ºC for 4 h and ground with mortar and pestle to get dried $MgFe_2O_4$ powder. The prepared $MgFe_2O_4$ particles was calcined at 400 ºC for 4 h to obtain $MgFe_2O_4$ nanoparticles (MF1) (Sajjadi, 2005).

Preparation of $MgFe_2O_4$ Nanoparticles using Formic Acid by Sol-Gel Method

Magnesium nitrate and iron nitrate were dissolved in distilled water to obtain solution (I). Formic acid was dissolved in distilled water and solution (II) was obtained. The solution (I) and (II) were mixed as molar ratio of formic acid and metal ion was 1:2 and then 5 mL of ethylene glycol was added to the mixture solution. The mixture solution was stirred with magnetic stirrer and heated at 70 ºC- 80ºC for 7 h to get $MgFe_2O_4$ gels. The gel was dried at 105 ºC for 4 h and ground with mortar and pestle to get dry $MgFe_2O_4$ powder. The prepared $MgFe_2O_4$ particles was calcined at 400 ºC for 4 h to obtain $MgFe_2O_4$ nanoparticles (MF2) (Sajjadi, 2005).

Characterizations of $MgFe_2O_4$Nanoparticles

Crystal structure and phase analysis were performed by X-ray diffraction (XRD) using Rigaku, D-Max 2200, Japan in Universities' Research Centre, Yangon. The elemental compositions of the two prepared samples were confirmed by using EDXRF 700 spectrometer in Department of Chemistry, Monywa University. The chemical bondings of crystals were studied by Fourier Transform Infrared (FT IR) spectroscopy in Department of Chemistry, Monywa University.

Determination of Crystalline Size and Interplanar Spacing

The crystallite size of $MgFe_2O_4$ can be calculated by using Debye-Scherrer formula (Leroy an Harold, 1950),

$$D = \frac{0.9\lambda}{\beta cos\theta} \quad \text{and}$$

interplanar spacing was computed by Bragg's equation,

$$d = \frac{\lambda}{2sin\theta}$$

Where, λ = the wave length of X-rays (1.54056Åfor Cu/K-alpha 1)

θ = the diffraction angle

β = full width at half maximum in radian

D =average crystal size

d = interplanar spacing

Results and Discussion

EDXRF Analysis of Magnesium Ferrite ($MgFe_2O_4$) Nanoparticles

The relative abundance of elements in magnesium ferrite synthesized with acetic acid (MF1) is shown in Table 1 and Figure 1. From the data, elements contained in MF1 were iron (64.555%) and magnesium (34.047%) and some of trace elements.

Elemental composition of magnesium ferrite MF2 synthesized with formic acid is shown in Table 2 and Figure 2. According to the experimental results, main elemental components were iron (70.886%) and magnesium (27.886%), and some trace elements.

Table 1 Elemental Composition in Magnesium Ferrite ($MgFe_2O_4$) Nanoparticles MF3

No	Elements	Amount (%)
1	Fe	64.555
2	Mg	34.047
3	Si	0.761
4	S	0.332
5	Mn	0.157
6	Ca	0.084
7	Cr	0.034
8	Cu	0.030

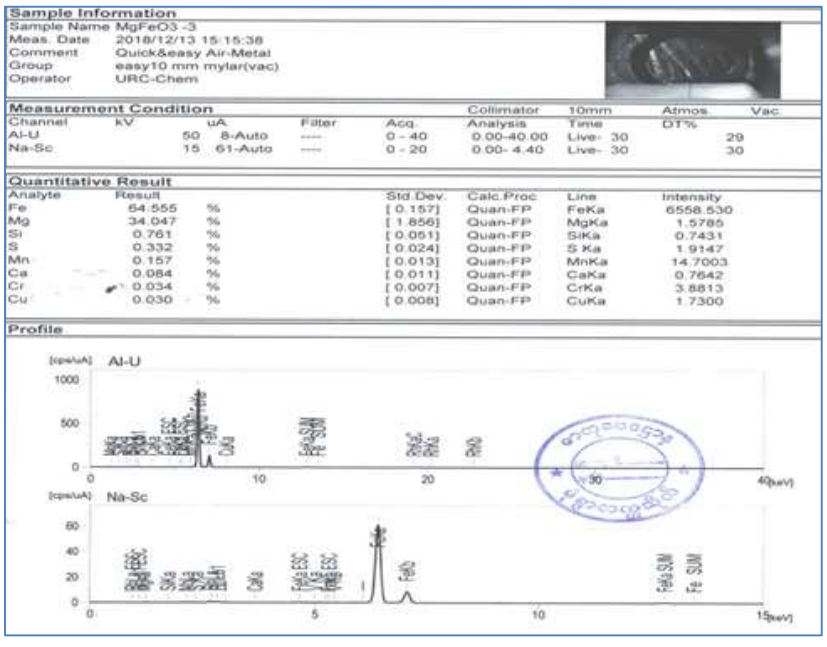

Figure 1 EDXRF spectrum of MF1 nanoparticles

Table 2 Elemental Composition in Magnesium Ferrite ($MgFe_2O_4$) Nanoparticles MF2

No	Element	Amount (%)
1	Fe	70.886
2	Mg	27.886
3	Si	0.806
4	S	0.348
5	Cr	0.075

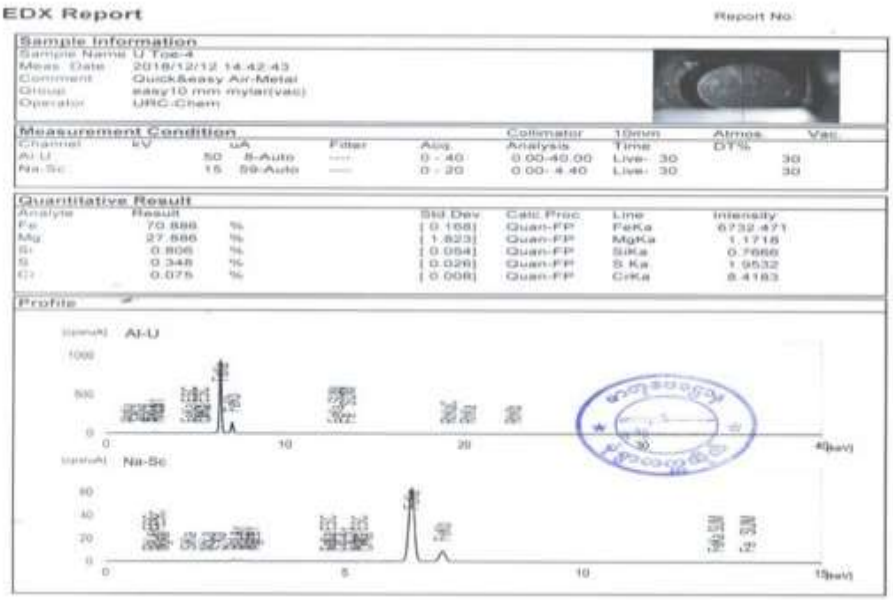

Figure 2 EDXRF spectrum of MF4 nanoparticles

FT IR Analysis of Magnesium ferrite ($MgFe_2O_4$) Nanoparticles

Magnesium ferrites (MF1 and MF2) were analyzed by FT-IR spectrophotometer. The characteristic features of FT IR spectra of MF1 and MF2 are shown in Figures 3 and 4, respectively. According to the FT IR spectral data as shown in Table 3, the stretching vibration of metal-oxygen bond of MF1 and MF2 were 523 cm^{-1} and 530 cm^{-1}, respectively. The region 520-630 cm^{-1} corresponds to stretching vibrations of metal ions in the tetrahedral sites (Kaur and Kaur, 2014). Anam *et al.* (2017) reported the stretching vibration of of Mg-O bond occured between 650-530 cm^{-1}.

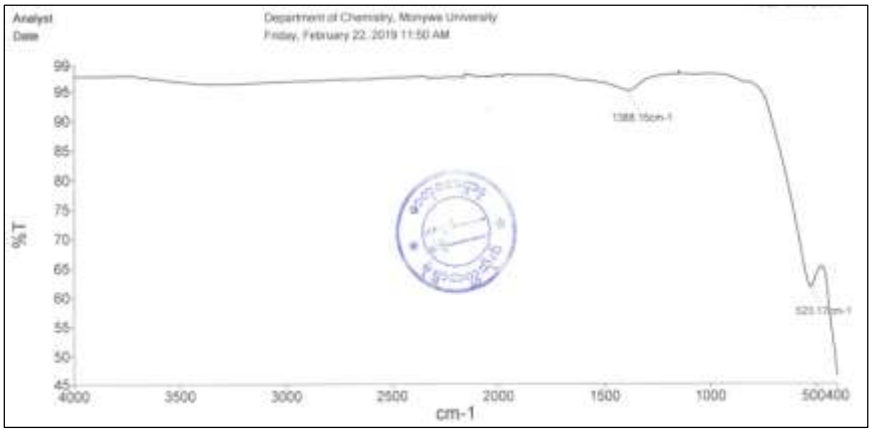

Figure 3 FT IR spectrum of MF1 nanoparticles

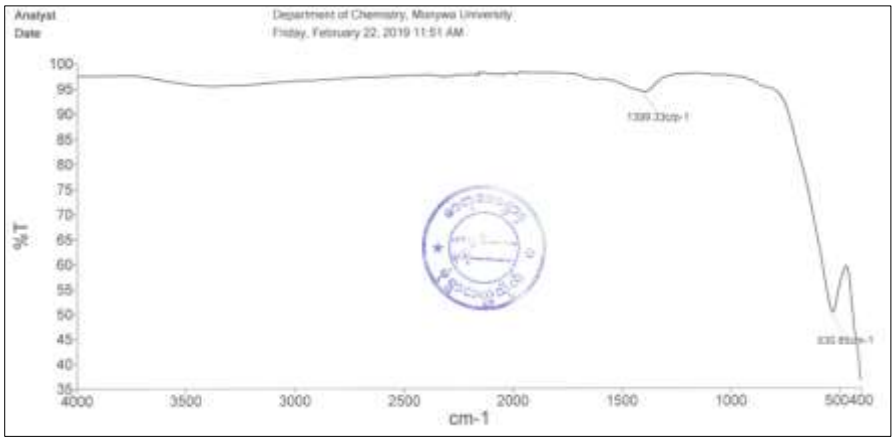

Figure 4 FT IR spectrum of MF2 nanoparticles

Table 3 FT IR Spectra Data for $MgFe_2O_4$ Nanoparticles

Sample	Wave number (cm^{-1})	Remark	*Reported value
MF1	523	stretching vibrations of metal ions in the tetrahedral sites	520-630 cm^{-1}
MF2	530	stretching vibrations of metal ions in the tetrahedral sites	520-630 cm^{-1}

* Kaur and Kaur (2014)

XRD Analysis of Magnesium Ferrite ($MgFe_2O_4$) Nanoparticles

Figures 5 and 6 show XRD diffractograms of magnesium ferrites MF1 and MF2, respectively. The XRD patterns were compared with the standard powder diffraction pattern. The major planes correspond to (111), (220), (311), (222), (400), (422) and (511) were found to be matched with the library data which confirmed the presence of magnesium ferrite. All the observed peaks and Miller indices of the prepared magnesium ferrite were in agreement with the reported values (Arulmurugan *et al*., 2005; Spiers *et a*l., 2004) for $MgFe_2O_4$. Tables 4 and 5 show the phase identification of prepared magnesium ferrite samples, MF1 and MF2, and their crystallite sizes respectively. Peak locations (2θ) and Miller indices are also shown in these tables. Only single phase of magnesium ferrite was observed in both MF 1 and MF 2. From their data, chemical formulae of these nanoparticles were magnesium ferrites (spinels). The crystallite sizes were calculated using Bragg angle, 2θ(degree) and β, radian by Debye-Scherrer formula, $D = 0.9\ \lambda/\beta \cos\theta$. According to the calculated data, the average crystallite size of MF 2 (magnesium ferrite using formic acid) was slightly higher (28.58 nm) than MF 1 (magnesium ferrite using acetic acid) (15.25 nm). These values were in the range of nanosize (1-100 nm). The difference in crystallite size was due to different preparation conditions for ferrite synthesis.

Tables 6 and 7 show lattice constants calculated from peak locations and Miller indices for MF1 and MF2 nanoparticles. From the data, lattice parameters of MF1 and MF2 were a= b= c= 0.836 nm and a = b=c= 0.839 nm, respectively. The crystal structures were indexed as face centered cubic having all odd or all even Miller indices. The volume of unit cells of prepared samples MF1 and MF2 were computed from their lattice parameters and found to be 506.17Å and 511.45Å, respectively.

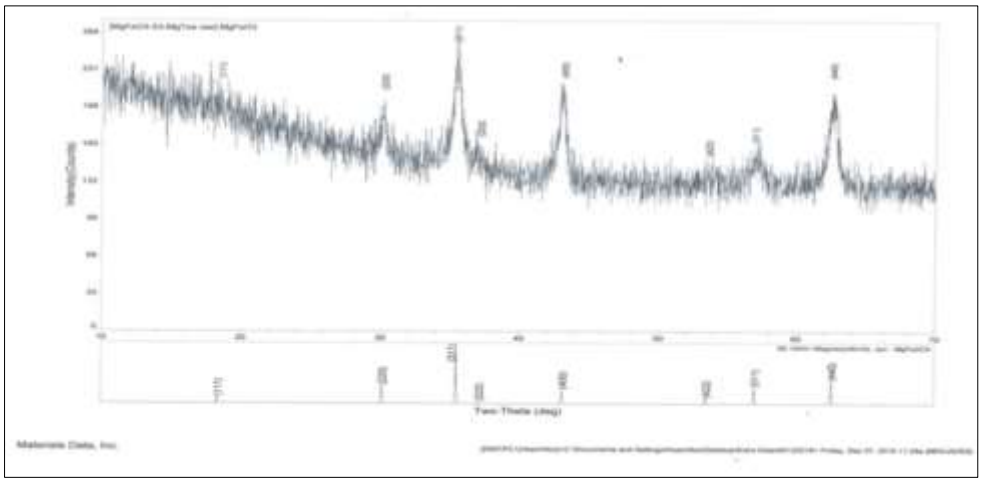

Figure 5 XRD diffractogram of MF1 nanoparticles

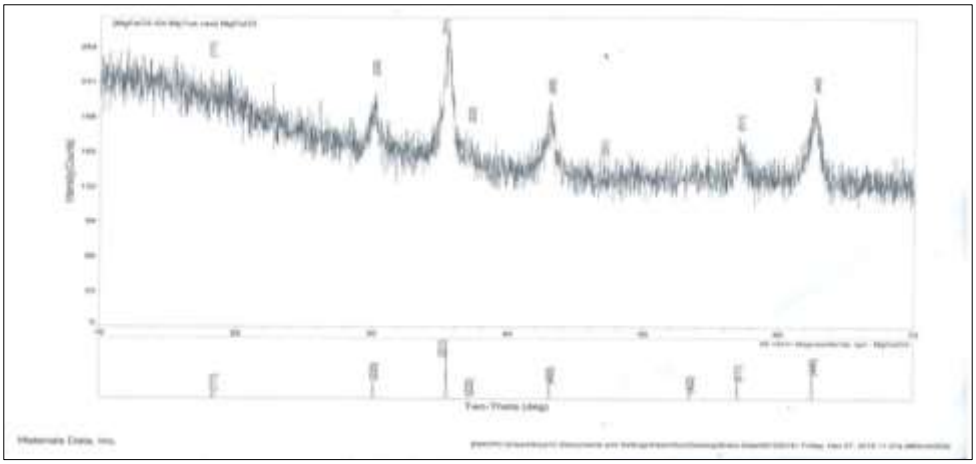

Figure 6 XRD diffractogram of MF2 nanoparticles

Table 4 Phase Identification and Crystallite Size of MF 1 Nanoparticles

No	Bragg angle,2θ (degree)	Miller indices (hkl)	Interplanar spacing,d(nm)	Phase ID	(β) radian	Crystallite size D (nm)
1	18.553	1 1 1	0.478	$MgFe_2O_4$	0.01216	11.55
2	30.210	2 2 0	0.296	$MgFe_2O_4$	0.00751	19.26
3	35.422	3 1 1	0.253	$MgFe_2O_4$	0.01021	14.29
4	37.155	2 2 2	0.242	$MgFe_2O_4$	0.01019	14.44
5	43.138	4 0 0	0.210	$MgFe_2O_4$	0.00899	16.71
6	53.556	4 2 2	0.171	$MgFe_2O_4$	0.00981	15.94
7	56.907	5 1 1	0.162	$MgFe_2O_4$	0.01178	13.46
8	62.516	4 4 0	0.148	$MgFe_2O_4$	0.01006	16.31

Range of crystallite size = 11.55 – 16.71 nm
Average crystallite size = 15.25 nm

Table 5 Phase Identification and Crystallite Size of MF 2 Nanoparticles

No	Bragg angle,2θ (degree)	Miller indices (hkl)	Interplanar spacing, d(nm)	Phase ID	(β) radian	Crystallite size D (nm)
1	18.199	1 1 1	0.487	$MgFe_2O_4$	0.00399	35.55
2	30.180	2 2 0	0.296	$MgFe_2O_4$	0.00957	15.07
3	35.585	3 1 1	0.252	$MgFe_2O_4$	0.01012	14.44
4	37.223	2 2 2	0.241	$MgFe_2O_4$	0.00191	77.03
5	43.115	4 0 0	0.021	$MgFe_2O_4$	0.0115	13.46
6	47.032	3 3 1	0.193	$MgFe_2O_4$	0.00412	37.47
7	57.072	5 1 1	0.161	$MgFe_2O_4$	0.00816	19.53
8	62.728	4 4 0	0.148	$MgFe_2O_4$	0.01009	16.12

Range of crystallite size = 13.46 – 77.03 nm
Average crystallite size = 28.58 nm

Table 6 Lattice Constants from Peak Locations and Miller Indices for MF1

No	Bragg angle (2θ)	Miller indices (hkl)	Inter planar spacingd (nm)	a-Axis (nm)	b-Axis (nm)	c-Axis (nm)
1	18.553	1 1 1	0.478	0.828	0.828	0.828
2	30.210	2 2 0	0.296	0.836	0.836	0.836
3	35.422	3 1 1	0.253	0.840	0.840	0.840
4	37.155	2 2 2	0.242	0.838	0.838	0.838
5	43.138	4 0 0	0.210	0.838	0.838	0.838
6	53.556	4 2 2	0.171	0.838	0.838	0.838

Table 7 Lattice Constants from Peak Locations and Miller Indices for MF2

No	Bragg angle (2θ)	Miller indices (hkl)	Inter planar spacing d(nm)	a-Axis (nm)	b-Axis (nm)	c-Axis (nm)
1	18.199	1 1 1	0.487	0.844	0.844	0.844
2	30.180	2 2 0	0.296	0.837	0.837	0.837
3	35.585	3 1 1	0.252	0.836	0.836	0.836
4	37.223	2 2 2	0.241	0.836	0.836	0.836
5	43.115	4 0 0	0.021	0.839	0.839	0.839
6	47.032	3 3 1	0.193	0.842	0.842	0.842

Conclusion

In this study, two types of magnesium ferrite ($MgFe_2O_4$) nanoparticles were synthesized from magnesium nitrate and ferric nitrate by sol-gel method with different acids such as acetic acid and formic acid. MF1 synthesized with acetic acid and MF2 synthesized with formic acid were characterized by modern sophisticated methods such as EDXRF, XRD and FTIR. From EDXRF data, the amount of magnesium and iron were found to be 34.047 % and 64.555 % for MF1 and 27.886 % and 70.886 % for MF2. Prepared magnesium ferrite samples were confirmed by the presence of the stretching band of metal-oxygen bonds appeared between 520-630 cm^{-1} in FT IR spectra. The XRD reults revealed the impurity free nanocrystalline spinel MgFe2O4 by showing no impurity peaks except magnesium ferrite.From the XRD results, the average crystallite sizes of

vibration prepared nanoparticles for MF1 and MF2 were found to be 15.25 nm and 28.58 nm, respectively, which were in the range of nanosize. The prepared magnesium ferrites were indexed as face centered cubic structure with equal lengths of 0.836 nm and0.839 nm for MF1 and MF 2, respectively. Thus, the sol-gel method is well suited for the synthesis of nano-sized spinel $MgFe_2O_4$.

Acknowledgements

I am extremely grateful to Dr Khin Maung Oo, Rector, University of Magway and Professor and Head, Dr Thidar Aung, Department of Chemistry, Magway University for their provision and suggestions of the research facilities.

References

Anam, A., Abad, A., Mohd, A. and Shams, U. (2017). "Microwave- Assisted MgO NP Catalyzed One- Pot Multicomponent Synthesis of Polysubstituted Steroidal Pyridines". *New Journal of Chemistry,* vol. 42(1), pp. 184-197

Arulmurugan,R., Jeyadevan, B.,Vaidyanathan,G. and Sendhilnathan,S.(2005). "Effect of Zinc Substitution on CoZn and Mn-Zn ferrite Nanoparticles Prepared by Coprecipitation",. *J. Magn. Magn. Mater*., vol., 288, pp. 470-477

Kaur,N. and Kaur, M. (2014). "Comparative Studies on Impact of Synthesis Methods on Structural and Magnetic Properties of Magnesium Ferrite Nanoparticles".*Processing and Application of Ceramics,* vol. 8 (3), pp.137–143

Leroy, A. and Harold, P. K. (1950). "Determination of Crystallite Size with the X-Ray Spectrometer". *Journal of Applied Physics*, **21** (1), 137-142

Sajjadi, S. P. (2005). "Sol-gel Process and its Application in Nanotechnology". *Journal of Polymer Engineering and Technology,* vol.23 (1), pp.38-41

Schmid, G.. (2010). *Nanoparticles: From Theory to Application*. Weinheim: 2nd, Wiley-VCH, 517-522

Spiers, H., Parkin,I.P., Pankhurst,Q.A., Affleck,L., Green, M., Caruana, D.J. ,Kuznetsov, M.V. ,Yao, J.,Vaughan, G., Terry, A. and Kvick, A.(2004). "Self Propagating High Temperature Synthesis of Magnesium Zinc Ferrites $Mg_xZn_{1-x}Fe_2O_4$: Thermal Imaging and Time Resolved X-ray Diffraction Experiments". *J. Mater. Chem*., vol. 14, pp. 1104 -1111

OPTIMIZATION THE EFFICIENCY OF ORGANIC AMENDMENTS FOR REMEDIATION OF INSECTICIDE-CONTAMINATED SOIL

May Thet Tun[1], Phyu Phyu Myint[2], Saw Hla Myint[3]

Abstract

The main aim of this research is to examine the optimization of the organic amendments for remediation of insecticide contaminated soil. The waste materials for crude protein contents, fish scale (*Cirrhinus cirrhosus*), chickpea shell *(Cicer arietinum* L.*)* and peanut shell (*Arachis hypogaeal* L.) were collected from Pyay Township, Bago Region. The crude proteins were extracted from the selected sources by trichloroacetic acid (TCA) method, and evaluated the yield % of nitrogen. The nitrogen contents of fish scale, chick pea shell and peanut shell were found to be 1.527 %, 0.901%, and 0.990%, respectively. Furthermore, the protein extract from selected sources were confirmed by chemical tests. According to the result, the fish scale waste was found to possess the highest content of protein. The fish scale could be potentially applied as a nitrogen source in the determination of soil enzyme activity and degradation of insecticide in soil. Before treatment, two types of amendments were prepared by fermentation for 10 days on mixing the samples viz., FSJ (fish scale-FS: Jaggery-J - 10:10 w/v) and FST (FS: Treacle-T - 10:10 w/v). A laboratory bench study was conducted to assess the removal efficiency of FSJ and FST on 1 ppm insecticide contaminated soil. Three different nitrogen additives from two natural sources; FSJ, FST and one chemical, NH_4-N source with a concentration 4%each treatment were applied on insecticide contaminated soil along with control (no treatment). The residual insecticide (as its metabolite 3-phenoxybenzoic acid 3-PBA) in soil samples extracted from the experimental plot was examined using UV-vis spectrophotometer. After five weeks treatment, the removal efficiency of FSJ and FST treatments was found significantly increased. The profile of soil urease activity in the treated and contaminated soil was also determined by Phenol-Hypochlorite method. The overall results indicated that appropriate waste- amendment application can promote the removal of PBA as well as maintain the activity of urease enzyme in soil.

Keywords: protein extraction, TCA method, waste amendment effect, contaminated soil, urease activity

Introduction

Nowadays, with global population exceeding seven billion, agriculture inexorably continues to play a very important role in the survival of mankind. Since many years, farmers have been used insecticides to kill unwanted insects and to control pests that infest crop. Nearly all insecticides have the potential to significantly alter ecosystems: many are toxic to humans and/or animals; some become concentrated as they spread along the food chain. The presence of these chemicals in both aquatic and terrestrial ecosystems has become an important issue globally. Agriculture and Toxicology provides information on the use of insecticides in pest management in order to enhance crop protection and their effects on nontarget organisms. Insecticides are agents of chemical or biological origin that control insects (Amweg *et al*., 2005). The widespread use of insecticides over the past 30 years has resulted in problems caused by their interaction with natural biological systems. The persistence of insecticides and their degradation products depends on how deeply they are mixed into the soil; even the most persistent compounds disappear relatively quickly when on the soil surface, yet when incorporated into the soil they are very persistent (Dileep, 2002).

Nitrogen (N) fertilizer application is an important measure to improve the soil fertility and crop yield, also it is one of the most management measure in agriculture. Soil microorganisms are important components of soil ecosystem, leading the nutrient cycle and energy flow meanwhile, it

[1] Assistant Lecturer, Department of Chemistry, University of Yangon
[2] Dr, Professor, Department of Chemistry, Loikaw University
[3] Dr, Part-Time Professor, Department of Chemistry, University of Yangon

plays an important role on the ecosystem stability and sustainability (Jingjing *et al*., 2015). Urease is the enzyme that degrades urea and is widely considered to be a good proxy of nitrogen (N) mineralisation. Urease is widely distributed in soils and was one of the first soil enzymes to be experimentally evaluated (Cordero *et al.,* 2019).

The aim of the present research work is to study the effect of nitrogen on remediation of pyrethroid insecticides in contaminated soil and determine the soil urease activities in the treated and contaminated soil.

Materials and Methods

The fish scale, chickpea shell and peanut shell were collected from Pyay market, Pyay Township, Bago Region and identified at Zoology and Botany Department of Pyay University. They were dried, ground well with a pestle and mortar into powder and stored in air-tight container. Figure 1 shows the collected samples used in this study. Treacle from Mya Ywar Sugar Factory, and jaggery residue from Tamikethar village were also collected.

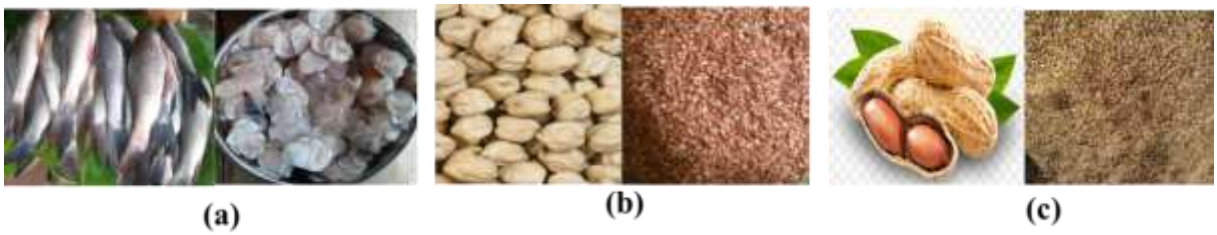

Figure 1 Photograph of samples: (a) fish and fish scale (b) chickpea and chickpea shell (c) peanut and peanut shell

Extraction of Protein from Waste Samples (TCA Method)

Dried powdered sample (1 g) was accurately weighed and extracted with an aliquot of ethanol: petroleum ether (2:1v/v) mixture with constant stirring for 15 min at 550 rpm. The sediment was washed again with pet-ether (200 mL) and stirred 15 min at 550 rpm. The residue was dried at room temperature to remove all traces of pet-ether and dissolved in 5-10 % trichloroacetic acid (TCA). The mixture was kept at 4ºC for about 4 h and filtered. Then 1M NaOH (100 mL) was added into the residue and stirrred for 1h at 550 rpm and filtered. After filtration, 3M HCl was added to the mixture and pH was adjusted to 4.2 and filtered. Next, 1M NaOH was added to get pH 9.0 and stirred for 1h at 550 rpm and filtered. After that, 3M HCl was added to adjust pH 4.2 and filtered. The residue was calculated to obtain percentage of pure protein.

Characterization of crude protein

The extracted crude protein was characterized by Qualitative tests for protein such as Xanthoproteic Test, Biuret Test and Millon's Test.

In Xanthoproteic Test, 2 mL of crude protein solution was taken in a test tube and 0.5 mL of concentrated HNO_3 was added and boiled. The mixture was cooled under tap water and concentrated ammonium hydroxide was added to make the solution alkaline. In Biuret Test, 3 mL of crude protein solution was taken in a test tube and added an equal amount of 10 % sodium sulphate solution. In Millon's Test, about 5 mL of protein solution was taken in a test tube and a few drops of Millon's reagent were added. After mixing thoroughly, the mixture was heated to the boiling point.

Collection of Soil Sample

The soil was collected from the surface layer (0-20 cm) of an agricultural field located in Tamikethar village (at 21°50′ latitude north and 96°40′ longitude east), Myingyan Township, Mandalay Region (Figure 2).

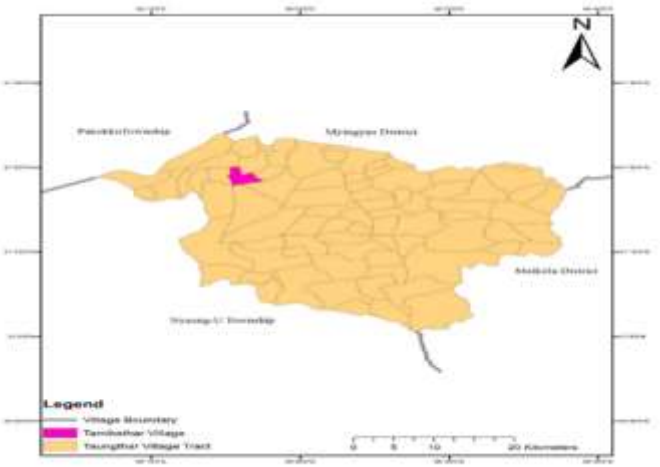

Figure 2 Location of Thamikethar Village

Determination of Physicochemical Properties of Soil Sample

The moisture content of the soil samples was determined according to the reported method. pH content of the soil sample was determined according to the standard method by using pH meter. EC content of the soil sample was determined by using electrical conductivity meter. Organic matter content of the soil sample was determined by using Walkley and Black method based upon the oxidizable organic matter content. Total N content was determined by using Kjeldahl's method. Cation exchange capacity content of the soil samples were determined according to the method of Kappen. Total P of the soil samples was determined by using Olsen method for neutral and alkaline soil (measured by spectrophotometer). Potassium content of the soil samples was determined by using ammonium acetate extraction method (measured by Flame photometer).

Experimental Design

Organic Amendment Samples Preparation

To make the organic amendment, 20 g of fish scale powder was put in a beaker, treacle or jaggery residue of an equal amount (1:1 weight ratio) was added, then mixed thoroughly using a glass rod. The beaker was covered with aluminium foil. The fish scale will have fermented in 14 days' period. The solution was extracted and used as organic amendments; FSJ and FST.

Determination of Insecticide-contaminated Soil Remediation

Fresh soil samples, each equivalent to 10 g of dry soil, were placed in 150 mL beakers and their water contents were adjusted to 60% of water holding capacity. Each treatment in triplicate was spiked with 1 mL cypermethrin (1000 µg/ml). Nitrogen source was added in the form of Nitrate-N by using nitrate fertilizer. FSJ and FST dissolved in water were also added separately into different beakers. All containers were covered with aluminium foil to ensure gas exchange and then incubated at 25 °C for 0 week, 1 week, 2 weeks etc. and up to the 5 week.

Determination of Insecticide Removal

The residue of insecticide was extracted from soil samples (10 g) using the reagent of methanol: dichloromethane (3:1 v/v). Each sample was shaken at 200 rpm for 15 min and then centrifuged at 5000 rpm for 15 min. Solution aliquots were then analyzed using an ultraviolet-visible (UV-vis) detector.

Determination of Urease Activity

The urease activity was determined by urea reduction method. Firstly, 10 g of fresh soil was placed in a 100 mL volumetric flask and treated with 1mL of toluene, 10 mL of buffer (pH-7) and 5 mL of 10 % urea solution (freshly prepared). After a thorough mixing the flask was incubated for 3 h at 37 ºC in dark. For the control, 5 mL of 10 % urea solution was replaced by 5 mL of sterile distilled water. After incubation the volume of the flask was made up to 100 mL with distilled water and shaken thoroughly and transferred the filtrate through Whatman No. 5 filter paper. The ammonia released as a result of urease activity was measured by indophenol blue method. In brief 0.5 mL filtrate was taken into a 25 mL volumetric flask and 5 mL of distilled water was added. Then 2 mL of phenolate solution (mixture of 20 mL of stock A (62.5 g phenol crystals dissolved in a minimum volume of methanol and made up the volume up to 100 mL with ethanol after adding 18.5 mL acetone and 20 mL of stock B (27 g NaOH dissolved in 100 mL distilled water and kept in freezer)) were added. Thereafter, 1.5 mL of sodium hypochlorite solution was added. The final volume of the flask was made up to 25 mL with distilled water and the blue colour was read out with the spectrophotometer at 630 nm.

Results and Discussion

Extraction of Protein from Waste Samples

The crude protein contents of fish scale, chickpea shell and peanut shell were found to be 1.527 %, 0.901 %, and 0.990 % respectively. According to this result, the fish scale waste was found to possess the highest content of protein.

Table 1 Protein Contents of Selected Waste Extracts

Sample	Protein content(%)
Fish scale	1.527
Chickpea shell	0.901
Peanut shell	0.990

Confirmation of the extracted protein from waste samples

In Xanthoproteic test, the crude protein samples extracted from the fish scale, chickpea shell and peanut shell were observed as yellow colour solutions**.** This observation inferred that amino acids like tyrosine, tryptophan, and phenylalanine were present in these waste samples. In Biuret Test, all extracted crude proteins were observed as violet colour solutions. So, these waste samples were indicated the presence of albumin. The intensity of the colour increased as the number of linkages involved in the proteins increased. The fish scale in Millon's Test did not give brick red colour whereas chickpea shell and peanut shell gave brick red precipitate. It was found that all samples gave positive results for Biuret test. These samples gave purple colour indicating the presence of proteins. However, tyrosine are present in chickpea shell and peanut shell according to Millon's test.

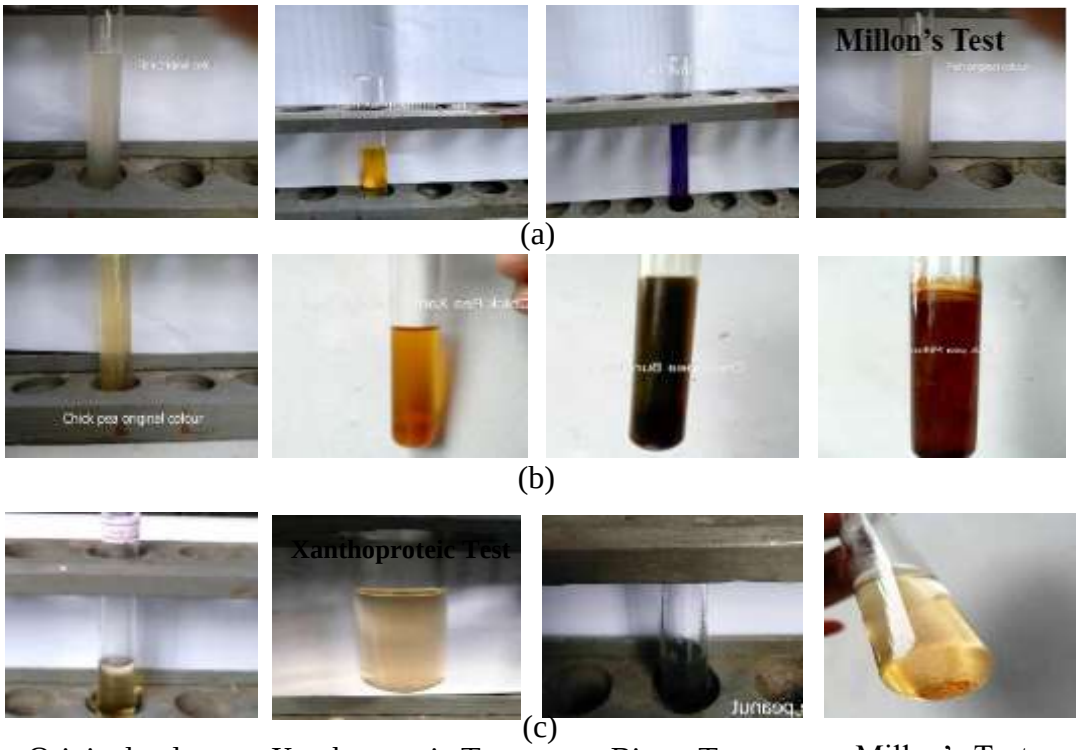

Figure 3 Photographs of confirmation tests for crude protein extracted from (a) fish scale sample (b) chickpea shell and (c) peanut shell samples

Physicochemical Properties of Soil Sample

The characteristics and physicochemical properties of soil sample are shown in Table 2. Soil pH value was found to be 8.22. The representative soil that used in this study was the type of moderate alkalinity. The data pointed out that the moisture content was 4.75 %. The moisture content of soil sample was sufficient for cultivation of plant. Moreover, 0.87 % of humus and 0.50% of organic carbon contents were found in the representative soil and it was found to have very low in organic matter content. The experimental data showed high in Ca (26.61 meq/ 100 g), medium in Mg (2.10 meq/100 g), low in K (0.62 meq/100 g) and Na (2.99 meq/100 g). The concentration of calcium helps in membrane stability maintenance of chromosome structure and enzyme inhibitor. Magnesium helps the movement of sugar within plant. Sufficient amount of potassium increases the size of grains or seeds and improves the quality of fruits and vegetables. The deficient K causes the shriveled seeds or fruits. Sodium is not essential element for plants but can be used in small quantities, similar to micronutrients, to aid in metabolism and synthesis of chlorophyll. The contents of total nitrogen, phosphorus and potassium were 0.09 %, 7.56 ppm and 28.99 mg/100g, respectively. An abundance of nitrogen promotes rapid growth with a greater development of green leaves and stems. The presence of sufficient available phosphorus is required for seed formation and crops maturity.

Table 2 Characteristics of the Soil Sample

Parameter		Content
Moisture (%)		4.75
pH Soil: Water 1:2:5		8.22
EC (mS/cm)		0.10
Organic Carbon (%)		0.50
Humus (%)		0.87
Total N (%)		0.09
CEC (meq/100 g)		32.32
Exchangeable cations	Ca^{2+}	26.61
	Mg^{2+}	2.10
	K^{+}	0.62
	Na^{+}	2.99
	H^{+}	Not detected
	Al^{3+}	Not detected
Available nutrients	P (ppm) (Olsen)	7.56
	K_2O (mg/100g)	28.99

Determination the organic amendments efficiency on soil remediation

The insecticide residue in soil was observed to be decreased gradually in all treatments after 5 - week period. It was found that the urea, FSJ and FST treatments significantly increased the degradation of cypermethrin in soil as compared with the control (no treatment) after 2-week period. After 5 weeks, the removal efficiency of FSJ and FST treatments were found significantly increased. These findings indicated that adequate addition of N could increase the degradation of cypermethrin but oversupplying N suppress it. However, the degradation levels were similar after a long enough incubation period.

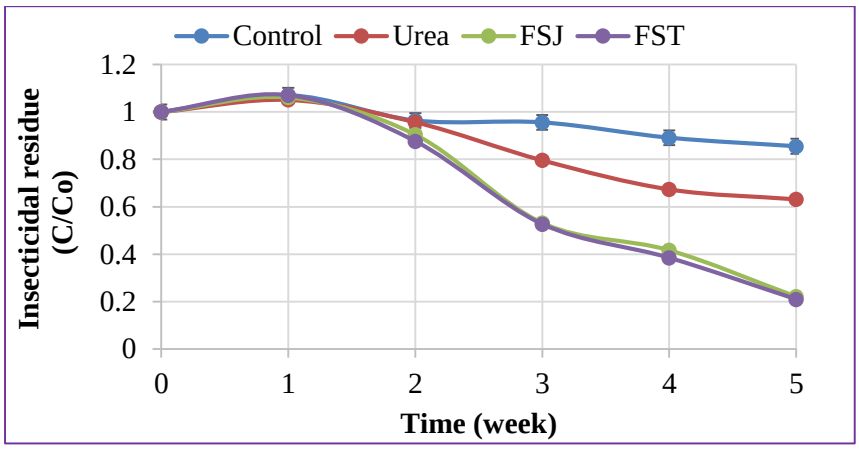

Figure 4 Insecticide residues in soil by different dosage of various amendments treatments

Enhancement of Urease Enzyme Activity

According to comparative study of all treatments, it was found that the urease activity was significantly increased by FSJ and FST treatments more than the control (no treatment) after 2-week and 3-week periods. The maximum urease activity levels were observed in the urea, FSJ

and FST treatments after 4 and 5 weeks. These results suggested that adequate additions of N stimulated soil microbial activity, which in turn enhanced degradation of cypermethrin.

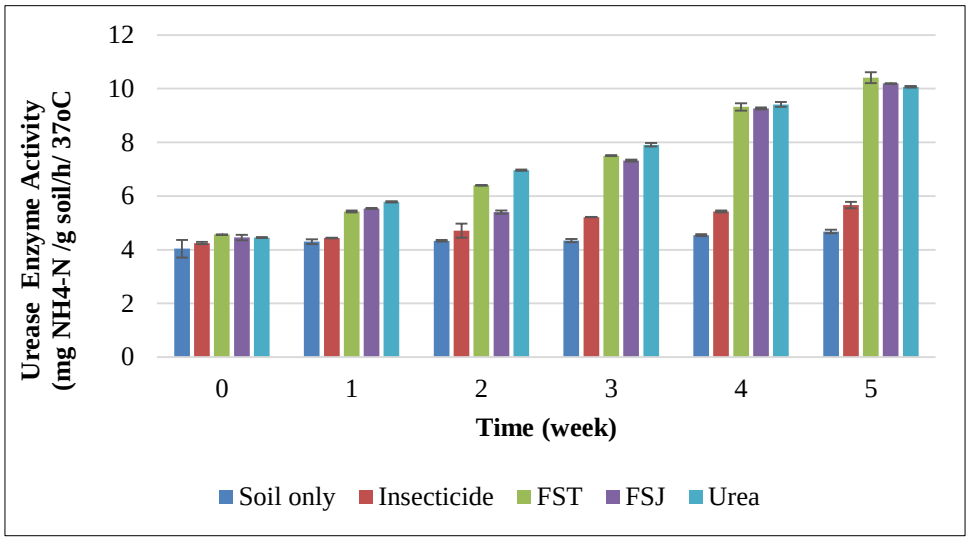

Figure 5 Urease enzyme activity of insecticide contaminated soil

Conclusion

The crude proteins were extracted from different waste materials, fish scale, chickpea shell and peanut shell by trichloroacetic acid (TCA) method, and the protein contents were found to be 1.527 %, 0.901% and 0.990%, respectively. Furthermore, the confirmation tests of protein in selected sources were done. According to this result, the fish scale waste was found to possess the highest content of protein. The fish scale could be potentially applied as nitrogen source in the determination of soil enzyme activities and remediation of insecticide in soil. The results of this study showed that addition of N at an adequate rate could enhance remediation of cypermethrin and its most persistent metabolite, PBA. Thus, in agricultural practice, adequate application of N fertilizer was an efficient method to reduce the accumulation of cypermethrin and PBA in soil and significantly decreased environmental risks, oversupplying N inhibited the degradation of cypermethrin and PBA in soil.

Acknowledgement

The authors would like to express their profound gratitude to the Myanmar Academy of Arts and Science for giving permission to submit this paper and to Professor and Head, Dr Daw Ni Ni Than, Department of Chemistry, University of Yangon, for her kind encouragement.

References

Amweg, E. L., Weston, D. P. and Ured, N. M. (2005). "Use and Toxicity of Pyrethroid Pesticides in the Central Valley, California, USA". *Environ. Toxicol. Chem*. vol. 24(4), pp.966- 972

Cordero, I., Helen, S. and Richard, D.B. (2019). "High Throughput Method for Measuring Urease Activity in Soil''. P *Soil Biol Biochem*., vol 134, pp.72-77

Dileep, K.S., (2002). "Microbial Degradatio of Insecticides: An Assessment for its Use in Bioremediation''. *Progress in Industrial Microbiology*, vol36, pp.175-188

Jingjing, S., Zhu, M., Yang, X., Zhang, C. and Yao, J. (2015). "Microbial, Urease Activities and Organic Matter Responses to Nitrogen Rate in Cultivated Soil''. *The Open Biotechnology Journal*, vol .9, pp. 14-20

PREPARATION OF WHITE STICKY RICE STARCH-CLAY NANOCOMPOSITE FILMS AND ITS APPLICATION

Htun Minn Latt*

Abstract

Plastic materials are not easily degradable and produce hazardous waste, causing environmental problem. In order to solve this problem, the uses of biodegradable polymers from renewable sources were generated. In this study, polymer films of polyvinyl alcohol (PVA)–white sticky rice starch were prepared by casting method. White sticky rice starch was extracted from white sticky rice grains collected from Myothit Township, Magway Region, and yield percentage was 64 %. Physicochemical properties such as pH, moisture percent, true density and bulk density and porosity of sticky rice starch were determined as 7.10, 10.51 %, 3.85 g mL^{-1}, 2.41 g mL^{-1} and 37.50 %, respectively. Semi-crystalline nature of the sticky rice starch with the average crystallite size of 51.65 nm was shown by XRD. Nanoclay was prepared from volcanic mud of Nagarpwak Taung in Minbu Township, Magway Region and the crystallite size was 30.79 nm. Nanocomposite films of PVA – starch – clay- glycerol were prepared by varying the ratios of nanostarch and nanoclay, i.e., 50:50 and 75:25. PVA – starch – clay- glycerol (75:25) film was found to have more flexible and plasticizing effect than the film with the ratio of 50:50. Biodegradability of these films was tested by soil burial method and the film with nanostarch and nanoclay with the ratio of 75:25 completely degraded after 18 days. For fruit coating application tomato fruits were dipped in prepared nanocomposite film and the tomato fruits were still fresh after 25 days compared to 8 days of non-coated tomato fruit.

Keywords: White sticky rice starch, clay, nanocomposite films, polyvinyl alcohol

Introduction

Plastics are widely used packaging materials for food and non-food products due to desirable material properties and low cost. However, the merits of plastic packaging have been overshadowed by its non-degradable nature, thereby leading to waste disposal problems. The public is also gradually coming around to perceive plastic packaging as something that uses up valuable and scarce non-renewable natural resources like petroleum. Moreover, the production of plastics is relatively energy intensive and it results in the release of large quantities of carbon dioxide as a by-product, which is often believed to cause, or at least contribute to global warming. Some recent research findings have also linked plastic packaging to some forms of cancer (El Amin, 2005; Kirsch, 2005). In order to solve problems generated by plastic waste many efforts have been done to obtain an environmental friendly material. Most of the researches are focused on substitute starch - based plastics by biodegradable materials with similar properties (Cyras *et al.*, 2008). Starch is known to be completely biodegradable in soil and water, and due to its cheap sources is one of the best candidates for replacing current synthetic plastics including packaging materials (Park *et al.*, 2003).

Packaging materials based on polymers that are derived from renewable sources may be a solution to the above problems. Such polymers include naturally existing proteins, cellulose, starches, and other polysaccharides, with or without modifications. These renewable polymers are not only important in the context of petroleum scarcity, but are also generally biodegradable under normal environmental conditions. Interest and research activity in the area of biopolymer packaging films have been especially intensive over the past 10 years (Krochta *et al.*, 1997; Tharanathan, 2003).

* Dr, Lecturer, Department of Chemistry, University of Magway

Materials and Methods

Extraction of Starch from Sticky Rice (White) Grain

The sticky rice (white) grains were collected from Myothit Township, Magway Region. Starch was extracted from sticky rice (white) grains. White sticky rice powders (200 g) were ground and the powder was passed through 250 mesh screen. Distilled water (250 mL) was added to the powder, stirred manually for 30 min and allowed to settle overnight. The supernatant was decanted off and this starch was subjected to a second washing and settled overnight. The supernatant was then decanted off and filtered through a double-layered cotton cloth. Then the starch obtained was dried in air for 48 h at room temperature. The starch lumps were powdered before it was stored in polyethene bag prior before use and the yield percent of sticky rice (white) starch powder was calculated. The yield percentage of starch powder was found to be 74.00 %.

Determination of Some Physicochemical Properties of Sticky Rice (White) Starch pH

Sticky rice (white) starch (1.0 g) was made into mucilage with 100 mL of distilled water and it was determined for pH with a pH meter (Oyster-15), which was previously calibrated with standard buffers of pH 4 and 7.

Moisture content

Moisture content of the white sticky rice sample was determined by using moisture analyzer (USA, MB-23) at Research Center, Magway University.

True density

The true density (D_t) of sticky rice (white) starch powder was determined by the liquid displacement method using xylene as the immersion fluid (Hasan *et al.*, 2014). Density bottle (10 mL) was filled with xylene solvent and then weighed and recorded. Sticky rice (white) starch powder (2 g) was added into the above bottle and weighed and recorded. True density of sticky rice (white) starch was calculated by the following formula:

$$D_t = \frac{W_p}{\left[\left(a + W_p\right) - b\right]} \times SG$$

where, D_t = true density

W_p = the weight of starch powder

SG = specific gravity of solvent (xylene, 0.962)

a = weight of bottle and solvent

b = weight of bottle, solvent and starch powder.

Bulk density

A clean dry 10 mL graduated cylinder was weighed. It was then filled with the dry white sticky rice sample to the 10 mL mark and reweighed. The graduated cylinder was placed in a tapping box and the cylinder was tapped gently until there is no more reduction in volume. The minimum volume was recorded and the bulk density was calculated.

$$\text{Density} = \frac{\text{Weight of sample (g) x 6.24}}{\text{Final volume of sample (mL)}}$$

Porosity

The porosity is related to the true density and bulk density. So, the porosity of starch was calculated by the method of Ohwoavworhua *et al*. (2007) as:

$$\text{Porosity} = \left(1 - \frac{\text{bulk density}}{\text{true density}}\right) \text{x } 100$$

Preparation of Starch Nanoparticles

Starch nanoparticles were prepared by hydrolyzing starch with H_2SO_4.The prepared starch powder of white sticky rice was suspended in 3 M H_2SO_4 at a concentration of 5% (w/v) and incubated in a shaker at 37°C and 100 rpm for 5 days. Then, the resultant solution was filtered using Whatman filter paper. The obtained H_2SO_4 hydrolyzed starch nanoparticles were dried at 60°C to constant weight.

Extraction of Nanoclay from Volcanic Mud

Nanoclay was extracted from volcanic mud of Nagarpwak Taung in Minbu Township. Firstly, 60 g of volcanic mud are placed into the first plastic container. Next, 8.4 L of distilled water was poured into the container. After keeping still a mixture of volcanic mud and water for 24 h, the mixture was stirred for 20 min and became liquid along with some solid precipitate. The mixture was then kept still for 48 h and precipitate was found at bottom of the first container. The liquid of the first plastic container was decanted into the second plastic container. The liquid was kept still in the second plastic container for 7 days, and precipitate was found at the bottom of the second container. The liquid of the second plastic container was decanted into the third plastic container. After 2 L of the liquid was taken from the third plastic container, the liquid was baked and heated on sand-bath. Then the remaining liquids were dried in an oven at 250 ^oC for 48 h and dried nanoclays were ground up to be powder.

Characterization of Nanostarch and Nanoclay

Surface morphology of nanostarch and nanoclay were examined by Scanning electron microscope (SEM), EVO– 18, ZEISS, Germany at Research Center, Magway University and structural property by XRD at Universities' Research Center, Yangon.

Preparation of Film

PVA-starch was taken in water in different composition (50:50 v/v and 75:25 v/v). The reaction mixture was stirred at 70ºC and 100 rpm until uniformity appeared. After cooling the solution at 35 ºC, all the solutions are mixed and modified with 30 % glycerol. A specified amount of Nano Clay (0.3 % by wt. of PVA-starch) was dissolved in the PVA-starch solution. The starch solution containing the clay was stirred at 70 °C and 100 rpm, held at that temperature for 20 min and then cooled to 50 °C. Then the solutions were poured into casting mold and dried in the oven at 75ºC to remove water contents. After complete drying, the films were stored in moisture free environment.

Investigation of Biodegradability of Films by Soil Burial Test

The biodegradability of the prepared PVA and PVA - starch - clay - glycerol films were investigated by soil-burial test. Firstly, composted soil under tamarind tree was collected and put into the different plastic boxes. The films (4″ × 6″ dimensions) were layered on the soil and then the films were covered with the same soil, the depth being 10 cm. The boxes were placed in the

laboratory and the moisture of the soil was maintained by sprinkling water at regular time intervals. The excess water was drained through a hole at the bottom of the box. The degradation of the samples was determined at regular time intervals (4 days) by carefully removing the sample from the soil and washing it gently with distilled water to remove soil from the film. They were taken out from the soil at an interval of 4 days until entirely degraded. Sample geometry on degradation was also recorded by photograph.

Study on Food Coating of Tomato Fruits

PVA-starch-clay-glycerol (75:25) mixture solution was prepared. Then tomato fruits were dipped in this solution for film coating and kept at room temperature. For control, these fruits were not treated with the PVA-starch-clay-glycerol mixture solution. The appearances of the fruits were observed daily.

Results and Discussion

Physicochemical Properties of White Sticky Rice

The physicochemical properties such as pH, moisture percent, true density and bulk density of white sticky rice starch were 7.1, 10.51 %, 3.85 gmL^{-1} and 2.41 gmL^{-1}, respectively. Porosity of starch was calculated to be 37.50 %. All data are shown in Table 1.

Table 1 Physicochemical Properties of White Sticky Rice Starch

No.	Parameter	Experimental values
1	pH	7.10
2	Moisture content (%)	10.51
3	True density (g mL^{-1})	3.85
4	Bulk density (g mL^{-1})	2.41
5	Porosity (%)	37.50

Characterization of Nanostarch and Nanoclay

Scanning electron microscopic (SEM) analysis of nanostarch

The surface morphology of nanostarch sample was examined by SEM micrograph as described in Figure 1. The sample was observed as polygonal shape for the starch granules with ununiform sizes.

X-Ray Powder diffraction studies on nanostarch

XRD pattern (Figure 2) of sticky rice starch shows strong diffraction peaks at 16.5^{o}, 21.0^{o}, and 23.09^{o} of 2θ. For the presence both sharp and diffuse diffraction in this XRD, sticky rice starch was observed to have semi-crystalline nature. Parallel double amylopectin molecules result in the formation of crystalline regions, while amylose molecules result in the formation of amorphous regions in the starch structure. The average crystallite size of nanostarch sample was calculated based on Sherrer formula and it was found to be 51.65 nm.

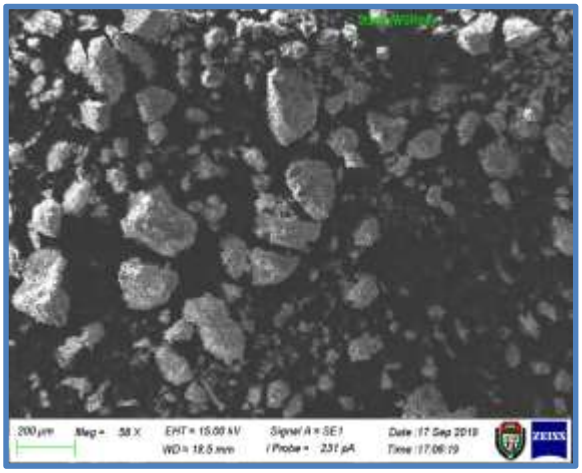

Figure 1 Scanning electron micrograph of nanostarch from white sticky rice

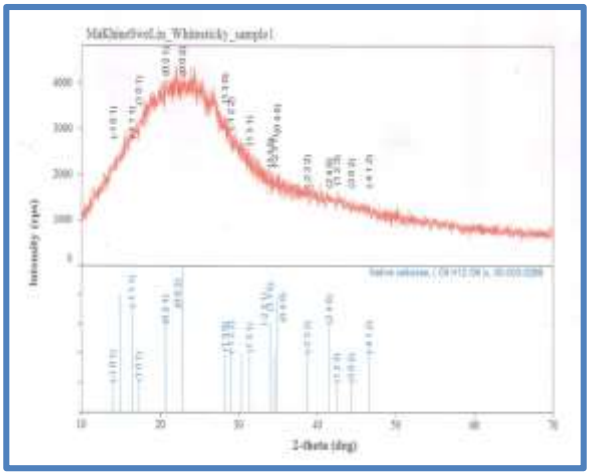

Figure 2 X-ray diffractogram of nanostarch from white sticky rice

Scanning electron microscopic (SEM) analysis of nanoclay

Nanoclay was extracted from volcanic mud of Nagarpwak Taung in Minbu Township. The surface morphology of nanoclay sample was examined by SEM micrograph as shown in Figures 3. From SEM micrograph, the sample was disordered pore system.

X-Ray powder diffraction studies on nanoclay

Crystalline nature of nanoclay was observed in X-ray powder diffractogram (Figure 4) because of the presence of sharp peaks. Nano - clay sample showed strong diffraction peaks at 12.45º, 18.72º, 20.79º, 25.12º, 26.57º, 31.63º and 45.40º of 2θ. The average crystallite size of nanoclay was determined from XRD pattern by using Scherrer equation. The average crystallite size of nanoclay was 30.79 nm.

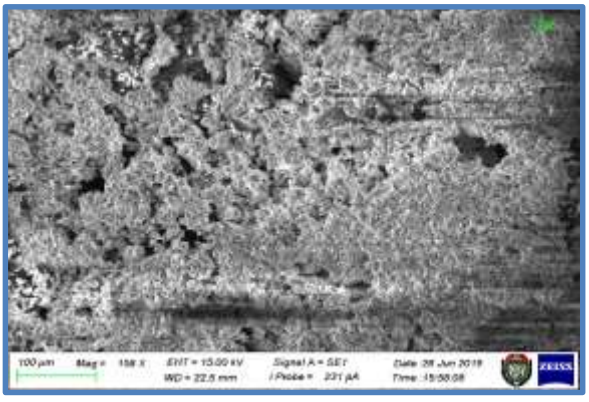

Figure 3 Scanning electron micrograph of nanoclay

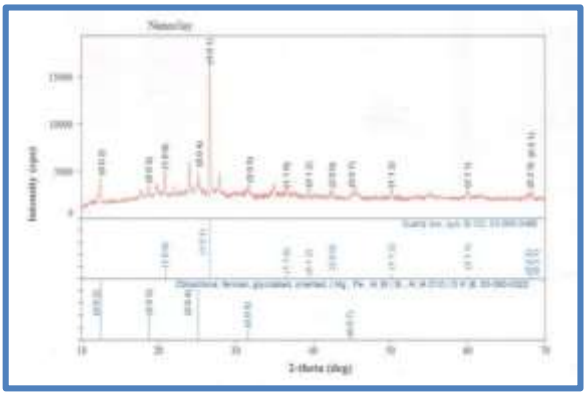

Figure 4 X-ray diffractogram of nanoclay

PVA-Starch- Clay – Glycerol Films with Different Concentrations

Nanocomposite films of PVA - starch - clay - glycerol were prepared by casting method. Different ratios (50:50 and 75:25) of nanocomposite films were made. Film with PVA – starch – clay- glycerol (75:25) was found to be flexible and plasticizing effect than the film with the ratio of 50:50 (Figure 5).

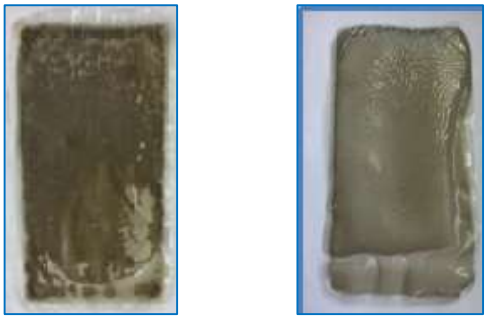

Figure 5 Prepared PVA-starch- clay - glycerol films with different concentrations

Soil Burial Test for Prepared Films

The natural biodegradation of these films in the soil environment were observed in soil burial method during 20 days. After 18 days, PVA – starch – clay – glycerol (75:25) film was completely destroyed.

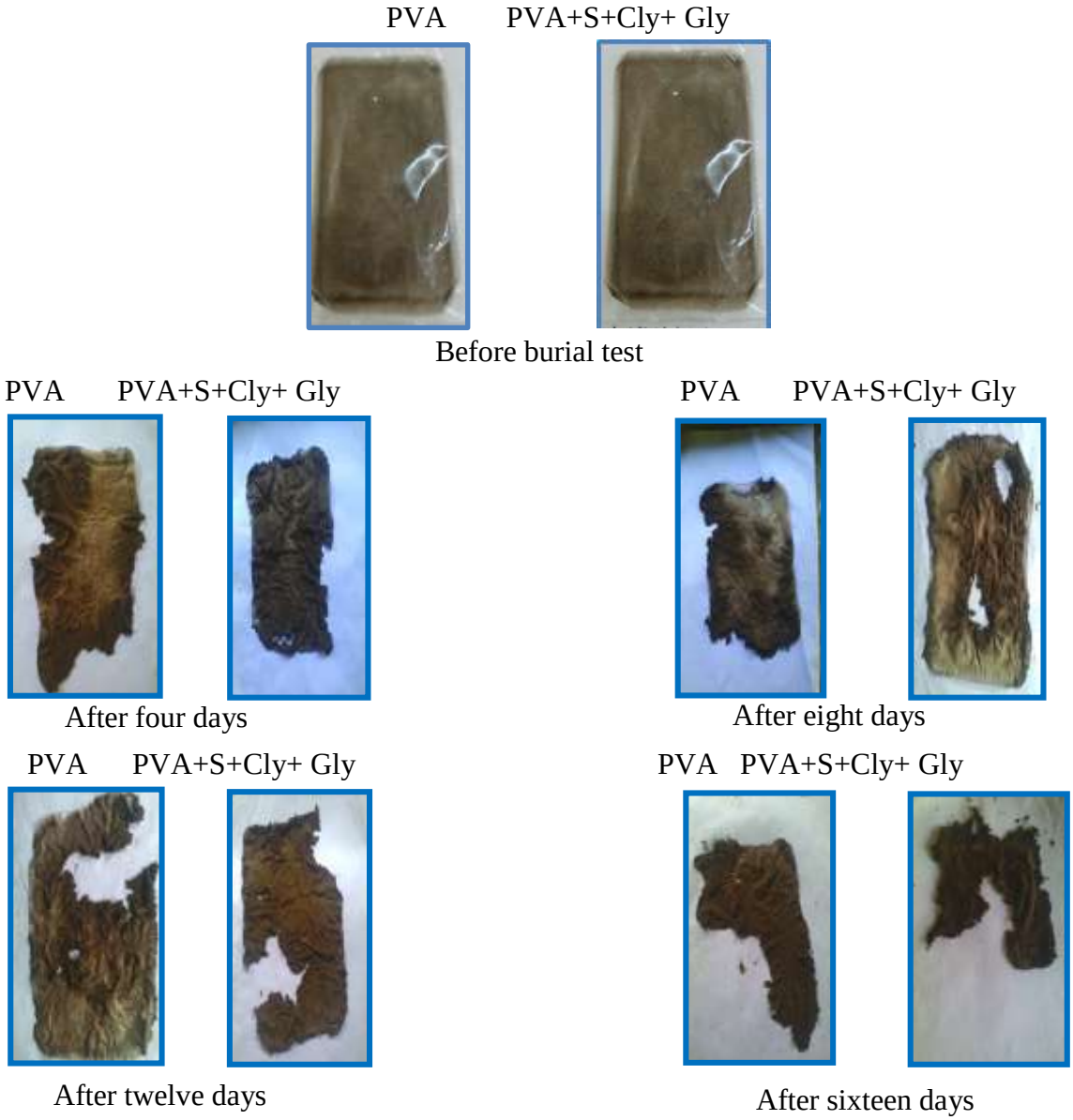

Figure 6 Soil burial tests for prepared films

Study on Food Coating of Tomato Fruits

Figures 7 to 9 show the physical appearances of tomato fruits. After 8 days, the tomato fruit without coating started to decay. The tomato fruit with coating was still fresh after 25 days. It was observed that PVA – starch – clay – glycerol (75:25) blended solution retreated ripening and decay.

Coating Non-coating

Figure 7 Coating and non-coating tomato fruits (after 1 day)

Coating Non-coating

Figure 8 Coating and non-coating tomato fruits (after 4 days)

Coating Non-coating

Figure 9 Coating and non- coating tomato fruits (after 8 days)

Conclusion

Polymer films of polyvinyl alcohol (PVA) - starch - clay - glycerol were successfully prepared by casting method. White sticky rice starch extracted from white sticky rice grains and prepared nanoclay from volcanic mud of Nagarpwak Taung in Minbu Township, Magway Region were used to prepare films. They were polygonal in shapes for the starch granules with non-uniform sizes and disordered pore system for nanoclay. XRD confirmed the nanosize of both sticky rice starch (51.65 nm) and nanoclay (30.79 nm). PVA - starch - clay- glycerol nanocomposite films with clay. PVA - starch - clay- glycerol (75:25) ratio showed to have more smooth and plasticizing effect than the film with the ratio of 50:50. The prepared film it was completely degraded after 18 days. In the study on food coating, the tomato fruit coated by PVA - starch - clay- glycerol (75:25) film was still fresh after 25 days whereas non-coating fruit started to decay after 8 days.

Acknowledgement

I would like to thank Dr Khin Maung Oo, Rector, Magway University, for his encouragement. I am really indebted to Dr Thidar Aung, Professor and Head of the Department of Chemistry, for her invaluable suggestions.

References

Cyras, V. P., Manfredi, L. B., Ton-That, M. T. and Vazquez, A. (2008). "Physical and Mechanical Properties of Thermoplastic Starch/montmorillonite Nanocomposite Films. *Carbohydrate Polymers*, vol., (73), pp. 55–63

El-Amin, A. (2005). *Common Plastics Packaging Chemical Linked to Cancer*. Food Production Daily e-newsletter, pp. 3-33

Hasan,M. M., Rana, M.S., Uddin,N., Rahman,K.J. and Chowdhury,S.S. (2014). "Comparative Evaluation of Solanum tuberosum L. and Manihot esculenta Starch as Pharmaceutical Excipients: Assessment by Preformulation Studies". *Bangladesh Pharmaceutical Journal*, vol.17(2), pp. 128-134, 2

Kirsch, C. (2005). *Compounds in Plastic Packaging Act as Environmental Estrogens Altering Breast Genes.* Eurek Alert e-newsletter.

Krochta, J. M. and De Mulder-Johnston, C. (1997). "Edible and Biodegradable Polymer Films: Challenges and Opportunities". *Food Technology*, vol.51, pp. 61-74

Ohwoavworhua, F.O, Ogah, E. and Kunle, O.O. (2005). "Preliminary Investigation of Physicochemical and Functional Properties of Alpha Cellulose Obtained from Waste Paper - A Potential Pharmaceutical Excipient". *J. Raw Mat. Res.* vol. 2, pp. 84- 93

Park, H. M., Lee, W. K., Park, C. Y., Cho, W. J. and Ha, C. S. (2003). "Environmentally Friendly Polymer Hybrids". *Journal of Materials Science*, vol., 38, pp. 909-915

Tharanathan, R. N. (2003). "Biodegradable Films and Composite Coatings: Past, Present and Future". *Trends Food Science Technology*, vol., 14, pp. 71-78

BIOSYNTHESIS OF SILVER NANOPARTICLES USING EXTRACTS OF NEEM LEAVES

Yoon Noe Aung[1], Ye Myint Aung[2], Nilar Kyi[3]

Abstract

The biosynthesis of silver nanoparticles from extracts of neem leaves was studied. In this research, silver nitrate was used as a metal precursor and nee[1]m leaves extract was taken as a reducing agent for synthesis of silver nanoparticles, AgNPs. The characteristics of silver nanoparticles were mainly confirmed by UV-Visible spectroscopy, Energy Dispersive X-ray Fluorescence (EDXRF) spectroscopy, X-ray Diffraction (XRD) analysis, Fourier Transform Infra-red (FT IR) spectroscopy and Scanning Electron Microscopy (SEM). In the biosynthesis process, effect of neem leaves extract and effect of stirring time on synthesized AgNPs were also studied. It was observed that the maximum wavelength of synthesized AgNPs was 410 nm that agreed with the literature value of the wavelength range of 400-500 nm for silver nanoparticles. The EDXRF data showed a percent relative abundance of Ag (50.108%) that confirmed the presence of silver in the suspension. From XRD data, the average crystallite size was calculated by Scherrer equation and found to be 37.14 nm. FT IR analysis showed the presence of the protein or amino acid group in neem extract which reduced Ag^+ ion into metallic Ag nanoparticles. In SEM analysis, it was found that the sample was likely to be well dispersed agglomerates of grains with narrow size distribution. As other evidence, the characteristic of AgNPs was observed by Tyndall effect. The antimicrobial activity of prepared AgNPs was also studied by the six microorganisms - *Bacillus subtilis*, *Staphylococcus aureus*, *Pseudomonas aeruginosa*, *Bacillus pumilus*, *Candida albicans* and *Escherichia coli.* It was observed the AgNPs suspension was more potent than neem extract only especially in *Bacillus pumilus* and *Escherichia coli* with the zone diameters of 15 mm.

Keywords: neem leaves extract, reducing agent, silver nitrate, antimicrobial activity

Introduction

Nanotechnology provides the ability to engineer the properties of materials by controlling their size, and this has driven research toward a multitude of potential uses for nanomaterials (Saifuddin *et al.*,2009). Nanoparticle synthesis and the study of their size and properties is of fundamental importance in the advancement of recent research. It is found that the optical, electronic, magnetic and catalytic properties of metal nanoparticles depend on their sizes, shape, and chemical surroundings.

Nanoparticles can be broadly grouped into two: namely organic and inorganic nanoparticles. Inorganic nanoparticles (such as metallic and semiconductor nanoparticles) exhibit intrinsic optical properties which may enhance the transparency of polymer-particles composites. For such reasons, inorganic nanoparticles have found special interest in studies devoted to optical properties in composites (Caseri, 2009). Green synthesis methods employing either biological microorganism or plant extracts have emerged as a simple and alternative to chemical synthesis. Generally, the green synthesis method involves three main steps, (1) solvent medium selection, (2) environmental benign reducing agent selection, and (3) non-toxic substances for nanoparticles stability selection. The synthesis of nanoparticles by using plant extracts can be advantageous over other biological processes because it eliminates the elaborate process of maintaining cell cultures and can be suitably scaled up for large scale production under non-aseptic environments (Loo *et al.*, 2012).

[1] Demonstrator, Department of Chemistry, Pathein University
[2.] Dr, Professor and Head, Department of Chemistry, Pathein University
[3.] Dr, Prorector (retired), Department of Chemistry, University of East Yangon

Azadirachta indica commonly known as Neem belongs to Meliaceae family, and is well known in India and its neighbouring countries for more than 200 years as one of the most versatile medicinal plant having a wide spectrum of biological activity. Every part of the tree has been used as a traditional medicine for house-hold remedy against various human ailments, from antiquity (Koul *et al.*, 1990). Antimicrobial capability of AgNPs allows them to be suitably employed in numerous household products such as textiles, food storage containers, home appliances and in medical devices (Marambio-Jones and Hoek, 2010). The most important application of silver and AgNPs is as topical ointments to prevent infection against burns and open wounds (Ip *et al*., 2006). The aim of this research is to study the biosynthesis of silver nanoparticles by using aqueous neem leaves extract and to determine the antimicrobial activities of synthesized AgNPs.

Materials and Methods

Sample Collection

In this experimental work, the leaves of *Azadirachta indica* A. Juss (Tama-kha) were collected from Pathein Township, Ayeyarwady Region, Myanmar. After collection, the scientific name of the plant was identified at Botany Department, Pathein University. The collected fresh samples were washed and air dried at room temperature for about one week and then they were ground into powder by a grinder. The dried powder samples were stored in air-tight containers.

Preparation of Neem Leaves Extract

The leaves were ground to get a fine powder and 30 g of dried powder was weighed in an electric balance and put into a beaker. A 100 mL of phosphate buffer, pH 9.0 and a 100 mL of distilled water were added into the sample, and then were boiled for 30 min. After cooling at room temperature, it was filtered with filter paper into the conical flask and then centrifuged at 6,000 rpm for 10 min and filtered. The filtrate was stored at 4 ºC for further experiments. The filtrate was used as reducing and stabilizing agent for 1 mM of $AgNO_3$ (Roy *et al.,* 2017).

Preparation of Silver Nanoparticles (AgNPs) Using Neem Leaves Extract

The extract of neem leaves (20 mL) was mixed with 50 mL of 1 mM silver nitrate ($AgNO_3$) solution in a conical flask under aseptic condition. The flask was magnetically stirred while heating at 50 ºC in dark for 5 h. A change in the colour was observed indicating the formation of silver nanoparticles. The solution was centrifuged at 6,000 rpm for 30 min to obtain the silver nanoparticles and the supernatant was discarded. The particles were repeatedly washed to ensure purity and dried at 100 °C in an oven (Roy *et al.,* 2017).

Effect of Different Volumes of Neem Leaves Extract

Each of the extract of neem leaves (10, 20, 30) mL was mixed with 50 mL of 1 mM silver nitrate ($AgNO_3$) solution in a conical flask under aseptic condition. The flask was magnetically stirred while heating at 50 ºC in dark for 5 h. A change in the colour was observed indicating the formation of silver nanoparticles. The solution was centrifuged at 6,000 rpm for 30 min to obtain the silver nanoparticles and the supernatant was discarded. The particles were repeatedly washed to ensure purity and dried at 100 °C in an oven.

Effect of Stirring Time

The extract of neem leaves (20 mL) was mixed with 50 mL of 1 mM silver nitrate ($AgNO_3$) solution in a conical flask under aseptic condition. The flask was magnetically stirred while heating at 50 ºC in dark for each about (3, 4, 5) h. A change in the colour was observed indicating the

formation of silver nanoparticles. The solution was centrifuged at 6,000 rpm for 30 min to obtain the silver nanoparticles and the supernatant was discarded. The particles were repeatedly washed to ensure purity and dried at 100 °C in an oven.

Characterization of Silver Nanoparticles

The silver nanoparticles prepared from neem leaves extract and silver nitrate ($AgNO_3$) was characterized by UV-Visible EDXRF, XRD, FTIR, and SEM techniques.

Determination of λ_{max} of AgNPs by UV-Visible Spectroscopic Method

The bio-reduction of the Ag^+ ions by the supernatant of the test plant extracts in the solutions and formation of silver nanoparticles were monitored by UV-1800 (Shimadzu) spectrophotometer operated at a resolution of 1 nm. The UV-Vis spectra of the samples were measured in the wavelength range of 300 - 600 nm. Distilled water was used to adjust the baseline.

Screening of Antimicrobial Activities

The antimicrobial activity of the crude extracts was performed by the agar well diffusion assay. The pathogenic test organisms were incubated in trypticase soy broth at appropriate temperature for 24 h. Nutrient agar medium containing meat extract (0.5 g), peptone (0.5 g), sodium chloride (0.25 g), agar (1.5 g) and 100 mL of distilled water were placed in a beaker and the contents were heated for 30 min. The nutrient agar medium was put into sterilized conical flask and plugged with cotton wool and then autoclaved at 121 ºC for 15 min. After cooled down to 40 ºC, one drop of suspended strain was inoculated to the nutrient agar with the help of a sterilized disposable pipette near the burner. About 20 mL of medium was poured into the sterilized petri dish and allowed to set the medium. Once solidified the dishes were stored for 2 h in a refrigerator. Two wells of 10 mm diameter each were cut out in the inoculated agar to place extract samples to be tested. The volume of each extract sample placed in each well was 0.2 mL. Two samples, namely neem leaves extract and AgNPs suspension were tested. The petri-dishes were then incubated at 37 ºC for 24 h, and the diameters of clear inhibition zone around the wells were measured (Collin, 1965).

Results and Discussion

Silver Nanoparticles Using Neem Leaves Extract

In this work, silver nanoparticles were synthesized by using silver nitrate and neem leaves extract. The silver nitrate was used as a metal precursor and neem leaves extract was used as a reducing agent. The formation of silver nanoparticles was confirmed through visual assessment. The reaction mixture turned to dark brown colour from brownish-yellow colour within 20 min indicating the formation of silver nanoparticles in the solution. Reduction of silver ion into silver particles during exposure to the leaf extracts could be followed by colour change. Silver nanoparticles exhibited dark yellowish-brown colour in aqueous solution due to the surface plasmon resonance phenomenon (Azizi *et al.,* 2013). Figure 1 shows the aqueous extract of neem leaves before and after synthesis of AgNPs.

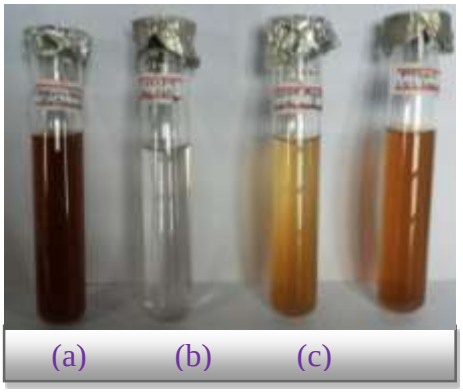

Figure 1 Photographs of (a) aqueous extract of neem leave extract (b) silver nitrate solution (1mM) (c) silver nanosuspension (after 20 min) and (d) silver nanosuspension (after 5 h)

Effect of Different Volumes of Neem Leaves Extract

The reducing agent gives the particles with narrower size distribution of the uniform size of AgNPs. The extracts of neem leaves (10, 20 and 30) mL were used in this work. The absorption spectra of AgNPs with different volumes of neem leaves extracts are shown in Table 1 and Figure 2. With the increasing reducing agent larger nanoparticle cluster were formed. The silver colloids exhibit absorbance in the visible region, and the wavelength at the maximum absorption highly shifts towards a longer one with the increase of leaf extracts (Dagmara *et al.,* 2012). Maximum absorbance of electromagnetic wave of visible range (400-500 nm) was observed in the literature where silver nanoparticles synthesized by using neem leaves extraction (De Silva *et al.,* 2013). In this study,the wavelength of maximum absorption was found at 410 nm which was in accordance with the literature value.

Table 1 Relationship between Absorbance of AgNPs Solution using Different Volumes of Neem Leaves Extract as a Function of Wavelength

Wavelength (nm)	Absorbance		
	10 mL	20 mL	30 mL
390	3.20	3.40	3.80
400	3.25	3.60	3.79
410	3.56	3.70	4.0
420	1.34	1.60	1.93
430	1.52	1.67	2.06
440	1.35	1.40	1.43
450	1.24	1.43	1.47
460	0.52	0.70	0.97
470	0.76	0.90	1.04

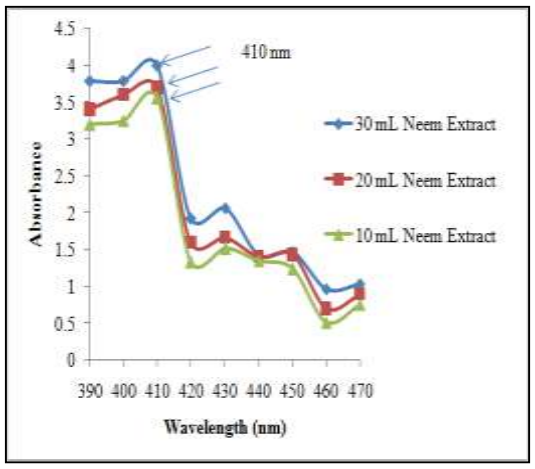

Figure 2 Changes of absorbance of silver nanoparticles with different volumes of neems leaves extract at different wavelengths

Effect of Stirring Time

The extract of neem leaves (20 mL) was mixed with 50 mL of 1 mM silver nitrate ($AgNO_3$) solution in a conical flask. The flask was kept in heat and magnetic stirrer at 50 ºC in dark for each about (3, 4, 5) h for stirring time. The colour intensity increased with the duration of stirring time. The position of absorption maxima does not change significantly during time interval of stirring (Table 2 and Figure 3).

Table 2 Absorbance of AgNPs Solution as a Function of Wavelength at Different Stirring Times

Wavelength (nm)	Absorbance		
	3 h	4 h	5 h
390	2.80	3.20	3.40
400	3.40	3.51	3.60
410	3.54	3.57	3.70
420	1.43	1.48	1.60
430	1.54	1.58	1.67
440	1.26	1.29	1.40
450	1.29	1.38	1.43
460	0.56	0.64	0.70
470	0.67	0.79	0.90

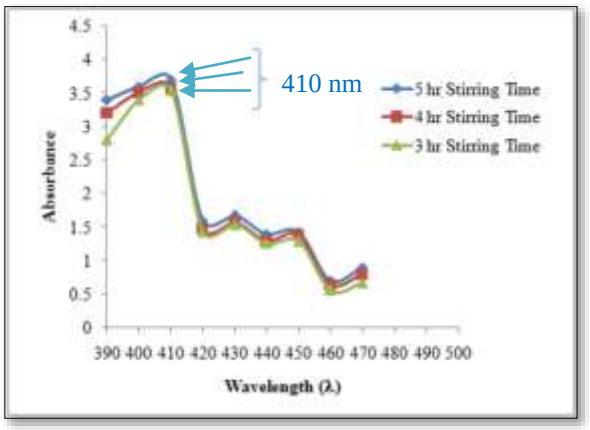

Figure 3 Changes of absorbance of silver nanoparticles with various stirring time at different wavelengths

EDXRF Analysis

EDXRF technique was used to verify the presence of silver in the resulting suspension. The percents of elements present in neem leaves extract and silver nanoparticles formed in the reaction media are shown in Figures 4 and 5. In the neem leaves extract, Ca (74.816%) and K (18.716%) were present as major constituents. Other elements: S (2.773%), Si (1.217%), Fe (1.018%), Sr (0.612%), Mn (0.443%), Br (0.214%) and Zn (0,191%) were present as minor constituents. By EDXRF data, Ag (50.108%), Ca (26.961%), K (17.323%), P (2.843%), S (1.065%), Mn (0.585%), Br (0.502%), Fe (0.340%), Sr (0.106%), Cu (0.079%), Zn (0.058%) and Rb (0.031%) were also present in AgNPs suspension.

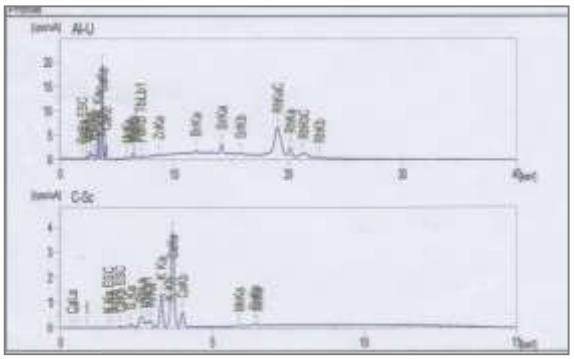

Figure 4 EDXRF spectrum of neem leaves extract

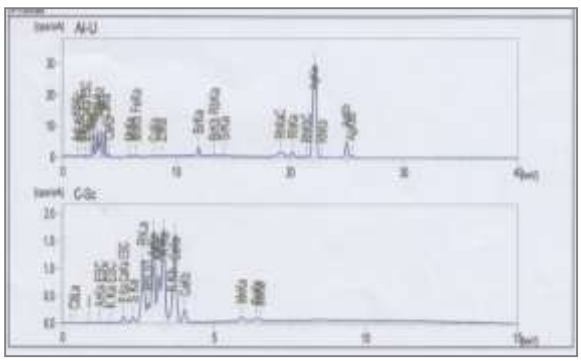

Figure 5 EDXRF spectrum of AgNPs suspension

XRD Analysis

The X-ray diffractogram of silver nanoparticles is shown in Figure 6. The synthesized AgNPs shows the crystalline nature. The average crystallite size of silver nanoparticles was calculated by using the Scherrer equation and found to be 37.14 nm.

FT IR Analysis

The FTIR spectra of neem leaf extract and silver nanoparticles are shown in Figures 7 and 8. The spectrum of neem extracts consist of the band at 3439 cm^{-1} attributed to the OH stretching vibration. The band appeared at 2933 cm^{-1} was due to the C-H stretching vibration in CH_2 and CH_3 groups. The absorption band corresponding to 1624 cm^{-1} was due to (NH) C=O stretching vibration of the characteristic of proteins. It may be concluded that protein or amino acid group present in neem extract reduced Ag^+ ion into metallic Ag nanoparticles. After reduction of $AgNO_3$, the additional peaks at 1383 cm^{-1} and 1066 $cm^{-1}$are related to AgNPs. Some peaks were disappeared in the reduction process of AgNPs (Silverstein, 1998).

SEM Analysis

The surface morphology of nanoparticles was examined by SEM micrograph. It was found that the sample was likely to be well-dispersed agglomerates of grains with narrow size distribution (Figure 9).

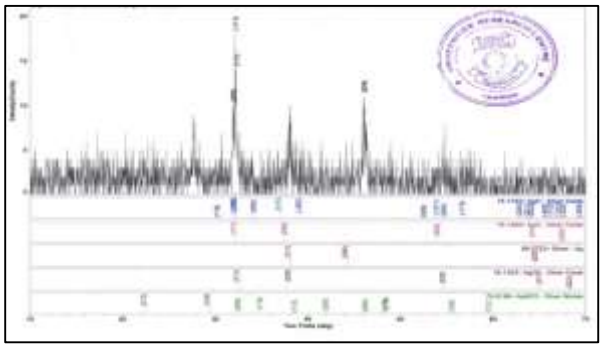

Figure 6 X-raydiffractogram of AgNPs suspension

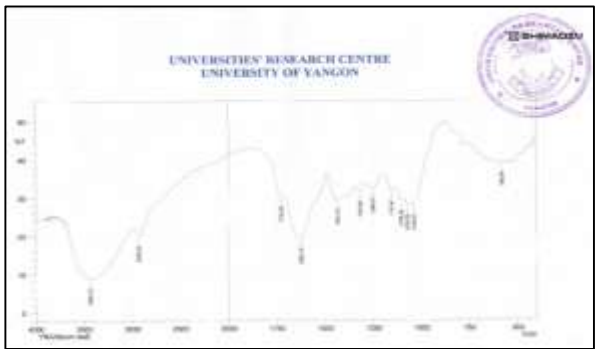

Figure 7 FT IR spectrum of neem leaves extract

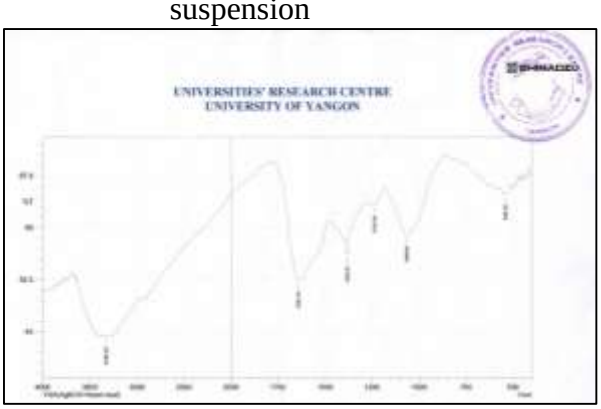

Figure 8 FT IR spectrum of AgNPs suspension

Figure 9 SEM micrograph of AgNPs suspension

Characteristic of AgNPs by Tyndall Effect

The presence of a colloidal suspension can be detected by the reflection of a laser beam from the particles. Because a laser pointer emits polarized light the pointer can be oriented such that the beam appears to disappear. If the colloidal particles are present, the laser beam can pass

and if the particles are absent, the beam cannot pass through the medium. It was found that the laser beam passed through the AgNPs suspension but did not pass through in silver nitrate solution (Figure 10). The particles are large enough that they do scatter light, and the Tyndall effect is observed.

Screening of Antimicrobial Activities

The selected strains are used to perform the antimicrobial activities for the neem leaves extract and synthesized silver nanoparticles. The antimicrobial activity screening of neem leaves crude extract and AgNPs were carried out against six species of microorganism *viz*., *Bacillus subtilis, Staphylococcus aureus, Pseudomonas aeruginosa, Bacillus pumilus, Candida albicans* and *Escherichia coli* by employing agar well diffusion method. It was observed that both neem extracts and AgNPs suspension showed antimicrobial activity against all test organisms except *Pseudomonas aeruginosa*. The AgNPs suspension was more potent than neem extract especially in *Bacillus pumilus* and *Escherichia coli* with the zone diameters of 15 mm (Table 3).

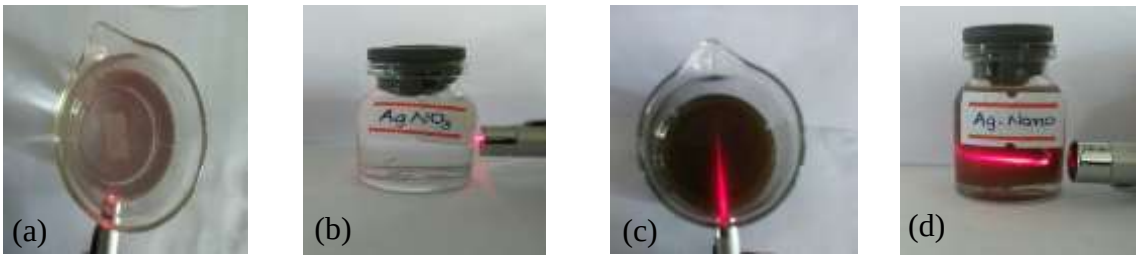

Figure 10 Photographs of Tyndall effect (a) $AgNO_3$ solutions (top view) (b) $AgNO_3$ solutions (side view) (c)Ag NPs suspension (top view) (d) Ag NPs suspension (side view)

Table 3 Antimicrobial Activity of Neem Leaves Extract and AgNPs Suspension

Samples	***B. subtilis***	***S. aureus***	***P. aeruginosa***	***B. pumilus***	***C albicans***	***E. coli***
Neem leaves extract	11 (+)	11 (+)	-	12 (+)	11 (+)	13 (+)
Ag NPs suspension	12 (+)	14 (+)	-	15 (++)	13 (+)	15 (++)

Conclusion

Silver nanoparticles were prepared by biosynthesis, green synthesis. The green synthesis of AgNPs is alternative to chemical method. It is a cheap, pollutant free and eco-friendly method. In this research, silver nitrate was taken as the metal precursor and neem leaves extract as a reducing agent. In this work, AgNPs were prepared by different volumes of neem leaves extract (10, 20 and 30 mL) and stirring times (3, 4 and 5 h) for synthesis process. The AgNPs suspension has been detected by UV-Visible absorption spectroscopy and the wavelength of maximum absorption was observed at 410 nm. By EDXRF data, silver suspension as nanoparticles showed silver content of 50.108%. From the XRD result, the average crystallite size of AgNPs was 37.14 nm. In FT IR analysis, the protein or amino acid group was present in neem extract to reduce Ag^+ ion into metallic AgNPs. In SEM analysis, the sample was likely to be well-dispersed agglomerates of grains with narrow size distribution. In this study, the presence of a colloidal suspension was detected by the reflection of a laser beam from AgNPs particles showing the Tyndall effect. Neem extract and AgNPs suspension showed the inhibitory effects against six tested organisms except *Pseudomonas aeruginosa.*

Acknowledgements

The authors would like to thank the Department of Higher Education, Ministry of Education, Myanmar, for the permission of doing this research and also to the Myanmar Academy of Arts and Science for allowing to present this paper.

References

Azizi , S.,Namvar ,F., Mahdavi ,M., Ahmad M.B. and Mohamad, R. (2013). "Biosynthesis of Silver Nanoparticles Using Brown Marine *Macroalga, Sargassum Muticum* Aqueous Extract". *Materials,* vol. 6, pp.5942-5950

Caseri, W. (2009). "Inorganic Nanoparticles as Optically Effective Additives for Polymers". *Chemical Engineering Communication.* vol. 196 (5), pp.549-572

Collins, C. H. (1965). *Microbial Methods*. London: Butterworth Pub. Co., pp.225-237

Dagmara, M., Agniezka, S. K., Zbigniew, W. and Zygmunt, K. (2012). "Silver Nanoparticles Synthesis with Different Concentrations of Polyvinylpyrrolidone". *Digest Journal of Nanomaterials and Biostructures*, vol. **7** (4), pp.1527-1534

De Silva, W.H., Vivehananthan, K. and Fernando, C.A.N. (2013). "Green Synthesis of Silver Nanoparticles Using *Azadirachta indica* (Neem) Leaf Extract". *Proceeding of 12th Agricultural Research Symposium,* pp. 30-31

Ip, M., Lui, S.L., Poon, V.K.M., Lung, I. and Burd, A. (2006). "Antimicrobial Activities of Silver Dressings: An In Vitro Comparison". *Journal of Medical Microbiology,vol.* 5, pp. 59-63

Koul, O., Isman, M.B. and Kethar, C.M. (1990). "Neem-a Traditional Medicine for Household Remedy". *Journal of Bot*, vol. 68, pp.70-73

Loo, Y.Y., Chieng,B.W., Nishibuchi,M. and Radu,S. (2012). "Synthesis of Silver Nanoparticles by Using Tea Leaf Extract from Camellia sinensis". *International Journal of Nanomedicine.*, vol. **7**. pp.4263-4267

Marambio-Jones, C., and Hoek, E.M.V. (2010). "A review of the Antibacterial Effects of Silver Nano Materials and Potential Implications for Human Health and the Environment". *Journal of Nanopart Res,* vol. 12, pp.135.

Roy,P., Das, B., Mohanty, A. and Mohapatra, S. (2017). "Green Synthesis of Silver Nanoparticles using *Azadirachta indica* Leaf Extract and its Antimicrobical Study". *Appl Nanosci*: vol. 7. pp.843-850

Saifuddin, N., Wong,C.W.and Yasumira,A. A.N.(2009). "Rapid Biosynthesis of Silver Nanoparticles Using Culture Supernatant of Bacteriavwith Microwave Irradiation". *E-.Journal of Chemistry,* vol 6(1), pp.61-70

Silverstein, R.M. (1998). *Spectrometric Identification of Organic Compound*. New York: 6th Edn., John Wiley and Sons, pp.215

SYNTHESIS AND CHARACTERIZATION OF IRON OXIDE (Fe_3O_4) PARTICLES BY CHEMICAL METHOD AND ITS APPLICATION

Aye Aye Mar[1], Myat Kyaw Thu[2], Thida[3], Ni Ni Than[4]

Abstract

Iron oxide particles with appropriate surface chemistry exhibit many interesting properties that can be exploited in a variety of biomedical application such as magnetic resonance imaging contrast enhancement, tissue repair, hyperthermia, drug delivery and in cell separation. In this study, $FeSO_4.7H_2O$, $NaNO_3$ and NaOH were used in the preparation of iron oxide by chemical method. The characteristic properties of iron oxide were studied by X-ray Diffraction (XRD), Fourier Transform Infrared (FT IR) spectroscopy and Scanning Electron Microscopy (SEM) and Thermogravimetric-Differential Thermal Analysis (TG-DTA). The crystalline nature of the prepared iron oxide was identified by XRD analysis. According to XRD data synthesized iron oxide (Fe_3O_4) by chemical method at 100 °C was naturally stabilized cubic structure and in the average crystallite size of 39.27 nm. In FT IR spectrum of iron oxide the peaks at 895 cm^{-1} and 457cm^{-1} are due to the vibration of Fe-O group. The SEM micrographs of iron oxide prepared by chemical method at 100ºC indicated that the particles are spherical in shape with a narrow size distribution. TG-DTA analysis showed two endothermic peaks and one exothermic peak. Sorption properties of the prepared iron oxide was studied by model congo red dye. Since, the value of separation factor R_L (from Langmuir isotherm) for this dye was 0.04, the adsorption was favourable adsorption.

Keywords: iron oxide, chemical method, congo red, separation factor, Langmui isotherm

Introduction

Iron and oxygen are two of the four most common elements in the Earth's crust, and iron oxide form naturally through the weathering of Fe-containing rocks both on land and in the oceans. Iron oxides are chemicals compounds composed of iron and oxygen. All together there are sixteen known iron oxides and oxyhyroxides. Iron oxides and oxyhydroxides are widespread in nature, play an important role in many geological and biological process, and are widely used by humans, e.g., as iron ores, pigments, catalyst, in thermite and hemoglobin. Common rust is a form of iron (III) oxides (Gareth, 2016). Iron oxide nanoparticles are iron oxide particles with diameters between about 1 and 100 nm. They have attracted much attention due to their fine magnetic properties and applications in modern science. The most common iron oxides for biomedical applications are magnetite (Fe_3O_4) and maghemite (γ-Fe_2O_3). Magnetite is a black magnetic mineral and is also called iron (II, III) oxide or ferrous ferrite. The molecular formula, Fe_3O_4, can also be written as $FeO.Fe_2O_3$, which consists of w*ü*stite (FeO) and hematite (Fe_2O_3). It has the strongest magnetism of all the natural minerals existing on the earth (Majewski and Thierry, 2007). Magnetite (Fe_3O_4) has an inverse spinel structure with oxygen forming a face-centered cubic system. In magnetite, all tetrahedral sites are occupied by Fe^{3+} and octahedral sites are occupied by both Fe^{3+} and Fe^{2+}. Maghemite (γ-Fe_2O_3) differs from magnetite in that all or most of the iron is in the trivalent state (Fe^{3+}) and by the presence of cation vacancies in the octahedral sites. Maghemite has a cubic unit cell in which each cell contains 32 O^{2-} ions, $21_{1/3}Fe^{3+}$ ions and $2_{2/3}$ vacancies. The cations are distributed randomly over the 8 tetrahedral and 16 octahedral sites (Laurent *et al*., 2008). Magnetic properties of nanomaterials are powerful manipulation and detection tools which are studied for a long time. Since magnetic fields are not harmful organism, magnetic nanoparticles can be used for biomedical in vivo and, of course, in vivo applications. The

[1] Dr, Lecturer, Department of Chemistry, University of Yangon
[2] Dr, Professor, Department of Chemistry, University of Yangon
[3] Dr, Associate Professor , Department of Chemistry, University of Yangon
[4] Dr, Professor and Head, Department of Chemistry, University of Yangon

latest researchers tell about high potential of magnetic nanoparticles in environments applications such as removal of heavy metals from waste water. Magnetic properties depend on size, shape, structure, crystallinity, synthesis method and chemistry of materials. The most widely investigated magnetic nanomaterials are iron, cobalt and nickel compounds and alloys (Shahoo *et al*., 2010). Iron (II, III) oxide, chemical formula Fe_3O_4 or Fe_2O_3. Black or grayish black colour mineral. Structure formula $[Fe^{3+}]$ Td$[Fe^{3+}Fe^{2+}]$ Oh O^{2-}, which means there is tetrahedral magnetic sub lattice, containing Fe^{3+} ions, an octahedral sub lattice, containing Fe^{3+} and Fe^{2+} ions. Spins from these two sub lattices are antiparallel so magnetite and magnetization occurs due to Fe^{2+} ions from octahedral sub lattice. Magnetite is sensitive to oxidation-oxygen transforms it to maghemite by oxidizing of Fe^{2+} ions (Lodhia *et al*., 2010)

Materials and Methods

Preparation of Iron Oxide

A 14 g of NaOH (0.35 mol) and 4.2495g of $NaNO_3$ (0.05 mol) were placed into a 1L beaker containing 150 mL distilled water. Then the volume was made up to 300 mL with distilled water. A 36.84 g of $FeSO_4.7H_2O$ was dissolved in distilled water and the volume made up to 250 mL in a 250 mL volumetric flask. The $FeSO_4$ solution was slowly added into the beaker containing solution mixture of NaOH and $NaNO_3$. The black precipitate was obtained and the sample was aged at room temperature for 16 days. Then, the sample was washed and filtered and then dried at temperature of 100 °C.

Characterization of the Prepared Iron Oxide Samples

Prepared iron oxide particles were qualitatively analyzed by X-ray diffractometer. Infrared Spectrometer (FT IR) with a scan speed of 16 scans/sec from 400 to 4000 cm^{-1} was used to identify the functional groups present in the sample. The SEM micrograph was obtained using JXA 840 A, JEOL Ltd., Japan, the permanent records obtained by the crystals feature. Thermal stability of the prepared sample was evaluated by simultaneous TG-DTA operated under air atmosphere. The measurements were carried out at a heating rate of 10.0 °C min^{-1} and scanning from 30 °C to 600 °C. `

Determination of Wavelength of Maximum Absorption (λ_{max}) of Congo Red and Construction of the Calibration Curve

To determine the wavelength of maximum absorption (λ_{max}) of congo red solution the absorbance values were recorded in the visible range of 400 - 600 nm by using using a UV-visible spectrophotometer. The calibration curve of congo red solution was constructed by using different concentrations of 10, 20, 30, 40 and 50 ppm solutions at the wavelength of maximum absorption of congo red.

Sorption of Congo Red on the Prepared Iron Oxide sample

Study on the effect of contact time on removal of congo red dye

A 0.5 g of magnetite was placed into the separate conical flasks and treated with 50 mL 30 ppm congro red solution at pH of 7. These experiments were performed with the same concentration of dye solution and the same amount of iron oxides samples. The flasks containing congo red and iron oxides as adsorbents were placed in the thermostatic shaker at room temperature. The contact time settings were 20,40,60,80,100 and 120 min. After shaking, the sample solutions were filtered off and the filtrates were spectrophotometrically measured at λ_{max}

495 nm. By the contact time setting, the removal percent of congo red dye onto iron oxide was calculated.

Study on the effect of dosage on removal of congo red dye

Dyes removal efficiency of iron oxide was determined by using different weights of 0.2, 0.4, 0.6, 0.8 and 1g. Each 50 mL of 30 ppm congo red solution adjusted to pH 7 was added into separate conical flasks. Then 0.2, 0.4, 0.6, 0.8 and 1g of each sample was added into each conical flask and the solution was agitated in thermostatic shaker at room temperature for 1h. Then the solution was removed from samples by filtration. The absorbance values of resultant solutions were measured at λ_{max} 495 nm using the spectrophotometer (Jain and Sikarwar, 2006).

Results and Discussion

Iron Oxide Prepared by Chemical Method

In this study, iron oxide was prepared by using chemical method at 100°C. The prepared iron oxides sample was black in colour as shown in Figure 1.

Figure 1 Prepared iron oxide

Characterization of Prepared Iron Oxide Samples

XRD

Figure 2 shows X-ray diffractogram of iron oxide sample obtained at 100 °C. Characteristic peaks of iron oxide appeared at 30.075º, 35.500º, 43.110º 57.049º and 62.662º of 2 θ values with corresponding Miller indices of (220), (311), (400), (511), (440) , respectively. The XRD pattern of the prepared iron oxide sample clearly matched with the standard library data of JCPDS-87-2334 magnetite. The diffraction angle, interplanar spacing and Miller Indices of prepared iron oxide sample are shown in Table 1. It was observed that the sample showed single phase of Fe_3O_4 with no impurity phase.The resultant iron oxide was indexed as cubic structure with a= 8.3851 Å (Table 2). Average crystallite size of prepared iron oxide sample was calculated by using Scherrer equation,

$$t = \frac{K\lambda}{\beta\cos\theta}$$

Where t = crystallite size in nanometers
K = Scherrer constant
θ = Diffraction angle of the peak under consideration of FWHM (º)
λ = wavelength (Å)
β = the broadening solely due to small crystallite size (FWHM radians).

The average crystallite size was found to be 39.27 nm.

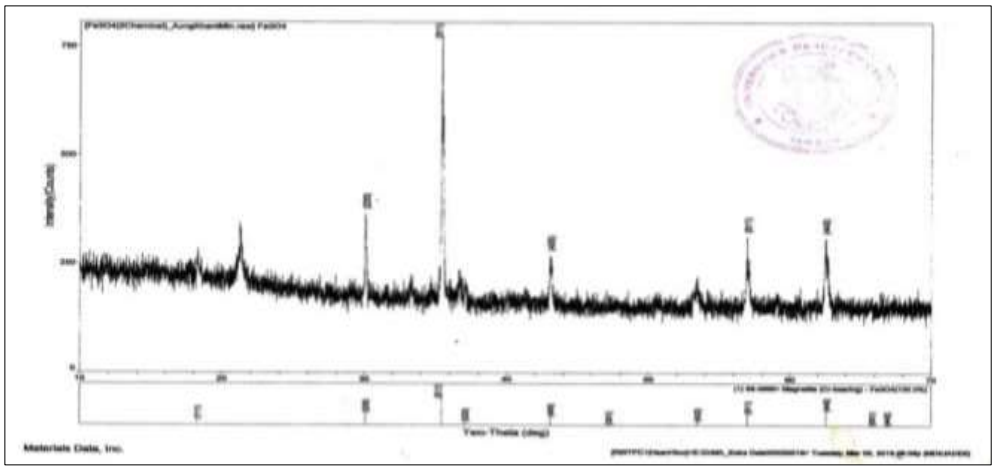

Figure 2 X-ray diffractogram of prepared iron oxide

Table 1 Diffraction Angle, Interplanar Spacing and Miller Indices of Prepared Iron Oxide

No.	Diffraction angle (2θ) (degree)	Interplanar spacing (Å)	Miller indices			Remark
			h	k	l	
1.	18.291	4.8463	1	1	1	Fe_3O_4
2.	30.075	2.9689	2	2	0	Fe_3O_4
3.	35.500	2.5266	3	1	1	Fe_3O_4
4.	37.124	2.4198	2	2	2	Fe_3O_4
5.	43.110	2.0966	4	0	0	Fe_3O_4
6.	47.179	1.9248	3	3	1	Fe_3O_4
7.	53.450	1.7128	4	2	2	Fe_3O_4
8.	57.049	1.6130	5	1	1	Fe_3O_4
9.	62.662	1.4814	4	4	0	Fe_3O_4
10.	65.755	1.4190	5	3	1	Fe_3O_4
11.	66.913	1.3972	4	4	2	Fe_3O_4

Table 2 Crystal Structure, Lattice Constant and Average Crystallite Size of Prepared Iron Oxide

No.	Sample	Crystal structure	Lattice constant (Å)	Aveage crystallite size (nm)
1.	Iron oxide	Cubic	8.3851	39.27

FT IR

Figure 3 shows FT IR spectrum of iron oxide sample obtained at 100 ° C and the spectral data are shown in Table 3. The absorption band at 3451 cm^{-1} was due to stretching vibration of hydroxyl functional group (O-H) on the surface of oxide particles or adsorbed water in the sample. Absorption peaks at 895 $cm^{-1}$and 457cm^{-1} are due to the vibration of Fe-O group in prepared iron oxide particles.

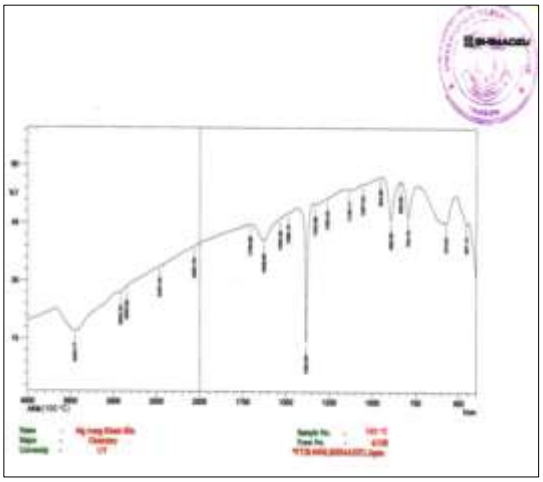

Figure 3 FT IR spectrum of prepared iron oxide

Table 3 FT IR Spectral Data of Prepared Iron Oxide (Fe_3O_4)

No.	Wavenumber (cm^{-1})	Literature value*(cm^{-1})	Assignment
1.	3451	3570-3200 (broad)	Stretching vibration of hydroxyl group
2.	895	1010-850(M=O)	Vibration of Fe-O group
3.	457	400-600 (M-O)	Vibration of Fe-O group

*Coates, 2000

Surface morphology of the iron oxide

Surface morphology of the prepared iron oxide sample was studied by using SEM as shown in Figure 4. The image of SEM represents spherical morphology of iron oxide particles. Mostly particles were in sphere form but particles with cubic shape were also observed. The SEM also revealed the agglomeration of iron oxide particles with a narrow size distribution. The particles have a narrow size distribution and the SEM micrograph indicates the porous nature of the surface.

TG- DTA data of iron oxide

TG and DTA curve of prepared iron oxide is shown in Figure 5. The temperature range was 30°C to 600°C. In TG analysis, the total weight loss percentage of the sample was 6.472 %. The initial weight loss observed below 200 °C corresponds to the removal of water existing on the surface of iron oxide. From DTA data, above 200 °C, exothermic peaks and endothermic peaks were observed due to the phase transformation. (Table 4).

Figure 4 SEM microphotograph of prepared iron oxide

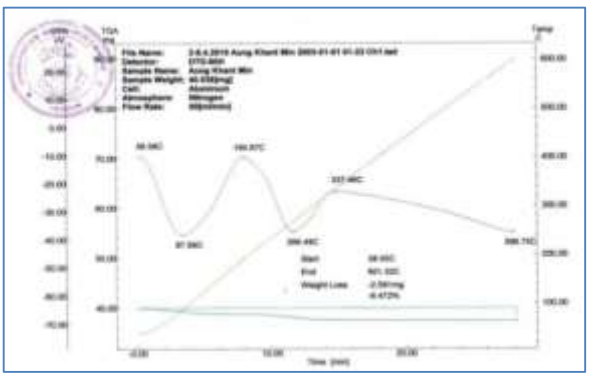

Figure 5 TG-DTA thermogram of prepared iron oxide

Table 4 TG-DTA Data of Prepared Iron Oxide

No.	Observed Temperature (ºC)	Weight Loss (%)	Interpretation
1.	87.89	0.859	Endothermic peak, removal of water existing on the surface
2.	190.87	1.845	Exothermic peak, oxidation reaction takes places
3.	266.49	1.963	endothermic peak, phase transition from Fe_3O_4 to Fe_2O_3*
4.	337.46	1.805	exothermic peaks, phase transition fromFe_3O_4 to Fe_2O_3*

*Khan *et al.*,2015

Absorption Spectrum and Calibration Curve of Congo Red

In this research, congo red solution was used to study the effect of sorption by prepared iron oxide. Figure 6 shows the absorption spectrum of congo red solution. The wavelength of maximum absorption was found at 495 nm. Standard calibration curve was constructed using concentrations of standard congo red solution at 495 nm. According to calibration curve (Table 5 and Figure 7), the straight line passed through the origin (R^2 = 0.9889) indicating that it obeyed Beer's Law.

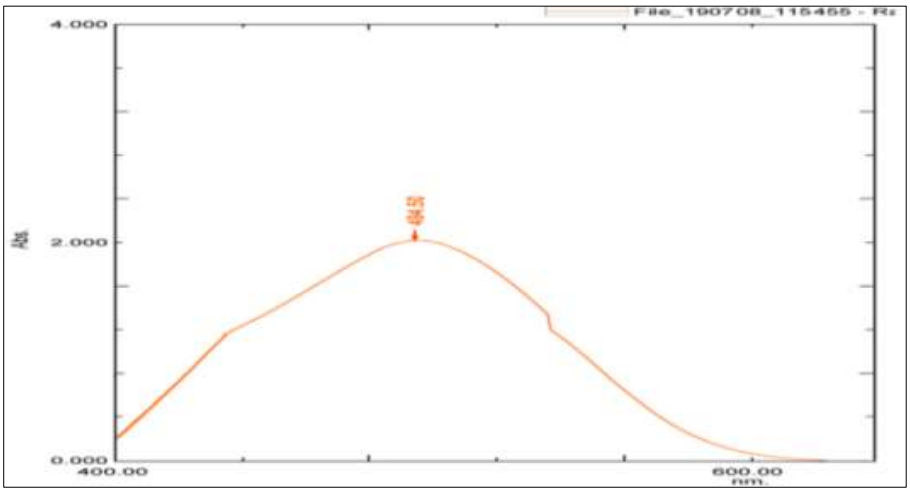

Figure 6 Absorption spectrum of congo red solution

Table 5 Relationship between Absorbance and Concentration of Standard Congo Red Solution

Concentrations (ppm)	Absorbance at 495 nm
10	0.15
20	0.33
30	0.45
40	0.57
50	0.68

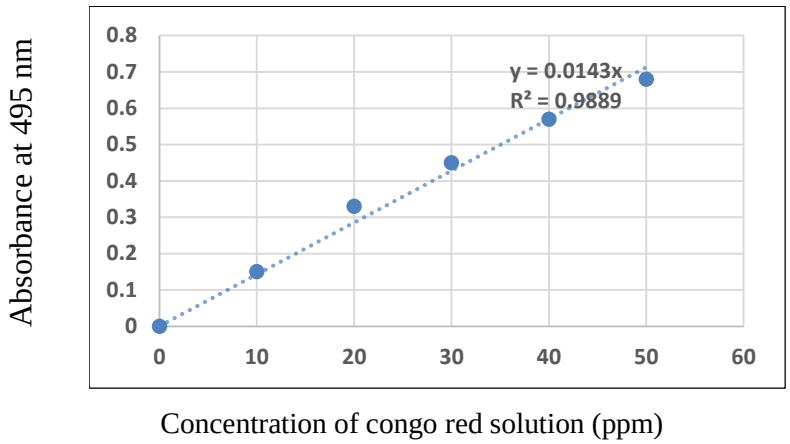

Figure 7 Calibration curve for standard congo red at 495 nm

Sorption of Congo Red onto Prepared Iron Oxide (Magnetite)

Effect of contact time

In the present work, sorption capacity of magnetite samples onto congo red was studied. Figure 8 shows a plot of removal percent of congo red as a function of contact time. As the contact time increased removal percent also increased.For the contact time of 120 min, 97.60 % of congo red were removed and adsorbed on magnetite sample.

Effect of dosage

The effect of dosage of the prepared iron oxide samples on the removal of congo red dye was studied by choosing the dosage of the prepared iron oxide samples from 0.2 to 1.0 g. Table 6 shows the relationship between dosage of magnetite with removal percentage of congo red and the corresponding histogram is depicted in Figure 9. By using 1.0 g of magnetite sample and 97.33% of congo red were removed and adsorbed on magnetite sample.

Langmuir Adsorption Parameters

An adsorption isotherm is characterized by certain constants, which express the surface properties and affinity of the adsorbent and can also be used to compare the adsorption capacities of the adsorbent for different adsorbate (Hall *et al.*, 1966). In this study, data from Langmuir plots of congo red sorption onto magnetite sample were obtained (Table 7). The correlation coefficient R^2 for congo red was 0.4751. This value indicated weak binding of congo red dyes to the surface of the magnetite iron oxide sample. The separation factor R_L for congo red was 0.04 (Table 8). R_L is the essential characteristic of the Langmuir isotherm which indicates the shape of isotherm that predicts whether an adsorption is favourable or unfavourable. Since the value of R_L between 0 and 1, sorption of congo red can be considered as favourable adsorption (McKay *et al.*,1982).

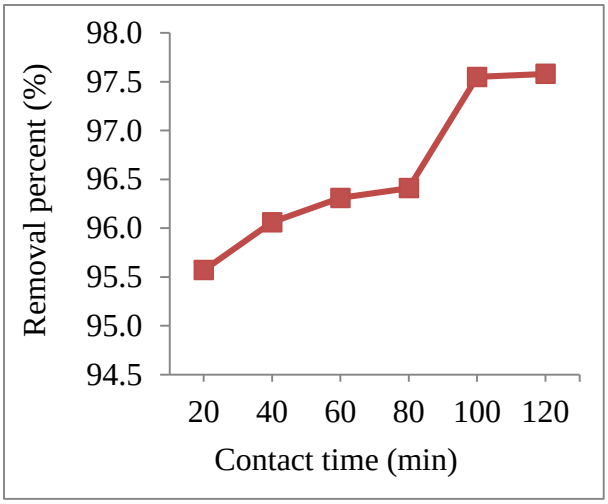

Experimental condition

Amount of magnetite = 0.5 g

Volume of solution = 50 mL

Concentration of dye = 30 ppm

pH = 7

Figure 8 Plot of congo red removal percent as a function of contact time

Table 6 Relationship between Dosage of Magnetite and Percent Removal of Congo Red

Dosage (g)	Absorbance	Ce (mg L^{-1})	Ci - Ce (mg L^{-1})	Removal (%)
0.2	0.013	0.95	29.05	96.83
0.4	0.014	1.02	28.98	96.60
0.6	0.007	0.51	29.49	98.30
0.8	0.010	0.73	29.27	97.57
1.0	0.011	0.80	29.20	97.33

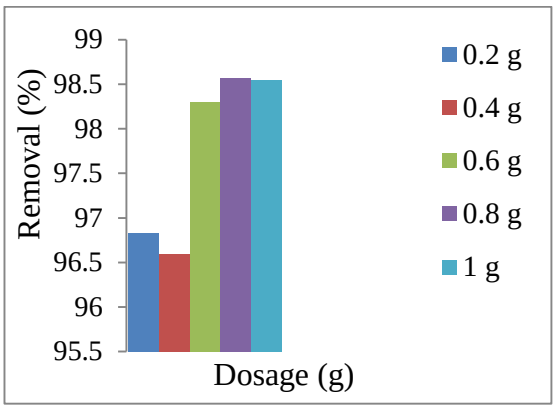

Figure 9 Histogram of removal percent of congo red with dosage of the prepared magnetite sample

Experimental condition

percent pH = 7

Contact time = 1 h

Concentration of dye = 30 ppm

Volume of congo red solution = 50 mL

Table 7 Equilibrium Data for Adsorption of Congo Red by Magnetite

Weight of sample m (g)	Absorbance	Final conc: C_e (mg L^{-1})	Amount of absorbed, x (mg)	q_e = x/m (mg g^{-1})	1/Ce (L/mg)	$1/q_e$ (gmg^{-1})
0.2	0.013	0.95	0.87	4.35	1.05	0.23
0.4	0.014	1.02	0.87	2.18	0.98	0.46
0.6	0.007	0.51	0.88	1.47	1.96	0.68
0.8	0.010	0.73	0.88	1.10	1.37	0.91
1.0	0.011	0.80	0.88	0.88	1.25	1.14

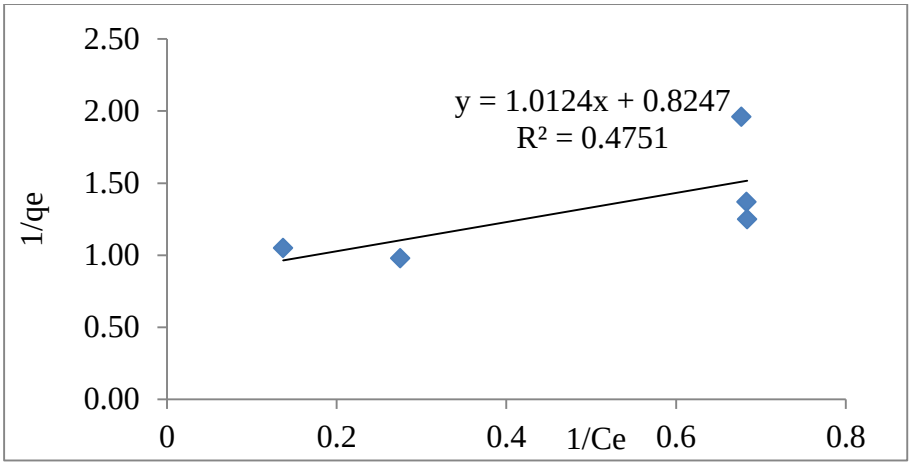

Figure 10 Langmuir plot of congo red adsorption onto magnetite sample

Table 8 Langmuir Isotherm Parameters for the Dyes

Dyes	Sorption coefficient K_L(x 10^{-2}L mg^{-1})	Sorption capacity q_{max} (mg g^{-1})	Correlation coefficient R^2	Separation factor R_L
Congo red	0.81	1. 21	0.4751	0.04

Conclusion

In this study, synthesis of iron oxide (Fe_3O_4) by chemical method was carried out and the dye removal properties of the prepared iron oxide was investigated. XRD data revealed the single phase of Fe_3O_4 with crystallites size of 39.27 nm. The FT IR spectrum of the prepared iron oxide showed the the peaks at 895 cm^{-1} and 457 cm^{-1} corresponding to the vibration of Fe-O groups. The particles are spherical in shape with a narrow size distribution as indicated by SEM. Moreover, iron oxide prepared was studied by TG-DTA analysis, it was found that total weight loss 6.472 %. Two exothermic peaks and two endothermic peaks were corresponding to the vaporization of moisture, phase transition and oxidation reaction takes place in the sample. For the contact time of 120 min, 97.60 % of congo red were sorbed on prepared iron oxide particles. So the prepared iron oxide sample was effective in removal of dyes in waste water treatment. In the dosage of 1g of prepared iron oxide sample in 50 mL of 30 ppm dye solution, percentage of sorbed congo red was 97.33 %. According to Langmuir adsorption parameters, it was found that weak binding of congo red dyes onto the surface of the iron oxide sample since the R^2 value for was 0.4751. Since the value of separation factor R_L for congo red dye was 0.04, the adsorption was favourable adsorption.

Acknowledgements

The authors would like to thank the Department of Higher Education, Ministry of Education, Yangon, Myanmar, for allowing us to carry out this research programme. Thanks are also extended to the Myanmar Academy of Arts and Science and for allowing to present this paper.

References

Coates, J. (2000). *Interpretation of Infrared Spectra, A Practical Approach.* In Encyclopedia of Analytical Chemistry. Meyers, A., (Ed.), Chichester: 2nd ed. John Wiley and Sons Ltd, p. 10815-10837

Gareth, S. P. (2016). "Iron Oxide Surfaces". *Surface science*, vol. 71, pp. 272-365

Hall, K. R.,Eagleton, L. C. , Acrivos, A. and Vermeulen,T. (1966). "Pore and Solid Diffusion Kinetics in Fixed-bed Adsorption under Constant-pattern Conditions". *Ing. Eng. Chem. Fund,* vol. 5, pp. 212-223

Jain, R. and Sikarwar,S. (2006). "Photocatalytic and Absorption Studies on the Removal of Dye Congo red from Wastewater". *Int. J. Environment and Pollution*, vol. 27, pp. 158-160

Khan, U.S., Amanullah, Manan, A., Khan,N. Mahmood,A.and Rahim, A.(2015). "Transformation Mechanism of Magnetite Nanoparticles". *Materials Science-Poland*, vol. 33(2), pp. 278-285

Laurent, S., Vander,E.L.M. and Robert, N. (2008). "Magnetic Iron Oxide Nanoparticles: Synthesis, Stabilization, Vectorization, Physicochemical Characterizations and Biological Applications". *Chemical Reviews*, vol. 108, pp. 2064-2110

Lodhia, J., Mandarano,G., Ferris, N.J., Eu,P. and Cowell,S.F. (2010). "Development and Use of Iron Oxide Nanoparticles (Part I): Synthesis of Iron Oxide Nanoparticles for MRI". *Biomedical Imaging and Intervention Journal*, vol. 6, pp. 1-11

Majewski, P. and Thierry, B. (2007). "Functionalized Magnetite Nanoparticles-synthesis, Properties, and Bio-applications". *Critical Reviews in Solid State and Material Science,* vol. 32, pp. 203-215

Mckay, G., Blair, H. S. and Gardner, J. R. (1982). "Adsorption of Dye on Chitin, I. Equilibrium Studies". *J. Appl. Polym. Sci.,* vol. 27, pp. 3043-3057

Shahoo, S. K., Agrawal, K., Polke, B.G. and Raha, K.C. (2010). " Characterization of γ and α-Fe_2O_3 Nanopowder Synthesized by Emulsion Precipitation Calcination Route and Rheological Behaviour of α-Fe_2O_3", *Inter. J. Engin. Sci & Tech.*, vol.2, pp. 118-126

OPTIMIZATION OF PULPING PROCESS OF BETEL NUT FIBER USING CENTRAL COMPOSITE DESIGN FOR THE PREPARATION OF CELLULOSE FIBER*

Kyi Tha Thaw[1], Soe Soe Than[2], Nwe Nwe Aung[3]

Abstract

Betel nut fiber was used to isolate cellulose fiber by four processing steps such as alkali hydrolysis using sodium hydroxide (pulping), bleaching using hydrogen peroxide, acid hydrolysis using sulphuric acid and homogenization. In the pulping of biomass, Central Composite Design of Response Surface Methodology was used to opt imize the yield of cellulose**.** Three variables such as alkali concentration, alkali volume and cooking time were considered as influencing factors on the yield of holocellulose, alpha cellulose and hemicellulose during alkali pulping process. The maximum yields of holocellulose, alpha cellulose and hemicellulose by % wt were 94.33±0.76, 80.17±1.89, and 13.83±1.75 under the optimum conditions. Cellulose fiber was analysed by thermogravimetric analysis (TGA), Fourier-transform infrared (FTIR) spectroscopy, scanning electron microscopy (SEM), and X-ray diffraction (XRD). The XRD results revealed high crystallinity of both the cellulose fiber and cellulose pulp, while the TGA thermograms indicated that the alkali and acid treatment completely removed lignin and hemicelluloses from the betel nut fiber. FTIR results reveal that the peaks in the range between 1200 and 1300 cm^{-1} were not observed in pulp and cellulose fiber which indicated the removal of hemicelluloses and lignin. SEM microphotograph showed that mercerization and acid hydrolysis lead to fibrillation and breakage of the fiber into smaller pieces which promote the effective surface area available for contact.

Keywords: Cellulose Fiber, Central Composite Design, Response Surface Methodology, Holocellulose, Alpha Cellulose, Hemicellulose

Introduction

The disposal of agricultural waste is becoming a problem especially in the intensive growing areas. The unmanaged agricultural waste in the plantation causes terrible odor and other decay-related problems. Agricultural waste and by-products are rich sources of cellulose and hemicelluloses. Lignocellulosic fibers from agricultural waste act low cost and more environmentally friendly replacement for wood in polymer composite. In the last few years, cellulose fibers have been a trendy research subject due to their high strength and stiffness combined with low weight and biodegradability **(**Liew *et al.*, 2015). Cellulose fibers are widely used in the paper and packaging products, automotive, furniture, sporting goods, electronics, pharmacy and cosmetic (Dungani *et al*., 2016). The betel nut fiber is a strong fibrous material covering the endosperm and constitutes about 60-80% of the total weight and volume of the areca fruit. The husk of betel nut fiber is composed of 55.82% cellulose, 34.28% hemicelluloses, 6.82% lignin, 1.80% moisture content and 1.28 % ash content. This highly cellulosic material is being used as a fuel and fabricated as value added products such as cushion, handcrafts and non-woven fabrics. Surface modifications of natural fibers by various chemical treatments are one of the most significant areas in the field of technical utilization of natural fiber reinforced polymer composites in various industrial sectors (Dhanalakshmi *et al*., 2015). Cellulose is physically and chemically surrounded by hemicellulose and lignin, with the links forming a lignocellulose matrix (Galiwango *et al*., 2019). Cellulose was extracted by industrial pulping processes. Most other constituents of the cell walls are broken down or solubilized and removed (Mohammadi *et al.*, 2011). The pulping processes are categorized as mechanical, thermal, semi-chemical or wholly chemical methods. Chemical pulping accomplished the degradation of lignin and

[1] Lecturer, Department of Industrial Chemistry, Dagon University
[2] Professor and Head, Department of Industrial Chemistry, University of Yangon
[3] Professor, Department of Industrial Chemistry, West Yangon University
[*] Best Paper Award Winning Paper in Industrial Chemistry (2020)

hemicelluloses into small water-soluble molecules which can be washed away from the cellulose fibers. Chemical methods include Kraft, sulphite, soda, and organosolv pulping processes (Azeez, 2018). During pulping, the reagents attack the lignin and hemicellulose on which the macromolecules are converted into low molecular weight that are soluble in the liquor. Pulping is not enough to eliminate all lignin and hemicellulose residue; therefore, additional bleaching process can be used (Pereira *et al*., 2011). Acid-alkali treatment is the most effective method for individual cellulose isolation from the complex structure of lignocellulose (Galiwango *et al*., 2019). Combination of sulphuric acid hydrolysis and homogenization methods to isolate cellulose nanofiber is reported to be convenient and has minimum effect on fiber properties (Chaturbhuj *et al.*, 2016). Sulphuric acid hydrolysis mainly removes the amorphus regions of the cellulose (Zhang *et al.*, 2019)

In this study, cellulose fiber was prepared from betel nut fiber. Conversion of non-woody biomass to cellulose fiber was conducted through pulping by alkali hydrolysis and bleaching followed by acid hydrolysis and homogenization.

Materials and Methods

Materials

Betel nut fiber was brought from betel nut farm, Thandwe Township, Rakhine State. Analar grade BDH products – acetic acid, hydrogen peroxide, sodium chlorite, sulphuric acid and commercial grade sodium hydroxide were purchased from Golden Lady Store – Chemical Trading, No. (114), 28th street, Pabeden Township.

Preparation of Cellulose Fiber

Sodium hydroxide was used as cooking liquor for conversion of betel nut fiber to pulp. Response Surface Methodology was used to optimize the maximum yield of alpha cellulose content in pulp with the process variables such as alkali concentration, alkali volume and hydrolyzing time during cooking process as shown in Table (1). Central Composite Design was chosen and (17) experimental runs were conducted as shown in Table (2).

Betel nut fiber was dried in sunlight about one week. Dried betel nut fiber was ground by using a grinder. Powder 50 g was treated with 464 mL of 48 % (w/v) sodium hydroxide for 4 hr for pulping process. After alkali treatment, it was washed with tap water and bleached with 30 % (v/v) hydrogen peroxide for one hour. It was then washed with purified water in order to remove excess hydrogen peroxide. After that, it was soaked in 10 % (v/v) acetic acid at room temperature for half an hour to remove excess sodium hydroxide and washed with water. The resulting pulp was dried in an oven at 100 ^{o}C for 6 hr. Dried pulp powder 30 g was treated with 600 mL of 20 % (w/v) sulphuric acid solution for 1 hr at 45 ^{o}C. After acid hydrolysis, it was soaked in sixfold of cold water to stop the reaction. After that it was washed with purified water until it was neutralized. It was then homogenized using ultra-turrax for 30 min. The resulting cellulose fiber was dried in an oven at 100 ^{o}C for 6 hr.

Table 1 Variables in Experimental Design for Pulping

Variables	Levels	
	Lower	Upper
Alkali Concentration% (w/v)	40	50
Alkali Volume (mL)	450	550
Hydrolysing time (hr.)	3	5

Table 2 Experimental Runs According to Central Composite Design for Pulping of Betel Nut Fiber

Run Order	Alkali Concentration (% w/v)	Alkali Volume (mL)	Hydrolysing Time (hr)
1.	50.00	550.00	5.00
2.	40.00	450.00	3.00
3.	45.00	415.91	4.00
4.	45.00	500.00	4.00
5.	36.59	500.00	4.00
6.	50.00	450.00	5.00
7.	45.00	500.00	5.68
8.	53.41	500.00	4.00
9.	45.00	500.00	4.00
10.	45.00	584.09	2.32
11.	45.00	500.00	3.00
12.	50.00	450.00	3.00
13.	40.00	550.00	5.00
14.	40.00	450.00	3.00
15.	50.00	500.00	3.00
16.	40.00	550.00	5.00
17.	45.00	500.00	4.00

Characterization of Cellulose Pulp and Cellulose Fiber of Betel Nut Fiber

Scanning Electron Microscopy (SEM)

Morphological study of raw material, cellulose pulp and cellulose fiber was conducted using JSM-5610, Jeol Ltd., Japan, scanning electron microscopy at the Universities' Research Center, University of Yangon.

Fourier Transform Infrared Spectroscopy (FTIR)

FTIR analysis was carried out to examine the changes in the functional groups in raw material, cellulose pulp and cellulose fiber. FTIR-8400, SHIMADZU, Japan was used to obtain the spectra of each sample. FTIR analysis was carried out at the Universities' Research Center, University of Yangon.

X-Ray Diffraction (XRD)

XRD analyses were performed for raw material, cellulose pulp and cellulose fiber using Regakuminiflex 600 Detax, Tokyo, Japan. XRD analysis was carried out at the Department of Physics, University of Yangon.

Thermogravimetric Analysis (TG-DTA)

Thermal stability of raw material, cellulose pulp and cellulose fiber were analyzed using Pyris Diamond TG-DTA High Temp.115V thermal analyzer DTG-60H. TG-DTA analysis was carried out at the Universities' Research Center, University of Yangon.

Determination of Alpha Cellulose Contents

Alpha cellulose was determined according to (ASTM 1104-56, 1978) and (TAPPI T 203 cm-99 (TAPPI 1999b)). Holocellulose, alpha cellulose and hemicellulose contents in resulting pulp were determined. Determination of holocellulose content was carried out according to the modified method of (Wise *et al*., 1946). Pulp 2 g was added to in a 250 mL Erlenmeyer flask. Pulp was dissolved in a solution of 1.5 g of sodium chlorite ($NaClO_2$) in 100 mL distilled water and 5 mL of 10% (v/v) acetic acid. The flask was placed into a water bath and kept at 70 ^oC for 30 min with frequent stirring (Wise *et al*., 1946). Furthermore 5 mL of acetic acid and 1.5 g $NaClO_2$ until 6 g of $NaClO_2$ had been added, after which, the flask was further heated for 30 min after the last addition of $NaClO_2$. It was then cooled to 10 ^oC. It was washed with acetone and allowed to be air-dried. Finally, the residue was transferred into desiccators and weighed until a constant weight was obtained.

Alpha-cellulose content of pulp was determined according to TAPPI T203 cm-99 (TAPPI 1999b). The holocellulose containing crucible was placed in a Syracuse watch glass, which contained water to a depth of 1 cm and 3 mL of 17.5 % (w/v) NaOH were added to each crucible. After 5 min, additional 3 mL of 17.5 % (w/v) NaOH solution was added. The contents were allowed to stand for 35 min, a total of 42 min contact time. After washing with 60 mL of distilled water, 5 mL of 10 % (v/v) acetic acid was added and 5 min later, the alpha-cellulose was washed with distilled water 60 mL, and then finally with acetone 20 mL. After washing, it was oven-dried to a constant weight, and the alpha-cellulose content calculated based on oven-dried weight. The hemicellulose content was calculated by subtracting the weight of alpha-cellulose from that of hollocellulose (TAPPI 1999b).

Results and Discussion

Pulping by alkali treatment with 17 experimental runs was conducted according to the experimental design. The second-order polynomial quadratic regression equations are stated in Eqns. (1) to (3). By solving these equations in matrix notation using MATLAB, the predicted and actual yield of celluloses are shown in Table (3). As can be seen in the table, high content of holocellulose (94.33±0.76) and alpha cellulose (80.17 ± 1.89 % (w/w)) have resulted. It is indicated that delignification and opening the structure of biomass was related to produce the alpha cellulose. The increase of alpha cellulose during the pulping process indicated the content of lignin and hemicelluloses decrease in the pulping and lignin was almost completely removed during bleaching (Soliman *et al*., 2017). The low level of alpha cellulose content indicates that the cellulose structure might be damaged (Kopania *et al*, 2012). Alkali treatment has a positive effect on the mechanical properties and interfacial adhesion of various types of natural fibers (Lazim *et al*., 2014). During chemical pulping, lignin and a large proportion of the hemicellulosess were removed and it opened up the fiber bundles. In addition, the high content of alpha cellulose indirectly indicated no damage of cellulose structure and cellulose content is the equal fiber content of pulp (Khalil *et al*., 2006). In soda pulping, NaOH tend to disperse to form alkali cellulose by the reaction of Cel-OH + NaOH $\rightarrow$ Cel-O-Na+H_2O (Kunusa *et al*., 2018). Three dimensional surfaces and contour plots were designed to investigate the interaction among the variables and to determine the optimum condition of each factor for maximum alpha cellulose content. The plots are shown in Figure 1 (a), (b) and (c).

$$\text{Holocellulose Content (\%)} = +77.11 - 0.19x_{1+} 1.09x_2 - 6.59x_3 + 0.94x_1x_2 - 0.31x_1x_3 - 1.06x_2x_3 + 2.16x_1^2 + 2.25x_2^2 + 3.58x_3^2 \quad \text{Eq}^n\ 1$$

Alpha Cellulose Content (%) = $+63.13-2.17x_1+ 1.27x_2 -6.02x_3+0.31x_1x_2-2.56x_1x_3-0.19x_2x_3+2.25x_1^2 +2.07x_2^2 +3.75x_3^2$ …….……. Eq^n 2

Hemicelluloses Content (%) = $+13.98+2.05x_1- 1.98x_2-0.57x_3 +0.63x_1x_2 +2.25x_1x_3 - 0.88x_2x_3-0.086x_1^2 +0.18x_2^2 – 0.17x_3^2$ ……..…. Eq^n 3

Table 3 Yield of Cellulose from the Pulping of Betel Nut Fiber under Optimum Conditions

Sr. No.	Alkali Concentration % (w/v)	Alkali Volume (mL)	Hydrolysing Time(hr)	Composition of Pulp	Predicted Yield %(w/w)	Actual Yield %(w/w)
1	44.40	475.60	3.08	Holocellulose	80.17	94.33±0.76
2	47.60	463.62	4.10	Alpha Cellulose	63.84	80.17±1.89
3	45.84	491.18	4.66	Hemicelluloses	13.88	13.83±1.75

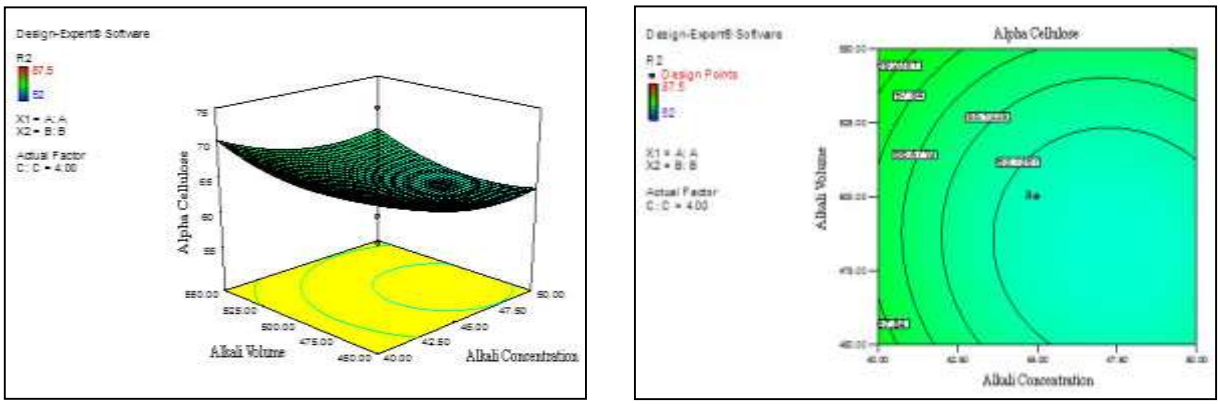

Figure 1 (a) 3-D Surface and Contour Plots of Alpha Cellulose Content for Betel Nut Fiber as a Function of Alkali Concentration and Alkali Volume

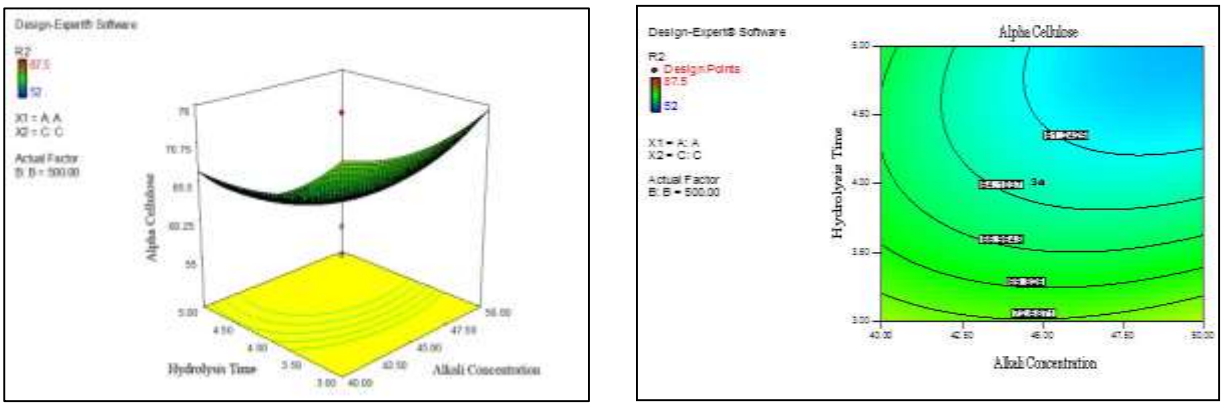

Figure 1 (b) 3-D Surface and Contour Plots of Alpha Cellulose Content for Betel Nut Fiber as a Function of Alkali Concentration and Hydrolysing Time

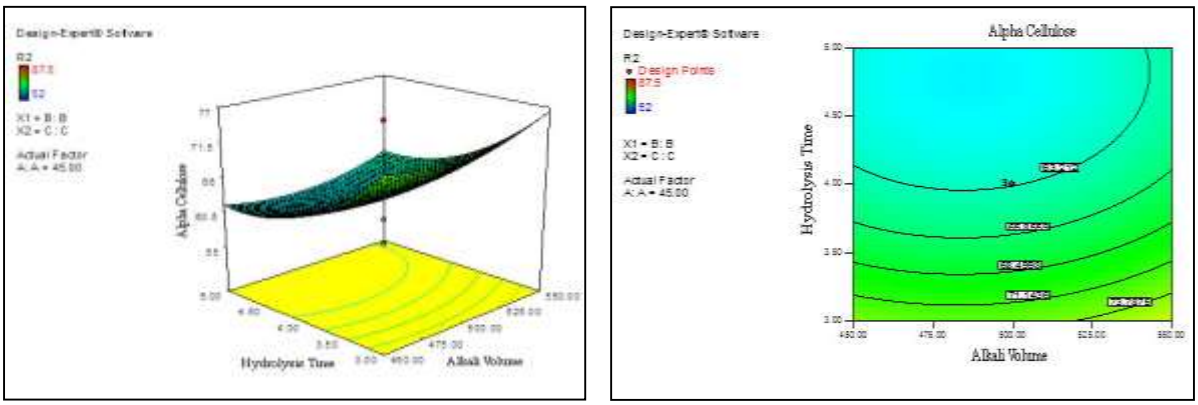

Figure 1 (c) 3-D Surface and Contour Plots of Alpha Cellulose Content for Betel Nut Fiber as a Function of Alkali Volume and Hydrolysing Time

After alkali and acid treatment, lignin and hemicelluloses were broken down and cellulose was separated. So the changes in structure of raw material, pulp and cellulose fiber were observed. Figure (2) represents the FTIR spectra of the raw material, cellulose pulp and cellulose fiber. All the samples exhibited a broad band in the region 3500 cm^{-1} - 3200 cm^{-1} that indicates the free O-H stretching of O-H groups in cellulose molecules. The prominent C-H stretching band was found at 2887.53 cm^{-1}, 2893.32 cm^{-1}, 2895.25 cm^{-1} and 2926 cm^{-1}. The peak at 1647.26 cm^{-1} for betel nut fiber and 1635.69 cm^{-1} in pulp were observed due to the -OH bending of absorbed water. The water molecule in the cellulose is very difficult to extract due to the cellulose-water interaction. The moisture was slightly absorbed in the space left vacant from the removal of hemicelluloses and lignin due to the alkali treatment. The higher moisture content is probably due to the higher cellulose content (Sofla *et al*., 2016). Lignin presented characteristic peak in the range 1200 cm^{-1}-1300 cm^{-1} corresponding to the aromatic skeletal vibration. These peaks are associated with C-O stretching of hemicelluloses and lignin. These peaks were not observed in pulp and cellulose fiber which indicated the removal of hemicelluloses and lignin. The high contents of alpha-cellulose and holocellulose were obtained as a result of the delignification and refining treatments, the opening of the lignocellulosic structure of the pulps, causing hemicelluloses hydrolysis and cleavage of lignin-hemicelluloses bonds, resulting in the removal of most of the hemicelluloses and almost all of the pulp lignin (Guimaraes *et al*., 2015). The alkaline cellulose is formed by stretching C-O and C-C group at around 1060 cm^{-1}. It was observed that these stretchings were found in the spectra of cellulose fibers. Beta glucosidic linkages between glucose units in cellulose presented the peak at around 900 cm^{-1}. The appearance of the signal at 896.93 cm^{-1} and 895.50 cm^{-1} were observed in pulp and cellulose fiber which is a typical structure of cellulose. The presence of this peak showed the increase in the percentage of cellulosic components after removal of non-cellulosic materials by chemical treatments (Wicaksono *et al.*, 2013). After the chemical treatment, the absorption bands at 1730 cm^{-1}, 1620 cm^{-1}, 1595 cm^{-1} and 1512 cm^{-1} were not observed on the spectrum of pulp and cellulose fiber. The bands at 1512 cm^{-1} and 1250 cm^{-1} were drastically reduced in FTIR spectrum of the pulp and cellulose fiber which indicated that most of the lignin was removed. After acid hydrolysis and homogenization treatment, the spectra of cellulose fiber were fairly close to that of the pulp.

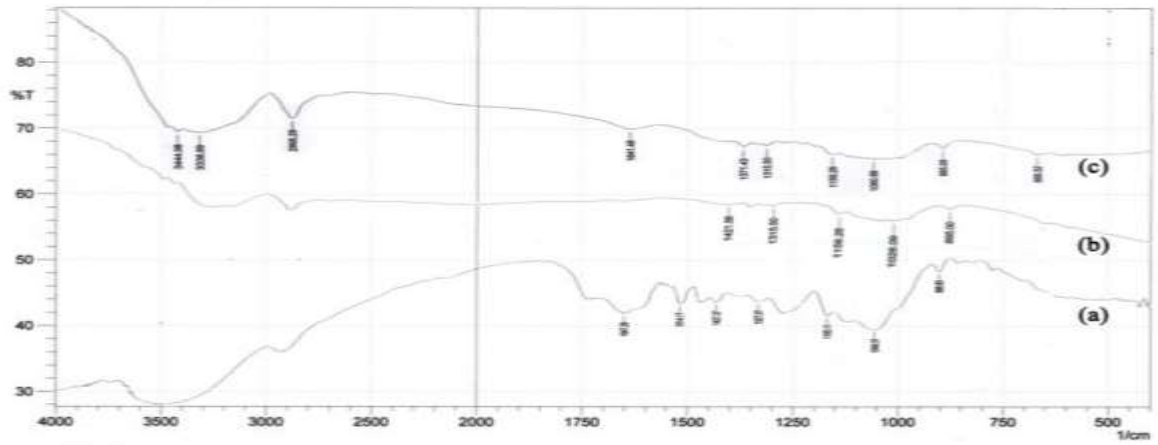

Figure 2 FTIR Spectra of (a) Betel Nut Fiber (b) Its Cellulose Pulp and (c) Its Cellulose Fiber

Figure (3) reveals the SEM images and represents the structure and shape of fiber matrix in betel nut fiber, cellulose pulp and cellulose fiber. The raw fiber was uneven and tangled with lignin binder. The raw fiber is composed of individual cells that are bound together by cemented components of lignin and hemicelluloses. The diameter of the betel nut fiber was found to be around 86.14 µm. After soda pulping, the resulted fiber had smooth and clear surfaces. It was observed that the surface of the fiber look smoother than the raw fibers due to the removal of the bundles. The bleaching process decreased the fiber diameter because of the removal of lignin. The bleaching treatment modified the surface of the fibers and it became smooth (Ireana *et al.*, 2014). After pulping and bleaching process, the fiber diameter for betel nut fiber further reduced to 9.92 µm respectively. Specifically, alkali treatment brought about the leaving pit-like pores on betel nut fiber. This was due to the removal of waxy layers from the surface (Lazim *et al*., 2014). Acid treatment of pulp could also weaken the structure of aggregate fibers and defribrilllation occurred (Wicaksono *et al*., 2013). It can also be seen that the cellulose fibers were smoother than the raw material and pulp. The size of the cellulose fiber was found to be 8.01µm.

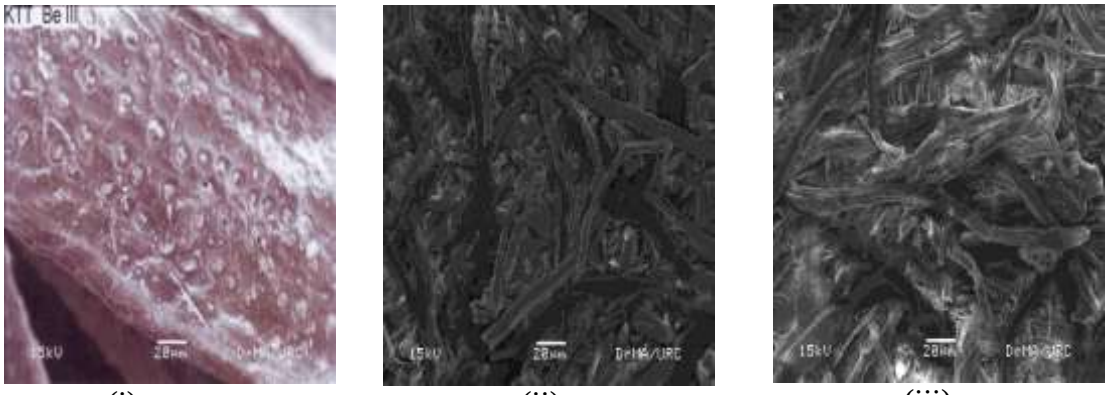

(i) (ii) (iii)

Figure 3 SEM Images of (i) Betel Nut Fiber (ii) Its Cellulose Pulp and (iii) Its Cellulose Fiber

Figure (4) shows the XRD patterns of the raw, pulp and cellulose fiber of the betel nut fiber. These were possible to observe a major diffraction peak for 2θ ranging between 22º and 23º, which corresponds to cellulose (002) crystallographic planes (Pereira *et al.*, 2011). The spectra corresponding to the untreated betel nut fiber showed wider diffraction pattern observing at 2θ ranging 22º. It was found for 2θ ranging between 12.32° and 22.30° for cellulose pulp and cellulose fiber of betel nut fiber. The high intensity peak associated with pulp and cellulose fiber was due to the removal of lignin and hemicelluloses with the consequent increase in the cellulose

index. The sharp diffraction peak is an indication of high crystallinity degree in the structure of the treated fibers (Alemdar and Sain, 2008). In diffraction pattern the narrower peaks indicates crystalline part of the material while the amorphous part of fibers presents as wider peaks. The Bragg angles of 16º, 22º and 35º are characteristics of cellulose and the peak corresponding to crystalline region that is located in a Bragg angle 2θ of 22º (Fonseca *et al*., 2015). Cellulose consists of both amorphous and crystalline regions whereas lignin and hemicelluloses display a completely amorphous structure. The sharp diffraction pattern was observed for the pulp and cellulose fiber. The structure of hemicelluloses was easily hydrolysed while the structure of cellulose was not easily broken by acid hydrolysis. Therefore, more sharper diffraction pattern was found in cellulose fiber than in pulp.

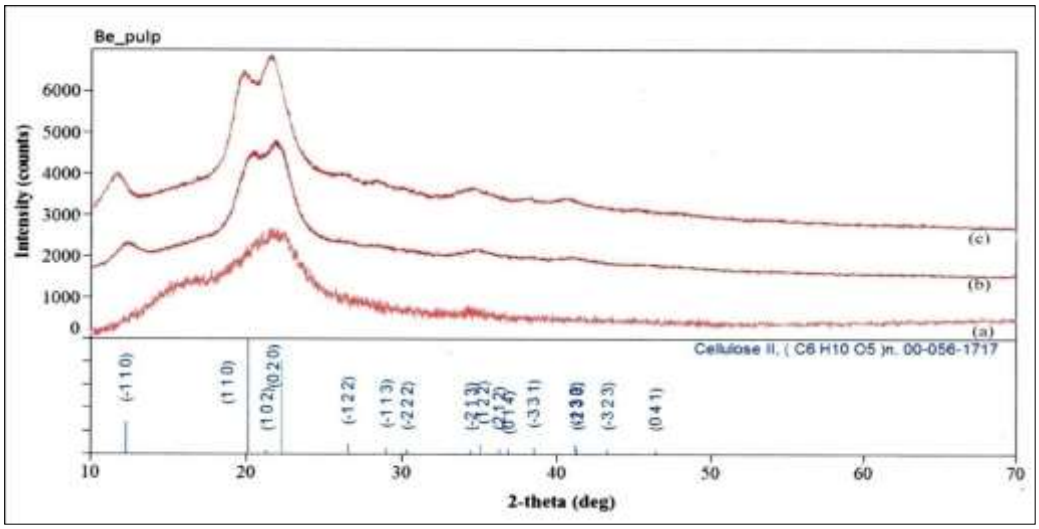

Figure 4 X-Ray Diffraction Analysis of (a) Betel Nut Fiber (b) Its Cellulose Pulp and (c) Its Cellulose Fiber

The resulting TGA curves as shown in Figure (5) indicated that small mass of loss was found at around 100 ºC due to the evaporation of absorbed moisture. According to the results, thermal stability of betel nut fiber is greater than that of pulp and cellulose fiber. Because betel nut fiber has higher lignin content. Lignin is different from hemicelluloses and cellulose, because it is composed of three kinds of benzene-propane units, being heavily cross-linked and having very high molecular weight. The thermal stability of lignin is thus very high, and it is difficult to decompose (Poletto *et al*., 2014). The curves of the raw material, cellulose pulp and cellulose fiber showed several different decomposition stages, which indicated the presence of different components. The temperature range where maximum mass loss rate occurred was related to the decomposition of hemicelluloses (225-325 ºC), lignin (250-500 ºC) and cellulose (305-375 ºC) as reported (Guimaraes *et al*., 2015). Betel nut fiber showed a lower original decomposition temperature about 220 ºC due to the presence of hemicelluloses and lignin. Pulp degradation began at a temperature approximately 330 ºC due to the removal of hemicelluloses and lignin after chemical extraction. Bleaching increased the thermal stability of the pulp (Guimaraes *et al*., 2015). Therefore, TG-DTA curves obtained for cellulose fiber revealed difference in thermal behavior in comparison to that of the pulp and raw materials due to the presence of sulfate groups, which promote dehydration reactions that release water and which can influence cellulose degradation reactions (Corradine *et al*., 2016).

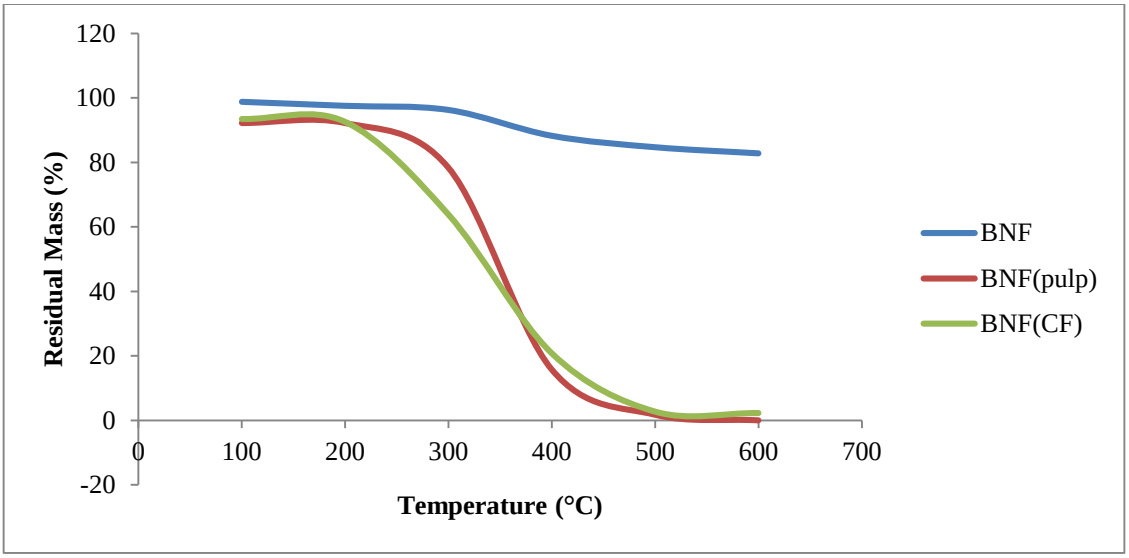

BNF = Betel Nut Fiber
BNF (pulp) =Cellulose Pulp of Betel Nut Fiber
BNF (CF) =Cellulose Fiber of Betel Nut Fiber

Figure 5 Thermogravimetric Analysis Graph of Betel Nut Fiber, It Cellulose Pulp and Its Cellulose Fiber

Conclusion

In this study, cellulose fiber was isolated from betel nut fiber through four steps, including alkali treatment, bleaching, acid hydrolysis and homogenization. Acid and alkaline conditions degrade lignin and hemicelluloses preserving the cellulose. After acid hydrolysis and homogenization, the spectra of cellulose fiber were fairly close to that of the pulp. The size of the cellulose fiber was observed to be 8.01µm. The sharp diffraction pattern was observed in cellulose fiber than in pulp and raw materials. TG-DTA analysis expressed that cellulose fiber revealed difference in thermal behavior in comparison to that of the pulp and raw materials due to the presence of sulfate groups.

Acknowledgements

I would like to express my gratitude to the Myanmar Academy of Arts and Science for allowing me to submit this article.

References

Alemdar. A, and Sain.M., (2008), "*Isolation and characterization of nanofibers from agricultural residues – Wheat straw and soy hulls,"*Bioresource Technology 99, 1664–1671

Azeez. M.A., (2018), "*Pulping of non-woody biomass*", DOI:10.5772/intechopen.79749

Chaturbhuj. K.S., Mustrapha.A., Masri.M.M., Owolabi.A.F, Syakir.M.I., Dungani.R., Paridah.M.T., Jawaid.M. and Khalil.H.P.S.A., (2016), " *Isolation and characterization of cellulose nanofibers from Gigantochloascortchinii of a reinforcement material,*" Journal of Nanomaterials, vol.2016 ,Articla ID 4024527

Corradini. E., Pineda.E.A.G., Correa.A.C., Teixeira.E.M. and Mattoso.L.H.C., (2016), "*Thermal Stability of Cellulose nanocrystals from curaua fiber isolation by acid hydrolysis*", Cellulose Chemistry and Technology, 50 (7-8), 737-743

Dhanalakshmi.S. Ramadev.P. and Basavaraju.B.(2016), "*Effect of chemical treatments on tensile strength of areca fiber reinforced natural rubber composites*", IOSR Journal of Applied Chemistry (IOSR-JAC) Volume 8, Issue 5 Ver. II e-ISSN: 2278-5736.

Dungani.R., Karina.M., Subyakto, Sulaeman.A., Hermawan.D. and Hadiyane.A., (2016), "Agricultural waste fibers towards substanability and advanced utilization: A review," Asian Journal, vol 15 (1-2); 42-55

Fonseca. H.C.O., Gascia.R.H.L., Ferreira.R.J., Silva.F.R.O., Jr.A.J.P. and Sakata.S.K., (2015), "*Thermal Stability of Cellulose nanocrystals from curaua fiber isolation by acid hydrolysis*", Cellulose Chemistry and Technology, 50 (7-8), 737-743

Galiwango. E., Rahman.N.S.A., Al- Marzouqi A. and Abu-Omar.M., (2019), "*Isolation*

and characterization of cellulose and α-cellulose from date palm biomass waste" Heliyon 5 e02937

Guimaraes. M., Batro.V.R., Novack.K.M., Neto.W.P.F., Mendes.L.M. and Tonoli.G.H.D., (2015), "*Preparation of cellulose nanofibrillation for their applications in biodegradable composites*," Journal of Nonoscience and Nanotechnology, vpl.15, 1-18

Ireana. Y.F.K. Abdul., H.Soharb., A.Astimar., D.Yalda., D.Rudi. and B.Amir., (2014), " *Exploration of a chemo-mechanical technique for the isolation of nanofibrillated cellulosic fiber from oil palm empty fruit bunch as a reinforcing agent in composites materials*", Polymers, 6, 2611-2624

Khalil.H.P.S.A., Alwani.S.M. and Omas.A.K.M., (2006), "*Chemical Composition, anatomy,lignin distribution and cell wall structure of Malaysis plant waste fibers*," Bio Resources 1 (2), 220-230

Kopanina. E., Wietecha.J. and Ciechanska.D., (2012), "*Studies on isolation of cellulose fiber from waste plant biomass*," vol.20, no. 6B (93), 167-172

Kunusa. W.R,Isa.I., AR Laliyo.L. andIyaba.H., (2018), "*FTIR, XRD and SEM analysis of microcrystalline cellulose (MCC) fibers from corncorbs in alkali treatment*," IOP Conf. series: Journal of Physics, 1028, 012199

Lazim. Y., Salit.S.M., Zaninudin.E.S., Mustapha.M. and Jawaid.M., (2014), "*Effect of alkali treatment on the physical, mechanical and morophological properties of waste betel nut (areca catechu) husk fiber*," peer-review article, Bioresources,9 (4), 7721-7736

Liew.F.K., Hamdan.S., Rahman.R., Rusop.M., Josephine.C.H.L., Hossen.F. and Rahman.M., (2015), "*Synthesis and characterization of cellulose from green bamboo by chemical treatment with mechanical process*," Journal of Chemistry, volume 2015, ID 212158, 6pages

Mohammadi. N.S., Nemati.M., Zaninudin.E.S., Samariha.A., abei.A., Ravanbakhsh.F., and Kiaei.M., (2011), " *Studying the effect of the age of a tree on chemical composition and degree of polymerization cellulose*," Indian Journal of Science and Technology Vol. 4 No. 12 (Dec 2011) ISSN: 0974- 6846

Petreira. P.H.F., Voorwald.H.C.J., Cioffi.M.O.H., Mulinari.D.R., Luz.S.M.D. and Silva.M.L.C.P.D., (2011)," *Sugarcane bagasse pulping and bleaching: thermal and chemical characterization,"* Bioresources, 6 (3), 2471-2482

Poletto. M., Juinor.H.L.O. and Zattera.A.J., (2014)., "*Native cellulose: structure, characterization and thermal properties",* Materials, ISSN 1996-1944, 7, 6105-6119

Sofla. M.R.K., Brown.R.J., Tsuzuki.T. and Rainey.T.J., (2016), "*A comparison of cellulose nanocrystals and cellulose nanofibers extracted from bagasse using acid and ball milling method*, "Advances in Nanoscience and Nanotechnology, 7,053004 (9pp)

Soliman.A.S., Shenata.M.S., Ahmad.F. and Abdel.A.M., (2017), "*Evaluation of paper pulp and paper making characteristics produce from different African woody trees grown in Egypt",* Research Journal of Forestry, vol.11(2), 19-27

Wicaksono.R., SyamsuK., Yuliasih.I. and Nasir.M, (2013)," *Cellulose nanofibers from cassvabagasse: characterization and application on tapioca-film,*" Chemistry Materials Research, Vol.3, No.13, I SSN 2224-3224 (Print) ISSN 2225-0956 (Online), 79-87

Zhang.G., Wu.F., Ma T., Zhang.B., Manyande.A. and Du.H., (2019)," *Preparation and characterization of cellulose fibers isolated from lettuce peel,*" Cellulose Chemistry and Technology, 53 (7-8), 677-684

COMPARATIVE STUDY ON THE CHARACTERISTICS OF ESSENTIAL OILS FROM SPEARMINT PLANTS (*MENTHA SPICATA* L.) BY MICROWAVE-ASSISTED HYDRODISTILLATION AND CONVENTIONAL METHODS

Saw Htet Thura Lin[1], Soe Soe Than[2], Khin Si Win[3]

Abstract

Essential oils from plant species have played an important role in the fields of food industry, drugs, mosquito repellent, perfumes and other chemicals of important economic values. In this research work, essential oils from spearmint plants (*Mentha spicata* L.) were extracted using a method of microwave-assisted hydrodistillation (MHD) and conventional methods such as steam distillation (SD) and hydrodistillation (HD). Microwave-assisted hydrodistillation is an advanced and innovative hydrodistillation technique, in which a microwave oven (250v-50Hz power source; 2450MHz, output power 800Watt) was used as the heating source. The effects of extraction time (15 min, 30 min, 45 min, 60 min and 75 min) for microwave-assisted hydrodistillation and (30 min, 60 min, 90 min, 120 min, 150 min and 180 min) for steam distillation and hydrodistillation on the yield of essential oils were investigated. It was found that the highest yield percent of spearmint essential oils obtained by steam distillation and hydrodistillation were 0.07 % w/w and 0.05 % w/w while that of 0.09 % w/w for microwave-assisted hydrodistillation. The physico-chemical properties of essential oils such as color, specific gravity, refractive index, acid value and solubility in ethanol were analyzed. The extracted essential oils were also identified by Gas Chromatography-Mass Spectrometry (GC-MS). It was observed that carvone in spearmint essential oils was the major key component, with the highest concentration in 58.63 % by steam distillation, 56.91 % by hydrodistillation and 59.49 % by microwave-assisted hydrodistillation.

Keywords: essential oils, spearmint plants, microwave-assisted hydrodistillation, steam distillation, hydrodistillation

Introduction

Essential oils are botanical extracts of various plant materials and they are extracted not only from flowers but from herbs, trees and various other plant materials. These essential oils are commercially used in different industries including food, beverages, pharmaceutical and cosmetics industries due to the multifunctional properties such as antiviral, antibacterial, insecticidal and antioxidant properties. However, essential oils are obtained very low yield, making it fragile substances (Teixeira *et al.,* 2013). The use of medicinal plants extracts including for spearmint (*Mentha spicata* L.) is a part of competitive market, which includes pharmaceuticals, food, cosmetics, and perfumery markets, mainly to use their active substance (Husnu, 2010). The essential oils extracted from spearmint plants containing mainly carvone 50-70 % w/w and menthone, have shown strong insecticidal and mutagenic activity (Hussain, 2009).

Essential oils can be isolated using several extraction methods that differ from one another by the time required for extraction, performance and energy consumption, etc. (Romdhane *et al.*, 2011). The conventional hydrodistillation and steam distillation remain the most common method used for the extraction of essential oils. However, these extraction methods have several disadvantages such as loss of the ability of some compounds of the extract due to thermal degradation, a long extraction time and the considerable consumption of energy (Wenqiang *et al.*, 2007). As a means to overcome this sort of drawbacks, an advanced and improved method such as microwave-assisted extraction, subcritical water extraction and ultrasound-assisted extraction have

[1] Demonstrator, Department of Industrial Chemistry, University of Yangon
[2] Professor and Head, Department of Industrial Chemistry, University of Yangon
[3] Professor, Department of Industrial Chemistry, University of Mandalay

been applied for the extraction of essential oils in order to shorten the extraction time, improve the extraction yield and reduce the operational costs.

Recently, microwave-assisted hydrodistillation (MHD) procedures for extracting essential oils have become attractive for use in laboratories and industries due to its effective heating, fast extraction process, high yield of oil, good quality of the extracts and also environmental friendly extraction technique (Wenqiang *et al.,* 2007). The aim of this research is to investigate the applicability of microwave-assisted hydrodistillation method as an alternative and effective technique over steam distillation and hydrodistillation in the extraction of essential oils based on the extraction yield and chemical compositions of essential oils obtained from native plant species, spearmint.

Materials and Methods

Materials

Fresh spearmint plants were collected from Hlegu Township, Yangon Region. Air-dried leaves were used as raw materials in this research work. Ethanol (95 %) and sodium sulfate were purchased from Empire Chemical Shop, 27th street, Pabedan Township, Yangon.

Preparation of Sample

The collected plant materials were thoroughly washed with tap water to remove the dirt. These plant materials were dried at room temperature for one day and cut into small pieces. Then, the small pieces of sample were ground using a grinder (Super Blender, Panasonic, Tokyo, Japan).

Extraction of Essential Oil from Spearmint Plants

Steam Distillation (SD)

The ground plant material, 400 g, was placed in a 1 L round bottom flask. This flask was then connected to a steam generating equipment (Clevenger-type apparatus). 1 L of water was boiled in a flat bottom flask. The generated steam was passed through the dried sample and the volatilized oil which passed through the condenser was collected in a receiver. Steam distillation was conducted for 3 hours. The distillate from the receiver was transferred into a separating funnel and left quiescently overnight for layer separation. The bottom layer, which is water, was withdrawn. The extracted essential oil was retained in the upper layer. The residual moisture in the extracted oil was removed using anhydrous sodium sulfate. Then, the resultant oil was put in an air tight amber glass bottle and stored in a cool and dry place.

Hydrodistillation (HD)

400 g of ground plant material was placed in a 1 L round bottom flask containing 400 mL of distilled water and hydrodistilled for 30 min, 60 min, 90 min, 120 min and 150 min using a Clevenger-type apparatus. The system was operated at a fixed power of 500 W and under the atmospheric pressure. The oil and water layers separation was conducted according to the above steam distillation method.

Microwave-assisted Hydrodistillation (MHD)

A modified domestic microwave oven model Electrolux EMM2331MK connected to the Clevenger apparatus was modified for microwave-assisted hydrodistillation operation as shown in Figure (1). The Electrolux EMM2331MK has 1150 W power consumption, 800 W output power with 250v-50Hz power source; 2450MHz. The cavity dimensions of the microwave oven were 220 × 340 × 320 mm.

The microwave-assisted hydrodistillation was conducted at microwave power 800 W for durations of 15 min, 30 min, 45 min, 60 min and 75 min. Firstly, 1 L of flat bottom flask containing 400 g of plant material with 400 mL of distilled water was put into the microwave oven cavity. A condenser which has been set on the top, outside the oven, was used to collect the extracted essential oils. Microwave-assisted hydrodistillation was conducted for 75 min.

The extracted essential oils were dehydrated using anhydrous sodium sulphate. The pure extracted essential oil was placed in an air tight amber glass bottle and stored in a clean and dry place.

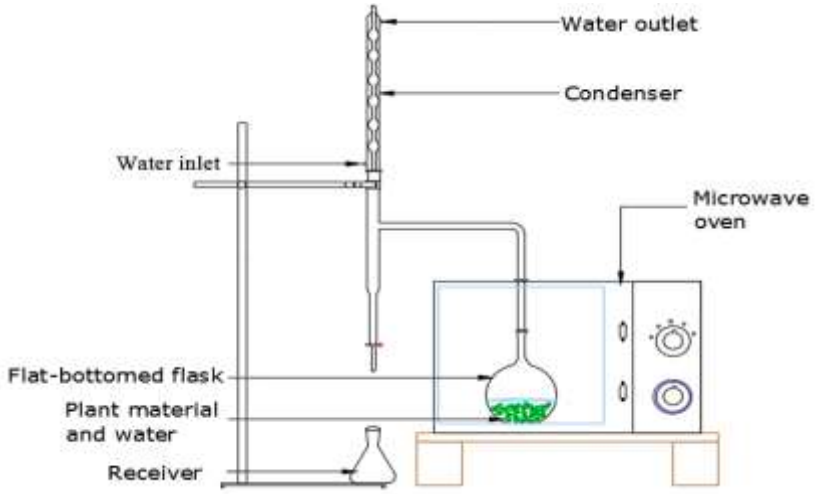

Figure 1 Microwave-Assisted Hydrodistillation Apparatus

Determination of Physico-chemical Properties of Extracted Essential Oils

The physico-chemical characteristics such as color, specific gravity, refractive index, acid value and solubility of the extracted essential oils from spearmint plants were analysed at room temperature. Lovibond Tintometer (Model No. E, England Made) was used to determine the color of essential oil. The specific gravity of extracted essential oil was determined using density bottle AOAC-2000(9.009). The refractive index was measured with an Abbe '60' type refractometer. The acid value was determined by AOAC-2000 (969.33) method. The solubility in alcohol was determined by AOAC-2000(2021.25) method.

Identification of Extracted Essential Oils by Gas Chromatography-Mass Spectroscopy (GC-MS) Analysis

The constituents in extracted essential oils were identified by GC-MS (PerkinElmer, Clarus 680 GC coupled to PerkinElmer, Clarus 600 MS Detector equipped with an Elite 5 MS capillary non polar column - 30.0 m length x 0.25 mm ID x 0.25 μm film thickness). The components of essential oils were identified based on their retention time and mass spectra, matching with National Institute of Standards and Technology (NIST05) libraries provided with computer controlling of the GC-MS system.

The GC-MS analysis of the extracted essential oils was conducted at the National Analytical Laboratory, Department of Research and Innovation, Ministry of Education, Yangon Region.

Results and Discussion

In this research work, essential oils were extracted from spearmint plants by steam distillation, hydrodistillation and microwave-assisted hydrodistillation methods. Figure (2) shows that the effect of extraction time on yield percent of extracted spearmint essential oil was graphically compared with steam distillation and hydrodistillation methods. According to the results of the research work, the amounts of essential oils extracted by both methods did not change significantly after 150 min. The extraction rate was high at the beginning of the extraction but it can be seen that no significant improvement in yield of oil after a certain period. From the point of view of distillation methods, the yield of essential oils from spearmint plants extracted by steam distillation was higher than that of hydrodistillation. Guenther, 1948 stated that the distillation of plant materials with high water content usually provides the problems to completely extract the essential oil. It was found that fresh spearmint herb, like most plants or plant parts with a high moisture content, cannot be exhausted completely by distillation, or only with great difficulty, and after long hours of distillation. It was also observed that yield of essential oils by hydrodistillation were slightly lower than that of steam distillation method.

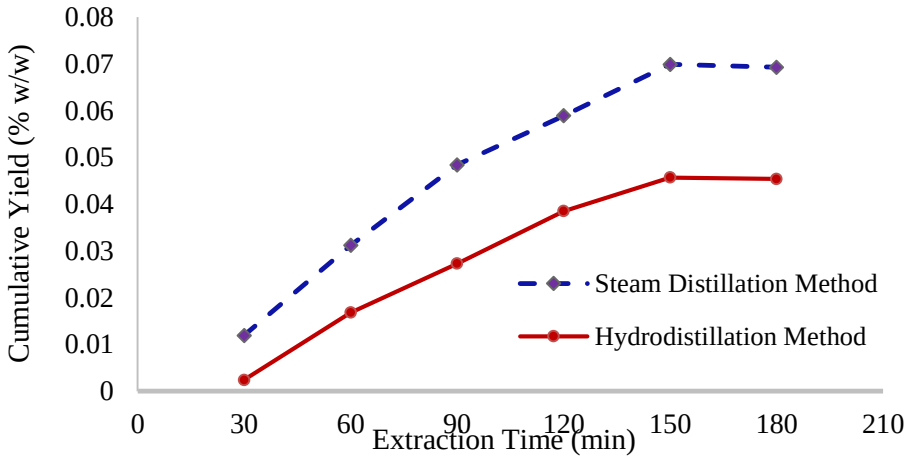

Figure 2 Effect of Extraction Time on the Yield Percent of Spearmint Essential Oils by Steam Distillation and Hydrodistillation

Figure (3) shows the effect of extraction time on the yield of oil from the spearmint plants by microwave-assisted hydrodistillation method. It can be seen that the extraction time of 45 min was found to obtain the highest yield of spearmint essential oil. When compared to the yields of essential oils obtained by steam distillation and hydrodistillation methods, the extraction time for microwave-assisted hydrodistillation was only 15 min whereas for steam distillation and hydrodistillation needed 30 min. This result shows that nearly 30 % w/w of the total yield of oil could be extracted using the microwave-assisted hydrodistillation within a short extraction time of 15 min.

The amount of yield resulted by microwave-assisted hydrodistillation after 45 min was almost similar to the oil obtained after 150 min by steam distillation and hydrodistillation methods. It can also be seen that the yield of essential oil extracted by microwave-assisted hydrodistillation was slightly higher than that of steam distillation and hydrodistillation methods.

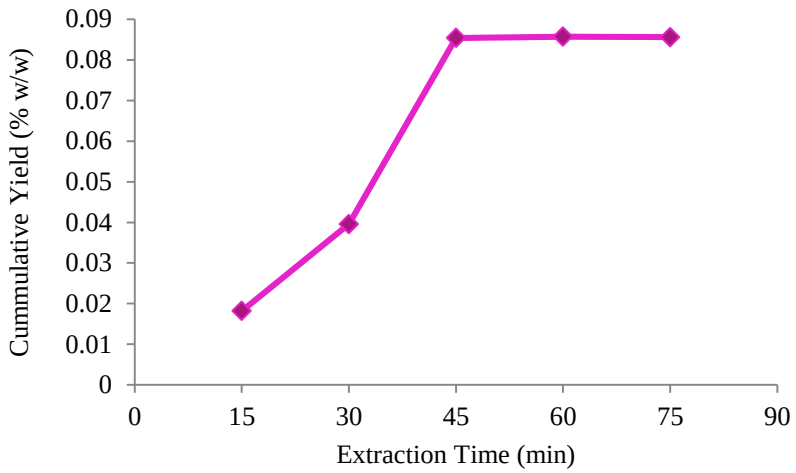

Figure 3 Effect of Extraction Time on the Yield Percent of Spearmint Essential Oil by Microwave-assisted Hydrodistillation

The results in Table (1) show that physico-chemical properties of essential oils from spearmint plants. Physico-chemical properties of essential oils are an assessment of the purity and quality of the volatile oil as well as for identification. Therefore, the specific gravity, refractive index, acid value and solubility were determined for the isolated essential oils from spearmint plants by steam distillation, hydrodistillation and microwave-assisted hydrodistillation methods. According to the results, it can be seen that specific gravity of extracted essential oil is less than 1 for all samples.

Barkatullah *et al*., (2012) stated that specific gravity of essential oils is less than one for all the oils except some plant oil like eugenol and cinnamon oils. The value of refractive index of essential oil extracted by steam distillation was 1.47, 1.48 for hydrodistillation but 1.45 for microwave-assisted hydrodistillation. Duarte *et al*., (2018) reported that the essential oils which have high refractive index, are sparingly soluble in water, and less dense than water and liquid at room temperature, but exception for trans-anethole (anise camphor) from the oil of anise (*Pimpinella anisum* L.). Guenther, 1948 stated that essential oils contain several volatile aroma compounds; often these are free fatty acid. Free fatty acids are considered as defect in oils/fats because these are degraded or become rancid. Hassan, (2019) reported that spearmint essential oil contains acid value 1.1 mg, specific gravity 0.81 and refractive index 1.49. Acid values of extracted essential oils are 1.35, 1.50 and 1.30 for steam distillation, hydrodistillation and microwave-assisted hydrodistillation, respectively. It can also be found that all the samples were miscible in ethanol. According to the literature study of essential oils, Gamarra *et al*., 2000 stated that physico-chemical properties of the plant oils can vary depending on the chemotype and biotype of the plant, the soil condition as well as the extractive process.

Table 1 Physico-chemical Properties of Spearmint Plants Essential Oils

Sr. No.	Parameters	Experimental Values		
		SD	HD	MHD
1	Color	Yellow 0.1, Blue 0.1	Yellow 0.1	Yellow 0.1, Blue 0.2
2	Refractive Index	1.47	1.48	1.45
3	Specific Gravity	0.84	0.90	0.89
4	Acid Value (mg KOH/g)	1.35	1.50	1.30
5	Solubility in ethanol	Soluble	Soluble	Soluble

SD – Steam Distillation HD – Hydrodistillation MHD – Microwave-assisted Hydrodistillation

From the results of the Table (2), carvone was found as the most dominant compound and followed by D-lemnene, Beta-phellandrene and Alpha-cardinol. It was also observed that concentrations of key component, carvone, found in the spearmint (*Mentha spicata* L.) essential oil, shown in Figure (4), were nearly the same in all methods. This finding is in accordance with the literature values. According to the literature review, Bayan *et al.*, (2018) reported that the Gas Chromatography-Mass Spectrometry (GC-MS) analysis of the essential oil from *Mentha spicata* L. contained the main component of carvone 56.94 % w/w, followed by limonene 11.63 % w/w, sabinene hydrate 7.04 % w/w and caryophyllene 4.06 % w/w. Moreover, Hassan, (2019) stated that D-carvone 51.91 % w/w, D-limonene 24.64 % w/w and eucalyptol 2.81 % w/w were found as major compounds of *Mentha viridis* leaves oil. GC-MS Chromatogram of extracted essential oil by steam distillation, hydrodistillation and microwave-assisted hydrodistillation are shown in Figures (5), (6) and (7).

However, some oxygenated monoterpenes compounds such as Beta-Ocimene, and Terpenen-4-ol cannot be found in the extracted essential oils by microwave-assisted hydrodistillaton and hydrodistillation methods. Handa *et al.*, (2008) stated that if refluxing was controlled like hydrodistillation, there will be losses of some oxygenated compounds and these could be dissolved into distilled water to some extent. Ranitha *et al.*, (2014) reported that there can be a difference for chemical compositions in extracted essential oil by microwave distillation. Microwave radiation can penetrate into biological materials and creates heat by interaction with polar molecules such as water. Therefore, water soluble constituents cannot be completely extracted by microwave-assisted hydrodistillation.

Figure 4 Spearmint Plants Essential Oil Extracted by Microwave-assisted Hydrodistillation Method

Table 2 Dominant Compounds in Extracted Essential Oils by Steam Distillation, Hydrodistillation and Microwave-assisted Hydrodistillation

Sr. No.	Compound Name	Retention Time (min)			Molecular Weight	Formula	Related Amount (% w/w)		
		SD	HD	MHD			SD	HD	MHD
1	3- Carene	3.08	3.38	3.24	136	$C_{10}H_{16}$	1.14	1.18	1.34
2	Beta-Phellandrene	3.81	3.84	3.64	136	$C_{10}H_{16}$	4.38	1.17	1.66
3	Gamma- Terpinene	3.94	3.68	3.75	136	$C_{10}H_{16}$	1.38	0.08	0.15
4	Beta-Pinene	3.99	-	3.76	134	$C_{10}H_{14}$	0.77	-	0.84
5	D-Limonene	4.67	4.05	4.31	154	$C_{10}H_{18}O$	19.64	24.30	22.19
6	Beta-Ocimene	4.79	-	-	154	$C_{10}H_{18}O$	0.27	-	-
7	Trans-Carveol	7.84	6.72	6.90	154	$C_{10}H_{18}O$	2.64	1.65	2.02
8	Terpenen-4-ol	-	6.18	6.72	154	$C_{10}H_{18}O$	-	8.91	3.65
9	Carvone	7.95	7.01	7.24	152	$C_{10}H_{16}O$	58.63	56.91	59.49
10	Beta-Bourbonene	9.73	-	9.04	154	$C_{10}H_{18}O$	1.12	-	2.92
11	Azulene,1,2,3,3A,4, 5,6,7-Octahydro-1,4-Dimethyl-7-(1-Methylethenyl)	8.19	-	-	204	$C_{15}H_{24}$	2.13	-	-
12	Caryophyllene	10.21	9.12	9.51	154	$C_{10}H_{18}O$	0.89	0.37	0.23
13	Dihydro-Cis-Alpha-Copaene-8-ol	10.25	10.25	10.28	222	$C_{15}H_{26}O$	2.40	2.86	2.10
14	Alpha-Cardinol	13.10	11.98	12.37	222	$C_{15}H_{26}O$	2.27	0.19	0.63

SD – Steam Distillation HD – Hydrodistillation MHD – Microwave-assisted Hydrodistillation

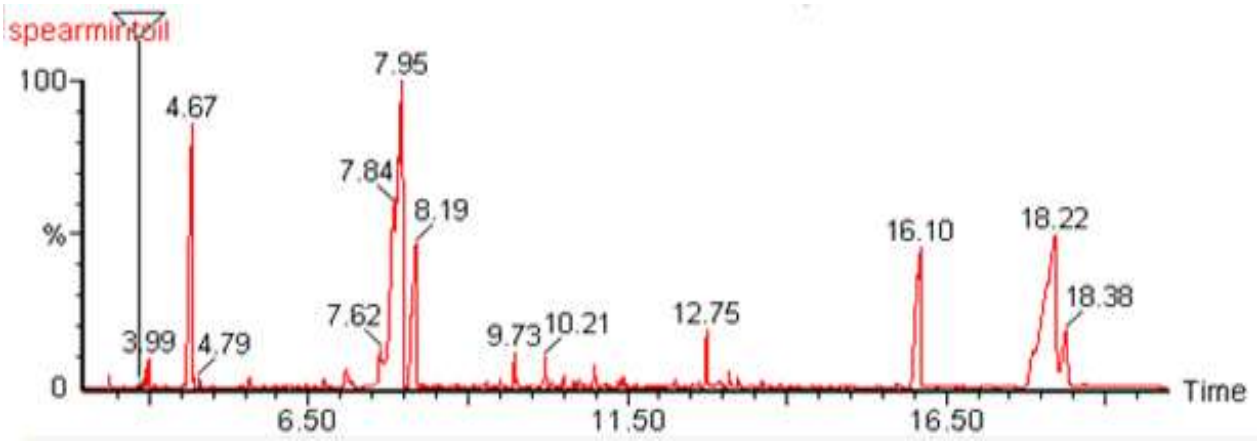

Figure 5 GC-MS Chromatogram of Extracted Spearmint Essential Oil by Steam Distillation

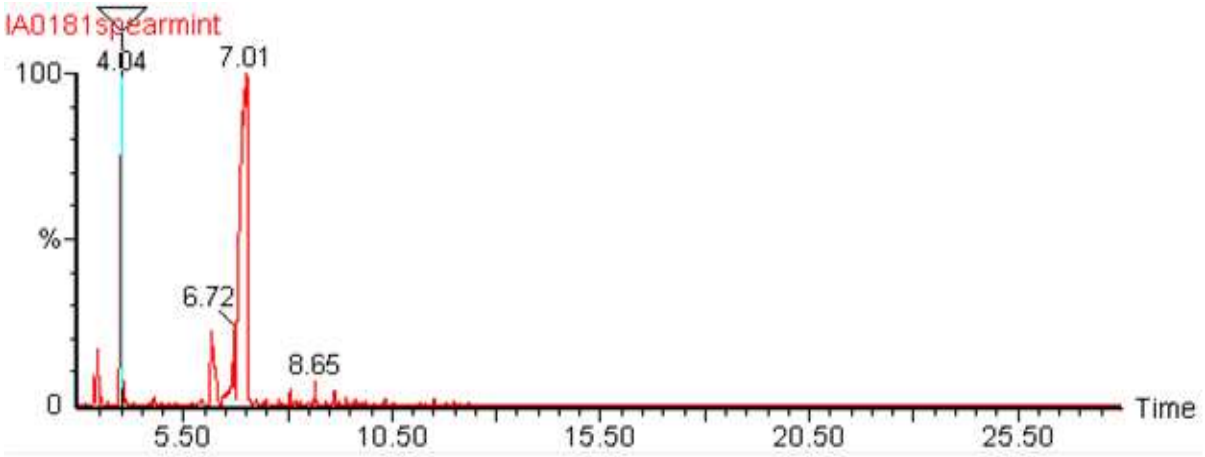

Figure 6 GC-MS Chromatogram of Extracted Spearmint Essential Oil by Hydrodistillation

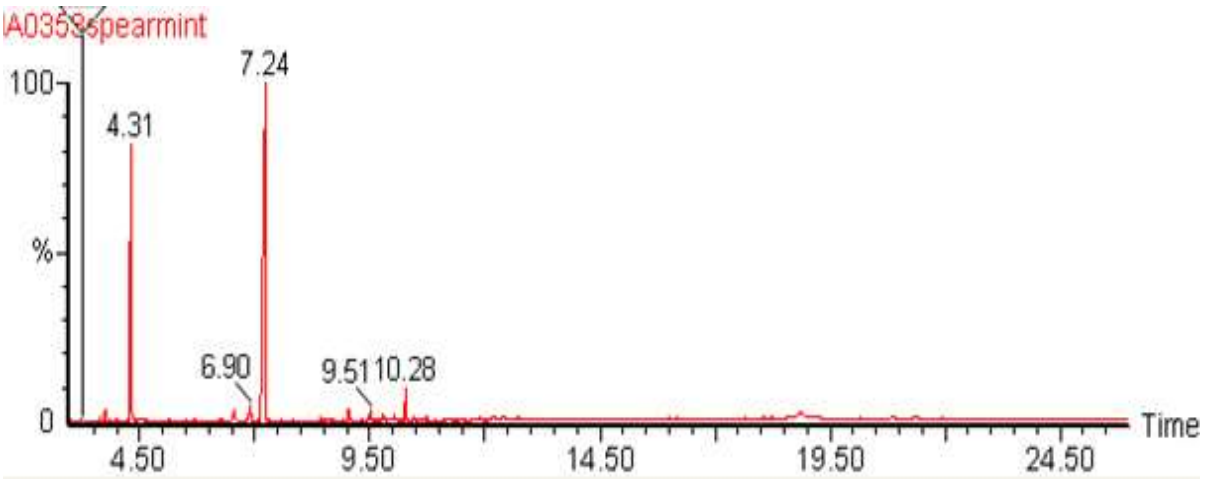

Figure 7 GC-MS Chromatogram of Extracted Spearmint Essential Oil by Microwave-assisted Hydrodistillation

Conclusion

In this research work, essential oils were successfully extracted by steam distillation, hydrodistillation and microwave-assisted hydrodistillation methods. Microwave-assisted hydrodistillation offered great advantages over conventional methods such as steam distillation and hydrodistllation. Microwave-assisted hydrodistillation technique was found to require shorter extraction time. In addition, GC-MS results proved that there were no significant difference between the components of essential oil extracted by microwave-assisted hydrodistillation and those obtained by steam distillation. However, the number of extracted components obtained by hydrodistillation method was found to be less than the other two methods. According to the substantial odor and yield of essential oil, saving of time, cost and energy with no significant changes in its constituents, microwave-assisted hydrodistillation technique was found to be a good alternative way in the extraction processes of essential oils from spearmint plants.

Acknowledgements

We would like to express our deep appreciation to the Myanmar Academy of Arts and Science for giving us the permission to submit this article.

References

AOAC, (2000). Official Methods of Analysis, Association of Official Analytical Chemists, 17th ed., Washington D.C., USA.

Barkatullah, Ibrar M, Rauf A. and Rahman I. U., (2012). Physico-chemical characterization of essential and fixed oils of Skimmia laureola and Zanthoxylum armatum, Middle-East Journal of Medicinal Plants Research 1(3): 51-58, ISSN 2309-8929.

Bayan, Y.,and Kusek M., (2018). Chemical Composition and Antifungal and Antibacterial Activity of Mentha Spicata L. Volatile Oil, Cien. Inv. Arg. 45(1):64-69.

Duarte, M. C. T., Duarte1 R. M. T., Rodrigues R. A. F., and Rodrigues M. V. N., (2018). Essential oils in food processing: chemistry, safety and applications - essential oils and their characteristics, First Edition,. Published by John Wiley & Sons Ltd.

Gamarra, F. M. C., Sakanaka L. S., Tambourgi E. B. and Cabral F. A., (2006). Influence on the quality of essential lemon (Citrus Aurantifolia) Oil by distillation process, Brazilian Journal of Chemical Engineering, Vol. 23, No. 01, pp. 147 – 151.

Guenther E., (1948). The Essential Oils, Volume one – History, Origin in plants, Production and Analysis, D. Van Nostrand Company, Inc., New York.

Handa, S. S., Singh Khanuja S. P., Longo G., and Rakesh D. D., (2008). Extraction technologies for medicinal and aromatic plants, Italy.

Hassan, H. A., Kabbashi, A. S., Abedallah, A., Wagh, Vithal, D. and Hamdi, O. A. A., (2019). Chemical Composition, Antioxidant Activity and Cytotoxicity of Essential Oil of *Mentha viridis*, Acta Scientific Medical Science 3.8 (2019):200-205.

Husnu, K. C., B., & Gerhard, B., (2010). Handbook of Essential Oils: Science, Technology, and Applications. New York: Taylor & Francis Group, http;//doi.org/ 10.7763.

Hussain, A.I., (2009). Characterization and Biological Activities of Essential Oils of Some Species of Lamiaceae. PhD Thesis, Faculty of Science, University of Agriculture, Faisalabad, Pakistan.

Ranitha M., Abdurahman, H. N., Sulaiman, Z. A., Nour, A. H., and Thana, R. S., (2014). A Comparative Study of Lemongrass (*Cymbopogon Citratus*) Essential Oil Extracted by Microwave-Assisted Hydrodistillation (MAHD) and Conventional Hydrodistillation (HD) Method, International Journal of Chemical Engineering and Applications, Vol. 5, No. 2, pp. 104 – 151.

Romdhane M. and Chemat F., (2011). Microwave steam diffusion for extraction of essential oil from orange peel: Kinetic data, extract's global yield and mechanism. Food Chemistry, 125: 255-261.

Wenqiang G., Shufen L., Ruixiang Y., Shaokun T. and Can Q., (2007). Comparison of essential oils of clove buds extracted with supercritical carbon dioxide and other three traditional extraction methods. Food Chemistry, 101: 1558-1564.

Teixeira B., Marques A., Ramo C., Neng N. R., Nogueira J. M. F., Saraiva J. A. and Nunes M. L., (2013). Chemical composition and antibacterial and antioxidant properties of commercial essential oils. Industrial Crops and Products, 43: 587-595.

EXTRACTION OF LIGNIN FROM SUGARCANE BAGASSE BY USING ALKALINE PROCESS AND ALCOHOLIC ALKALINE PROCESS

Phyo Ei Ei Swe[1], Soe Soe Than[2] and Lei Lei Aung[3]

Abstract

The present work was focused on the extraction of lignin from sugarcane bagasse by two extraction processes: alkaline process and alcoholic alkaline process. A Box-Behnken Design of Response Surface Methodology (RSM) was chosen to investigate the optimum conditions of extraction process. Three independent variables in two processes consisting of concentration of solvent, volume of solvent and extraction time were determined based on the yield of lignin. The optimum conditions in alkaline process were found at NaOH concentration of 15%, NaOH volume of 304 mL and extraction time of 2 hr with predicted final lignin yield of 35.62 (%w/w). In alcoholic alkaline process, the optimum conditions were observed at NaOH concentration of 15%, alcoholic NaOH volume of 303 mL and extraction time of 3 hr with predicted lignin yield of 57.19 (%w/w). Predicted values were observed to be in good agreement with experimental values. Then the functional groups present in prepared lignins were identified by using UV-visible spectroscopy and Fourier Transform Infrared Spectroscopy (FTIR). The prepared samples were confirmed as lignin due to the presence of phenolic hydroxyl groups, carbonyl groups and methoxy groups.

Keywords: sugarcane bagasse, lignin, alkaline process, alcoholic alkaline process, response surface methodology

Introduction

The lignocellulosic biomasses such as agricultural wastes, crops and wood wastes are renewable resources for making of chemicals and fuels. The main constituents such as cellulose, hemicellulose and lignin are strongly bonded together to form a lignocellulosic matrix. The lignocellulosic biomasses are difficult to break down the components and digest the hemicellulose due to their structural features (Behera et al., 2014). After the cellulose, lignin is the second most plentiful natural bio polymer. Lignin is hard to break down or remove because of its strong lignocellulosic structure (Cesarino et al., 2012). It consists of three major phenylpropanoid monomers mostly the hydroxycinnamyl alcohols: coniferyl alcohol (G), sinapyl alcohol (S) and p-coumaryl alcohol (H). It can be substituted in expensive phenol part because it is bio-renewable, inexpensive and non-toxic natural polymer (Ji et al., 2018). Lignin can be taken out from Sulfur processes (Sulfite process and Kraft process) in pulping industry (Cao et al., 2018). Lignosulfonate lignin and Kraft lignin are sulfur-containing lignins and thus they are not only low in reactivity but also tend to be corrosive to the equipment. Moreover, the presence of sulfur renders them hazardous for the environment. Sulfur free processes such as solvent pulping process and alkaline pulping process can be used to alter the chemical structure of isolated lignin polymers. Lignin can be extracted from numerous biomasses by using various treatment processes such as physical treatment (milling and grinding), chemical treatment (acid, alkali and organic solvents), physicochemical treatment (steam explosion, hydrothermolysis and wet oxidation) and biological treatment (enzymatic hydrolysis) or their combination. Organosolvents have been used to extract high quality and pure lignin but the yield of lignin was very low (D. Li et al., 2020). Alkali pretreatment have been used to separate lignin binding with hemicellulose and also to enhance the digestibility of hemicellulose. However, in the conventional method of NaOH pretreatment, half or more amount of the hemicellulose is dissolved in black liquor (Tsegaye et al., 2019). The present

[1] Lecturer, Department of Industrial Chemistry, West Yangon University.
[2] Professor and Head, Department of Industrial Chemistry, University of Yangon.
[3] Professor, Department of Industrial Chemistry, University of Yangon.

study was aimed to extract the lignin from sugarcane bagasse by the alkaline process and alcoholic alkaline process and to analyze the characteristics of prepared lignins.

Materials and Methods

Materials

Sugarcane Bagasses (*Saccharum officinarum*) were collected from Kyun-Lay Village, Kyaiklat Township, Ayeyarwady Region. Ethanol (99%), n-Hexane (95%), Sulphuric acid (98%) and Sodium hydroxide (Analar grade (B.D.H, England)) were purchased from Academy Chemical Shop, Pabedan Township, Yangon Region.

Methods

Analysis of Sugarcane Bagasse

Determination of Lignin Content

Lignin was determined according to ASTM D 1106-56 (1977). The dried sample 1 g was weighed and transferred to a beaker, then 10 mL of 72% sulphuric acid was added carefully and the mixture was stirred with a glass rod. The mixture was diluted with water until the final volume was 300 mL. The solution was refluxed at 100°C for 3 hr and then filtered with vacuum filter. The filter containing lignin residues was dried in an oven at 105°C for 12 hr, cooled in a desiccator for 15 min and then weighed accurately. The cycle of heating, cooling and weighing were repeated until a constant weight was obtained.

$$\text{Lignin content (\%)} = \frac{\text{Weight of lignin}}{\text{Weight of initial sample}} \times 100$$

Determination of Holocellulose Content

Holocellulose content was determined by using ASTM D 1104-56 (1978). Sample 2 g was dissolved into 150 mL of distilled water and the mixture was added into a 250 mL Erlenmeyer flask. $NaClO_2$ 1 g and 3 mL of 10% acetic acid were added while slowly shaking the flask. The flask was placed into a water bath and heated at 70 to 80°C for 30 min. Further addition of 1 g of $NaClO_2$ and 3 mL of 10% acetic acid were conducted until 4 g of $NaClO_2$ had been added into the mixture. Then the flask was further heated for 30 min. After cooling, the sample was filtered and washed with hot water until free of acid. Then the insoluble portion was dried in an oven at 105°C for 4 hr, placed in a desiccator and weighed. The cycle of heating, cooling and weighing were repeated until a constant weight was obtained.

$$\text{Holocellulose content (\%)} = \frac{\text{Weight of holocellulose}}{\text{Weight of initial sample}} \times 100$$

Determination of Alpha-cellulose Content

Alpha cellulose content was determined according to ASTM D 1103-60 (1978). Holocellulose 3 g was placed into a 250 mL Erlenmeyer flask. The sample was then treated with 50 mL of 17.5% NaOH for 30 min and then 50 mL of distilled water was added to it. The reaction was continued for 5 min. The contents were filtered by using vacuum filtration. The residue was washed first with 50 mL of 8.3% NaOH, then with 40 mL of 10% acetic acid and finally, with hot water. After that, the cellulose was dried in an oven at 103 ± 2°C, placed in a desiccator and weighed. The process of heating, cooling and weighing were repeated until a constant weight was obtained.

$$\text{Alpha cellulose content (\%)} = \frac{\text{Weight of alpha cellulose}}{\text{Weight of holocellulose}} \times 100$$

Determination of Hemicellulose Content

The hemicellulose content was obtained by subtracting the weight of alpha-cellulose content from that of holocellulose content (TAPPI 1999b).

Determination of Moisture Content

The moisture content of sugarcane bagasse was determined by AOAC method no. 942.05 (AOAC 2000). Sample 5 g was weighed accurately in a clean, dry and previously weighed dish. The sample was dried at 105ºC for 3 hr in a hot air oven. After drying, the sample was removed from the oven and placed in a desiccator for 30 min and weighed accurately. The cycle of heating, cooling and weighing were repeated until a constant weight was obtained. The percentage moisture content was obtained as follows:

$$\text{Moisture content (\%)} = \frac{\text{Initial weight of sample} - \text{Final weight of sample}}{\text{Initial weight of sample}} \times 100$$

Determination of Ash Content

The ash content of sugarcane bagasse was determined according to AOAC method no. 942.05 (AOAC 2000). Sample 5 g was weighed in a clean and previously weighed porcelain crucible and ignited in a muffle furnace at 600ºC for 4 hr. The crucible containing the ash was placed in a desiccator for 30 min and weighed. Heating, cooling and weighing were repeated until a constant weight was attained. The following formula was used to calculate the percentage of ash content.

$$\text{Ash content (\%)} = \frac{\text{Weight of ash}}{\text{Weight of sample}} \times 100$$

Extraction of Lignin from Sugarcane Bagasse

Bagasse powder (<0.42 mm in size) was pretreated with n-Hexane (95 %) in solid to liquid ratio of 1:16 g/mL at 70˚C for 6 hr in a Soxhlet extractor to remove the minor constituents (extractives) such as wax, tannin. Then the solid residues were dried in a hot air oven at 60˚C until a constant weight was obtained.

Pretreated solid residues 25 g were heated with 300 mL of hot distilled water at 120˚C for half an hour in a heating mantle and then filtered on filter cloth. In alkaline process, the solid residues were treated with 304 mL of 15% NaOH solution at 100°C for 2 hr in two neck flat-bottomed flask equipped with condenser and magnetic stirrer. In alcoholic alkaline process, the concentration of ethanol was kept constant at 64% to make the alcoholic NaOH solution. In this process, the solid residues were treated with 15% NaOH concentration, 303 mL of alcoholic NaOH at 100°C for 3 hr. After the reaction time, the mixture was filtered about three times under vacuum filtration. The lignin in the black filtrate was precipitated with 50% H_2SO_4 in order to adjust pH 2-3. Then the precipitated lignin was filtered through vacuum filtration and washed with hot distilled water to reach neutral pH (Runcang Sun et al., 1998). Then the lignin cake was dried in hot air oven at 60°C until a constant weight was obtained. In alcoholic alkaline process, ethanol was recovered from the black liquor by distillation.

Process Optimization by Response Surface Methodology (RSM)

Response Surface Methodology (RSM) was used to determine the optimum conditions of lignin extraction from bagasse by using two processes with the process independent variables such as concentration of solvents (%w/v), volume of solvents (mL) and extraction time (hr) as shown in Table (1). Box-Behnken Design was chosen by using the statistical software (Design Expert, version 11, Stat Ease Inc.,) and the 15 experimental runs were conducted as shown in Table (2).

Table 1 Variables in Experimental Design for Extraction of Lignin from Sugarcane Bagasse with Alkaline Process and Alcoholic Alkaline Process

Variables	Symbols	Levels			
		Alkaline Process		Alcoholic Alkaline Process	
		Lower	Upper	Lower	Upper
Concentration of solvent (w/v %)	X_1	10	20	10	20
Volume of solvent (mL)	X_2	200	400	200	400
Extraction Time (hr)	X_3	1	3	2	4

Table 2 Experimental Runs According to Box-Behnken Design for Lignin Extraction from Sugarcane Bagasse

Run Order	Alkaline Process			Alcoholic Alkaline Process		
	Concentration of NaOH (%w/v)	Volume of NaOH (mL)	Extraction Time (hr)	Concentration of NaOH (%w/v)	Volume of Alcoholic NaOH (mL)	Extraction Time (hr)
1	10	400	2	15	200	4
2	15	300	2	15	300	3
3	15	200	3	20	200	3
4	15	300	2	20	400	3
5	20	400	2	10	400	3
6	20	300	1	20	300	4
7	15	400	3	15	400	4
8	15	200	1	15	400	2
9	10	300	3	15	300	3
10	10	200	2	15	200	2
11	15	300	2	10	300	4
12	20	300	3	10	300	2
13	10	300	1	15	300	3
14	20	200	2	10	200	3
15	15	400	1	20	300	2

Characterization of Extracted Lignin

Physico-chemical properties (moisture content, ash content and melting point) of lignin were investigated. Moisture content and ash content were determined by using AOAC method no. 934.06 and 942.05 (AOAC 2000).

Determination of Melting Point

The melting points of isolated lignins were measured in open capillary tube by using Gallenkamp melting point apparatus. The melting point of lignin was determined at the Chemistry Department, West Yangon University.

UV-visible Analysis

The resultant lignin was identified in Shimadzu UV-visible Spectrophotometer (UV-1800) at the Customer Support and Laboratory, Amtt, Mayangone Township, Yangon Region.

Fourier-Transform Infrared (FTIR) Analysis

FTIR analysis was carried out to determine the functional groups of extracted lignin using IR-Tracer 100 S (SHIMADZU, Japan) at the Universities' Research Center, University of Yangon.

Results and Discussion

The chemical compositions such as lignin, alpha-cellulose, hemicellulose, moisture and ash of sugarcane bagasse are shown in Table (3). Lignin is the second most abundant constituent after cellulose in sugarcane bagasse. The compositions of bagasse can be different depending on its location, variety and agricultural practices (X. Li, 2004).

Table 3 Chemical Composition of Sugarcane Bagasse

Sr No.	Components	Composition (% w/w)
1.	Lignin	38.1 ± 0.2
2.	Alpha-cellulose	47.41 ± 0.67
3.	Hemicellulose	32.35 ± 0.68
4.	Moisture	2.39 ± 0.79
5.	Ash	2.33 ± 0.58

Table (4) shows experimental and predicted yield of lignin from bagasse by alkaline extraction process. It was found that the predicted values by statistical design software were in good agreement with the experimental values. Alkali can be used to enhance the digestibility of hemicellulose and to disrupt lignin binding with hemicellulose. The model regression equation giving lignin content as a function of alkali concentration, alkali volume and extraction time in alkaline process is shown in equation (1). This equation was solved by using MATLAB.

$$\text{Lignin Content (\% w/w)} = 35.24 + 5.84X_1 + 7.11X_2 + 6.39X_3 - 0.600X_1X_2 + 1.95X_1X_3 + 0.4475X_2X_3 - 6.69X_1^2 - 5.29X_2^2 - 6.39X_3^2 \quad \text{---------- eq (1)}$$

Table 4 Experimental and Predicted Yield of Lignin by Alkaline Process

Run Order	Experimental Factors			Response (lignin %)	
	X_1 (%w/v)	X_2 (mL)	X_3 (hr)	Experimental Values (Y) (% w/w)	Predicted Values (% w/w)
1	10	400	2	25.23	25.12
2	15	300	2	35.3	35.24
3	15	200	3	22.43	22.39
4	15	300	2	35.28	35.24
5	20	400	2	35.53	35.60
6	20	300	1	19.76	19.65
7	15	400	3	37.50	37.50
8	15	200	1	10.50	10.50
9	10	300	3	20.65	20.76
10	10	200	2	9.78	9.71
11	15	300	2	35.13	35.24
12	20	300	3	36.4	36.33
13	10	300	1	11.8	11.87
14	20	200	2	22.48	22.59
15	15	400	1	23.78	23.82

The effect of alkali concentration and volume on lignin content at a constant extraction time of 2 hr is presented in Figure (1, a). It was observed that increasing the concentration and volume of NaOH increased the lignin yield. The effect of alkali concentration and extraction time at constant alkali volume of 304 mL is shown in Figure (1, b). It can be seen that increasing the reaction time did not significantly increase the lignin yield; however, increasing the concentration of NaOH increased the lignin content. The interactive effect of volume of NaOH and extraction time on lignin content at constant alkali concentration of 15% is pointed out in Figure (1, c). This figure shows that the lignin content rises with an increase in volume of NaOH and extraction time.

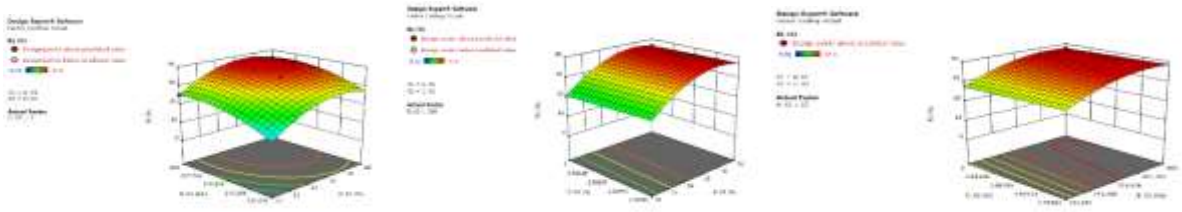

(a) (b) (c)

Figure 1 3D Surface Plot for Interaction of (a) Concentration and Volume of NaOH (b) Concentration of NaOH and Extraction Time (c) Volume of NaOH and Extraction Time in Lignin Extraction by Alkaline Process

Table (5) shows experimental and predicted yield of lignin from bagasse by alcoholic alkaline extraction process. It was observed that the values predicted by statistical design software were in agreement with the experimental values. A combination of alkali with ethanol treatments would liberate the recalcitrant structure of lignocelluloses, achieving a relatively high yield of lignin (RunCang Sun et al., 2002).

Table 5 Experimental and Predicted Yield of Lignin by Alcoholic Alkaline Process

Run Order	Experimental Factors			Response (lignin %)	
	X_1 (%w/v)	X_2 (mL)	X_3 (hr)	Experimental Values (Y) (% w/w)	Predicted Values (% w/w)
1	15	200	4	47.68	47.61
2	15	300	3	55.86	56.81
3	20	200	3	43.56	44.17
4	20	400	3	56.12	56.22
5	10	400	3	50.21	49.61
6	20	300	4	57.78	57.24
7	15	400	4	58.93	59.36
8	15	400	2	48.56	48.63
9	15	300	3	55.84	56.81
10	15	200	2	33.25	32.82
11	10	300	4	48.76	48.93
12	10	300	2	35.6	36.14
13	15	300	3	58.72	56.81
14	10	200	3	34.2	34.10
15	20	300	2	44.68	44.51

The model regression equation for lignin content as a function of alkali concentration, alcoholic alkaline volume and extraction time in alcoholic alkaline process is shown in equation (2).

$$\text{Lignin Content (\% w/w)} = 56.81 + 4.17X_1 + 6.89X_2 + 6.38X_3 - 0.8625X_1X_2 - 0.0150X_1X_3 - 1.02 X_2X_3 - 5.59X_1^2 - 5.19\ X_2^2 - 4.51X_3^2 \quad \text{-------- eq (2)}$$

The interactive effect of alkali concentration and volume of alcoholic alkaline on lignin content at a constant extraction time of 3 hr is shown in Figure (2, a). It was found that decreasing the concentration of NaOH and rising the volume of alcoholic NaOH increased the lignin yield. Figure (2, b) pointed out that the effect of alkali concentration and extraction time at constant alcoholic alkaline volume of 303 mL. It can be observed that increasing the extraction time improved the lignin content but rising the concentration of NaOH reduced the lignin content. The effect of volume of alcoholic NaOH and extraction time on lignin content at constant alkali concentration of 15% is presented in Figure (2, c). This figure shows that the lignin content rises with an increase in volume of alcoholic NaOH and extraction time.

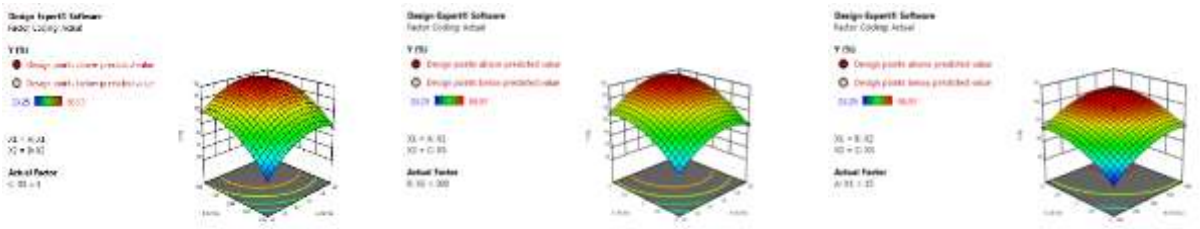

(a) (b) (c)

Figure 2 3D Surface Plot for Interaction of (a) Concentration of NaOH and Volume of Alcoholic NaOH (b) Concentration of NaOH and Extraction Time (c) Volume of Alcoholic NaOH and Extraction Time in Lignin Extraction by Alcoholic Alkaline Process

Table (6) shows the actual values and predicted values of lignin under optimum conditions. The optimum conditions in alkaline process were 304 mL of 15% of NaOH and 2 hr extraction time to obtain 35.62% of lignin and that in alcoholic alkaline process were 303 mL of 15% of NaOH and 3 hr extraction time to achieve 57.19% of lignin. The optimum conditions under predicted values were validated by repeating the experiments about 3 times. As can be seen in the Table (6), lignin contents are (37.13±0.34 (% w/w)) for alkaline process and (56.75±0.03 (% w/w)) for alcoholic alkaline process. It was indicated that alcoholic alkaline process has a positive effect on lignin yield.

Table 6 Actual Values and Predicted Values of Lignin under Optimum Conditions

Sr No.	Extraction Process	Concentration (%)	Volume (mL)	Reaction Time (hr)	Predicted Value (% w/w)	Actual Value (% w/w)
1.	Alkaline	15	304	2	35.62	37.13±0.34
2.	Alcoholic Alkaline	15	303	3	57.19	56.75±0.03

The physico-chemical characteristics of lignin such as moisture, ash and melting point are shown in Table (7). According to the results, the moisture content and melting point of lignin extracted by alkaline process were higher than that of lignin extracted by alcoholic alkaline process. Most of the extracted lignin did not provide sharp melting point and the melting point depends on the extraction process and molecular weight of lignin. The ash content of lignin from alkaline process was lower than that from alcoholic alkaline process. The ash content of lignin sample depends on the biomass type and extraction process (Chen et al., 2013).

Table 7 Physico-chemical Characteristics of Lignin

Sr No.	Extraction Process	Moisture (% w/w)	Ash (% w/w)	Melting Point (°C)
1.	Alkaline	2.39 ± 0.79	1.24 ± 0.11	263-269
2.	Alcoholic Alkaline	3.07 ± 0.15	1.07 ± 0.04	200-206

During alkaline and alcoholic alkaline treatments, holocellulose was broken down and the lignin was separated. Figures 3 (a) shows UV-spectrum of lignin extracted from bagasse by alkaline process. It was found that the phenolic hydroxyl group contributes to the absorption band of lignin at 282 nm in alkaline process. Figure 3 (b) points out UV-spectrum of lignin extracted from bagasse by alcoholic alkaline process. It can be seen that the hydroxyl group gives the absorption band of lignin at 238 nm and also phenolic hydroxyl group supplies the wavelength of lignin at 288 nm in alcoholic alkaline process. The characteristic absorption minimum of lignin provides the etherified hydroxyl groups near 280 nm. The absorption peaks within the range from 277 to 282 nm supply the unconjugated quaiacyl and 3,4-dimethoxy-phenyl model compounds (Jablonský et al., 2015).

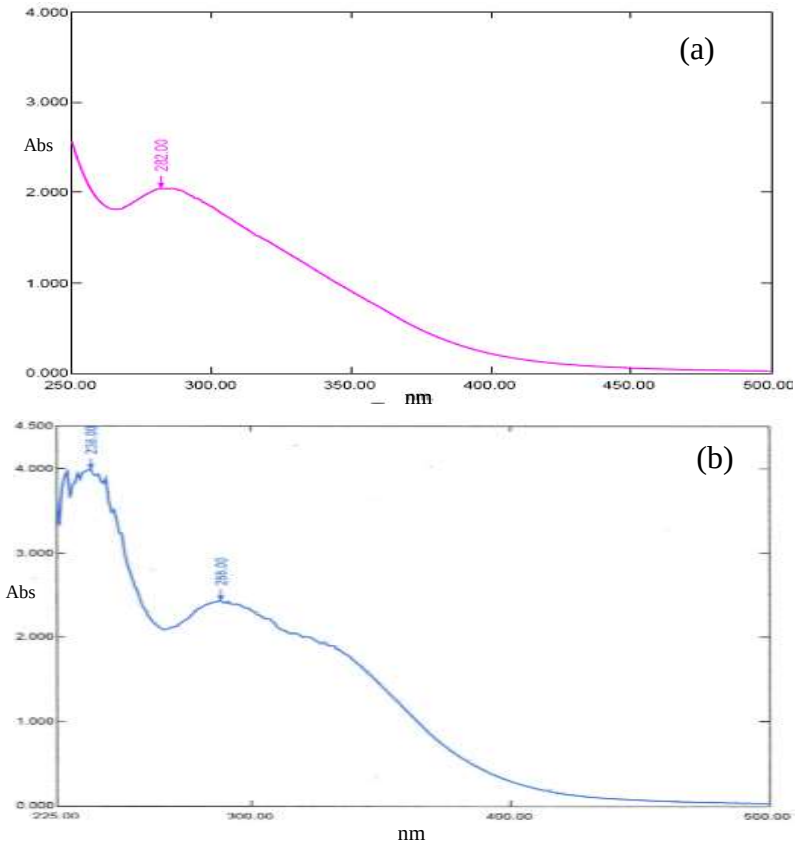

Figure 3 UV-Spectrum of Lignin Extracted by (a) Alkaline Process and (b) Alcoholic Alkaline Process

Figure 4 (a) and (b) represent the FTIR spectra of lignin extracted from bagasse by alkaline process and alcoholic alkaline process. The absorption peaks of both lignins at (3855 cm^{-1}) belonged to the stretching vibration of hydrogen bonded OH group in alcohol. A wide absorption bands at 3375 cm^{-1} for alkaline process and 3381 cm^{-1} for alcoholic alkaline process are assigned to hydroxyl groups in phenolic and aliphatic structures. The absorption peaks at (2939 and 2908 cm^{-1}) in two processes predominantly arise from CH stretching in aromatic methoxy group and in methyl and methylene groups of side chains. The bands (2337, 2110,1950 cm^{-1}) in alkaline process and 2386 cm^{-1} in alcoholic alkaline process arise C-H-stretching in the lignin molecules. The bands at (1710 cm^{-1}) was observed in alcoholic alkaline process but it was absent in alkaline process. In the carbonyl/carboxyl region, weak medium bands were found at 1705–1720 cm^{-1} that indicates the stretching of C=O group in these lignin (Boeriu et al., 2004). The weak absorption peak at 1699 cm^{-1} in alkaline process resulting in the asymmetry and broadening of the more intense bands may originate from both protein impurity and water associated with lignin. This peak was not observed in alcoholic alkaline process which indicated that lignin extracted by this process has no impurity. The bands at (1599, 1514, 1512, 1462, 1425 cm^{-1}) are assigned to C–H deformation combined with aromatic ring vibration. The bands at (1329 cm^{-1} in alkaline process and 1327 cm^{-1} in alcoholic alkaline process) belong to O-H stretching vibrations in alcohol and phenol. Spectra of hardwood and all non-wood lignins show a band at 1326 cm^{-1}, which is characteristic for syringyl (S) ring plus guaiacyl (G) ring. The bands at (1041, 993, 987, 895,835, 638 cm^{-1}) to COC group out of plane deformation (trans) which further indicated that the lignin with conjugated units was isolated by aqueous alkaline solution (Boeriu et al., 2004). From the analysis of IR-spectra of lignin, it may be inferred that lignins consist of ionizable groups (carboxylic acid and phenol groups) and polar functional groups (hydroxyl, carbonyl and methoxy group) abundantly.

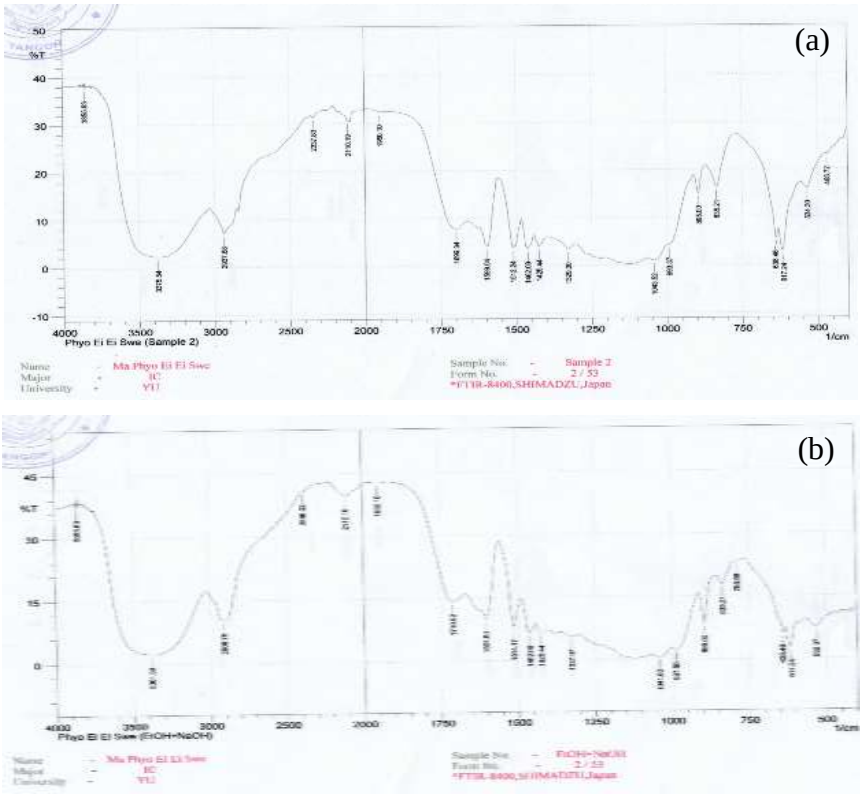

Figure 4 FT-IR Spectrum of Lignin Extracted by (a) Alkaline Process (b) Alcoholic Alkaline Process

Conclusion

In this research work, lignin was extracted from sugarcane bagasse by using alkaline process and alcoholic alkaline process. Box-Behnken Design was used to obtain the optimum conditions of lignin extraction by two processes. From the economical point of view, alcoholic alkaline extraction process was found to be the most suitable process because of the maximum yield of lignin and also ethanol can be recovered from black liquor by distillation. The analysis of UV and FT-IR spectra of lignin indicated that lignins extracted by both processes consisted of ionizable groups (carboxylic acid and phenyl) and polar functional groups (hydroxyl and methoxy). The lignin in alcoholic alkaline process also contains C=O stretching vibration of unconjugated ketone, carbonyl and ester at the wave number around 1710 cm^{-1}. Moreover, the band around 1699cm^{-1} indicating the presence of a small amount of impurities was not found in lignin from alcoholic alkaline process but this peak was observed in lignin from alkaline process.

Acknowledgements

I would like to express my greatest appreciation to the Myanmar Academy of Arts and Science for allowing me to summit this paper.

References

AOAC, (2000). Official Methods of Analysis, Association of Official Analytical Chemists, 17th ed., Washington D.C., USA.

Behera, S., Arora, R., Nandhagopal, N., & Kumar, S. (2014). Importance of chemical pretreatment for bioconversion of lignocellulosic biomass. *Renewable and Sustainable Energy Reviews*, 36, 91–106.

Boeriu, C. G., Bravo, D., Gosselink, R. J., & van Dam, J. E. (2004). Characterisation of structure-dependent functional properties of lignin with infrared spectroscopy. *Industrial Crops and Products*, 20(2), 205–218.

Cao, L., Iris, K. M., Liu, Y., Ruan, X., Tsang, D. C., Hunt, A. J., Ok, Y. S., Song, H., & Zhang, S. (2018). Lignin valorization for the production of renewable chemicals: State-of-the-art review and future prospects. *Bioresource Technology*, 269, 465–475.

Cesarino, I., Araujo, P., Domingues Júnior, A. P., & Mazzafera, P. (2012). An overview of lignin metabolism and its effect on biomass recalcitrance. *Brazilian Journal of Botany*, 35(4), 303–311.

Chen, F., Zhou, W., Yao, H., Fan, P., Yang, J., Fei, Z., & Zhong, M. (2013). Self-assembly of NiO nanoparticles in lignin-derived mesoporous carbons for supercapacitor applications. *Green Chemistry*, 15(11), 3057–3063.

Jablonsky, M., Kocis, J., Haz, A., & Sima, J. (2015). Characterization and comparison by UV spectroscopy of precipitated lignins and commercial lignosulfonates. *Cellulose Chemistry and Technology*, 49(3–4), 267–274.

Ji, X., Dong, Y., Nguyen, T. T., Chen, X., & Guo, M. (2018). Environment-friendly wood fibre composite with high bonding strength and water resistance. *Royal Society Open Science*, 5(4): 172002.

Li, D., Long, L., & Ding, S. (2020). Alkaline organosolv pretreatment of different sorghum stem parts for enhancing the total reducing sugar yields and p-coumaric acid release. *Biotechnology for Biofuels*, 13(1), 1–14.

Li, X. (2004). Physical, chemical, and mechanical properties of bamboo and its utilization potential for fiberboard manufacturing. *LSU Master's Theses*, 866.

Sun, R., Fang, J., & Rowlands, P. (1998). Physico-chemical and thermal characterization of alkali-soluble lignins from wheat straw. *Polymer Journal*, 30(4), 289–294.

Sun, R., Wang, S. Q., Zhu, W., & Wang, X. Y. (2002). Ester and ether linkages between hydroxycinnamic acids and lignins from wheat, rice, rye, and barley straws, maize stems, and fast-growing poplar wood. *Industrial Crops and Products*, 15(3), 179–188.

Tsegaye, B., Balomajumder, C., & Roy, P. (2019). Alkali pretreatment of wheat straw followed by microbial hydrolysis for bioethanol production. *Environmental Technology*, 40(9), 1203–1211.

PREPARATION OF NATURAL DYE POWDER EXTRACT FROM MANGO (NETTE) BARK AND APPLICATION ON COTTON FABRIC

Sandar Win[1], Khin Thet Ni[2]

Abstract

This research concerns with the preparation of natural dye powder extract from *Mangifera indica* L. (Mango) bark. Natural dye solution was extracted from mango bark by using water, alkaline, acidic and alcoholic medium. The resultant concentrated dye solutions were dried in an oven at 60°C. Alcoholic medium was selected based on the yield percent and absorbance value and the dye powder was prepared at the various ethanol-water ratio, solid to liquid ratio, extraction temperature and time. The chemical compounds present in dye powder were studied by phytochemical methods and the functional groups were identified by FT-IR spectroscopy. Furthermore, content of moisture, ash and heavy metals in natural dye powder were also determined. The dye powder was then applied on cotton fabrics by using mordant with pre-mordanting, post-mordanting and simultaneous mordanting and dyeing methods. Fastness tests especially for washing, rubbing and light on dyed cotton fabrics were also studied.

Keywords: mango bark, extraction, natural dye powder, dyeing, mordant, fastness

Introduction

Natural dyes are basically elements of natural resources, and these dyes are generally classified as plant, animal, mineral, and microbial dyes based on their source of origin, colour, application and chemical nature. Natural dyes can reduce environmental pollution and they are renewable and biodegradable. The experience with natural dyeing has given an understanding of plants to find in the neighborhood. Finding textiles colors in plants that grow easily and fast has lead into a new colors that give unusual and interesting shades. These natural colors have luxuriance and luster that synthetics can never achieve. It has become a common exception that natural dyes only produce beiges and browns and colour ranging from yellow to black. In reality, vibrant, fast natural colors can be produced, which are comparable with and often surpass the colors of synthetics(Padma Shree Vankar, 2017).

Natural dyes are either substantive, meaning that which do not require a mordant, or adjective, they require a mordant. Adjective dyes are mordanted with a metallic salt or with the addition tannin tannic acid to the dye bath. Examples of such dyes are logwood, madder, cochineal, cutch and lac. In their refined state, adjective dyes are generally only slightly coloured and produce poor shades when used alone.

Mordants (from Latin mordere, 'to bite', because the mordant consume away the surface of the fibre so that the dye can seep in) are chemicals in the form of metallic salts which are generally used to make an affinity between the fibre and the dye.

The main objective of the mordant when used with adjective dyes is to open up the pores so that the dye can penetrate the fibres, thereby supporting in the fixation of the dyestuffs on the substrate. However, mordants can also be used with dyes which may be applied directly to the fiber. In this case their function is to form an insoluble compound with the dyestuff within th fibre itself, thereby improving the fastness properties of the dyed material (Patel, 2011).

The bark of the mango tree contains tannin (16-20%) and may be used for tanning purposes; it contains resinous matter. The bark yields a colouring matter which produces beautiful, through light, yellow shades on cotton, silk and wool; in conjuction with tumeric and lime, the bark dyes

[1] Dr, Lecturer, Department of Industrial Chemistry, Dagon University

[2.] Dr, Professor and Head (Retired)Department of Industrial Chemistry, University of Yangon

cotton a bright rose-pink. Mangiferine has been isolated from the bark (The Wealth of India,1985).

Thus, the objectives of this study are to prepare natural dye powder extract from mango bark, to determine the optimum conditions for the extraction of natural dye powder, to prepare dye powder with low cost and high yield, to study the colour developed on cotton fabric dyed with extracted dye powder.

Materials and Methods

Materials

Mango bark (Nette) was collected from selected old trees in Amarapura Township, Mandalay Region. For solvent extraction, 95% ethanol was used to extract natural dye solution from mango bark.

Methods

Before extraction of natural dyestuff, the bark were rinsed with water and dried at room temperature. After cleaning and drying, the samples were powdered by grinder. These powder samples were screened by passing through mesh no-42 screen and stored in plastic bags for further works.

Preparation of Natural Dye Powder Extract from Mango (Nette) Bark Using Different Media

Natural dye was extracted as liquid form from mango bark powder (-42 mesh) by using different media such as pure water , 1% acetic acid, 50% ethanol and 0.5% sodium carbonate solution (Excutive summary,2010).

Mango bark powder 10 g was placed in a 3-neck round-bottomed flask. 100 ml of pure water was added into the flask (solid to liquid ratio 1:10) and the flask was kept for 5 hours. The flask was heated by a water bath at 60˚C. The extraction time was kept for 1 hour. Then the extracted dye solution was concentrated and dried at 60˚C for 6 hours in an oven.

Similar experiments were carried out using different media as described above. The absorbance value of dye powder extract was studied by UV/VIS spectrometer. Among the different media, alcoholic medium was selected as the most suitable medium due to its yield percent and absorbance value. Yield percent of natural dye powder extract was calculated based on weight of mango bark powder.

Determination of Optimum Conditions for Preparation of Natural Dye Powder Extract from Mango Bark

The optimum conditions for the preparation of natural dye powder extract was studied by varying the ethanol and water ratio in the range of (50:50, 40:60, 30:70, 20:80) and solid to liquid ratio (10:100 to 10:250) while the other variables like weight of bark, extraction temperature and extraction time as described were fixed.

The effect of temperature on the dye extraction was studied by varying the extraction temperature in the range of (60, 70, 80, 90˚C) and the effect of extraction time in the range of (1, 2 , 3 and 4) hours were also studied.

Phytochemical Investigation of Natural Dye Powder Extract

Phytochemical tests were carried out to study the main compounds which are present or absent in samples. Test for alkaloids, polyphenol, flavonoids, glycosides, phenolics, sugars, saponins, lipophilics, proteins and tannin were performed according to the procedures prescribed in the Text Book of "A Guide to Modern Techniques of Plant Analysis''.

Physico-chemical Characterization of Natural Dye Powder Extract from Mango Bark

The physico-chemical properties of natural dye powder extract from mango bark such as content of moisture, ash and heavy metals in natural dye powder were also determined. The heavy metal contents (As, Pb and Cd) were determined by using Atomic Absorption Spectrophotometer (AAS, Model No. AA-6200).

Dyeing Process of Cotton Fabrics

Mercerization

Firstly, 5 g of caustic soda were dissolved in 2 L of warm water before adding to the cotton fabrics. To prepare mercerized cotton fabrics, 1 yard of cotton fabric was simmered in caustic soda solution for 60 min and rinsed with water. After the finishing of this step, cotton fabric was put into vinegar solution (4ml acetic acid in 1L of water) for 30 min to neutralize it. To prepare clean cotton fabric, neutralized fabric was rinsed with water and then dried at room temperature. After that, it was tested with a few drops of iodine. If purple black colour did not appear, the fabrics had been mercerized.

Mordanting

In this method, mordant solution was prepared by heating 0.05 g copper (II) sulphate with 200 ml water to obtain a volume of material to liquor ratio of 10:200. This mordant solution was heated at 80˚C and cleaned fabric (10" × 10") was simmered in this solution for about 45 minutes. During mordanting , the fabric was frequently stirred to obtain good penetration of mordants into the fabric. After that, the mordanted fabric was rinsed with water.

Dyeing

For dyeing of mercerized cotton fabric, 3 g of extracted natural dye powder and 200 ml of water was heated at 80°C and mercerized cotton fabric was simmered in this solution for 30 minutes. Then the fabric was rinsed with water and allowed to air drying. In this research, pre-mordanting method, post-mordanting method and simultaneous mordanting and dyeing method were used. In pre-mordanting method, mordanting was done before dyeing and in post-mordanting method, mordanting was done after dyeing. In simultaneous mordanting and dyeing method, mordant, dye powder and cotton fabric were added in a pot and treated together.

Testing the Colour Fastness of Dyed Fabrics

After dyeing, testing the colour fastness of dyed fabrics was carried out. In the dyeing process, fastness of textile substrates such as washing, rubbing and light were determined.

Washing Fastness

Launder Meter washing machine, Model L-4 (containing 4-rack testing bottle) washing machine was used and Test No.3 of ISO 105 was used to assess the colour fastness to

washing. 2 g/litre of soap solution was added to the jar (material to liquor ratio of 1:50) and the soap solution was preheated at 60˚C. Then the composite sample was placed in the jar and treated at 60˚C for 30 minutes. After washing, the specimen was rinsed with water for 3 times and dried at room temperature.

Rubbing Fastness

The rubbing fastness of dyed fabric was determined by a Crock Meter, JIS.L 0823 / 0849 with a rubbing finger, comprising a cylinder of 1.6 cm diameter moving to and fro along a straight line of 10 cm track on the specimen with a load of 900 g was used.

Light Fastness

The cabinet consists of a glass-covered enclosure of wood was used for light fastness test to protect the specimens from rain and weather. The dyed fabrics measuring (2 in × 1.5 in) of the material to be tested were cut out. These specimens were placed on the rack and the cabinet was covered. Then the specimens were exposed on sunny days between 9 a.m. to 3 p.m. for 7 days. The change in colour is assessed by comparing with the original dyed fabrics.

Results and Discussion

The effect of extraction medium on yield percent of natural dye powder extract was studied by using different polarity solvent (water, acetic, ethanol) and nonpolar solution (sodium carbonate). The results are shown in Table 1. Ethanol was chosen because alcohol group has high polarity than most non-polar but lower polar than water [9]. From the research, it was observed that alcoholic medium was suitable because it gave the maximum yield percent of dye powder and the results are shown in Table(1).

Table 1 Effect of Extraction Medium on the Yield Percent of Natural Dye Powder Extract using Different Media

Weight of mango bark powder = 10 g

Sr. No.	Extraction Medium*	Solid-Liquid Ratio	Extraction Condition		NDPE (g)	Yield (%)
			Temp (˚C)	Time (hr.)		
1	Water	1:10	60	1	1.4	14
2	1% Acetic acid	1:10	60	1	1.4	14
3	50% Ethanol**	1:10	60	1	2.0	20
4	0.5% Sodium carbonate solution	1:10	60	1	1.7	17

Note: NDPE = Natural dye powder extract, * (Excutive summary,2010) ** Suitable condition

According to the Beer-lambert law, absorbance value is directly proportational to concentration of dye solution and the alcoholic medium was selected because of the maximum absorbance value of 1.3. The results are shown in Table (2). Based on these results, acetic acid showed the lowest absorbance in most of stated concentration. The second lowest absorbance of overall result is water extract which has the slightest increment of absorbance compare with acetic acid. Ethanol is a polar solvent which can attract all kinds of active substances such as antioxidant, as well as good absorbance and low reactive toxicity [9].

Table 2 Absorbance Values of Natural Dye Powder Extract using Different Media

Sr.No.	Extraction Medium	Pigment*	Wavelength λ_{max} (nm)		Absorbance Values
			NDPE	Literature**	
1	Water	Mangiferin	260	258	0.6
2	1% Acetic acid	Mangiferin	259	258	0.5
3	50% Ethanol	Mangiferin	260	258	1.3
4	0.5% Sodium carbonate solution	Mangiferin	263	258	0.9

Note: NDPE = Natural dye powder extract

* and * * = Harbone, A Guide to Modern Technique of Plant Analysis.

The effect of ethanol- water ratio and solid to liquid ratio on the yield of dye powder are shown in Tables (3) and (4). According to the results in Table (3), it was clearly seen that ethanol:water ratio of 30:70 gave highest yield percent of dye powder.

Table 3 Effect of Ethanol-Water Ratio on the Yield Percent of Natural Dye Powder Extract

Weight of mango bark powder = 10 g
Soaking time = 5 hr.

Sr. No.	Solvent Ratio (ml)		Solid-Liquid Ratio	Extraction Condition		NDPE (g)	Yield (%w/w)
	Ethanol	Water		Temp. (˚C)	Time (hr.)		
1	50	50	1:10	60	1	2	20
2	40	60	1:10	60	1	1.7	17
3*	30	70	1:10	60	1	2.1	21
4	20	80	1:10	60	1	1.8	18

Note: NDPE = Natural dye powder extract * Suitable condition

The data in Table (4) indicates that yield percent of dye powder increases with increase in solid to liquid ratio from 10:100 to 10:200 but decreases at 10:250. From the results, solid to liquid ratio of 10:200 gives the maximum yield percent of dye powder.

Table 4 Effect of Solid to Liquid Ratio on the Yield Percent of Natural Dye Powder Extract

Weight of mango bark powder = 10 g , Soaking time = 5 hr.
Ethanol : Water = 30 : 70

Sr. No.	Solid to Liquid Ratio	Soaking Time (hr)	Extraction Condition		NDPE (g)	Yield (%w/w)
	MBP : Liquid (g) : (ml)		Temp. (˚C)	Time (hr.)		
1	10:100	5	60	1	2.1	21
2	10:150	5	60	1	2.5	25
3	10:200*	5	60	1	3.0	30
4	10:250	5	60	1	1.9	19

Note: MBP = Mango bark powder NDPE = Natural dye powder extract * Suitable condition

Table (5) tabulates the results of the effect of extraction temperature on the yield of dye powder. It was found that extraction temperature 80ºC was found to be the most favourable condition with respect to yield percent.

Table 5 Effect of Temperature on the Yield Percent of Natural Dye Powder Extract

Weight of mango bark powder = 10 g ,
Solid to liquid ratio = 10:200 , Ethanol and water ratio = 30:70

Sr. No.	Extraction Temp. (˚C)	Soaking Time (hr.)	Extraction Time (hr.)	NDPE (g)	Yield (%w/w)
1	60	5	1	2.2	30
2	70	5	1	2	29
3	80*	5	1	2.5	32
4	90	5	1	2.1	31

Note: NDPE = Natural dye powder extract *Suitable condition

According to the results of Table (6), maximum yield percent of dye powder is observed with 1 hour extraction time but after that decrease in yield of dye powder is observed.

Table 6 Effect of Extraction Time on the Yield Percent of Dye Powder Extract

Weight of mango bark powder = 10 g ,
Solid to liquid ratio = 10:200 , Ethanol and water ratio = 30:70

Sr. No.	**Extraction Time (hr.)**	**Soaking Time (hr.)**	**Extraction Temp. (˚C)**	**NDPE (g)**	**Yield (%w/w)**
1	1*	5	80	2.5	32
2	2	5	80	2	30
3	3	5	80	2.3	23
4	4	5	80	2.2	22

Note: NDPE = Natural dye powder extract *Suitable condition

From the results of Tables (3) to (6), the maximum yield percent of dye powder was obtained by using ethanol:water ratio of 30:70, solid to liquid ratio of 10:200 and extraction temperature and time were 80˚C and 1 hour.

From the results of phytochemical investigations shown in Table (7), it can be seen that extracted dye powder contains alkaloids, polyphenols, flavonoids, glycosides, phenolics, saponins, lipophilics and tannins.

Table 7 Phytochemical Characteristics of Natural Dye Powder Extract from Mango Bark

Sr. No.	Test	Extract	Reagents	Observation	Inference
1	Alkaloids	1% HCl	(i) Dragendroff's reagent (ii) Mayer's reagent	(i)Orange ppt (ii)Cream ppt	+ +
2	Polyphenols	EtOH	1%$FeCl_3$ + 1%$K_3[Fe(CN)_6]$	Green-blue colour	+
3	Flavonoids	EtOH Benzene	HCl (conc:) + Mg turnings 10% $FeCl_3$	Pink colour Greenish blue colour	+ +
4	Glycosides	H_2O	10% $FeCl_3$	Purple colour	+
5	Phenolics	H_2O	10% $FeCl_3$	Purple colour	+
6	Sugars	H_2O	Benedict's solution	Red ppt	_
7	Saponins	H_2O EtOH	$NaHCO_3$ H_2SO_4 (conc:)	Froth Red colour	+ +
8	Lipophilics	H_2O	0.5 N KOH	Deep colour	+
9	Proteins	H_2O	10% NaOH + 3% $CaSO_4$	Red	_
10	Tannin	H_2O	2% NaCl, 1% $FeCl_3$	Deep blue ppt	+

Note : + = Present - = Absent

Heavy metals are found everywhere in the environment and enters through human activities, mining, power generation, leaded gasoline. Humans risk to exposure from environmental concentrations that occur naturally or human activities. [10] The results in Table (8) indicate that 8.51% w/w moisture content, 7.99 % w/w ash content and heavy metals (0.09 ppm of As, 0.27 ppm of Pb, 0.13 ppm of Cd) were observed in natural dye powder extract. The standard permissible limits of heavy metals by WHO and FDA are 3 ppm of As, 1ppm of Pb and 1 ppm of Cd. From the results, the level of arsenic, lead and cadmium were found to be below the WHO and FDA maximum permissible limits.

Table 8 Physico-Chemical properties of Natural Dye Powder Extract from MangoBark

Sr. No.	Parameter	Contents	Literature*
1	Moisture (%w/w)	8.51	-
2	Ash (%w/w)	7.99	-
3	Arsenic (As) (ppm)	0.09	3
4	Lead (Pb) (ppm)	0.27	1
5	Cadmium (Cd) (ppm)	0.13	1

* (Lakshmi. T,2015)

Mango bark contain very high levels of phenolic compounds, mainly mangiferin and protocatechic acid, catechin, mangiferin, alanine, glycine, γ-amino-butyric acid, kinic acid, shikimic acid, etc were present. Figure (1) shows the FT-IR Spectra of natural dye powder extract. An occurrence of a strong band at 3342 cm^{-1} confirmed –OH stretching frequency of alcohol or phenol group. The C=C stretching vibrations at 1616 cm^{-1} confirmed the presence of aromatic or phenol groups. The band at 1452 cm^{-1} confirmed the C-H in-plane bending vibration. C-H in plane bending vibration of aromatic compounds were found at 1369 cm^{-1} and 1286 cm^{-1}. The band at 1200-1000 cm^{-1} was attributed to C-O stretching vibration. Another characteristics peak occurred at less than 1000 cm^{-1} were characteristics of C-H bending

vibrations. According to FT-IR analysis the colour compounds such as, polyphenols, flavonoids, phenolic, glycosides and tannin were present in dye powder.

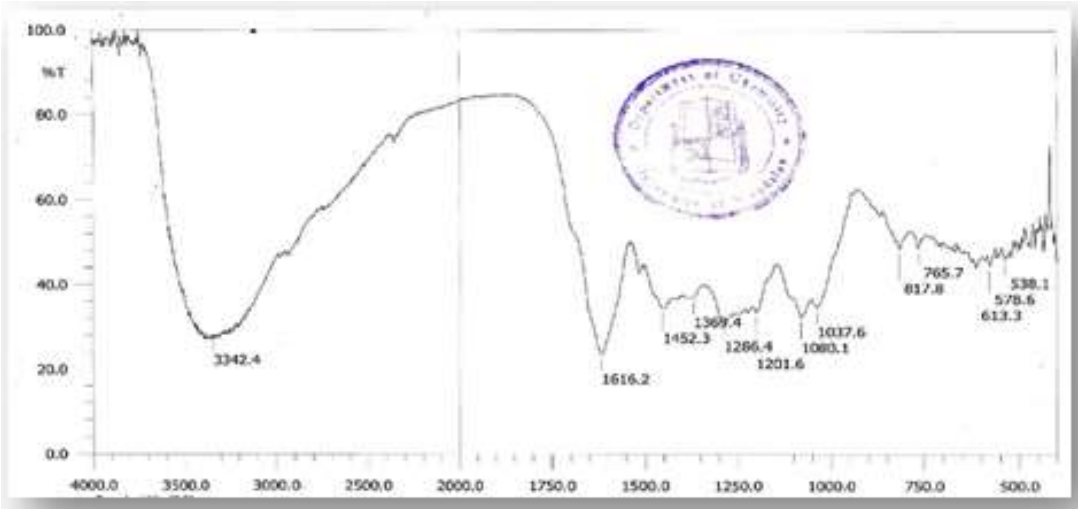

Figure 1 FT-IR Spectrum of Natural Dye Powder Extract

The data in Table (9) indicates that post-mordanting method with $CuSO_4$ mordant was found to be the most suitable condition due to its washing fastness grade of 4-5 (Good-Excellent). From the light fastness of dyed cotton fabrics, a slight change in colour was observed in different dyeing methods.

Table 9 Colour Fastness of Dyed Cotton fabrics Mordanted with $CuSO_4$

Cotton Fabric = 10 g (10" – 10") Dyeing temperature and time = 80˚C,30min
Mordanting temperature and time = 80˚C ,45 min. Volume of mordant solution = 200 ml
Volume of 1.5 % w/v of dye solution = 200 ml

Sr. No.	Method	$CuSO_4$ % (w/v)	Washing Test (60˚C , 30 min)		Rubbing Test 900g , 10 times		Light Test (7 days)
			Change of shade	Staining on Cotton	Dry	Wet	
1	Pre-mordanting	0.05	2-3	4	4-5	3-4	4
2	Post-mordanting*	0.05	4-5	4-5	4-5	4	4
3	Simultaneous mordanting and dyeing	0.05	2-3	4	4-5	3-4	4

Notes : * Suitable method
Fastness rating 1 = Very poor, 2=Poor, 3=Fair, 4=Good, 5=Excellent (Lyle, 1977

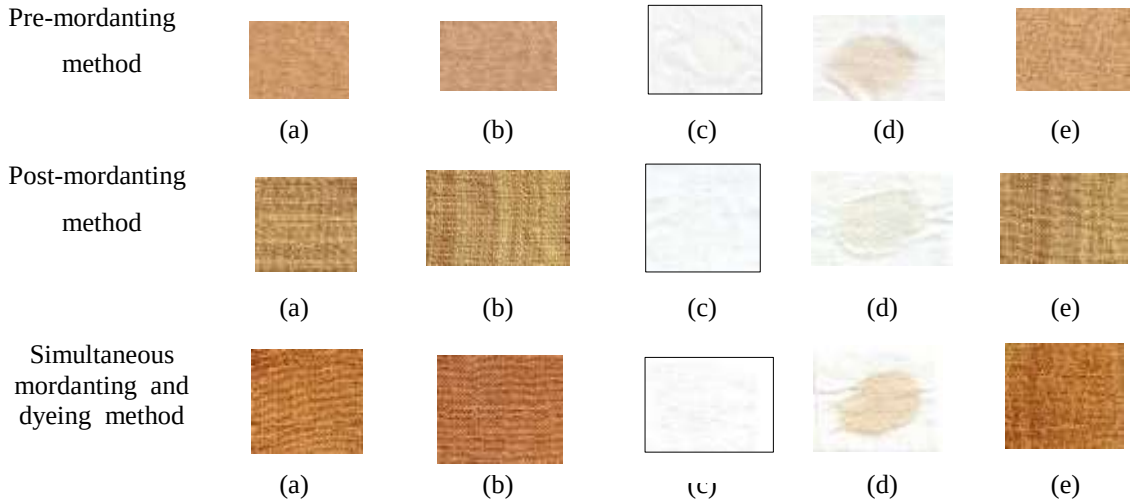

Figure 2 Color Fastness of Cotton Fabrics Dyeing with Natural Dye Powder Extract
(a) Original Sample (b)Washing Fastness (c) Dry Rubbing Test
(d) Wet Rubbing Test (e) Light Test

Conclusion

Natural dye powder was prepared from mango bark using water, alcoholic, acidic and alkaline method. Among the four medium alcoholic medium is the best because it gives the maximum yield percent and maximum absorbance value. For the preparation of natural dye powder from mango bark, the most suitable extraction conditions are mango bark powder to water ratio (1:20), ethanol-water ratio (3:7) and extraction temperature and time were 80˚C and 1 hour. According to the results obtained from phytochemical test and FT-IR analysis, it was found that the colour compounds such as alkaloids, polyphenols, flavonoids, glycosides, phenolics, saponins, lipophilics and tannins were present in dye powder. From the analysis of natural dye powder extract by AAS standard method, it can be seen that the presence of toxic heavy metals are below the WHO and FDA maximum permissible limits. It was evident that good fastness results were found in fabric dyed by post- mordanting method with copper (II) sulphate mordant due to its washing fastness grade of 4-5 (Good- Excellent). Moreover, variations in color shade were found when three mordanting methods were compared. As a result, good light fastness can be observed in all cotton fabrics dyed with all dyeing methods.

Acknowledgements

The author would like to express deepest gratitude to Myanmar Academy of Arts and Science for allowing to present this paper.

References

Bechtold. T. and Mussak. R. (2009). Hand book of natural colorants, John Wiley& Sons Ltd, United Kingdom.

Excutive summary. (2010, May 3). Retrieved from htpp://www.dsir.gov.in / reports/tmreps/vegdye.pdf.

Harbone, J.B. (1984). Phytochemical methods, 2nd Edition, Ruhard Clay Ltd., Great Britain.

Handayani I. S. V. and Waris R. (2018). Identification and antioxidant activity of alamanda leaf (Allamanda Cathartica L.) Based On Solvent Pro. of ISER 125th Int. Conf. of Malacca, Malaysia, 3rd – 4th May.

Lakshmi.T., Rajendran. R. and Ezhilarasan. D.(2015). Atomic absorption spectrophotometric analysis of heavy metals in acacia catechu willd. *International Journal of Pharmacognosy and Phytochemical Research*, 7(4), 777-781., Retrieved from htpps://www.researchgate.net.

Lyle and Siegert. D. (1977). Performance of textile, United States of America.

Moeyes. M. (1993). Natural dyeing in Thailand, White Lotus Co., Ltd, Bangkok.

Moore, J.A. and Dalrymple, D.L. (1976). Experimental methods in organic chemistry. 2nd.Edition., Saunders Company, London.

Patel, B. H. (2011). Handbook of textile and industrial dyeing, vol 1, UK, Woodhead Publishing Limited, pp. 412.

The Wealth of India. (1985). A dictionary of indian raw materials and products council of scientific and industrial research, New Delhi.

Vankar. P. S. (2017). Natural dyes for textiles.Woodhead Publishing.

WHO. (2001) Arsenic and arsenic compounds.environmental health criteria, Geneva: World Health Organization. P. 224.

APPLICATION OF WATER QUALITY INDEX (WQI) METHOD TO ASSESS THE WATER QUALITY OF DALA TOWNSHIP, YANGON REGION, MYANMAR

Theint Theint Nway[1], Seinn Lei Aye[2] and Min Myint[3]

Abstract

Nowadays, water quality issues have become a significant concern due to the growth of population, urban expansion and technological development. The current study is conducted to investigate the water quality status of Dala Township, using the Water Quality Index (WQI) method. The WQI was used to aggregate the diverse parameters into a single term that is helpful for the selection of appropriate treatment technique to meet the drinking water standard. In this study, the WQI of ground and surface water samples were evaluated by analyzing the various parameters such as pH, total hardness, total dissolved solid, conductivity, chloride, nitrate, sulphate, calcium, dissolved oxygen and biological oxygen demand. The WQI values for all the samples were found in the range of 51 - 78. The highest value of WQI was observed in the river water sample and the lowest WQI value was observed in ground water sample. Results of the assessment confirmed that the WQI values of all the water sources are high and they are not suitable for direct consumption.

Keywords: Water Quality Index (WQI), drinking water standard, parameters

Introduction

Unsafe drinking water is one of the main problems in developing countries. Scarcity of clean and potable water often hit various parts of the world due to the dry season and pollution of water resources. Nowadays, water quality issue has become a significant concern due to the growth of population, urban expansion and socio-economic development (Kumar et al., 2005).

Seawater intrusion into the surface water and ground water sources is a serious problem in coastal regions worldwide. Dala Township is located on the opposite side of Yangon downtown across Yangon River which runs from Yangon to the Gulf of Martaban of the Andaman Sea. The township has a total land area of 224 square kilometers and consists of 24 wards and 23 village tracts (including 54 villages). It has a population of 172,857 people living in 37,912 households. Ground water is not trusted as a source for drinking water due to the salt intrusion. Therefore, most of the people in this area rely on fresh water ponds for drinking water. When the rainwater collecting in ponds it dries out seasonally, local people have to use salty ground water or fresh water brought across from Yangon River. Nowadays, local residents obtain YCDC water distribution system but it is still insufficient (https//:www. mmtimes.com/ dala-residents).

This study is intended to assess the quality of water for drinking purposes in Dala Township using the Water Quality Index (WQI) method. WQI is the most effective method to monitor the surface as well as ground water pollution. It provides a single number that expresses the overall water quality based on the different parameters (Selvam et al., 2014). There are so many types of WQI methods. Some of the most commonly used methods to evaluate the WQI are Weight Arithmetic Water Quality Index (WAWQI), the Canadian Council of Ministers of the Environment Water Quality Index (CCMEWQI), Oregon Water Quality Index (OWQI) and Nemerow Pollution Index. In this study, the calculation of WQI was done using the Weight Arithmetic Water Quality Index (WAWQI) method.

[1] Assistant Lecturer, Department of Industrial Chemistry, West Yangon University
[2] Dr. Professor, Department of Water and Environment Studies, University of Yangon
[3] Dr. Professor and Head (Retd.), Department of Industrial Chemistry, Dagon University

Materials and Methods

Sampling

Ground water samples were collected from three tube wells in Kamakasit Quarter, Set Myay Quarter and Nyaung Gone Village, Dala Township, Yangon Region. Surface water samples were taken from ponds and Yangon River nearby Kamakasit Quarter, Set Myay Quarter and Nyaung Gone village, Dala Township, Yangon Region.

Tube well water samples were collected at a depth of 50 ft, 60 ft and 80 ft after 2 minutes of pumping to obtain the deep water as the test sample using (1 L) capacity with screwed cap polyethylene bottles previously cleaned with deionized water. Pond water samples were collected at a depth of 2 ft below the surface level to avoid surface debris using (1 L) capacity stainless steel sampling bottle previously cleaned with deionized water and transferred to the (1 L) capacity with screwed cap sterilized polyethylene bottle. River water samples were collected at a distance of about 20 ft from the riverbank and at a depth of 5 ft below the surface of the river using (1 L) capacity stainless steel sampling bottle previously cleaned with deionized water. Then it was readily transferred to the (1 L) capacity with screwed cap sterilized polyethylene bottle. After collection, each bottle was clearly marked the name and date of sampling. Then the collected sampling bottles were placed in an ice box with ice cubes to main the temperature at 4^{o}C and immediately transported to the laboratory (APHA 2005). Water samples were collected from September 2019 to March 2020 (during monsoon and post-monsoon seasons). The location map of sampling site is shown in Figure (1).

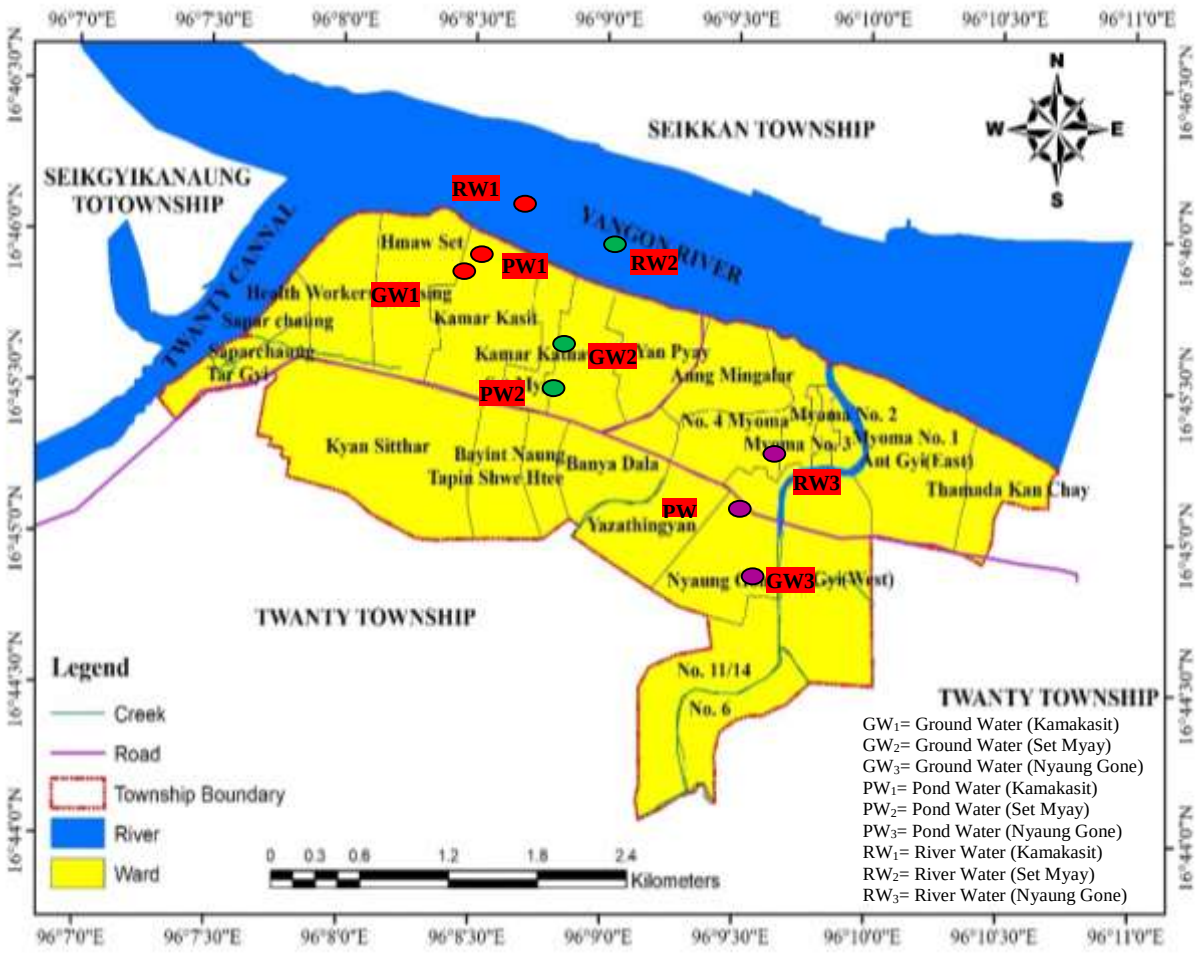

Figure 1 Location Map of Sample Collection Area

Analysis of Water Sample

For the assessment of water quality, ten important parameters were determined such as pH, total hardness, total dissolved solid (TDS), conductivity, chloride, nitrate, sulphate, calcium, dissolved oxygen (DO) and biological oxygen demand (BOD) and compared with the WHO Drinking Water Standard. Parameters were analyzed by using the LaMotte pH 5 Plus Meter (5-0035-01), LaMotte Con 6 Plus Conductivity Meter (5-0038-02), LaMotte TDS 6 Meter (5-0036-02), LaMotte Smart 3 Colorimeter (1910) and DO and BOD Meter (HANNA HI5421).

Assessment of Water Quality by WQI Method

WQI is an effective method to assess the quality and ensure the sustainable safe use of water for drinking purposes. It integrates several water quality parameters into a mathematical equation that rates the water quality with number (Yogendra & Puttaiah, 2008). In this study, ten important parameters were chosen for the calculation of WQI and has been calculated by using the recommended WHO Drinking Water Standard. The calculation of the WQI was done using Weighted Arithmetic Water Quality Index (WAWQI) method (Brown et al., 1972). WQI is in the following form:

$$WQI_{WA} = \sum W_i Q_i / \sum W_i$$

where W_i is the relative weight of i^{th} parameter and Q_i is the water quality rating scale of i^{th} parameter. The value of W_i and Q_i are calculated using the following equation:

$$W_i = k / S_i$$

$$k = 1/ \sum S_i$$

$$Q_i = 100 \left[(V_i - V_{id})/ (S_i - V_{id})\right]$$

where V_i is the observed value or measurable value of the i^{th} parameter, k is the proportionality constant, S_i is the standard permissible value of the i^{th} parameter and V_{id} is the ideal value of the i^{th} parameter in drinking water. In that case, all the ideal values V_{id} are taken as zero for drinking water except pH and DO. For pH, V_{id} is 7.0 and a standard maximum permissible value is 8.5 mg/L. Therefore, the quality rating scale for pH is calculated as follows:

$$Q_{ipH} = 100 \left\lfloor(V_{ipH} - 7.0) / (8.5 - 7.0)\right\rfloor$$

where V_{ipH} is the observed value of pH. For DO, V_{id} is 14.6 mg/L and the standard maximum permissible value for drinking water is 5 mg/L. Therefore, its quality rating scale is calculated as follows:

$$Q_{iDO} = 100 \left[(V_{iDO} - 14.6) / (5.0 - 14.6)\right]$$

where V_{iDO} is the observed value of dissolved oxygen. The WQI value can be categorized into five classes: ranking between 0 - 25 represents excellent water quality, ranking between 25 - 50 represents good water quality, ranking between 51 - 75 represents poor water quality, ranking between 76 - 100 represents very poor quality and above 100 represents water is excessively polluted and unsuitable for drinking.

Results and Discussion

In this study, the suitability of water quality for domestic purpose was assessed based on WQI values. The principal factor in calculating the WQI is the selection of water quality parameters. Parameters having low permissible limits are more harmful to the water quality because a slight increase affects these values to a great extent. In this investigation ten parameters

such as pH, total hardness, total dissolved solid, conductivity, chloride, nitrate, sulphate, calcium, DO and BOD were analysed.

Dala Township is located in the lower part of the Ayeyarwady delta region. Due to the proximity of the Andaman Sea (about 34 kilometers), the majority of the streams that flow in the lower delta are characterized by a high level of salinity. Firstly, Table (1) shows the characteristics of ground water samples. It could be seen that pH, nitrate and BOD values of ground water samples fall within the acceptable limit. Therefore, the ground water sources of the study area were microbially safe but total hardness, sulphate and calcium content do not fall within the standard limit. EC is directly related to the dissolved ions present in the water. TDS designates the general nature of water quality or salinity. Water containing above 500mg/L is regarded undesirable for domestic uses. Similarly, Chloride in excess of 100mg/L imparts a salty taste and concentration in excess of 100mg/L may cause physiological damage (River, 2011). Observed TDS, EC and chloride values of ground water samples ranged between 1805 - 3400 mg/L, 3610 - 6800 µS/cm and 1580 - 3110 mg/L respectively and significantly higher than the standard limit. It could be revealed that the ground water sources were severely intruded with salt. The vast amount of TDS, EC and chloride content were found in the tube well water of Kamasit Quarter (GW_1) because it is the nearest place to the Yangon Riverbank and located in the downstream area.

Table 1 Characteristics of Ground Water Samples

Sr No.	Parameters	GW_1	GW_2	GW_3	Standard Values*
1.	pH	6.9±0.21	6.72±0.92	7.1±0.14	6.5 - 8.5
2.	Total Hardness (mg/L)	372±45	305±58	288±21	200
3.	TDS(mg/L)	3400±62	1805±54	3140±46	500
4.	EC(µS/cm)	6800±71	3610±85	6280±73	1000
5.	Chloride(mg/L)	3110±65	1580±53	2780±44	250
6.	Nitrate(mg/L)	0.10±0.03	0.12±0.01	0.12±0.006	10
7.	Sulphate(mg/L)	404±31	256±23	391±17	200
8.	Calcium(mg/L)	80±7	106±12	98±10	75
9.	DO(mg/L)	3.4±0.1	3.7±0.13	3.2±0.05	>5
10.	BOD(mg/L)	1.38±0.039	1.32±0.03	1.41±0.09	<5

*W.H.O (2017), "Guideline for Drinking Water Quality." WHO/SDE/WSH/03.04/09/Rev

The quantity of total oxygen dissolved in a water body is expressed as dissolved oxygen (DO) and its concentration depend on physical, chemical and biological activities of the water body. Estimation of DO is essential in surface water pollution control. The total amount of oxygen required by aerobic microorganisms for complete degradation of organic wastes present in a water body is termed as biological oxygen demand (BOD). When BOD levels are elevated, DO levels decrease because of the oxygen that is available in the water is being consumed by the microorganisms (https://www.coursehero.com/file/37889371 /BOD forwebsite-1pdf/).

Table (2) shows the characteristics of surface water samples; pond water and river water sources. It could be observed that physico- chemical properties of pond water sources fall within the permissible limit but BOD levels slightly higher than the standard limit. The highest BOD level (6.59 mg/L) was found in the pond water sample of Nyaung Gone Village. River water sources are mostly contaminated with dissolved ions and organic matter due to the tidal effect and human activity. According to the results, the highest BOD level (7.3 mg/L) was found in the river water sample of Set Myay Quarter. Moreover, TDS, EC and chloride values of river water samples ranged between 899 - 1873 mg/L, 1797 - 3746 µS/cm and 428 - 902 mg/L respectively and

significantly higher than the standard limit. The present analysis revealed that DO level of the pond and river water fall within the acceptable limit but BOD levels slightly higher than the permissible limit. Therefore, it could be assumed that pond water and river water sources were slightly contaminated with organic matter and the direct consumption of this source is not safe for drinking purpose.

Table 2 Characteristics of Surface Water Samples

Sr No.	Parameters	PW_1	PW_2	PW_3	RW_1	RW_2	RW_3	Stand -ard Values*
1.	pH	6.79±1.1	6.97±0.9	6.82±1.3	7.2±0.1	7.1±0.04	7.2±0.12	6.5 - 8.5
2.	Total Hardness (mg/L)	54±7	49±8.9	57±8	121±29	188±31	130±15	200
3.	TDS(mg/L)	185±18	163±27	189±11	899±70	1281±41	1873±68	500
4.	EC(µS/cm)	370±22	326±17	378±14	1797±55	2562±67	3746±82	1000
5.	Chloride (mg/L)	25±5	21±3.6	32±2.4	470±47	428±75	902±88	250
6.	Nitrate (mg/L)	0.12±0.02	0.09±0.001	0.12±0.016	0.19±0.04	0.28±0.08	0.2±0.034	10
7.	Sulphate (mg/L)	0.04±0.013	0.08±0.003	0.09±0.006	7.2±4.3	6.5±2.01	9.6±3.5	200
8.	Calcium (mg/L)	17±1.01	21±1.82	25±0.15	64±6.3	89±8.7	69±5.9	75
9.	DO(mg/L)	6.17±2.6	6.28±3.1	5.97±2.8	6.63±3.5	6.58±2.1	6.78±3	>5
10.	BOD (mg/L)	6.25±2.2	6.4±3.43	6.59±3.1	7.02±3.5	7.3±2.1	6.8±3.7	<5

*W.H.O (2017), "Guideline for Drinking Water Quality." WHO/SDE/WSH/03.04/09/Rev

Tables (3), (4) and (5) show the calculated values of WQI for the ground water. The WQI value of ground water samples were found in the range of 51- 63. According to the WQI value, the ground water samples were found to be poor of category because they contain a high content of dissolved ions depending on the soil conditions of water passage.

Table 3 Calculation of Water Quality Index Value of Ground Water from Kamakasit Quarter (GW_1)

Sr No.	Parameters	Observed values (V_i)	Standard Values* (S_i)	Unit Weight(W_i)	Quality Rating Scale (Q_i)	$W_i Q_i$
1.	pH	6.9	6.5 - 8.5	0.181	- 6.67	-1.21
2.	Total Hardness(mg/L)	372	200	0.0077	186	1.43
3.	TDS(mg/L)	3400	500	0.0031	680	2.108
4.	EC(µS/cm)	6800	1000	0.00154	680	1.047
5.	Chloride(mg/L)	3110	250	0.0062	1244	7.713
6.	Nitrate(mg/L)	0.10	10	0.154	1.0	0.154
7.	Sulphate(mg/L)	404	200	0.0077	202	1.56
8.	Calcium(mg/L)	80	75	0.021	106.4	2.234
9.	DO(mg/L)	3.4	>5	0.308	116.7	35.9
10.	BOD(mg/L)	1.38	<5	0.308	27.6	8.5
				$\sum W_i = 1$		$\sum W_i Q_i$=59
$WQI = \sum W_i Q_i / \sum W_i$= 59						

*W.H.O (2017), "Guideline for Drinking Water Quality." WHO/SDE/WSH/03.04/09/Rev/

Table 4 Calculation of Water Quality Index Value of Ground Water from Set Myay Quarter (GW_2)

Sr No.	Parameters	Observed values (V_i)	Standard Values* (S_i)	Unit Weight(W_i)	Quality Rating Scale (Q_i)	$W_i Q_i$
1.	pH	6.72	6.5 - 8.5	0.181	-18.6	-3.37
2.	Total Hardness(mg/L)	305	200	0.0077	152.5	1.174
3.	TDS(mg/L)	1805	500	0.0031	361	1.119
4.	EC(µS/cm)	3610	1000	0.00154	361	0.556
5.	Chloride(mg/L)	1580	250	0.0062	632	3.918
6.	Nitrate(mg/L)	0.12	10	0.154	1.2	0.185
7.	Sulphate(mg/L)	256	200	0.0077	128	0.986
8.	Calcium(mg/L)	106	75	0.021	141.3	2.97
9.	DO(mg/L)	3.7	>5	0.308	114	35
10.	BOD(mg/L)	1.32	<5	0.308	26.4	8.13
				$\sum W_i = 1$		$\sum W_i Q_i$=51
$WQI = \sum W_i Q_i / \sum W_i$= 51						

*W.H.O (2017), "Guideline for Drinking Water Quality." WHO/SDE/WSH/03.04/09/Rev/

Table 5 Calculation of Water Quality Index Value of Ground Water from Nyaung Gone Village (GW_3)

Sr No.	Parameters	Observed values (V_i)	Standard Values* (S_i)	Unit Weight(W_i)	Quality Rating Scale (Q_i)	$W_i Q_i$
1.	pH	7.1	6.5 - 8.5	0.181	6.67	1.207
2.	Total Hardness (mg/L)	288	200	0.0077	144	1.108
3.	TDS (mg/L)	3140	500	0.0031	628	1.947
4.	EC(µS/cm)	6280	1000	0.00154	628	0.967
5.	Chloride (mg/L)	2780	250	0.0062	1112	6.894
6.	Nitrate(mg/L)	0.12	10	0.154	1.2	0.185
7.	Sulphate(mg/L)	391	200	0.0077	195.5	1.505
8.	Calcium(mg/L)	98	75	0.021	130.67	2.744
9.	DO(mg/L)	3.2	>5	0.308	118.75	36.58
10.	BOD(mg/L)	1.41	<5	0.308	28.2	8.69
				$\sum W_i = 1$		$\sum W_i Q_i$=63
$WQI = \sum W_i Q_i / \sum W_i$= 63						

*W.H.O (2017), "Guideline for Drinking Water Quality." WHO/SDE/WSH/03.04/09/Rev/

Tables (6), (7) and (8) show the calculated values of WQI for the pond water. The WQI value of pond water samples were found in the range of 64- 68. According to the WQI value, the pond water samples were also found to be poor of category because BOD level do not fall within the permissible limit. Although the dissolved ions content in pond water were low, the BOD level were higher than that of ground water and river water.

Table 6 Calculation of Water Quality Index Value of Pond Water from Kamakasit Quarter (PW_1)

Sr No.	Parameters	Observed values (V_i)	Standard Values* (S_i)	Unit Weight(W_i)	Quality Rating Scale (Q_i)	$W_i Q_i$
1.	pH	6.79	6.5 - 8.5	0.181	-14	-2.534
2.	Total Hardness(mg/L)	54	200	0.0077	27	0.21
3.	TDS(mg/L)	185	500	0.0031	37	0.1147
4.	EC(µS/cm)	370	1000	0.00154	37	0.057
5.	Chloride(mg/L)	25	250	0.0062	10	0.062
6.	Nitrate(mg/L)	0.12	10	0.154	1.2	0.185
7.	Sulphate(mg/L)	0.04	200	0.0077	0.02	0.00015
8.	Calcium(mg/L)	17	75	0.021	22.67	0.476
9.	DO(mg/L)	6.17	>5	0.308	87.8	27.042
10.	BOD(mg/L)	6.25	<5	0.308	125	38.5
				$\sum W_i = 1$		$\sum W_i Q_i$=64
$WQI = \sum W_i Q_i / \sum W_i$= 64						

*W.H.O (2017), "Guideline for Drinking Water Quality." WHO/SDE/WSH/03.04/09/Rev/

Table 7 Calculation of Water Quality Index Value of Pond Water from Set Myay Quarter (PW_2)

Sr No.	Parameters	Observed values (V_i)	Standard Values* (S_i)	Unit Weight (W_i)	Quality Rating Scale (Q_i)	$W_i Q_i$
1.	pH	6.97	6.5 - 8.5	0.181	-2	-0.36
2.	Total Hardness(mg/L)	49	200	0.0077	24.5	0.189
3.	TDS (mg/L)	163	500	0.0031	32.6	0.101
4.	EC(µS/cm)	326	1000	0.00154	32.6	0.050
5.	Chloride (mg/L)	21	250	0.0062	8.4	0.052
6.	Nitrate(mg/L)	0.09	10	0.154	0.9	0.139
7.	Sulphate(mg/L)	0.08	200	0.0077	0.04	0.0003
8.	Calcium(mg/L)	21	75	0.021	28	0.588
9.	DO(mg/L)	6.28	>5	0.308	86.7	26.7
10.	BOD(mg/L)	6.4	<5	0.308	128	39.4
				$\sum W_i = 1$		$\sum W_i Q_i$=67
$WQI = \sum W_i Q_i / \sum W_i$= 67						

*W.H.O (2017), "Guideline for Drinking Water Quality." WHO/SDE/WSH/03.04/09/Rev/

Table 8 Calculation of Water Quality Index Value of Pond Water from Nyaung Gone Village (PW_3)

Sr No.	Parameters	Observed values (V_i)	Standard Values* (S_i)	Unit Weight(W_i)	Quality Rating Scale (Q_i)	$W_i Q_i$
1.	pH	6.82	6.5 - 8.5	0.181	-12	-2.172
2.	Total Hardness(mg/L)	57	200	0.0077	28.5	0.22
3.	TDS (mg/L)	189	500	0.0031	37.8	0.117
4.	EC(µS/cm)	378	1000	0.00154	37.8	0.058
5.	Chloride (mg/L)	32	250	0.0062	12.8	0.079
6.	Nitrate(mg/L)	0.12	10	0.154	1.2	0.185
7.	Sulphate(mg/L)	0.09	200	0.0077	0.045	0.0003
8.	Calcium(mg/L)	25	75	0.021	33.33	0.699
9.	DO(mg/L)	5.97	>5	0.308	89.9	27.7
10.	BOD(mg/L)	6.59	<5	0.308	132	41
				$\sum W_i = 1$		$\sum W_i Q_i$=68
$WQI = \sum W_i Q_i / \sum W_i$= 68						

*W.H.O (2017), "Guideline for Drinking Water Quality." WHO/SDE/WSH/03.04/09/Rev/

Tables (9), (10) and (11) show the calculated values of WQI for the river water. The WQI value of river water samples were found in the range of 76 - 78. According to the WQI value, the river water samples were found to be very poor of category because they were also contaminated with dissolved solids and BOD level were higher than the acceptable limit. It indicated that river water sources were contaminated with dissolved ions and organic matter. Therefore, it is unsuitable for direct consumption.

Table 9 Calculation of Water Quality Index Value of River Water from Kamakasit Quarter (RW_1)

Sr No.	Parameters	Observed values (V_i)	Standard Values* (S_i)	Unit Weight (W_i)	Quality Rating Scale (Q_i)	$W_i Q_i$
1.	pH	7.2	6.5 - 8.5	0.181	13.3	2.41
2.	Total Hardness(mg/L)	121	200	0.0077	60.5	0.47
3.	TDS (mg/L)	899	500	0.0031	179.8	0.56
4.	EC(µS/cm)	1797	1000	0.00154	179.8	0.277
5.	Chloride (mg/L)	470	250	0.0062	188	1.166
6.	Nitrate(mg/L)	0.19	10	0.154	1.9	0.29
7.	Sulphate(mg/L)	7.2	200	0.0077	3.6	0.028
8.	Calcium(mg/L)	64	75	0.021	85.3	1.791
9.	DO(mg/L)	6.63	>5	0.308	83	25.6
10.	BOD(mg/L)	7.02	<5	0.308	140	43
				$\sum W_i = 1$		$\sum W_i Q_i$=76
$WQI = \sum W_i Q_i / \sum W_i$= 76						

*W.H.O (2017), "Guideline for Drinking Water Quality." WHO/SDE/WSH/03.04/09/Rev/

Table 10 Calculation of Water Quality Index Value of River Water from Set Myay Quarter (RW_2)

Sr No.	Parameters	Observed values (V_i)	Standard Values* (S_i)	Unit Weight (W_i)	Quality Rating Scale (Q_i)	$W_i Q_i$
1.	pH	7.1	6.5 - 8.5	0.181	6.67	1.207
2.	Total Hardness(mg/L)	188	200	0.0077	94	0.72
3.	TDS (mg/L)	1281	500	0.0031	256	0.794
4.	EC(µS/cm)	2562	1000	0.00154	256	0.395
5.	Chloride (mg/L)	428	250	0.0062	171.2	1.061
6.	Nitrate(mg/L)	0.28	10	0.154	2.9	0.45
7.	Sulphate(mg/L)	6.5	200	0.0077	3.25	0.025
8.	Calcium(mg/L)	89	75	0.021	118.67	2.492
9.	DO(mg/L)	6.58	>5	0.308	84	26
10.	BOD(mg/L)	7.3	<5	0.308	146	45
				$\sum W_i = 1$		$\sum W_i Q_i$=78
$WQI = \sum W_i Q_i / \sum W_i$= 78						

*W.H.O (2017), "Guideline for Drinking Water Quality." WHO/SDE/WSH/03.04/09/Rev/

Table 11 Calculation of Water Quality Index Value of River Water from Nyaung Gone Village (RW_3)

Sr No.	Parameters	Observed values (V_i)	Standard Values* (S_i)	Unit Weight (W_i)	Quality Rating Scale (Q_i)	$W_i Q_i$
1.	pH	7.2	6.5 - 8.5	0.181	13.33	2.413
2.	Total Hardness(mg/L)	130	200	0.0077	65	0.5
3.	TDS(mg/L)	1873	500	0.0031	374.6	1.161
4.	EC(µS/cm)	3746	1000	0.00154	374.6	0.577
5.	Chloride(mg/L)	902	250	0.0062	360.8	2.237
6.	Nitrate(mg/L)	0.2	10	0.154	2	0.308
7.	Sulphate(mg/L)	9.6	200	0.0077	4.8	0.037
8.	Calcium(mg/L)	69	75	0.021	92	1.932
9.	DO(mg/L)	6.78	>5	0.308	81.5	25
10.	BOD(mg/L)	6.8	<5	0.308	136	42
				$\sum W_i = 1$		$\sum W_i Q_i$=76
$WQI = \sum W_i Q_i / \sum W_i$= 76						

*W.H.O (2017), "Guideline for Drinking Water Quality." WHO/SDE/WSH/03.04/09/Rev/

A comparative analysis for all the water samples are shown in Figure (2). As a result, all the WQI values of water samples fall within the poor and very poor categories. Therefore, the effective water treatment method for the study area was needed for domestic purposes. For reducing the dissolved ions level, the water will be treated with ion exchange method, lime soda softening method, capacitive deionization method and reverse osmosis membrane can be used. The BOD level can be reduced by using the chemicals, advanced oxidation process and membrane bioreactor can be used.

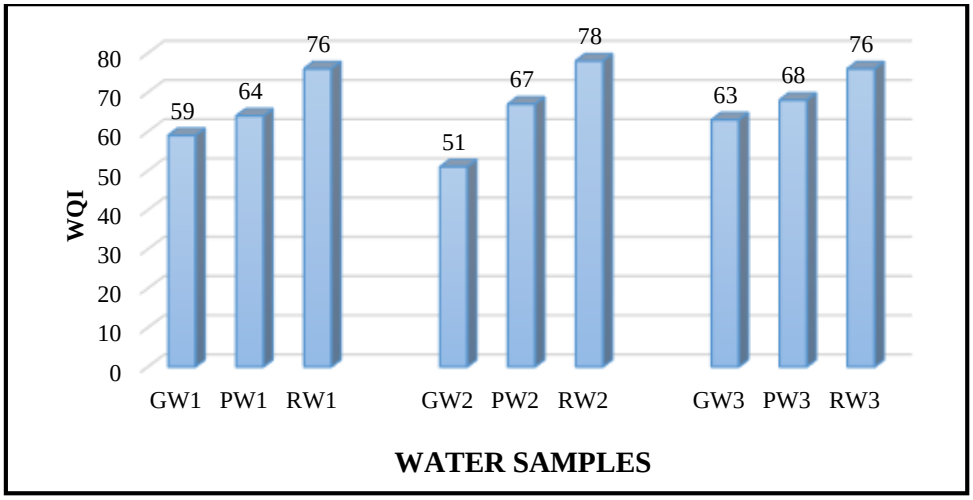

Figure 2 Water Quality Index of Water Samples

Conclusion

Improvement of water supply structures and water treatment system are possible solutions to improve the quality of drinking water. In Dala Township, the ground water sources were mostly contaminated with dissolved solids and considerably higher than the acceptable range of WHO Drinking Water Standard. The BOD level of pond water sources slightly higher than the standard value but the other remaining parameters fall within the acceptable limit. Moreover, the river water sources were also contaminated with dissolved solids and BOD level were higher than the acceptable limit. Based on the observed WQI value, it can be concluded that the overall water quality of Dala Township was impair and the effective water treatment systems are required to develop for the community residents of this area.

Acknowledgement

We would like to express our deep appreciation to the Myanmar Academy of Arts and Science for giving us the permission to submit this article.

References

APHA, (2005). Standard Methods for Examination of Water and Wastewater, 20th edition, Washington, DC.

Brown, R. M., McClelland, N. I., Deininger, R. A., & O'Connor, M. F. (1972). A water quality index—crashing the psychological barrier. In *Indicators of environmental quality* (pp. 173–182). Springer.

EPA, (2009). Environmental impact and benefits assessment for final effluent guidelines and standards for the construction and development category. Office of Water, Washington, DC. EPA-821-R-09-012.

Kumar, R., Singh, R. D., & Sharma, K. D. (2005). Water resources of India. *Current Science*, 794–811.

River, U. (2011). Seasonal Assessment of Physico—Chemical Concentration of Polluted Urban River: A Case of Ala River in Southwestern—Nigeria. *Research Journal of Environmental Sciences*, *5*(1), 22–35.

Selvam, S., Manimaran, G., Sivasubramanian, P., Balasubramanian, N., & Seshunarayana, T. (2014). GIS-based evaluation of water quality index of groundwater resources around Tuticorin coastal city, South India. *Environmental Earth Sciences*, *71*(6), 2847–2867.

W.H.O (2017), Guideline for Drinking Water Quality. WHO/SDE/WSH/03.04/09/Rev/1.

Yogendra, K., & Puttaiah, E. T. (2008). Determination of water quality index and suitability of an urban waterbody in Shimoga Town, Karnataka. *Proceedings of Taal2007: The 12th World Lake Conference*, *342*, 346.

https//:www. mmtimes.com/ dala-residents

https://www.coursehero.com/file/37889371/BODforwebsite-1pdf/